A continent-wide hunt for critical minerals p. 883

Summer reading for scientists of every stripe p. 888

3D-printed glass chills out pp. 895 & 960

Science

$15
2 JUNE 2023
SPECIAL ISSUE
science.org
AAAS



PRIMATE GENOMES

PRIMATE GENOMES

RESEARCH ARTICLES

A global catalog of whole-genome diversity from 233 primate species p. 906

Phylogenomic analyses provide insights into primate evolution p. 913

Pervasive incomplete lineage sorting illuminates speciation and selection in primates p. 925

Hybrid origin of a primate, the gray snub-nosed monkey p. 926

Adaptations to a cold climate promoted social evolution in Asian colobine primates p. 927

Genome-wide coancestry reveals details of ancient and recent male-driven reticulation in baboons p. 928

The landscape of tolerated genetic variation in humans and primates p. 929

Rare penetrant mutations confer severe risk of common diseases p. 930

RELATED ITEMS

NEWS STORY p. 881

SCIENCE ADVANCES RESEARCH ARTICLE BY ZHANG *ET AL*. 10.1126/SCIADV.ADD3580

SCIENCE ADVANCES RESEARCH ARTICLE BY BI *ET AL*. 10.1126/SCIADV.ADC9507

By **Sacha Vignieri**

Humans are primates. If we weren't able to do things like write poetry and drive cars, we would likely be classified as another species of great ape, along with our closest cousins—chimpanzees, bonobos, gorillas, and orangutans. Thus, understanding the genomes, evolutionary history, sociality, and, some might argue, even ecology of modern primates greatly informs our understanding of ourselves.

Species in the order Primates include not only humans and our closest relatives but also species that occupy a wide array of habitats, from savanna to tropical forest and even to mountainous areas, where snow is a regular occurrence. In this special issue, the sequencing of more than 230 primate genomes, globally, reveals patterns of speciation across the entire order as well as the contributions of hybridization to diversification and how adaptations to cold have contributed to the evolution of social structure. In addition, the genomes are used to characterize rare mutations associated with disease risk in humans.

Primates not only have a past that helps us understand ourselves but also an uncertain future—more than 60% are threatened with extinction. The knowledge gained through this first, large effort to characterize their genomes will, hopefully, also lead to an increased understanding of how to conserve the other members of our own order.

10.1126/science.adi8248

A male olive baboon (*Papio anubis*) peers curiously into the camera.

PHOTO: ANUP SHAH/NPL/MINDEN PICTURES



RESEARCH ARTICLE

PRIMATE GENOMES

A global catalog of whole-genome diversity from 233 primate species

Lukas F. K. Kuderna[1,2]*†, Hong Gao[2], Mareike C. Janiak[3], Martin Kuhlwilm[1,4,5], Joseph D. Orkin[1,6], Thomas Bataillon[7], Shivakumara Manu[8,9], Alejandro Valenzuela[1], Juraj Bergman[7,10], Marjolaine Rousselle[7], Felipe Ennes Silva[11,12], Lidia Agueda[13], Julie Blanc[13], Marta Gut[13], Dorien de Vries[3], Ian Goodhead[3], R. Alan Harris[14], Muthuswamy Raveendran[14], Axel Jensen[15], Idrissa S. Chuma[16], Julie E. Horvath[17,18,19,20,21], Christina Hvilsom[22], David Juan[1], Peter Frandsen[22], Joshua G. Schraiber[2], Fabiano R. de Melo[23], Fabrício Bertuol[24], Hazel Byrne[25], Iracilda Sampaio[26], Izeni Farias[24], João Valsecchi[27,28,29], Malu Messias[30], Maria N. F. da Silva[31], Mihir Trivedi[9], Rogerio Rossi[32], Tomas Hrbek[24,33], Nicole Andriaholinirina[34], Clément J. Rabarivola[34], Alphonse Zaramody[34], Clifford J. Jolly[35], Jane Phillips-Conroy[36], Gregory Wilkerson[37], Christian Abee[37], Joe H. Simmons[37], Eduardo Fernandez-Duque[38], Sree Kanthaswamy[39], Fekadu Shiferaw[40], Dongdong Wu[41], Long Zhou[42], Yong Shao[41], Guojie Zhang[43,42,44,45,46], Julius D. Keyyu[47], Sascha Knauf[48], Minh D. Le[49], Esther Lizano[1,50], Stefan Merker[51], Arcadi Navarro[1,52,53,54], Tilo Nadler[55], Chiea Chuen Khor[56], Jessica Lee[57], Patrick Tan[58,59,56], Weng Khong Lim[59,58,60], Andrew C. Kitchener[61], Dietmar Zinner[62,63,64], Ivo Gut[13], Amanda D. Melin[65,66,67], Katerina Guschanski[68,15], Mikkel Heide Schierup[7], Robin M. D. Beck[3], Govindhaswamy Umapathy[8,9], Christian Roos[69], Jean P. Boubli[3], Jeffrey Rogers[14]*, Kyle Kai-How Farh[2]*, Tomas Marques Bonet[1,50,13,52]*

The rich diversity of morphology and behavior displayed across primate species provides an informative context in which to study the impact of genomic diversity on fundamental biological processes. Analysis of that diversity provides insight into long-standing questions in evolutionary and conservation biology and is urgent given severe threats these species are facing. Here, we present high-coverage whole-genome data from 233 primate species representing 86% of genera and all 16 families. This dataset was used, together with fossil calibration, to create a nuclear DNA phylogeny and to reassess evolutionary divergence times among primate clades. We found within-species genetic diversity across families and geographic regions to be associated with climate and sociality, but not with extinction risk. Furthermore, mutation rates differ across species, potentially influenced by effective population sizes. Lastly, we identified extensive recurrence of missense mutations previously thought to be human specific. This study will open a wide range of research avenues for future primate genomic research.

The order Primates includes over 500 recognized species that display an array of morphological, physiological, and behavioral adaptations (*1*). Spanning a broad range of social systems, locomotory styles, dietary specializations, and habitat preferences, these species rightly attract attention from scientists with equally diverse research interests. Because humans are members of the order Primates, we also find many important and informative biological parallels between ourselves and other primates. The analysis of nonhuman primate genomes has long been motivated by a desire to understand human evolutionary origins, human health, and disease. However, past comparative genomic analyses have mainly focused on a relatively small number of species (*2*, *3*), thus providing a limited understanding of genome variability in only a few key lineages, such as members of the great apes (*4*–*10*) or macaques (*11*–*13*). Furthermore, low numbers of wild-born individuals in these studies potentially result in assessments of diversity that may not reflect natural populations (*3*). To gain a more complete picture of how evolution has shaped genomic variation across primates, large-scale sequencing of many species and individuals is necessary, especially within previously neglected lineages such as strepsirrhines (lemurs, lorises, galagos, and relatives) and platyrrhines (monkeys of the Americas). The need for a more complete understanding of primate genetic diversity in the wild, and its determinants, is urgent given the current extinction crisis driven by climate change, habitat loss, and illegal trading and hunting (*14*). At present, 60% of the world's primate species are threatened with extinction, and current trends are likely to exacerbate the rates of biodiversity loss in the near future (*14*, *15*). The analysis of whole-genome sequences allows estimation of genetic diversity and evaluation of its association with ecological traits, degrees of inbreeding, and phylogenetic relationships, all metrics relevant to primate conservation genomics.

High-coverage genome sequences of 233 primate species

We sequenced the genomes of 703 individuals from 211 primate species on the Illumina NovaSeq 6000 platform (*16*). For 78% of individuals, the available amount of DNA permitted us to generate polymerase chain reaction–free libraries. We sequenced paired-end reads of 151 base pairs (bp) to an average production target of at least 100 gigabases (Gb), resulting in an average mapped coverage of 32.4× per individual (15.3 to 77.6×) (*16*). We expanded our dataset by including 106 individuals representing 29 species from previously published studies to maximize phylogenetic diversity (*8*, *17*–*24*). Altogether, we compiled data from 809 individuals from 233 primate species, amounting to 47% of the 521 currently recognized species (*14*). Our sampling covers 86% of primate genera (69), and all 16 families. More than 72% of individuals in this study are wild-born. Furthermore, 58% of species in our dataset are classified as threatened with extinction by the International Union for Conservation of Nature (IUCN) [i.e., classified in the categories vulnerable (VU), endangered (EN), and critically endangered (CR)], and 30 species are critically endangered. It is worth noting that among the species we sampled are some of the world's most endangered primates, which face an extremely high risk of extinction in the wild. Examples include the Western black crested gibbon (*Nomascus concolor*), with an estimated 1500 individuals left in the wild and scattered across an array of discontinuous habitats, and the northern sportive lemur (*Lepilemur septentrionalis*), with roughly 40 individuals estimated to remain in the wild, inhabiting an area potentially as small as 12 km^2 (*25*, *26*).

For 100 species, we generated sequencing data from more than one individual, and for 36 species from five or more individuals, 29 of which belong to newly sequenced species. We thus gathered broad primate taxonomic coverage by compiling species from all major geographic regions currently inhabited by primates, including the Americas, mainland Africa, Madagascar, and Asia (Fig. 1A). The data presented here provide the foundation for several additional studies in this issue, informing important and diverse topics including hybrid speciation and reticulation among primates (*27*) and predicting the landscape of tolerated mutations in the human genome (*28*).

Owing to technical challenges inherent to short-read assembly, we aligned our data to a backbone of 32 reference genomes for further analyses, most of which are derived from long-read sequencing technologies (*16*). These references are well distributed across the primate phylogeny and result in a median pairwise distance between the focal and reference species of 6.6×10^{-3} substitutions per site (0 to 4.1×10^{-2}), which is within the range of previous projects using a similar approach (*8*). To ensure our estimates of genetic diversity over these phylogenetic distances are minimally

biased, we compared pairs of diversity estimates in which reads from one species were mapped to its own reference as well as mapped to another species reference. Across 19 species pairs that fully cover the phylogenetic distances between focal species and reference in our data, we find heterozygosity estimates to be highly correlated (Pearson's $r = 0.97$, $p = 6.8 \times 10^{-12}$). Overall, we find a median value of 2.4 Gb per individual to be callable across all references, thus enabling genome-wide comparisons.

Genetic diversity across primates

Heterozygosity in primates spans over an order of magnitude, with values ranging from 0.41×10^{-3} heterozygotes per base pair (het × bp^{-1}) to 7.14×10^{-3} het × bp^{-1} (Fig. 1C). We observe the lowest levels of diversity in the golden snub-nosed monkey (*Rhinopithecus roxellana*) at about one heterozygous position every 2400 bp. Only 15 species have a lower median genetic diversity than humans, the primate with by far the largest census size. Among these are several Asian colobines, but also the aye-aye, the western hoolock gibbon, and the Guinea baboon. There are marked differences in genetic diversity across genera, families, and geographic regions, with high-diversity species found among cercopithecines from mainland Africa and lemurs in Madagascar (Fig. 1B). Among cercopithecines, guenons of the genus *Cercopithecus* are almost exclusively responsible for high diversity with a median value of 4.54×10^{-3} het × bp^{-1}, more than double the primate-wide median. Some members of this tribe also show large historical effective population sizes, and there are several known instances of past and present interspecific hybridization (*29*–*32*). We further observe high diversity across several genera of lemurs, which are among the most endangered primates, primarily owing to rapid habitat loss and severe population decline. Examples include members of the true lemurs (*Eulemur* spp.), bamboo lemurs (*Hapalemur* spp.), and sifakas (*Propithecus* spp.).

We investigated whether genetic diversity estimates are correlated with extinction risk in primates, a subject of previous debate (*17*, *33*, *34*). Despite our broad sampling, we find no global relationship between numerically coded IUCN extinction risk categories and estimated heterozygosity [$p > 0.05$, phylogenetic generalized least squares (PGLS)] (Fig. 2A) (*16*). Because genetic diversity is strongly determined by long-term demographic history, rapid recent population declines such as those currently experienced by many primate species are unlikely to be detected in a cross-species comparison. Instead, temporal datasets within the same species are better suited to quantify recent changes in genetic diversity (*35*). Nevertheless, comparing genetic diversity for non-threatened [least concern (LC), near-threatened (NT)] and threatened (VU, EN, CR) species within the same family consistently uncovers lower diversity among species in the threatened categories for all families with more than one species in both categories, although not all comparisons reach statistical significance ($p < 0.05$, Mann–Whitney U test) (Fig. 2B). The only exception is Lorisidae, which showed no difference in genetic diversity between non-threatened and threatened species.

To further assess the potential impact of recent population decline, we analyzed runs of homozygosity (RoH) across species. We focused on tracts with a minimum length of one megabase (Mb), which in humans indicate recent inbreeding (*8*). The order-wide median fraction of the genome in RoH is 5.1%, and individual values vary substantially, reaching over 50%. We find critically endangered species, such as the white-headed langur (*Trachypithecus leucocephalus*), the eastern gorilla (*Gorilla beringei*), and mongoose lemur (*Eulemur mongoz*), among the species with the highest proportion of RoHs (Fig. 2C). However, some species not currently classified as threatened, such as Azara's owl monkey (*Aotus azarae*) and the northern greater galago (*Otolemur garnettii*), also have a high fraction of the genome in RoHs. Although the overall conservation status of these two species might not be worrisome, some individuals may belong to smaller local populations, which can exacerbate inbreeding. We find 13 critically endangered species with lower than the primate-wide average fractions of their genomes in RoHs, among them the three douc langur species (*Pygathrix*

[1]IBE, Institute of Evolutionary Biology (UPF-CSIC), Department of Medicine and Life Sciences, Universitat Pompeu Fabra. PRBB, C. Doctor Aiguader N88, 08003 Barcelona, Spain. [2]Illumina Artificial Intelligence Laboratory, Illumina Inc.; Foster City, CA 94404, USA. [3]School of Science, Engineering & Environment, University of Salford, Salford M5 4WT, UK. [4]Department of Evolutionary Anthropology, University of Vienna, Djerassiplatz 1, 1030 Vienna, Austria. [5]Human Evolution and Archaeological Sciences (HEAS), University of Vienna, Austria. [6]Département d'anthropologie, Université de Montréal, 3150 Jean-Brillant, Montréal, QC H3T 1N8, Canada. [7]Bioinformatics Research Centre, Aarhus University, Aarhus, Denmark. [8]Academy of Scientific and Innovative Research (AcSIR), Ghaziabad 201002, India. [9]Laboratory for the Conservation of Endangered Species, CSIR-Centre for Cellular and Molecular Biology, Hyderabad 500007, India. [10]Section for Ecoinformatics and Biodiversity, Department of Biology, Aarhus University, Aarhus, Denmark. [11]Research Group on Primate Biology and Conservation, Mamirauá Institute for Sustainable Development, Estrada da Bexiga 2584, CEP 69553-225, Tefé, Amazonas, Brazil. [12]Evolutionary Biology and Ecology (EBE), Département de Biologie des Organismes, Université libre de Bruxelles (ULB), Av. Franklin D. Roosevelt 50, CP 160/12, B-1050 Brussels Belgium. [13]CNAG-CRG, Centre for Genomic Regulation (CRG), Barcelona Institute of Science and Technology (BIST), Baldiri I Reixac 4, 08028 Barcelona, Spain. [14]Human Genome Sequencing Center and Department of Molecular and Human Genetics, Baylor College of Medicine, Houston, TX 77030, USA. [15]Department of Ecology and Genetics, Animal Ecology, Uppsala University, SE-75236 Uppsala, Sweden. [16]Tanzania National Parks, Arusha, Tanzania. [17]North Carolina Museum of Natural Sciences, Raleigh, NC 27601, USA. [18]Department of Biological and Biomedical Sciences, North Carolina Central University, Durham, NC 27707, USA. [19]Department of Biological Sciences, North Carolina State University, Raleigh, NC 27695, USA. [20]Department of Evolutionary Anthropology, Duke University, Durham, NC 27708, USA. [21]Renaissance Computing Institute, University of North Carolina at Chapel Hill, Chapel Hill, NC 27599, USA. [22]Copenhagen Zoo, 2000 Frederiksberg, Denmark. [23]Universidade Federal de Viçosa, Viçosa, Brazil. [24]Universidade Federal do Amazonas, Departamento de Genética, Laboratório de Evolução e Genética Animal (LEGAL), Manaus, Amazonas 69080-900, Brazil. [25]Department of Anthropology, University of Utah, Salt Lake City. UT 84102, USA. [26]Universidade Federal do Para, Bragança, Para, Brazil. [27]Research Group on Terrestrial Vertebrate Ecology, Mamirauá Institute for Sustainable Development, Tefé, Amazonas, Brazil. [28]Rede de Pesquisa para Estudos sobre Diversidade, Conservação e Uso da Fauna na Amazônia – RedeFauna, Manaus, Amazonas, Brazil [29]Comunidad de Manejo de Fauna Silvestre en la Amazonía y en Latinoamérica – ComFauna, Iquitos, Loreto, Peru. [30]Universidade Federal de Rondônia, Porto Velho, Rondônia, Brazil. [31]Instituto Nacional de Pesquisas da Amazônia, Manaus, AM, Brazil. [32]Instituto de Biociências, Universidade Federal do Mato Grosso, Cuiabá, MT, Brazil. [33]Department of Biology, Trinity University, San Antonio, TX 78212, USA. [34]Life Sciences and Environment, Technology and Environment of Mahajanga, University of Mahajanga, Mahajanga, Madagascar. [35]Department of Anthropology, New York University, New York, NY 10003, USA. [36]Department of Neuroscience, Washington University School of Medicine in St. Louis, St. Louis, MO 63110, USA. [37]Keeling Center for Comparative Medicine and Research, MD Anderson Cancer Center, Bastrop TX 78602, USA. [38]Department of Anthropology, Yale University, New Haven, CT 06511, USA. [39]School of Mathematical and Natural Sciences, Arizona State University, Phoenix, AZ 85004, USA. [40]Guinea Worm Eradication Program, The Carter Center Ethiopia, Addis Ababa, Ethiopia. [41]State Key Laboratory of Genetic Resources and Evolution, Kunming Institute of Zoology, Chinese Academy of Sciences, Kunming, Yunnan 650223, China. [42]Center for Evolutionary and Organismal Biology, Zhejiang University School of Medicine, Hangzhou 310058, China. [43]Villum Centre for Biodiversity Genomics, Section for Ecology and Evolution, Department of Biology, University of Copenhagen, DK-2100 Copenhagen, Denmark. [44]State Key Laboratory of Genetic Resources and Evolution, Kunming Institute of Zoology, Chinese Academy of Sciences, Kunming, Yunnan 650223, China. [45]Liangzhu Laboratory, Zhejiang University Medical Center, 1369 West Wenyi Road, Hangzhou 311121, China. [46]Women's Hospital, School of Medicine, Zhejiang University, 1 Xueshi Road, Shangcheng District, Hangzhou 310006, China. [47]Tanzania Wildlife Research Institute (TAWIRI), Head Office, P.O. Box 661, Arusha, Tanzania. [48]Institute of International Animal Health/One Health, Friedrich-Loeffler-Institut, Federal Research Institute for Animal Health, 17493 Greifswald–Insel Riems, Germany. [49]Department of Environmental Ecology, Faculty of Environmental Sciences, University of Science and Central Institute for Natural Resources and Environmental Studies, Vietnam National University, Hanoi, Vietnam. [50]Institut Català de Paleontologia Miquel Crusafont, Universitat Autònoma de Barcelona, Barcelona, Spain. [51]Department of Zoology, State Museum of Natural History Stuttgart, Stuttgart, Germany. [52]Institució Catalana de Recerca i Estudis Avançats (ICREA) and Universitat Pompeu Fabra. Pg. Luís Companys 23, 08010 Barcelona, Spain. [53]Centre for Genomic Regulation (CRG), The Barcelona Institute of Science and Technology, Av. Doctor Aiguader, N88, 08003 Barcelona, Spain. [54]BarcelonaBeta Brain Research Center, Pasqual Maragall Foundation, C. Wellington 30, 08005 Barcelona, Spain. [55]Cuc Phuong Commune, Nho Quan District, Ninh Binh Province, Vietnam. [56]Genome Institute of Singapore, Agency for Science, Technology and Research, Singapore. [57]Mandai Nature, 80 Mandai Lake Road, Singapore. [58]SingHealth Duke-NUS Institute of Precision Medicine (PRISM), Singapore. [59]Cancer and Stem Cell Biology Program, Duke-NUS Medical School, Singapore [60]SingHealth Duke-NUS Genomic Medicine Centre, Singapore. [61]Department of Natural Sciences, National Museums Scotland, Chambers Street, Edinburgh EH1 1JF, UK, and School of Geosciences, Drummond Street, Edinburgh EH8 9XP, UK. [62]Cognitive Ethology Laboratory, Germany Primate Center, Leibniz Institute for Primate Research, 37077 Göttingen, Germany. [63]Department of Primate Cognition, Georg-August-Universität Göttingen, 37077 Göttingen, Germany. [64]Leibniz ScienceCampus Primate Cognition, 37077 Göttingen, Germany. [65]Department of Anthropology and Archaeology, University of Calgary, 2500 University Dr NW, Calgary, AB T2N 1N4, Canada. [66]Department of Medical Genetics, University of Calgary, 3330 Hospital Drive NW, HMRB 202, Calgary, AB T2N 4N1, Canada. [67]Alberta Children's Hospital Research Institute, University of Calgary, 3330 Hospital Drive NW, HMRB 202, Calgary, AB T2N 4N1, Canada. [68]Institute of Ecology and Evolution, School of Biological Sciences, University of Edinburgh, Edinburgh, UK. [69]Gene Bank of Primates and Primate Genetics Laboratory, German Primate Center, Leibniz Institute for Primate Research, Kellnerweg 4, 37077 Göttingen, Germany.
***Corresponding author. Email: lkuderna@illumina.com (L.F.K.K.); jr13@bcm.edu (J.R.); kfarh@illumina.com (K.K.-H.F.); tomas.marques@upf.edu (T.M.B.)**
†Present address: Illumina Artificial Intelligence Laboratory, Illumina Inc., Foster City, CA 94404, USA.

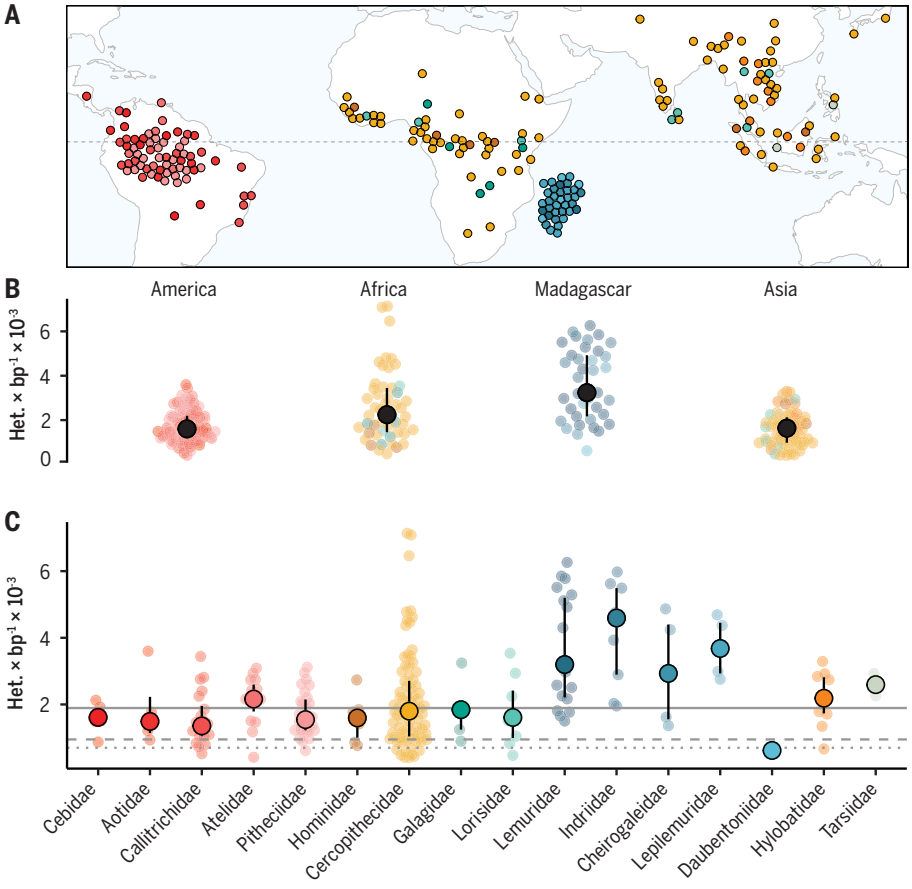


Fig. 1. Genetic diversity in primates across geographic regions and families. (**A**) Sampling range of species analyzed in this project. Each point represents the approximate species range centroid of all sampled species with available ranges. Points are repelled to avoid overplotting. (**B**) Heterozygosity stratified by geographic region. Solid black circles and whiskers represent median values and interquartile range. (**C**) Median species heterozygosity by family. Solid circles and whiskers represent median and interquartile range. Solid gray line denotes primate-wide median heterozygosity; dashed and dotted lines denote human heterozygosity for African and bottlenecked out-of-Africa populations, respectively. Points are colored according to the family a species belongs to, as denoted on the *x* axis of (C).

cinerea, *P. nemaeus*, *P. nigripes*), red-tailed sportive lemur (*Lepilemur ruficaudatus*), and Verreaux's sifaka (*Propithecus verreauxi*). We find no overall relationship between extinction risk and degree of inbreeding deduced from the total fraction of the genome in RoHs (Pearson's $r = 0.03$, $p = 0.71$). This implies that RoHs are not a good predictor of extinction risk in primates and suggests that many critically endangered species are threatened by nongenetic factors, likely reflecting population declines that have been too fast to be detectable on the genomic level. Given the potential importance of functional variation to conservation efforts, we sought to quantify the proportion of loss of functional variation in each lineage (*34*, *36*). To this end, we quantified stop-gain and missense mutations and normalized them by the number of synonymous mutations to account for lineage-specific differences in evolutionary rates. We found inverse relationships between the missense/synonymous ratios (Pearson's $r = -0.35$, $p = 9.3 \times 10^{-8}$) and, to a lesser extent, stop-gain/synonymous ratios and heterozygosity across primates, suggesting effects of purifying selection on deleterious variation, although the latter does not reach statistical significance (Pearson's $r = -0.12$, $p = 0.082$). We do not find deleterious variations as measured by the stop-gain/synonymous ratio to be correlated with extinction risk (Pearson's $r < 0.01$, $p = 0.94$). Nevertheless, we caution that the varying quality of the references and their annotations, together with potential changes in gene structure between the references and analyzed species, might add noise to the comparisons across our references.

A time-calibrated nuclear phylogeny of primates

We generated a genome-wide nuclear phylogeny of ultraconserved elements (UCEs) and 500 bp of their flanking regions, a widely used marker that enables easy detection of sequence orthologs across species (*37*). To this end, we identified the location of ~3500 UCE probes across all primate genomes and generated individual gene trees for each locus using a maximum-likelihood approach (*38*–*40*). We used the resulting trees as input for a coalescent analysis to obtain the topology of the species tree, which has strong support at most nodes and recovers all currently recognized primate families, tribes, and genera as monophyletic (*41*–*44*). We used a newly established set of 27 well-justified fossil calibration points to constrain the timing of key phylogenetic divergences among different lineages (*45*). We estimate the split between Haplorhini and Strepsirrhini to have happened between 63.3 and 58.3 million years (Ma) ago, and thus the radiation of crown Primates is entirely within the Paleocene. We find the deepest divergence within tarsiers to be notably recent at 15.2 to 9.5 Ma, which, together with fossil evidence, implies considerable extinction along the long branch leading to extant tarsiers (*46*–*49*). All interfamilial relationships within our phylogeny receive strong support [posterior probability (PP) = 1], except for the position of Aotidae (owl monkeys), which is weakly supported as sister to Callitrichidae (marmosets and tamarins) rather than Cebidae (capuchin and squirrel monkeys) (PP = 0.56). We consider the precise relationship among these three families to remain uncertain. Lastly, we estimate the human–chimpanzee divergence between 9.0 and 6.9 Ma, and thus slightly older than other recent analyses, although these overlap our confidence intervals (*41*–*43*).

Taking advantage of our rich resequencing data, we generated a tree topology that includes two individuals per species for all species with more than one sequenced individual. We observe paraphyletic or polyphyletic placements of these individuals in 17 species, possibly calling several currently established species boundaries into question (Fig. 3). These cases could result from genetic structure interpreted as species delimitation, incomplete lineage sorting, or hybridization, and most are also observed at the mitochondrial level (*16*, *50*–*53*). Although some instances of hybridization have previously been described, such as among different species of langurs (*54*), we find most of the paraphyletic or polyphyletic placements among platyrrhines. These include 13 species, among them capuchins, squirrel monkeys, howler monkeys, uakaris, sakis, and titis, and point to the need for more taxonomic studies using genomic data in this group (*55*). Finally, we retrieve previously unknown phylogenetic relationships for species that were sequenced for the first time in this study, such as different species of howler monkeys (e.g., *Alouatta puruensis*, or *A. juara*).

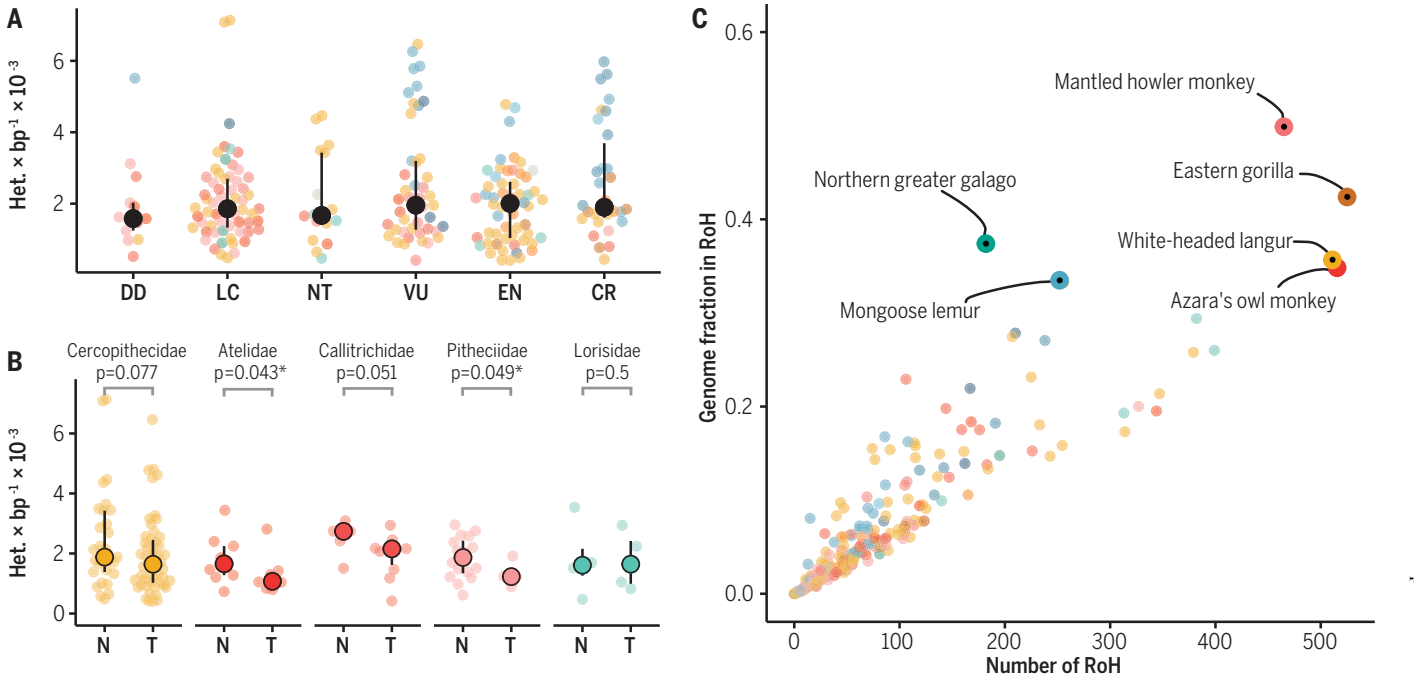


Fig. 2. Runs of homozygosity and impact of extinction risk on diversity (**A**) Relationship between IUCN extinction risk categories and heterozygosity. Solid black circles and bars denote median and IQR. (**B**) Partition into threatened (T: VU, EN, CR) and nonthreatened (N: LC, NT) categories for all families with more than one species in either partition. Significant differences ($p < 0.05$, one-sided rank-sum test) are marked with an asterisk. (**C**) Median number of tracts of homozygosity versus median proportion of the genome in runs of homozygosity per species. Species with a fraction over 1/3 are highlighted. Solid black dots within highlights denote threatened species (VU, EN, CR).

Determinants of diversity and mutation rate

We used the topology of the species tree and 614 UCE alignments, for which we had full species coverage, to estimate branch lengths as the number of substitutions per site. We combined this with our dated phylogeny and published estimates of generation times to estimate mutation rates per generation for all primate species from their substitution rates (*16*). Although we caution that we cannot rule out potential biases in these estimates, such as the effects of selection or uncertainties in fossil calibration, they agree well with published estimates for overlapping species on the basis of trio sequencing (Spearman's $r = 0.85$, $p = 0.02$; Fig. 4C). Our estimated mutation rates (μ) per generation vary between 0.25×10^{-8} and 1.62×10^{-8} (Fig. 4A), showing a considerably larger range than previously reported (*56*). We observe the lowest estimate per generation in Lemuridae and find highly variable estimates across some families such as Cebidae and Lorisidae, which also have variable generation times (8 to 17 and 4.6 to 9 years per generation, respectively). The highest estimates of μ are in great apes. We find a significant and positive correlation between μ per generation and the generation time (Spearman's $r = 0.36$, $p = 1.89 \times 10^{-8}$), which partly counteracts a generation-time effect on the yearly mutation rate. The latter is therefore larger in species with a shorter generation time (Fig. 4E). Together, variation in effective population size (N_e) and generation time explain roughly half of the observed variation in mutation rates among extant species.

We used our estimates of μ and estimates of genetic diversity π based on median heterozygosity to get an estimate of the effective population sizes $N_e = \pi/(4 \times \mu)$. We find multiple species belonging to different families of lemurs, as well as several species of guenons within the Cercopithecidae, with the largest N_e estimates, often exceeding 2×10^5 (Fig. 4B). For several critically endangered lemur species, e.g., the northern sportive lemur (*Lepilemur septentrionalis*), the red-tailed sportive lemur (*Lepilemur ruficaudatus*), or the Alaotra reed lemur (*Hapalemur alaotrensis*), these likely surpass census sizes by a considerable margin. We find multiple members of the genera *Cercopithecus* and *Eulemur* exhibiting high N_e values, which may be driven by interspecific hybridization observed in these species. Conversely, we observe comparatively low N_e estimates in great apes, lorises, and platyrrhines (Fig. 4B) (*16*).

The drift-barrier hypothesis (*57*, *58*) predicts that μ per generation should decrease with N_e, because new mutations affecting fitness are predominantly deleterious, and the ability to select for lower mutation rate increases with the population size. We tested for a relationship between μ and N_e, while controlling for the relationship between μ and generation time in a PGLS model, and observed a significantly lower mutation rate for species with higher N_e. We find around 45% of the variation in μ to be explained by N_e, thus lending apparent support to the drift-barrier hypothesis (*59*). However, we caution that although this pattern is consistent with the drift-barrier hypothesis, N_e is estimated by the division of π by μ, which at least partially explains the negative relationship. Additionally, our estimates of μ assume homogeneous levels of evolutionary constraint on the UCEs and flanking regions used to estimate divergence time and substitution rate. Should there be a strong covariation between substitution rates in these regions and effective size in branches, underlying variation in N_e along the branches of the phylogeny can act as a confounder of apparent variation in mutation rates and thus further complicate a formal test of the drift-barrier hypothesis.

To further disentangle what factors might contribute to the levels of genetic diversity and mutation rates, we compiled a list of 32 traits that can be summarized by grouping them into the broader categories of body mass, life history, activity budget, ranging patterns, climatic niche, social organization, sexual selection, diet composition, social systems, mating systems, and natal

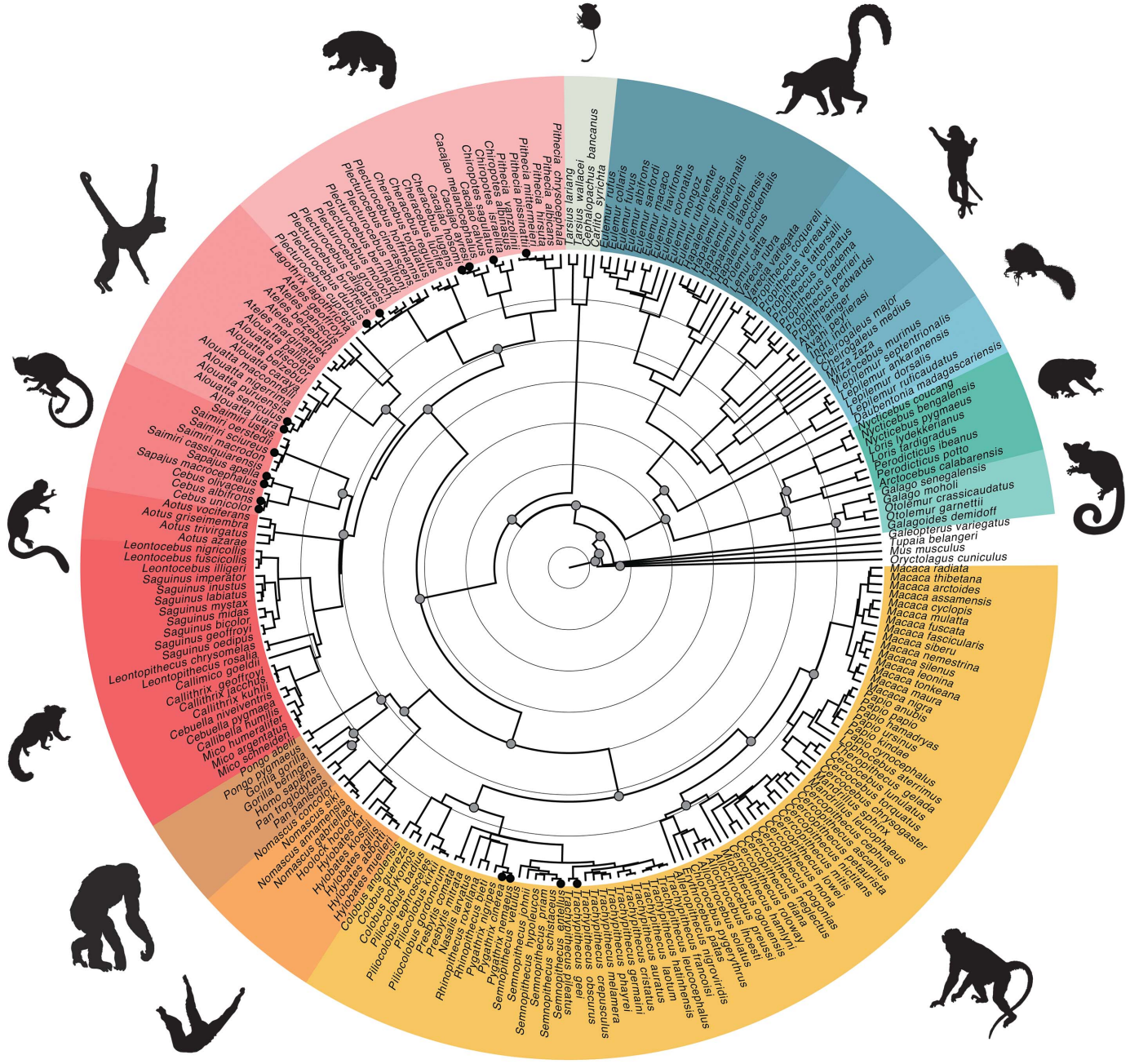


Fig. 3. Fossil-calibrated nuclear time tree. Concentric background circles mark 10-million-year intervals; solid gray circles in internal nodes show fossil calibration points (*36*); species marked with solid circles at tips show paraphyly or polyphyly when including additional individuals to estimate the topology.

dispersal mode (*60*–*62*). To account for potential phylogenetic inertia in trait evolution, we generated PGLS models using either genetic diversity or mutation rate as the response variable and individual traits as the predictors. We find traits within mating systems, activity budget, climatic niche, ranging patterns, and life history to be significant predictors of diversity ($p < 0.05$), and traits within the former three categories remaining so after accounting for multiple testing (Benjamini-Hochberg correction, false discovery rate = 0.05). Species organized in single-male polygynous mating systems show lower diversity than the background ($r^2_{\text{pred}} = 0.11$, $p_{\text{corr}} = 1.53 \times 10^{-2}$), consistent with expectations of reduced contribution of allelic diversity from males (*63*). Within the climatic niche, we observe a gradient of diversity declining from south to north ($r^2_{\text{pred}} = 0.28$, $p_{\text{corr}} = 1.45 \times 10^{-5}$), which is driven by highly diverse lemur species in the Southern Hemisphere. We also find a significant correlation with mean temperature and amount of precipitation ($r^2_{\text{pred}} = 0.33$, $p_{\text{corr}} = 1.97 \times 10^{-4}$). It is worth noting that these measurements are not highly correlated with each other (Pearson's r −0.27 to 0.17), and the relationships are thus at least partly independent. Lastly, within the activity budget, we find the amount of time spent socializing to be correlated with diversity ($r^2_{\text{pred}} = 0.11$, $p_{\text{corr}} = 5.56 \times 10^{-3}$). However, we caution that the measurement of activity budget is difficult to standardize across species, and interpreting this relationship is thus challenging. We find no significant impact of life-history traits such as body mass or longevity on genetic diversity

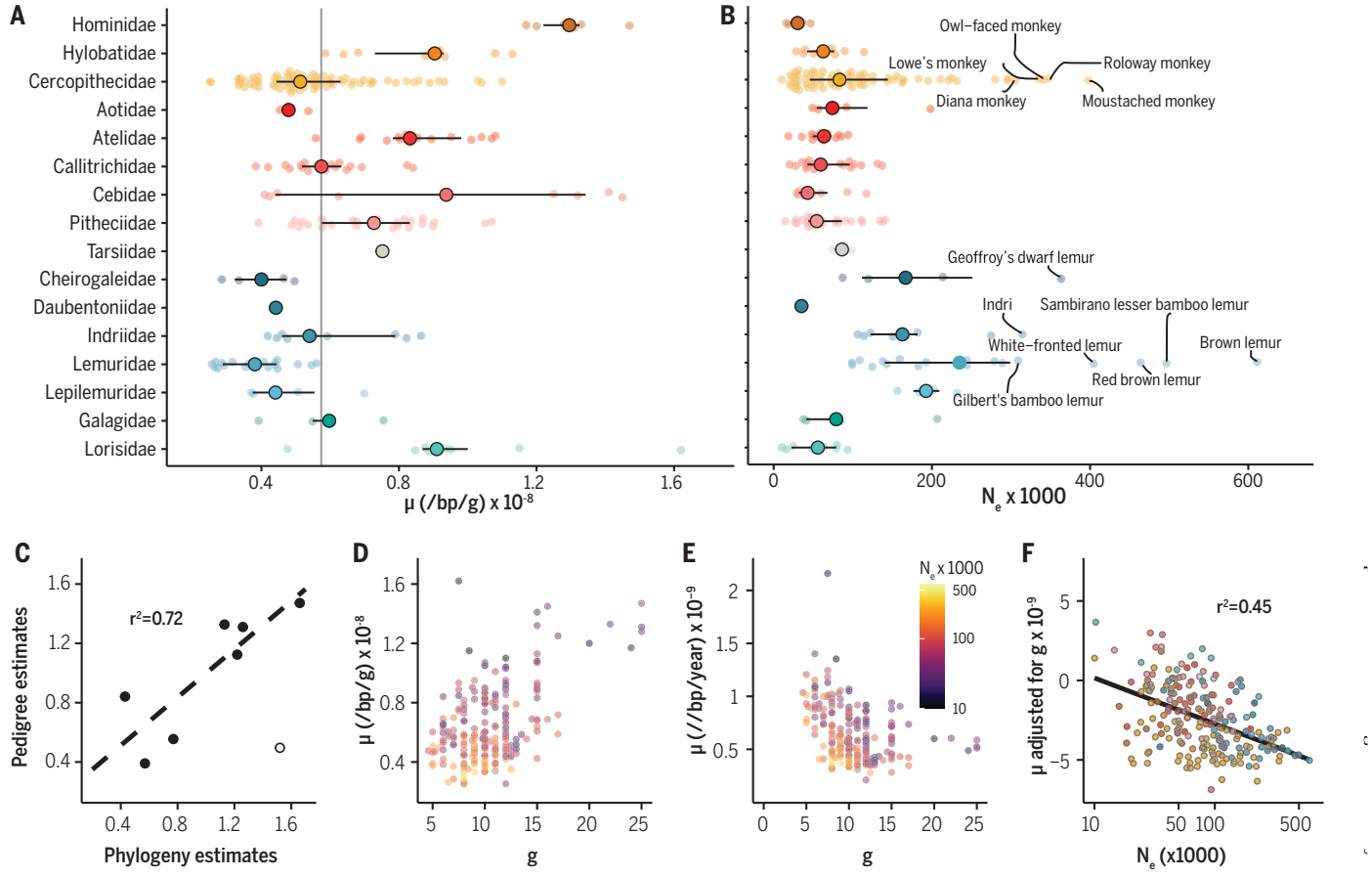


Fig. 4. Estimates of mutation rates and effective population size. (**A**) Distribution of estimates of the per-generation mutation rate across primate families (μ). Large solid circles denote median, and horizontal bars denote the interquartile range. The gray line denotes the primate-wide median. (**B**) Distribution of N_e estimates across primate families. Species with effective population size above 3×10^5 are highlighted. (**C**) Comparison of pedigree-based estimates of μ for great apes (*79*, *80*), olive baboon (*81*), rhesus macaque (*82*), and common marmoset (*83*) show a high correlation between the two estimates (Spearman's $r = 0.85$, $p = 0.02$). The open circle denotes the estimate for the mouse lemur (*84*), which was excluded from the comparison as an outlier (*16*). Data for trio estimates were derived from (*85*). (**D**) Positive correlation between estimates of per-generation mutation rates and generation times (g) (Pearson's $r = 0.53$, $p = 2.1 \times 10^{-17}$). (**E**) Inverse relationship between yearly mutation rate and generation time. Circles in (D) and (E) are colored by the effective population size N_e (Pearson's $r = -0.34$, $p = 3.1 \times 10^{-7}$). (**F**) Relationship between per-generation mutation rate, adjusted by first regressing the effects of generation time, and effective population size. The relationship is highly significant after phylogenetic correction ($r^2 = 0.45$, $p < 0.001$).

within primates, although body mass is significant before accounting for multiple testing. These relationships have been previously described, albeit for broader evolutionary distances, including a wider range of genetic diversity and body mass (*64*, *65*). We additionally calculated the relationship of the traits above to our mutation rate estimates. After correcting for multiple testing, we did not find any significant predictors of μ.

Variants specific to the human lineage

Finally, we revisited a previously published catalog of 647 high-frequency human-specific missense changes, i.e., amino acid–altering variants that putatively emerged specifically in the human lineage and quickly rose to high frequency or fixation (*66*). This catalog was mainly defined by looking at derived sites segregating at high frequency in anatomically modern humans, at which archaic hominins (Neanderthals and Denisovans) carry the ancestral allele. Although insufficient to explain the whole spectrum of human uniqueness, such a catalog should contain prime candidates for some of its molecular underpinnings. We sought to determine how often the putatively human-specific derived allele occurs at orthologous positions across the genomes of other primate species analyzed in this study. We find 63% (406) of high-frequency human-specific missense changes to occur in at least one other primate species and 55% in more than two, segregating at high frequency (>0.9) within the sampled individuals of a species (Fig. 5). This suggests that mutational recurrence generally might be widespread across primates. We find mutation pairs in recurrent high-frequency human-specific missense changes enriched in T-C and A-G mutations, and to a lesser extent in C-T and G-A compared with nonrecurrent ones.

We leveraged our data to generate a more stringent picture of the mutations that arose specifically in the human lineage and have not emerged elsewhere in primates. We identified alleles present in anatomically modern humans at a frequency of at least 99.9% that differ in state from a set of four high-coverage archaic hominins genomes (*67*–*70*). We ensured that the human allele represents the derived state by requiring the ancestral allele to be present at a frequency of >99% in a genetic diversity panel of 139 previously published great ape genomes (*8*, *9*, *71*, *72*). The resulting 24,374 candidates include a conservative set of 124 missense coding mutations affecting 107 different genes, among which are 17 previously undescribed changes affecting 12 genes (*66*).

We further sought to detect which genes have not shown frequent allele recurrence in other primate species. To this end, we removed variants that we found to reoccur in >1% of

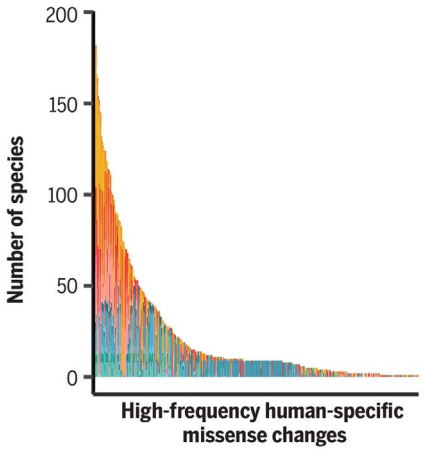


Fig. 5. Recurrent putative high-frequency human-specific missense changes. Each bar on the *x* axis represents a high-frequency human-specific missense change with the same allele found in a different species. Color schemes are the same as presented in Figs. 1 and 2.

species at a frequency of >0.1%. In this set, we find 89 missense changes, affecting 80 distinct genes. We observe no enrichment for functional categories or association to diseases among them. Within our catalog, we also find the two amino acid differences with demonstrated functional differences between humans and Neanderthals: The ancestral allele in *NOVA1* (neuro-oncological ventral antigen 1) leads to a slower development of cortical organoids and modifies synaptic protein interactions (*73*); the human-derived allele of the adenylosuccinate lyase gene (*ADSL*) leads to a reduced de novo synthesis of purines in the brain (*74*). Furthermore, changes in mitotic spindle-associated genes previously reported to be under positive selection (*SPAG5, KIF18A*) maintain their status as distinctively human (*75*). This may have had an impact on neurogenesis during development (*76*), although this hypothesis has not been experimentally validated. We find a specifically human change in *TMPRSS2*, a main factor in the response to severe acute respiratory syndrome coronavirus 2 (SARS-CoV-2) infection with known functional variants that have possibly been under selection in some human populations (*77*).

Analogous to the above, we additionally generated a catalog of sites that are fixed across great apes but differ from rhesus macaque (*Macaca mulatta*). Among these 11.2 million variants, we find 1 million without observed recurrences beyond apes, corresponding to mutations specific to the great ape lineage. These contain 3792 missense variants affecting 2970 different genes that are significantly enriched for multiple cilia-related functional categories, such as axoneme assembly, motile cilium assembly, nonmotile cilium assembly, cilium-dependent cell motility, and epithelial cilium movement involved in extracellular fluid movement, suggesting that the evolution of ape-specific features of cilia have been important in shaping the lineage leading to our own species. The disruption of normally functioning cilia can lead to an array of heterogeneous pathologies in humans, collectively known as ciliopathies. Among 187 genes with established links to different ciliopathies, we find 30% to be affected by ape-specific missense changes (*78*) ($p < 0.01$, Fisher's exact test). More generally, we also find an overall significant enrichment of genes with nonrecurrent ape-specific missense changes among genes with disease association in OMIM (Online Mendelian Inheritance in Man) ($p < 0.01$, Fisher's exact test), suggesting that—to some degree—variants that give rise to the ape-specific phenotype, and thus ultimately also to the human one, affect a greater proportion of the genes that make us susceptible to diseases than would be expected by chance.

REFERENCES AND NOTES

1. A. B. Rylands, R. A. Mittermeier, in *Primate Behavioral Ecology, 6th edition*, K. B. Strier, Ed. (Routledge, New York, 2021), pp. 407–428.
2. L. F. Kuderna, P. Esteller-Cucala, T. Marques-Bonet, *Curr. Opin. Genet. Dev.* **62**, 65–71 (2020).
3. J. D. Orkin, L. F. K. Kuderna, T. Marques-Bonet, *Annu. Rev. Anim. Biosci.* **9**, 103–124 (2021).
4. Chimpanzee Sequencing and Analysis Consortium, *Nature* **437**, 69–87 (2005).
5. D. P. Locke *et al.*, *Nature* **469**, 529–533 (2011).
6. A. Scally *et al.*, *Nature* **483**, 169–175 (2012).
7. K. Prüfer *et al.*, *Nature* **486**, 527–531 (2012).
8. J. Prado-Martinez *et al.*, *Nature* **499**, 471–475 (2013).
9. A. Nater *et al.*, *Curr. Biol.* **27**, 3576–3577 (2017).
10. Z. N. Kronenberg *et al.*, *Science* **360**, eaar6343 (2018).
11. R. A. Gibbs *et al.*, *Science* **316**, 222–234 (2007).
12. W. C. Warren *et al.*, *Science* **370**, eabc6617 (2020).
13. C. Xue *et al.*, *Genome Res.* **26**, 1651–1662 (2016).
14. A. Estrada *et al.*, *Sci. Adv.* **3**, e1600946 (2017).
15. C. S. Mantyka-Pringle *et al.*, *Biol. Conserv.* **187**, 103–111 (2015).
16. See supplementary materials.
17. Zoonomia Consortium, *Nature* **587**, 240–245 (2020).
18. L. Wang *et al.*, *Gigascience* **8**, giz098 (2019).
19. Z. Liu *et al.*, *Mol. Biol. Evol.* **37**, 952–968 (2020).
20. B. J. Evans *et al.*, *R. Soc. Open Sci.* **4**, 170351 (2017).
21. Z. Fan *et al.*, *Mol. Phylogenet. Evol.* **127**, 376–386 (2018).
22. D. Vanderpool *et al.*, *PLOS Biol.* **18**, e3000954 (2020).
23. L. Yu *et al.*, *Nat. Genet.* **48**, 947–952 (2016).
24. N. Osada, K. Matsudaira, Y. Hamada, S. Malaivijitnond, *Genome Biol. Evol.* **13**, evaa209 (2021).
25. E. E. Louis *et al.*, Lepilemur septentrionalis. The IUCN Red List of Threatened Species 2020; https://dx.doi.org/10.2305/IUCN.UK.2020-2.RLTS.T11622A115567059.en.
26. C. Coudrat, B. Rawson, P. Phiaphalath, F. Pengfei, C. Roos, M. H. Nguyen, IUCN Red List of Threatened Species: Nomascus concolor. *IUCN Red List of Threatened Species* (2015); https://www.iucnredlist.org/species/39775/17968556.
27. E. F. Sørensen *et al.*, *Science* **380**, eabn8153 (2023).
28. H. Gao *et al.*, *Science* **380**, eabn8197 (2023).
29. T. van der Valk *et al.*, *Mol. Biol. Evol.* **37**, 183–194 (2020).
30. K. M. Detwiler, *Int. J. Primatol.* **40**, 28–52 (2019).
31. Y. A. de Jong, T. M. Butynski, *Primate Conserv.* **25**, 43–56 (2010).
32. H. Svardal *et al.*, *Nat. Genet.* **49**, 1705–1713 (2017).
33. D. Spielman, B. W. Brook, R. Frankham, *Proc. Natl. Acad. Sci. U.S.A.* **101**, 15261–15264 (2004).
34. J. C. Teixeira, C. D. Huber, *Proc. Natl. Acad. Sci. U.S.A.* **118**, e2015096118 (2021).
35. T. van der Valk, D. Díez-Del-Molino, T. Marques-Bonet, K. Guschanski, L. Dalén, *Curr. Biol.* **29**, 165–170.e6 (2019).
36. J. A. Robinson *et al.*, *Sci. Adv.* **5**, eaau0757 (2019).
37. B. C. Faircloth *et al.*, *Syst. Biol.* **61**, 717–726 (2012).
38. S. Naser-Khdour, B. Q. Minh, W. Zhang, E. A. Stone, R. Lanfear, *Genome Biol. Evol.* **11**, 3341–3352 (2019).
39. D. T. Hoang, O. Chernomor, A. von Haeseler, B. Q. Minh, L. S. Vinh, *Mol. Biol. Evol.* **35**, 518–522 (2018).
40. S. Kalyaanamoorthy, B. Q. Minh, T. K. F. Wong, A. von Haeseler, L. S. Jermiin, *Nat. Methods* **14**, 587–589 (2017).
41. P. Perelman *et al.*, *PLOS Genet.* **7**, e1001342 (2011).
42. M. S. Springer *et al.*, *PLOS ONE* **7**, e49521 (2012).
43. M. D. Reis *et al.*, *Syst. Biol.* **67**, 594–615 (2018).
44. C. Zhang, M. Rabiee, E. Sayyari, S. Mirarab, *BMC Bioinformatics* **19** (suppl 6), 153 (2018).
45. D. de Vries, R. M. D. Beck, *Palaeontol. Electron.* **26**, 1–52 (2023).
46. J. B. Rossie, X. Ni, K. C. Beard, *Proc. Natl. Acad. Sci. U.S.A.* **103**, 4381–4385 (2006).
47. J. S. Zijlstra, L. J. Flynn, W. Wessels, *J. Hum. Evol.* **65**, 544–550 (2013).
48. Y. Chaimanee, R. Lebrun, C. Yamee, J.-J. Jaeger, *Proc. Biol. Sci.* **278**, 1956–1963 (2011).
49. X. Ni, Q. Li, L. Li, K. C. Beard, *Science* **352**, 673–677 (2016).
50. J. Tung, L. B. Barreiro, *Curr. Opin. Genet. Dev.* **47**, 61–68 (2017).
51. C. Fontsere, M. de Manuel, T. Marques-Bonet, M. Kuhlwilm, *BioEssays* **41**, e1900123 (2019).
52. J. Sukumaran, L. L. Knowles, *Proc. Natl. Acad. Sci. U.S.A.* **114**, 1607–1612 (2017).
53. M. C. Janiak *et al.*, *Mol. Ecol.* **31**, 3888–3902 (2022).
54. C. Roos *et al.*, *BMC Evol. Biol.* **11**, 77 (2011).
55. M. G. M. Lima *et al.*, *Mol. Phylogenet. Evol.* **124**, 137–150 (2018).
56. M. Chintalapati, P. Moorjani, *Curr. Opin. Genet. Dev.* **62**, 58–64 (2020).
57. T. Ohta, *Nature* **246**, 96–98 (1973).
58. W. Sung, M. S. Ackerman, S. F. Miller, T. G. Doak, M. Lynch, *Proc. Natl. Acad. Sci. U.S.A.* **109**, 18488–18492 (2012).
59. M. Lynch, *Trends Genet.* **26**, 345–352 (2010).
60. J. M. Kamilar, N. Cooper, *Philos. Trans. R. Soc. London B Biol. Sci.* **368**, 20120341 (2013).
61. A. R. DeCasien, S. A. Williams, J. P. Higham, *Nat. Ecol. Evol.* **1**, 112 (2017).
62. S. Shultz, C. Opie, Q. D. Atkinson, *Nature* **479**, 219–222 (2011).
63. B. Charlesworth, *Nat. Rev. Genet.* **10**, 195–205 (2009).
64. H. Ellegren, N. Galtier, *Nat. Rev. Genet.* **17**, 422–433 (2016).
65. J. Romiguier *et al.*, *Nature* **515**, 261–263 (2014).
66. M. Kuhlwilm, C. Boeckx, *Sci. Rep.* **9**, 8463 (2019).
67. K. Prüfer *et al.*, *Science* **358**, 655–658 (2017).
68. F. Mafessoni *et al.*, *Proc. Natl. Acad. Sci. U.S.A.* **117**, 15132–15136 (2020).
69. R. E. Green *et al.*, *Science* **328**, 710–722 (2010).
70. D. Reich *et al.*, *Nature* **468**, 1053–1060 (2010).
71. Y. Xue *et al.*, *Science* **348**, 242–245 (2015).
72. M. de Manuel *et al.*, *Science* **354**, 477–481 (2016).
73. C. A. Trujillo *et al.*, *Science* **371**, eaax2537 (2021).
74. V. Stepanova *et al.*, *eLife* **10**, e58741 (2021).
75. S. Peyrégne, J. Kelso, B. M. Peter, S. Pääbo, *eLife* **11**, e75464 (2022).
76. S. Pääbo, *Cell* **157**, 216–226 (2014).
77. S. Jeon *et al.*, *Mol. Cells* **44**, 680–687 (2021).
78. J. F. Reiter, M. R. Leroux, *Nat. Rev. Mol. Cell Biol.* **18**, 533–547 (2017).
79. S. Besenbacher, C. Hvilsom, T. Marques-Bonet, T. Mailund, M. H. Schierup, *Nat. Ecol. Evol.* **3**, 286–292 (2019).
80. M. D. Kessler *et al.*, *Proc. Natl. Acad. Sci. U.S.A.* **117**, 2560–2569 (2020).
81. F. L. Wu *et al.*, *PLOS Biol.* **18**, e3000838 (2020).
82. L. A. Bergeron *et al.*, *Gigascience* **10**, giab029 (2021).
83. C. Yang *et al.*, *Nature* **594**, 227–233 (2021).
84. C. Ryan Campbell *et al.*, bioRxiv (2020), p. 724880.
85. L. A. Bergeron *et al.*, *eLife* **11**, e73577 (2022).

ACKNOWLEDGMENTS

The authors thank the Veterinary and Zoology staff at Wildlife Reserves Singapore for help in obtaining the tissue samples, as well

as the Lee Kong Chian Natural History Museum for storage and provision of the tissue samples. We thank H. Doddapaneni, D. M. Muzny, and M. C. Gingras for their support of sequencing at the Baylor College of Medicine Human Genome Sequencing Center. We appreciate the support of R. Gibbs, director of HGSC, for this project and thank Baylor College of Medicine for internal funding. We thank P. Karanth (IISc) and H. N. Kumara (SACON) for collecting and providing some of the samples from India. We acknowledge the support provided by the Council of Scientific and Industrial Research (CSIR), India, to G.U. for the sequencing at the Centre for Cellular and Molecular Biology (CCMB), India. Silhouettes in Fig. 3 were obtained from phylopic.org. The silhouette for *Propithecus* is credited to Terpsichores and has been published under CC BY-SA 3.0. All other silhouettes are under public domain. This is Duke Lemur Center publication #1559. E.F.D. thanks the Ministry of Production and the Environment of Formosa Province in Argentina for the research presented here. Samples from Amazônia, Brazil, were accessed under SisGen no. A8F3D55. **Funding:** L.F.K.K. was supported by an EMBO STF 8286. M.K. was supported by "la Caixa" Foundation (ID 100010434), fellowship code LCF/BQ/PR19/11700002, and by the Vienna Science and Technology Fund (WWTF) [10.47379/VRG20001]. J.D.O. was supported by "la Caixa" Foundation (ID 100010434) and the European Union's Horizon 2020 research and innovation program under the Marie Skłodowska-Curie grant agreement No 847648. The fellowship code is LCF/BQ/PI20/11760004. F.E.S. has received funding from the European Union's Horizon 2020 research and innovation programme under the Marie Skłodowska-Curie grant agreement no. 801505. FES also received funds from the Conselho Nacional de Desenvolvimento Científico e Tecnológico (CNPq) (Process nos.: 303286/2014-8, 303579/2014-5, 200502/2015-8, 302140/2020-4, 300365/2021-7, 301407/2021-5, 301925/2021-6), International Primatological Society (Conservation grant), The Rufford Foundation (14861-1, 23117-2, 38786-B), the Margot Marsh Biodiversity Foundation (SMA-CCO-G0023, SMA-CCOG0037), and Primate Conservation Inc. (no. 1713 and no. 1689). Fieldwork for samples collected in the Brazilian Amazon was funded by grants from Conselho Nacional de Desenvolvimento Científico e Tecnológico (CNPq/SISBIOTA Program 563348/2010-0), Fundação de Amparo à Pesquisa do Estado do Amazonas (FAPEAM/SISBIOTA 2317/2011), and Coordenação de Aperfeiçoamento de Pessoal de Nível Superior (CAPES AUX 3261/2013) to IPF. Sampling of nonhuman primates in Tanzania was funded by the German Research Foundation (KN1097/3-1 to S.K. and RO3055/2-1 to C.R.) and by the US National Science Foundation (BNS83-03506 to J.P.-C.). No animals in Tanzania were sampled purposely for this study. Details of the original study on *Treponema pallidum* infection can be requested from S.K. Sampling of baboons in Zambia was funded by US NSF grant BCS-1029451 to J.P.-C., C.J.J., and J.R. The research reported in this manuscript was also funded by the Vietnamese Ministry of Science and Technology's Program 562 (grant no. ĐTĐL. CN-64/19) to M.D.L. A.N.C. is supported by PID2021-127792NB-I00 funded by MCIN/AEI/10.13039/501100011033 (FEDER Una manera de hacer Europa)" and by "Unidad de Excelencia María de Maeztu", funded by the AEI (CEX2018-000792-M) and Departament de Recerca i Universitats de la Generalitat de Catalunya (GRC 2021 SGR 0467). A.D.M. was supported by the National Sciences and Engineering Research Council of Canada and Canada Research Chairs program. T.M.B. is supported by funding from the European Research Council (ERC) under the European Union's Horizon 2020 research and innovation programme (grant agreement no. 864203), PID2021-126004NB-100 (MICIIN/FEDER, UE) and Secretaria d'Universitats i Recerca and CERCA Programme del Departament d'Economia i Coneixement de la Generalitat de Catalunya (GRC 2021 SGR 00177). M.C.J, D.d.V. I.G., R.M.D.B., and J.P.B. were supported by a UKRI NERC standard grant (NE/T000341/1). S.M.A. was supported by a BINC fellowship from the Department of Biotechnology (DBT), India. *Aotus azarae* samples from Argentina where obtained with grant support to E.F.-D. from the Zoological Society of San Diego, Wenner-Gren Foundation, the L.S.B. Leakey Foundation, the National Geographic Society, the US National Science Foundation (NSF-BCS-0621020, 1232349, 1503753, 1848954; NSF-RAPID-1219368, NSF-FAIN-1952072; NSF-DDIG-1540255; NSF-REU 0837921, 0924352, 1026991), and the US National Institute on Aging (NIA- P30 AG012836-19, NICHD R24 HD-044964-11). J.H.S. was supported in part by the NIH under award number P40OD024628 - SPF Baboon Research Resource. K.G. was supported by the Swedish Research Council VR (2020-03398). This research is supported by the National Research Foundation Singapore under its National Precision Medicine Programme (NPM) Phase II Funding (MOH-000588) and administered by the Singapore Ministry of Health's National Medical Research Council. **Author contributions:** Conceptualization: T.M.B., K.K.-H.F., J.R. Methodology & analysis: L.F.K.K., H.G., M.C.J., M.K., J.D.O., S.M., A.V., J.B., M.R., R.M.D.B., T.M.B., K.K.-H.F., J.R., T.B., Y.S., L.Z., J.G.S., D.d.V., I.G., A.J., J.P.B., M.R., R.A.H. Fieldwork & sample acquisition: J.P.B., C.R., G.U., K.G., F.E.S., F.R.D.-M., F.B., H.B., I.S., I.F., J.V., M.M., M.N.F.d.S., M.T., R.R., T.H., A.M., D.Z., A.C.K., W.K.L., C.C.K., P.T., J.L., S.M., M.D.L., S.K., J.D.K., F.S., E.F.-D., J.H.S., C.A., G.W., J.P.-C., C.J.J., A.Z., C.J.R., N.A., C.H., P.F., I.S.C., J.H., J.R. Topic section leaders: L.F.K.K., J.P.B., M.H.S., R.M.D.B., K.G., C.R., G.U., A.M., T.M.B. Sequencing: L.A., M.G., J.E.H., J.B., G.U., E.L., R.A.H., M.R. Supervision: T.M.B., K.K.-H.F., J.R., M.H.S., R.M.D.B., G.Z., D.W., D.J., J.P.B. Writing – original draft: L.F.K.K., T.M.B. Writing – review and editing: All authors. **Competing interests:** L.F.K.K., H.G., J.G.S., and K.K.-H.F. are employees of Illumina Inc. as of the submission of this manuscript. **Data and materials availability:** All sequencing data have been deposited at the European Nucleotide Archive under the accession number PRJEB49549. **License information:** Copyright © 2023 the authors, some rights reserved; exclusive licensee American Association for the Advancement of Science. No claim to original US government works. https://www.sciencemag.org/about/science-licenses-journal-article-reuse

SUPPLEMENTARY MATERIALS

science.org/doi/10.1126/science.abn7829
Materials and Methods
Supplementary Text
Figs. S1 to S111
Tables S1 to S30
References (*86*–*190*)
Data S1 to S6

View/request a protocol for this paper from *Bio-protocol*.

Submitted 19 December 2021; accepted 6 February 2023
10.1126/science.abn7829

PRIMATE GENOMES

Phylogenomic analyses provide insights into primate evolution

Yong Shao[1]†, Long Zhou[2]†, Fang Li[3,4], Lan Zhao[5], Bao-Lin Zhang[1], Feng Shao[6], Jia-Wei Chen[7], Chun-Yan Chen[8], Xupeng Bi[2], Xiao-Lin Zhuang[1,9], Hong-Liang Zhu[7], Jiang Hu[10], Zongyi Sun[10], Xin Li[10], Depeng Wang[10], Iker Rivas-González[11], Sheng Wang[1], Yun-Mei Wang[1], Wu Chen[12], Gang Li[13], Hui-Meng Lu[14], Yang Liu[13], Lukas F. K. Kuderna[15,16], Kyle Kai-How Farh[16], Peng-Fei Fan[17], Li Yu[18], Ming Li[19], Zhi-Jin Liu[20], George P. Tiley[21], Anne D. Yoder[21], Christian Roos[22], Takashi Hayakawa[23,24], Tomas Marques-Bonet[15,25,33,34], Jeffrey Rogers[26], Peter D. Stenson[27], David N. Cooper[27], Mikkel Heide Schierup[11], Yong-Gang Yao[9,28,29,30], Ya-Ping Zhang[1,29,30], Wen Wang[1,8,29], Xiao-Guang Qi[5]*, Guojie Zhang[1,2,3,31]*, Dong-Dong Wu[1,29,30,32]*

Comparative analysis of primate genomes within a phylogenetic context is essential for understanding the evolution of human genetic architecture and primate diversity. We present such a study of 50 primate species spanning 38 genera and 14 families, including 27 genomes first reported here, with many from previously less well represented groups, the New World monkeys and the Strepsirrhini. Our analyses reveal heterogeneous rates of genomic rearrangement and gene evolution across primate lineages. Thousands of genes under positive selection in different lineages play roles in the nervous, skeletal, and digestive systems and may have contributed to primate innovations and adaptations. Our study reveals that many key genomic innovations occurred in the Simiiformes ancestral node and may have had an impact on the adaptive radiation of the Simiiformes and human evolution.

The order Primate contains >500 species from 79 genera and 16 families (*1*), with new species continuing to be discovered (*2*–*5*), making primates the third most speciose order of living mammals after bats (Chiroptera) and rodents (Rodentia). As our closest living relatives, nonhuman primates play important roles in the cultures and religions of human societies (*1*). Many nonhuman primate species have been widely used as animal models because of their genetic, physiological, and anatomical similarities to humans, allowing the efficacy and safety of newly developed drugs and vaccines to be tested (*6*). For example, since the emergence of COVID-19, macaques have served as important models in the research and development of vaccines (*7*–*16*). Primates display considerable morphological, behavioral, and physiological diversity and hold the key to understanding the evolution of our own species, particularly the evolution of human phenotypes such as high-level cognition (*17*, *18*).

Nonhuman primates occupy a wide range of diverse habitats in the tropical forest, savanna, semidesert, and subtropical regions of Asia, Central and South America, and Africa, and humans have spread across much of the earth's surface. Nevertheless, according to the International Union for Conservation of Nature (IUCN) Red Lists, >33% of primate species are critically endangered or vulnerable, ~60% are threatened with extinction, and ~75% are experiencing population decline (*1*). With global climate change and increasing anthropogenic interference, the conservation status of primates has attracted global scientific and public awareness.

Despite the importance of nonhuman primates, reference genomes have been sequenced in <10% of species (*19*–*27*), which both impedes research and hampers conservation efforts. Here, we present high-quality reference genomes for 27 primate species with long-read sequencing generated from our first-phase program of the Primate Genome Project.

Assembly and annotation of 27 new primate reference genomes

We applied long-read genome-sequencing technologies, including Pacbio and Nanopore, to sequence the genomes of 27 nonhuman primate species from 26 genera of 11 families (table S1). Long reads were self-polished and assembled, and the genome assemblies were further corrected and polished by paired-end short reads sequenced from the same individuals (tables S2 to S4). We also used sequencing data generated by high-throughput chromosome conformation capture technology (*28*) to anchor assembled contigs into chromosomes for four species (fig. S1 and table S4). The sizes of the new genome assemblies of the primate species under study ranged from ~2.4×10^9 base pairs (Gbp) (*Daubentonia madagascariensis*) to ~3.1 Gbp (*Erythrocebus patas*), which were mostly consistent with the k-mer–based estimations (fig. S2 and table S5), with a high average contig N50 length of ~15.9×10^6 base pairs (Mbp) (table S6). All of the genome assemblies yielded BUSCO complete scores >92% (table S6). A method that integrates de novo and homology-based strategies was applied to annotate all genomes with protein sequences from human, chimpanzee, gorilla, orangutan, and mouse as references for homology-based gene model prediction. Between 20,066 and 21,468 protein-coding genes were predicted in these genome assemblies (table S7). Further, we also identified ~24.2 Mbp of primate-specific highly conserved elements by using whole-genome alignments between all primates and nine other mammals (fig. S3).

[1]State Key Laboratory of Genetic Resources and Evolution, Kunming Natural History Museum of Zoology, Kunming Institute of Zoology, Chinese Academy of Sciences, Kunming 650201, China. [2]Center of Evolutionary & Organismal Biology, and Women's Hospital at Zhejiang University School of Medicine, Hangzhou 310058, China. [3]Section for Ecology and Evolution, Department of Biology, University of Copenhagen, DK-2100 Copenhagen, Denmark. [4]Institute of Animal Sex and Development, ZhejiangWanli University, Ningbo 315100, China. [5]Shaanxi Key Laboratory for Animal Conservation, College of Life Sciences, Northwest University, Xi'an 710069, China. [6]Key Laboratory of Freshwater Fish Reproduction and Development (Ministry of Education), Southwest University School of Life Sciences, Chongqing 400715, China. [7]BGI-Shenzhen, Shenzhen 518083, China. [8]School of Ecology and Environment, Northwestern Polytechnical University, Xi'an 710072, China. [9]Kunming College of Life Science, University of the Chinese Academy of Sciences, Kunming 650204, China. [10]Grandomics Biosciences, Beijing 102206, China. [11]Bioinformatics Research Centre, Aarhus University, DK-8000 Aarhus, Denmark. [12]Guangzhou Zoo & Guangzhou Wildlife Research Center, Guangzhou 510070, China. [13]College of Life Sciences, Shaanxi Normal University, Xi'an 710119, China. [14]School of Life Sciences, Northwestern Polytechnical University, Xi'an 710072, China. [15]Institute of Evolutionary Biology (UPF-CSIC), PRBB, 08003 Barcelona, Spain. [16]Illumina Artificial Intelligence Laboratory, Illumina Inc, San Diego, CA 92122, USA. [17]School of Life Sciences, Sun Yat-sen University, Guangzhou, Guangdong 510275, China. [18]State Key Laboratory for Conservation and Utilization of Bio-Resource in Yunnan, School of Life Sciences, Yunnan University, Kunming 650091, China. [19]CAS Key Laboratory of Animal Ecology and Conservation Biology, Institute of Zoology, Chinese Academy of Sciences, Beijing 100101, China. [20]College of Life Sciences, Capital Normal University, Beijing 100048, China. [21]Department of Biology, Duke University, Durham, NC 27708, USA. [22]Gene Bank of Primates and Primate Genetics Laboratory, German Primate Center, Leibniz Institute for Primate Research, 37077 Göttingen, Germany. [23]Faculty of Environmental Earth Science, Hokkaido University, Sapporo, Hokkaido 060-0810, Japan. [24]Japan Monkey Centre, Inuyama, Aichi 484-0081, Japan. [25]Catalan Institution of Research and Advanced Studies (ICREA), Passeig de Lluís Companys, 23, 08010 Barcelona, Spain. [26]Human Genome Sequencing Center, Department of Molecular and Human Genetics, Baylor College of Medicine, Houston, TX 77030, USA. [27]Institute of Medical Genetics, School of Medicine, Cardiff University, Cardiff CF14 4XN, UK. [28]Key Laboratory of Animal Models and Human Disease Mechanisms of Chinese Academy of Sciences & Yunnan Province, Kunming Institute of Zoology, Chinese Academy of Sciences, Kunming 650201, China. [29]Center for Excellence in Animal Evolution and Genetics, Chinese Academy of Sciences, Kunming 650201, China. [30]National Resource Center for Non-Human Primates, Kunming Primate Research Center, and National Research Facility for Phenotypic & Genetic Analysis of Model Animals (Primate Facility), Kunming Institute of Zoology, Chinese Academy of Sciences, Kunming 650107, China. [31]Liangzhu Laboratory, Zhejiang University Medical Center, Hangzhou 311121, China. [32]KIZ-CUHK Joint Laboratory of Bioresources and Molecular Research in Common Diseases, Kunming Institute of Zoology, Chinese Academy of Sciences, Kunming 650204, China. [33]CNAG-CRG, Centre for Genomic Regulation (CRG), Barcelona Institute of Science and Technology (BIST), 08028 Barcelona, Spain. [34]Institut Català de Paleontologia Miquel Crusafont, Universitat Autònoma de Barcelona, Edifici ICTA-ICP, c/ Columnes s/n, 08193 Cerdanyola del Vallès, Barcelona, Spain.
***Corresponding author. Email: wudongdong@mail.kiz.ac.cn (D.-D.W.); guojiezhang@zju.edu.cn (G.Z.); qixg@nwu.edu.cn (X.-G.Q.)** †These authors contributed equally to this work.

The Primate Genome Project also generated high-quality reference genomes for another 16 primate species that were used in the accompanying papers to reveal hybrid speciation during the rapid radiation of the macaques (*29*), the homoploid hybrid speciation in the snub-nosed monkey *Rhinopithecus* genus (*30*), social evolution in the Asian colobines driven by cold adaptation (*31*), and the evolutionary adaptations of slow lorises (*32*). All genomic data have been published openly and can be freely accessed in the National Center for Biotechnology Information (NCBI) Assembly Database under the accession information described in this study.

A genomic phylogeny of living primates

We next performed phylogenomic analyses comprising the 27 newly generated genomes, another 22 published primate genomes, one long-read genome from *Nycticebus pygmaeus* reported in an accompanying paper (*32*), and two close relatives of primates, the Sunda flying lemur (*Galeopterus variegatus*) and the Chinese tree shrew (*Tupaia belangeri chinensis*) (*33*), as outgroups (table S8). We constructed whole-genome–wide phylogenetic trees using ExaML under a GTR+GAMMA model (*34*). Altogether, ~433.5 Mbp of gap-free data for syntenic orthologous sequences were retrieved

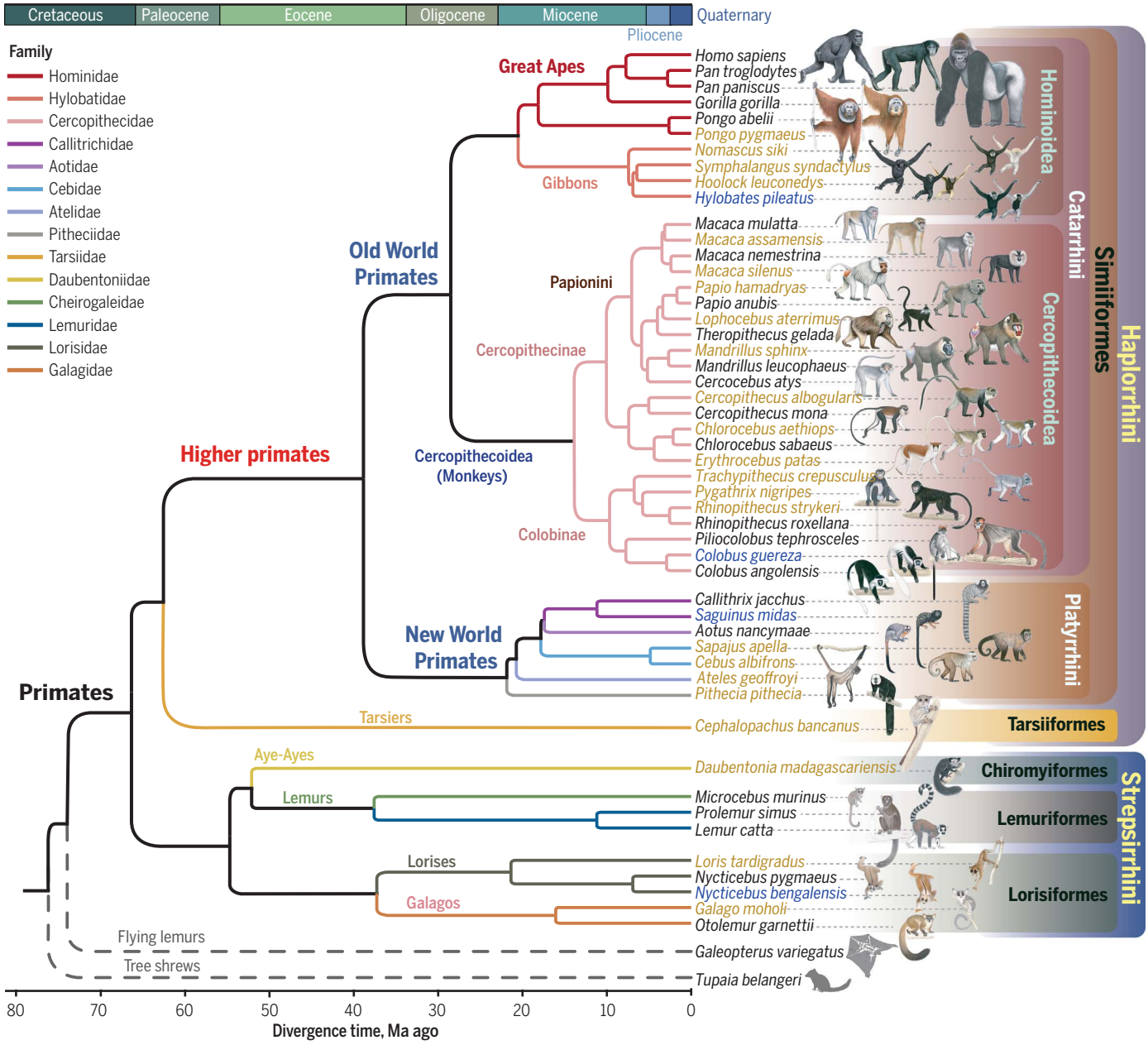


Fig. 1. Genomic phylogeny of primates. The maximum likelihood method was used to infer the primate species tree from whole-genome sequences across 52 species, including 50 primate species and two outgroup species (the Sunda flying lemur and the Chinese tree shrew) with 100 bootstraps under a GTR+GAMMA model. The divergence time was estimated using fossil calibrations (fig. S11) and the MCMCtree algorithm. The yellow and blue species names represent those genomes newly produced in this study. The genomes of the species marked in blue were assembled at the chromosome level. The genomes of the species marked in black were downloaded from the NCBI and Ensembl databases (table S8). Monkey pictures are copyrighted by Stephen D. Nash/IUCN/SSC Primate Specialist Group and are used in this study with their permission.

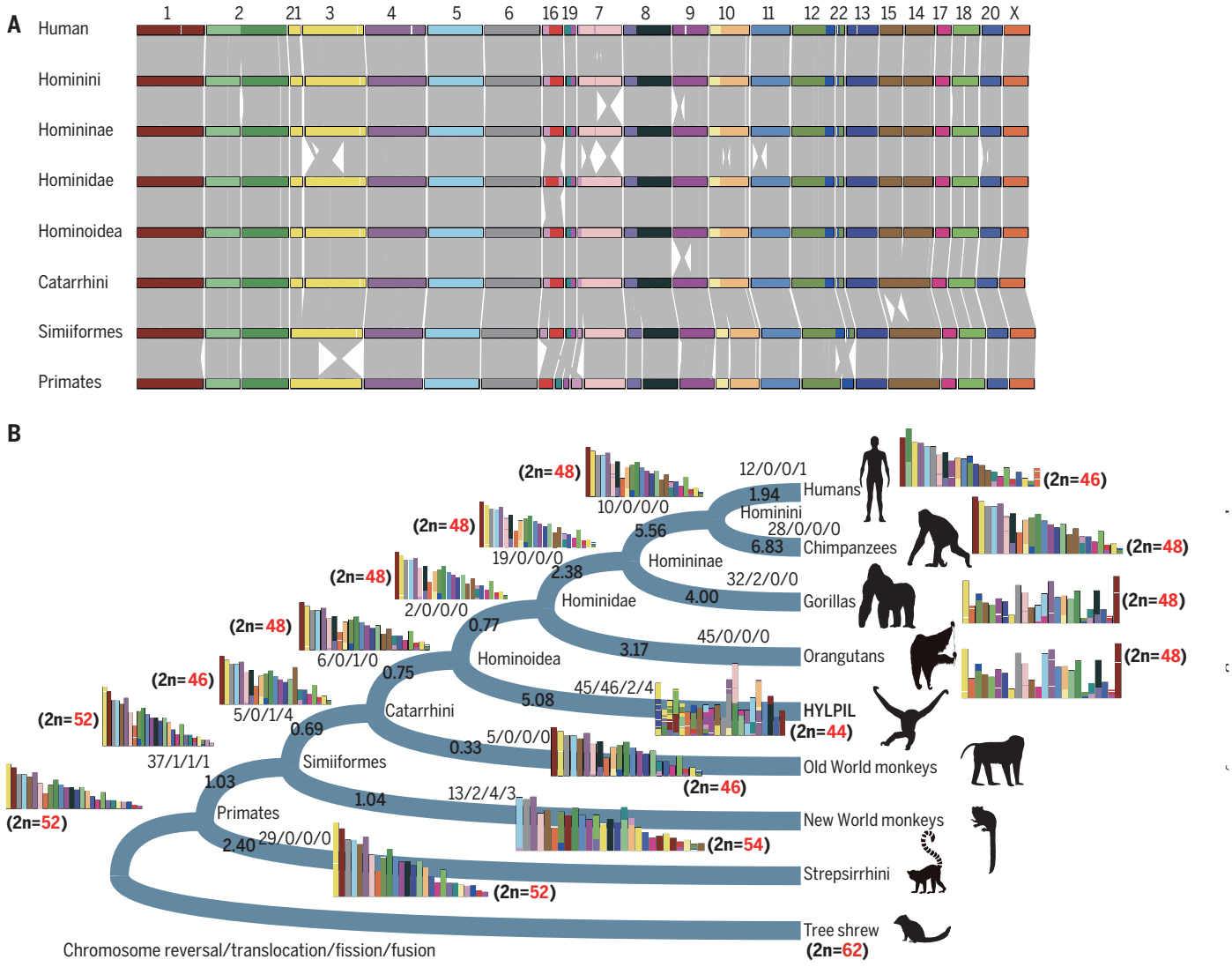


Fig. 2. Reconstruction of primate ancestral chromosomes. (**A**) Chromosome evolution patterns from the primate common ancestral lineage leading to the human lineage. Chromosomes are colored on the basis of human homologies. (**B**) Karyotype evolution and genome rearrangement. The rates of genomic rearrangement are highlighted in black bold font. Chromosome variations from ancestral nodes to derived branches are shown by pathways including chromosome reversal, translocation, and fission and fusion events, which are shown by number, e.g., reversal, translocation, fission, and fusion. "HYLPIL" represents the gibbon *Hylobates pileatus*, the genome of which was assembled at the chromosome level.

from the whole-genome alignments (table S9) and used to infer the primate phylogeny, yielding a high-resolution whole-genome nucleotide evidence tree with identical topology to a previous tree derived from 54 nuclear gene regions from 186 living primates (*35*). This tree has 100% bootstrap support for all evolutionary nodes, with the exception of the node ((*Symphalangus syndactylus*, *Hoolock leuconedys*), *Hylobates pileatus*) among gibbon genera with 90% bootstrap support (Fig. 1 and figs. S4 and S5). The evolution of gibbons has been characterized by their rapid karyotypic changes and remains controversial in primate phylogeny at the genus level (*24*, *35*, *36*). To confirm the phylogeny of this node, we also generated partitioned trees with orthologous protein-coding genes, exon codons with first and second positions, fourfold degenerate sites, and conserved nonexonic elements (figs. S6 to S9). The tree from conserved nonexonic elements yielded the identical topologies for the gibbon lineages with the whole-genome nucleotide evidence trees (fig. S9). However, the trees from orthologous protein-coding genes and exon codons with first and second positions and fourfold degenerate sites, respectively, supported the alternative topologies, ((*Nomascus*, *Hylobates*), (*Symphalangus*, *Hoolock*)) and ((*Nomascus*, (*Symphalangus*, *Hoolock*)), *Hylobates*) (figs. S6 to S8). The two topologies were shown in previous studies based on variants called by mapping short reads to the reference genome of *Nomascus leucogenys* (*24*, *36*).

Our analyses again confirmed the phylogenetic challenge within the gibbon lineage, which has experienced pronounced adaptive radiation within an extremely short evolutionary time period (*24*, *35*). Consistently, we observed extremely short internal branches in this lineage on the phylogeny. A comparative analysis using CoalHMM (*37*) across primate lineages showed that the gibbon lineage represents one of the lineages with the highest frequency of incomplete lineage sorting (*38*), supporting a previous study based on population data (*24*). Specifically, the two gibbon branches showed incomplete lineage-sorting

proportions of 57 and 61%, respectively, but the species topology inferred from incomplete lineage-sorting analyses was identical to those presented herein (figs. S4 and S10).

Using the whole-genome nucleotide evidence tree and fossil calibration data (*35*, *39*) (Fig. 1 and fig. S11), the divergence dating of living primates was estimated by means of the MCMCtree algorithm (*40*) (Fig. 1 and fig. S12). We estimated that the most recent common ancestor of all primates evolved between 64.95 and 68.29 million years (Ma) ago, which is close to the estimate given in the latest phylogenetic study across mammals (*41*), suggesting that the origin of the primate group was near the Cretaceous–Tertiary boundary at 66 Ma ago. We also estimated that the most recent common ancestor of Strepsirrhini appeared between 52.57 and 56.56 Ma ago, and that of the Simiiformes emerged between 35.65 and 42.55 Ma ago (Fig. 1 and fig. S12).

Genomic structure and evolution of primates

Karyotype evolution and genome rearrangement

The speciation process is often accompanied by karyotypic evolution, which also affects genome evolution and gene function (*42*–*44*). We reconstructed the ancestral karyotype evolutionary process across primate lineages (table S10) and observed an overall conserved pattern of chromosome-level synteny (Fig. 2A). The numbers of ancestral karyotypes of Catarrhini ($2n$ = 46) and Hominoidea ($2n$ = 48) were consistent with previous inferences derived from the fluorescence in situ hybridization data of bacterial artificial chromosomes (*45*) (Fig. 2A). However, we deduced that both of the ancestral karyotypes of primates and Simiiformes had a diploid number of $2n$ = 52 (Fig. 2A) rather than $2n$ = 50 as previously suggested (*45*), recovering a fission event in chromosome 8 that was observed in the common ancestor of primates (Fig. 2A and fig. S13). Fusion and fission are the most common mechanisms of karyotype evolution in primates, as exemplified by the fusion of chromosome 2, which occurred specifically in the human lineage (*45*). Our analyses further identified at least one fission and one fusion during the emergence of the Simiiformes, as well as one fission and four fusions associated with the Catarrhini node (Fig. 2B and fig. S13), resulting in the contemporary karyotype structure of our own. The rapid change of karyotypes in the Simiiformes also led to an increased chromosome number in New World monkeys, which have the largest number of chromosomes across primates. We further estimated the rate of genome rearrangement by taking into account all large-scale genomic rearrangement events, including reversions, translocations, fusions, and fissions, in key evolutionary nodes from the primate common ancestral lineage leading to the human lineage. We observed an increasing rate of rearrangement in the Homininae (*Gorilla-Homo-Pan*) (~2.38/Ma) and particularly in the Hominini (*Homo-Pan*) (~5.56/Ma) (Fig. 2B), which contradicts the Hominini slowdown hypothesis on the nucleotide substitution rates (*35*).

Lineage-specific segmental duplication

We next compiled segmental duplication maps (segmental duplication length ≥5 kbp) for primates and five outgroup species (fig. S14 and table S11). Compared with other primate lineages, we observed a marked increase in the number of lineage-specific segmental duplications (n = 221) in the great ape genomes (Fig. 3A and table S12), consistent with previous findings describing a burst of segmental duplications in the great ape ancestor (*46*). These specific segmental duplications in great apes overlapped with 57 protein-coding genes (table S13), 20 of which were highly expressed in the human brain (fig. S15). We also observed lineage-specific segmental duplications in other primate groups producing lineage-specific new genes that might have contributed to the evolution of these lineages (table S13). We further explored the functions of all genes overlapping segmental duplications in primate genomes (table S13) against the Human Gene Mutation Database (*47*), and found that a high proportion of these genes (52.8%) have been reported to be associated with inherited conditions including autism, intellectual disabilities, and other developmental disorders (Fig. 3B and table S14).

Evolution of genome size and transposable elements

Compared with other mammalian groups, the primates on average have a relatively large genome size (*48*, *49*). Among primates, the lemurs (Lemuriformes and Chiromyiformes) were found to be characterized by a significantly smaller genome size (~2.36 Gbp) than other groups such as the lorisoids (Lorisiformes: Lorisdae and Galagidae, ~2.70 Gbp), New World monkeys (~2.82 Gbp), Old World monkeys (~2.91 Gbp), and Hominoidea (~2.96 Gbp) (P < 0.05, Mann-Whitney U test) (fig. S16). The increase of genome size in the Simiiformes can be attributed to the expansion of transposable elements (figs. S16 to S18 and table S15), especially *Alu* elements, ~300 nucleotide short interspersed sequence elements (SINEs) that make up ~11% of the human genome (*50*–*54*). We observed that the genomes of lemurs exhibited a relative paucity of SINEs, especially *Alu* (~3.87%), which is less than one-third of the proportion noted in other lineages (figs. S16 to S18). By contrast, the *Alu* elements in both Simiiformes and Lorisiformes experienced major bursts of retrotranspositional activity at ~40 to 45 and ~34 to 39 Ma ago independently (fig. S19). Specifically, we noticed a substantial expansion of the *AluS*-related subclasses, especially *AluSx* in the Simiiformes, whereas the *AluJ*-related subclasses (especially *AluJb*) were the dominant subclasses of *Alu* in the Lorisiformes (fig. S20).

Variation in the nucleotide substitution rate

We estimated the overall nucleotide substitution rate in primates to be ~1.1×10^{-3} substitutions per site per million years (Fig. 3C, fig. S21, and table S16), which is much lower than the average rate for mammals (~2.7×10^{-3}) and birds (~1.9×10^{-3}) (*55*). However, the nucleotide substitution rate exhibited a high degree of heterogeneity between primate lineages, potentially caused by differences with respect to life history traits (*56*–*58*). The New World monkeys evolved the fastest at ~1.4×10^{-3} substitutions per site per million years (Fig. 3C and fig. S21). We confirmed the hominoid "slowdown" (*35*, *59*–*61*) hypothesis by detecting a reduced substitution rate in hominoids (~0.8×10^{-3} substitutions per site per million years) (fig. S21). Our analysis and a previous study (*62*) suggested that tarsiers, as the most basal haplorrhines, potentially evolved with a rapid substitution rate compared with other primates (fig. S21).

Evolution of protein-coding genes

We obtained a high-confidence orthologous gene set comprising 10,185 orthologs across 50 primate species, along with the Sunda flying lemur and the Chinese tree shrew. On the basis of the whole-genome nucleotide evidence tree topology of primates, we calculated the ratio of the rates of nonsynonymous (d_N) to synonymous (d_S) substitutions for each ortholog to explore the evolutionary constraints operating on coding regions. We estimated the evolutionary rate of tissue-specific expressed genes for different tissues across evolutionary clades in primates based on the observation that tissue-specific expressed genes are generally conserved across diverse species (*63*, *64*), and observed that testis- and spleen-specific expressed genes generally displayed higher values of d_N/d_S (Fig. 3D and figs. S22 and S23) than other tissue-specific expressed genes, corroborating the rapid evolution of the reproductive and immune systems in primates (*65*, *66*). By contrast, brain-specific expressed genes generally showed a high degree of conservation with lower d_N/d_S values, as previously reported, despite the rapid evolution of primate cognitive functions (*67*).

Next, we detected 82 positively selected genes in the common ancestral lineage of primates by comparison with other mammalian species (table S17) using the codeml algorithm under the branch-site model with a likelihood rate test in PAML4 (*40*, *68*). We found that these positively selected genes were significantly enriched in genes exhibiting high-level

expression in brain, bone marrow, and testis (table S18). In particular, close to 37% (30 genes) of positively selected genes exhibited biased expression in the brain (tables S18 and S19), and we found that some of them (e.g., *SPTAN1*, *MYT1L*, and *SHMT1*) could have important roles in brain function, because deleterious mutations of these genes have been reported to cause brain disorders (*69*–*71*) such as epilepsy and schizophrenia. These genes may be important candidates for involvement in the evolution of the primate brain because of their functional importance. Our results suggest that some positively selected genes in the primate ancestral lineage may have been involved in the rapid evolution of their brain functions despite the general conservation of brain-specific expressed genes. In addition, several immune-related genes (e.g., *XRCC6* and *CD2*) (table S17) also experienced positive selection in the primate ancestor, suggesting that the adaptive immune system might also have contributed to primate evolution.

An increased level of genomic change in the ancestor of the Simiiformes

To provide new insights into the genetic underpinnings of primate phenotypic evolution, we performed various comparative genomic analyses, including the identification of positively selected genes, genes having conserved noncoding regions that have been subject to lineage-specific accelerated evolution (*72*), and expanded gene families in different primate lineages (*68*). An increased level of genomic evolutionary changes, as reflected by the high numbers of positively selected genes, lineage-specific accelerated regions, and expanded gene families, was observed in the Simiiformes ancestor (Fig. 4A). Consistently, the Simiiformes have also experienced rapid evolution of a series of complex traits, unlike

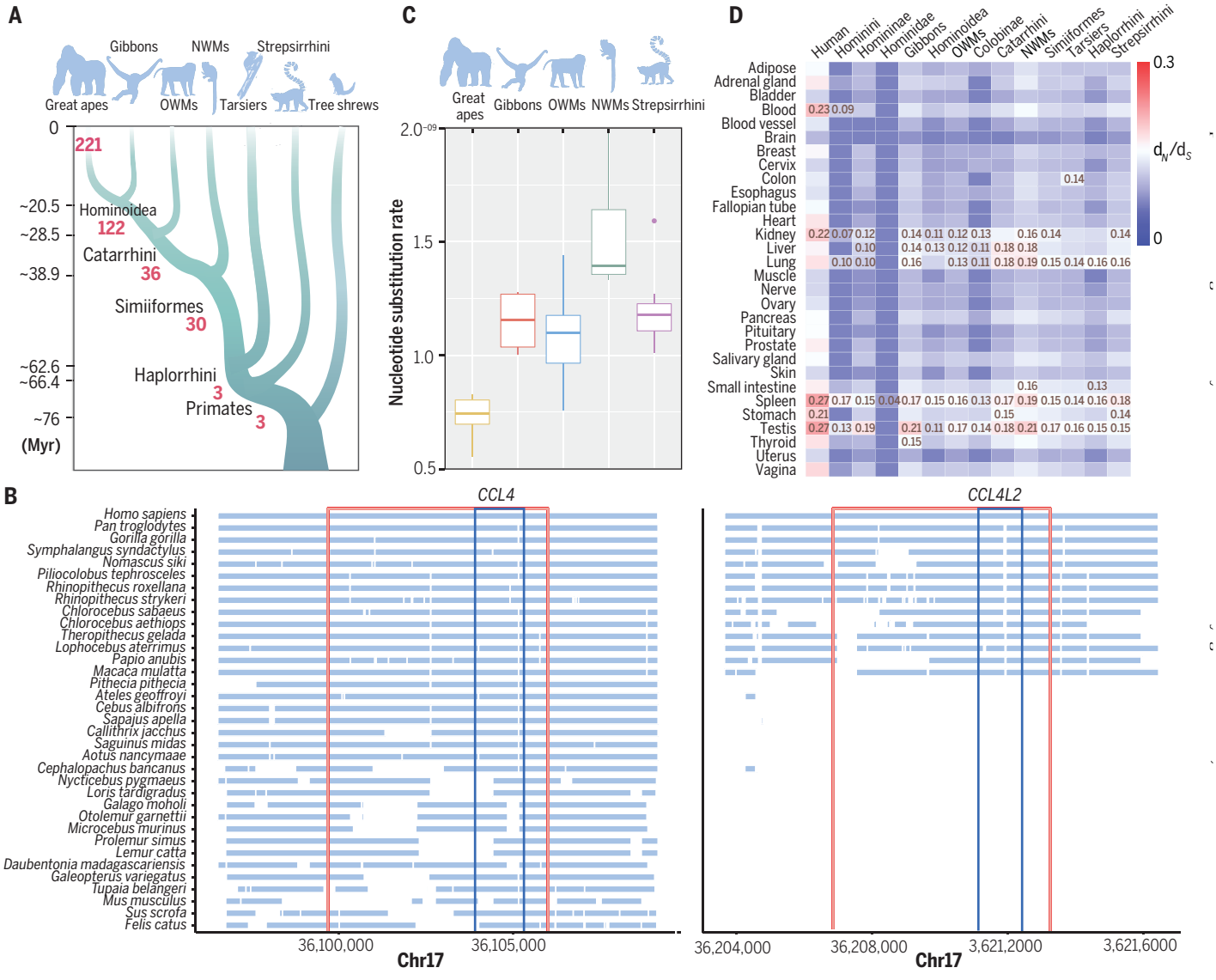


Fig. 3. Structural evolution in primate genomes. (**A**) Evolutionary pattern of lineage-specific segmental duplications in primates. The numbers of lineage-specific segmental duplications are shown in red. The largest number of segmental duplications was found in the great ape lineage. OWMs, Old World monkeys; NWMs, New World monkeys. (**B**) Example of specific segmental duplications during evolution of the genome in Catarrhini. A gene pair overlapping the segmental duplication (left, *CCL4*; right, *CCL4L2*) is associated with HIV susceptibility. The red and green boxes represent the segmental duplication region and the overlapping gene pair, respectively. (**C**) Substitution rates across five evolutionary branches in primates. (**D**) Evolutionary constraints of tissues across diverse lineages in primates. The evolutionary constraints of tissues are shown by the d_N/d_S median of tissue-specific expressed genes in different evolutionary nodes among primates.

the Strepsirrhini and Tarsiiformes. For example, the Simiiformes generally exhibit a larger brain volume and body mass than the Strepsirrhini and Tarsiiformes (Fig. 4B) (*73*, *74*). Functional enrichment analyses showed that the associated genes relevant to these rapid genomic changes in the Simiiformes ancestor (tables S20 to S22) were overrepresented in functions related to the nervous system and development, such as postsynaptic density, synapses, and the negative regulation of the canonical Wnt signaling pathway (table S23).

Additional analyses indicated that various candidate genes in the Simiiformes ancestral lineage, comprising 168 positively selected genes, 273 genes associated with lineage-specific accelerated regions, and 14 expanded gene families, were enriched in central nervous system terms, i.e., brain, cerebrum, cerebellum, hippocampus, and cerebral cortex (table S24). More specifically, five genes participated in pathway axon guidance (Fig. 4C), being expressed in the human brain at a high level (table S25). Axon guidance represents a key stage in the formation of a neural network (*75*, *76*) and may have been an important influence on brain volume. In this pathway, two semaphorin genes, *SEMA3B* and *SEMA3D*, which are critical for central nervous system patterning (*77*, *78*), experienced positive selection and served as a gene associated with the lineage-specific accelerated region, respectively. These two genes, together with another three genes associated with the lineage-specific accelerated regions, *EPHA3*, *RAC1*, and *NTNG2*, are known to be important for brain development (*79*–*81*). Furthermore, eight genes were assigned under the term "Hippo signaling pathway" (Fig. 4D), an evolutionarily conserved signaling pathway that controls organ or body size by regulating cell growth, proliferation, and apoptosis in a range of animals from flies to humans (*82*–*84*). Genes involved in neuronal network formation and the control of organ size appear to have undergone adaptive evolution in the Simiiformes ancestral lineage and may have been responsible for specific phenotypic changes, particularly the progressive

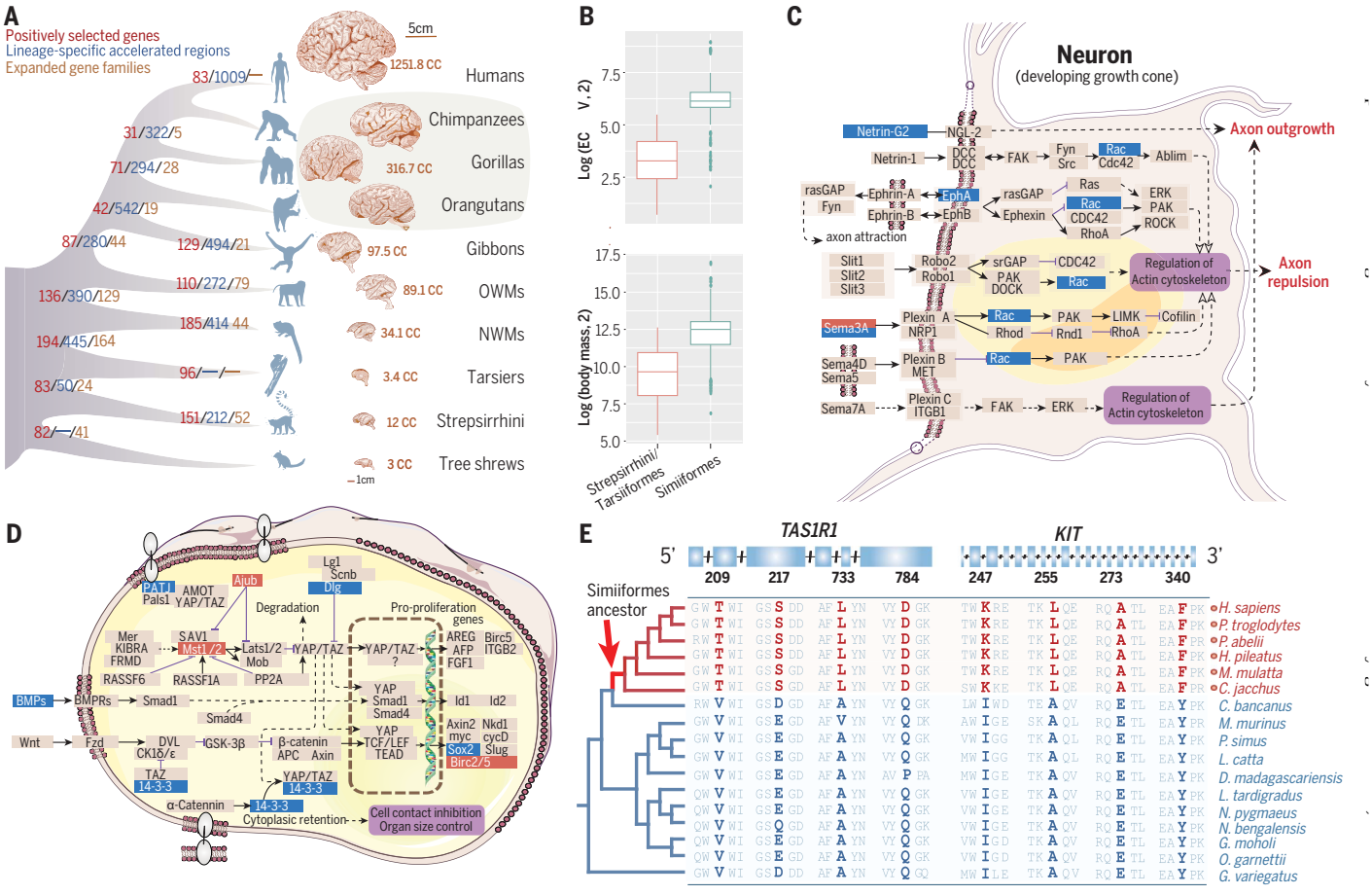


Fig. 4. Genomic changes and phenotype evolution in the ancestor of the Simiiformes. (**A**) Increased level of genomic evolutionary change, including positively selected genes, lineage-specific accelerated regions, and significantly expanded gene families, seen in the Simiiformes ancestral lineage. The brain sizes and brain structures are shown in representative evolutionary groups of primates. The brain sizes across primate and outgroup species are derived from previous studies (*156*, *157*). Brain images are from the Michigan State University Comparative Mammalian Brain Collections (www.brainmuseum.org). (**B**) Representative phenotype variations, including brain size and body mass, between the Strepsirrhini and Tarsiiformes and the Simiiformes. Statistical significance was assessed by the Mann-Whitney *U* test as $P < 0.05$. (**C**) Candidate genes involved in the axon guidance KEGG pathway (hsa04360). Genes relating to genomic changes in the Simiiformes ancestral lineage are shown in this pathway. The protein product of the positively selected gene in the Simiiformes ancestral lineage, *SEMA3B*, is shown in red. The protein products of genes associated with lineage-specific accelerated regions, *EPHA3*, *RAC1*, *NTNG2*, and *SEMA3D*, are shown in blue. (**D**) The Hippo signaling pathway (hsa04390), which is involved in organ size and body size, with candidates including positively selected genes and genes associated with lineage-specific accelerated regions. The gene products for positively selected genes (*LIMD1*, *BIRC3*, and *STK3*) in the Simiiformes ancestral lineage are shown in red, and the products of genes associated with lineage-specific accelerated regions (*PATJ*, *SOX2*, *BMP2*, *DLG2*, and *YWHAQ*) in the Simiiformes ancestral lineage are shown in blue. (**E**) Multiple sequence alignments of two positively selected genes, *TAS1R1* and *KIT*, along the Simiiformes ancestral lineage. The phylogenetic position of the Simiiformes ancestor is indicated by a red arrow.

increase in brain volumes and body sizes compared with the Tarsiiformes and Strepsirrhini.

A major phenotypic difference between the Strepsirrhini and Tarsiiformes and the Simiiformes is nocturnal versus diurnal life history. The visual system has diverged substantially between the Strepsirrhini and Tarsiiformes and the Simiiformes such that the diurnal Simiiformes have much smaller corneal sizes (relative to their eyes) and higher visual acuity than the Strepsirrhini and Tarsiiformes (*85*). Consistent with this phenotypic difference, we detected positive selection signals in three genes, *NPHP4*, *GRHL2*, and *SLC39A5*, which are associated with eye development (Gene Ontology identifier: 0001654) in the Simiiformes ancestral lineage. An intragenic deletion in *NPHP4* causes recessive cone-rod dystrophy with a predominant loss of cone function in the dachshund (*86*). *GRHL2* encodes a transcription factor that suppresses epithelial-to-mesenchymal transition; ectopic *GRHL2* expression caused by mutation accelerates cell state transition and leads to posterior polymorphous corneal dystrophy and vision function disruption (*87*). The *GRHL2* gene has the highest number of positively selected sites in the Simiiformes ancestor compared with the other genes involved in eye development (fig. S24). *TAS1R1* encodes a taste receptor that can form a heterodimer with TAS1R3 to elicit the umami taste (*88*). We found that *TAS1R1* also experienced positive selection with four positively selected sites in the Simiiformes ancestor (Fig. 4E). The rapid and concerted evolution of taste receptors and vision could have helped the diurnal Simiiformes to locate and identify food. The detailed functional consequences of these amino acid changes might be worthy of further study.

Compared with the Strepsirrhini and Tarsiiformes, the Simiiformes generally exhibit darker skin pigmentation and a less bright coat color (fig. S25) (*89*). We identified two pigmentation-related genes, *KIT* and *CREB3L4*, that participate in the melanogenesis pathway that evolved under positive selection (detected by the branch-site model) in the Simiiformes ancestor (Fig. 4E). Melanocytes play an important role during the formation of skin and coat colors in mammals by regulating melanin-related genes (*90*). *KIT*, a proto-oncogene, encodes a receptor tyrosine kinase that regulates cell migration, proliferation, and differentiation in melanocytes and plays a key role in melanin deposition (*91*, *92*). *KIT* also communicates with *MITF*, a key gene in the formation of melanin that regulates the development of melanocytes (*93*–*95*).

Genetic mechanisms underlying primate phenotype evolution

Primates have evolved diverse phenotypic traits to adapt to their challenging environments. Here, we sought to investigate the evolution of complex phenotypes in the brain, skeletal system, digestive system, and sense organs, as well as body size, in primates.

Brain evolution

In primates, brain volumes range from <~2 cm^3 in the mouse lemur to ~1300 cm^3 in human (*73*). To reveal the genetic changes that might underlie brain evolution in primates, we detected signals of positive selection in brain development genes using a branch-site model in PAML in key evolutionary nodes in the primate phylogeny. A total of 34 brain genes were found to be under positive selection in one of the primate evolutionary nodes (table S26) (*68*). Four of them, *SLC6A4*, *NR2E1*, *NIPBL*, and *XRCC6*, were under positive selection in the common ancestor of all primates, whereas 30 were under positive selection in other primate ancestral nodes leading to the evolution of humans (table S26). These results appear to suggest that primates underwent continuous brain evolution over an extended period of evolutionary time. Knockout experiments in mice on many of these positively selected genes have shown brain function impairment. For instance, the *NIPBL* gene interacts with *ZFP609* to regulate the migration of cortical neurons, and its mutations are frequently involved in brain neurological defects encompassing intellectual disability and seizures (*96*). We identified two amino acid residues in the NIPBL protein that experienced adaptive change in the common ancestor of all primate lineages (fig. S26).

Microcephaly is characterized by severe neurological defects, the small brain size being caused by a disturbance of the proliferation of nerve cells (*97*). Some genes involved in microcephaly have been proposed as candidates for involvement in the evolution of brain size (*98*–*100*). We also searched for positive selection signals in the 1113 coding genes involved in microcephaly (g:Profiler identifier HP:0000252). In total, 65 positively selected genes with functional roles in microcephaly were identified, along with the primate ancestor leading to the human lineage (table S27), suggesting that microcephaly genes may have been involved in the marked evolutionary expansion of brain size that characterizes primates, especially in those crucial evolutionary nodes characterized by a sharp increase in the degree of cortical folding (gyrification) and brain volume (*101*).

We next sought to investigate the roles of regulatory elements in the evolution of primate brain size. We first identified noncoding regions that were highly conserved and under strong purifying selection across all primates and detected signals of accelerated evolution in four lineages: the Simiiformes ancestor (table S21), the Catarrhini ancestor (table S28), the ancestor of great apes (table S29), and the human lineage (table S30), representing crucial evolutionary nodes for the enlargement of primate brain size (*101*) (fig. S27). These lineage-specific accelerated regions should be under strong positive selection specifically in the targeted lineages and might contribute to the adaptation or innovation of these lineages (*72*). We found 15 genes associated with lineage-specific accelerated regions in the common ancestor of the great apes that showed particularly high expression in the human fetal brain (fig. S27 and table S31) (P = 0.023, modified Fisher's exact test). More than half of these genes have been reported to have roles in brain development and function (*102*–*109*). For example, knockout of the transcription factor–encoding *MEF2C* in a mouse model resulted in impaired neuronal differentiation and smaller somal size among neural progenitor cells (*108*). Coincidentally, the lineage-specific accelerated region of this gene was detected in the great ape ancestral lineage. The *DLG5* gene, which is required for the polarization of citron kinase in mitotic neural precursors, also contains a lineage-specific accelerated region in the great ape lineage, and $DLG5^{-/-}$ mice have smaller brains and thinner neocortices (*109*, *110*).

We further investigated the evolution of neurotransmitters, which mediate the neurogenesis process (*111*, *112*) and also play a role in the regulation of brain size (*111*). We detected 12 positively selected genes and 39 genes associated with lineage-specific accelerated regions in the ancestral nodes leading to the human lineage that were found to be involved in the release, transportation, and reception of neurotransmitter signals (Fig. 5A and fig. S28). These genes participate in diverse neurotransmitter systems: glutamatergic, dopaminergic, cholinergic, and GABAergic synapses and the synaptic vesicle cycle. Among these, five positively selected genes and 33 genes associated with lineage-specific accelerated regions are highly expressed in the human brain (table S32). It is likely that at least some of these genomic changes affecting the neurotransmitter signaling pathway might have played a role in primate brain evolution.

Evolution of the skeletal system and limbs

The arboreal lifestyle coevolved with adaptive changes of the skeletal system and limb development. Genes functioning in bone development are likely to have been especially important for the adaptive radiation of the primates. We identified four positively selected genes, *PIEZO1*, *EGFR*, *BMPER*, and *NOTCH2*, that were involved in bone development (*113*–*116*) in the ancestral lineage of primates (table S17). Bone development requires the recruitment of osteoclast precursors from the surrounding mesenchyme, thereby actuating the key events of bone growth, such as marrow cavity formation, capillary

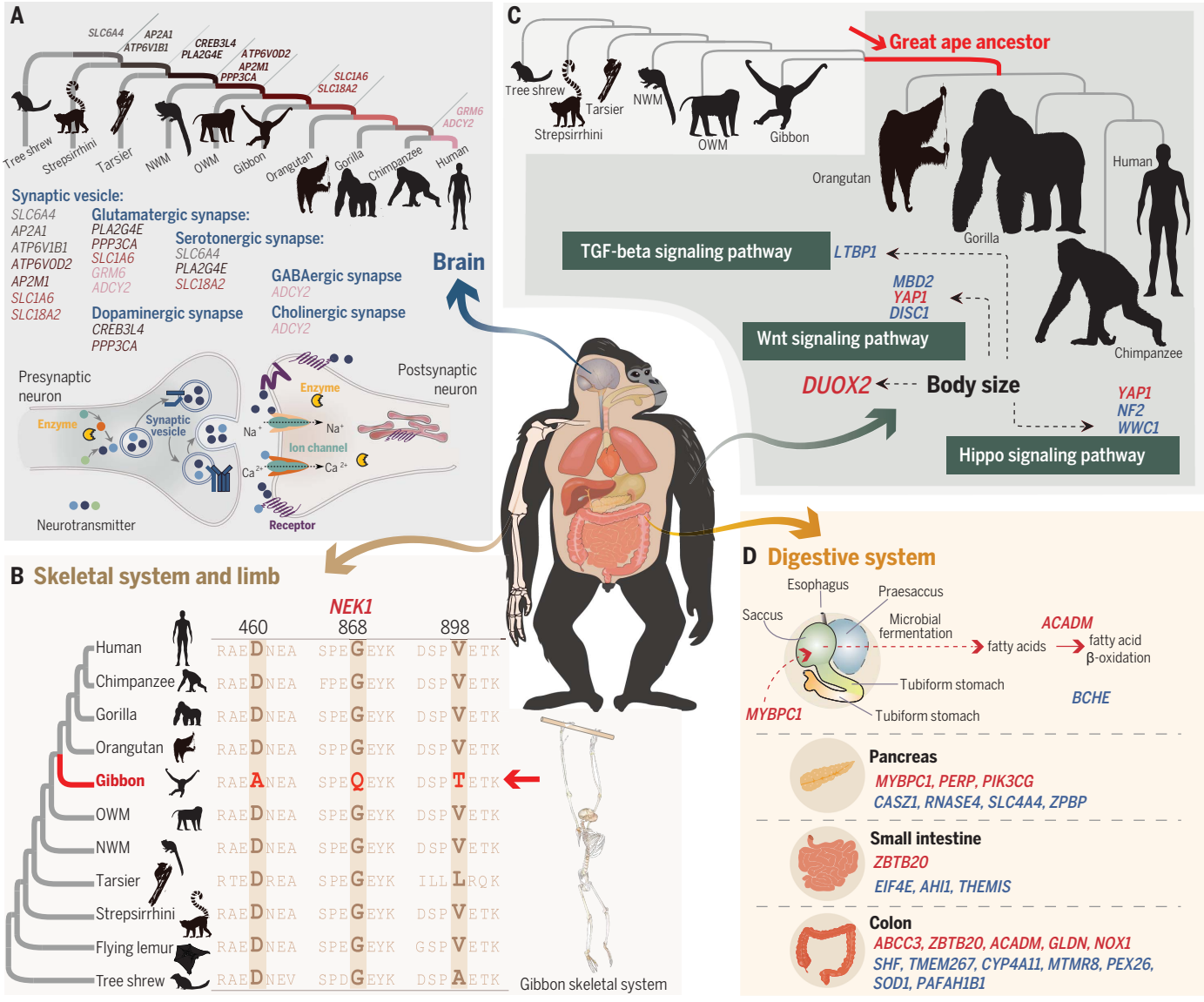


Fig. 5. Associations between genomic evolutionary characteristics and phenotypic traits in primates. (**A**) Positively selected genes and genes associated with lineage-specific accelerated regions from the primate ancestral lineage leading to the human lineage that are involved in transport, release, and receptors in neurotransmitter signaling. (**B**) The *NEK1* gene, which is involved in upper limb bone development, was under positive selection with three positively selected sites in the gibbon ancestral lineage. The gibbon ancestor is shown in red. (**C**) Eight positively selected genes and genes associated with lineage-specific accelerated regions from the great ape ancestral lineage involved in the TGF-β, Wnt, and Hippo signaling pathways. (**D**) Positively selected genes and genes associated with lineage-specific accelerated regions involved in the evolution of the digestive system in the Colobinae ancestral lineage. Genes marked in red and blue represent positively selected genes and genes associated with lineage-specific accelerated regions, respectively, in this lineage.

invasion, and matrix remodelling. The mechanical sensing protein PIEZO1 accommodates bone homeostasis through osteoclast-osteoblast cross-talk (*113*). Osteoclasts then influence osteoblast formation and differentiation through the secretion of some soluble factors (*117*). *EGFR* negatively regulates mTOR signaling during osteoblast differentiation to control bone development (*114*). The *NOTCH2* gene regulates cancellous bone volume and microarchitecture in osteoblast precursors (*116*, *118*).

Although tails vary in length and shape across the primates, they generally play key roles in relation to locomotion (*119*). This notwithstanding, the tail was lost in some primate lineages, including the common ancestor of the apes (*120*, *121*). We retrieved 151 genes associated with lineage-specific accelerated regions in the common ancestral lineage of the apes (table S33), including *KIAA1217* (sickle tail protein homolog) (figs. S29 and S30). Mutations in *KIAA1217* are associated with malformations of the notochord and caudal vertebrae in humans, and in mice they affect the development of the vertebral column, leading to a characteristic short tail due to a reduced number of caudal vertebrae (*122*, *123*). Thus, the lineage-specific accelerated region may serve as a regulator of the expression of *KIAA1217*, because this lineage-specific accelerated region, residing in the vicinity of *KIAA1217* in the ape lineage, overlaps with the enhancer EH38E1455433 (pELS) (fig. S31). High-throughput chromosome conformation capture data (fig. S32) also showed that this lineage-specific accelerated region is located in the same topologically associated domain as *KIAA1217*, suggesting that they may physically interact with each other. Furthermore, the

lesser apes (gibbons) are of particular interest because of their dominant locomotor style, brachiation (*124*, *125*). This locomotor adaptation was accompanied by the acquisition of distinct morphological characteristics, particularly the elongated forelimb, representing one of the most intriguing phenotypic traits in gibbons that enables them to travel through the canopy at high speed (*126*). We found that positive selection has operated on four genes related to upper limb bone morphology in the gibbon ancestral lineage (table S34). Of these, *NEK1*, which encodes a serine or threonine kinase, contains the most positively selected sites (Fig. 5B). Functional studies have shown that genetic variants in this gene can influence bone length and shorten the humerus and femur in humans (*127*, *128*). Therefore,

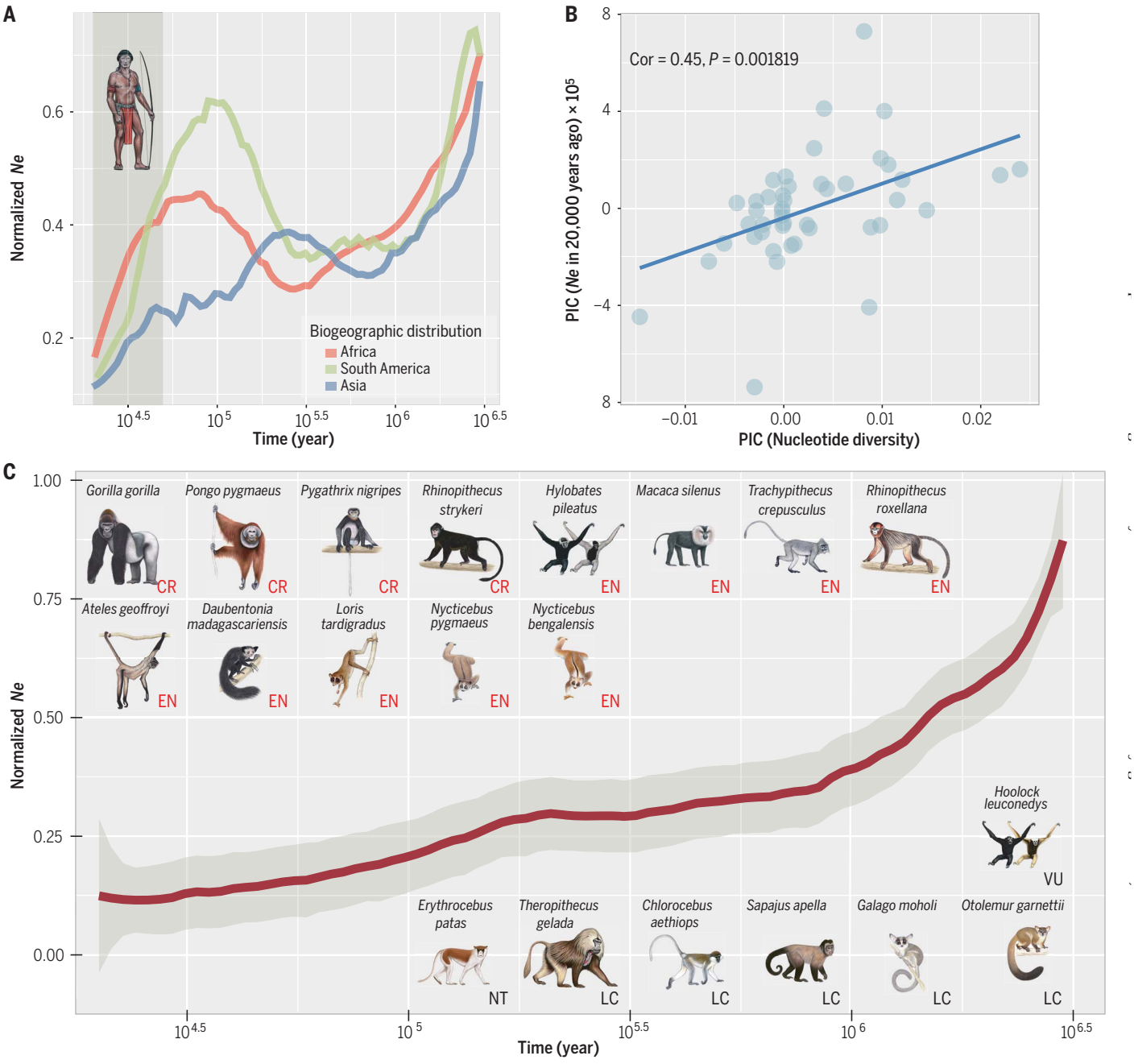


Fig. 6. Demographic history of nonhuman primates. (**A**) Primate species grouped according to their biogeographic distribution (Africa, Asia, or South America). The plot shows the normalized demographic history of all species within each biogeographic region. The normalized N_e was inferred by dividing the estimated value of N_e for each species at each time point by its maximum value. *Callithrix jacchus* was removed from this analysis because the genome was derived from an inbred individual. The time period from 50,000 to 20,000 years ago (late Pleistocene) is indicated by a gray background. (**B**) Correlation analysis between nucleotide diversity and N_e after phylogenetic corarection using the Ape library in R (http://ape-package.ird.fr/). N_e represents the median value of effective population size for each species 20,000 years ago. (**C**) Nearly half (n = 20) of all nonhuman primate species experienced a continual decline in N_e over the past 3 million years. These include the 13 critically endangered or endangered species shown in red. The IUCN Red List status is shown for each species in the inserted plot: CR, critically endangered; EN, endangered; VU, vulnerable; NT, near threatened; and LC, least concern.

positive selection acting on genes related to upper limb bone morphology may have been important in the acquisition of the elongated forelimb, a key adaptive trait for the unique brachiating locomotion style of gibbons.

Evolution of body size in primates

Like other mammalian groups (*129*, *130*), extant primate species exhibit a large range of body sizes, from dwarf galagos and mouse lemurs (~60 to 70 g) at one end of the spectrum to male gorillas (>200 kg in some individuals) at the other (*131*). Thus, primate body size has experienced significant divergence, particularly for the great apes with their substantial enlargement in body size. We detected several positively selected genes in the common ancestors of the great apes that might have contributed to the evolution of this trait. *DUOX2* encodes a protein involved in a critical step of thyroid hormone synthesis, and mutations in *DUOX2* are known to cause decreased body size in mouse and panda (*132*, *133*). This gene experienced strong positive selection in the great ape ancestral lineage (P = 0.018, χ^2 test) (Fig. 5C and table S35). Additionally, we found several genes involved in the transforming growth factor-β (TGF-β) signaling pathway (e.g., *LTBP1*) or the Wnt signaling pathway (e.g., *MBD2*, *YAP1*, and *DISC1*), two of the best known pathways participating in bone development and body size (*48*), that were either under strong positive selection in the great apes or had lineage-specific accelerated regions in this lineage (Fig. 5C and tables S29 and S35).

Several positively selected genes and genes associated with lineage-specific accelerated regions in the great ape ancestor were also significantly overrepresented in the Hippo signaling pathway (P = 0.045, modified Fisher's exact test) (table S36), which has been implicated in the determination of organ and body size (*82*). When combining all positively selected genes, genes associated with lineage-specific accelerated regions, and expanded gene families in the Simiiformes ancestral lineage, which markedly increased their body size compared with non-Simiiformes lineages (Fig. 4B), we also detected diverse candidate genes with adaptive changes in the Hippo signaling pathway. These results indicate potentially important roles for the Hippo pathway in body size changes in these two nodes during primate evolution.

Evolution of the digestive system

Primate lineages have evolved diverse dietary habits and specialized digestive functions (*134*). In particular, leaf-eating colobines, an African and Asian subfamily (Colobinae) of Old World monkeys, have evolved a uniquely specialized and compartmentalized foregut in which there are discrete alkaline and acidic sections to cope with their folivorous diet and microbial fermentation can take place (*135*, *136*). Although colobines eat leaves, fruits, flowers, and seeds, they typically focus much of their feeding time on leaves (estimated range: ~34 to 81% of their annual diet) (*135*). Accordingly, these leaf-eaters are well adapted in terms of meeting their energy metabolism requirements and balancing micronutrients and protein intake while also dealing with the toxins contained in their food plants (*137*).

In the ancestor of the Colobinae, we identified a number of pivotal digestive genes that underwent positive selection (table S37). Acyl-CoA dehydrogenase, encoded by the *ACADM* gene, is an important lipolytic enzyme that catalyzes the initial step in each cycle of mitochondrial fatty acid β-oxidation and plays a key role in metabolizing fatty acids derived from ingested foods (*138*). Energy-rich short-chain volatile fatty acids are produced by the microbial fermentation process and absorbed by the host, thus making an important contribution to the energy budget of colobines (*135*). Therefore, rapid evolution of this gene, with two positively selected sites (V75M and A138C), may have been important for the absorption of fatty acids by colobines (Fig. 5D and fig. S33). *NOX1*, which is highly expressed in the colon, was identified as being under positive selection in the ancestor of the Colobinae (Fig. 5D and tables S37 and S38). *NOX1*-dependent reactive oxygen species production can further regulate microorganism homeostasis in the ileum of mice (*139*). The rumens of ruminants and the saccus stomachs of colobines have developed a similar adaptive strategy to allow the microbial fermentation of high-fiber foods, and therefore are an example of convergent evolution. We found that *MYBPC1*, which has been shown to contribute to morphological and functional differences in the bovine rumen (*140*), also underwent positive selection in the ancestor of the Colobinae (Fig. 5D and table S37). In addition, 100 genes associated with lineage-specific accelerated regions were identified in the ancestral lineage of the Colobinae (table S39). Several of these genes were also highly expressed in the stomach, colon, pancreas, and small intestine (Fig. 5D and table S38). Of these, *RNASE4* encodes a vital digestive enzyme, pancreatic ribonuclease 4, and is a paralog of *RNASE1*, which is known to have undergone adaptive evolution by gene duplication in leaf-eating colobines and howler monkeys (*26*, *141*). Colobines may therefore have acquired adaptations to allow them to digest fatty acids and ribonucleic acids, and their unique foregut and intestinal microbiota enabled them to cope with their folivorous diet.

Evolution of sensory organs

In many mammals, olfaction is the dominant sense and provides much of the sensory information upon which animals rely to navigate, forage, and avoid predators or for social behavior and courtship (*134*). Most Strepsirrhini species are nocturnal, whereas most Simiiformes are diurnal with well-developed color vision systems attuned to their priorities in diurnal activity (*142*–*145*). By contrast, olfactory sensitivity appears to have decreased in the Simiiformes compared with the Strepsirrhini (*134*, *146*, *147*). Consistent with these findings, we found that the copy number of several specific olfactory receptor gene families was significantly reduced in the Simiiformes. For example, the olfactory receptor gene family *OR52A* underwent a significant contraction in the Simiiformes (40 species), with only ~0.7 copies on average, in contrast to the ~3.4 average copies in the Strepsirrhini (nine species) (figs. S34 and S35) ($P = 4.072 \times 10^{-5}$, Mann-Whitney U test). Anatomically, Strepsirrhini are characterized by the presence of a rhinarium, a moist and naked surface around the tip of the nose that is present in most mammals, including dogs and cats, but has been lost in the Simiiformes (*134*, *147*). Olfactory bulb volume, which correlates with olfactory receptor neuron population size, is also larger in the Strepsirrhini than in the Simiiformes (*146*, *148*). The *LHX2* gene, which participates in olfactory bulb development (*149*, *150*), experienced positive selection in the ancestor of the Strepsirrhini (P = 0.03, χ^2 test; table S40).

Demographic history of nonhuman primates

The IUCN lists more than one-third of primates as critically endangered or vulnerable (*1*). To evaluate the effects of climate change and human activity on the recent population declines in these primates, we inferred their demographic histories over the past million years by using the pairwise sequentially Markovian coalescent model (*151*) for each species in this study (fig. S36 and tables S16 and S41). Our data showed that most nonhuman primate species experienced rapid population declines during the late Pleistocene (Fig. 6A and fig. S37), consistent with the record of a large mass extinction of mammals during this period (*48*, *152*). Although we did not observe a significant difference between endangered species and other species in terms of nucleotide diversity (fig. S38 and table S42), we did detect a significant positive correlation between the median effective population size (N_e) over the past ~20,000 years and nucleotide diversity (P = 0.002, Pearson's product-moment correlation after phylogenetic correction) (Fig. 6B and table S42), indicating a long-term effect of N_e decline on the loss of genetic diversity. According to the historical demographic patterns, we further clustered all nonhuman primate species with similar trends of historical N_e, and found that 20 species experienced a

continual N_e decline over the past 3 million years (Fig. 6C). Sixty-five percent of these species are now listed as endangered or critically endangered (Fig. 6C and fig. S39). This ratio is twice that of the remaining species, suggesting that the prehistoric environmental effects (e.g., habitat fragmentation) (*26*) may also have driven population decline and contributed to the current endangered status of these species well before human interference in the modern era.

Conclusions

Understanding the evolution and genetic basis of human-specific traits requires a systematic comparison of genomes along the primate lineages. Previous studies of primate genomes have focused on genomic changes in the human lineage that influenced brain functions and other traits (*120*, *153*–*155*). Our comparative phylogenomic analyses across primate lineages have revealed some of the accumulated genomic changes at different primate ancestral nodes that may have contributed to the evolution of unique human traits. Of particular interest, we report a hitherto unreported increase in the rate of genomic change in the Simiiformes common ancestor that may have played a role in the later diversification of Simiiformes and the evolution of humans. Our comparative genomic analyses also yielded insights into the genetic basis of phenotypic diversity across primate lineages. With the rich diversity of morphology and physiology among nonhuman primates, further genomic analyses covering all primate species will provide an indispensable resource for comparative studies allowing expansion of the scope of biomedical research programs using primates as model systems. Further, increased knowledge of the genomic makeup and variations of nonhuman primates should help to identify risk factors for genetic disorders and enhance wildlife health management in both wild and captive members of these species.

REFERENCES AND NOTES

1. A. Estrada *et al*., *Sci. Adv.* **3**, e1600946 (2017).
2. C. Roos *et al*., *Zool. Res.* **41**, 656–669 (2020).
3. A. Nater *et al*., *Curr. Biol.* **27**, 3487–3498.e10 (2017).
4. P. F. Fan *et al*., *Am. J. Primatol.* **79**, e22631 (2017).
5. C. Li, C. Zhao, P. F. Fan, *Am. J. Primatol.* **77**, 753–766 (2015).
6. J. Rogers, R. A. Gibbs, *Nat. Rev. Genet.* **15**, 347–359 (2014).
7. B. Rockx *et al*., *Science* **368**, 1012–1015 (2020).
8. A. Chandrashekar *et al*., *Science* **369**, 812–817 (2020).
9. Q. Gao *et al*., *Science* **369**, 77–81 (2020).
10. J. Yu *et al*., *Science* **369**, 806–811 (2020).
11. V. J. Munster *et al*., *Nature* **585**, 268–272 (2020).
12. N. B. Mercado *et al*., *Nature* **586**, 583–588 (2020).
13. K. S. Corbett *et al*., *N. Engl. J. Med.* **383**, 1544–1555 (2020).
14. N. van Doremalen *et al*., *Nature* **586**, 578–582 (2020).
15. B. N. Williamson *et al*., *Nature* **585**, 273–276 (2020).
16. T. Z. Song *et al*., *Zool. Res.* **41**, 503–516 (2020).
17. W. Enard, S. Pääbo, *Annu. Rev. Genomics Hum. Genet.* **5**, 351–378 (2004).
18. Z. N. Kronenberg *et al*., *Science* **360**, eaar6343 (2018).
19. Chimpanzee Sequencing and Analysis Consortium, *Nature* **437**, 69–87 (2005).
20. R. A. Gibbs *et al*., *Science* **316**, 222–234 (2007).
21. A. Scally *et al*., *Nature* **483**, 169–175 (2012).
22. Marmoset Genome Sequencing and Analysis Consortium, *Nat. Genet.* **46**, 850–857 (2014).
23. D. P. Locke *et al*., *Nature* **469**, 529–533 (2011).
24. L. Carbone *et al*., *Nature* **513**, 195–201 (2014).
25. L. Yu *et al*., *Nat. Genet.* **48**, 947–952 (2016).
26. X. Zhou *et al*., *Nat. Genet.* **46**, 1303–1310 (2014).
27. A. O. Ayoola *et al*., *Mol. Biol. Evol.* **38**, 876–890 (2021).
28. D. M. Bickhart *et al*., *Nat. Genet.* **49**, 643–650 (2017).
29. B.-L. Zhang *et al*., *Sci. Adv.* **9**, eadd3580 (2023).
30. H. Wu *et al*., *Science* **380**, eabl4997 (2023) .
31. X.-G. Qi *et al*., *Science* **380**, eabl8621 (2023).
32. M.-L. Li *et al*., *Proc. Natl. Acad. Sci. U. S. A.* **119**, e2123030119 (2022).
33. M. S. Ye *et al*., *Zool. Res.* **42**, 692–709 (2021).
34. A. M. Kozlov, A. J. Aberer, A. Stamatakis, *Bioinformatics* **31**, 2577–2579 (2015).
35. P. Perelman *et al*., *PLOS Genet.* **7**, e1001342 (2011).
36. C. M. Shi, Z. Yang, *Mol. Biol. Evol.* **35**, 159–179 (2018).
37. A. Hobolth, O. F. Christensen, T. Mailund, M. H. Schierup, *PLOS Genet.* **3**, e7 (2007).
38. I. Rivas-González *et al*., *Science* **380**, eabn4409 (2022).
39. D. Vanderpool *et al*., *PLOS Biol.* **18**, e3000954 (2020).
40. Z. Yang, *Mol. Biol. Evol.* **24**, 1586–1591 (2007).
41. S. Álvarez-Carretero *et al*., *Nature* **602**, 263–267 (2022).
42. C. Liu *et al*., *Sci. Adv.* **7**, eabe9459 (2021).
43. E. E. Eichler, D. Sankoff, *Science* **301**, 793–797 (2003).
44. Y. Yin *et al*., *Nat. Commun.* **12**, 6858 (2021).
45. R. Stanyon *et al*., *Chromosome Res.* **16**, 17–39 (2008).
46. T. Marques-Bonet *et al*., *Nature* **457**, 877–881 (2009).
47. P. D. Stenson *et al*., *Hum. Genet.* **139**, 1197–1207 (2020).
48. L. Chen *et al*., *Science* **364**, eaav6202 (2019).
49. J. D. Smith, J. W. Bickham, T. R. Gregory, *Genome* **56**, 457–472 (2013).
50. S. Shen *et al*., *Proc. Natl. Acad. Sci. U.S.A.* **108**, 2837–2842 (2011).
51. G. E. Liu, C. Alkan, L. Jiang, S. Zhao, E. E. Eichler, *Genome Res.* **19**, 876–885 (2009).
52. T. Hayakawa, Y. Satta, P. Gagneux, A. Varki, N. Takahata, *Proc. Natl. Acad. Sci. U.S.A.* **98**, 11399–11404 (2001).
53. P. Kuehnen *et al*., *PLOS Genet.* **8**, e1002543 (2012).
54. J. Jurka, *Curr. Opin. Genet. Dev.* **14**, 603–608 (2004).
55. G. Zhang *et al*., *Science* **346**, 1311–1320 (2014).
56. P. Moorjani, C. E. Amorim, P. F. Arndt, M. Przeworski, *Proc. Natl. Acad. Sci. U.S.A.* **113**, 10607–10612 (2016).
57. E. Fontanillas, J. J. Welch, J. A. Thomas, L. Bromham, *BMC Evol. Biol.* **7**, 95 (2007).
58. A. Wong, *Mol. Biol. Evol.* **31**, 1432–1436 (2014).
59. W. H. Li, M. Tanimura, *Nature* **326**, 93–96 (1987).
60. M. E. Steiper, N. M. Young, *Mol. Phylogenet. Evol.* **41**, 384–394 (2006).
61. S. H. Kim, N. Elango, C. Warden, E. Vigoda, S. V. Yi, *PLOS Genet.* **2**, e163 (2006).
62. J. Schmitz *et al*., *Nat. Commun.* **7**, 12997 (2016).
63. L. Fang *et al*., *Genome Res.* **30**, 790–801 (2020).
64. B. Y. Liao, J. Zhang, *Mol. Biol. Evol.* **23**, 1119–1128 (2006).
65. G. J. Wyckoff, W. Wang, C. I. Wu, *Nature* **403**, 304–309 (2000).
66. T. Boehm, *Curr. Biol.* **22**, R722–R732 (2012).
67. H. Y. Wang *et al*., *PLOS Biol.* **5**, e13 (2007).
68. Materials and methods are available as supplementary materials.
69. J. Tohyama *et al*., *J. Hum. Genet.* **60**, 167–173 (2015).
70. P. Mansfield, J. N. Constantino, D. Baldridge, *Am. J. Med. Genet. B. Neuropsychiatr. Genet.* **183**, 227–233 (2020).
71. M. Maekawa *et al*., *J. Neurochem.* **115**, 1374–1385 (2010).
72. X. Bi *et al*., *Sci. Adv.* 10.1126/sciadv.adc9507 (2023).
73. J. K. Rilling, T. R. Insel, *Neuroreport* **10**, 1453–1459 (1999).
74. K. Isler *et al*., *J. Hum. Evol.* **55**, 967–978 (2008).
75. C. Plachez, L. J. Richards, *Curr. Top. Dev. Biol.* **69**, 267–346 (2005).
76. M. A. Robichaux, C. W. Cowan, *Curr. Top. Behav. Neurosci.* **16**, 19–48 (2014).
77. J. Falk *et al*., *Neuron* **48**, 63–75 (2005).
78. M. A. Wolman, Y. Liu, H. Tawarayama, W. Shoji, M. C. Halloran, *J. Neurosci.* **24**, 8428–8435 (2004).
79. C. Kudo, I. Ajioka, Y. Hirata, K. Nakajima, *J. Comp. Neurol.* **487**, 255–269 (2005).
80. M. V. Tejada-Simon, *J. Neurochem.* **133**, 767–779 (2015).
81. S. L. Eastwood, P. J. Harrison, *Neuropsychopharmacology* **33**, 933–945 (2008).
82. D. Pan, *Genes Dev.* **21**, 886–897 (2007).
83. S. H. Patel, F. D. Camargo, D. Yimlamai, *Gastroenterology* **152**, 533–545 (2017).
84. R. H. Gokhale, A. W. Shingleton, *Wiley Interdiscip. Rev. Dev. Biol.* **4**, 335–356 (2015).
85. E. C. Kirk, *Anat. Rec. A Discov. Mol. Cell. Evol. Biol.* **281**, 1095–1103 (2004).
86. A. C. Wiik *et al*., *Genome Res.* **18**, 1415–1421 (2008).
87. P. Liskova *et al*., *Am. J. Hum. Genet.* **102**, 447–459 (2018).
88. Y. Toda *et al*., *Curr. Biol.* **31**, 4641–4649.e5 (2021).
89. J. M. Kamilar, B. J. Bradley, *J. Biogeogr.* **38**, 2270–2277 (2011).
90. S. Hu *et al*., *PeerJ* **8**, e9402 (2020).
91. M. C. Garrido, B. C. Bastian, *J. Invest. Dermatol.* **130**, 20–27 (2010).
92. J. M. Grichnik, *J. Invest. Dermatol.* **126**, 945–947 (2006).
93. Y. Mizutani, N. Hayashi, M. Kawashima, G. Imokawa, *Arch. Dermatol. Res.* **302**, 283–294 (2010).
94. R. Kitamura *et al*., *J. Pathol.* **202**, 463–475 (2004).
95. B. Wen *et al*., *Pigment Cell Melanoma Res.* **23**, 441–447 (2010).
96. D. L. C. van den Berg *et al*., *Neuron* **93**, 348–361 (2017).
97. G. H. Mochida, C. A. Walsh, *Curr. Opin. Neurol.* **14**, 151–156 (2001).
98. S. H. Montgomery, I. Capellini, C. Venditti, R. A. Barton, N. I. Mundy, *Mol. Biol. Evol.* **28**, 625–638 (2011).
99. L. Shi, M. Li, Q. Lin, X. Qi, B. Su, *BMC Biol.* **11**, 62 (2013).
100. L. Shi, B. Su, *Zool. Res.* **40**, 236–238 (2019).
101. J. Rogers *et al*., *Neuroimage* **53**, 1103–1108 (2010).
102. S. V. Puram *et al*., *Genes Dev.* **25**, 2659–2673 (2011).
103. A. Yamada *et al*., *Mol. Cell. Neurosci.* **56**, 234–243 (2013).
104. R. Kusano *et al*., *FEBS Lett.* **590**, 3606–3615 (2016).
105. M. Talarowska, J. Szemraj, M. Kowalczyk, P. Gałecki, *Med. Sci. Monit.* **22**, 152–160 (2016).
106. A. K. Pandey, L. Lu, X. Wang, R. Homayouni, R. W. Williams, *PLOS ONE* **9**, e88889 (2014).
107. A. Graziano, G. Foffani, E. B. Knudsen, J. Shumsky, K. A. Moxon, *PLOS ONE* **8**, e54350 (2013).
108. H. Li *et al*., *Proc. Natl. Acad. Sci. U.S.A.* **105**, 9397–9402 (2008).
109. Y. Chang, O. Klezovitch, R. S. Walikonis, V. Vasioukhin, J. J. LoTurco, *Cell Cycle* **9**, 1990–1997 (2010).
110. M. R. Sarkisian, *Cell Cycle* **9**, 1876 (2010).
111. D. A. Berg, L. Belnoue, H. Song, A. Simon, *Development* **140**, 2548–2561 (2013).
112. P. Levitt, J. A. Harvey, E. Friedman, K. Simansky, E. H. Murphy, *Trends Neurosci.* **20**, 269–274 (1997).
113. L. Wang *et al*., *Nat. Commun.* **11**, 282 (2020).
114. M. Linder *et al*., *Cell Death Differ.* **25**, 1094–1106 (2018).
115. F. Xiao *et al*., *Cell. Physiol. Biochem.* **45**, 1927–1939 (2018).
116. S. Zanotti, E. Canalis, *Bone* **62**, 22–28 (2014).
117. J. M. Kim, C. Lin, Z. Stavre, M. B. Greenblatt, J. H. Shim, *Cells* **9**, 2073 (2020).
118. S. Zanotti, E. Canalis, *Endocr. Rev.* **37**, 223–253 (2016).
119. M. Schmidt, *Adv. Sci. Res.* **5**, 23–39 (2011).
120. Y. He *et al*., *Nat. Commun.* **10**, 4233 (2019).
121. S. A. Williams, G. A. Russo, *Evol. Anthropol.* **24**, 15–32 (2015).
122. K. Semba *et al*., *Genetics* **172**, 445–456 (2006).
123. N. Al Dhaheri *et al*., *Am. J. Med. Genet. A.* **182**, 1664–1672 (2020).
124. J. R. Usherwood, J. E. Bertram, *J. Exp. Biol.* **206**, 1631–1642 (2003).
125. J. R. Usherwood, S. G. Larson, J. E. Bertram, *Am. J. Phys. Anthropol.* **120**, 364–372 (2003).
126. S. M. Cheyne, in *Primate Locomotion: Linking Field and Laboratory Research*, K. D'Août, E. E. Vereecke, Eds. (Springer, NY, 2011), pp. 201–213.
127. C. Thiel *et al*., *Am. J. Hum. Genet.* **88**, 106–114 (2011).
128. J. El Hokayem *et al*., *J. Med. Genet.* **49**, 227–233 (2012).
129. J. M. Vazquez, V. J. Lynch, *eLife* **10**, e65041 (2021).
130. J. G. M. Thewissen, L. N. Cooper, J. C. George, S. Bajpai, *Evolution (N. Y.)* **2**, 272–288 (2009).
131. W. L. Jungers, in *Size and Scaling in Primate Biology*, W. L. Jungers, Ed. (Springer, 1985), pp. 345–381.
132. A. M. Rudolf *et al*., *Natl. Sci. Rev.* **9**, nwab125 (2021).
133. K. R. Johnson *et al*., *Mol. Endocrinol.* **21**, 1593–1602 (2007).
134. J. G. Fleagle, *Primate Adaptation and Evolution* (Academic, 2013).
135. K. Milton, *Int. J. Primatol.* **19**, 513–548 (1998).
136. I. Matsuda, C. A. Chapman, M. Clauss, *J. Morphol.* **280**, 1608–1616 (2019).
137. M. C. Janiak, *Evol. Anthropol.* **25**, 253–266 (2016).
138. J. J. Kim, R. Miura, *Eur. J. Biochem.* **271**, 483–493 (2004).

139. C. Matziouridou *et al*., *Mucosal Immunol.* **11**, 774–784 (2018).
140. C.-J. Li, R. W. Li, R. L. Baldwin Vi, *Agric. Sci.* **9**, 619–638 (2018).
141. M. C. Janiak, A. S. Burrell, J. D. Orkin, T. R. Disotell, *Sci. Rep.* **9**, 20366 (2019).
142. P. Pontarotti, *Evolutionary Biology: Mechanisms and Trends* (Springer, 2012).
143. N. J. Dominy, P. W. Lucas, *Nature* **410**, 363–366 (2001).
144. N. G. Caine, N. I. Mundy, *Proc. Biol. Sci.* **267**, 439–444 (2000).
145. A. C. Smith, H. M. Buchanan-Smith, A. K. Surridge, D. Osorio, N. I. Mundy, *J. Exp. Biol.* **206**, 3159–3165 (2003).
146. S. Heritage, *PLOS ONE* **9**, e113904 (2014).
147. A. Matsui, Y. Go, Y. Niimura, *Mol. Biol. Evol.* **27**, 1192–1200 (2010).
148. T. D. Smith, K. P. Bhatnagar, *Anat. Rec. B New Anat.* **279**, 24–31 (2004).
149. A. Berghard, A. C. Hägglund, S. Bohm, L. Carlsson, *FASEB J.* **26**, 3464–3472 (2012).
150. J. Hirota, P. Mombaerts, *Proc. Natl. Acad. Sci. U.S.A.* **101**, 8751–8755 (2004).
151. H. Li, R. Durbin, *Nature* **475**, 493–496 (2011).
152. A. D. Barnosky, P. L. Koch, R. S. Feranec, S. L. Wing, A. B. Shabel, *Science* **306**, 70–75 (2004).
153. X. Luo *et al*., *Cell* **184**, 723–740.e21 (2021).
154. C. Yang *et al*., *Nature* **594**, 227–233 (2021).
155. G. Dumas, S. Malesys, T. Bourgeron, *Genome Res.* **31**, 484–496 (2021).
156. J. K. Rilling, *Evol. Anthropol.* **15**, 65–77 (2006).
157. H. Stephan, H. Frahm, G. Baron, *Folia Primatol. (Basel)* **35**, 1–29 (1981).
158. Genome annotation GFF files at Mendeley Data for: Y. Shao *et al*., Phylogenomic analyses provide insights into primate evolution, Mendeley (2023).
159. Genome annotation GFF files at Figshare for: Y. Shao *et al*., Phylogenomic analyses provide insights into primate evolution, Figshare (2023); https://doi.org/10.5061/dryad.8w9ghx3qj.
160. Gene sequences for: Y. Shao *et al*., Phylogenomic analyses provide insights into primate evolution, Dryad (2023).

ACKNOWLEDGMENTS

We are grateful to the many individuals in our host institutions who provided support for this project. **Funding:** This work was supported by the Strategic Priority Research Program of the Chinese Academy of Sciences (grants XDPB17 and XDB31020000); the National Natural Science Foundation of China (grants 31822048 and 32270500); the CAS Light of West China Program (grant xbzg-zdsys-202213); the Yunnan Fundamental Research Project (grant 2019FI010); the Animal Branch of the Germplasm Bank of Wild Species of Chinese Academy of Science (Large Research Infrastructure Funding); the International Partnership Program of Chinese Academy of Sciences (grant 152453KYSB20170002); a Villum Investigator Grant (25900 to G.Z.); the Japan Society for the Promotion of Science (JSPS KAKENHI grants 16K18630, 19K16241, 20H04987, 21H04919, and 21KK0106); Hokkaido University Sousei Tokutei Research; and JSPS Bilateral Joint Research Project (JPJSBP grant 120219902 to T.H.). T.M.B. was supported by funding from the European Research Council (ERC) under the European Union's Horizon 2020 research and innovation programme (grant 864203), PID2021-126004NB-100 (MICIIN/FEDER, UE), and Secretaria d'Universitats i Recerca and CERCA Programme del Departament d'Economia i Coneixement de la Generalitat de Catalunya (GRC 2021 SGR 00177). **Author contributions:** D.D.W. and G.J.Z. led the project. D.D.W., G.J.Z., and X.G.Q. conceived and designed the research. Y.S., L.Z, F.L., L.Z., B.L.Z., F.S., J.W.C., C.Y.C., X.P.B., X.L.Z., H.L.Z., I.R.G., S.W., Y.M.W., L.K., G.L., H.M.L., Y.L., and P.D.S. performed comparative genomics analysis. L.Z., J.H., Z.Y.S., X.L., D.P.W., and K.F. contributed genome sequencing, assembly, and annotation. P.F.F., M.L., Z.J.L., G.P.T., A.D.Y., C.R., T.H., T.M.B., and J.R. collected samples. J.R. and T.M.B. generated some genome assemblies for comparative genomics analysis. C.R., G.P.T., J.R., L.Y., M.H.S., D.N.C., Y.G.Y., Y.P.Z., W.W., and X.G.Q. provided comments for improving the manuscript. Y.S., X.G.Q., and L.Z. plotted and revised the figures. Y.S. drafted the manuscript. D.D.W., G.J.Z., and Y.S. wrote the manuscript. D.N.C. edited the manuscript. All authors approved the final manuscript. **Competing interests:** J.R. is also a core scientist at the Wisconsin National Primate Research Center, University of Wisconsin, Madison. Employees of Illumina, Inc., are indicated in the list of author affiliations. The authors declare no competing financial interests. **Data and materials availability:** All 27 primate genome assemblies and the raw genome long- and short-read sequencing data have been deposited at the NCBI Assembly Database (https://www.ncbi.nlm.nih.gov/assembly/) and the Sequence Read Archive Database (https://www.ncbi.nlm.nih.gov/sra/) under accessible BioProject accession codes PRJNA785018 and PRJNA911016. All genome annotation GFF files have been uploaded to the Mendeley Data database (*158*) and the Figshare database (*159*). The positively selected genes and their sequence alignments have been uploaded to a public Dryad dataset (*160*). **License information:** Copyright © 2023 the authors, some rights reserved; exclusive licensee American Association for the Advancement of Science. No claim to original US government works. https://www.science.org/about/science-licenses-journal-article-reuse

SUPPLEMENTARY MATERIALS

science.org/doi/10.1126/science.abn6919
Materials and Methods
Figs. S1 to S39
Tables S1 to S42
References (*161–237*)
MDAR Reproducibility Checklist

Submitted 16 December 2021; accepted 26 January 2023
10.1126/science.abn6919

RESEARCH ARTICLE SUMMARY

PRIMATE GENOMES

Pervasive incomplete lineage sorting illuminates speciation and selection in primates

Iker Rivas-González†, Marjolaine Rousselle†, Fang Li†, Long Zhou, Julien Y. Dutheil, Kasper Munch, Yong Shao, Dongdong Wu, Mikkel H. Schierup*, Guojie Zhang*

INTRODUCTION: Incomplete lineage sorting generates gene trees that are incongruent with the species tree. Incomplete lineage sorting has been described in many phylogenetic clades, including birds, marsupials, and primates. For example, the level of incomplete lineage sorting in the human-chimp-gorilla branch adds up to ~30%, which means that, even though our closest primate relatives are chimps, 15% of our genome resembles more the gorilla than the chimp genome, and another 15% groups the chimp with the gorilla first.

RATIONALE: Although incomplete lineage sorting is usually regarded as an obstacle for phylogenetic reconstruction, it holds valuable information about the evolutionary history of the species because its extent depends on the ancestral effective population sizes and the time between speciation events. Additionally, recurrent ancestral selective processes are expected to influence how the proportion of incongruent trees varies along the genome, which makes incomplete lineage sorting a useful tool to study ancient evolutionary events. In this study, we estimate the incomplete lineage sorting landscape by running a coalescent hidden Markov model in species trios along a 50-way primate genome alignment. We then leverage the signal of incomplete lineage sorting to reconstruct ancestral effective population parameters and to analyze the genomic determinants that influence the sorting of lineages.

RESULTS: We find widespread incomplete lineage sorting across the primate tree in 29 nodes, some reaching as much as 64% of the genome. Combining CoalHMM with a machine learning pipeline, we reconstruct the speciation times of the primate phylogeny without the need for fossil calibrations. Our speciation time estimates are more recent than divergence times, and they are in agreement with previous estimates based on fossil evidence. Our reconstructed ancestral effective population sizes show that they increase toward the past.

We additionally detect regions that have low or high incomplete lineage sorting levels consistently across several nodes. We show that incomplete lineage sorting proportions increase with the recombination rate in the genomic region—a difference that translates into an up to fourfold variation in the inferred local effective population size. Moreover, we report low levels of incomplete lineage sorting on the X chromosome. This reduction is more pronounced than expected under neutral evolution, which suggests that selective forces affect the X chromosome more strongly than the autosomes, reducing the effective population size of the X chromosome and, subsequently, the levels of incomplete lineage sorting.

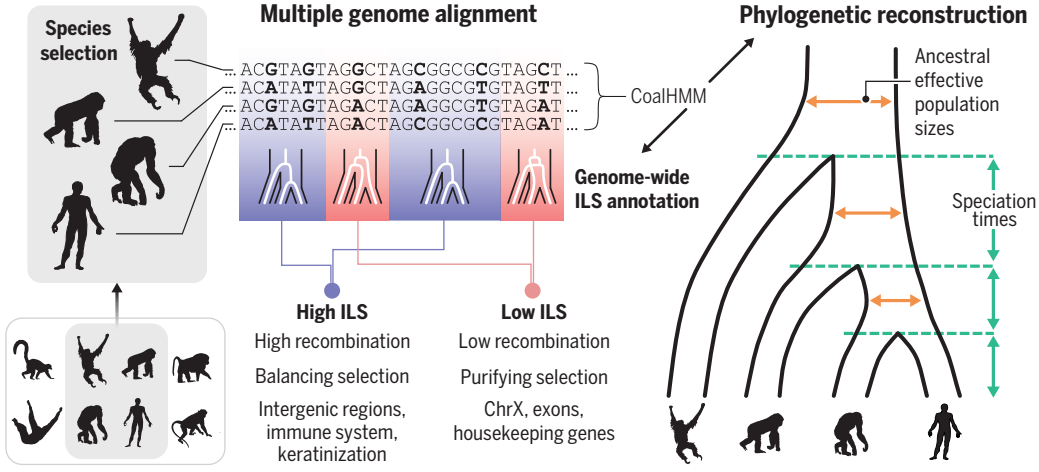
We further assess how selection affects the distribution of incomplete lineage sorting patterns by comparing the incomplete lineage sorting proportions of exons with those in intergenic regions. We find that there is an overall decrease in the levels of incomplete lineage sorting in exons that amounts to a reduction of 31% in the local effective population size as compared with intergenic regions.

Finally, we perform a gene ontology enrichment analysis on low– and high–incomplete lineage sorting genes. We find that immune system genes show large proportions of incomplete lineage sorting for many of the nodes, whereas housekeeping genes with basic cell functions show a lack of incomplete lineage sorting.

CONCLUSION: Most molecular-based methods that aim at timing a species tree provide estimates of divergence times, which are confounded by ancestral population sizes compared with the actual speciation times. We showed that using the coalescent theory and the signal of incomplete lineage sorting allows us to accurately estimate speciation times and ancestral population sizes in the primate tree, gaining key insights regarding some aspects of primate biology. Our study also emphasizes the prevalence of natural selection at linked sites that shapes the landscape of both genetic diversity and incomplete lineage sorting along the primate genome. ■

The list of author affiliations is available in the full article online.
*Corresponding author. Email: mheide@birc.au.dk (M.H.S.); guojiezhang@zju.edu.cn (G.Z.)
†These authors contributed equally to this work.
Cite this article as I. Rivas-González *et al.*, *Science* **380**, eabn4409 (2023). DOI: 10.1126/science.abn4409

READ THE FULL ARTICLE AT
https://doi.org/10.1126/science.abn4409



Inference of the speciation history and the genomic landscape of natural selection in primates from patterns of incomplete lineage sorting. CoalHMM was used to capture the signal of incomplete lineage sorting (ILS) segments along the genomes of 50 primate species and to estimate coalescent parameters—i.e., the ancestral effective population sizes and speciation times. Moreover, the genome-wide variation in the levels of incomplete lineage sorting allowed for the inference of selective processes in primates. ChrX, X chromosome.

RESEARCH ARTICLE

PRIMATE GENOMES

Pervasive incomplete lineage sorting illuminates speciation and selection in primates

Iker Rivas-González[1]†, Marjolaine Rousselle[1]†, Fang Li[2,3,4]†, Long Zhou[5,6], Julien Y. Dutheil[7,8], Kasper Munch[1], Yong Shao[9], Dongdong Wu[9,10,11,12], Mikkel H. Schierup[1]*, Guojie Zhang[5,6,9,13,14]*

Incomplete lineage sorting (ILS) causes the phylogeny of some parts of the genome to differ from the species tree. In this work, we investigate the frequencies and determinants of ILS in 29 major ancestral nodes across the entire primate phylogeny. We find up to 64% of the genome affected by ILS at individual nodes. We exploit ILS to reconstruct speciation times and ancestral population sizes. Estimated speciation times are much more recent than genomic divergence times and are in good agreement with the fossil record. We show extensive variation of ILS along the genome, mainly driven by recombination but also by the distance to genes, highlighting a major impact of selection on variation along the genome. In many nodes, ILS is reduced more on the X chromosome compared with autosomes than expected under neutrality, which suggests higher impacts of natural selection on the X chromosome. Finally, we show an excess of ILS in genes with immune functions and a deficit of ILS in housekeeping genes. The extensive ILS in primates discovered in this study provides insights into the speciation times, ancestral population sizes, and patterns of natural selection that shape primate evolution.

Comparative genomics can offer insights into population processes deep in phylogenetic history. As a result of recombination, different parts of our genomes have different genealogical histories (*1*, *2*). Therefore, when speciation occurs, the genes of the resulting descendants can be traced back to different ancestors, each coalescing at different times that stochastically depend on both the species population size and natural selection acting on each gene. If the time between two consecutive speciation events is short and/or the effective population size (*Ne*) is large, then genes from the two most closely related species may coalesce deeper in the past than the time of the oldest speciation event. This can result in genealogical histories that are different from the species tree—a phenomenon called incomplete lineage sorting (ILS). ILS has affected the evolutionary history of the human genome as well as many other groups (*3*–*5*). Around 30% of the human genome does not follow the ((human, chimpanzee), gorilla) speciation tree (*2*, *6*–*8*), with 15% of nucleotide positions grouping human and gorilla, and 15% grouping gorilla and chimpanzee.

Although the phylogenetic incongruences produced by ILS can hamper gene tree reconstruction from single loci, they offer an opportunity to learn about the population history of species sitting in deep ancestral branches of the phylogeny (*6*, *9*–*11*). We can, for example, estimate the actual times when species split as opposed to the more ancient average time to the most recent common ancestor, and we can measure how natural selection, directly or indirectly, affected the genomic diversity of the ancestral species. For example, Dutheil *et al.* (*12*) have concluded that the lack of ILS on the X chromosome in the human-chimp ancestor first reported by Patterson *et al.* (*13*) was likely a result of several episodes of very strong positive selection.

The recent effort to de novo assemble a large number of primate genomes makes it possible to extend the study of ILS to many more nodes across the primate phylogeny, allowing estimation of the speciation times and the forces that shaped genetic diversity in the ancestral species. With many independent replicates of the ILS process, we can learn about common targets of natural selection during primate diversification. In this work, we apply an extended version of the CoalHMM model (*14*) to a whole-genome alignment of 50 primate species (10 prosimians, 7 New World monkeys, 23 Old World monkeys, and 10 great and lesser apes). We report high levels of ILS on 29 of the total number of internal branches, and we estimate dates of the speciation times independently of fossil calibration that are in concordance with available fossil evidence. Additionally, we report recombination rate, ancestral effective population sizes, and selection as major genomic and functional determinants that have shaped the patterns of ancestral primate diversity.

Results

ILS is pervasive on most branches of the primate tree

We applied CoalHMM to the internal branches of the primate tree for 50 species used in Shao *et al.* (*15*) and shown in Fig. 1A, using combinations of quartets of species from the genome-wide alignment (see the supplementary materials, section 4). After filtering out ambiguously aligned regions, we used posterior decoding to infer segments of the alignment best supported by either the species topology or any of the two possible discordant topologies. Figure 1A shows the level of autosomal ILS detected on individual branches of the phylogeny. Branch lengths represent estimated genomic divergence times obtained by dividing substitution rates of the ExaML Gamma model by an estimate of the yearly mutation rate of each branch (supplementary materials, sections 3 and 7). We found appreciable genome-wide ILS proportions between 5 and 64% on 29 of the 49 branches, which implies that, on these branches, a large proportion of the genome follows a different gene genealogy from that of the species tree (Fig. 1A). The length distribution of the genome segments supporting the discordant topologies (i.e., topologies V2 and V3 in Fig. 1A, inset) depends mainly on the effective population size of the examined branch and is expected to follow a geometric distribution. Except for a deficiency of very short segments, this assumption is generally met in our analysis (fig. S7). We also show that the mean length of segments supporting both the species topology and the discordant topologies varies substantially among nodes, with mean lengths for discordant segments between 100 and 1000 base pairs for individual branches (fig. S7). This shows that single genes, which typically cover >20 kb in the genome, rarely have just one phylogenetic history when ILS is prominent.

A previous study based on the phylogenies of 1700 genes concluded that hybridization

[1]Bioinformatics Research Centre, Aarhus University, DK-8000 Aarhus C, Denmark. [2]BGI-Research, BGI-Wuhan, Wuhan 430074, China. [3]Institute of Animal Sex and Development, ZhejiangWanli University, Ningbo 315104, China. [4]BGI-Research, BGI-Shenzhen, Shenzhen 518083, China. [5]Evolutionary & Organismal Biology Research Center, Zhejiang University School of Medicine, Hangzhou 310058, China. [6]Women's Hospital, School of Medicine, Zhejiang University, Shangcheng District, Hangzhou 310006, China. [7]Max Planck Institute for Evolutionary Biology, Plön, Germany. [8]Institute of Evolution Sciences of Montpellier (ISEM), CNRS, University of Montpellier, IRD, EPHE, 34095 Montpellier, France. [9]State Key Laboratory of Genetic Resources and Evolution, Kunming Institute of Zoology, Chinese Academy of Sciences, Kunming, Yunnan 650223, China. [10]Center for Excellence in Animal Evolution and Genetics, Chinese Academy of Sciences, Kunming, Yunnan 650223, China. [11]National Resource Center for Non-Human Primates, Kunming Primate Research Center, and National Research Facility for Phenotypic and Genetic Analysis of Model Animals (Primate Facility), Kunming Institute of Zoology, Chinese Academy of Sciences, Kunming, Yunnan 650107, China. [12]Kunming Natural History Museum of Zoology, Kunming Institute of Zoology, Chinese Academy of Sciences, Kunming, Yunnan 650223, China. [13]Liangzhu Laboratory, Zhejiang University Medical Center, Hangzhou 311121, China. [14]Villum Centre for Biodiversity Genomics, Section for Ecology and Evolution, Department of Biology, University of Copenhagen, DK-2100 Copenhagen, Denmark.
***Corresponding author. Email: mheide@birc.au.dk (M.H.S.); guojiezhang@zju.edu.cn (G.Z.)**
†These authors contributed equally to this work.

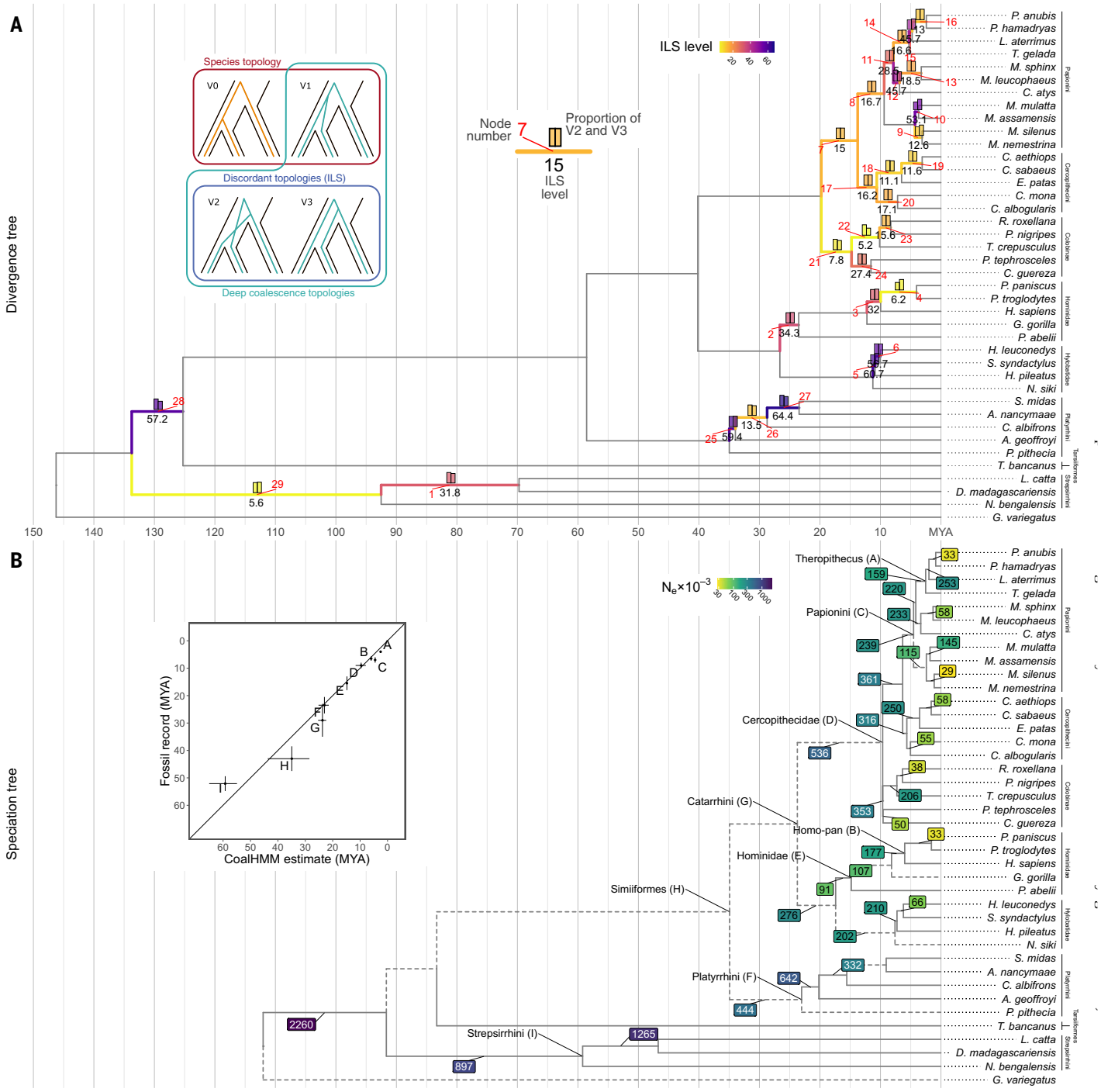


Fig. 1. Phylogenetic tree of primates, with scaled divergence times or speciation times as branch lengths. (**A**) Divergence time tree scaled with estimated mutation rate for individual branches (supplementary materials, section 7). Percentage ILS (the sum of V2 and V3 topologies; see inset) is plotted as branch color and marked with numbers for those branches with >5% of ILS. Only the subset of 38 species that were used to infer the ILS of the colored branches are plotted for clarity. The two columns on top of each branch show the relative frequency of bases attributed to V2 and V3, respectively. The numbers in red denote individual branches referenced in subsequent figures. The taxonomic classification is shown to the right of the phylogeny. (**B**) Speciation time tree with branch lengths in units of million years (MYA) as estimated from CoalHMM and scaled with estimated ancestral mutation rates for individual branches (supplementary materials, section 7). The annotations in colored rectangles refer to the inferred ancestral effective population sizes. Branches without enough information to infer speciation times using CoalHMM (i.e., branches with <5% ILS) are shown as dashed lines. Here, speciation times are instead estimated by subtracting an assumed population size (the CoalHMM estimate of the ancestral population size of the closest branch) from the divergence time rescaled by mutation rate per generation (supplementary materials, section 10). The inset panel shows the correlation between the split times estimated by CoalHMM and the dated fossil record. Each point corresponds to an evolutionary node in the right panel. Horizontal lines correspond to the bootstrapped standard deviation of the estimated branch length, and vertical lines represent the standard deviation of the fossil date estimates (data are shown in table S4).

events are as common in the deeper branches of the primate tree as they are today between related extant species of many primate groups (*16*, *17*). To estimate to what extent the phylogenetic incongruence that the model attributes to ILS is affected by widespread hybridization on the deeper branches, we investigated the relative frequency, nucleotide divergence, and length of the genomic fragments assigned to the two discordant topologies on each internal branch. If explained by ILS, the three measures should all be equal for the two discordant topologies, whereas hybridization is expected to cause one of the discordant topologies to be more frequent, and the genomic segments supporting the predominant topology should be, on average, longer and less divergent than those supporting the other discordant topology. On most of the 29 internal branches, we observe near-equal proportions of genomic positions assigned to the two discordant topologies (see the proportions of V2 versus V3 in Fig. 1A), and we find that the fragments have very similar size distributions (fig. S7). After correcting for different substitution rates (supplementary materials, section 9), we also find that segments with the two discordant topologies are close to equally divergent (figs. S17 and S19). Exceptions to these general patterns are found within the recent macaque, gibbon, and lesser apes divergences. In these cases, evidence of introgression has also been reported previously (*16*, *18*, *19*). However, even in those cases, ILS is the predominant cause of incongruent genealogies in the primate tree (*20*) (supplementary materials, section 9). It is possible that hybridizations occurred between related species in deeper branches, as is observed in several extant genera. However, if a pair of hybridizing species did not both leave extant descendant species (as is likely because most species die out), this would not have been distinguishable from deep coalescences in causing ILS. Thus, we cannot completely exclude that gene flow occurred at ancestral branches—only that it did not leave detectable evidence of ancient hybridization.

The level of ILS generally increases with shorter internal branch lengths (Fig. 1A). In the taxon sampling of our present dataset, we find that ILS is particularly ubiquitous in Old World monkeys, which have undergone rapid speciation events. Notably, however, 32% ILS is estimated even on a very long and deep branch within Strepsirrhini and 57% on the branch separating tarsiers from Strepsirrhini (branch 1 and branch 28, respectively; Fig. 1A), which suggests very large ancestral population sizes in these nodes that can also be predicted from the short size of the ILS fragments (fig. S7). Furthermore, the very high levels of ILS in gibbons and Old World monkeys, particularly macaques and baboons, explain the long-standing difficulty to resolve their phylogenetic relationships (*16*, *19*, *21*, *22*).

Speciation times and ancestral effective population sizes in the primate tree

The reconstruction of the dated history of a group of species is typically based on genomic divergence rates turned in divergence times through fossil calibrations (*23*–*25*). However, the genomic divergence times in species with large populations and long generation times can be much further back in time than the time when species actually split. The expected time for genomic coalescence on an ancestral branch is 2 × *Ne* generations older than the times of speciation. For an ancient population with an *Ne* of 200,000 and a generation time of 10 years, the average expected genomic divergence time would be 4 million years further back in time than the actual species split time. The analysis of incongruences produced by ILS via CoalHMM allows direct estimation of speciation times as opposed to divergence times as well as estimation of the ancestral effective population sizes.

We used the estimated parameters using CoalHMM together with simulations and a random forest model to derive ancestral effective population sizes and speciation times in all nodes with >5% of ILS (supplementary materials, section 10, and fig. S20). We then rescaled the parameters by estimated yearly mutation rates, which we derived from the relationship between pedigree-based yearly mutation rate and generation time, and the relationship between inferred body mass of extant and ancestral species and generation time (*26*, *27*) (supplementary materials, section 7). The resulting tree (fig. S21) was close to ultrametric and was linearized to make the speciation time tree shown in Fig. 1B (and that in fig. S22).

We infer ancestral effective population sizes that vary more than an order of magnitude within the primate phylogeny. In the few cases where ancestral effective population sizes of primate lineages have been estimated by other approaches, they are in good agreement with our estimates (*21*, *28*–*30*). For instance, Warren *et al.* (*29*) have estimated effective population sizes in the ancestors of the *Chlorocebus* lineage at around 40,000 using a multiple sequentially Markovian coalescent (MSMC) approach, when we infer an ancestral population size of 58,000, and Schrago and Seuánez (*21*) have estimated *Ne* in the ancestors of *Aotus* and Callitrichinae to >240,000 using a MSMC approach, when we infer an ancestral population size of 330,000. Most estimated ancestral *Ne* values are higher than effective population sizes estimated for primates today. This might reflect the fact that the ancestors of primates had smaller body sizes (*31*), which is known to be associated with larger population sizes, or that lineages with small population sizes are more likely to go extinct, leaving no descendants to sample from (*32*). As expected, population size estimates are negatively correlated with the median segment size of the discordant topologies (fig. S24). We also find an expected negative correlation between our estimate of ancestral *Ne* and the efficiency of purifying selection measured as dN/dS (the ratio of nonsynonymous to synonymous mutations) on the ancestral branches (fig. S25; $P = 0.0015$) and an expected negative correlation between average segment length and dN/dS (fig. S26).

Our inferred species split times are generally in good agreement with independent estimates from the fossil record when these exist (Fig. 1B, inset, and table S4), which supports that our approach can also infer speciation times on nodes that lack fossil evidence without the need for fossil calibration. Previous studies extrapolating the speciation time on the basis of pedigree-based mutation rates back in time have generally led to estimated times much further back in time than those suggested by the fossil record (*6*, *33*, *34*). We see two reasons for this. First, the large effective population sizes imply that divergence-based estimates of split times are several million years further back in time than the actual species split times. Second, our analysis rescales branch lengths by yearly mutation rates dependent on body size and generation time.

Highly variable frequency of ILS along the genome

Under selective neutrality, ILS is expected to occur at random along the genome. However, if natural selection, either directly or indirectly, affects the coalescent process of a genomic region, the sorting of lineages with deep coalescence will not be random (*12*, *35*, *36*). We painted all the genomes of the 29 ancestral branches by the level of ILS in 100-kb windows displayed as horizon plots (*37*, *38*) (fig. S8) and found many regions that experienced either high or low levels of ILS in the same genomic positions across several ancestral nodes in the primate phylogeny. We therefore integrated the ILS inference across the 29 branches using normalized ILS scores displayed in a single horizon plot showing the general pattern of ILS with the human genome coordinates as reference (Fig. 2A). This integrated signal of ILS shows that certain regions have consistently high or low levels of ILS. As an example, ILS is reduced in a large genomic region from 40 to 60 Mb on chromosome 3 (chr3) (Fig. 2B), which suggests either repeated selective sweeps or strong background selection (*11*, *36*). By contrast, the human lymphocyte antigen–major histocompatibility complex (HLA-MHC) cluster on position 27 to 33 Mb on chr6 has several regions showing

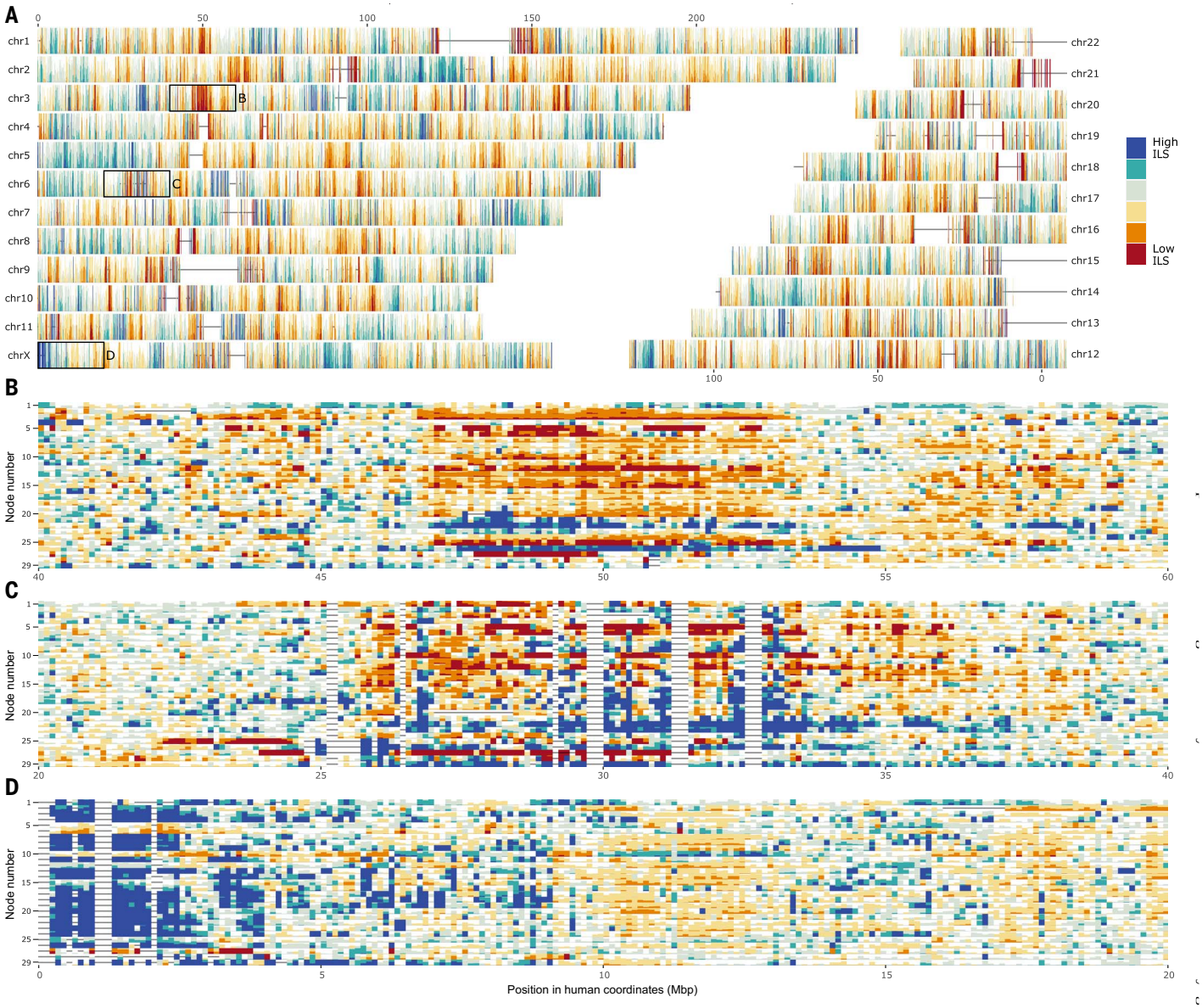


Fig. 2. Genome-wide distribution of ILS levels. (**A**) Horizon plot of the mean z-standardized ILS values in 100-kb windows (*x* coordinates in megabases). Red colors represent regions low in ILS, and blue colors represent high-ILS regions. Missing data are represented by a horizontal line. Regions marked with a rectangle in (A) are zoomed in. (**B** to **D**) A low-ILS region in chr3 (B), the MHC in chr6 (C), and the PAR region of the X chromosome (D). (B) to (D) are all horizon plots for all of the 29 individual nodes, where each node is mapped to Fig. 1A, inset. Mbp, mega–base pairs.

extremely high ILS, likely as a result of balancing selection (Fig. 2C). Additionally, the pseudoautosomal region (PAR) on position 0 to 2.7 Mb on the X chromosome also contains much higher ILS than the rest of the X chromosome (Fig. 2D) and, in many nodes, much higher ILS than the autosomal average. These and many other consistent patterns suggest that there are genomic and/or functional determinants of ILS that persist across the primate phylogeny.

Determinants of the variation in ILS along the genome

Recombination is not expected to directly affect the amount of ILS but can do so indirectly because the amount of recombination determines the efficacy of both positive and negative selection and, thus, the amount of diversity that is lost because of selection at linked genomic positions. A general observation of a positive correlation between nucleotide diversity and the recombination rate in extant species, including humans, has been interpreted as evidence for both the action of linked selection and as a mutagenic effect of recombination (*39*–*41*). ILS patterns will not be affected by the latter, so we investigated how ILS depends on recombination rate by extrapolating the human pedigree–based recombination map (*42*) at a 100-kb scale to the whole primate phylogeny. We inferred ILS levels and the corresponding relative local *Ne* as a function of recombination rate divided into ten bins (fig. S15 and supplementary materials, section 8). We find that the *Ne* of genomic regions with the highest recombination rate is typically 1.3-fold to fourfold larger than that in the lowest recombination bin (Fig. 3A), which implies that linked selection has removed a large proportion of the diversity in the ancestral species. Additionally, the extent of the effect of linked selection on genetic variation that we observe is likely underestimated because the present-day human recombination map is an imperfect proxy of the recombination landscape in ancestral species separated by tens of million years from humans.

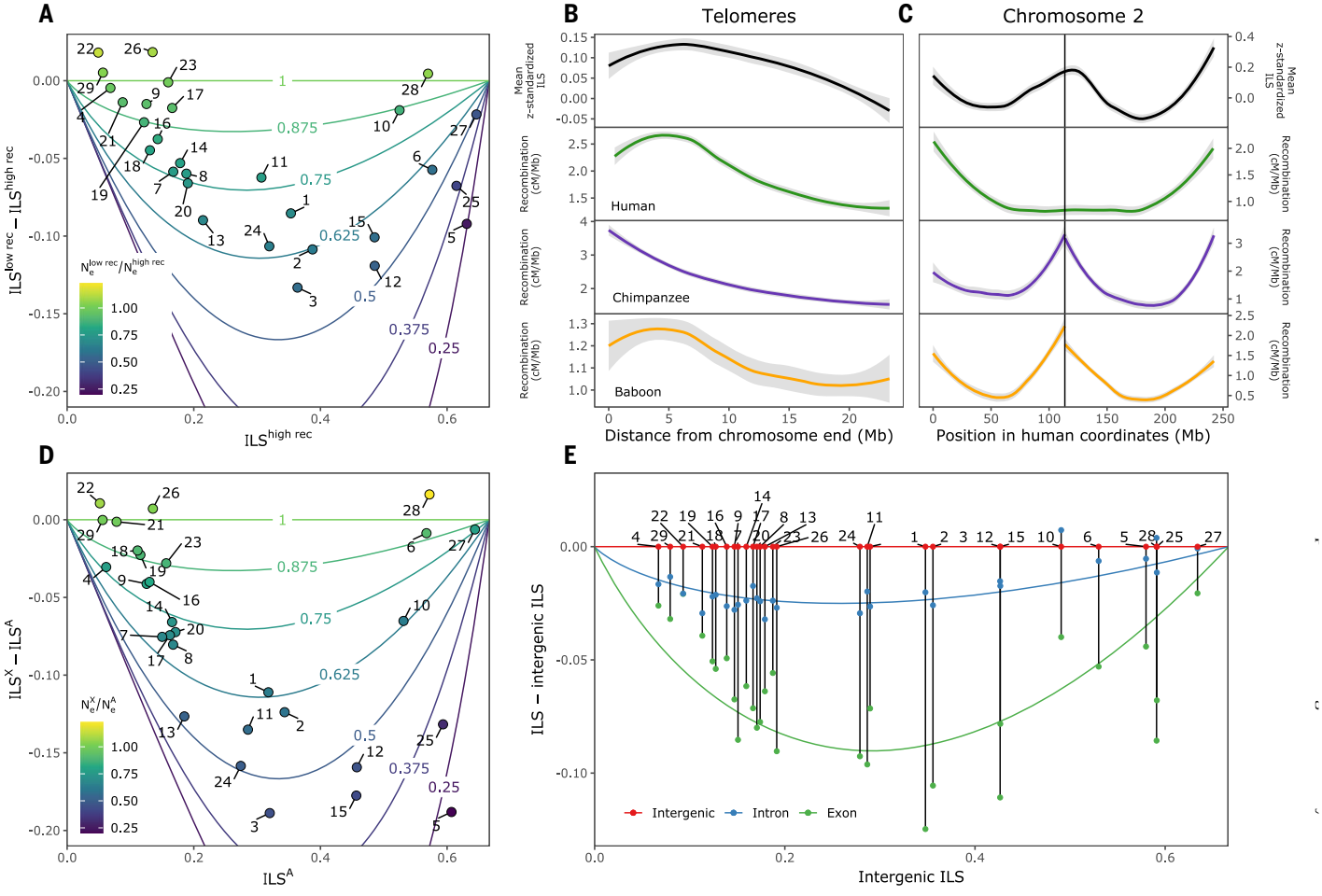


Fig. 3. Determinants of variation in ILS and corresponding *Ne*. (**A**) Difference in the proportion of ILS between the lowest recombination and the highest recombination deciles against the proportion of ILS in the highest recombination decile. Each numbered point represents a node in the phylogeny mapped to Fig. 1A, inset. The color and lines represent the relative change in *Ne* between the low and high recombination deciles, calculated using eq. S3 in the supplementary materials, section 8. (**B** and **C**) Comparison of the mean z-standardized proportion of ILS across 29 branches and the human (green), chimp (purple), and baboon (orange) recombination maps in the telomeres (B) and in chr2 (C). In (C), the fusion point is represented by a vertical line. (**D**) Difference between the ILS proportion of chromosome X and autosomes, where each numbered point is a node in the phylogeny mapped to Fig. 1A, inset. The color and lines represent the relative change in *Ne* between chromosome X and autosomes, calculated using eq. S3 in the supplementary materials, section 8. (**E**) Difference between the proportion of ILS in either exons (green) or introns (blue) and intergenic regions (red). Each numbered point and the corresponding vertical line represent one of 29 nodes in the phylogeny, mapped to Fig. 1A, inset. The colored lines represent fitted models that translate into a constant reduction in *Ne* across nodes.

Telomeres recombine more frequently than the rest of the genome (*42*–*45*). The integrated signal across all nodes and autosomal telomeres (Fig. 3B) shows a peak in the telomeric ILS that agrees with human (*42*), chimpanzee (*45*), and olive baboon (*46*) recombination maps at the tips of the chromosomes. Moreover, there is an increased signal of ILS at around position 114 Mb of chr2 (in human coordinates) (Fig. 3C), which corresponds to the remnants of an ancient telomere-telomere fusion affecting only the human lineage (*47*). Notably, we can only detect the corresponding peak in recombination in this region using the recombination map of nonhuman primate species, which suggests that, although big chromosomal rearrangements might markedly change the present-day recombination patterns, ILS can still be used to infer the ancestral recombination landscape in the primate phylogeny (*48*).

We next contrasted the ILS on the X chromosome with that on the autosomes. Because males only carry a single copy of the X chromosome in primates, and, consequently, it has a smaller effective population size, the X chromosome is expected to have lower ILS. We find that the X chromosome has an overall lower amount of ILS compared with the autosomal average (Fig. 3D and fig. S6), with the decrease corresponding to the *Ne* of chromosome X being between 50 and 75% of that of the autosomes. Under random mating and unbiased sex ratio, the Ne_X/Ne_A ratio is expected to equal 75% (*49*). However, in primates, males typically have the highest variance of reproductive success (*50*), which is at odds with our observed ratios smaller than 0.75 (Fig. 3D).

Previous surveys of chromosome X to autosome diversity have also often reported ratios below 0.75—e.g., 0.6 in non-African humans (*51*), 0.4 in gorillas, 0.5 in orangutans (*52*), and 0.3 in macaques (*53*). These observations have often been ascribed to differences in male and female mutation rates and recent bottleneck effects affecting the X chromosome diversity more than the autosomal diversity (*54*). However, sex differences in mutation rates should not affect ILS inference, and bottlenecks are unlikely as a general explanation throughout the primate phylogeny. We thus conclude that the large reduction in ILS on the X chromosome is likely a result of linked selection targeting the X chromosome to a

larger extent than the autosomes, as has been reported previously in the human-chimpanzee ancestral species (*12*). The 1.5- to 2.7-Mb PAR of the X chromosome is very high in ILS in most ancestral species (fig. S8). This is consistent with its very high recombination rate in males—~22 times the genome average rate, which minimizes the effect of linked selection—and its high polymorphism in great apes (*55*).

The strong positive correlation between ILS and recombination (fig. S15) suggests that positive and negative selection events had a strong impact on the removal of diversity in the ancestral species. These selective events are more likely enriched in genes, so we contrasted the amount of ILS in coding regions, introns, and intergenic regions (Fig. 3E). We find that, for all internal branches, $ILS_{exon} < ILS_{intron} < ILS_{intergenic}$. We estimate that a constant average reduction in the *Ne* of exons of 31% compared with the *Ne* in intergenic regions across the primate nodes would amount to the observed decrease in exonic ILS ($P < 2 \times 10^{16}$; SD = 1.4). Additionally, introns have an estimated average reduction in *Ne* of 10% compared with intergenic regions ($P < 2 \times 10^{16}$; SD = 0.5), which we interpret as a direct effect of their closer physical proximity to exons, leaving intronic ILS more strongly affected by linked selection than intergenic ILS.

ILS and gene function

Finally, we investigated whether certain gene categories are more likely to experience high levels of ILS than others—either because they experience less purifying selection and adaptive evolution or because they are more likely to be under balancing selection. We performed gene ontology enrichment tests with ILS as the response variable (supplementary materials, section 12).

We identify the most significant gene ontology terms enriched for either high or low ILS genes across the primate nodes and plot the gene ontology terms as a function of their average dN/dS ratio (Fig. 4A). As expected, more selectively constrained gene categories have significantly lower ILS than the genic average (correlation coefficient, $r = 0.35$; $P = 2.68 \times 10^{-10}$). These include many house-keeping gene categories and genes categories associated with chromosome organization and regulation. The *PIAS3* gene involved in transcriptional modulation is an example of consistently low ILS (Fig. 4B, left; other examples are in fig. S27).

Notably, the two gene ontologies with the highest ILS are "cornification" and/or "keratinization" and "immune response regulation." Corfinication (enriched for high ILS in 12 nodes) and keratinization (enriched for high ILS in 17 nodes) are tightly related gene ontology terms that include epidermal and keratinization genes. Primates exhibit an extraordinary degree of color variation across

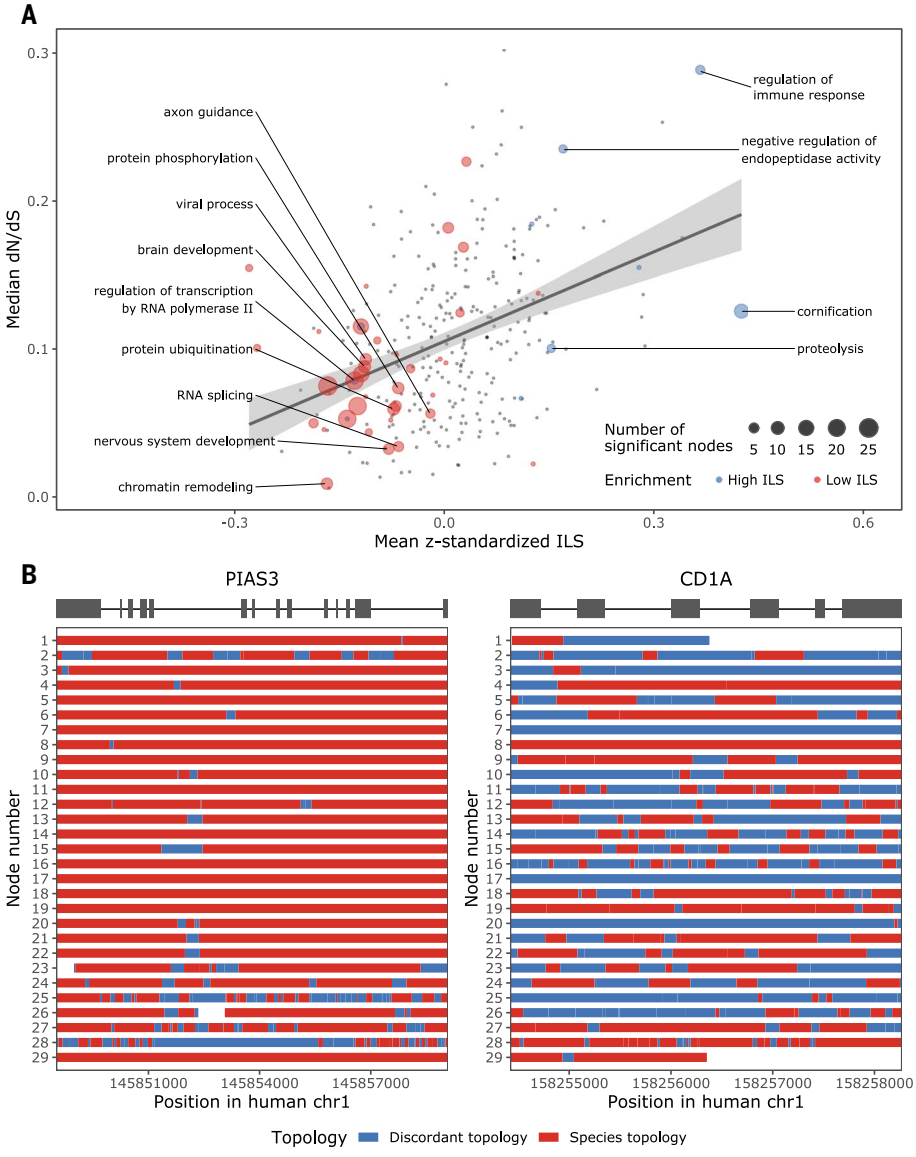


Fig. 4. ILS and gene function. (**A**) relationship between the ILS and the median dN/dS for each gene ontology term. Each data point corresponds to one gene ontology term, where the median dN/dS across all 29 nodes is plotted on the *y* axis, and the mean z-standardized ILS across all 29 nodes is represented on the *x* axis. Blue points are gene ontology terms that are significantly enriched for high ILS in at least one node, and red points correspond to gene ontology terms significantly enriched for low ILS. The size of the data points represents the number of nodes for which that gene ontology term has been significantly detected in the enrichment test. (**B**) Examples of genes with consistently low ILS (*PIAS3*, left) or consistently high ILS (*CD1A*, right). Each row corresponds to the inferred topologies (V0 or V1 in blue, and V2 or V3 in red) per genomic position for each node in the primate phylogeny. The top gray bar represents exons (in thick lines) and introns (in thin lines).

and within species and even in different parts of the body (*56*, *57*), which highlights the importance of the phenotypic evolution of skin in primates. This high diversity of coloration is crucial as social and sexual signaling and is often under stabilizing selection or positive selection that is closely linked with the high variations of primates in ecological niches, color vision, mating, and social systems (*58*). Additionally, some of the keratin gene families exhibit high levels of gene duplication and high functional diversification in primates (*59*–*61*).

Immune response regulation genes have been reported to evolve under balancing selection in primates (*62*), consistent with their enrichment in high-ILS genes. The MHC in chr6 is an outstanding region enriched for ILS, especially in Old World monkeys. Many other genes related to the immune response in genomic locations other than the HLA are also high in ILS. The detailed ILS pattern for the

CD1A gene (chr1) involved with innate immune response (Fig. 4B, right; other examples in fig. S28) reveals a higher ILS proportion in this gene above the average across the 29 nodes. Other examples are the ULBP family and killer cell immunoglobulin-like receptor (KIR) proteins. This last family is highly diverse, and it is consistent with patterns of balancing selection in several present-day human populations (*63*, *64*) and other primates (*65*).

Conclusion

The inference of ILS on many nodes in the primate phylogeny allows us to estimate speciation times and ancestral population sizes directly from genomic divergence data. We found that the effective population sizes have been very large in early primate evolution, at least in most lineages that have descendants today. This explains why the genomic divergence times estimates are much further back in time than the actual speciation times and why estimates of speciation events from trio-based germline mutation rates are often further back in time than the dating with fossil records.

The high levels of ILS in most nodes of the primate phylogeny made it possible to investigate the forces that shape genetic diversity along the genome in a complementary way to what has been done extensively using genome diversity data for individual species. We find that ILS depends strongly on the recombination rate, likely illustrating that a large part of genetic diversity is being removed by selection at linked sites. This dependency may partly explain Lewontin's paradox that the difference in genetic diversity across species is smaller than predicted from differences in neutral effective population sizes (*66*, *67*). The prevalence of natural selection at linked sites influencing diversity in ancestral nodes and thus ILS is also clear from the reduced ILS in introns compared with intergenic regions. The X chromosome appears to undergo more natural selection than the autosomes, perhaps as a consequence of male hemizygosity or possibly its strong role in male reproduction. Finally, ILS patterns also illuminate gene categories under balancing selection, particularly related to cornification or keratinization and immune functions, often experiencing different genealogical history compared with the speciation process.

Materials and methods summary

Data, alignment, and species tree

Our dataset consists of 50 primate species, including 27 newly sequenced ones and an outgroup, *Galeopterus variegatus*. For detailed information on sequencing and assembling, see the accompanying paper (*15*). We generated pairwise genome alignments using LASTZ (v1.04.00) for each species versus the human genome then using MULTIZ (v11.2) for multiway alignments. After removing columns of the alignment containing gaps in any of the species, we randomly chose half of the columns to run ExaML with the GAMMA model with 100 bootstraps. We report the tree with the highest maximum likelihood (fig. S1).

CoalHMM

We designed a divide-and-conquer, automated CoalHMM pipeline to fit a hidden Markov model where hidden states are four different topologies (Fig. 1A, inset), namely the species tree topology (V0), the deep coalescent topology following the species tree (V1), or one of two alternative topologies incongruent with the species tree (V2 and V3) (*14*). We defined each branch with a quartet of genomes and extracted them from the 51-way alignment using MafFilter (*68*). We removed columns containing only gaps and merged consecutive blocks that were <200 nucleotides apart. Chunks of <2000 nucleotides were filtered out, and blocks were divided into groups containing roughly 1 Mb alignment each (fig. S2B). CoalHMM was first run in a subset of 1-Mb groups of blocks, and the means of each of the estimated population parameters (tau1, tau2, theta1, theta2, c2, rho, and all the GTR model values) were recovered and used as starting parameters for the second CoalHMM run on all the other 1-Mb groups of blocks (fig. S2D). The posterior probabilities for each of the four hidden states were collected for each 1-Mb run and mapped to human coordinates (fig. S2E). All the code for processing the files and running CoalHMM is unified using a gwf workflow (https://gwf.app/), which can be accessed via https://github.com/rivasiker/autocoalhmm.

Genomic determinants of ILS

We used the latest deCODE human recombination map from Halldorsson *et al.* (*42*), the chimpanzee recombination map from Auton *et al.* (*45*), and the olive baboon recombination map from Sørensen *et al.* (*46*) to divide the genome into 10 equally sized recombination bins at a 100-kb resolution. We then calculated the mean ILS for each bin.

We retrieved intron and exon information from the knownGene UCSC Genome Browser table for hg38 (*69*–*71*) and kept only protein-coding genes that appear in the knownCanonical UCSC Genome Browser table (*72*). After trimming for size (supplementary materials, section 8), ILS level was calculated for exons and introns separately.

Introgression

We compared the level of divergence between sister species for segments of the genome attributed with the four different topologies to assess whether the level of incongruences that we report could be influenced by introgression. We used MafFilter to extract, filter, and concatenate segments and computed the percentage of mismatch as a measure of divergence between the sister species of the alignment (i.e., species 1 and species 2 for the segments assigned to the states V0 or V1, species 1 and species 3 for the segments assigned to the states V2, and species 2 and species 3 for the segments assigned to the states V3). We performed nonparametric Tukey-Kramer tests to compare the distribution of V0 segments versus V2 versus V3 segments divergence.

Population parameters reconstruction

The population parameters tau1, tau2, theta1, theta2, c2, and rho (defined as in fig. S20) outputted by CoalHMM are biased because of the use of a restricted set of four possible topologies to model the continuity of possible coalescence times (*14*), so we developed a machine learning–based procedure to learn how the different combinations of parameter values influence the bias of each parameter and then used this knowledge to predict the bias on real data. Briefly (but see supplementary materials, section 10), we ran CoalHMM on alignment blocks simulated under a grid of known combinations of population parameters using msprime (*73*). We then used the simulated versus estimated population parameters to train a random forest model and estimated the bias in our data on the basis of the estimates outputted by CoalHMM on the primate dataset.

dN/dS

We recovered 9972 coding gene alignments and filtered for orthologous genes where at least 41 out of the 50 primate species and the outgroup were present. Protein alignments were aligned using PRANK (*74*) and then filtered by Gblocks (*75*). Nucleotide alignments were generated by applying the protein alignment and site selection to the corresponding nucleotide sequences. We estimated branch-specific dN/dS ratios using the branch model of Codeml from PAML 4 (*23*). Results are reported in table S5.

Gene ontology

A gene ontology (GO) enrichment test was carried out for both high-ILS and low-ILS genes in each node using GOATOOLS (*76*). Gene annotations were downloaded from the National Center for Biotechnology Information's file transfer protocol (FTP) server (ftp://ftp.ncbi.nlm.nih.gov/gene/DATA/gene2go.gz). For each branch, genes were assigned to be high in ILS if their exonic ILS was in the top 30%, whereas genes were classified as low ILS if they were in the bottom 30%. The significance level for the enrichment test was set to 0.05 after false discovery rate correction. A full list of the enriched gene ontology terms can be found in table S6.

REFERENCES AND NOTES

1. M. Nei, *Molecular Evolutionary Genetics* (Columbia Univ. Press, 1987).
2. T. Mailund, K. Munch, M. H. Schierup, Lineage sorting in apes. *Annu. Rev. Genet.* **48**, 519–535 (2014). doi: 10.1146/annurev-genet-120213-092532; pmid: 25251849
3. A. Suh, L. Smeds, H. Ellegren, The Dynamics of Incomplete Lineage Sorting across the Ancient Adaptive Radiation of Neoavian Birds. *PLOS Biol.* **13**, e1002224 (2015). doi: 10.1371/journal.pbio.1002224; pmid: 26284513
4. K. Wang *et al*., Incomplete lineage sorting rather than hybridization explains the inconsistent phylogeny of the wisent. *Commun. Biol.* **1**, 169 (2018). doi: 10.1038/s42003-018-0176-6; pmid: 30374461
5. F. Alda *et al*., Resolving Deep Nodes in an Ancient Radiation of Neotropical Fishes in the Presence of Conflicting Signals from Incomplete Lineage Sorting. *Syst. Biol.* **68**, 573–593 (2019). doi: 10.1093/sysbio/syy085; pmid: 30521024
6. A. Scally *et al*., Insights into hominid evolution from the gorilla genome sequence. *Nature* **483**, 169–175 (2012). doi: 10.1038/nature10842; pmid: 22398555
7. Z. N. Kronenberg *et al*., High-resolution comparative analysis of great ape genomes. *Science* **360**, eaar6343 (2018). doi: 10.1126/science.aar6343; pmid: 29880660
8. Y. Mao *et al*., A high-quality bonobo genome refines the analysis of hominid evolution. *Nature* **594**, 77–81 (2021). doi: 10.1038/s41586-021-03519-x; pmid: 33953399
9. A. Hobolth, O. F. Christensen, T. Mailund, M. H. Schierup, Genomic relationships and speciation times of human, chimpanzee, and gorilla inferred from a coalescent hidden Markov model. *PLOS Genet.* **3**, e7 (2007). doi: 10.1371/journal.pgen.0030007; pmid: 17319744
10. A. Siepel, Phylogenomics of primates and their ancestral populations. *Genome Res.* **19**, 1929–1941 (2009). doi: 10.1101/gr.084228.108; pmid: 19801602
11. K. Prüfer *et al*., The bonobo genome compared with the chimpanzee and human genomes. *Nature* **486**, 527–531 (2012). doi: 10.1038/nature11128; pmid: 22722832
12. J. Y. Dutheil, K. Munch, K. Nam, T. Mailund, M. H. Schierup, Strong selective sweeps on the X chromosome in the human-chimpanzee ancestor explain its low divergence. *PLOS Genet.* **11**, e1005451 (2015). doi: 10.1371/journal.pgen.1005451; pmid: 26274919
13. N. Patterson, D. J. Richter, S. Gnerre, E. S. Lander, D. Reich, Genetic evidence for complex speciation of humans and chimpanzees. *Nature* **441**, 1103–1108 (2006). doi: 10.1038/nature04789; pmid: 16710306
14. J. Y. Dutheil *et al*., Ancestral population genomics: The coalescent hidden Markov model approach. *Genetics* **183**, 259–274 (2009). doi: 10.1534/genetics.109.103010; pmid: 19581452
15. Y. Shao *et al*., Phylogenomic analyses provide insights into primate evolution. *Science* **380**, eabn6919 (2023). doi: 10.1126/science.abn6919
16. D. Vanderpool *et al*., Primate phylogenomics uncovers multiple rapid radiations and ancient interspecific introgression. *PLOS Biol.* **18**, e3000954 (2020). doi: 10.1371/journal.pbio.3000954; pmid: 33270638
17. J. Tung, L. B. Barreiro, The contribution of admixture to primate evolution. *Curr. Opin. Genet. Dev.* **47**, 61–68 (2017). doi: 10.1016/j.gde.2017.08.010; pmid: 28923540
18. N. Osada *et al*., Ancient genome-wide admixture extends beyond the current hybrid zone between *Macaca fascicularis* and *M. mulatta*. *Mol. Ecol.* **19**, 2884–2895 (2010). doi: 10.1111/j.1365-294X.2010.04687.x; pmid: 20579289
19. K. R. Veeramah *et al*., Examining phylogenetic relationships among gibbon genera using whole genome sequence data using an approximate bayesian computation approach. *Genetics* **200**, 295–308 (2015). doi: 10.1534/genetics.115.174425; pmid: 25769979
20. Y. Song *et al*., Genome-wide analysis reveals signatures of complex introgressive gene flow in macaques (genus *Macaca*). *Zool. Res.* **42**, 433–449 (2021). doi: 10.24272/j.issn.2095-8137.2021.038; pmid: 34114757
21. C. G. Schrago, H. N. Seuánez, Large ancestral effective population size explains the difficult phylogenetic placement of owl monkeys. *Am. J. Primatol.* **81**, e22955 (2019). doi: 10.1002/ajp.22955; pmid: 30779198
22. D. Silvestro *et al*., Early Arrival and Climatically-Linked Geographic Expansion of New World Monkeys from Tiny African Ancestors. *Syst. Biol.* **68**, 78–92 (2019). doi: 10.1093/sysbio/syy046; pmid: 29931325
23. Z. Yang, PAML 4: Phylogenetic analysis by maximum likelihood. *Mol. Biol. Evol.* **24**, 1586–1591 (2007). doi: 10.1093/molbev/msm088; pmid: 17483113
24. F. Ronquist *et al*., MrBayes 3.2: Efficient Bayesian phylogenetic inference and model choice across a large model space. *Syst. Biol.* **61**, 539–542 (2012). doi: 10.1093/sysbio/sys029; pmid: 22357727
25. R. Bouckaert *et al*., BEAST 2.5: An advanced software platform for Bayesian evolutionary analysis. *PLOS Comput. Biol.* **15**, e1006650 (2019). doi: 10.1371/journal.pcbi.1006650; pmid: 30958812
26. L. Bromham, The genome as a life-history character: Why rate of molecular evolution varies between mammal species. *Phil. Trans. R. Soc. B* **366**, 2503–2513 (2011). doi: 10.1098/rstb.2011.0014; pmid: 21807731
27. G. W. C. Thomas *et al*., Reproductive Longevity Predicts Mutation Rates in Primates. *Curr. Biol.* **28**, 3193–3197.e5 (2018). doi: 10.1016/j.cub.2018.08.050; pmid: 30270182
28. C. G. Schrago, The effective population sizes of the anthropoid ancestors of the human–chimpanzee lineage provide insights on the historical biogeography of the great apes. *Mol. Biol. Evol.* **31**, 37–47 (2014). doi: 10.1093/molbev/mst191; pmid: 24124206
29. W. C. Warren *et al*., The genome of the vervet (*Chlorocebus aethiops sabaeus*). *Genome Res.* **25**, 1921–1933 (2015). doi: 10.1101/gr.192922.115; pmid: 26377836
30. R. Burgess, Z. Yang, Estimation of hominoid ancestral population sizes under bayesian coalescent models incorporating mutation rate variation and sequencing errors. *Mol. Biol. Evol.* **25**, 1979–1994 (2008). doi: 10.1093/molbev/msn148; pmid: 18603620
31. M. E. Steiper, E. R. Seiffert, Evidence for a convergent slowdown in primate molecular rates and its implications for the timing of early primate evolution. *Proc. Natl. Acad. Sci. U.S.A.* **109**, 6006–6011 (2012). doi: 10.1073/pnas.1119506109; pmid: 22474376
32. J. J. O'Grady, D. H. Reed, B. W. Brook, R. Frankham, What are the best correlates of predicted extinction risk? *Biol. Conserv.* **118**, 513–520 (2004). doi: 10.1016/j.biocon.2003.10.002
33. M. Chintalapati, P. Moorjani, Evolution of the mutation rate across primates. *Curr. Opin. Genet. Dev.* **62**, 58–64 (2020). doi: 10.1016/j.gde.2020.05.028; pmid: 32634682
34. F. L. Wu *et al*., A comparison of humans and baboons suggests germline mutation rates do not track cell divisions. *PLOS Biol.* **18**, e3000838 (2020). doi: 10.1371/journal.pbio.3000838; pmid: 32804933
35. A. Hobolth, J. Y. Dutheil, J. Hawks, M. H. Schierup, T. Mailund, Incomplete lineage sorting patterns among human, chimpanzee, and orangutan suggest recent orangutan speciation and widespread selection. *Genome Res.* **21**, 349–356 (2011). doi: 10.1101/gr.114751.110; pmid: 21270173
36. K. Munch, K. Nam, M. H. Schierup, T. Mailund, Selective sweeps across twenty millions years of primate evolution. *Mol. Biol. Evol.* **33**, 3065–3074 (2016). doi: 10.1093/molbev/msw199; pmid: 27660295
37. J. Heer, N. Kong, M. Agrawala, "Sizing the horizon: The effects of chart size and layering on the graphical perception of time series visualizations" in *CHI '09: Proceedings of the SIGCHI Conference on Human Factors in Computing Systems* (Association for Computing Machinery, 2009), pp. 1303–1312.
38. C. Perin, F. Vernier, J.-D. Fekete, "Interactive horizon graphs: Improving the compact visualization of multiple time series" in *CHI '13: Proceedings of the SIGCHI Conference on Human Factors in Computing Systems* (Association for Computing Machinery, 2013), pp. 3217–3226.
39. M. W. Nachman, Single nucleotide polymorphisms and recombination rate in humans. *Trends Genet.* **17**, 481–485 (2001). doi: 10.1016/S0168-9525(01)02409-X; pmid: 11525814
40. F. Pratto *et al*., DNA recombination. Recombination initiation maps of individual human genomes. *Science* **346**, 1256442 (2014). doi: 10.1126/science.1256442; pmid: 25395542
41. B. Arbeithuber, A. J. Betancourt, T. Ebner, I. Tiemann-Boege, Crossovers are associated with mutation and biased gene conversion at recombination hotspots. *Proc. Natl. Acad. Sci. U.S.A.* **112**, 2109–2114 (2015). doi: 10.1073/pnas.1416622112; pmid: 25646453
42. B. V. Halldorsson *et al*., Characterizing mutagenic effects of recombination through a sequence-level genetic map. *Science* **363**, eaau1043 (2019). doi: 10.1126/science.aau1043; pmid: 30679340
43. F. Pardo-Manuel de Villena, C. Sapienza, Recombination is proportional to the number of chromosome arms in mammals. *Mamm. Genome* **12**, 318–322 (2001). doi: 10.1007/s003350020005; pmid: 11309665
44. A. Kong *et al*., A high-resolution recombination map of the human genome. *Nat. Genet.* **31**, 241–247 (2002). doi: 10.1038/ng917; pmid: 12053178
45. A. Auton *et al*., A fine-scale chimpanzee genetic map from population sequencing. *Science* **336**, 193–198 (2012). doi: 10.1126/science.1216872; pmid: 22422862
46. E. F. Sørensen *et al*., Genome-wide coancestry reveals details of ancient and recent male-driven reticulation in baboons. *Science* **380**, eabn8153 (2023). doi: 10.1126/science.abn8153
47. J. W. Ijdo, A. Baldini, D. C. Ward, S. T. Reeders, R. A. Wells, Origin of human chromosome 2: An ancestral telomere-telomere fusion. *Proc. Natl. Acad. Sci. U.S.A.* **88**, 9051–9055 (1991). doi: 10.1073/pnas.88.20.9051; pmid: 1924367
48. K. Munch, T. Mailund, J. Y. Dutheil, M. H. Schierup, A fine-scale recombination map of the human–chimpanzee ancestor reveals faster change in humans than in chimpanzees and a strong impact of GC-biased gene conversion. *Genome Res.* **24**, 467–474 (2014). doi: 10.1101/gr.158469.113; pmid: 24190946
49. B. Vicoso, B. Charlesworth, Effective population size and the faster-X effect: An extended model. *Evolution* **63**, 2413–2426 (2009). doi: 10.1111/j.1558-5646.2009.00719.x; pmid: 19473388
50. C. Dubuc, A. Ruiz-Lambides, A. Widdig, Variance in male lifetime reproductive success and estimation of the degree of polygyny in a primate. *Behav. Ecol.* **25**, 878–889 (2014). doi: 10.1093/beheco/aru052; pmid: 25024637
51. A. Keinan, J. C. Mullikin, N. Patterson, D. Reich, Accelerated genetic drift on chromosome X during the human dispersal out of Africa. *Nat. Genet.* **41**, 66–70 (2009). doi: 10.1038/ng.303; pmid: 19098910
52. J. Prado-Martinez *et al*., Great ape genetic diversity and population history. *Nature* **499**, 471–475 (2013). doi: 10.1038/nature12228; pmid: 23823723
53. N. Osada *et al*., Finding the factors of reduced genetic diversity on X chromosomes of *Macaca fascicularis*: Male-driven evolution, demography, and natural selection. *Genetics* **195**, 1027–1035 (2013). doi: 10.1534/genetics.113.156703; pmid: 24026095
54. J. E. Pool, R. Nielsen, Population size changes reshape genomic patterns of diversity. *Evolution* **61**, 3001–3006 (2007). doi: 10.1111/j.1558-5646.2007.00238.x; pmid: 17971168
55. J. Bergman, M. Heide Schierup, Population dynamics of GC-changing mutations in humans and great apes. *Genetics* **218**, iyab083 (2021). doi: 10.1093/genetics/iyab083; pmid: 34081117
56. S. E. Santana, J. Lynch Alfaro, M. E. Alfaro, Adaptive evolution of facial colour patterns in Neotropical primates. *Proc. Biol. Sci.* **279**, 2204–2211 (2012). doi: 10.1098/rspb.2011.2326; pmid: 22237906
57. H. Rakotonirina, P. M. Kappeler, C. Fichtel, Evolution of facial color pattern complexity in lemurs. *Sci. Rep.* **7**, 15181 (2017). doi: 10.1038/s41598-017-15393-7; pmid: 29123214
58. J. G. Fleagle, *Primate Adaptation and Evolution* (Academic Press, 2013).
59. B. Jackson *et al*., Late cornified envelope family in differentiating epithelia—Response to calcium and ultraviolet irradiation. *J. Invest. Dermatol.* **124**, 1062–1070 (2005). doi: 10.1111/j.0022-202X.2005.23699.x; pmid: 15854049
60. D.-D. Wu, D. M. Irwin, Y.-P. Zhang, Molecular evolution of the keratin associated protein gene family in mammals, role in the evolution of mammalian hair. *BMC Evol. Biol.* **8**, 241 (2008). doi: 10.1186/1471-2148-8-241; pmid: 18721477
61. H. Niehues *et al*., Late cornified envelope (LCE) proteins: Distinct expression patterns of LCE2 and LCE3 members suggest nonredundant roles in human epidermis and other epithelia. *Br. J. Dermatol.* **174**, 795–802 (2016). doi: 10.1111/bjd.14284; pmid: 26556599
62. A. Cagan *et al*., Natural selection in the great apes. *Mol. Biol. Evol.* **33**, 3268–3283 (2016). doi: 10.1093/molbev/msw215; pmid: 27795229
63. K. J. Guinan *et al*., Signatures of natural selection and coevolution between killer cell immunoglobulin-like receptors (KIR) and HLA class I genes. *Genes Immun.* **11**, 467–478 (2010). doi: 10.1038/gene.2010.9; pmid: 20200544
64. V. Béziat, H. G. Hilton, P. J. Norman, J. A. Traherne, Deciphering the killer-cell immunoglobulin-like receptor system at super-resolution for natural killer and T-cell biology. *Immunology* **150**, 248–264 (2017). doi: 10.1111/imm.12684; pmid: 27779741
65. J. Bruijnesteijn, N. G. de Groot, R. E. Bontrop, The Genetic Mechanisms Driving Diversification of the *KIR* Gene Cluster in Primates. *Front. Immunol.* **11**, 582804 (2020). doi: 10.3389/fimmu.2020.582804; pmid: 33013938
66. R. C. Lewontin, *The Genetic Basis of Evolutionary Change* (Columbia Univ. Press, 1974).

67. R. B. Corbett-Detig, D. L. Hartl, T. B. Sackton, Natural selection constrains neutral diversity across a wide range of species. *PLOS Biol.* **13**, e1002112 (2015). doi: 10.1371/journal.pbio.1002112; pmid: 25859758
68. J. Y. Dutheil, in *Statistical Population Genomics*, J. Y. Dutheil, Ed., vol. 2090 of *Methods in Molecular Biology* (Humana, 2020), pp. 21–48.doi: 10.1007/978-1-0716-0199-0_2
69. W. J. Kent *et al*., The human genome browser at UCSC. *Genome Res.* **12**, 996–1006 (2002). doi: 10.1101/gr.229102; pmid: 12045153
70. D. Karolchik *et al*., The UCSC Table Browser data retrieval tool. *Nucleic Acids Res.* **32**, D493–D496 (2004). doi: 10.1093/nar/gkh103; pmid: 14681465
71. F. Hsu *et al*., The UCSC known genes. *Bioinformatics* **22**, 1036–1046 (2006). doi: 10.1093/bioinformatics/btl048; pmid: 16500937
72. J. Harrow *et al*., GENCODE: The reference human genome annotation for The ENCODE Project. *Genome Res.* **22**, 1760–1774 (2012). doi: 10.1101/gr.135350.111; pmid: 22955987
73. J. Kelleher, A. M. Etheridge, G. McVean, Efficient Coalescent Simulation and Genealogical Analysis for Large Sample Sizes. *PLOS Comput. Biol.* **12**, e1004842 (2016). doi: 10.1371/journal.pcbi.1004842; pmid: 27145223
74. A. Löytynoja, in *Multiple Sequence Alignment Methods*, D. Russell, Ed., vol. 1079 of *Methods in Molecular Biology* (Humana Press, 2014), pp. 155–170.
75. G. Talavera, J. Castresana, Improvement of phylogenies after removing divergent and ambiguously aligned blocks from protein sequence alignments. *Syst. Biol.* **56**, 564–577 (2007). doi: 10.1080/10635150701472164; pmid: 17654362
76. D. V. Klopfenstein *et al*., GOATOOLS: A Python library for Gene Ontology analyses. *Sci. Rep.* **8**, 10872 (2018). doi: 10.1038/s41598-018-28948-z; pmid: 30022098
77. I. Rivas-González, rivasiker/autocoalhmm: v1.0.0, version 1.0.0, Zenodo (2022); https://doi.org/10.5281/zenodo.7277715.

ACKNOWLEDGMENTS

We thank GenomeDK for the computations; T. Bataillon, A. Hobolth, and M. Coll Macià for their valuable insights; and the two anonymous reviewers whose comments helped improve the manuscript. **Funding:** The study was supported by grants NNF18OC0031004 from the Novo Nordisk Foundation and 6108-00385 from the Independent Research Fund Denmark, Natural Sciences, to M.H.S. This work was also supported by the Strategic Priority Research Program of the Chinese Academy of Sciences (XDB31020000), the International Partnership Program of the Chinese Academy of Sciences (no. 152453KYSB20170002), and the Villum Foundation (no. 25900) to G.Z. **Author contributions:** I.R.-G. and M.R. performed conceptualization, methodology, software, formal analysis, visualization, and writing. F.L. and L.Z. performed methodology, software, and formal analysis. Y.S. and D.W. performed data generation. J.Y.D. performed methodology, software, and revision. K.M. performed revision. M.H.S. and G.Z. performed conceptualization, writing, and supervision. **Competing interests:** The authors declare no competing interests. **Data and materials availability:** The primate alignment can be retrieved from Shao *et al*. (*15*). The code used to run CoalHMM on the primate alignment is available on Github (https://github.com/rivasiker/autocoalhmm) and Zenodo (*77*). The ILS tracts in 100-kb windows for each node can be retrieved from file S1. **License information:** Copyright © 2023 the authors, some rights reserved; exclusive licensee American Association for the Advancement of Science. No claim to original US government works. https://www.science.org/about/science-licenses-journal-article-reuse

SUPPLEMENTARY MATERIALS

science.org/doi/10.1126/science.abn4409
Materials and Methods
Figs. S1 to S29
Tables S1 to S6
File S1
References (*78*–*99*)
MDAR Reproducibility Checklist

View/request a protocol for this paper from *Bio-protocol*.

Submitted 28 November 2021; accepted 19 January 2023
10.1126/science.abn4409

RESEARCH ARTICLE SUMMARY

PRIMATE GENOMES

Hybrid origin of a primate, the gray snub-nosed monkey

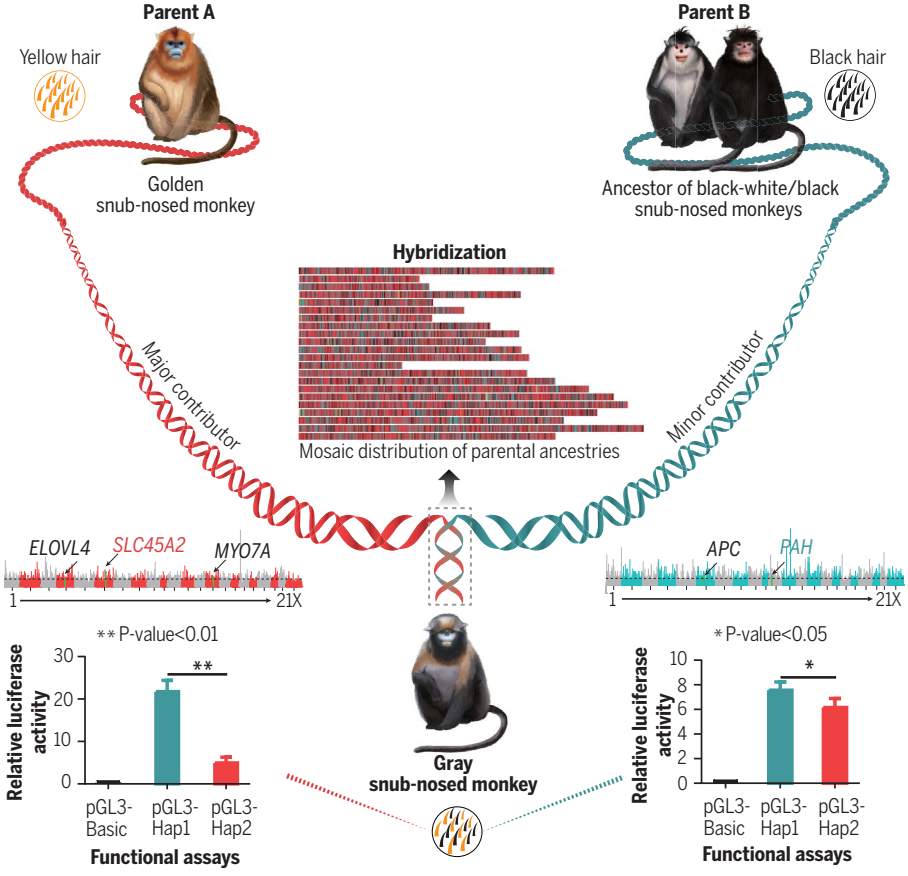
Hong Wu†, Zefu Wang†, Yuxing Zhang†, Laurent Frantz, Christian Roos, David M. Irwin, Chenglin Zhang, Xuefeng Liu, Dongdong Wu, Song Huang, Tongtong Gu, Jianquan Liu*, Li Yu*

INTRODUCTION: Hybridization is increasingly recognized as an important evolutionary force for generating species and phenotypic diversity in plants and animals. This is especially common in lineages that can tolerate whole-genome duplication and increased levels of ploidy. However, the role of hybridization in generating species and phenotypic diversity of lineages without polyploidization is underappreciated, especially in nonhominoid mammals.

RATIONALE: The snub-nosed monkey genus *Rhinopithecus* comprises five allopatric and morphologically differentiated species, the black-white snub-nosed monkey *Rhinopithecus bieti*, the black snub-nosed monkey *Rhinopithecus strykeri*, the golden snub-nosed monkey *Rhinopithecus roxellana*, the gray snub-nosed monkey *Rhinopithecus brelichi*, and the Tonkin snub-nosed monkey *Rhinopithecus avunculus*. They possess the same chromosome number, and it has been speculated that they have hybridized in the past. To examine the speciation histories of these species, we generated a chromosome-level high-quality reference genome assembly for the black-white snub-nosed monkey and analyzed 106 resequenced genomes of individuals from all five species. We conducted multiple population genomic analyses—including ADMIXTURE, D-statistics, phylogenetic reconstruction, and evolutionary scenario simulations—to investigate the genomic admixture of these species. We further applied genomic selective scans and functional assays to reveal the likely genetic basis of mosaic coat coloration of the hybrid species. Possible mechanisms of premating and postmating reproductive isolation barriers between the hybrid species and its parents are briefly discussed.

RESULTS: We show that historical hybridization directly resulted in the origin of the gray snub-nosed monkey. Population genomic analyses provided evidence for apparent genomic admixture across genomes of all gray snub-nosed monkeys from two parental lineages, the golden snub-nosed monkey and an ancestor of the black-white/black snub-nosed monkeys, with the majority of genome derived from the golden snub-nosed monkey. As a result of hybridization, the hybrid species possesses a mosaic of the color patterns of its parents. Genomic selection scans and functional assays identify several key melanogenesis-related genes (*PAH*, *APC*, *SLC45A2*, *MYO7A*, and *ELOVL4*). Alleles of these genes were alternately inherited from each parent, likely producing the mosaic coat coloration of the hybrid monkey and promoting premating reproductive isolation of the hybrid species from both parents. In addition, alternate inheritance of divergent alleles at many loci, especially those involved in genetic incompatibility between the parents, may have contributed to postmating reproductive isolation of the gray snub-nosed monkey.

CONCLUSION: We report a notable example of hybrid speciation in primates and present a detailed evolutionary scenario from the genomic admixture to the likely reproductive isolation establishment owing to alternate inheritance of divergent alleles from parents. This study highlights the underappreciated role of interspecific hybridization in species and phenotypic diversity in mammals. ■



The hybrid origin and genetic basis of mosaic coat coloration for the gray snub-nosed monkey. Interspecific hybridization between the golden snub-nosed monkey and the ancestor of black-white/black snub-nosed monkeys led to the genomic admixture of the gray snub-nosed monkey. Alleles of positively selected genes related to melanogenesis were alternately inherited from parental lineages A and B and contributed to the mosaic coat coloration of the hybrid species.

The list of author affiliations is available in the full article online.
*Corresponding author. Email: yuli@ynu.edu.cn (L.Y.); liujq@nwipb.ac.cn (J.L.)
†These authors contributed equally to this work.
Cite this article as H. Wu *et al.*, *Science* **380**, eabl4997 (2023). DOI: 10.1126/science.abl4997

READ THE FULL ARTICLE AT
https://doi.org/10.1126/science.abl4997

RESEARCH ARTICLE

PRIMATE GENOMES

Hybrid origin of a primate, the gray snub-nosed monkey

Hong Wu[1]†, Zefu Wang[2]†, Yuxing Zhang[1]†, Laurent Frantz[3,4], Christian Roos[5], David M. Irwin[6], Chenglin Zhang[7], Xuefeng Liu[7], Dongdong Wu[8], Song Huang[9], Tongtong Gu[1], Jianquan Liu[2,10]*, Li Yu[1]*

Hybridization is widely recognized as promoting both species and phenotypic diversity. However, its role in mammalian evolution is rarely examined. We report historical hybridization among a group of snub-nosed monkeys (*Rhinopithecus*) that resulted in the origin of a hybrid species. The geographically isolated gray snub-nosed monkey *Rhinopithecus brelichi* shows a stable mixed genomic ancestry derived from the golden snub-nosed monkey (*Rhinopithecus roxellana*) and the ancestor of black-white (*Rhinopithecus bieti*) and black snub-nosed monkeys (*Rhinopithecus strykeri*). We further identified key genes derived from the parental lineages, respectively, that may have contributed to the mosaic coat coloration of *R. brelichi*, which likely promoted premating reproductive isolation of the hybrid from parental lineages. Our study highlights the underappreciated role of hybridization in generating species and phenotypic diversity in mammals.

Hybridization is increasingly recognized as an important evolutionary force for generating species and phenotypic diversity in plants and animals (*1*–*4*). This is especially common in lineages that can tolerate whole-genome duplication and increased levels of ploidy (*5*). However, the role of hybridization in generating species and phenotypic diversity of lineages without polyploidization is underappreciated, especially in nonhominoid mammals. In this study, we report historical hybridization among a group of snub-nosed monkeys (*Rhinopithecus*) that resulted in the origin of a hybrid species.

The genus *Rhinopithecus* includes five allopatric and morphologically differentiated species (the black-white snub-nosed monkey *Rhinopithecus bieti*, the black snub-nosed monkey *Rhinopithecus strykeri*, the golden snub-nosed monkey *Rhinopithecus roxellana*, the gray snub-nosed monkey *Rhinopithecus brelichi*, and the Tonkin snub-nosed monkey *Rhinopithecus avunculus*) (Fig. 1). They possess the same chromosome number, and it has been speculated that they have hybridized in the past (*6*–*8*). To examine the speciation histories of these species, we generated a chromosome-level high-quality reference genome assembly (270-fold coverage) for the black-white snub-nosed monkey and analyzed 106 resequenced genomes of individuals from all five species (12.12-fold coverage on average) (fig. S1 and tables S1 to S3). Our comprehensive analyses of these data supported the hybrid origin of the gray snub-nosed monkey and identified several key genes that may have contributed to the mosaic coat coloration and premating reproductive isolation of this hybrid species.

Apparent genetic mixture across genome of the gray snub-nosed monkey

Analyses by means of ADMIXTURE set at two postulated ancestral populations ($K = 2$) showed that all individuals of the gray snub-nosed monkey possessed an admixed genome derived from two parental lineages: the golden snub-nosed monkey (parent A) and an ancestral lineage of the black-white/black snub-nosed monkeys (parent B), with the majority of genome derived from the golden snub-nosed monkey (69 and 61.75% of autosomal and X chromosomal components, respectively) (Fig. 2A and fig. S2). Principal components analyses (PCA) supported this finding, placing the gray snub-nosed monkey in an intermediate position between its two presumed parental lineages (Fig. 2B). Furthermore, both analyses that were conducted on down-sampled datasets, to avoid unbalanced sampling effects, yielded similar results (figs. S3 to S8). The mixed genomic ancestry of the gray snub-nosed monkey was stable across all examined individuals with the ancestry proportion and tract length of the golden snub-nosed monkey (parent A, the major contributor) significantly larger than

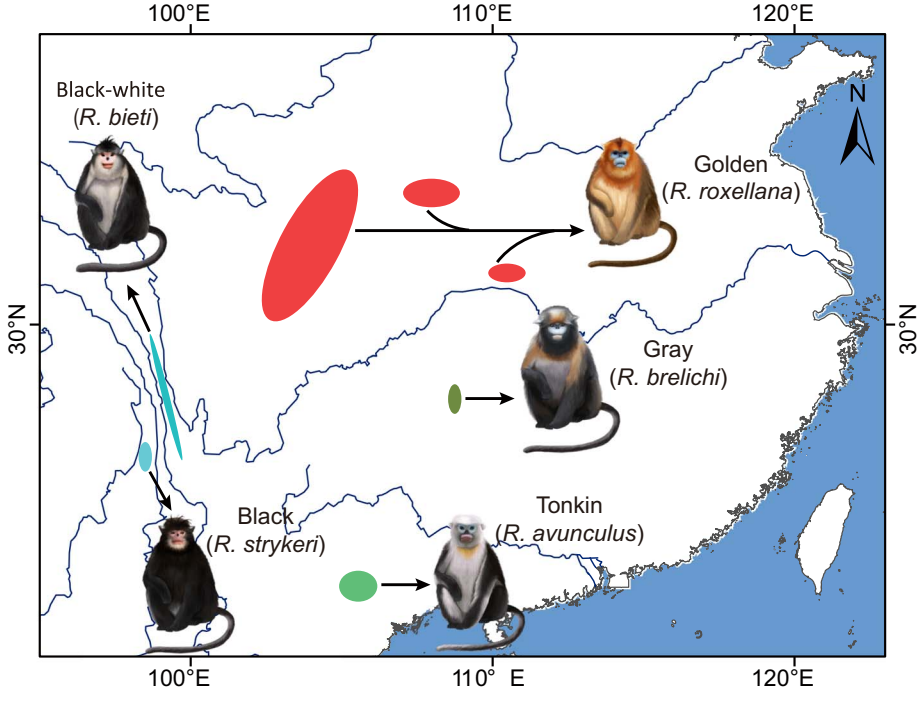


Fig. 1. Geographic distributions of the five snub-nosed monkey species.

[1]State Key Laboratory for Conservation and Utilization of Bio-Resource in Yunnan, School of Life Sciences, Yunnan University, Kunming 650091, China. [2]Key Laboratory for Bio-resource and Eco-environment of Ministry of Education, College of Life Sciences, Sichuan University, Chengdu 610065, China. [3]Palaeogenomics Group, Department of Veterinary Sciences, Ludwig Maximilian University of Munich, D-80539 Munich, Germany. [4]School of Biological and Behavioural Sciences, Queen Mary University of London, London E1 4NS, UK. [5]Gene Bank of Primates and Primate Genetics Laboratory, German Primate Center, Leibniz Institute for Primate Research, 37077 Göttingen, Germany. [6]Department of Laboratory Medicine and Pathobiology, University of Toronto, Toronto, Canada. [7]Beijing Key Laboratory of Captive Wildlife Technologies in Beijing Zoo, Beijing, China. [8]Kunming Institute of Zoology, Chinese Academy of Sciences, Kunming, China. [9]Kunming Zoo, Kunming, China. [10]State Key Laboratory of Herbage Improvement and Grassland Agro-Ecosystem, College of Ecology, Lanzhou University, Lanzhou 730000, China.
***Corresponding author. Email: yuli@ynu.edu.cn (L.Y.); liujq@nwipb.ac.cn (J.L.)**
†These authors contributed equally to this work.

that of the ancestor to the black-white/black snub-nosed monkeys (parent B, the minor contributor) (Fig. 2, C and D, and fig. S9). This indicates that the dual ancestry of the gray snub-nosed monkey is unlikely to have arisen from recent introgression (*9*).

We further evaluated whether this admixed ancestry arose from ancient hybridization by using phylogenetic and D-statistics analyses as well as f_d scans (*10*, *11*). We built 27,943 trees across the genome using 100-kb windows and found three major topologies (Fig. 3A). The most common tree topology (Tree-1; 62.34% of the total) (Fig. 3A) was identical to that of the previously reported species tree in which the gray snub-nosed monkey clustered with the golden snub-nosed monkey (parent A) (*12*). By contrast, the second-most common tree topology (Tree-2; 22.64% of the total) (Fig. 3A) supported the clustering of the gray snub-nosed monkey with the ancestor of the black-white/black snub-nosed monkeys (parent B). Only 14.54% of the trees displayed a topology (Tree-3) (Fig. 3A) in which the gray snub-nosed monkey diverged from its two presumed parental lineages. Both Tree-1 and Tree-2 types were significantly more common than Tree-3 (both $P < 2.2 \times 10^{-16}$; Student's t test). In addition, windows of the genome supporting Tree-1 and Tree-2 were significantly larger than those supporting Tree-3 ($P < 2.2 \times 10^{-16}$ and $P = 1.12 \times 10^{-3}$, respectively; Mann-Whitney U test) (Fig. 3, A and B). Such conflicts of tree topologies more likely arose from the effects of hybridization than incomplete lineage sorting, under which all tree topologies are expected to have similar proportions and distributions of window sizes. Signals of historical hybridization were also evident from analyses of D-statistics and f_d genomic scans (fig. S10 and tables S4 to S5), and as found for other species with a history of hybridization (*13*), recombination rate was significantly ($P < 0.05$) lower in the major ancestral genome component of the gray snub-nosed monkey genome (derived in this case from the golden snub-nosed monkey, parent A) than in the minor component (derived from the ancestor of the black-white/black snub-nosed monkeys, parent B) (Fig. 2, C and D, and fig. S11).

Genomic coalescent simulation further supports the hybrid origin of the gray snub-nosed monkey

To determine whether the hypothesis of a hybrid origin was more likely than other speciation hypotheses, we extracted the joint site frequency spectrum from population genomic data of the gray snub-nosed monkey and its two assumed parental lineages and used coalescent simulations to infer the most likely evolutionary scenario for the origin of the gray snub-nosed monkey (fig. S12 and table S6). The best-fitting model (model 18 in Fig. 3C and tables S6 and S7) again supported a

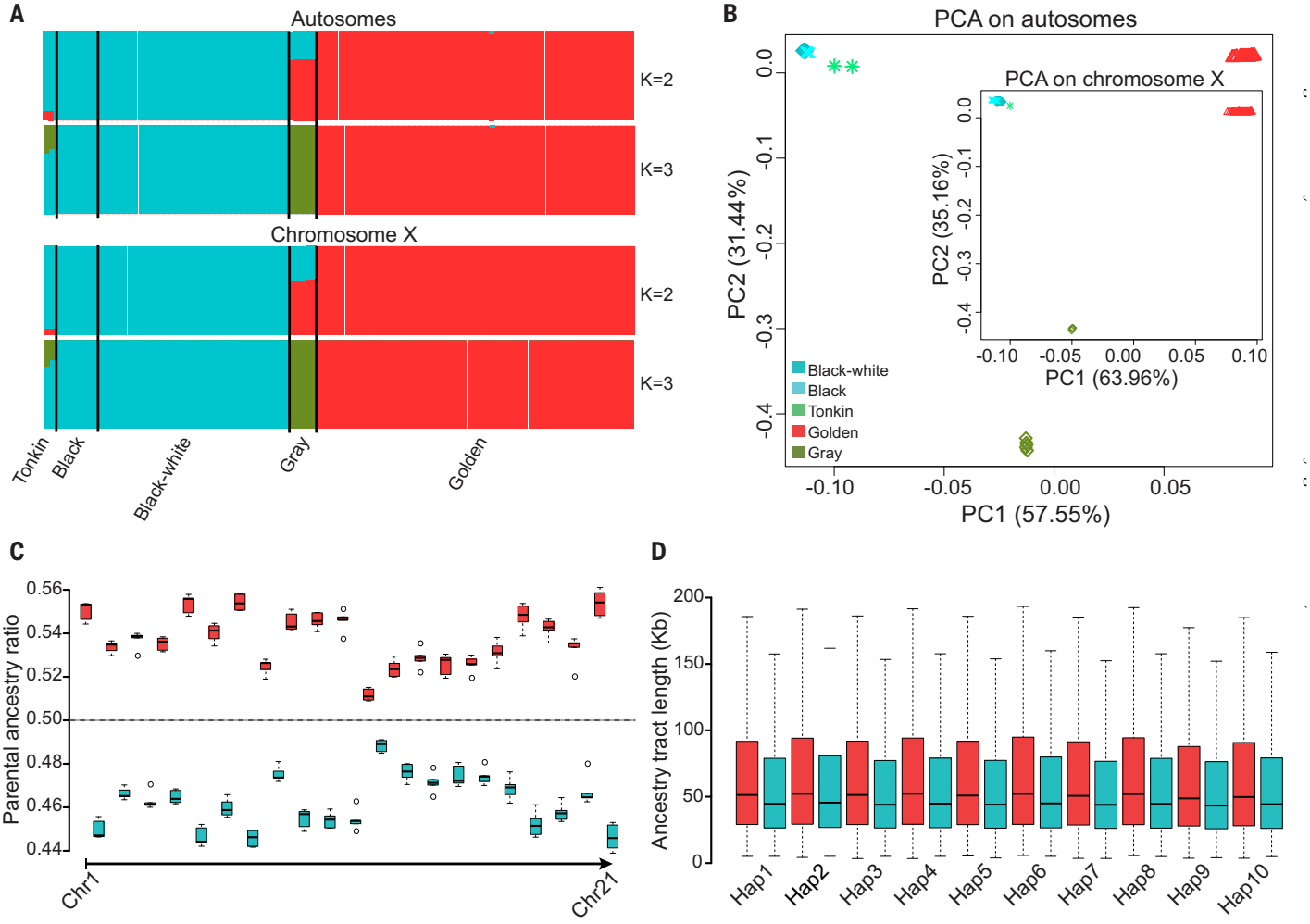


Fig. 2. ADMIXTURE, PCA, and genomic parental ancestry tract analyses. (**A**) ADMIXTURE results for 106 snub-nosed monkeys. (**B**) PCA results for 106 snub-nosed monkeys. (**C**) Ancestry proportions across all autosomes of the gray snub-nosed monkey that were contributed by parent A (red) and parent B (blue). (**D**) Boxplots of the ancestry tract lengths. Red, ancestry inherited from parent A (the golden snub-nosed monkey); blue, ancestry inherited from parent B (the ancestor of the black-white/black snub-nosed monkeys). For the five gray snub-nosed monkeys, 10 haploid genomes were calculated, respectively (Hap1 to Hap10).

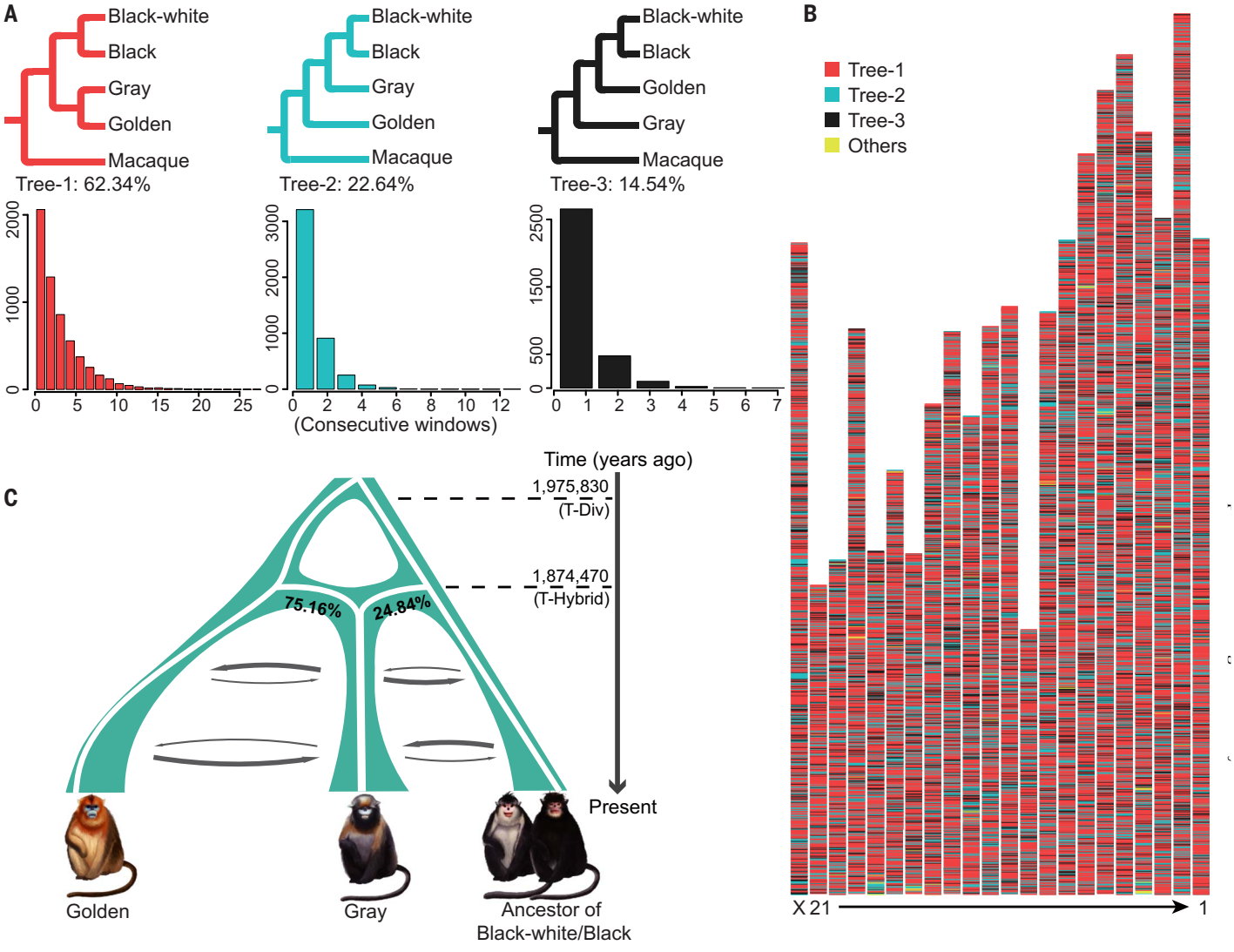


Fig. 3. Genomic phylogenetic analysis and evolutionary scenario simulation. (**A**) The major three phylogenetic tree topologies and their distributions in consecutive windows. (**B**) Genomic distributions of all topologies identified. (**C**) The best-fitting evolutionary scenario inferred by coalescent simulation. T-Div is the time of divergence of *Rhinopithecus*. T-Hybrid is the time of the hybridization between the two parental lineages. The respective genetic contributions of the two parents to the hybrid origin species, the gray snub-nosed monkey, are 24.84 and 75.16%. Curved arrows of different thicknesses indicate the magnitudes of subsequent interspecific gene flows.

hybrid origin of the gray snub-nosed monkey from the golden snub-nosed monkey and the ancestral lineage of black-white/black snub-nosed monkeys, with more ancestry contributed by the golden snub-nosed monkey than the other lineage. Because both maternal mitochondrial genome and paternal Y-linked gene trees (fig. S13) supported a sister relationship of the gray snub-nosed monkey and the golden snub-nosed monkey, we tested whether a hybridization-backcrossing scenario (fig. S12, models 20 and 21) could explain this. This showed that the fit of these models was not significantly better than that of the pure hybrid-origin scenario (model 18) (table S6). Therefore, other mechanisms—including mitonuclear incompatibility, maternal or paternal replacement of hybrid offspring in a small population (*9*), and purging of minor parental ancestry in low recombination regions—could have contributed to the sister relationship observed in the mitochondrial genome/Y-linked gene trees, and to the different genetic contributions from the two parents to the gray snub-nosed monkey during its hybrid origin.

Genetic basis of the mosaic coat coloration of the gray snub-nosed monkey

We next assessed whether genomic admixture gave rise to the peculiar pattern of hair coloration of the gray snub-nosed monkey, which displays a mosaic of the color coat patterns of both parental lineages, with golden hair on the head and deltoid regions similar to that of the golden snub-nosed monkeys, and black hair on the lateral limbs (arms and legs) similar to that of the black-white/black snub-nosed monkeys. We first used spectrophotometric measurement to quantify the amount of two melanogenesis-related pigments (eumelanin and pheomelanin) produced by melanocytes in hairs of the gray snub-nosed monkey and its two parental representatives. We found that hairs on the head and deltoid regions of the golden snub-nosed monkey showed higher pheomelanin/eumelanin ratios than those from the same regions in the black-white snub-nosed monkey. The gray snub-nosed monkey possessed elevated pheomelanin/eumelanin ratios on its head and deltoid regions similar to those

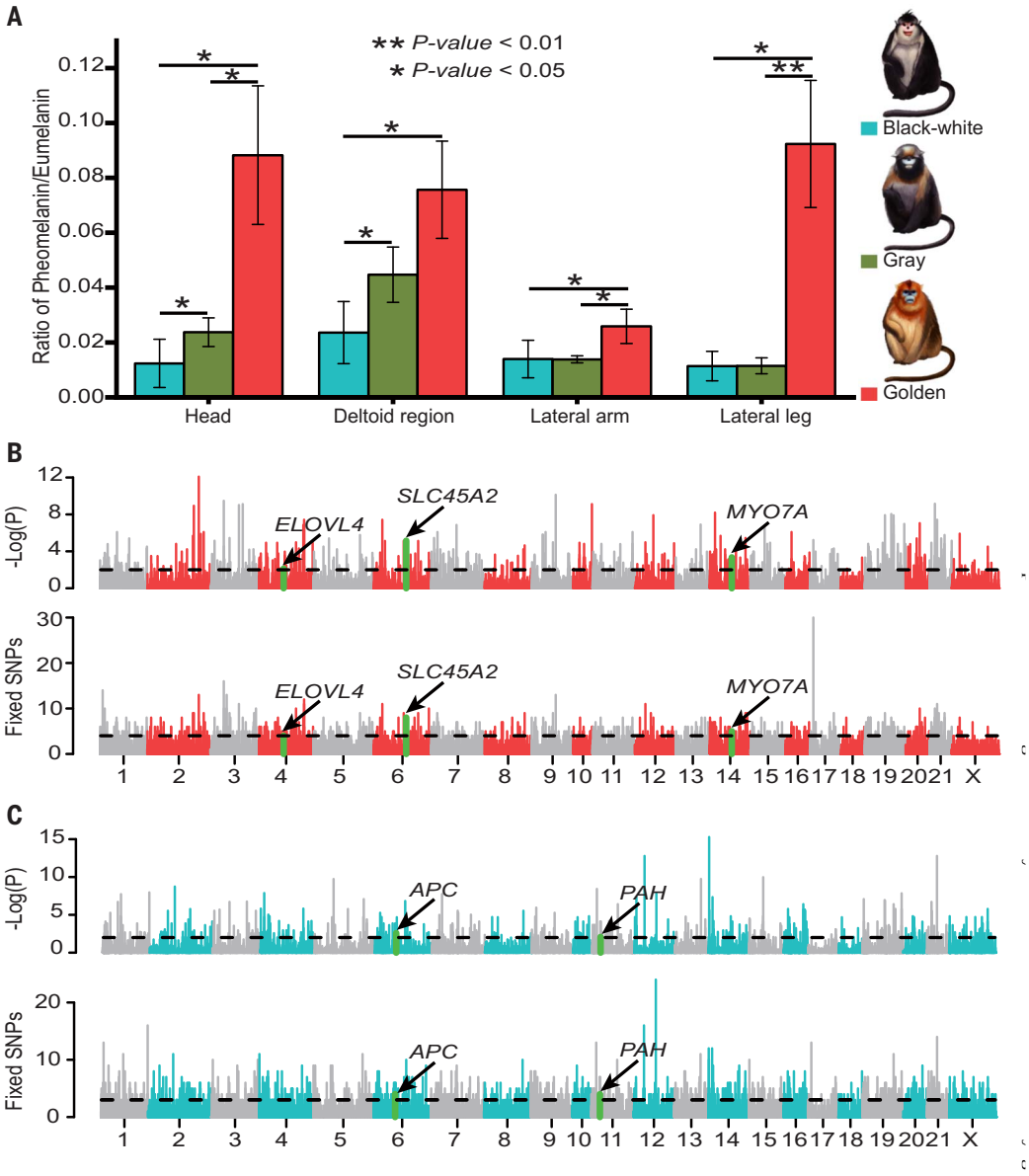


Fig. 4. Quantitative measurement of melanogenesis-related pigments and genomic positive selection analyses. (**A**) Spectrophotometric measurement of eumelanin and pheomelanin in different body parts of the gray snub-nosed monkey and two parental representatives, the golden and the black-white snub-nosed monkeys. (**B**) PSGs identified in the gray snub-nosed monkey derived from the golden snub-nosed monkey population. Three melanogenesis-related PSGs are indicated with arrows. (**C**) PSGs identified in the gray snub-nosed monkey derived from the black-white/black snub-nosed monkey populations. Two melanogenesis-related PSGs are indicated with arrows.

of the golden snub-nosed monkey but exhibited decreased ratios on its lateral limbs similar to those of the black-white snub-nosed monkey (Fig. 4A).

We used a method developed recently (*13*) to identify positively selected genes (PSGs) that co-occur in a hybrid and one of its parents, which may account for their respective phenotypic and physiological similarities. In this way, we identified 416 PSGs shared by the hybrid gray snub-nosed monkey and the golden snub-nosed monkey (parent A) and 414 PSGs by the gray snub-nosed monkey and the ancestor of the black-white/black snub-nosed monkeys (parent B) (Fig. 4, B and C). The PSGs represent genes that were under selection in each parent lineage before hybridization and were alternatively inherited by the gray snub-nosed monkey during its origin. Some of these PGSs were found to be involved mainly in functions related to melanogenesis (fig. S14). Among them, five PSGs (*PAH*, *APC*, *SLC45A2*, *MYO7A*, and *ELOVL4*) (Fig. 4, B and C) have been reported to be related to pigmentation in the eye retina, skin, and coat and hair (*14*–*18*). Haplotype analyses of these five genes showed that the *SLC45A2*, *MYO7A*, and *ELOVL4* genes of the gray snub-nosed monkey were derived from the golden snub-nosed monkey (parent A), whereas the *PAH* and *APC* genes were inherited from the ancestor of the black-white/black snub-nosed monkeys (parent B) (Fig. 5A and fig. S15). Previous studies in mammals (including humans) have reported that reduced expression of the *SLC45A2* gene (parent A–derived) results in lower melanosomal pH and promotes the synthesis of pheomelanin in melanocytes (*16*, *19*), leading to light or blonde skin or coat colors (*20*, *21*). By contrast, higher expression of the *PAH* gene (parent B–derived), which encodes a limiting enzyme for the conversion of phenylalanine to tyrosine during melanin synthesis (*14*, *22*), is associated with darker skin or coat color in humans and mice (*14*, *23*).

All fixed single-nucleotide polymorphisms (SNPs) between species in *SLC45A2* and *PAH* genes were located in promotor regions. Luciferase reporter assays of SNPs in *SLC45A2* showed that alleles derived from both the gray snub-nosed monkey and the golden snub-nosed monkey (parent A) caused significantly lower transcriptional activity than those from the ancestral lineage of the black-white/black snub-nosed monkeys (parent B) (Fig. 5B and fig. S16), suggesting that this gene likely plays a role in the development of the yellow coat

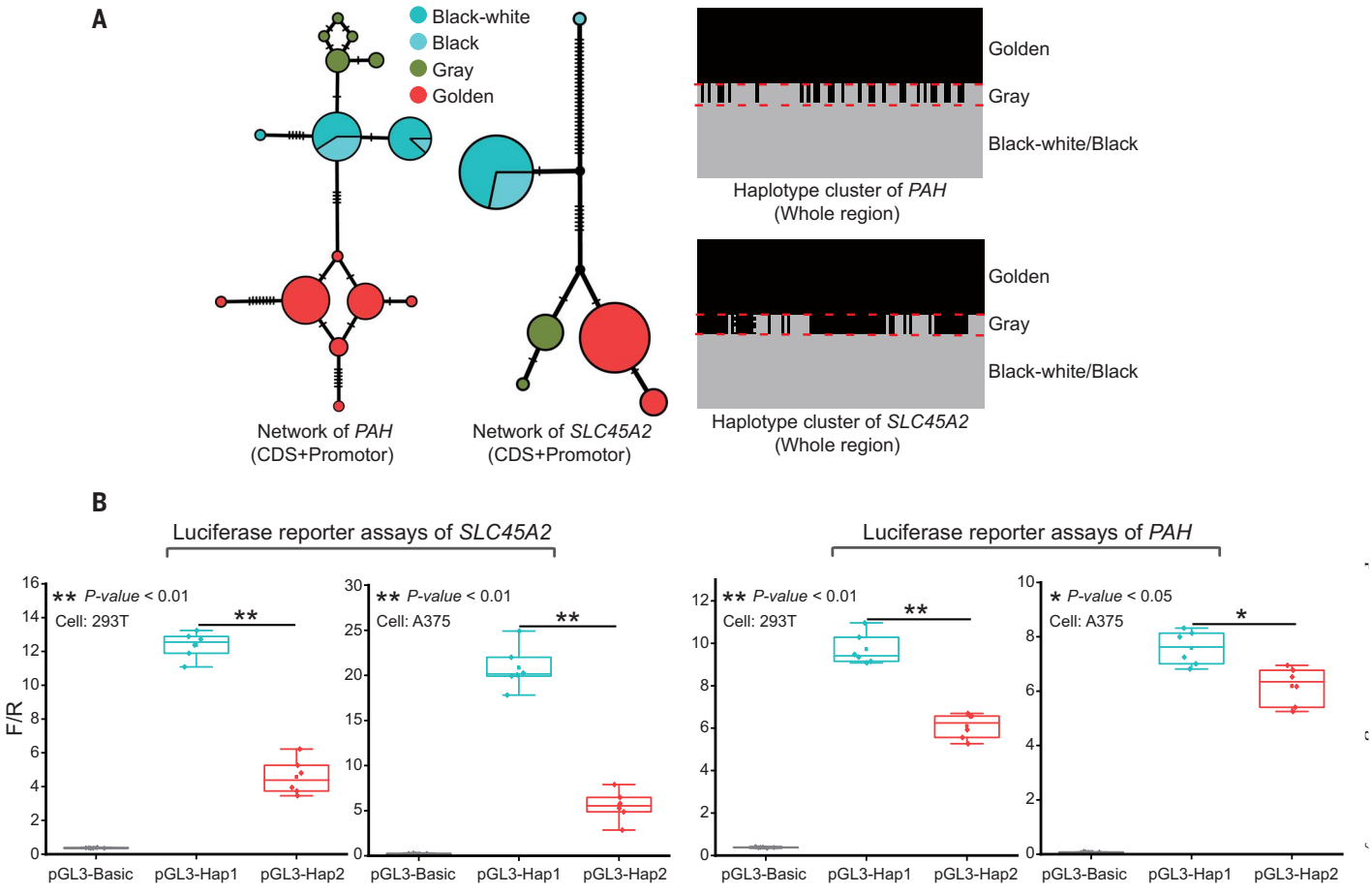


Fig. 5. Haplotype analyses and functional assays of melanogenesis-related genes *PAH* and *SLC45A2*. (**A**) Haplotype analyses of *SLC45A2* and *PAH* genes. (**B**) Luciferase reporter assays of *SLC45A2* and *PAH* genes. For each candidate gene, 293T and A375 cell lines were used. Blue, transcriptional activities induced by alleles derived from both the black-white/black and the gray snub-nosed monkeys; red, transcriptional activities induced by alleles derived from both the golden and the gray snub-nosed monkeys.

color parts of the gray snub-nosed monkey. On the other hand, luciferase reporter assays of fixed SNPs in *PAH* showed that alleles derived from both the gray snub-nosed monkey and parent B caused significantly higher transcriptional activity than those from parent A (Fig. 5B and fig. S17), suggesting that this gene contributes to the development of the dark color areas of the coat of the gray snub-nosed monkey. Together, these results indicate that selection acting on early hybrids caused the retention and loss of alleles of these genes inherited from the two parental lineages, which in turn changed the pheomelanin/eumelanin ratio in their different parts of the body to produce the distinctive mosaic coat coloration found in the gray snub-nosed monkey.

Discussion

Our study has produced evidence for genomic admixture among species of the genus *Rhinopithecus* and a hybrid origin of the gray snub-nosed monkey (Fig. 6). All of these species are highly endangered primates, and as yet, it has not been possible to quantify premating and postmating reproductive isolation (RI) barriers between them or to determine whether hybridization led to the possible origin of such barriers between the gray snub-nosed monkey and its parents (*24*–*26*). However, we have obtained evidence that allele recombination in the hybrid of different genes affecting type and distribution of hair pigmentation between the two assumed parental lineages likely produced the mosaic coat coloration of the gray snub-nosed monkey. Such phenotypic differentiation between species is known to be important in mate recognition and choice in birds (*27*), other primates (*28*, *29*), and mammals (*30*), thus creating effective premating RI (Fig. 6). Additionally, we might expect postmating RI to have arisen in the hybrid lineage through alternate fixing of alleles at different loci involved in genetic incompatibility [Bateson-Dobzhansky-Muller (BDM) incompatibility model] between the parents (*31*, *32*). We found that alleles at numerous loci of the gray snub-nosed monkey are derived alternately from its two parents (more than 18,000 SNPs and more than 10,000 genes involved from each parent) (table S8). Although many of these allelic differences might be expected to be neutral in effect (*31*), it is feasible that some have caused the hybrid species to exhibit BDM genetic incompatibility with both parents at its origin. Alternately inherited alleles of multiple genes in the gray snub-nosed monkey are associated with reproduction (such as sperm development, oocyte maturation, and fertility) (figs. S18 and S19 and tables S9 and S10) and show high levels of divergence between the two parent lineages. If these divergent alleles are involved in hindering reproduction between these parental lineages, their inheritance in the hybrid might have caused postmating RI to have developed between the hybrid and each parent, thus adding to the likely premating RI (Fig. 6). Premating isolation owing to differences in coat coloration pattern (together with

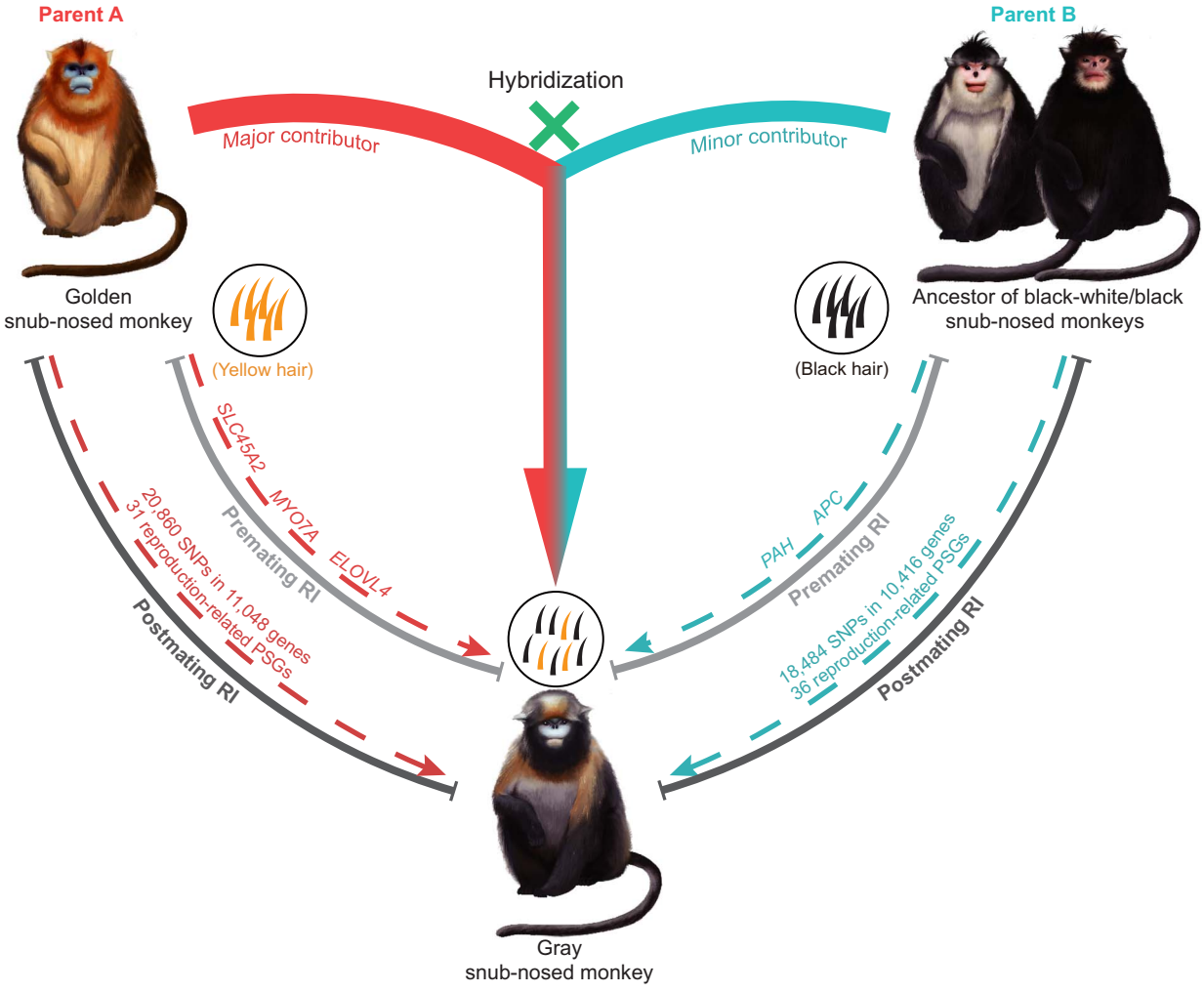


Fig. 6. Evolutionary scenario of the hybrid origin for the gray snub-nosed monkey. Genome of the gray snub-nosed monkey was generated by the historical hybridization between the golden snub-nosed monkey (parent A) and the ancestor of the black-white/black snub-nosed monkeys (parent B). Under the hybrid origin context, melanogenesis-related PSGs derived from parent A (*SLC45A2*, *MYO7A*, and *ELOVL4*) and from parent B (*PAH* and *APC*) are likely to contribute to the mosaic coat coloration of the gray snub-nosed monkey, which may promote the establishment of premating RI. In addition, alleles at numerous loci (more than 18,000 SNPs and more than 10,000 genes involved from each parent) and 67 PSGs related to reproduction of the gray snub-nosed monkey derived alternately from its two parents may promote the establishment of postmating RI.

geographic isolation) could accelerate the development of such genetic incompatibility between the hybrid and its parents (*31*, *33*).

REFERENCES AND NOTES

1. J. Mallet, Hybridization as an invasion of the genome. *Trends Ecol. Evol.* **20**, 229–237 (2005). doi: 10.1016/j.tree.2005.02.010; pmid: 16701374
2. S. A. Taylor, E. L. Larson, Insights from genomes into the evolutionary importance and prevalence of hybridization in nature. *Nat. Ecol. Evol.* **3**, 170–177 (2019). doi: 10.1038/s41559-018-0777-y; pmid: 30697003
3. D. A. Marques, J. I. Meier, O. Seehausen, A combinatorial view on speciation and adaptive radiation. *Trends Ecol. Evol.* **34**, 531–544 (2019). doi: 10.1016/j.tree.2019.02.008; pmid: 30885412
4. R. Abbott *et al.*, Hybridization and speciation. *J. Evol. Biol.* **26**, 229–246 (2013). doi: 10.1111/j.1420-9101.2012.02599.x; pmid: 23323997
5. J. Mallet, Hybrid speciation. *Nature* **446**, 279–283 (2007). doi: 10.1038/nature05706; pmid: 17361174
6. T. Geissmann *et al.*, A new species of snub-nosed monkey, genus *Rhinopithecus* Milne-Edwards, 1872 (Primates, Colobinae), from northern Kachin state, northeastern Myanmar. *Am. J. Primatol.* **73**, 96–107 (2011). doi: 10.1002/ajp.20894; pmid: 20981682
7. X. Zhou *et al.*, Whole-genome sequencing of the snub-nosed monkey provides insights into folivory and evolutionary history. *Nat. Genet.* **46**, 1303–1310 (2014). doi: 10.1038/ng.3137; pmid: 25362486
8. H. L. Xu *et al.*, Construction, characterization and chromosomal mapping of bacterial artificial chromosome (BAC) library of Yunnan snub-nosed monkey (*Rhinopithecus bieti*). *Chromosome Res.* **12**, 251–262 (2004). doi: 10.1023/B:CHRO.0000021946.13556.40; pmid: 15125639
9. B. M. Moran *et al.*, The genomic consequences of hybridization. *eLife* **10**, e69016 (2021). doi: 10.7554/eLife.69016; pmid: 34346866
10. N. Patterson *et al.*, Ancient admixture in human history. *Genetics* **192**, 1065–1093 (2012). doi: 10.1534/genetics.112.145037; pmid: 22960212
11. S. H. Martin, J. W. Davey, C. D. Jiggins, Evaluating the use of ABBA-BABA statistics to locate introgressed loci. *Mol. Biol. Evol.* **32**, 244–257 (2015). doi: 10.1093/molbev/msu269; pmid: 25246699
12. L. Yu *et al.*, Genomic analysis of snub-nosed monkeys (*Rhinopithecus*) identifies genes and processes related to high-altitude adaptation. *Nat. Genet.* **48**, 947–952 (2016). doi: 10.1038/ng.3615; pmid: 27399969
13. Z. Wang *et al.*, Hybrid speciation via inheritance of alternate alleles of parental isolating genes. *Mol. Plant* **14**, 208–222 (2021). doi: 10.1016/j.molp.2020.11.008; pmid: 33220509
14. K. U. Schallreuter *et al.*, Regulation of melanin biosynthesis in the human epidermis by tetrahydrobiopterin. *Science* **263**, 1444–1446 (1994). doi: 10.1126/science.8128228; pmid: 8128228
15. I. Hwang *et al.*, Neural stem cells inhibit melanin production by activation of Wnt inhibitors. *J. Dermatol. Sci.* **72**, 274–283 (2013). doi: 10.1016/j.jdermsci.2013.08.006; pmid: 24016750
16. P. Wiriyasermkul, S. Moriyama, S. Nagamori, Membrane transport proteins in melanosomes: Regulation of ions for pigmentation. *Biochim. Biophys. Acta Biomembr.* **1862**, 183318 (2020). doi: 10.1016/j.bbamem.2020.183318; pmid: 32333855
17. V. S. Lopes *et al.*, Retinal gene therapy with a large *MYO7A* cDNA using adeno-associated virus. *Gene Ther.* **20**, 824–833 (2013). doi: 10.1038/gt.2013.3; pmid: 23344065
18. G. Karan *et al.*, Lipofuscin accumulation, abnormal electrophysiology, and photoreceptor degeneration in mutant

ELOVL4 transgenic mice: A model for macular degeneration. *Proc. Natl. Acad. Sci. U.S.A.* **102**, 4164–4169 (2005). doi: 10.1073/pnas.0407698102; pmid: 15749821
19. J. Ancans *et al*., Melanosomal pH controls rate of melanogenesis, eumelanin/phaeomelanin ratio and melanosome maturation in melanocytes and melanoma cells. *Exp. Cell Res.* **268**, 26–35 (2001). doi: 10.1006/excr.2001.5251; pmid: 11461115
20. X. Xu *et al*., The genetic basis of white tigers. *Curr. Biol.* **23**, 1031–1035 (2013). doi: 10.1016/j.cub.2013.04.054; pmid: 23707431
21. R. A. Sturm, D. L. Duffy, Human pigmentation genes under environmental selection. *Genome Biol.* **13**, 248 (2012). doi: 10.1186/gb-2012-13-9-248; pmid: 23110848
22. K. U. Schallreuter, S. Kothari, B. Chavan, J. D. Spencer, Regulation of melanogenesis—Controversies and new concepts. *Exp. Dermatol.* **17**, 395–404 (2008). doi: 10.1111/j.1600-0625.2007.00675.x; pmid: 18177348
23. H. J. Oh, E. S. Park, S. Kang, I. Jo, S. C. Jung, Long-term enzymatic and phenotypic correction in the phenylketonuria mouse model by adeno-associated virus vector-mediated gene transfer. *Pediatr. Res.* **56**, 278–284 (2004). doi: 10.1203/01.PDR.0000132837.29067.0E; pmid: 15181195
24. M. Schumer, G. G. Rosenthal, P. Andolfatto, How common is homoploid hybrid speciation? *Evolution* **68**, 1553–1560 (2014). doi: 10.1111/evo.12399; pmid: 24620775
25. L. H. Rieseberg, Hybrid origins of plant species. *Annu. Rev. Ecol. Syst.* **28**, 359–389 (1997). doi: 10.1146/annurev.ecolsys.28.1.359
26. M. Schumer *et al*., Natural selection interacts with recombination to shape the evolution of hybrid genomes. *Science* **360**, 656–660 (2018). doi: 10.1126/science.aar3684; pmid: 29674434
27. S. P. Turbek *et al*., Rapid speciation via the evolution of pre-mating isolation in the Iberá Seedeater. *Science* **371**, eabc0256 (2021). doi: 10.1126/science.abc0256; pmid: 33766854
28. S. Winters, W. L. Allen, J. P. Higham, The structure of species discrimination signals across a primate radiation. *eLife* **9**, e47428 (2020). doi: 10.7554/eLife.47428; pmid: 31928629
29. W. L. Allen, M. Stevens, J. P. Higham, Character displacement of *Cercopithecini* primate visual signals. *Nat. Commun.* **5**, 4266 (2014). doi: 10.1038/ncomms5266; pmid: 24967517
30. P. W. Hedrick, D. W. Smith, D. R. Stahler, Negative-assortative mating for color in wolves. *Evolution* **70**, 757–766 (2016). doi: 10.1111/evo.12906; pmid: 26988852
31. M. Schumer, R. Cui, G. G. Rosenthal, P. Andolfatto, Reproductive isolation of hybrid populations driven by genetic incompatibilities. *PLOS Genet.* **11**, e1005041 (2015). doi: 10.1371/journal.pgen.1005041; pmid: 25768654
32. J. S. Hermansen *et al*., Hybrid speciation through sorting of parental incompatibilities in Italian sparrows. *Mol. Ecol.* **23**, 5831–5842 (2014). doi: 10.1111/mec.12910; pmid: 25208037
33. J. W. Kadereit, The geography of hybrid speciation in plants. *Taxon* **64**, 673–687 (2015). doi: 10.12705/644.1

ACKNOWLEDGMENTS

Funding: This project was supported equally by grants from the National Natural Science Foundation of China (NSFC) (31925006) and the Strategic Priority Research Program of the Chinese Academy of Sciences (XDB31000000) and further by NSFC projects (91731311, 91731301, and 31590821) and Fundamental Research Funds for the Central Universities (SCU2019D013 and 2020SCUNL207). We thank T. Zou for conducting the haplotype analyses. **Author contributions:** L.Y. and J.L. designed the project and wrote the manuscript. H.W. and Z.W. performed data analyses and wrote the manuscript. Y.Z. performed practical experiments. L.F., C.R., and D.M.I. revised the paper. C.Z., X.L., D.W., and S.H. performed sample collection. T.G. performed data analyses. **Competing interests:** The authors declare no competing interests. **Data and materials availability:** Newly generated genome assembly and raw data are available through CNCB (BioProject accession no. PRJCA007648) and NCBI (BioProject accession no. PRJNA744006). **License information:** Copyright © 2023 the authors, some rights reserved; exclusive licensee American Association for the Advancement of Science. No claim to original US government works. https://www.science.org/about/science-licenses-journal-article-reuse

SUPPLEMENTARY MATERIALS

science.org/doi/10.1126/science.abl4997
Materials and Methods
Figs. S1 to S19
Tables S1 to S10
References (*34*–*81*)
MDAR Reproducibility Checklist

Submitted 17 July 2021; accepted 6 July 2022
10.1126/science.abl4997

RESEARCH ARTICLE SUMMARY

PRIMATE GENOMES

Adaptations to a cold climate promoted social evolution in Asian colobine primates

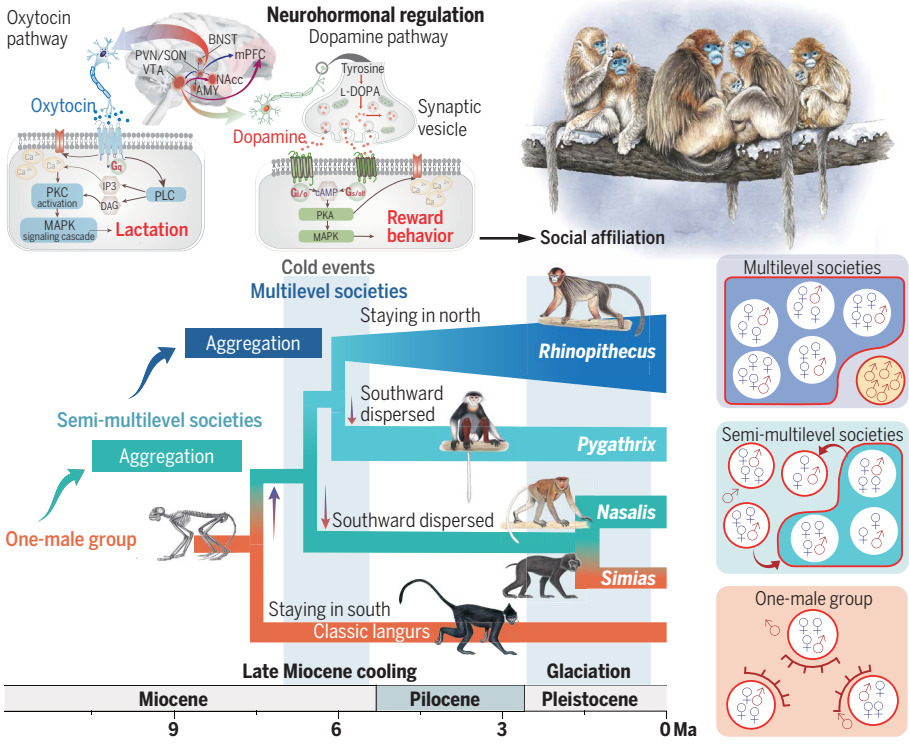
Xiao-Guang Qi*†, Jinwei Wu†, Lan Zhao†, Lu Wang, Xuanmin Guang, Paul A. Garber, Christopher Opie, Yuan Yuan, Runjie Diao, Gang Li, Kun Wang, Ruliang Pan, Weihong Ji, Hailu Sun, Zhi-Pang Huang, Chunzhong Xu, Arief B. Witarto, Rui Jia, Chi Zhang, Cheng Deng, Qiang Qiu, Guojie Zhang, Cyril C. Grueter*, Dongdong Wu*, Baoguo Li*

INTRODUCTION: Primates have evolved a diverse set of social systems, from solitary living to large multilevel societies. The traditional socioecological model explains this diversity as a response to changing environments, which shaped patterns of cooperation and competition for resources and predator defense. However, the socioecological model does not explain why sympatric species living in the same environment exhibit different social systems. There is a growing consensus that primate social organization shows a strong phylogenetic signal as a result of shared inheritance from a common ancestor and evolved stepwise along with species differentiation. This implies a genetic basis for the evolution of animal social systems. However, the genomic mechanisms that underlie the expression of primate social systems remain poorly understood.

RATIONALE: Asian colobines, a subfamily of Old World monkeys, are represented by seven genera and 55 species that are distributed from tropical rainforests to snow-covered mountains. They exhibit four distinct types of social organization and provide a good model for examining the mechanisms that drive social evolution from a common ancestral state to the diverse systems present today. By integrating new genomic data across all seven colobine genera with paleoenvironmental information, the fossil record, social organization characteristics, social behavioral characteristics, and ecological niche modeling, we constructed a socioecological-genomic framework to identify selective pressures that form the genetic basis for social evolution in Asian colobines.

RESULTS: To understand the evolutionary process of social systems in Asian colobines, we first reconstructed their phylogenetic relationships using whole-genome data. In contrast to the previous hypothesis of three major clades, our study reveals that Asian colobines split into two clades: the odd-nosed monkeys and the classical langurs. Our phylogenetic analyses detected a strong signal in colobine social evolution, suggesting that these social systems evolved in a stepwise manner, with ancestral one-male, multifemale groups fusing into semi-multilevel societies characterized by fission-fusion and then merging into complex multilevel societies. Consistent with our ecological results indicating that extant colobine primates that inhabit colder environments tend to live in larger groups, we found that adaptations driven by ancient cold events, including the late Miocene cooling and Pleistocene glacial periods, played an important role in promoting these changes in social evolution. Furthermore, our genomic analyses revealed that these cold events promoted the selection of genes involved in energy metabolism and neurohormonal regulation. In particular, more-efficient dopamine and oxytocin pathways developed in odd-nosed monkeys, which might have resulted in the prolongation of maternal care and lactation, favoring infant survival in cold environments. These adaptive changes also appear to have strengthened interindividual affiliation, increased male-male tolerance, and facilitated the stepwise social aggregation from independent one-male, multifemale groups to large multilevel societies in Asian colobines.

CONCLUSION: Our results reveal a stepwise evolutionary scenario of social organization in Asian colobines. We show that ancient glacial events selected for neurohormonal regulation, including dopamine and oxytocin pathways that promoted aggregation from one-male, multifemale groups into large multilevel societies. Our study demonstrates a direct link between a genomically regulated adaptation and social evolution in primates and offers new insights into the mechanisms that underpin behavioral evolution across animal taxa. ■



Adaptation for survival in cold climates facilitated evolution of social behavior in colobine monkeys. Cold environments promoted the social evolution of Asian colobines in a stepwise manner. Genomic changes in neurohormonal regulation, including in the dopamine and oxytocin pathways, improved social affiliation in odd-nosed monkeys and thus promoted social aggregations from independent one-male, multifemale groups into large multilevel societies. Ma, million years ago.

The list of author affiliations is available in the full article online.
*Corresponding author: Email: qixg@nwu.edu.cn (X.G.Q.); baoguoli@nwu.edu.cn (B.G.L.); wudongdong@mail.kiz.ac.cn (D.D.W.); cyril.grueter@uwa.edu.au (C.C.G.)
†These authors contributed equally to this work.
Cite this article as X. G. Qi *et al.*, *Science* **380**, eabl8621 (2023). DOI: 10.1126/science.abl8621

READ THE FULL ARTICLE AT
https://doi.org/10.1126/science.abl8621

RESEARCH ARTICLE

PRIMATE GENOMES

Adaptations to a cold climate promoted social evolution in Asian colobine primates

Xiao-Guang Qi[1]*†, Jinwei Wu[1]†, Lan Zhao[1]†, Lu Wang[1], Xuanmin Guang[2], Paul A. Garber[3], Christopher Opie[4], Yuan Yuan[5], Runjie Diao[6], Gang Li[7], Kun Wang[5], Ruliang Pan[1], Weihong Ji[8], Hailu Sun[2], Zhi-Pang Huang[1], Chunzhong Xu[9], Arief B. Witarto[10], Rui Jia[7], Chi Zhang[2], Cheng Deng[6], Qiang Qiu[5], Guojie Zhang[11], Cyril C. Grueter[12]*, Dongdong Wu[11]*, Baoguo Li[1]*

The biological mechanisms that underpin primate social evolution remain poorly understood. Asian colobines display a range of social organizations, which makes them good models for investigating social evolution. By integrating ecological, geological, fossil, behavioral, and genomic analyses, we found that colobine primates that inhabit colder environments tend to live in larger, more complex groups. Specifically, glacial periods during the past 6 million years promoted the selection of genes involved in cold-related energy metabolism and neurohormonal regulation. More-efficient dopamine and oxytocin pathways developed in odd-nosed monkeys, which may have favored the prolongation of maternal care and lactation, increasing infant survival in cold environments. These adaptive changes appear to have strengthened interindividual affiliation, increased male-male tolerance, and facilitated the stepwise aggregation from independent one-male groups to large multilevel societies.

Primates have evolved a diverse set of social systems (*1*–*3*). From solitary living and small families to large multilevel societies, evolution associated with varied behavioral tactics has allowed primates to successfully exploit a wide range of habitats (*4*–*9*). The socioecological model explains the diversity of primate social systems as a response to changing environments, which shaped patterns of cooperation and competition for resources and predator defense (*10*–*12*). However, the socioecological model does not explain why sympatric species can live in the same environment but exhibit different social systems (*13*, *14*).

Evidence increasingly supports that the social system of different primate taxa is likely inherited from a recent common ancestor, rather than evolving as a direct adaptation to current environmental conditions (*15*, *16*). For example, although they inhabit the same rainforest, white-handed gibbons form monogamous pairs, whereas Thomas's langurs live in a one-male, multifemale polygynous group; long-tailed macaques live in multimale, multifemale groups; and Bornean orangutans live solitarily with occasional social contact (*17*). Therefore, there is a growing consensus that certain components of social systems have a strong phylogenetic signal (*5*, *18*) and evolved in a stepwise manner in conjunction with species differentiation (*16*, *19*). However, the genomic mechanisms that constrain or promote the expression of primate social systems remain poorly understood (*20*, *21*).

Asian colobines, a subfamily of Old World monkeys, are represented by seven genera and 55 species that are distributed from tropical rainforests to snow-covered mountains. They exhibit four distinct types of social organization and provide a good model for examining the multiple mechanisms that have driven their social evolution from a common ancestral state to the diverse systems that are present today (Fig. 1 and data S1). These Asian colobines are categorized into two clades (*22*). The classical langurs (genera *Presbytis*, *Semnopithecus*, and *Trachypithecus*) are each principally characterized by a one-male, multifemale unit; polygynous mating; and strict male territorial defense. In addition, a small number of species in this clade such as the Himalayan gray langur (*Semnopithecus schistaceus*) and the Indochinese langur (*Trachypithecus crepusculus*) exploit high-altitude forests and occasionally form cohesive larger multimale, multifemale groups (Fig. 1C). By contrast, species in the odd-nosed monkey clade exhibit a wide spectrum of social systems. Simakobus (genus *Simias*) live in independent one-male, multifemale units, whereas doucs (genus *Pygathrix*) and proboscis monkeys (genus *Nasalis*) live in distinct nonterritorial one-male, multifemale units, which seasonally fuse into a single breeding band or aggregate together at nighttime sleeping sites (*23*) (data S1). We term these semi-multilevel societies because this social system is characterized by flexibility in switching between independent one-male, multifemale units and multilevel societies. The last group of odd-nosed monkeys are the snub-nosed monkeys (genus *Rhinopithecus*). They live in typical multilevel societies, which are composed of several core one-male, multifemale units embedded within a stable and larger social matrix and associated all-male bachelor bands (*24*).

In this study, we integrated newly acquired de novo high-quality genome data representing all seven colobine genera with paleoenvironmental information, the fossil record, type of social organization, level of intrasexual tolerance, and ecological databases from 2189 habitat locations (data S2) of 48 extant Asian colobine species. This allowed us to construct a comparative dynamic socioecological-genomic framework that identifies the genetic basis of social evolution in primates.

Phylogeny reconstruction

To understand the social evolution of Asian colobines, we clarified their phylogenetic relationships and natural histories. To resolve previous inconsistencies concerning colobine phylogenetic relationships (*25*, *26*), we sequenced and analyzed seven de novo genomes of species from all seven genera of Asian colobines [supplementary materials (SM) section 3.3.1]. Based on a combination of the concatenation method and the coalescent method, a new phylogenomic tree was reconstructed from a total of 4992 one-to-one orthologs (fig. S7). With calibrations from new fossil discoveries, we were able to develop greater precision in divergence time estimates (Fig. 2A). This new high-confidence topological structure enabled us to trace the evolutionary history of social systems in Asian colobines. The results revealed that Asian colobines split into two well-supported clades: the odd-nosed monkeys and the classical langurs. The genera *Presbytis*, *Semnopithecus*, and *Trachypithecus* are best described as a monophyly of the classical langurs (Fig. 2A). These results contrast with the hypothesis of three major clades, with *Presbytis* located at the basal position of an independent monophyly, which was proposed in previous studies (*27*, *28*).

Phylogenetic signal of social evolution

To understand how the set of social organizations of extant Asian colobines was shaped by their phylogenetic lineage, we used phylogeny trait reconstruction modeling. Based on

[1]College of Life Sciences, Northwest University, Xi'an, China. [2]BGI-Shenzhen, Shenzhen, China. [3]Department of Anthropology, University of Illinois, Urbana, IL, USA. [4]Department of Anthropology and Archaeology, University of Bristol, Bristol, UK. [5]College of Ecological and Environmental Sciences, Northwestern Polytechnical University, Xi'an, China. [6]College of Life Sciences, Nanjing Normal University, Nanjing, China. [7]College of Life Sciences, Shaanxi Normal University, Xi'an, China. [8]School of Natural and Computational Sciences, Massey University, Auckland, New Zealand. [9]Shanghai Wild Animal Park Development Co., Shanghai, China. [10]Faculty of Medicine, Universitas Pertahanan, Jabodetabek, Indonesia. [11]Kunming Institute of Zoology, Chinese Academy of Sciences, Kunming, China. [12]School of Human Sciences, The University of Western Australia, Perth, WA, Australia.
*Corresponding author. Email: qixg@nwu.edu.cn (X.G.Q.); baoguoli@nwu.edu.cn (B.G.L.); wudongdong@mail.kiz.ac.cn (D.D.W.); cyril.grueter@uwa.edu.au (C.C.G.)
†These authors contributed equally to this work.

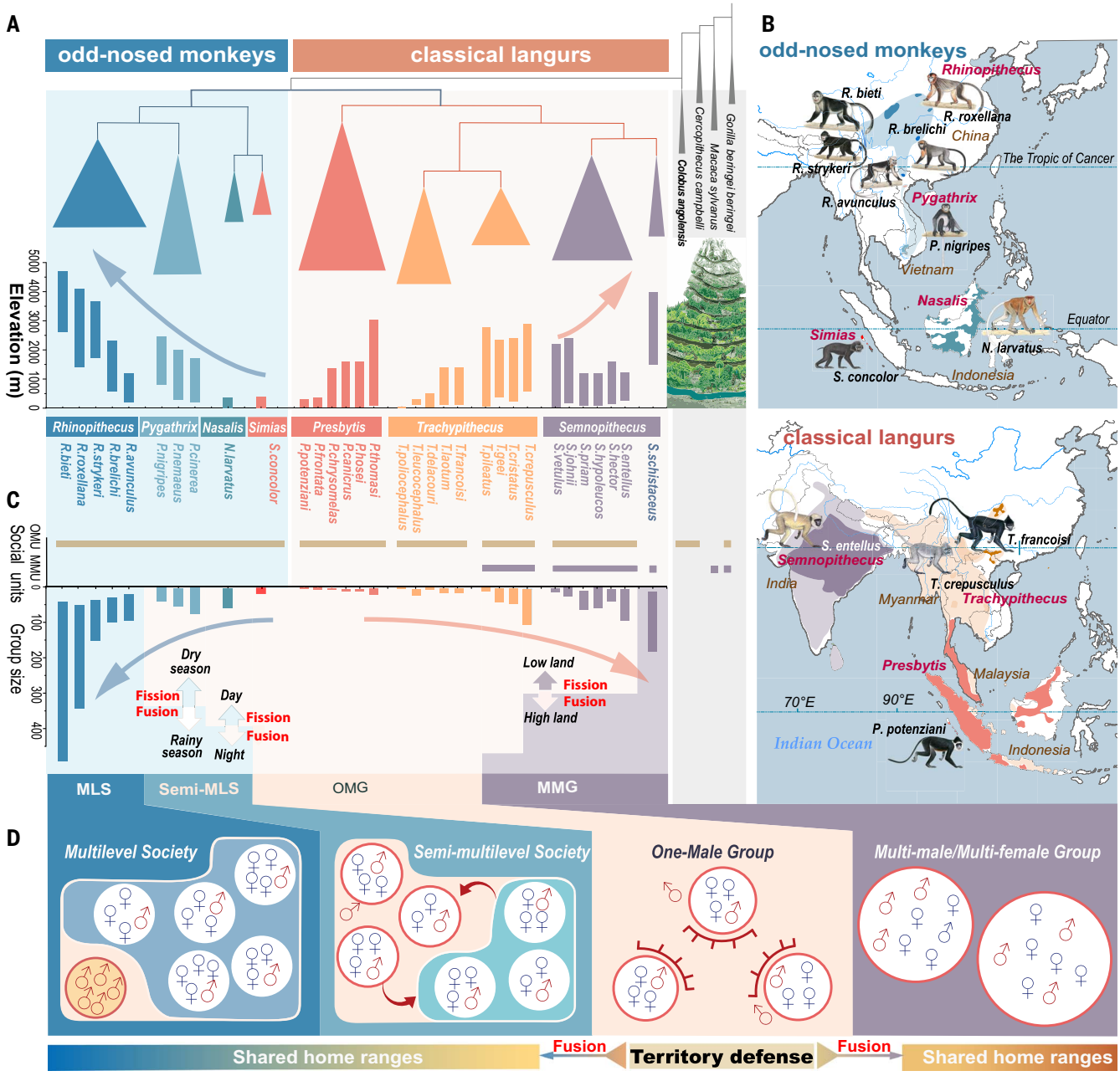


Fig. 1. Taxonomy and the social systems of Asian colobines. (**A**) Classification and vertical distribution of Asian colobines. (**B**) Geographical distribution of odd-nosed monkeys and classical langurs. (**C**) Group size increases with increasing elevation and latitude in both odd-nosed monkeys and classical langur species. MMU, multimale, multifemale unit; OMU, one-male, multifemale unit. (**D**) Stepwise evolution of social systems in Asian colobines. MLS, multilevel society; MMG, multimale, multifemale group; OMG, one-male group. [Credits: All monkey illustrations are copyrighted 2014 by Stephen D. Nash/IUCN/SSC Primate Specialist Group and used with permission]

the new phylogenomic tree (fig. S2, data S3, and SM section 3), we used Pagel's λ (*29*) and Phylo.D (*30*) to evaluate the strength of the phylogenetic signal in their social evolution. The results showed a strong signal [Pagel's λ = 0.81, log likelihood (LL) = 34.98, probability of λ resulting from Brownian model ($P_{\lambda_Brownian}$) = 1; estimated Phylo.D (D) = −0.44, probability of D resulting from Brownian model ($P_{D_Brownian}$) = 0.87] in colobine social evolution (table S6 and SM section 4.1). Next, we used a macroevolutionary model fitting analysis to compare the fit factors of phylogenetically associated models [λ, κ, δ, early burst (EB)] with nonphylogenetic models (white-noise model) in Asian colobines. The results showed that the likelihood of each of the four phylogenetically associated models was significantly higher than that of the white-noise model (table S10). These results indicate that during their evolutionary history, phylogeny was a relevant driving factor rather than a random factor in colobine sociality (SM section 4.1.2).

To verify whether social evolution in Asian colobines was stepwise, we compared ordered (stepwise) models with an unordered evolution model using MultiState in BayesTraits. By comparing the marginal likelihoods among the three candidate stepwise models (SM section 4.1.3) and the unrestricted model (unordered model) (fig. S2), a strong Bayes factor (log $BF_{model_OMM\ or\ OSM}$ >10; see SM section 4.1.3) suggested that Asian colobine social systems evolved in a stepwise manner (fig. S2A

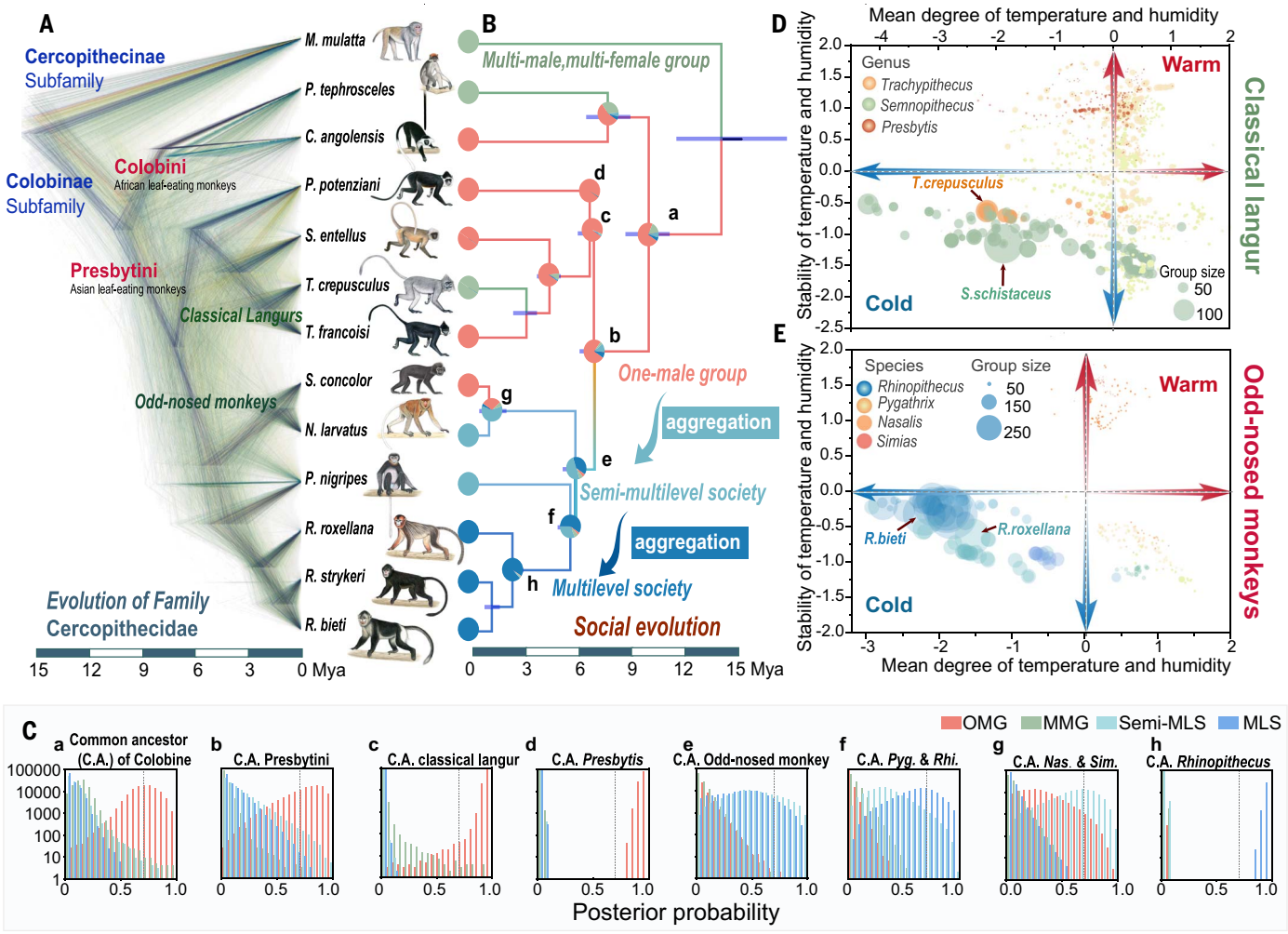


Fig. 2. Phylogenetic relationship and social system evolution in Asian colobines. (**A**) DensiTree presentation of phylogenetic trees of orthologous genes. Gene trees with a clade probability larger than 30% are shown. Mya, million years ago. (**B**) Social system evolution in Asian colobines. The pie chart at each ancestral node shows the reconstructed ancestral social state. Different colors correspond to the estimated social systems and are proportional to their posterior probability. (**C**) The posterior distributions of the probabilities (*x* axis) of each of the ancestral nodes marked in (B). C.A., common ancestor. (**D**) High principal components PC1 scores indicate high temperature and humidity. (**E**) Low principal components PC2 scores indicate wide ranges of seasonality, annual temperature, and precipitation. The scatter size in a species is proportional to its group size. [Credits: All monkey illustrations are copyrighted 2014 by Stephen D. Nash/IUCN/SSC Primate Specialist Group and used with permission]

and table S8). Therefore, we investigated these lineage-specific evolutionary pathways in greater detail.

We traced the set of social conditions for each of the ancestral nodes using a Bayesian phylogenetic framework (SM section 4.1.4 and Fig. 2B). The results showed that the most likely ancestral social state of Asian colobines (Fig. 2B) was an independent one-male, multifemale unit [probability of ancestral state (ASP_{OMU}) = 0.76 ± 0.16]. Based on the Bayesian phylogenetic framework results, we identified three lineages of ancestral Asian colobines, each with a different social evolutionary history (Fig. 2B and fig. S2). The first lineage retained the ancestral one-male, multifemale unit system that is present in most of the classical langurs, such as *Presbytis* (Fig. 2, B and C). The second lineage included a small number of classical langurs, such as the Indochinese langur (*T. crepusculus*) (Fig. 2B), that inhabit mountainous regions and tend to merge into larger multimale, multifemale groups. This contrasts with their sister species that live in warmer lowland regions and form single or independent one-male, multifemale units.

The third evolutionary pathway is related to the stepwise aggregation of core one-male, multifemale units into multilevel societies that characterize the odd-nosed monkey clade. The Bayesian phylogenetic framework results indicate that in this lineage, the ancestral independent one-male, multifemale units aggregated into semi-multilevel societies after splitting from the common ancestor of the odd-nosed monkey clade about 6.5 million (7.0 million to 5.7 million) years (Ma) ago (Figs. 2, B and C, and 3A). Subsequently, the lineage leading to the extant doucs (*Pygathrix*) and proboscis monkeys (*Nasalis*) inherited this social system, with multiple one-male, multifemale units sharing a home range through a process of fusion-fission (data S1 and S7). *Simias*, by contrast, independently reverted to an ancestral-like social system characterized by independent one-male, multifemale units. Our results indicate that the snub-nosed monkeys (*Rhinopithecus*) represent the second step of social aggregation from semi-multilevel societies to typical multilevel societies, with multiple one-male, multifemale units forming a large stable breeding band in which residents travel, rest, and feed together throughout the year. The breeding band, which may include more than 100 individuals,

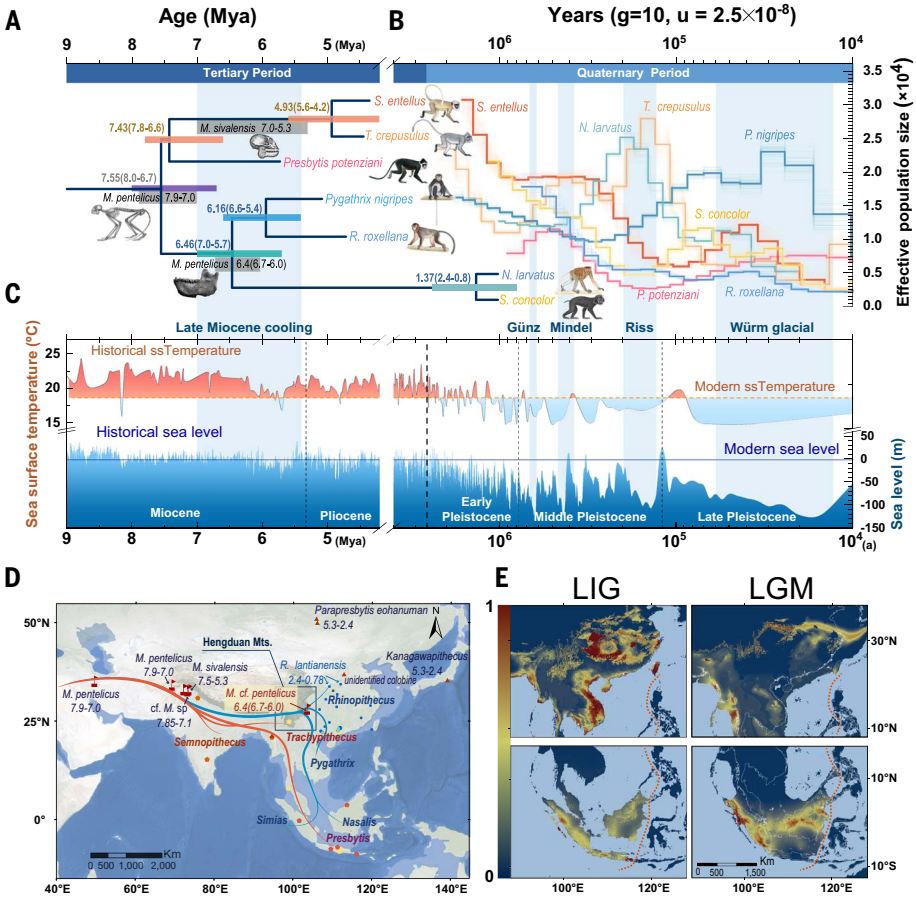


Fig. 3. Natural history of Asian colobines. (**A**) Reconstructed phylogenetic relationship of Asian colobines. The node bars indicate the 95% confidence interval for each branch. (**B**) Demographic history of seven Asian colobines estimated by PSMC. The regions marked with a vertical blue bar correspond to glacial periods. g, generation time; u, mutation rate. (**C**) Historical sea surface temperature and relative sea level over the past 9 Ma. (**D**) A new dispersal scenario proposed for Asian colobines. The orange line shows the proposed route of the odd-nosed clade (fossil records shown as dots), and the green line represents the classical langurs (fossil records shown as pentagons). (**E**) Ecological niche modeling for odd-nosed monkeys during the Last Interglacial (LIG; ~116 thousand to 130 thousand years before the present) and the Last Glacial Maximum (LGM; ~26.5 thousand to 19.0 thousand years before the present) period. [Credits: All monkey illustrations are copyrighted 2014 by Stephen D. Nash/IUCN/SSC Primate Specialist Group and used with permission]

is shadowed by all-male bachelor bands (Fig. 2B). These results demonstrate that social evolution in Asian colobines represents a newly discovered two-step pathway from ancestral independent one-male, multifemale units to large aggregated multilevel societies. This pathway is distinct from that of African papionins (e.g., gelada, hamadryas baboon), whose multilevel societies evolved through the internal fissioning of large multimale, multifemale groups (*4*, *31*).

Social systems under contrasting environments

To understand how ecological factors have shaped primate social evolution, we constructed an Asian colobine ecological dataset (data S2) based on 19 bioclimatic variables that were extracted from a total of 2189 current locations across the ranges of 48 extant Asian colobine species (data S2). Based on principal components analyses, we found that species that are presently distributed in colder, drier, and more seasonal climates tend to live in larger groups, whereas species that inhabit warmer and moister environments tend to form smaller groups (Fig. 2, D and E). The mean and stability of temperature and humidity were identified as the main factors that affect group size in odd-nosed monkeys (which explained 84.8% of the variance) and classical langurs (which explained 85.7% of the variance) (table S9). Furthermore, the random-walk model for continuous traits in BayesTraits (*32*) showed that group size was negatively correlated with annual mean temperature [Pagel's λ = 0.59; correlation coefficient (R) = −0.69; log BF = 17.75, which is greater than 10], indicating that cold conditions may have selected for increased group size in both clades of Asian colobines (SM section 4.3.2). This pattern of enhanced sociality in cold and dry environments has also been reported in Australian rodents (*33*) and cooperative breeding birds (*34*). In the case of Asian colobines, transitions from one social system to another appear to have occurred at ancient evolutionary nodes and have been retained over long periods of time. This suggests that colobine social systems may reflect adaptations to ancient environmental conditions rather than a direct response to current environmental conditions.

Evolutionary history and radiation

Assuming that ancient ecological factors played an important role in promoting stepwise social evolution (Figs. 1 and 2), we traced the natural and social evolutionary history of Asian colobines over the past 8 Ma. This was accomplished by integrating data from new discoveries in the fossil record (data S4), paleogeology, paleogeography, paleoclimate, and historical sea level dynamics (data S5), as well as the present geographical distribution of individual Asian-colobine taxa (data S2). Using BioGeography with Bayesian and likelihood evolutionary analysis, we reconstructed the ancestral distribution pattern of Asian colobines (SM section 4.4.3 and fig. S12). In comparing the likelihoods of the resulting candidate models, with results from geographic and multiple-state speciation and extinction analyses (SM section 4.4.2 and fig. S11), we found that ancient dispersal routes and geographic isolation appear to have played important roles in Asian colobine speciation (Fig. 3D).

In contrast to the previous hypothesis that ancestral colobines dispersed into Asia via a northern route through China (*35*), we combined data on newly reported *Mesopithecus* fossils (7.9 to 7.0 Ma ago) found in Pakistan, Iran, and Afghanistan (SM section 4.4.5 and fig. S3) that support an alternative scenario. The common ancestor of Asian colobines, *Mesopithecus*, first entered Eastern Asia via the Indian subcontinent during the late Miocene (10.8 to 7.8 Ma ago) (Fig. 3D and data S4). Integrating this scenario with divergence times estimated from our newly constructed phylogenomic tree, we suggest that *Mesopithecus* spread throughout India and then divided into two clades at about 7.6 (8.0 to 6.7) Ma ago (Fig. 3, A and D).

One clade likely gave rise to the common ancestor of classical langurs, including *Presbytis*, *Semnopithecus*, and *Trachypithecus*, within a monophyletic clustering (Fig. 3A). Because of the uplifting of the Himalayas, some elements of this radiation spread eastward through the Indo-China Peninsula into warmer tropical forests in Sundaland during the late Miocene, around 7.4 (7.8 to 6.6) Ma ago. This group

evolved into the genus *Presbytis* (Fig. 3, A and D). During the Pliocene, about 4.9 (5.6 to 4.2) Ma ago, other members of this clade divided into two populations. One remained in the Indian subcontinent and evolved into *Semnopithecus*, whereas the other migrated eastward, spreading into southwest China and the Indo-China Peninsula in the Pleistocene. This lineage evolved into the genus *Trachypithecus* (Fig. 3, A and D).

Cold events promoted social aggregation in odd-nosed monkeys

In contrast to the classical langurs, our results suggest that cold events played an important role in adaptation and social aggregation along with speciation in the common ancestor of odd-nosed monkeys (Fig. 3). Combined with the new fossil *Mesopithecus pentelicus*, which was found in Zhaotong, Yunnan Province, China (identified as the most recent common ancestor of the odd-nosed monkey clade) (*36*) and was dated to 6.4 (6.7 to 6.0) Ma ago during Late Miocene Cooling (7.0 to 5.4 Ma ago), we propose that the ancestor of odd-nosed monkeys dispersed eastward from the Indian subcontinent, along the uplifted Himalayas, and then dispersed into the southeastern margin of the Tibetan Plateau (Hengduan Mountains region) (7.6 to 6.5 Ma ago) (Fig. 3, A and C). Paleoenvironmental evidence shows that after their arrival, the common ancestor of odd-nosed monkeys encountered a cooler and drier climate caused by the rapid uplifting of the Hengduan Mountains (8.0 to 6.0 Ma ago) during a global cooling period in the late Miocene (Fig. 3D and data S5). An additional changing monsoon climate in the area has also enhanced the cooling effects (fig. S3 and data S5). These events coincided with the evolution from an ancestral one-male, multifemale unit to a semi-multilevel society in odd-nosed monkeys (Figs. 2B and 3B). The results indicate that adaptations related to these cold events appear to have resulted in larger and more aggregated social groups in the odd-nosed monkey clade (Fig. 3).

Subsequently, the ancestors of odd-nosed monkeys evolved into four genera (Fig. 2A). Along with these cold events, the common ancestor of proboscis monkeys (*Nasalis*) and simakobus (*Simias*) migrated southward, crossing the land bridge that connected isolated islands in Southeast Asia (Sundaland) at about 6.5 (7.0 to 5.7) Ma ago. This radiation dispersed into tropical forests as far as Sumatra and Borneo (Fig. 3, D and E), facilitated by a fall in sea level caused by expanding ice sheets in the polar regions during glacial events (Fig. 3 and fig. S3).

The ecological niche modeling and pairwise sequentially Markovian coalescent (PSMC) analyses suggest that alternating glacial and interglacial events during the Pleistocene resulted in reconnection and disconnection of land bridges as well as the expansion and contraction of suitable habitats (Fig. 3, B and E). This led to the isolation and divergence of proboscis monkeys and simakobus about 1.4 (2.4 to 0.8) Ma ago (Fig. 3, A and D). This dispersal scenario is consistent with the semi-multilevel society social grouping pattern maintained by proboscis monkeys, even though they presently inhabit warmer environments. By contrast, simakobus, which today only inhabit the Mentawai Islands west of Sumatra, reverted to independent one-male groups, similar to the Asian colobine ancestral condition.

The remaining odd-nosed monkeys gave rise to the common ancestor of doucs (*Pygathrix*) and snub-nosed monkeys (*Rhinopithecus*), which adapted to the cold climate present in the northern region of East Asia during the Late Miocene Cooling (6.5 to 6.2 Ma ago). Later, a branch of this radiation migrated south into the Indo-China Peninsula and evolved into *Pygathrix* at 6.2 (6.6 to 5.4) Ma ago (Fig. 3A). The PSMC analysis also showed that an expansion in the effective population size of doucs was associated with an increase in cold temperatures during the middle and late Pleistocene glacial event (Fig. 3B). Compared with the semi-multilevel societies of proboscis monkeys, in which nonterritorial one-male, multifemale units aggregate together only at night, the semi-multilevel societies of doucs are characterized by an extended aggregation period during the rainy season. The more cohesive semi-multilevel societies of doucs appear to be related to a longer period of inhabiting glacial environments in colder northern regions compared with proboscis monkeys.

By contrast, the snub-nosed monkeys (genus *Rhinopithecus*) evolved from an ancestral lineage that remained in the north and experienced all major Pleistocene glacial cold events in high-latitude forests (data S1 and S2). Today, four of the five *Rhinopithecus* species are constrained to high-altitude temperate mountain forests up to 4500 m. These habitats are characterized by relatively cool summers and extended cold winters. This includes the golden snub-nosed monkeys (*Rhinopithecus roxellana*), which occupy the northern-most distribution of all colobine species (Fig. 1B). Through stepwise social evolution, snub-nosed monkeys evolved a social system distinguished by larger group size, increased male intrasexual tolerance, and the stable social aggregation of one-male, multifemale units that characterize their typical multilevel societies (Fig. 2B).

Colobine genomic evolution

These phylogenetic-based and cold-driven evolutionary scenarios point to a potential genetic mechanism that promoted the stepwise process of social aggregation in Asian colobines. Ecological pressures may have selected for genomic changes early in colobine evolution that promoted an expansion of prosocial behaviors. Therefore, to identify the genetic basis of primate social evolution, in addition to the reference genomes of two African colobines as outgroups, we provide 10 genomes that represent all seven genera of Asian colobines, including six genomes from all four genera of odd-nosed monkeys (table S2).

Given that the ancestor of the odd-nosed monkey clade was initially aggregated into semi-multilevel groups in response to glacial events, based on the genomes of four extant genera, we reconstructed the genome of the common ancestor of odd-nosed monkeys using likelihood-based and maximum parsimony methods. Based on the branch-site and branch model in phylogenetic analysis by maximum likelihood (PAML) (*37*) and the evolutionary rate model (*38*), we compared the adaptive divergence between the ancestral odd-nosed monkey and other primates in coding genes, as well as the conserved model generated by PhastCons (*39*) and the aov.phylo model in GEIGER (*40*) for comparison of the conserved noncoding elements (CNEs). For coding genes, we identified 78 candidate positively selected genes and 371 candidate rapidly evolving genes from a total of 17,191 one-to-one orthologous genes from whole-genome alignment. We then filtered these candidate genes to reduce false-positive results (SM section 5.1.6) and detected 30 positively selected genes and 228 rapidly evolving genes ($P < 0.05$) (tables S14 and S16). After obtaining the QQplot from all orthologous genes (fig. S15) and the false discovery rate corrections, we further noticed a set of genes with higher levels of significance (tables S14 and S16). These genes are associated with multiple functions, for example, cold-related energy metabolism as the positively selected gene *HMCN2*, which is involved in lipid metabolism (*41*) and may aid in energy maintenance in cold environments. We also identified *LTBP2* and *FLNC* as rapidly evolving genes, which are involved in adipocyte differentiation and fat degradation (*42*, *43*) and may be associated with nonshivering thermogenesis to increase body heat during periods of low temperature (*44*). In addition, we found a set of rapidly evolving genes (table S16) related to neurohormonal regulation, such as *DLGAP3* and *AP2A1*, which are involved in neurotransmission systems, such as the neurotransmission system that involves 5-hydroxytryptamine, which regulates grooming and other social behaviors (*45*, *46*).

In addition, we obtained a total of 23,038 CNEs and 4351 ultraconserved noncoding elements (UCNEs) and identified 636 specific CNEs and 283 fast-evolving UCNEs ($P < 0.05$) in ancestral odd-nosed monkeys that distinguished them from the outgroups (SM section 5.1.2 and Fig. 4A). Focusing on the selected

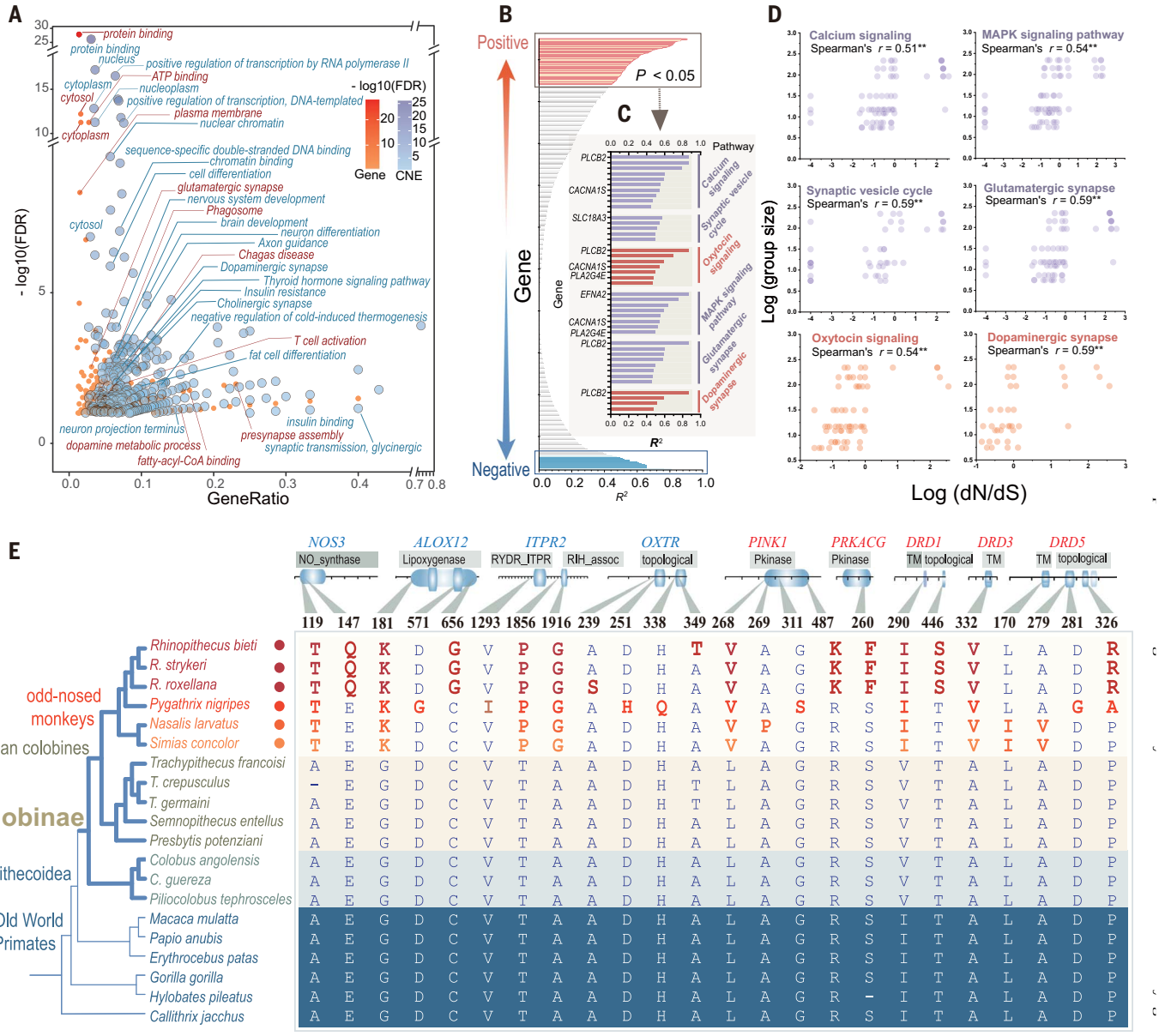


Fig. 4. Genome landscape of Asian colobines associated with social evolution. (**A**) Enrichment analysis of specific CNEs (blue dots) and genes (red dots) in the common ancestor of odd-nosed monkeys. The full results are shown in tables S19 and S22. FDR, false discovery rate. (**B**) Genome-wide PGLS analyses between the evolutionary rate and group size across Asian colobines. Genes enclosed in rectangles indicate that their evolutionary rate (dN/dS, where N is the number of nonsynonymous sites and S is the number of synonymous sites) is significantly correlated with group size. R^2, coefficient of determination. (**C**) The correlation coefficients of each of the genes in each of the distinguished pathways. (**D**) Regression analysis between dN/dS and group size of the pathways. (**E**) Genes exhibit specific mutations in the odd-nosed monkeys. Genes involved in the oxytocin pathway are colored blue, whereas those involved in the dopamine pathway are colored red.

genes and UCNE- and CNE-associated genes, we annotated these genes to the Gene Ontology terms and the Kyoto Encyclopedia of Genes and Genomes (KEGG) pathway database and performed gene enrichment analyses using the KEGG Orthology Based Annotation System (KOBAS) (*47*) (SM section 5.2). The results showed that most of the high-ranking significant Gene Ontology terms and the pathways were involved in immunity, fat metabolism, and adaptations to a high-cellulose diet (Fig. 4A and fig. S17). These pathways are associated with energy- and heat-acquiring pathways that maintain body temperature to survive in the cold, such as the phagosome and Chagas pathways (SM section 5.2 and table S18). In addition, based on the evolutionary rate model, the analysis of rapidly evolving Gene Ontology terms also distinguished similar patterns as the enrichment analyses described earlier in this section, such as mammary gland development, fatty acid metabolism, and cellular glucose homeostasis (figs. S17 and S18). Importantly, both of these analyses revealed that genes associated with neurohormonal regulation were significantly enriched (Fig. 4A). These results imply that cold-related energy metabolism and neurohormonal evolution appear to have jointly evolved in the common ancestor of the odd-nosed monkey clade.

Genome-wide association with social evolution

Based on these results, we investigated genomic changes in all extant Asian colobines that are relevant to social aggregation by exploring the potential genes and pathways that

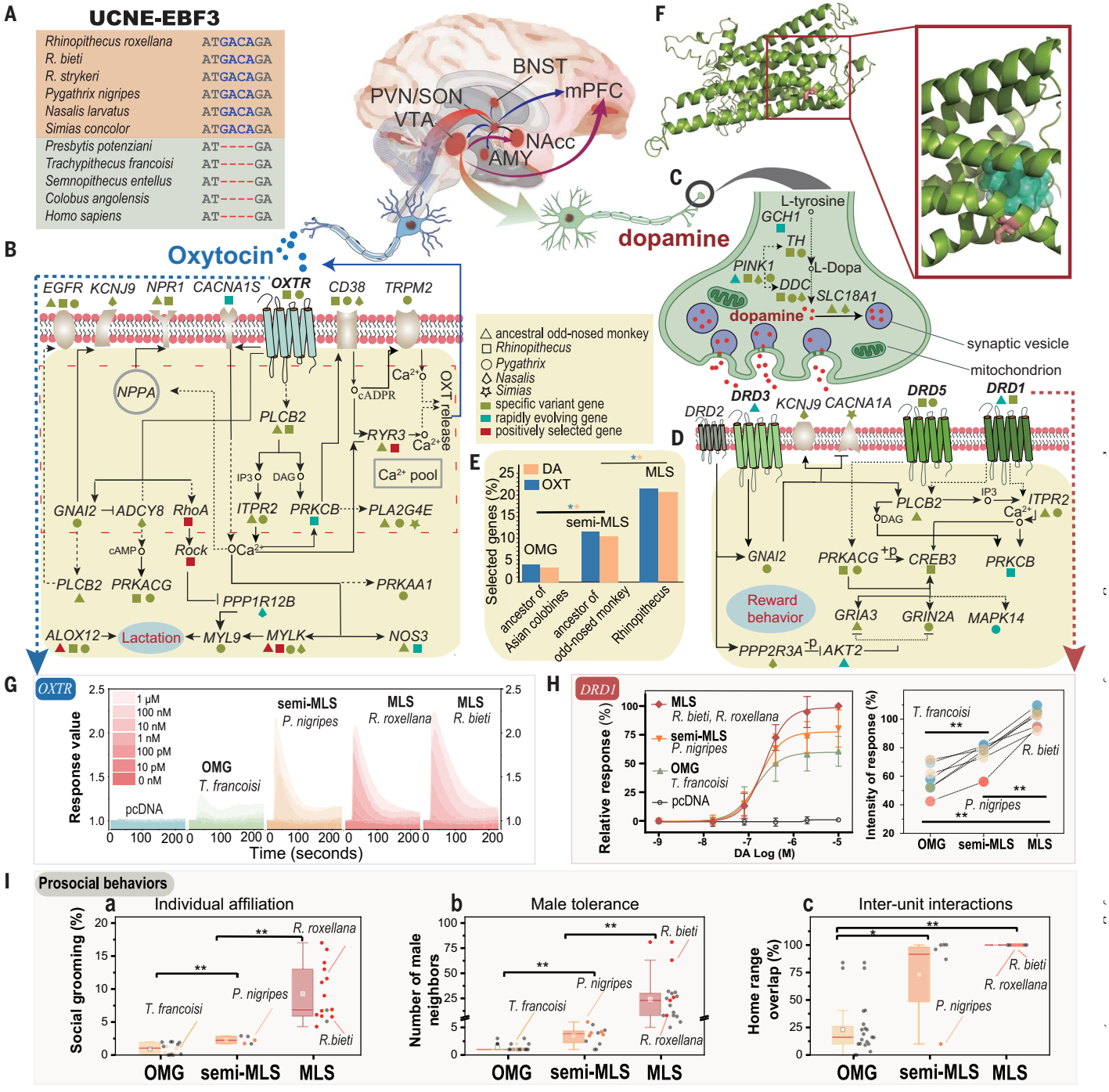


Fig. 5. Mutations in genes that encode proteins in the oxytocin and dopamine pathways and functional validation in odd-nosed monkeys. (**A**) Nucleotides inserted into the UCNEs in odd-nosed monkeys. (**B**) Genetic changes identified in the oxytocin pathway. (**C** and **D**) Genetic changes identified in the dopamine synthesis process as well as signal transduction in and cellular regulation of the dopamine pathway. (**E**) Comparison of the proportion of selected genes in the oxytocin (OXT) and dopamine (DA) pathways. (**F**) Three-dimensional views of the DRD1 protein of douc monkeys. (**G** and **H**) The in vitro receptor activity tests for OXTR and DRD1. *R. roxellana* and *R. bieti* share the same DRD1 amino acid sequence. (**I**) Prosocial behavioral characteristics related to the oxytocin and dopamine pathways in Asian colobines. For (H) and (I), *$P < 0.05$ and **$P < 0.01$.

correlated with the group-size spectrum from one-male, multifemale groups to multilevel societies. First, we constructed an orthologous gene set that focused on neurohormonal systems from nine genomes, including those of extant odd-nosed monkeys and classical langurs. Following the a priori candidate genes method (*48*, *49*), we obtained a total of 2103 orthologous genes that are defined as or exhibited annotations in neurohormonal regulation and social behavior from Gene Ontology and the KEGG pathway database (table S25). Focusing on these 2103 genes, we next performed correlation analyses and used mean group size as a continuous variable to represent

different forms of social organization to compare the evolutionary rate of each gene across species. Based on a phylogenetic generalized least squares (PGLS) regression analysis (*50*) (SM section 5.4), we detected 213 genes that were positively correlated and 66 genes that were negatively correlated with group size (Fig. 4B and table S26).

Then, focusing on these correlated genes, we performed two independent analyses, the enrichment analyses and the pathway correlation analyses to distinguish the specific pathways that correlated with group size. The enrichment analyses from these 213 and 66 genes using KOBAS distinguished 349 pathways that exhibited significant *P* values after correction for false discovery rates. We then ranked these pathways based on the *P* values (table S28). For the pathway correlation analyses, we focused on the 213 positively correlated genes, which may serve multiple functions across pathways, and recategorized these genes into 105 corresponding pathways. By comparing the evolutionary rate for each gene of each species in a pathway with mean group size in the corresponding species, we estimated the Spearman's correlation coefficients for each pathway. We then ranked these pathways by their correlation coefficients (tables S29 and S30 and SM section 5.4).

The results of both analyses showed that high-ranking pathways were primarily associated with categories of energy metabolism, neural signal transmission regulation, and immunity that may relate to group living (tables S28 and S29). For example, the regulation of lipolysis in adipocytes is associated with glucose and lipid metabolism (*51*). These pathways are relevant to energy demands and utilization and help to maintain body temperature and compensate for heat loss in cold environments (*52*). These high-ranking pathways also include those involved during the bacterial invasion of epithelial cells, which are reported to facilitate infection avoidance (*53*, *54*). These same pathways also appear to function in cellulose fermentation by the gut microbiome, which is related to the folivorous diet of colobine primates (*55*). In addition, both analyses indicated that the remaining high-ranking pathways are engaged in neural signal transmission and regulation, such as the sphingolipid signaling pathway, which is associated with brain development and neural system maintenance (*56*) (SM section 5.4), as well as the particular hormones such as glutamate, dopamine, oxytocin, and 5-hydroxytryptamine (tables S28 and S29).

Moreover, both of the analyses distinguished pathways related to materials that function in neuron structure and the neuronal connectivity system, including axon guidance, cholinergic synapse, and synaptic vesicles (tables S28 and S29). The enrichment analyses also distinguished dendrite, dendritic spine, synapse, and neuron projection as high-ranking Gene Ontology terms (table S28). These findings lay the structural foundation for signal transduction in the neural interaction network (*57*). Importantly, based on the enrichment analyses, the axon guidance and cholinergic systems, which were the first- and the sixth-highest-ranking pathways estimated from the KEGG database, are reported to affect and control dopamine release (*58*). Moreover, these analyses also distinguished the mitogen-activated protein kinase signaling and glutamatergic synapse pathways, which mediate downstream calcium signaling for the oxytocin and dopamine pathways (Fig. 4, C and D, and tables S29 and S30). These neurotransmitter systems, and the particular hormone types that they serve, suggest that neurohormonal regulation, including the oxytocin and dopamine pathways, is significantly related to group size in extant Asian colobines.

Therefore, we explored how neurohormonal systems, including the dopamine and oxytocin pathways, function in social behavior and the evolution of social group size. Oxytocin and dopamine play essential roles in maternal reward attachment, strengthening the mother-infant bond and maintaining nursing (*59*–*63*). Mammals living in colder environments tend to increase maternal investment, such as prolonging lactation and huddling periods to avoid infant exposure during the cold season (*64*–*66*). Therefore, we hypothesized that in response to cold temperatures, more efficient oxytocin and dopamine pathways were selected for in the odd-nosed monkeys, resulting in enhanced maternal care and infant survival. Furthermore, higher levels of oxytocin and dopamine also promote interindividual affiliation, mitigate intergroup conflict, and increase social bonding (*67*, *68*). This could have facilitated increased cooperation and neighbor-male tolerance (*69*, *70*) and thus may have favored social aggregation from independent one-male, multifemale groups to multilevel societies.

Rapid evolution in the oxytocin and dopamine pathways is related to social aggregation

To understand the adaptive changes in the oxytocin and dopamine pathways, we compared all 104 oxytocin-related and 96 dopamine-related orthologous genes (table S31) among snub-nosed monkeys, which represent a multilevel society; ancestral odd-nosed monkeys, which represent a semi-multilevel society; and classical langurs, which form independent one-male, multifemale units. By using PAML (*37*), hypothesis testing using phylogenies (*71*), and specific amino acid change (*72*), our results show that 22 (21.2%) genes in the oxytocin pathway and 20 (20.8%) genes in the dopamine pathway were selected in species that form multilevel societies. This is significantly higher than the 12 (11.5%) and 10 (10.4%) genes selected in the same pathways of species that form semi-multilevel societies (SM section 5.5 and tables S32 and S33), as well as significantly higher than the four (3.8%) and three (3.1%) genes selected in Asian classical langurs that form independent one-male, multifemale groups (chi-square test; Fig. 5E). This pattern of genome-wide change in neuron structures to signal transmission across different clades is consistent with differences in the level of social aggregation from one-male, multifemale units to multilevel societies.

In the case of the ancestral odd-nosed monkeys that initially formed semi-multilevel societies, a suite of gene changes was identified in the oxytocin pathway (Fig. 5B and table S32). These include *RYR3*, which showed specific mutations that affect oxytocin release, and *ALOX12*, which was positively selected and regulates downstream milk secretion (Fig. 4E and table S31). In the dopamine pathway, specific variations in genes and noncoding regulatory regions were identified (Fig. 5, A, C, and D), for example, genes that affect dopamine-regulation processes, such as *PINK1*, which is responsible for dopamine synthesis; *SLC18A1*, which influences dopamine transport; and *GRIA3*, which functions in reward behavior (fig. S23). In particular, we found that dopamine receptor genes *DRD1* and *DRD3* were rapidly evolving genes in the ancestral odd-nosed monkey clade (table S32). These G protein–coupled receptors (GPCRs), which are precise targets located in the cell membrane, play an important role in binding extracellular dopamine and transmit signals for intracellular downstream responses (Fig. 5D). Taken together, these findings suggest that the oxytocin and dopamine pathways evolved rapidly in ancestral odd-nosed monkeys, presumably in response to the initial aggregation required to form a semi-multilevel society.

Based on these findings, we examined the specific amino acid changes in oxytocin and dopamine pathway genes in each of the extant species of odd-nosed monkeys after their radiation from their common ancestor. A total of 22, 20, 10, and 6 genes in the oxytocin pathway and 20, 15, 9, and 4 genes in the dopamine pathway were identified in snub-nosed monkeys, which represent multilevel societies; doucs and proboscis monkeys, which represent semi-multilevel societies; and pig-tailed simakobus, which represent one-male, multifemale units, respectively (SM section 5.5 and tables S31 to S35). For example, *DRD5*, which encodes a dopamine receptor, had specific mutations in extant multilevel societies and semi-multilevel societies species (Fig. 4D) that were not present in one-male, multifemale unit species. In particular, specific amino acid changes in genes *CD38* and *RYR1*, which are associated with oxytocin downstream regulation, and the coding

region of the gene *OXTR* were present in multilevel society and semi-multilevel society species but were absent in one-male, multifemale unit species (Fig. 5B and tables S31 to S35). By contrast, *GCH1* and *PRKCB*, which are associated with dopamine synthesis and downstream response regulation, were selected in multilevel society species but not in semi-multilevel society species or one-male, multifemale unit species (Figs. 4E and 5, C and D; and table S32). Furthermore, the multilevel society species exhibited a shared threonine-to-serine mutation in *DRD1*, which encodes a dopamine receptor, in contrast to semi-multilevel society species or one-male, multifemale unit species (Fig. 4E), which do not. These genetic changes in the oxytocin and dopamine pathways reveal changing patterns in the neurohormonal regulation system that appear related to different levels of affiliation behavior (Fig. 2B).

Considering the importance of receptors in intercellular signal transduction and intracellular downstream responses, we used GPCR-I-TASSER to construct three-dimensional models to simulate protein expression in four oxytocin and dopamine receptors in snub-nosed monkeys, doucs, and François' langurs, representing a multilevel society, a semi-multilevel society, and a one-male, multifemale unit species, respectively (*73*) (Fig. 5F and fig. S22). The results indicate that a specific amino acid change of valine to isoleucine, located in the sixth transmembrane region of *DRD1*, was present in the odd-nosed monkey clade, which represents the ancestral aggregation from one-male, multifemale units to semi-multilevel societies (Fig. 5F). This mutation site was simulated to lie close to the binding pocket and thus may affect dopamine binding activity in the odd-nosed monkey clade; this mutation is not present in *DRD1* in Asian classical langurs and African colobus monkeys of the subfamily Colobinae, which represent independent one-male, multifemale units (Fig. 5F). In addition, the specific amino acid change of threonine to serine in *DRD1* in snub-nosed monkey species that live in multilevel societies was modeled to locate the conserved topological domain. This domain, which is located in the C-terminal domain of the GPCR protein (fig. S22), plays an important function in G protein coupling and activation (*74*) and thus may enhance intracellular G protein binding in these species compared with other species of colobines (fig. S22).

To confirm the functional expression of these receptors, we conducted cellular experiments that synthesized each sequence of *DRD1* and *OXTR* of the corresponding species, and these were then transferred in vitro into human embryonic kidney 293 (HEK293) cells. The results showed that the expressed DRD1 had higher binding efficiency in multilevel society species than in semi-multilevel society species ($P < 0.05$; Fig. 5H). Furthermore, the binding efficiency of the expressed DRD1 in species that exhibit either of these types of social organization was significantly higher than that in species with an independent one-male, multifemale unit social organization ($P < 0.05$; Fig. 5H). This finding is consistent with the pattern shown by three-dimensional modeling. In addition, *OXTR* had a significantly higher binding efficiency in multilevel society and semi-multilevel society species than in independent one-male, multifemale unit species ($P < 0.05$; Fig. 5G). These results demonstrate a correlation between species with increased social aggregation and increased binding efficiency of their dopamine and oxytocin receptors.

Overall, our results show integrated differences that involve multiple genetic changes across various biological processes genome wide, which are linked to neurohormonal regulation, including the oxytocin and dopamine pathways. These changes are consistent with differences in social organization and intermale tolerance in Asian colobine species and may underpin their ability to form large, stable, and cohesive groups.

Increased behavioral affiliation is related to oxytocin and dopamine regulation

To verify changes in social behavior in response to different levels of neurohormonal regulation, including the oxytocin and dopamine expression, we compared the strength of social affiliation among species represented by each of the three types of social organization. We constructed a behavioral dataset related to social affiliation that involved 17 behavioral categories collected from information reported in 45 extant species of Asian colobines (data S1, S2, S6, and S7). Analysis of variance (ANOVA) tests revealed that neighbor-male tolerance; interactions between one-male, multifemale units; and time spent in social grooming as a percentage of daily time budgets were significantly higher in multilevel society species than in semi-multilevel society species and independent one-male, multifemale unit species (Fig. 5I). This is consistent with the expression results of in vitro experiments, which support our contention that genomic changes in the regulation of neurohormonal systems, including the oxytocin and dopamine pathways, may promote affiliative behaviors that are more pronounced in cold-adapted species.

Conclusion

In this study, we found that Asian colobines that inhabit colder environments tend to live in larger, more complex groups. By constructing a socioecological-genomic framework, we found that instead of evidence of direct adaption to current environmental conditions, historical patterns of dispersal, phylogenetic species radiations, and adaptations to ancient environmental conditions played a more critical role in the social evolution of Asian colobines. Cold adaptations during ancient glacial events in ancestral odd-nosed monkeys appear to have favored the selection of the neurohormonal regulation system, from neuron structure to signal transmission, which includes the dopamine and oxytocin pathways. These changes in the dopamine and oxytocin pathways appear to function in strengthening social bonds, in facilitating male-male tolerance, and in shaping social affiliation. This process played an important role in promoting social aggregation from small, independent one-male groups into larger multilevel societies. Our study identifies, for the first time, a genomically regulated adaptation that is linked to stepwise social evolution in primates and offers new insights into the mechanisms that underpin diverse behavioral evolution across a range of animal taxa.

Materials and methods summary

Sequencing and assembly

We sequenced seven Asian colobine genomes by using four technologies, including long-read sequencing of Oxford Nanopore or PacBio SMART, paired-end sequencing, and high-throughput chromosome conformation capture (Hi-C). Different de novo assemblies were performed using FALCON v.0.4.0 (*75*), wtdbg2 v.2.4.1 (*76*), and SOAPdenovo2 v. 1.0 (*77*) according to the sequencing strategy used. Genomes with Hi-C reads were further scaffolded to chromosome based on LACHESIS (*78*) or 3D-DNA (*79*).

Dataset resources

We compiled the datasets of social, behavioral, and ecological traits of Asian colobines using published information (SM section 2), which include (i) social organization, such as group size and composition (data S1); (ii) mating system (data S1); (iii) social structure, which is defined as social interactions and communication, including the proportion of the activity budget devoted to social grooming (data S6); (iv) ecological (bioclimatic) variables based on occurrence location coordinates (data S2); and (v) paleoecological data based on the fossil record, paleoclimate, and paleogeography across Asia (SM section 2.2).

Ecological analyses

Ecological niche modeling was conducted using Maxent to reconstruct species distribution in the present climate and under paleoclimates. Principal components analysis was used to extract two main characters from 19 climate variables for 2189 species occurrences in the R package Multivariate Exploratory Data Analysis and Data Mining with FactoMineR v.3.6.1 (*80*). Geographic information was processed in ArcGIS (ArcGIS version 10.6, Environmental Systems Research Institutes, Inc., Redlands, CA, USA).

Reconstruction of phylogenomic relationships

One-to-one orthologs for phylogenomic relationship reconstruction were generated with OrthoFinder v.2.0.9 (*81*). Then, these orthologous genes were used to generate two dependent datasets, including a concatenated coding sequence alignment and the fourfold degenerate sites. For each dataset, a tree was constructed with the concatenation method of IQ-TREE v.1.6.12 (*82*) and coalescent method of Astral v.2.0 (*83*), respectively. The divergence time was estimated using MCMCtree v.4.5 (*37*).

Phylogenetic analyses

Pagel's λ was estimated using the R package GEIGER v.2.0.6 (*40*). The Phylo.D was estimated using R package CAPER v.1.0.1 (*50*), and the probability of the estimated *D* resulting from the Brownian phylogenetic structure was marked as $P_{D_Brownian}$. BayesTraits v.3.0.2 (*32*) was used to infer the social system state for each ancestral node, which was determined by calculating the ancestral state posterior probability. A random-walk Markov chain Monte Carlo procedure in BayesTraits v.3.0.2 was used to infer the correlated evolution between bioclimatic variables and group size.

Reconstruction of ancestral geographic ranges

We reconstructed the ancestral range through multiple biogeographical models (e.g., DIVA, DEC, or BayAreaLike) using Reconstruct Ancestral State in Phylogenies 4.2 (*84*). The best model generated was used to reconstruct the range in each ancestral node.

Demographic history reconstruction

Demographic history was inferred using PSMC v.0.6.5 (*85*) under a hidden Markov model. Paired-end Illumina sequences were aligned to the repeat-masked genome assembly of each species using the Burrows-Wheeler Alignment tool v.0.7.17-r1188 (*86*). Then, consensus sequences were generated using Sequence Alignment/Map format tools v.1.3.1 (*87*). Each PSMC test was examined with 100 bootstrap replicates.

Comparative genomics analyses

Divergent (fast-evolving) UCNEs were identified by using the R package GEIGER v.2.0.6 (*40*). PhyloFit v1.4 (*88*) and phastConsv1.4 (*39*) were used to infer CNEs. Orthologous genes were constructed by using LAST v.last982 (*89*). The pairwise synteny alignment analysis was conducted for Asian colobine species as well as outgroups, with the human genome serving as the reference. Then, the corresponding orthologous sequences were extracted based on the gff file of the human genome. The Gene Ontology and KEGG pathway enrichment analyses were conducted using KOBAS v.3.0 (*47*). Selection pressure tests were implemented by both branch-site models and branch models using PAML v.4.9 (*37*) through a likelihood ratio test and strict filter criterion. An episodic positive selection signal was detected using the mixed effects model of evolution (*90*) implemented in Hypothesis Testing using Phylogenies v.2.5.25 (*71*). Rapidly evolving Gene Ontology terms were identified following the evolutionary model and method proposed by Wang *et al.* (*38*). Specific mutations were identified following the specific amino acid change pipeline from Chen *et al.* (*72*) and were further examined if they were located in functional regions using the protein families database Pfam v.1.6 (*91*). Genome-wide associations with social evolution were explored using PGLS regression analyses in the R package Comparative Analysis of Phylogenetics and Evolution in R (CAPER) v.1.0.1 (*50*).

Protein structure modeling

The 3D protein structure of the functional region was simulated by GPCR-I-TASSER (*73*) and then visualized using PyMOL (the PyMOL molecular graphics system, version 2.0, Schrödinger, LLC). The binding cavity was explored with the docking simulations in Dock vina (*92*).

In vitro expression assay

For in vitro experiments, orthologous sequences were synthesized by General Biosystems Corporation Limited (Anhui, China). All genes were cloned into pcDNA3.1-V5-His vector separately and expressed in HEK293 cells. After 48 hours, the supernatant was removed, the cells were rinsed twice with phosphate-buffered saline (PBS), and then multiple solutions were added for an enzyme-linked immunosorbent assay experiment. Absorbance measurements were conducted at 370 nm within 30 min. Results were analyzed using GraphPad Prism. Statistical significance was set at <0.05, mean ± SD.

Measurement of receptor activity

For DRD1, luciferase activities were determined using luciferase assay kits (Beyotime, Shanghai, China). In the case of OXTR, fluorescence was measured using microplate reader SYNERGY H1 (BioTek Instruments). HEK293 cells transfected with pcDNA were used as a control in all luciferase experiments.

REFERENCES AND NOTES

1. T. Clutton-Brock, Sexual selection in males and females. *Science* **318**, 1882–1885 (2007). doi: 10.1126/science.1133311; pmid: 18096798
2. J. C. Mitani, J. Call, P. M. Kappeler, R. A. Palombit, J. B. Silk, *The Evolution of Primate Societies* (Univ. Chicago Press, 2012).
3. P. M. Kappeler, C. P. van Schaik, Evolution of primate social systems. *Int. J. Primatol.* **23**, 707–740 (2002). doi: 10.1023/A:1015520830318
4. C. C. Grueter *et al.*, Multilevel organisation of animal sociality. *Trends Ecol. Evol.* **35**, 834–847 (2020). doi: 10.1016/j.tree.2020.05.003; pmid: 32473744
5. D. Lukas, T. H. Clutton-Brock, The evolution of social monogamy in mammals. *Science* **341**, 526–530 (2013). doi: 10.1126/science.1238677; pmid: 23896459
6. T. Clutton-Brock, Cooperation between non-kin in animal societies. *Nature* **462**, 51–57 (2009). doi: 10.1038/nature08366; pmid: 19890322
7. J. B. Silk, S. C. Alberts, J. Altmann, Social bonds of female baboons enhance infant survival. *Science* **302**, 1231–1234 (2003). doi: 10.1126/science.1088580; pmid: 14615543
8. J. B. Silk, Social components of fitness in primate groups. *Science* **317**, 1347–1351 (2007). doi: 10.1126/science.1140734; pmid: 17823344
9. X.-G. Qi *et al.*, Satellite telemetry and social modeling offer new insights into the origin of primate multilevel societies. *Nat. Commun.* **5**, 5296 (2014). doi: 10.1038/ncomms6296; pmid: 25335993
10. A. Koenig, C. J. Scarry, B. C. Wheeler, C. Borries, Variation in grouping patterns, mating systems and social structure: What socio-ecological models attempt to explain. *Philos. Trans. R. Soc. London Ser. B* **368**, 20120348 (2013). doi: 10.1098/rstb.2012.0348; pmid: 23569296
11. J. F. Eisenberg, N. A. Muckenhirn, R. Rundran, The relation between ecology and social structure in Primates. *Science* **176**, 863–874 (1972). doi: 10.1126/science.176.4037.863; pmid: 17829291
12. P. M. Kappeler, A framework for studying social complexity. *Behav. Ecol. Sociobiol.* **73**, 13 (2019). doi: 10.1007/s00265-018-2601-8
13. C. H. Janson, Primate socio-ecology: The end of a golden age. *Evol. Anthropol.* **9**, 73–86 (2000). doi: 10.1002/(SICI)1520-6505(2000)9:2<73:AID-EVAN2>3.0.CO;2-X
14. T. Clutton-Brock, C. Janson, Primate socioecology at the crossroads: Past, present, and future. *Evol. Anthropol.* **21**, 136–150 (2012). doi: 10.1002/evan.21316; pmid: 22907867
15. P. M. Kappeler, Evolution. Why male mammals are monogamous. *Science* **341**, 469–470 (2013). doi: 10.1126/science.1242001; pmid: 23908214
16. S. Shultz, C. Opie, Q. D. Atkinson, Stepwise evolution of stable sociality in primates. *Nature* **479**, 219–222 (2011). doi: 10.1038/nature10601; pmid: 22071768
17. R. A. Mittermeier, A. B. Rylands, D. E. Wilson, Eds., *Primates*, vol. 3 of *Handbook of the Mammals of the World* (Lynx Edicions, 2013).
18. C. Opie, Q. D. Atkinson, R. I. Dunbar, S. Shultz, Male infanticide leads to social monogamy in primates. *Proc. Natl. Acad. Sci. U.S.A.* **110**, 13328–13332 (2013). doi: 10.1073/pnas.1307903110; pmid: 23898180
19. P. M. Kappeler, L. Pozzi, Evolutionary transitions toward pair living in nonhuman primates as stepping stones toward more complex societies. *Sci. Adv.* **5**, eaay1276 (2019). doi: 10.1126/sciadv.aay1276; pmid: 32064318
20. G. E. Robinson, R. D. Fernald, D. F. Clayton, Genes and social behavior. *Science* **322**, 896–900 (2008). doi: 10.1126/science.1159277; pmid: 18988841
21. R. I. M. Dunbar, S. Shultz, Evolution in the social brain. *Science* **317**, 1344–1347 (2007). doi: 10.1126/science.1145463; pmid: 17823343
22. E. H. M. Sterck, "The behavioral ecology of colobine monkeys" in *The Evolution of Primate Societies*, J. C. Mitani, J. Call, P. M. Kappeler, R. A. Palombit, J. B. Silk (Univ. Chicago Press, 2012), pp. 66–87.
23. L. R. Ulibarri, K. N. Gartland, Group composition and social structure of red-shanked doucs (*Pygathrix nemaeus*) at Son Tra Nature Reserve, Vietnam. *Folia Primatol.* **92**, 191–202 (2021). doi: 10.1159/000518594; pmid: 34535600
24. X.-G. Qi *et al.*, Male cooperation for breeding opportunities contributes to the evolution of multilevel societies. *Proc. Biol. Sci.* **284**, 20171480 (2017). doi: 10.1098/rspb.2017.1480; pmid: 28954911
25. X. Wang, Y. Zhang, L. Yu, Summary of phylogeny in subfamily Colobinae (Primate: Cercopithecidae). *Chin. Sci. Bull.* **58**, 2097–2103 (2013). doi: 10.1007/s11434-012-5624-y
26. X. P. Wang *et al.*, Phylogenetic relationships among the colobine monkeys revisited: New insights from analyses of complete mt genomes and 44 nuclear non-coding markers. *PLOS ONE* **7**, e36274 (2012). doi: 10.1371/journal.pone.0036274; pmid: 22558416
27. K. N. Sterner, R. L. Raaum, Y.-P. Zhang, C.-B. Stewart, T. R. Disotell, Mitochondrial data support an odd-nosed colobine clade. *Mol. Phylogenet. Evol.* **40**, 1–7 (2006). doi: 10.1016/j.ympev.2006.01.017; pmid: 16500120
28. A. Antonelli *et al.*, Toward a self-updating platform for estimating rates of speciation and migration, ages, and relationships of taxa. *Syst. Biol.* **66**, 152–166 (2017). pmid: 27616324
29. M. Pagel, Inferring the historical patterns of biological evolution. *Nature* **401**, 877–884 (1999). doi: 10.1038/44766; pmid: 10553904

30. S. A. Fritz, A. Purvis, Selectivity in mammalian extinction risk and threat types: A new measure of phylogenetic signal strength in binary traits. *Conserv. Biol.* **24**, 1042–1051 (2010). doi: 10.1111/j.1523-1739.2010.01455.x; pmid: 20184650
31. L. Swedell, T. Plummer, A Papionin multilevel society as a model for hominin social evolution. *Int. J. Primatol.* **33**, 1165–1193 (2012). doi: 10.1007/s10764-012-9600-9
32. M. Pagel, A. Meade, Bayesian analysis of correlated evolution of discrete characters by reversible-jump Markov chain Monte Carlo. *Am. Nat.* **167**, 808–825 (2006). doi: 10.1086/503444; pmid: 16685633
33. R. C. Firman, D. R. Rubenstein, J. M. Moran, K. C. Rowe, B. A. Buzatto, Extreme and variable climatic conditions drive the evolution of sociality in Australian rodents. *Curr. Biol.* **30**, 691–697.e3 (2020). doi: 10.1016/j.cub.2019.12.012; pmid: 32008900
34. W. Jetz, D. R. Rubenstein, Environmental uncertainty and the global biogeography of cooperative breeding in birds. *Curr. Biol.* **21**, 72–78 (2011). doi: 10.1016/j.cub.2010.11.075; pmid: 21185192
35. C. Roos *et al*., Nuclear versus mitochondrial DNA: Evidence for hybridization in colobine monkeys. *BMC Evol. Biol.* **11**, 77 (2011). doi: 10.1186/1471-2148-11-77; pmid: 21435245
36. X. Ji *et al*., Oldest colobine calcaneus from East Asia (Zhaotong, Yunnan, China). *J. Hum. Evol.* **147**, 102866 (2020). doi: 10.1016/j.jhevol.2020.102866; pmid: 32862123
37. Z. Yang, PAML 4: Phylogenetic analysis by maximum likelihood. *Mol. Biol. Evol.* **24**, 1586–1591 (2007). doi: 10.1093/molbev/msm088; pmid: 17483113
38. K. Wang *et al*., Morphology and genome of a snailfish from the Mariana Trench provide insights into deep-sea adaptation. *Nat. Ecol. Evol.* **3**, 823–833 (2019). doi: 10.1038/s41559-019-0864-8; pmid: 30988486
39. A. Siepel *et al*., Evolutionarily conserved elements in vertebrate, insect, worm, and yeast genomes. *Genome Res.* **15**, 1034–1050 (2005). doi: 10.1101/gr.3715005; pmid: 16024819
40. M. W. Pennell *et al*., geiger v2.0: An expanded suite of methods for fitting macroevolutionary models to phylogenetic trees. *Bioinformatics* **30**, 2216–2218 (2014). doi: 10.1093/bioinformatics/btu181; pmid: 24728855
41. X. Miao, W. Liu, B. Fan, H. Lin, Transcriptomic heterogeneity of Alzheimer's disease associated with lipid genetic risk. *Neuromolecular Med.* **22**, 534–541 (2020). doi: 10.1007/s12017-020-08610-6; pmid: 32862331
42. D. Halbgebauer *et al*., Latent TGFβ-binding proteins regulate UCP1 expression and function via TGFβ2. *Mol. Metab.* **53**, 101336 (2021). doi: 10.1016/j.molmet.2021.101336; pmid: 34481123
43. S. C. Goetsch, C. M. Martin, L. J. Embree, D. J. Garry, Myogenic progenitor cells express filamin C in developing and regenerating skeletal muscle. *Stem Cells Dev.* **14**, 181–187 (2005). doi: 10.1089/scd.2005.14.181; pmid: 15910244
44. J. H. Lee *et al*., The role of adipose tissue mitochondria: Regulation of mitochondrial function for the treatment of metabolic diseases. *Int. J. Mol. Sci.* **20**, 4924 (2019). doi: 10.3390/ijms20194924; pmid: 31590292
45. J. M. Welch *et al*., Cortico-striatal synaptic defects and OCD-like behaviours in *Sapap3*-mutant mice. *Nature* **448**, 894–900 (2007). doi: 10.1038/nature06104; pmid: 17713528
46. E. Marcello *et al*., Endocytosis of synaptic ADAM10 in neuronal plasticity and Alzheimer's disease. *J. Clin. Invest.* **123**, 2523–2538 (2013). doi: 10.1172/JCI65401; pmid: 23676497
47. C. Xie *et al*., KOBAS 2.0: A web server for annotation and identification of enriched pathways and diseases. *Nucleic Acids Res.* **39**, W316–W322 (2011). doi: 10.1093/nar/gkr483; pmid: 21715386
48. K. He *et al*., Echolocation in soft-furred tree mice. *Science* **372**, eaay1513 (2021). doi: 10.1126/science.aay1513; pmid: 34140356
49. T. S. Simonson *et al*., Genetic evidence for high-altitude adaptation in Tibet. *Science* **329**, 72–75 (2010). doi: 10.1126/science.1189406; pmid: 20466884
50. D. Orme, R. Freckleton, G. Thomas, T. Petzoldt, S. Fritz, N. Isaac, W. Pearse, caper: Comparative analysis of phylogenetics and evolution in R. version 3.5.3. (2012); http://CRAN.R-project.org/package=caper.
51. R. E. Duncan, M. Ahmadian, K. Jaworski, E. Sarkadi-Nagy, H. S. Sul, Regulation of lipolysis in adipocytes. *Annu. Rev. Nutr.* **27**, 79–101 (2007). doi: 10.1146/annurev.nutr.27.061406.093734; pmid: 17313320
52. G. J. Tattersall *et al*., Coping with thermal challenges: Physiological adaptations to environmental temperatures. *Compr. Physiol.* **2**, 2151–2202 (2012). doi: 10.1002/cphy.c110055; pmid: 23723035
53. E. A. Archie, J. Tung, Social behavior and the microbiome. *Curr. Opin. Behav. Sci.* **6**, 28–34 (2015). doi: 10.1016/j.cobeha.2015.07.008
54. C. L. Nunn, S. Altizer, *Infectious Diseases in Primates: Behavior, Ecology and Evolution* (Oxford Univ. Press, 2006).
55. F. Rubino *et al*., Divergent functional isoforms drive niche specialisation for nutrient acquisition and use in rumen microbiome. *ISME J.* **11**, 932–944 (2017). doi: 10.1038/ismej.2016.172; pmid: 28085156
56. A. S. B. Olsen, N. J. Færgeman, Sphingolipids: Membrane microdomains in brain development, function and neurological diseases. *Open Biol.* **7**, 170069 (2017). doi: 10.1098/rsob.170069; pmid: 28566300
57. S. B. Laughlin, T. J. Sejnowski, Communication in neuronal networks. *Science* **301**, 1870–1874 (2003). doi: 10.1126/science.1089662; pmid: 14512617
58. C. Liu *et al*., An action potential initiation mechanism in distal axons for the control of dopamine release. *Science* **375**, 1378–1385 (2022). doi: 10.1126/science.abn0532; pmid: 35324301
59. L. J. Young, Z. Wang, The neurobiology of pair bonding. *Nat. Neurosci.* **7**, 1048–1054 (2004). doi: 10.1038/nn1327; pmid: 15452576
60. S. C. Sealfon, C. W. Olanow, Dopamine receptors: From structure to behavior. *Trends Neurosci.* **23**, S34–S40 (2000). doi: 10.1016/S1471-1931(00)00025-2; pmid: 11052218
61. L. W. Hung *et al*., Gating of social reward by oxytocin in the ventral tegmental area. *Science* **357**, 1406–1411 (2017). doi: 10.1126/science.aan4994; pmid: 28963257
62. Y. Liu, Z. X. Wang, Nucleus accumbens oxytocin and dopamine interact to regulate pair bond formation in female prairie voles. *Neuroscience* **121**, 537–544 (2003). doi: 10.1016/S0306-4522(03)00555-4; pmid: 14568015
63. S. D. Preston, The rewarding nature of social contact. *Science* **357**, 1353–1354 (2017). doi: 10.1126/science.aao7192; pmid: 28963241
64. T. A. Mousseau, C. W. Fox, The adaptive significance of maternal effects. *Trends Ecol. Evol.* **13**, 403–407 (1998). doi: 10.1016/S0169-5347(98)01472-4; pmid: 21238360
65. T. Burton *et al*., Adaptive maternal investment in the wild? Links between maternal growth trajectory and offspring size, growth, and survival in contrasting environments. *Am. Nat.* **195**, 678–690 (2020). doi: 10.1086/707518; pmid: 32216673
66. T. Pääkkönen, J. Leppäluoto, Cold exposure and hormonal secretion: A review. *Int. J. Circumpolar Health* **61**, 265–276 (2002). doi: 10.3402/ijch.v61i3.17474; pmid: 12369117
67. L. Samuni *et al*., Oxytocin reactivity during intergroup conflict in wild chimpanzees. *Proc. Natl. Acad. Sci. U.S.A.* **114**, 268–273 (2017). doi: 10.1073/pnas.1616812114; pmid: 28028227
68. M. Kosfeld, M. Heinrichs, P. J. Zak, U. Fischbacher, E. Fehr, Oxytocin increases trust in humans. *Nature* **435**, 673–676 (2005). doi: 10.1038/nature03701; pmid: 15931222
69. T. E. Ziegler, C. Crockford, Neuroendocrine control in social relationships in non-human primates: Field based evidence. *Horm. Behav.* **91**, 107–121 (2017). doi: 10.1016/j.yhbeh.2017.03.004; pmid: 28284710
70. A. Charlet, V. Grinevich, Oxytocin mobilizes midbrain dopamine toward sociality. *Neuron* **95**, 235–237 (2017). doi: 10.1016/j.neuron.2017.07.002; pmid: 28728017
71. S. L. Pond, S. D. Frost, S. V. Muse, HyPhy: Hypothesis testing using phylogenies. *Bioinformatics* **21**, 676–679 (2005). doi: 10.1093/bioinformatics/bti079; pmid: 15509596
72. L. Chen *et al*., Large-scale ruminant genome sequencing provides insights into their evolution and distinct traits. *Science* **364**, eaav6202 (2019). doi: 10.1126/science.aav6202; pmid: 31221828
73. J. Zhang, J. Yang, R. Jang, Y. Zhang, GPCR-I-TASSER: A hybrid approach to G protein-coupled receptor structure modeling and the application to the human genome. *Structure* **23**, 1538–1549 (2015). doi: 10.1016/j.str.2015.06.007; pmid: 26190572
74. L. Spomer *et al*., A membrane-proximal, C-terminal α-helix is required for plasma membrane localization and function of the G protein-coupled receptor (GPCR) TGR5. *J. Biol. Chem.* **289**, 3689–3702 (2014). doi: 10.1074/jbc.M113.502344
75. C. S. Chin *et al*., Phased diploid genome assembly with single-molecule real-time sequencing. *Nat. Methods* **13**, 1050–1054 (2016). doi: 10.1038/nmeth.4035; pmid: 27749838
76. J. Ruan, H. Li, Fast and accurate long-read assembly with wtdbg2. *Nat. Methods* **17**, 155–158 (2020). doi: 10.1038/s41592-019-0669-3; pmid: 31819265
77. R. Luo *et al*., SOAPdenovo2: An empirically improved memory-efficient short-read de novo assembler. *Gigascience* **1**, 18 (2012). doi: 10.1186/2047-217X-1-18; pmid: 23587118
78. J. N. Burton *et al*., Chromosome-scale scaffolding of de novo genome assemblies based on chromatin interactions. *Nat. Biotechnol.* **31**, 1119–1125 (2013). doi: 10.1038/nbt.2727; pmid: 24185095
79. O. Dudchenko *et al*., De novo assembly of the *Aedes aegypti* genome using Hi-C yields chromosome-length scaffolds. *Science* **356**, 92–95 (2017). doi: 10.1126/science.aal3327; pmid: 28336562
80. S. Lê, J. Josse, F. Husson, FactoMineR: An R package for multivariate analysis. *J. Stat. Softw.* **25**, 1–18 (2008). doi: 10.18637/jss.v025.i01
81. D. M. Emms, S. Kelly, OrthoFinder: Phylogenetic orthology inference for comparative genomics. *Genome Biol.* **20**, 238 (2019). doi: 10.1186/s13059-019-1832-y; pmid: 31727128
82. L. T. Nguyen, H. A. Schmidt, A. von Haeseler, B. Q. Minh, IQ-TREE: A fast and effective stochastic algorithm for estimating maximum-likelihood phylogenies. *Mol. Biol. Evol.* **32**, 268–274 (2015). doi: 10.1093/molbev/msu300; pmid: 25371430
83. S. Mirarab *et al*., ASTRAL: Genome-scale coalescent-based species tree estimation. *Bioinformatics* **30**, i541–i548 (2014). doi: 10.1093/bioinformatics/btu462; pmid: 25161245
84. Y. Yu, C. Blair, X. He, RASP 4: Ancestral state reconstruction tool for multiple genes and characters. *Mol. Biol. Evol.* **37**, 604–606 (2020). doi: 10.1093/molbev/msz257; pmid: 31670774
85. H. Li, R. Durbin, Inference of human population history from individual whole-genome sequences. *Nature* **475**, 493–496 (2011). doi: 10.1038/nature10231; pmid: 21753753
86. H. Li, R. Durbin, Fast and accurate short read alignment with Burrows-Wheeler transform. *Bioinformatics* **25**, 1754–1760 (2009). doi: 10.1093/bioinformatics/btp324; pmid: 19451168
87. H. Li *et al*., The sequence alignment/map format and SAMtools. *Bioinformatics* **25**, 2078–2079 (2009). doi: 10.1093/bioinformatics/btp352; pmid: 19505943
88. M. J. Hubisz, K. S. Pollard, A. Siepel, PHAST and RPHAST: Phylogenetic analysis with space/time models. *Brief. Bioinform.* **12**, 41–51 (2011). doi: 10.1093/bib/bbq072; pmid: 21278375
89. S. M. Kiełbasa, R. Wan, K. Sato, P. Horton, M. C. Frith, Adaptive seeds tame genomic sequence comparison. *Genome Res.* **21**, 487–493 (2011). doi: 10.1101/gr.113985.110; pmid: 21209072
90. B. Murrell *et al*., Detecting individual sites subject to episodic diversifying selection. *PLOS Genet.* **8**, e1002764 (2012). doi: 10.1371/journal.pgen.1002764; pmid: 22807683
91. M. Punta *et al*., The Pfam protein families database. *Nucleic Acids Res.* **40**, D290–D301 (2012). doi: 10.1093/nar/gkr1065; pmid: 22127870
92. O. Trott, A. J. Olson, AutoDock Vina: Improving the speed and accuracy of docking with a new scoring function, efficient optimization, and multithreading. *J. Comput. Chem.* **31**, 455–461 (2010). pmid: 19499576

ACKNOWLEDGMENTS

We appreciate Z. Wang, J. Chang, and T. Wang from the Discipline Development Department of Northwest University for their support. We appreciate the support of the Life Periodic Plan of BGI and especially thank Y. Yin for assistance. We thank L. Yang from Nanning Zoo for help with sampling and Y. Xu, Q. Liang, and Y. Xie from Novogene for their support in genome assembly for the black-shanked douc monkey (*Pygathrix nigripes*). This study was supported through the Discipline Construction Project of Northwest University. We especially thank W. Wang and P. Shi for thoughtful comments on this manuscript. **Funding:** This work was supported by the National Science Foundation of China (32170512, 31622053, 31900314, 32001099, and 31730104), the Strategic Priority Research Program of the Chinese Academy of Sciences (XDB31020302), the Promotional Project for the Innovation Team, the Department of Science and Technology of Shaanxi Province (2018TD-017), and the Key Project of Basic Discipline Research Plan of Shaanxi Academy (2022). **Author contributions:** X.G.Q. conceived and designed the research; J.W.W., X.M.G., L.W., Q.Q., K.W., G.L., C.Z., Y.Y., D.D.W., and X.G.Q. contributed to genomic sequencing and data analyses. L.Z., C.O., C.C.G., and X.G.Q. performed the ecological analysis and phylogenetic reconstruction of social systems. R.J.D., J.W.W., L.Z., and C.D. performed cellular functional experiments. X.G.Q., J.W.W., L.Z., and P.A.G. wrote the manuscript. H.L.S., Z.P.H., C.Z.X., and A.B.W. helped with sample collection. B.G.L., G.J.Z., R.J., R.L.P., and W.H.J. added materials and helped to revise the manuscript, and all authors approved the final manuscript. **Competing interests:** The

authors declare no competing financial interests. **Data and materials availability:** Genome assemblies and DNA sequencing data have been deposited into the National Center for Biotechnology Information (NCBI) database under reference nos. PRJNA658634, PRJNA658635, PRJNA658636, PRJNA752402, and PRJNA752403. Other resources and data are available in the supplementary materials. **License information:** Copyright © 2023 the authors, some rights reserved; exclusive licensee American Association for the Advancement of Science. No claim to original US government works. https://www.science.org/about/science-licenses-journal-article-reuse

SUPPLEMENTARY MATERIALS

science.org/doi/10.1126/science.abl8621
Materials and Methods
Figs. S1 to S23
Tables S1 to S37
References (*93*–*445*)
Data S1 to S7
MDAR Reproducibility Checklist

Submitted 11 August 2021; accepted 6 July 2022
10.1126/science.abl8621

RESEARCH ARTICLE SUMMARY

PRIMATE GENOMES

Genome-wide coancestry reveals details of ancient and recent male-driven reticulation in baboons

Erik F. Sørensen *et al.*

INTRODUCTION: As a widespread but comparatively young clade of six parapatric species, the baboons (*Papio* sp.) exemplify a frequently observed pattern of mammalian diversity. In particular, they provide analogs for the population structure of the multibranched prehuman lineage that occupied a similar geographic range before the hegemony of "modern" humans, *Homo sapiens*. Despite phenotypic and genetic differences, interspecies hybridization has been described between baboons at several locations, and population relationships based on mitochondrial DNA (mtDNA) do not correspond with relationships based on phenotype. These previous studies captured the broad outlines of baboon population genetic structure and evolutionary history but necessarily used data that were limited in genomic and geographical coverage and therefore could not adequately document inter- and intrapopulation variation. In this study, we analyzed whole-genome sequences of 225 baboons representing all six species and 19 geographic sites, with 18 local populations represented by multiple individuals.

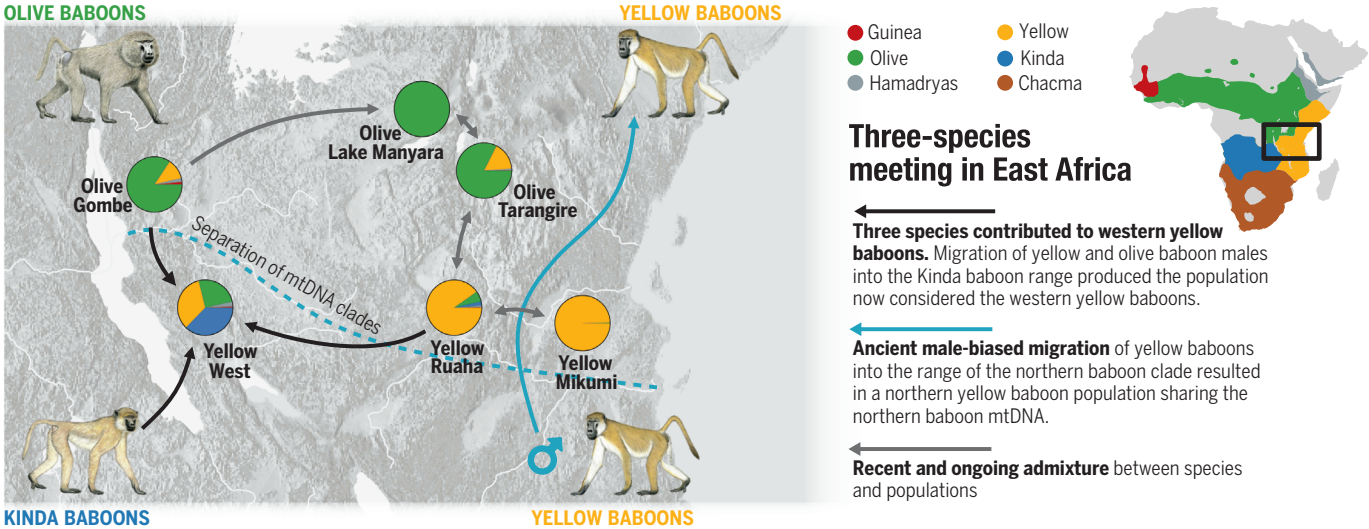
RATIONALE: Recent studies have identified several mammalian species groups in which genetically distinct lineages have hybridized to generate complex reticulate phylogenies. Baboons provide a valuable context for studying processes generating such population and phylogenetic complexity because extant parapatric species form hybrid zones in several regions of Africa, allowing for direct observation of ongoing introgression. Furthermore, prior studies of nuclear and mtDNA and phenotypic diversity have demonstrated gene flow among differentiated lineages but were unable to develop the detailed picture of process and history that is now possible using whole-genome sequences and modern computational methods. To address these questions, we designed a study that would provide a more fine-grained picture of recent and ancient genetic reticulation by comparing phenotypes and autosomal, X and Y chromosomal, and mtDNA sequences, along with polymorphic insertions of repetitive elements across multiple baboon populations.

RESULTS: Using deep whole-genome sequence data from 225 baboons representing multiple populations, we identified several previously unknown geographic sites of gene flow between genetically distinct populations. We report that yellow baboons (*P. cynocephalus*) from western Tanzania are the first nonhuman primate found to have received genetic input from three distinct lineages. We compared the ancestry shared among individuals, estim… separately from the X chromosome and a… somes, to distinguish shared ancestry due to ancestral population relationships from coancestry as a result of recent male-biased immigration and gene flow. This reveals directionality and sex bias of recent gene flow in several locations. Analyses of population differences within species quantified different degrees of interspecies introgression among populations with an essentially identical phenotype.

CONCLUSION: The population genetic structure and history of introgression among baboon lineages are even more complex than predicted from observed phenotypic diversity and prior studies of limited genetic data. Single populations can carry genetic contributions from more than two ancestral sources. Populations that appear homogeneous on the basis of observable phenotype can display different levels of interspecies introgression. The evolutionary dynamics and current structure of baboon population diversity indicate that other mammals displaying differentiated and geographically separate species may also have more-complex histories than anticipated. This may also be true for the morphologically defined hominin taxa from the past 4 million years. ■

All authors and affiliations appear in the full article online.
Corresponding authors: Kyle K.-H. Farh (kfahr@illumina.com); Tomas Marques-Bonet (tomas.marques@upf.edu); Kasper Munch (kaspermunch@birc.au.dk); Christian Roos (croos@dpz.eu); Jeffrey Rogers (jr13@bcm.edu)
Cite this article as E. F. Sørensen *et al.*, *Science* 380, eabn8153 (2023). DOI: 10.1126/science.abn8153

READ THE FULL ARTICLE AT
https://doi.org/10.1126/science.abn8153



Ancient and recent admixture among baboons: Complex population substructure and reticulation revealed by whole-genome sequencing. Pie charts represent recent ancestry of East African populations, with species contributions colored as in the inset map. Patterns of mixed ancestry differ substantially, even among conspecific populations. This suggests a complex history of recurrent interpopulational gene flow, driven predominantly by male migration. Comparably complex admixture probably also occurred among early hominins.

RESEARCH ARTICLE

PRIMATE GENOMES

Genome-wide coancestry reveals details of ancient and recent male-driven reticulation in baboons

Erik F. Sørensen[1]†, R. Alan Harris[2]†, Liye Zhang[3]†, Muthuswamy Raveendran[2]†, Lukas F. K. Kuderna[4,5], Jerilyn A. Walker[6], Jessica M. Storer[7], Martin Kuhlwilm[4,8,9], Claudia Fontsere[4], Lakshmi Seshadri[3], Christina M. Bergey[10], Andrew S. Burrell[11], Juraj Bergman[1,12], Jane E. Phillips-Conroy[13,14], Fekadu Shiferaw[15], Kenneth L. Chiou[16,17], Idrissa S. Chuma[18], Julius D. Keyyu[19], Julia Fischer[20,21,22], Marie-Claude Gingras[2], Sejal Salvi[2], Harshavardhan Doddapaneni[2], Mikkel H. Schierup[1], Mark A. Batzer[6], Clifford J. Jolly[11], Sascha Knauf[23], Dietmar Zinner[20,21,22], Kyle K.-H. Farh[5]*, Tomas Marques-Bonet[4,24,25,26]*, Kasper Munch[1]*, Christian Roos[3,27]*, Jeffrey Rogers[2]*

Baboons (genus *Papio*) are a morphologically and behaviorally diverse clade of catarrhine monkeys that have experienced hybridization between phenotypically and genetically distinct phylogenetic species. We used high-coverage whole-genome sequences from 225 wild baboons representing 19 geographic localities to investigate population genomics and interspecies gene flow. Our analyses provide an expanded picture of evolutionary reticulation among species and reveal patterns of population structure within and among species, including differential admixture among conspecific populations. We describe the first example of a baboon population with a genetic composition that is derived from three distinct lineages. The results reveal processes, both ancient and recent, that produced the observed mismatch between phylogenetic relationships based on matrilineal, patrilineal, and biparental inheritance. We also identified several candidate genes that may contribute to species-specific phenotypes.

Our understanding of the evolutionary processes involved in the origin of biological diversity has changed considerably over the past two decades. Genetic analyses have demonstrated that hybridization and interspecies gene flow between closely related mammalian species occur more often than previously assumed (*1*, *2*). Traditional studies of natural hybridization among populations and species have relied on phenotypic variation and a few informative genetic markers (*3*, *4*). However, access to large-scale genomic datasets now allows more extensive analyses (*5*–*7*) demonstrating that, in some cases, complex reticulations rather than dichotomously branching phylogenetic trees more accurately represent evolutionary histories.

Among primates, humans included, the number of genera found to exhibit complex histories of interspecific reticulation has recently grown markedly (*2*, *8*–*12*). Baboons (genus *Papio*) have long been recognized as a prime example of interspecies gene flow, with several hybrid zones between the six currently recognized parapatric species [Guinea baboons (*P. papio*), hamadryas baboons (*P. hamadryas*), olive baboons (*P. anubis*), yellow baboons (*P. cynocephalus*), Kinda baboons (*P. kindae*), and chacma baboons (*P. ursinus*); Fig. 1; for the rationale behind the classification of these major forms as species rather than subspecies, see (*13*)] (*14*–*17*). Previous analyses have identified substantial discrepancies in species-level phylogenies inferred using information from nuclear DNA, mitochondrial DNA (mtDNA), and phenotypes, indicating para- and polyphyletic relationships and suggesting a complex history of differentiation and admixture (*18*–*21*). Recent comparisons of whole-genome sequence (WGS) data across *Papio* species illustrated the extent of genetic exchange between phenotypically distinct species (*22*–*25*). These studies were, however, restricted to one or two populations per species and therefore unable to analyze wider geographic patterns of genetic diversity or compare the local effects of interspecific contact.

This study provides a detailed WGS-based analysis of coancestry and genomic exchange across all six baboon species, including multiple populations within olive and yellow baboons. We generated deep [>30×; table S1 (*13*)] WGS data from 225 wild baboons representing 19 localities (Fig. 1 and table S2), describing variation within and among localities for autosomes, X and Y chromosomes, mtDNA, and other genetic features such as insertions of *Alu* repeats and long interspersed elements (LINEs). In addition to analyzing population structure using autosomal single-nucleotide variants (SNVs) and repetitive elements, we compared coancestry inferred from autosomal and X chromosomal data to reveal sex-biased effects on genetic population structure. Our results provide the most extensive analysis of genetic diversity in baboons to date and reveal processes, both recent and in the distant past, that resulted in the discrepancies documented among the phylogenetic relationships based on matrilineal, patrilineal, and biparental inheritance. The evidence indicates the radiation that produced the six extant species began more than 1 million years ago. The lineages that diverged around that time have since experienced extensive admixture, as reflected in their current genetic composition. We suggest that these findings inform predictions for similar systems such as hominin and early human evolution, for which baboons have long been recognized as a model (*26*–*29*).

Results

WGS analysis across multiple populations of baboons provides a fine-grained picture of present-day population structure and the evolutionary history that generated it. Results of this analysis also document additional locations of ongoing admixture among genetically distinct lineages. Our analyses of SNVs strongly support the existence of differentiated clades including the six recognized species, despite well-known hybrid zones between parapatric

[1]Bioinformatics Research Centre, Aarhus University, 8000 Aarhus, Denmark. [2]Human Genome Sequencing Center and Department of Molecular and Human Genetics, Baylor College of Medicine, Houston, TX 77030, USA. [3]Primate Genetics Laboratory, German Primate Center, Leibniz Institute for Primate Research, 37077 Göttingen, Germany. [4]Institute of Evolutionary Biology (UPF-CSIC), PRBB, Dr. Aiguader 88, 08003 Barcelona, Spain. [5]Artificial Intelligence Lab, Illumina Inc., San Diego, CA 92122, USA. [6]Department of Biological Sciences, Louisiana State University, Baton Rouge, LA 70803, USA. [7]Institute for Systems Biology, Seattle, WA 98109, USA. [8]Department of Evolutionary Anthropology, University of Vienna, 1030 Vienna, Austria. [9]Human Evolution and Archaeological Sciences (HEAS), University of Vienna, 1030 Vienna, Austria. [10]Department of Genetics, Human Genetics Institute of New Jersey, Rutgers University, Piscataway, NJ 08854, USA. [11]Department of Anthropology, New York University, New York, NY 10003, USA. [12]Section for Ecoinformatics and Biodiversity, Department of Biology, Aarhus University, 8000 Aarhus C, Denmark. [13]Department of Neuroscience, Washington University School of Medicine in St. Louis, St. Louis, MO 63110, USA. [14]Department of Anthropology, Washington University in St. Louis, St. Louis, MO 63130, USA. [15]The Carter Center Ethiopia, Addis Ababa, Ethiopia. [16]Center for Evolution and Medicine, Arizona State University, Tempe, AZ 85281, USA. [17]School of Life Sciences, Arizona State University, Tempe, AZ 85281, USA. [18]Tanzania National Parks, Arusha, Tanzania. [19]Tanzania Wildlife Research Institute, Arusha, Tanzania. [20]Cognitive Ethology Laboratory, German Primate Center, Leibniz Institute for Primate Research, 37077 Göttingen, Germany. [21]Department of Primate Cognition, Georg-August-Universität Göttingen, 37077 Göttingen, Germany. [22]Leibniz ScienceCampus Primate Cognition, 37077 Göttingen, Germany. [23]Institute of International Animal Health/One Health, Friedrich-Loeffler-Institut, Federal Research Institute for Animal Health, 17493 Greifswald–Insel Riems, Germany. [24]Catalan Institution of Research and Advanced Studies (ICREA), Passeig de Lluis Companys, 23, 08010 Barcelona, Spain. [25]CNAG-CRG, Centre for Genomic Regulation (CRG), Barcelona Institute of Science and Technology, Baldiri i Reixac 4, 08028 Barcelona, Spain. [26]Institut Catala de Paleontologia Miquel Crusafont, Universitat Autonoma de Barcelona, Edifici ICTA-ICP, cl Columnes s/n, 08193 Cerdanyola del Valles, Barcelona, Spain. [27]Gene Bank of Primates, German Primate Center, Leibniz Institute for Primate Research, 37077 Göttingen, Germany.
***Corresponding author. Email: kfahr@illumina.com (K.K.-H.F.); tomas.marques@upf.edu (T.M.-B.); kaspermunch@birc.au.dk (K.M.); croos@dpz.eu (C.R.); jr13@bcm.edu (J.R.)**
†These authors contributed equally to this work.

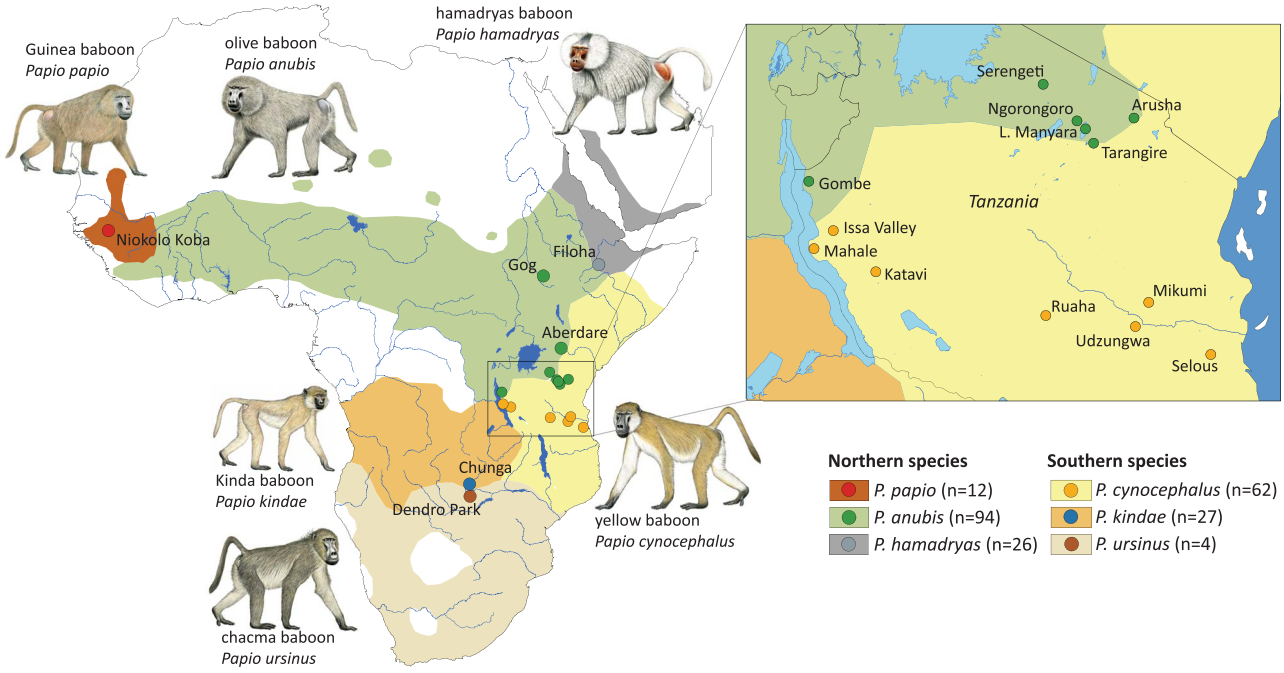


Fig. 1. Distribution of the six baboon species and sampling sites. Species distributions are modified from (*20*). The inset map shows sampling sites in Tanzania. Numbers of samples per species are given in parentheses. [Illustrations of male baboons by Stephen Nash, used with permission]

species. The initial divergence of evolutionary lineages separates the three northern species (hamadryas, olive, and Guinea baboons) from the three southern species (Kinda, yellow, and chacma baboons). Analyses of population structure (Fig. 2, A to C, and figs. S1 to S4) and phylogenomic maximum-likelihood (ML) trees using autosomal, X and Y chromosomal, and mtDNA data (figs. S5 to S8) are consistent with the initial north–south split and with greater overall divergence among southern than northern baboons [see also (*23*)]. Principal components analyses (PCAs) and ML trees of autosomal and X chromosomal data separate the western Tanzanian yellow baboons located at Mahale and Katavi into their own cluster distinct from eastern Tanzanian yellow baboons from Mikumi, Selous, Ruaha, and Udzungwa as well as from Kinda baboons. However, the Y chromosomal phylogenies, including one based on *Alu* insertions (fig. S9), show six main clusters largely corresponding to the six species and place most western yellow baboons with Kinda baboons. Other western yellow baboons cluster in that analysis with eastern yellow and one olive baboon, providing a clear example of admixture processes not revealed by the whole-genome phylogeny.

Across the genome of each individual, we identified the most recent coancestry among all other sampled individuals [using ChromoPainter (*30*)]. The corresponding first two principal components (Fig. 2C) show extensive variation among yellow baboons and confirm the primary north–south split. This split is also apparent in the clustering using fineSTRUCTURE (*30*) (Fig. 2B). ML trees for autosomes and X and Y chromosomes (figs. S5 to S7) all support the conclusions reached by PCA, with two individuals falling outside their expected species clades [samples PD0266 and PD0662, also anomalous in the PCAs; figs. S1, S2, S10, and S11 (*13*)]. As discussed below, the Y chromosomal phylogeny places Kinda baboons basal to all others (fig. S7).

Unsupervised cluster algorithms group individuals largely by species (see ADMIXTURE analysis; Fig. 2D and fig. S12) with $K = 7$ as the preferred number of clusters. However, in species for which we sampled more than one population (olive and yellow baboons), we find local genetic differences and evidence for a complex evolutionary history (detailed discussion below). These results are also supported by an analysis of LINE-1 (L1) insertions (fig. S13), an independent class of genetic marker that is less prone to parallel mutations. The pelage phenotypes on which taxonomy was traditionally based are generally very consistent within species over wide geographic ranges (*31*). Yet we find high genomic variation within and among conspecific populations. Heterozygosity ranges from 0.0006 to 0.0026 (average: 0.0018) per base pair across the six species, and from 0.0006 to 0.0029 across the 19 localities, with the lowest values in Guinea baboons (table S3 and figs. S14 to S17). The coancestry matrix and its PCA (Fig. 2, B and C) differentiates the various sampling localities and is therefore consistent with the ADMIXTURE analysis (Fig. 2D), showing that the sampled populations within both yellow and olive baboons can be distinguished genetically. The yellow baboons in Mikumi (Fig. 2B, box H) share pelage and morphological phenotypes with those in Ruaha despite being genetically distinct. Western yellow baboons from Mahale and Katavi (Fig. 2B, box F) exhibit phenotypic traits (somewhat smaller body size than Mikumi baboons, especially in terms of cranial metrics; aspects of coat color, with some individuals having pink skin around the eyes and sporadic occurrence of white-furred infants) in which they resemble Kinda baboons (*32*). The coancestry matrix (Fig. 2B) further shows that yellow baboons from Mahale and Katavi (box F) exhibit greater genetic similarity with Kinda (box E) and chacma baboons (box G) than with their supposed conspecifics from eastern Tanzania (box H). Similarly, all olive baboons (except for those from Tarangire) share a very consistent pelage and external phenotype. However, ADMIXTURE (Fig. 2D) and ChromoPainter (Fig. 2B) analyses identify clear evidence of genetic differences between the Ethiopian Gog olive baboons and the Tanzanian olive baboons of Lake Manyara and Ngorongoro. Furthermore, the Serengeti population is more similar genetically to both the Gombe and Aberdare populations than to the Ngorongoro or Lake Manyara populations, which are geographically much closer.

We used the SNV data to reconstruct the history of population size for each baboon locality (Fig. 3A and figs. S18 to S21). The estimated effective population sizes (N_e) were all essentially the same and on the order of 100,000 until about 1.0 million to 1.2 million

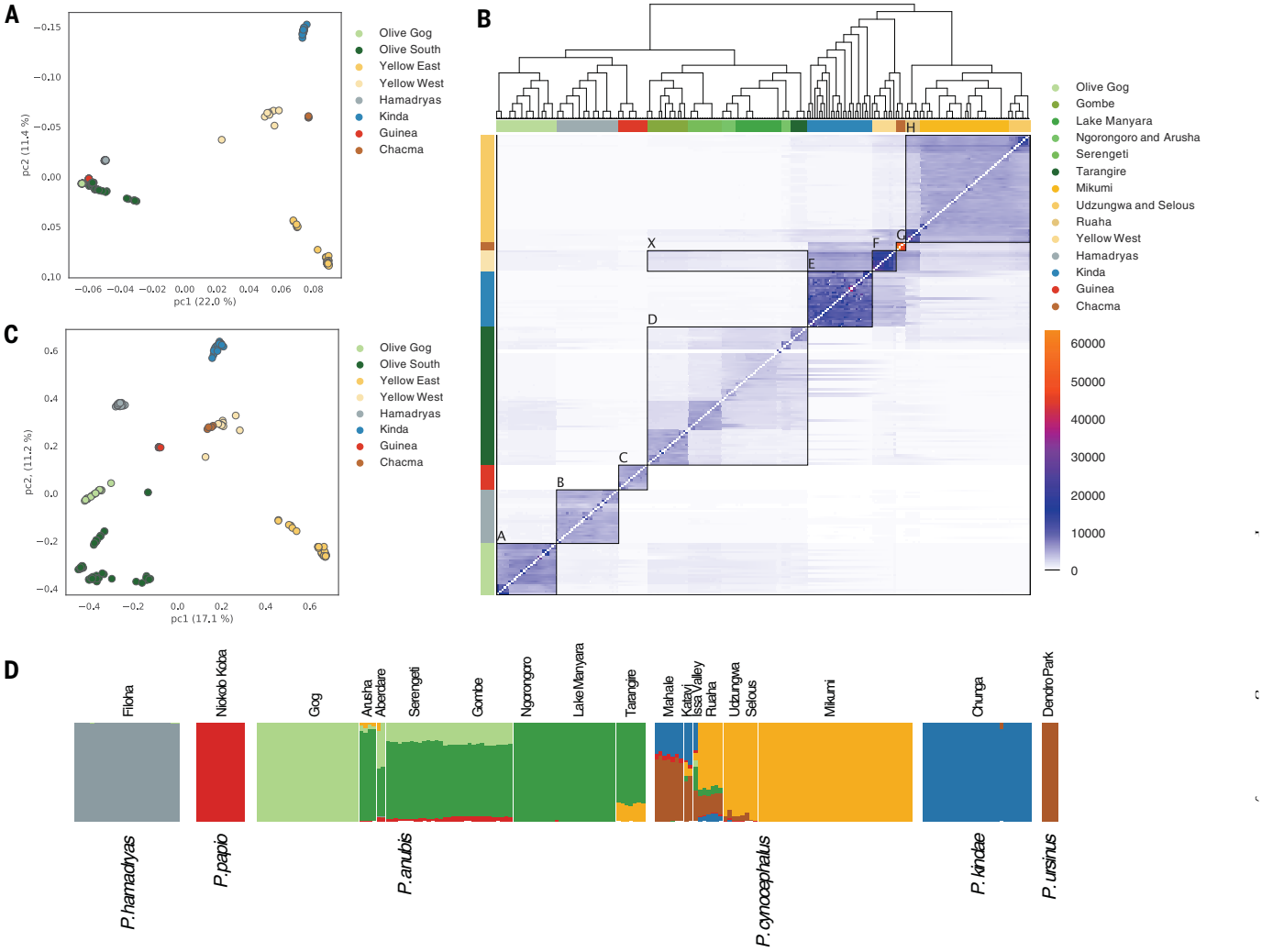


Fig. 2. Population structure and coancestry of the six baboon species. (**A**) PCA of autosomal SNVs. (**B**) ChromoPainter coancestry matrix with fineSTRUCTURE dendrogram. Each row in the coancestry matrix represents an individual and illustrates how its most recent common ancestry is distributed across all other sampled individuals. The ordering of individuals is the same for rows and columns. The row color labels are the same as in (A) and correspond to clusters shown for eight populations labeled with boxes: A, Gog olive (Ethiopia); B, hamadryas; C, Guinea; D, southern olive (Kenya and Tanzania); E, Kinda; F, western yellow; G, chacma; H, eastern yellow; X, olive coancestry in western yellows suggesting admixture (see alternate fineSTRUCTURE figure, fig. S4). Color labels below the dendrogram represent the 14 groups named in the figure legend. (**C**) PCA of the coancestry matrix. (**D**) ADMIXTURE plot with the preferred grouping of baboons into seven clusters (K = 7; for K = 2 to 10, see fig. S12).

years ago, which is consistent with the prior dating of the initial north–south divergence (*23*). At the separation, the N_e of northern populations fell below that of the southern populations, supporting the idea that the genus arose in southern Africa, and a daughter population from this basal stock spread to the north, then to the west, losing genetic diversity in serial founding events. The suggestion that Guinea baboons represent the descendants of those groups that were at the leading edge of that dispersal for the longest distance and time (*33*) is supported by the lower heterozygosity in that sample relative to all other baboon species (table S3). Also, whole-genome *Alu* and L1 insertion–based phylogenies place western yellow baboons with Kinda baboons, whereas Guinea baboons are basal among baboons, and hamadryas baboons are the sister taxon to olive and southern baboons (figs. S22 and S23). These findings may result from Guinea baboons and, to a lesser extent, hamadryas baboons losing polymorphic derived *Alu* and L1 insertions through drift as they dispersed north from the southern geographic origin (*34*).

Earlier studies provided clear evidence for hybridization and gene flow across the contact zones between pairs of parapatric species (*15*–*17*, *24*, *25*, *35*). In this study, we present evidence for additional ancient and recent arenas for gene flow between species pairs. Species tree reconstruction [ASTRAL (*36*)] using window-based ML trees (50- and 500-kb window size) produced inconsistent branching patterns among datasets, and only 58 to 70% of gene trees fit the species tree at the quartet level (figs. S24 and S25). Both incomplete lineage sorting (ILS) and gene flow are likely contributing to this discordance, which is expected to be larger for smaller windows. In addition, a qualitative visualization of these trees (figs. S24 and S25) shows a network-like pattern, again indicating complexity. There is greater shared genetic drift (measured by *f3* outgroup statistics) among eastern yellow baboon localities (Udzungwa, Selous, Mikumi, Ruaha), whereas western yellow baboons tend to cluster with Kinda baboons (fig. S26). In admixture graphs (Fig. 3B), Kinda baboons are, similarly to the description in (*23*), represented as a fusion product of populations from southern and ancestral northern clades, whereas the western yellow baboons share

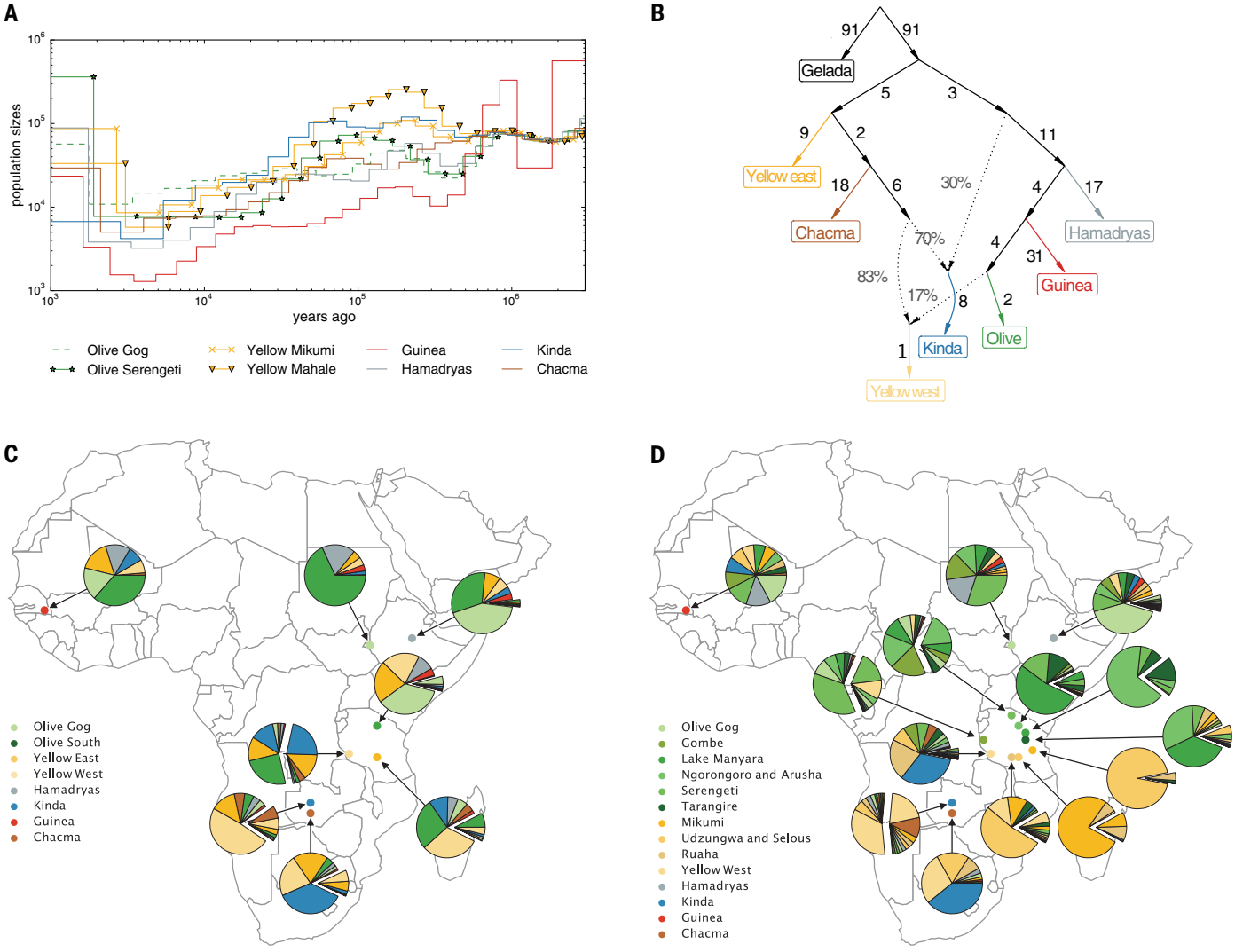


Fig. 3. Population history and complex reticulation between baboon populations. (**A**) MSMC2 plots using a mutation rate of 0.9 × 10^{-8} and a generation time of 11 years (*23*). (**B**) Admixture graph of the populations used in this study, based on 48,730,011 single-nucleotide variants with data for all individuals, and a predefined number of two admixture events. Numbers on solid branches correspond to the estimated drift in f2 units of squared frequency difference; labels on dotted edges give admixture proportions. (**C**) Globetrotter analysis of the eight major regional populations. The pie chart for each cluster shows ancestry contributions from other clusters. Expanded wedges represent ancestry that can be attributed to recent admixture (<56 generations, bootstrap $P < 0.05$). (**D**) Same as (C), but for 14 populations separating each major sampling location (here, expanded wedges represent ancestry that can be attributed to admixture more recent than 95 generations, bootstrap $P < 0.05$).

ancestry with both Kinda and olive baboons. More complex graphs (tables S4 and S5 and figs. S27 to S29) might be supported, but they failed to give replicable results, likely owing to complex reticulation and multiple gene flow events at different times and between different local populations, which now obscure the processes involved.

Taken as a whole, this expanded dataset does not support the previous suggestion that Kinda baboons result from a recent fusion event (*23*) as shown in Fig. 3B. In PCA plots using genome-wide SNVs, Kinda baboons do not fall intermediate between northern and southern clades but in fact are quite distinct (Fig. 2A and figs. S1 and S2). Some ML trees (i.e., Y chromosome data; fig. S7) place Kinda baboons as a sister clade to all other baboons, whereas other trees (autosomes and X chromosome data; figs. S5 and S6) lump them together with yellow and chacma baboons into the southern clade. These results are more consistent with the idea that Kinda baboons show substantial genetic similarity to both northern and southern clade baboons because they are basal and phenotypically resemble the ancestral form from which all extant species are derived. Fossil evidence suggests a southern African origin for baboons (*34*), and the mtDNA haplotypes of Kinda and western yellow baboons (Fig. 4 and fig. S8) (*21*) suggest that their range in tropical southern Africa may include the area of origin of both northern and southern primary branches. Broader aspects of Y chromosome data also do not support Kinda baboons as a fusion product; Kinda baboon Y haplotypes are found in western yellow baboons but not in olive baboons, and no olive baboon mtDNA has been observed in any Kinda baboon to date. Finally, Kinda baboons share more polymorphic *Alu* insertions with geladas than do other *Papio* species, possibly the result of a period of coexistence and hybridization between their ancestors (*37*).

We analyzed the genetic relationships among the eight major regional baboon populations that constitute our samples: the four single-locality populations of chacma, Kinda, hamadryas,

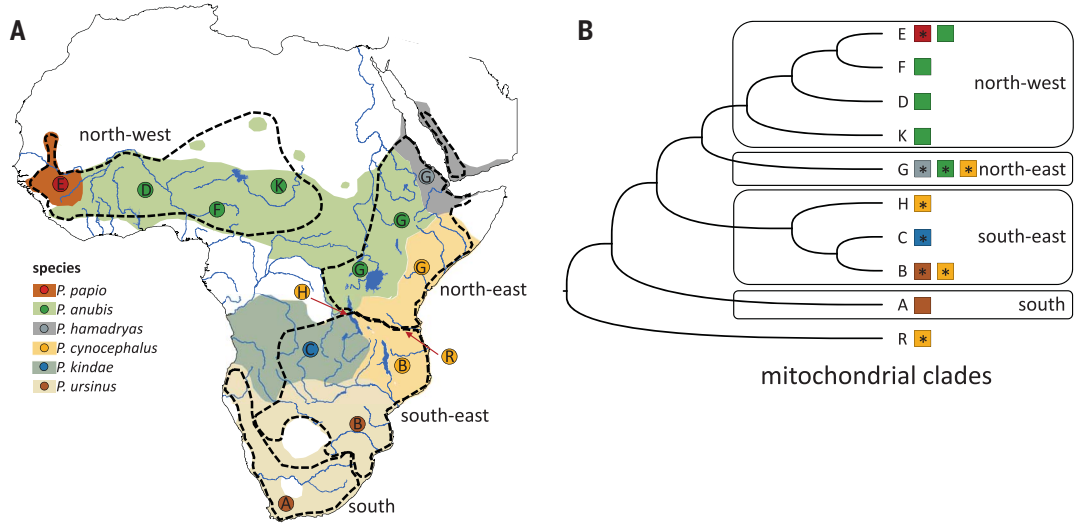


Fig. 4. Geographic distribution of mtDNA clades and mtDNA phylogeny. (**A**) Distribution ranges of baboon species and the four main mtDNA clades (south, southeast, northeast, northwest, dashed lines) including major mitochondrial lineages (A to R). (**B**) Phylogeny based on complete mtDNA genomes (see also fig. S8). Clade designation follows (*20*, *21*), and asterisks indicate lineages from which mtDNA genomes have been generated in this study. For identical haplotypes, see table S7.

and Guinea baboons and two groups each of yellow (western and eastern) and olive (Gog and southern) baboons. By modeling the recent ancestry along the chromosomes of individual baboons [Globetrotter (*38*)], we can represent each group as a mixture of recent ancestry with the remaining seven groups (Fig. 3C). In most of the groups, we can identify a contribution from recent admixture events (the oldest identifiable event estimated at 56 generations; table S6) separate from contributions of older admixture and retention of ancestral polymorphism (bootstrap $P < 0.01$ unless otherwise noted). In Fig. 3, C and D, we distinguish the recent admixture from more-ancient shared ancestry by showing the recent admixture estimates as expanded (exploded) wedges.

We identified a large amount of shared ancestry between southern olive and eastern yellow baboons not concordant with the overall phylogeny (Fig. 3C). This is also expressed in the coancestry matrix (Fig. 2B, box X) and is additional evidence of persistent admixture between both species (*15*, *17*, *22*, *25*). Furthermore, western yellow baboons from Mahale and Katavi share substantial ancestry with eastern yellow, Kinda, and southern olive baboons. This cannot be explained as a retention of ancient shared variation present before the origin of the six major branches, because there is no equivalent sharing with chacma, hamadryas, or Guinea baboons. This finding is, therefore, the first evidence that a single population (western yellow baboons) contains measurable admixture contributions from more than two distinct lineages. Comparing the ancestry of recently admixing populations (expanded wedges in Fig. 3C) to that of each other group identifies recent admixture from Gog into southern olive baboons, between western and eastern yellow baboons, from southern olive baboons into eastern yellow baboons ($P = 0.04$), between Kinda and chacma baboons ($P = 0.02$), and between Kinda and western yellow baboons. Repeating the Globetrotter analysis assuming 14 populations representing all major sampling locations differentiates olive and yellow baboon populations (Fig. 3D) and reveals a complex system of recent gene flow (all events < 95 generations) between: (i) olive baboon populations, (ii) yellow baboon populations, (iii) yellow and Tarangire olive baboons, (iv) western yellow and Gombe olive baboons, and (v) Tarangire olive baboons and Ruaha yellow baboons. These results do not imply direct migration of males (e.g., individual males moving from Gog to Serengeti) but rather, more plausibly, the overall consequences of many incremental gene flow events distributing alleles long distances over multiple generations.

This is not the first study to suggest that the history of genetic differentiation and reticulation among baboons is complex. Previous studies (*10*, *18*–*21*, *33*, *39*, *40*) showing widespread phenotype-mitochondrial discordance strongly suggest that nuclear swamping (i.e., the immigration of males into a phenotypically different population, largely or completely displacing the nuclear DNA composition and phenotype of the invaded population, without changing its mtDNA composition) has been a major contributing process. The present study found a similar discordance between the expanded mtDNA phylogeny (Fig. 4 and fig. S8) on the one hand and the new autosomal and Y-chromosomal phylogenies generated in this study on the other (figs. S5 and S7). Thus, our WGS findings strongly support previous suggestions, based only on mtDNA and phenotype data, that nuclear swamping has been a major factor generating the current pattern of baboon genetic and phenotypic variation.

The dense sampling of mtDNA provides important information about matrilineal ancestry. However, as a single locus, mtDNA represents only one of many possible genealogies generated by ILS and admixture. To test the hypothesis that nuclear swamping produced the discord observed between mtDNA phylogenies and relationships derived from comparisons of phenotype, we contrasted ancestry proportions across the X chromosome and the similarly sized chromosome 8, each contributing thousands of individual genealogies. Admixture by hemizygous males introduces disproportionately more autosomal than X chromosomal sequence, rendering shared X chromosome ancestry a better representation of deep species relationships before admixture. We found that the X chromosome of our chacma baboons derives more ancestry from yellow baboons than their chromosome 8 does (0.47 versus 0.62, paired *t* test, $P = 0.005$; Fig. 5A), suggesting that male-biased admixture from the ancestors of chacma baboons into the southern range of yellow baboons produced northern chacma baboons, including the grayfooted chacma baboons (*P. ursinus griseipes*) that we analyze in this study. This observation is consistent with the close relationship between mtDNA found in southernmost yellow and northern chacma baboons (clade B in Fig. 4) (*19*, *40*). The most compelling evidence of male-biased admixture is the relationship between western yellow and Kinda baboons. The ancestry profile of western yellow baboons (Fig. 5B) is very different from eastern yellow baboons (Fig. 5C). Western yellow baboons share more ancestry with Kinda baboons on the X chromosome than on chromosome 8 (0.27 versus 0.44, paired *t* test, $P = 0.025$), whereas Kinda baboons contain twice as much western yellow baboon ancestry on the X chromosome as on chromosome 8 (0.23 versus 0.55, paired *t* test, $P = 1.8 \times 10^{-13}$; Fig. 5D). Furthermore, eastern yellow baboons share more X chromosomal ancestry with western yellow baboons than

chromosome 8 ancestry (0.16 versus 0.20, paired *t* test, $P = 3.1 \times 10^{-9}$; Fig. 5B). Together these observations indicate that western yellow baboons were produced mainly from males carrying haplotypes that originated among eastern yellow and southern olive baboons migrating into the ancestral range of Kinda baboons, replacing Kinda baboon autosomes more than they replaced Kinda baboon X chromosomes. As a result, western yellow baboons carry genetic input from three distinct lineages.

In addition to patterns of shared ancestry among populations and species, we used two strategies to seek preliminary evidence for species-specific genetic adaptations in baboons. First, we used PLINK (*41*) to identify SNVs enriched in one species relative to all others (table S8). Genes containing possibly functional SNVs enriched in a given taxon were correlated with species phenotypes using Gene Ontology (GO) (*42*) terms and literature searches. We also used OmegaPlus (*43*) to test those gene regions for evidence of selective sweeps. Across all species, 1,342,371 SNVs met the criteria for being enriched in one particular species, including 4337 missense and 76 stop-gained SNVs (table S8). We next searched this list of candidates for genes annotated as influencing known traits of that species. Among them, SNV_1 (Table 1 and fig. S32), a missense variant in serine protease 8 (*PRSS8*), has a 0.96 allele frequency (AF) in hamadryas baboons and a 0.02 AF in the geographically adjacent Gog olive baboons (absent in other species). *PRSS8* increases epithelial sodium channel activity and mediates sodium reabsorption through the kidneys (*44*). *PRSS8* is under positive selection in the desert-adapted canyon mouse (*Peromyscus crinitus*) (*45*), and hamadryas baboons inhabit the most arid environment of all baboons (*46*). SNV_2 (Table 1 and fig. S33) has a 1.0 AF in both hamadryas and Guinea baboons and is absent from other species. This is a missense variant in neurexin 1 (*NRXN1*), which is associated with the GO term "social behavior." *Nrxn1* knockout mice exhibit changes in male aggression (*47*). Guinea and hamadryas baboons differ from others in the genus in exhibiting a multilevel male-philopatric social organization with substantial male-male tolerance (*29*, *48*). This contrasts with the matrilineal, male-dispersing social organization typical and likely ancestral for the genus. This observation is compatible with the speculation that until "swamped" by males from olive and yellow baboon populations, male-philopatric "pre-Guinea" and "pre-hamadryas" baboon populations occupied the northern savanna-woodland belt and much of the East African savanna-woodland corridor (*33*). SNV_3 (Table 1 and fig. S34) has a 1.0 AF in Kinda baboons and a 0.05 AF in yellow baboons (western yellow baboons and Ruaha) and one Serengeti olive baboon. This is a missense variant in the pigmentation-associated agouti signaling protein (*ASIP*). In mice, this gene affects melanin synthesis, shifting eumelanin production (black and brown hair) to phaeomelanin (red and yellow hair) (*49*). Kinda baboons display several distinctive coat color traits, including a substantial proportion of infants with white natal coats (*16*).

In our second approach to functional variation, we searched for genomic regions of elevated differentiation between pairs of closely related species [for details, see (*13*)]. We sought to

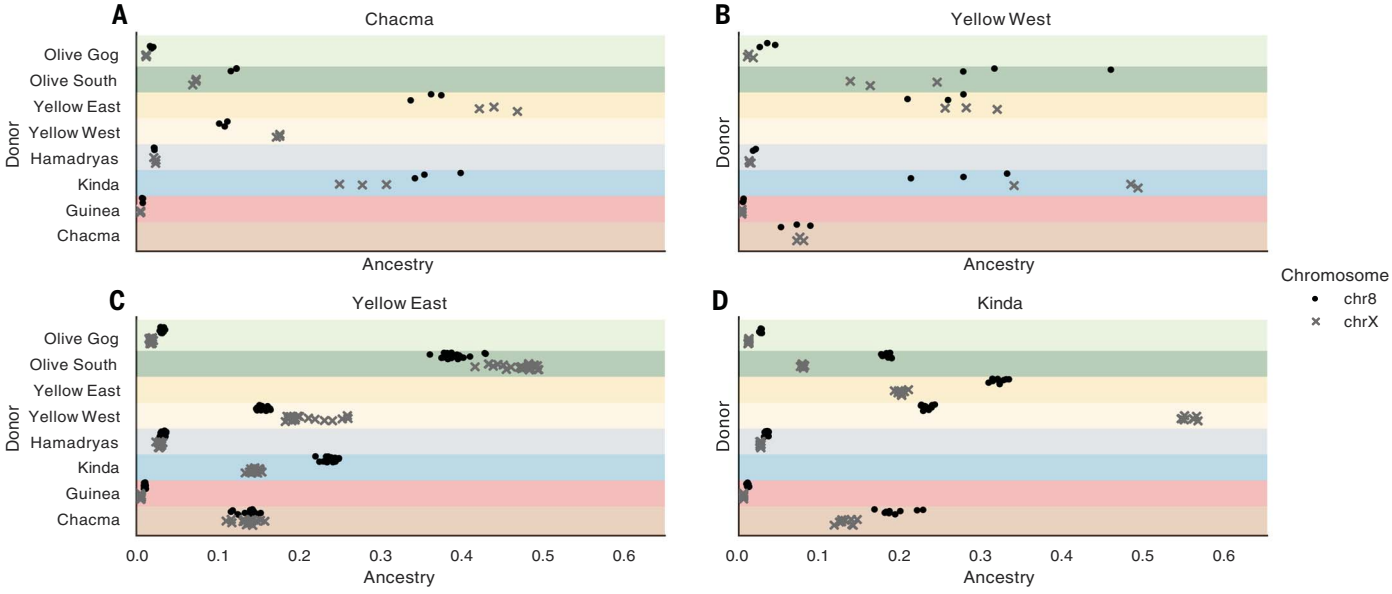


Fig. 5. Differential ancestry profiles on the X chromosome and an autosome. (**A**) Ancestry proportions of female chacma baboons. Each marker represents the fraction of total chromosome ancestry of one individual that is assigned to each of the remaining donor populations. Black dots and gray crosses represent ancestry proportions of chromosomes 8 and X, respectively. (**B**) Same as (A), but for female western yellow baboons. (**C**) Same as (A), but for female eastern yellow baboons. (**D**) Same as (A), but for female Kinda baboons. For additional profiles, see figs. S10, S30, and S31.

Table 1. Species enriched SNV statistics. Cluster and OmegaPlus statistics for the hamadryas and Guinea baboon shared SNV_2 are shown for hamadryas baboons. CADD and REVEL scores from human annotations predict functional impact of mutations (see supplementary materials).

SNV ID	SNV	PLINK *P* value	Cluster length (base pairs)	SNVs in cluster	OmegaPlus (percentile)	CADD PHRED	REVEL
SNV_1	20:27347531:G:T	1.40×10^{-78}	64,284	24	5.59 (1.8%)	0.001	0.351
SNV_2	13:49896439:G:C	9.72×10^{-101}	126,701	96	11.01 (0.3%)	7.266	N/A
SNV_3	10:30107617:T:C	2.52×10^{-69}	39,912	58	4.92 (0.7%)	19.140	0.080

determine whether regions with the strongest evidence of differentiation (windows in the top 0.1%) were enriched for genes with particular GO terms. Genomic regions most distinct between Kinda and yellow baboons were enriched for genes linked to skeletal development and morphogenesis (P value adjusted for false discovery rate, $P = 1.77 \times 10^{-4}$; tables S9 to S11 and fig. S35), including limb development (e.g., embryonic forelimb morphogenesis, adjusted $P = 0.02$). This enrichment was driven by one region on chromosome 3 containing a HOXA gene cluster (fig. S36) and may influence the distinctively small size and gracile, long-limbed build of Kinda baboons (*16*). Genes linked to male sexual differentiation were also increased in regions highly differentiated between Kinda and yellow baboons (adjusted $P = 0.0484$), possibly related to the reduced sexual dimorphism in Kinda baboons (*50*).

Discussion

Our expanded whole-genome dataset provides several insights into genetic reticulation and the evolutionary history of multiple local populations of baboons. Previous work showed that gene flow occurs among phenotypically and genetically distinct baboon species and pointed to nuclear swamping as a major contributing process. Our study extends and adds higher resolution to this picture, using genetic data to confirm hybrid zones that were previously suspected from field observation of phenotypic variation alone. We also identify the first local population (western Tanzanian yellow baboons) that has clear evidence for genetic contributions from three genetically distinct lineages.

While our results substantially extend our knowledge of baboon evolutionary history, some gaps remain. The richness of evolutionary detail to be derived from denser sampling is indicated by our results from East African populations. More extensive genetic surveys are needed to document other regions with complex biogeographic and evolutionary history, including the olive–Guinea baboon interface in West Africa (*21*), and regions of southern Africa where chacma baboons have experienced both ancient and recent periods of genetic divergence and reticulation (*39*, *40*). Other geographic regions, for example, the northern savanna-woodland belt west of our Gog population, have not been studied and would likely provide further information, especially regarding the origins and history of olive and Guinea baboons. Nevertheless, our dense sampling in East Africa clearly identifies previously unknown arenas of gene flow and documents the complexity of the evolutionary history of baboons in this region.

Our results lead to several substantive conclusions. With regard to methods, we find that while comparison of mtDNA and phenotypic variation is effective in detecting nuclear swamping, analyses comparing levels of shared ancestry across the X chromosome to that across autosomes provide a more quantitative assessment of demographic processes and genetic history. Second, we conclude that Kinda baboons are not the product of a recent fusion event. Instead, they are more likely close to the basal ancestor of all extant baboons. Next, we find additional support for the prior observation that the primary separation of northern and southern baboon species is the result of dispersal from the south to the north, with Guinea baboons recognized as the most recent occupants of the leading edge of that dispersal. Despite the sharp gradient of phenotypes that is characteristic of baboon interspecies contact zones, gene flow distributes the introgressed alleles far from the regions of obvious hybridization. And finally, we report that extant western yellow baboons carry genetic contributions from three genetically different baboon lineages.

The patterns of local, regional, and species-level genetic structure in baboons are likely a valuable model for population structure in other primate clades that consist of multiple closely related species, such as African green monkeys [genus *Chlorocebus* (*51*)] and macaques [genus *Macaca* (*52*)]. Clades in other mammalian orders are also revealing complex, often reticulated, evolutionary histories similar to those of baboons [e.g., polar bears (*53*, *54*), giraffes (*7*), and deer (*55*)]. The results for baboons also provide informative parallels and contrasts to the evolutionary differentiation and relationships among early human ancestors that arose, differentiated, and admixed over a time span remarkably similar to that of baboon cladogenesis (*56*).

Materials and methods summary

Extended materials and methods are presented in the supplementary materials. Descriptions of procedures used for sampling baboons in the wild, preparing and sequencing genomic libraries, analyzing variation among animals, and inferring phylogenetic relationships, as well as other aspects of study methods, are provided.

Samples and DNA sequencing

Blood samples from 225 baboons and two geladas were gathered in accordance with local regulations. Genomic DNA was extracted from blood, and libraries were prepared for sequencing on the NovaSeq 6000 platform (Illumina).

Variant calling and phasing

We used BWA-MEM to map reads to the Panu_3.0 baboon and the Mmul_10 rhesus assemblies. GATK was used to call variants following best practices. Panu_3.0 SNVs were phased using WhatsHap and SHAPEIT.

Population structure and phylogenetic analyses

Population structure based on SNVs was examined using PCA, ADMIXTURE, and fastSTRUCTURE. Phylogenetic trees based on autosomal and sex chromosome SNVs and Geneious assembled mitochondrial genomes were generated using IQ-TREE and visualized with FigTree. Polymorphic mobile elements were identified using DELLY and MELT. STRUCTURE and MELT were used to analyze population structure of L1 and *Alu* elements. PAUP was used to generate maximum parsimony trees from *Alu* and L1 elements. We used MSMC2 to infer baboon demographic history and population structure through time. Admixture graphs and *f*3 outgroup statistics were generated using ADMIXTOOLS 2.

Inference of most recent coancestry along each chromosome

ChromoPainter was used to infer the most recent coancestry along chromosomes, and fineSTRUCTURE was used to identify relationships between individuals on the basis of their most recent coancestry. We used Globetrotter to compute P values for a coancestry contribution from recent admixture.

Functional variation

Functional genetic variation among study animals was examined using PLINK for association analyses and OmegaPlus for identification of selective sweeps. We performed differentiation-based scans for selection using windowed F_{ST} values.

REFERENCES AND NOTES

1. M. L. Arnold, Y. Sapir, N. H. Martin, Genetic exchange and the origin of adaptations: Prokaryotes to primates. *Philos. Trans. R. Soc. London Ser. B* **363**, 2813–2820 (2008). doi: 10.1098/rstb.2008.0021; pmid: 18522920
2. R. R. Ackermann *et al.*, Hybridization in human evolution: Insights from other organisms. *Evol. Anthropol.* **28**, 189–209 (2019). doi: 10.1002/evan.21787; pmid: 31222847
3. N. H. Barton, G. M. Hewitt, Analysis of hybrid zones. *Annu. Rev. Ecol. Syst.* **16**, 113–148 (1985). doi: 10.1146/annurev.es.16.110185.000553
4. T. E. Dowling, C. L. Secor, The role of hybridization and introgression in the diversification of animals. *Annu. Rev. Ecol. Syst.* **28**, 593–619 (1997). doi: 10.1146/annurev.ecolsys.28.1.593
5. M. de Manuel *et al.*, The evolutionary history of extinct and living lions. *Proc. Natl. Acad. Sci. U.S.A.* **117**, 10927–10934 (2020). doi: 10.1073/pnas.1919423117; pmid: 32366643
6. S. Lamichhaney *et al.*, Female-biased gene flow between two species of Darwin's finches. *Nat. Ecol. Evol.* **4**, 979–986 (2020). doi: 10.1038/s41559-020-1183-9; pmid: 32367030
7. R. T. F. Coimbra *et al.*, Whole-genome analysis of giraffe supports four distinct species. *Curr. Biol.* **31**, 2929–2938.e5 (2021). doi: 10.1016/j.cub.2021.04.033; pmid: 33957077
8. M. L. Arnold, A. Meyer, Natural hybridization in primates: One evolutionary mechanism. *Zoology* **109**, 261–276 (2006). doi: 10.1016/j.zool.2006.03.006; pmid: 16945512
9. R. E. Green *et al.*, A draft sequence of the Neandertal genome. *Science* **328**, 710–722 (2010). doi: 10.1126/science.1188021; pmid: 20448178
10. D. Zinner, M. L. Arnold, C. Roos, The strange blood: Natural hybridization in primates. *Evol. Anthropol.* **20**, 96–103 (2011). doi: 10.1002/evan.20301; pmid: 22034167
11. J. Tung, L. B. Barreiro, The contribution of admixture to primate evolution. *Curr. Opin. Genet. Dev.* **47**, 61–68 (2017). doi: 10.1016/j.gde.2017.08.010; pmid: 28923540
12. C. Fontsere, M. de Manuel, T. Marques-Bonet, M. Kuhlwilm, Admixture in mammals and how to understand its functional implications: On the abundance of gene flow in mammalian

species, its impact on the genome, and roads into a functional understanding. *BioEssays* **41**, e1900123 (2019). doi: 10.1002/bies.201900123; pmid: 31664727
13. Detailed information is provided in the supplementary materials.
14. U. Nagel, A comparison of anubis baboons, hamadryas baboons and their hybrids at a species border in Ethiopia. *Folia Primatol. (Basel)* **19**, 104–165 (1973). doi: 10.1159/000155536; pmid: 4201907
15. J. Tung, M. J. E. Charpentier, D. A. Garfield, J. Altmann, S. C. Alberts, Genetic evidence reveals temporal change in hybridization patterns in a wild baboon population. *Mol. Ecol.* **17**, 1998–2011 (2008). doi: 10.1111/j.1365-294X.2008.03723.x; pmid: 18363664
16. C. J. Jolly, A. S. Burrell, J. E. Phillips-Conroy, C. Bergey, J. Rogers, Kinda baboons (*Papio kindae*) and grayfoot chacma baboons (*P. ursinus griseipes*) hybridize in the Kafue river valley, Zambia. *Am. J. Primatol.* **73**, 291–303 (2011). doi: 10.1002/ajp.20896; pmid: 21274900
17. M. J. E. Charpentier *et al*., Genetic structure in a dynamic baboon hybrid zone corroborates behavioural observations in a hybrid population. *Mol. Ecol.* **21**, 715–731 (2012). doi: 10.1111/j.1365-294X.2011.05302.x; pmid: 21988698
18. D. E. Wildman *et al*., Mitochondrial evidence for the origin of hamadryas baboons. *Mol. Phylogenet. Evol.* **32**, 287–296 (2004). doi: 10.1016/j.ympev.2003.12.014; pmid: 15186814
19. D. Zinner, L. F. Groeneveld, C. Keller, C. Roos, Mitochondrial phylogeography of baboons (*Papio* spp.): Indication for introgressive hybridization? *BMC Evol. Biol.* **9**, 83 (2009). doi: 10.1186/1471-2148-9-83; pmid: 19389236
20. D. Zinner, J. Wertheimer, R. Liedigk, L. F. Groeneveld, C. Roos, Baboon phylogeny as inferred from complete mitochondrial genomes. *Am. J. Phys. Anthropol.* **150**, 133–140 (2013). doi: 10.1002/ajpa.22185; pmid: 23180628
21. C. Roos *et al*., New mitogenomic lineages in *Papio* baboons and their phylogeographic implications. *Am. J. Phys. Anthropol.* **174**, 407–417 (2021). doi: 10.1002/ajpa.24186; pmid: 33244782
22. J. D. Wall *et al*., Genomewide ancestry and divergence patterns from low-coverage sequencing data reveal a complex history of admixture in wild baboons. *Mol. Ecol.* **25**, 3469–3483 (2016). doi: 10.1111/mec.13684; pmid: 27145036
23. J. Rogers *et al*., The comparative genomics and complex population history of *Papio* baboons. *Sci. Adv.* **5**, eaau6947 (2019). doi: 10.1126/sciadv.aau6947; pmid: 30854422
24. K. L. Chiou *et al*., Genome-wide ancestry and introgression in a Zambian baboon hybrid zone. *Mol. Ecol.* **30**, 1907–1920 (2021). doi: 10.1111/mec.15858; pmid: 33624366
25. T. P. Vilgalys *et al*., Selection against admixture and gene regulatory divergence in a long-term primate field study. *Science* **377**, 635–641 (2022). doi: 10.1126/science.abm4917; pmid: 35926022
26. C. J. Jolly, A proper study for mankind: Analogies from the Papionin monkeys and their implications for human evolution. *Am. J. Phys. Anthropol.* **116** (suppl. 33), 177–204 (2001). doi: 10.1002/ajpa.10021; pmid: 11786995
27. S. Elton, Forty years on and still going strong: The use of hominin-cercopithecid comparisons in palaeoanthropology. *J. R. Anthropol. Inst.* **12**, 19–38 (2006). doi: 10.1111/j.1467-9655.2006.00279.x
28. C. J. Jolly, "Analogies and models in the study of the early hominins" in *Early Hominin Paleoecology*, M. Sponheimer, J. A. Lee-Thorp, K. E. Reed, P. S. Ungar, Eds. (Colorado Univ. Press, 2013), pp. 437–455.
29. J. Fischer *et al*., Insights into the evolution of social systems and species from baboon studies. *eLife* **8**, e50989 (2019). doi: 10.7554/eLife.50989; pmid: 31711570
30. D. J. Lawson, G. Hellenthal, S. Myers, D. Falush, Inference of population structure using dense haplotype data. *PLOS Genet.* **8**, e1002453 (2012). doi: 10.1371/journal.pgen.1002453; pmid: 22291602
31. C. J. Jolly, "Species, subspecies, and baboon systematics" in *Species, Species Concepts, and Primate Evolution*, W. H. Kimbel, L. B. Martin, Eds. (Plenum, 1993), pp. 67–101.
32. M. V. Anandam *et al*., "Family Cercopithecidae (Old World monkeys) – species accounts of Cercopithecidae" in *Handbook of the Mammals of the World, Vol. 3 Primates*, R. A. Mittermeier, A. B. Rylands, D. E. Wilson, Eds. (Lynx, 2013), pp. 628–753.
33. C. J. Jolly, Philopatry at the frontier: A demographically driven scenario for the evolution of multilevel societies in baboons (*Papio*). *J. Hum. Evol.* **146**, 102819 (2020). doi: 10.1016/j.jhevol.2020.102819; pmid: 32736063
34. C. C. Gilbert, S. R. Frost, K. D. Pugh, M. Anderson, E. Delson, Evolution of the modern baboon (*Papio hamadryas*): A reassessment of the African Plio-Pleistocene record. *J. Hum. Evol.* **122**, 38–69 (2018). doi: 10.1016/j.jhevol.2018.04.012; pmid: 29954592
35. T. J. Bergman, J. E. Phillips-Conroy, C. J. Jolly, Behavioral variation and reproductive success of male baboons (*Papio anubis* x *Papio hamadryas*) in a hybrid social group. *Am. J. Primatol.* **70**, 136–147 (2008). doi: 10.1002/ajp.20467; pmid: 17724672
36. C. Zhang, M. Rabiee, E. Sayyari, S. Mirarab, ASTRAL-III: Polynomial time species tree reconstruction from partially resolved gene trees. *BMC Bioinformatics* **19** (suppl. 6), 153 (2018). doi: 10.1186/s12859-018-2129-y; pmid: 29745866
37. J. A. Walker *et al*., *Alu* insertion polymorphisms shared by *Papio* baboons and *Theropithecus gelada* reveal an intertwined common ancestry. *Mob. DNA* **10**, 46 (2019). doi: 10.1186/s13100-019-0187-y; pmid: 31788036
38. G. Hellenthal *et al*., A genetic atlas of human admixture history. *Science* **343**, 747–751 (2014). doi: 10.1126/science.1243518; pmid: 24531965
39. R. Sithaldeen, J. M. Bishop, R. R. Ackermann, Mitochondrial DNA analysis reveals Plio-Pleistocene diversification within the chacma baboon. *Mol. Phylogenet. Evol.* **53**, 1042–1048 (2009). doi: 10.1016/j.ympev.2009.07.038; pmid: 19665055
40. C. Keller, C. Roos, L. F. Groeneveld, J. Fischer, D. Zinner, Introgressive hybridization in southern African baboons shapes patterns of mtDNA variation. *Am. J. Phys. Anthropol.* **142**, 125–136 (2010). pmid: 19918986
41. S. Purcell *et al*., PLINK: A tool set for whole-genome association and population-based linkage analyses. *Am. J. Hum. Genet.* **81**, 559–575 (2007). doi: 10.1086/519795; pmid: 17701901
42. Gene Ontology Consortium, The Gene Ontology resource: Enriching a GOld mine. *Nucleic Acids Res.* **49**, D325–D334 (2021). doi: 10.1093/nar/gkaa1113; pmid: 33290552
43. N. Alachiotis, A. Stamatakis, P. Pavlidis, OmegaPlus: A scalable tool for rapid detection of selective sweeps in whole-genome datasets. *Bioinformatics* **28**, 2274–2275 (2012). doi: 10.1093/bioinformatics/bts419; pmid: 22760304
44. T. Narikiyo *et al*., Regulation of prostasin by aldosterone in the kidney. *J. Clin. Invest.* **109**, 401–408 (2002). doi: 10.1172/JCI0213229; pmid: 11828000
45. J. P. Colella *et al*., Limited evidence for parallel evolution among desert-adapted *Peromyscus* deer mice. *J. Hered.* **112**, 286–302 (2021). doi: 10.1093/jhered/esab009; pmid: 33686424
46. D. Zinner *et al*., Comparative ecology of Guinea baboons (*Papio papio*). *Primate Biol.* **8**, 19–35 (2021). doi: 10.5194/pb-8-19-2021; pmid: 34109265
47. H. M. Grayton, M. Missler, D. A. Collier, C. Fernandes, Altered social behaviours in neurexin 1α knockout mice resemble core symptoms in neurodevelopmental disorders. *PLOS ONE* **8**, e67114 (2013). doi: 10.1371/journal.pone.0067114; pmid: 23840597
48. L. Swedell *et al*., Female "dispersal" in hamadryas baboons: Transfer among social units in a multilevel society. *Am. J. Phys. Anthropol.* **145**, 360–370 (2011). doi: 10.1002/ajpa.21504; pmid: 21469076
49. J. Voisey, A. van Daal, Agouti: From mouse to man, from skin to fat. *Pigment Cell Res.* **15**, 10–18 (2002). doi: 10.1034/j.1600-0749.2002.00039.x; pmid: 11837451
50. M. Petersdorf, A. H. Weyher, J. M. Kamilar, C. Dubuc, J. P. Higham , Sexual selection in the Kinda baboon. *J. Hum. Evol.* **135**, 102635 (2019). doi: 10.1016/j.jhevol.2019.06.006; pmid: 31421317
51. H. Svardal *et al*., Ancient hybridization and strong adaptation to viruses across African vervet monkey populations. *Nat. Genet.* **49**, 1705–1713 (2017). doi: 10.1038/ng.3980; pmid: 29083404
52. Y. Song *et al*., Genome-wide analysis reveals signatures of complex introgressive gene flow in macaques (genus *Macaca*). *Zool. Res.* **42**, 433–449 (2021). doi: 10.24272/j.issn.2095-8137.2021.038; pmid: 34114757
53. J. A. Cahill *et al*., Genomic evidence for island population conversion resolves conflicting theories of polar bear evolution. *PLOS Genet.* **9**, e1003345 (2013). doi: 10.1371/journal.pgen.1003345; pmid: 23516372
54. J. A. Cahill *et al*., Genomic evidence of widespread admixture from polar bears into brown bears during the last ice age. *Mol. Biol. Evol.* **35**, 1120–1129 (2018). doi: 10.1093/molbev/msy018; pmid: 29471451
55. F. J. Combe, L. Jaster, A. Ricketts, D. Haukos, A. G. Hope, Population genomics of free-ranging Great Plains white-tailed and mule deer reflects a long history of interspecific hybridization. *Evol. Appl.* **15**, 111–131 (2021). doi: 10.1111/eva.13330; pmid: 35126651
56. Y. Liu, X. Mao, J. Krause, Q. Fu, Insights into human history from the first decade of ancient human genomics. *Science* **373**, 1479–1484 (2021). doi: 10.1126/science.abi8202; pmid: 34554811

ACKNOWLEDGMENTS

We thank all countries and their respective governmental and nongovernmental institutions that supported sampling and sample analysis. Specifically, we thank the government of the United Republic of Tanzania, Ministry for Education and Vocational Training, Commission for Science and Technology, Ministry for Natural Resources and Tourism, Ministry for Agriculture, Natural Resources, Livestock and Fisheries, Department of Forestry and Non-renewable Natural Resources, Tanzania Wildlife Authority, Tanzania Wildlife Research Institute, Tanzania National Parks (Y. A. Kiwango, R. Kaitila, I. A. V. Lejora), Ngorongoro Conservation Area Authority, Sokoine University of Agriculture (R. R. Kazwala), National Institute for Medical Research (C. C. Lubinza, S. G. M. Mfinanga), Jane Goodall Institute (I. F. Lippende, D. A. Collins), and the Greater Mahale Ecosystem Research and Conservation Project (A. Piel, F. A. Stewart). In Zambia, we thank the government of Zambia, the Zambia Wildlife Authority (J. Chulu, E. Matokwani; Chilanga), the staff of Kafue National Park, and the Department of Veterinary and Livestock Development (Y. Sinkala, Lusaka). In Ethiopia, we thank the government of Ethiopia, the Ethiopian Public Health Institute (E. Abate, Addis Ababa), the Guinea Worm Eradication Program of The Carter Center (J. Zingeser, E. Ruiz-Tiben, Z. Tadesse; Addis Ababa) as well as J. Else, H. Marshall, and the logistics team in Gog Woreda. In Senegal, we thank the Diréction des Parcs Nationaux and Ministère de l'Environnement et de la Protéction de la Nature de la République du Sénégal for permission to work in the Niokolo Koba National Park. We particularly thank former conservators of the park Colonel O. Kane and Commandant M. Gueye for their cooperation and logistical support during the study period and all the staff and field assistants of the CRP Simenti, in particular M. Faye, A. Louis Nyafouna, E. Dansokho, L. Diedhiou, M. Dieng, and T. Sonko, for their support in the field. **Funding:** This work was funded by "la Caixa" Foundation (ID 100010434), fellowship code LCF/BQ/PR19/11700002 (M.K.); the Vienna Science and Technology Fund (WWTF) (10.47379/VRG20001) (M.K.); German Research Foundation grants FI707/9-1, KN1097/3-1/3-1, KN1097/4-1, ZI548/5-1, and RO3055/2-1 (J.F., S.K., D.Z., and C.R.); Novo Nordisk Foundation grant 0058553 (E.F.S. and K.M.); R01 GM59290 (M.A.B.); and internal funding from Baylor College of Medicine (J.R.). T.M.B. is supported by funding from the European Research Council under the European Union's Horizon 2020 research and innovation programme (grant 864203), PID2021-126004NB-100 (MICIIN/FEDER, UE) and Secretaria d'Universitats i Recerca and CERCA Programme del Departament d'Economia i Coneixement de la Generalitat de Catalunya (GRC 2021 SGR 00177). **Author contributions:** Conceptualization: K.K.-H.F., T.M.-B., C.R., and J.R. Data curation: E.F.S., R.A.H., L.Z., M.R., and L.F.K.K. Formal analysis: E.F.S., R.A.H., L.Z., M.R., J.A.W., J.M.S., M.K., C.F., L.S., C.M.B., A.S.B., J.B., K.M., and C.R. Funding acquisition: K.K.-H.F., T.M.-B., K.M., C.R., and J.R. Investigation: E.F.S., R.A.H., L.Z., M.R., L.F.K.K., J.A.W., J.M.S., M.K., C.F., L.S., C.M.B., A.S.B., J.B., M.H.S., M.A.B., C.J.J., K.M., and C.R. Methodology: M.K., C.F., C.M.B., M.-C.G., S.S., H.D., M.A.B., S.K., D.Z., T.M.-B., K.M., C.R., and J.R. Project administration: K.M., C.R., and J.R. Resources and sample acquisition: C.M.B., A.S.B., J.E.P.-C., F.S., K.L.C., I.S.C., J.D.K., J.F., C.J.J., S.K., D.Z., C.R., and J.R. Supervision: T.M.-B., K.M., C.R., and J.R. Visualization: E.F.S., R.A.H., L.Z., J.A.W., J.M.S., M.K., C.F., C.M.B., D.Z., K.M., and C.R. Writing – original draft: E.F.S., R.A.H., L.Z., J.A.W., M.K., C.F., C.M.B., C.J.J., D.Z., T.M.-B., K.M., C.R., and J.R. Writing – review & editing: All authors. **Competing interests:** L.F.K.K. and K.K.-H.F. are employees of Illumina Inc. All other authors declare that they have no competing interests. **Data and materials availability:** The sequencing data used in these analyses are available through the Short Read Archive under BioProject accession PRJEB49549. Additional data are available in the supplementary materials. **License information:** Copyright © 2023 the authors, some rights reserved; exclusive licensee American Association for the Advancement of Science. No claim to original US government works. https://www.science.org/about/science-licenses-journal-article-reuse

SUPPLEMENTARY MATERIALS

science.org/doi/10.1126/science.abn8153
Materials and Methods
Supplementary Text S1 to S5
Figs. S1 to S36
Tables S1 to S11
References (*57*–*114*)
MDAR Reproducibility Checklist

Submitted 23 December 2021; accepted 27 September 2022
10.1126/science.abn8153

RESEARCH ARTICLE SUMMARY

PRIMATE GENOMES

The landscape of tolerated genetic variation in humans and primates

Hong Gao†, Tobias Hamp†, Jeffrey Ede, Joshua G. Schraiber, Jeremy McRae, Moriel Singer-Berk, Yanshen Yang, Anastasia S. D. Dietrich, Petko P. Fiziev, Lukas F. K. Kuderna, Laksshman Sundaram, Yibing Wu, Aashish Adhikari, Yair Field, Chen Chen, Serafim Batzoglou, Francois Aguet, Gabrielle Lemire, Rebecca Reimers, Daniel Balick, Mareike C. Janiak, Martin Kuhlwilm, Joseph D. Orkin, Shivakumara Manu, Alejandro Valenzuela, Juraj Bergman, Marjolaine Rousselle, Felipe Ennes Silva, Lidia Agueda, Julie Blanc, Marta Gut, Dorien de Vries, Ian Goodhead, R. Alan Harris, Muthuswamy Raveendran, Axel Jensen, Idriss S. Chuma, Julie E. Horvath, Christina Hvilsom, David Juan, Peter Frandsen, Fabiano R. de Melo, Fabrício Bertuol, Hazel Byrne, Iracilda Sampaio, Izeni Farias, João Valsecchi do Amaral, Mariluce Messias, Maria N. F. da Silva, Mihir Trivedi, Rogerio Rossi, Tomas Hrbek, Nicole Andriaholinirina, Clément J. Rabarivola, Alphonse Zaramody, Clifford J. Jolly, Jane Phillips-Conroy, Gregory Wilkerson, Christian Abee, Joe H. Simmons, Eduardo Fernandez-Duque, Sree Kanthaswamy, Fekadu Shiferaw, Dongdong Wu, Long Zhou, Yong Shao, Guojie Zhang, Julius D. Keyyu, Sascha Knauf, Minh D. Le, Esther Lizano, Stefan Merker, Arcadi Navarro, Thomas Bataillon, Tilo Nadler, Chiea Chuen Khor, Jessica Lee, Patrick Tan, Weng Khong Lim, Andrew C. Kitchener, Dietmar Zinner, Ivo Gut, Amanda Melin, Katerina Guschanski, Mikkel Heide Schierup, Robin M. D. Beck, Govindhaswamy Umapathy, Christian Roos, Jean P. Boubli, Monkol Lek, Shamil Sunyaev, Anne O'Donnell-Luria, Heidi L. Rehm, Jinbo Xu, Jeffrey Rogers*, Tomas Marques-Bonet*, Kyle Kai-How Farh*

INTRODUCTION: Millions of people have received genome and exome sequencing to date, a collective effort that has illuminated for the first time the vast catalog of small genetic differences that distinguish us as individuals within our species. However, the effects of most of these genetic variants remain unknown, limiting their clinical utility and actionability. New approaches that can accurately discern disease-causing from benign mutations and interpret genetic variants on a genome-wide scale would constitute a meaningful initial step towards realizing the potential of personalized genomic medicine.

RATIONALE: As a result of the short evolutionary distance between humans and nonhuman primates, our proteins share near-perfect amino acid sequence identity. Hence, the effects of a protein-altering mutation found in one species are likely to be concordant in the other species. By systematically cataloging common variants of nonhuman primates, we aimed to annotate these variants as being unlikely to cause human disease as they are tolerated by natural selection in a closely related species. Once collected, the resulting resource may be applied to infer the effects of unobserved variants across the genome using machine learning.

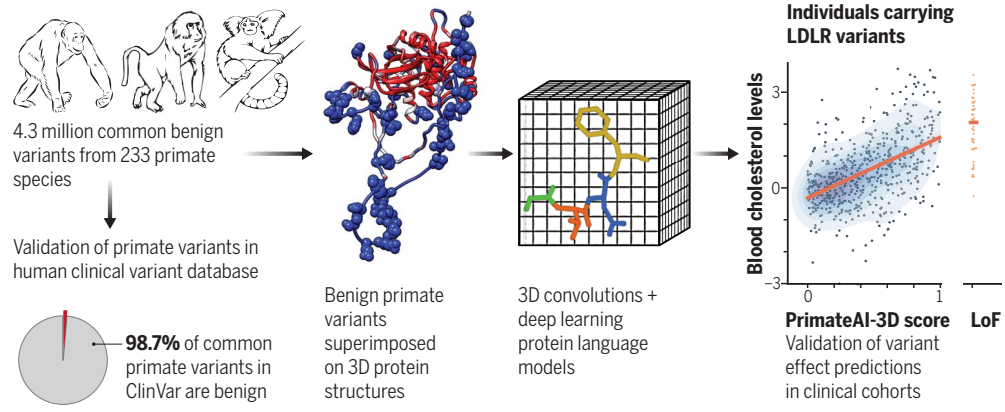
RESULTS: Following the strategy outlined above we obtained whole-genome sequencing data for 809 individuals from 233 primate species and cataloged 4.3 million common missense variants. We confirmed that human missense variants seen in at least one nonhuman primate species were annotated as benign in the ClinVar clinical variant database in 99% of cases. By contrast, common variants from mammals and vertebrates outside the primate lineage were substantially less likely to be benign in the ClinVar database (71 to 87% benign), restricting this strategy to nonhuman primates. Overall, we reclassified more than 4 million human missense variants of previously unknown consequence as likely benign, resulting in a greater than 50-fold increase in the number of annotated missense variants compared to existing clinical databases.

To infer the pathogenicity of the remaining missense variants in the human genome, we constructed PrimateAI-3D, a semisupervised 3D-convolutional neural network that operates on voxelized protein structures. We trained PrimateAI-3D to separate common primate variants from matched control variants in 3D space as a semisupervised learning task. We evaluated the trained PrimateAI-3D model alongside 15 other published machine learning methods on their ability to distinguish between benign and pathogenic variants in six different clinical benchmarks and demonstrated that PrimateAI-3D outperformed all other classifiers in each of the tasks.

CONCLUSION: Our study addresses one of the key challenges in the variant interpretation field, namely, the lack of sufficient labeled data to effectively train large machine learning models. By generating the most comprehensive primate sequencing dataset to date and pairing this resource with a deep learning architecture that leverages 3D protein structures, we were able to achieve meaningful improvements in variant effect prediction across multiple clinical benchmarks. ■

The list of author affiliations is available in the full article.
*Corresponding author. Email: tomas.marques@upf.edu (T.M.B.); jr13@bcm.edu (J.R.); kfarh@illumina.com (K.F.)
†These authors contributed equally to this work.
Cite this article as H. Gao *et al.*, *Science* **380**, eabn8197 (2023). DOI: 10.1126/science.abn8197

READ THE FULL ARTICLE AT
https://doi.org/10.1126/science.abn8197



PrimateAI-3D, a deep learning model trained on millions of benign primate variants. Common primate variants generated from 233 primate species (left) were validated as benign (98.7%) in the human ClinVar database. Voxelized protein structures (middle) with benign primate variants (spheres) were used to train a 3D convolution neural network to predict variant pathogenicity based on regional enrichment or depletion of primate variants. The resulting model was validated in independent clinical cohorts, as illustrated by the correlation of PrimateAI-3D scores and blood cholesterol levels for UK Biobank individuals (right).

RESEARCH ARTICLE

PRIMATE GENOMES

The landscape of tolerated genetic variation in humans and primates

Hong Gao[1]†, Tobias Hamp[1]†, Jeffrey Ede[1], Joshua G. Schraiber[1], Jeremy McRae[1], Moriel Singer-Berk[2], Yanshen Yang[1], Anastasia S. D. Dietrich[1], Petko P. Fiziev[1], Lukas F. K. Kuderna[1,3], Laksshman Sundaram[1], Yibing Wu[1], Aashish Adhikari[1], Yair Field[1], Chen Chen[1], Serafim Batzoglou[1]‡, Francois Aguet[1], Gabrielle Lemire[2,4], Rebecca Reimers[4,5], Daniel Balick[5,6], Mareike C. Janiak[7], Martin Kuhlwilm[3,8,9], Joseph D. Orkin[3,10], Shivakumara Manu[11,12], Alejandro Valenzuela[3], Juraj Bergman[13,14], Marjolaine Rousselle[13], Felipe Ennes Silva[15,16], Lidia Agueda[17], Julie Blanc[17], Marta Gut[17], Dorien de Vries[7], Ian Goodhead[7], R. Alan Harris[18], Muthuswamy Raveendran[18], Axel Jensen[19], Idriss S. Chuma[20], Julie E. Horvath[21,22,23,24,25], Christina Hvilsom[26], David Juan[3], Peter Frandsen[26], Fabiano R. de Melo[27], Fabrício Bertuol[28], Hazel Byrne[29], Iracilda Sampaio[30], Izeni Farias[28], João Valsecchi do Amaral[31,32,33], Mariluce Messias[34,35], Maria N. F. da Silva[36], Mihir Trivedi[12], Rogerio Rossi[37], Tomas Hrbek[28,38], Nicole Andriaholinirina[39], Clément J. Rabarivola[39], Alphonse Zaramody[39], Clifford J. Jolly[40], Jane Phillips-Conroy[41], Gregory Wilkerson[42]§, Christian Abee[42], Joe H. Simmons[42], Eduardo Fernandez-Duque[43,44], Sree Kanthaswamy[45], Fekadu Shiferaw[46], Dongdong Wu[47], Long Zhou[48], Yong Shao[47], Guojie Zhang[48,49,50,51,52], Julius D. Keyyu[53], Sascha Knauf[54], Minh D. Le[55], Esther Lizano[3,56], Stefan Merker[57], Arcadi Navarro[3,58,59,60], Thomas Bataillon[13], Tilo Nadler[61], Chiea Chuen Khor[62], Jessica Lee[63], Patrick Tan[62,64,65], Weng Khong Lim[64,65,66], Andrew C. Kitchener[67,68], Dietmar Zinner[69,70,71], Ivo Gut[17,72], Amanda Melin[73,74,75], Katerina Guschanski[19,76], Mikkel Heide Schierup[13], Robin M. D. Beck[7], Govindhaswamy Umapathy[11,12], Christian Roos[77], Jean P. Boubli[7], Monkol Lek[78], Shamil Sunyaev[5,6], Anne O'Donnell-Luria[2,4,79], Heidi L. Rehm[2,79,80], Jinbo Xu[1,81], Jeffrey Rogers[18]*¶, Tomas Marques-Bonet[3,17,56,58]*, Kyle Kai-How Farh[1]*

Personalized genome sequencing has revealed millions of genetic differences between individuals, but our understanding of their clinical relevance remains largely incomplete. To systematically decipher the effects of human genetic variants, we obtained whole-genome sequencing data for 809 individuals from 233 primate species and identified 4.3 million common protein-altering variants with orthologs in humans. We show that these variants can be inferred to have nondeleterious effects in humans based on their presence at high allele frequencies in other primate populations. We use this resource to classify 6% of all possible human protein-altering variants as likely benign and impute the pathogenicity of the remaining 94% of variants with deep learning, achieving state-of-the-art accuracy for diagnosing pathogenic variants in patients with genetic diseases.

A scalable approach for interpreting the effects of human genetic variants and their impact on disease risk is urgently needed to realize the promise of personalized genomic medicine (*1*–*3*). Out of more than 70 million possible protein-altering variants in the human genome, only ~0.1% are annotated in clinical variant databases such as ClinVar (*4*), with the remainder being variants of uncertain clinical significance (*5*, *6*). Despite collaborative efforts by the scientific community, the rarity of most human genetic variants has meant that progress toward deciphering personal genomes has been incremental (*7*, *8*). Consequently, clinical sequencing tests frequently return without definitive diagnoses, a frustrating outcome for both patients and clinicians (*9*, *10*). In certain cases patients must be recontacted and diagnoses reversed when the presumed pathogenic variant was later found to be a common variant in previously understudied human populations (*11*–*13*). Common variants can often be ruled out as the cause of penetrant genetic disease, because their high frequency in the population indicates that they are tolerated by natural selection, aside from rare exceptions due to founder effects and balancing selection (*14*–*16*).

An emerging strategy for solving clinical variant interpretation on a genome-wide scale is the use of information from closely related primate species to infer the pathogenicity of orthologous human variants (*17*). Because chimpanzees and humans share 99.4% protein sequence identity (*18*), a protein-altering variant present in one species can be expected to produce similar effects on the protein in the other species. By conducting population sequencing studies in closely related nonhuman primate species, it is feasible to systematically catalog common variants and rule these out as pathogenic in humans, analogous to how sequencing more diverse human populations has helped to advance clinical variant interpretation (*8*, *17*). Nonetheless, earlier work (*17*) was limited by the very small primate population sequencing datasets available, which bounded the number of common variants discovered and the scale of machine learning classifiers that could be trained.

Results

A database of 4.3 million benign missense variants across the primate lineage

To expand upon this strategy, we sequenced 703 individuals from 211 primate species and aggregated these with data from previous studies (*19*–*26*), yielding a total of 809 individuals from 233 species. We identified 4.3 million unique missense (protein-altering) variants and 6.7 million unique synonymous (nonprotein altering) variants (Fig. 1A), after excluding variants at positions that lacked unambiguous 1:1 mapping with humans, or that resulted in nonconcordant amino acid translation outcomes because of changes at neighboring nucleotides (fig. S1). The species selected for sequencing represent close to half of the 521 extant primate species on Earth (*27*) and cover all major primate families, from Old World monkeys and New World monkeys to lemurs and tarsiers. We targeted a small number of individuals per species (3.5 on average) to ensure that we primarily sampled common variants that have been filtered by natural selection rather than rare mutations (fig. S2).

Compared with the genome Aggregation Database (gnomAD) cohort of 141,456 human individuals from diverse populations (*28*, *29*), the primate sequencing cohort contained ~20% more exome variants despite sequencing 1/175th the number of individuals (Fig. 1A and fig. S3), attesting to the notable genetic diversity present in nonhuman primate species (*19*, *30*), many of which are critically endangered (*31*). The overlap of primate variants with gnomAD was low, consistent with independent mutational origins in each species (fig. S3). Out of the 22 million possible synonymous variants in the human genome, 30% were observed in the primate cohort, compared with just 6% of possible missense mutations (Fig. 1B). Because de novo mutations would have laid down unbiased proportions of missense and synonymous variants, the observed depletion of missense mutations in the primate cohort is consistent with most of the newly-arising human missense mutations being removed by natural selection as a result of their deleteriousness (*8*, *32*–*34*). The surviving missense variants are seen at high frequencies in primate populations and represent a subset of missense variants that have tolerated filtering by natural selection and are unlikely to be pathogenic (*35*).

Missense variants from the primate cohort are strongly enriched for benign consequence in the ClinVar clinical variant database (Fig. 1C). Among ClinVar variants with higher review

levels (two stars or above, indicating consensus by multiple submitters) (*4*), missense variants found in at least one nonhuman primate species were benign or likely benign ~99% of the time, compared with 63% for ClinVar missense variants in general and 80% for missense variants seen in gnomAD (Fig. 1C). The high fraction of pathogenic variants in gnomAD is consistent with most of these variants having arisen recently. Indeed, recent exponential human population growth introduced large numbers of rare variants through random de novo mutation (95% of variants in the gnomAD cohort are at <0.01% population allele frequency), without sufficient time for selection to purge deleterious variants from the population (*36*–*40*). Consequently, the gnomAD cohort provides a comparatively unfiltered look at variation caused by random mutations, whereas primate common variants represent the subset of random mutations that have survived.

The regions of human disease genes that were most densely populated by ClinVar pathogenic variants were also strongly depleted for primate common variants, with examples shown for *CACNA1A* (Fig. 1D) and *CREBBP* (fig. S4), genes responsible for familial epilepsy (*41*, *42*) and Rubinstein-Taybi syndrome (*43*, *44*). Missense variants in the gnomAD cohort were partially depleted within these same critical regions (Fig. 1D and fig. S4), indicating that humans and primates experience similar selective pressures. However, deleterious variants were incompletely removed in humans, consistent with the shorter amount of time they were exposed to natural selection.

Prior to using primate data as an indicator of benign consequence in a diagnostic setting, it is vital to understand why a handful of human pathogenic ClinVar variants appear as tolerated common variants in primates. Our clinical laboratory independently reviewed evidence for each of the 36 ClinVar pathogenic variants that appeared in the primate cohort, according to ACMG guidelines (*14*). Among these 36 variants, 8 were reclassified as variants of uncertain significance based on insufficient evidence of pathogenicity in the literature and an additional 9 were hypomorphic or mild clinical variants (table S1). The remaining 19 variants appear to be truly pathogenic in humans and are presumably tolerated in primates because of primate-human differences, such as interactions with changes in the neighboring sequence context (*45*, *46*). In one such example, a compensatory synonymous sequence change at an adjacent nucleotide explains why the variant is benign in primates but creates a pathogenic splice defect in humans (Fig. 1E). We also expect that some of the variants identified among primates are rare pathogenic variants by chance, despite the small number of individuals sequenced within each species. By expanding our cohort to sequence a large number of individuals per species, we would definitively exclude rare variation from our catalog of primate variation, as well as grow the database of benign variants to improve clinical variant interpretation.

As evolutionary distance from humans increases, cases in which the surrounding sequence context has changed sufficiently to alter the

[1]Illumina Artificial Intelligence Laboratory, Illumina Inc., Foster City, CA, 94404, USA. [2]Program in Medical and Population Genetics, Broad Institute of MIT and Harvard, Boston, MA, 02142, USA. [3]Institute of Evolutionary Biology (UPF-CSIC), PRBB, Dr. Aiguader 88, 08003 Barcelona, Spain. [4]Division of Genetics and Genomics, Department of Pediatrics, Boston Children's Hospital, Harvard Medical School, Boston, MA, 02115, USA. [5]Department of Biomedical Informatics, Harvard Medical School, Boston, MA, 02115, USA. [6]Division of Genetics, Brigham and Women's Hospital, Harvard Medical School, Boston, MA, 02115, USA. [7]School of Science, Engineering & Environment, University of Salford, Salford M5 4WT, UK. [8]Department of Evolutionary Anthropology, University of Vienna, Djerassiplatz 1, 1030 Vienna, Austria. [9]Human Evolution and Archaeological Sciences (HEAS), University of Vienna, 1030 Vienna, Austria. [10]Département d'anthropologie, Université de Montréal, 3150 Jean-Brillant, Montréal, QC H3T 1N8, Canada. [11]Academy of Scientific and Innovative Research (AcSIR), Ghaziabad 201002, India. [12]Laboratory for the Conservation of Endangered Species, CSIR-Centre for Cellular and Molecular Biology, Hyderabad 500007, India. [13]Bioinformatics Research Centre, Aarhus University, Aarhus 8000, Denmark. [14]Section for Ecoinformatics & Biodiversity, Department of Biology, Aarhus University, 8000 Aarhus, Denmark. [15]Research Group on Primate Biology and Conservation, Mamirauá Institute for Sustainable Development, Estrada da Bexiga 2584, Tefé, Amazonas, CEP 69553-225, Brazil. [16]Evolutionary Biology and Ecology (EBE), Département de Biologie des Organismes, Université libre de Bruxelles (ULB), Av. Franklin D. Roosevelt 50, CP 160/12, B-1050 Brussels, Belgium. [17]CNAG-CRG, Centre for Genomic Regulation (CRG), Barcelona Institute of Science and Technology (BIST), Baldiri i Reixac 4, 08028 Barcelona, Spain. [18]Human Genome Sequencing Center and Department of Molecular and Human Genetics, Baylor College of Medicine, Houston, TX 77030, USA. [19]Department of Ecology and Genetics, Animal Ecology, Uppsala University, SE-75236 Uppsala, Sweden. [20]Tanzania National Parks, Arusha, Tanzania. [21]North Carolina Museum of Natural Sciences, Raleigh, NC 27601, USA. [22]Department of Biological and Biomedical Sciences, North Carolina Central University, Durham, NC 27707, USA. [23]Department of Biological Sciences, North Carolina State University, Raleigh, NC 27695, USA. [24]Department of Evolutionary Anthropology, Duke University, Durham, NC 27708, USA. [25]Renaissance Computing Institute, University of North Carolina at Chapel Hill, Chapel Hill, NC 27599, USA. [26]Copenhagen Zoo, 2000 Frederiksberg, Denmark. [27]Universidade Federal de Viçosa, Viçosa, 36570-900, Brazil. [28]Universidade Federal do Amazonas, Departamento de Genética, Laboratório de Evolução e Genética Animal (LEGAL), Manaus, Amazonas, 69080-900, Brazil. [29]Department of Anthropology, University of Utah, Salt Lake City, UT 84102, USA. [30]Universidade Federal do Para, Guamá, Belém - PA, 66075-110, Brazil. [31]Research Group on Terrestrial Vertebrate Ecology, Mamirauá Institute for Sustainable Development, Tefé, Amazonas, 69553-225, Brazil. [32]Rede de Pesquisa para Estudos sobre Diversidade, Conservação e Uso da Fauna na Amazônia – RedeFauna, Manaus, Amazonas, 69080-900, Brazil. [33]Comunidad de Manejo de Fauna Silvestre en la Amazonía y en Latinoamérica – ComFauna, Iquitos, Loreto, 16001, Peru. [34]Universidade Federal de Rondonia, Porto Velho, Rondônia, 78900-000, Brazil. [35]PPGREN - Programa de Pós-Graduação "Conservação e Uso dos Recursos Naturais and BIONORTE - Programa de Pós-Graduação em Biodiversidade e Biotecnologia da Rede BIONORTE, Universidade Federal de Rondonia, Porto Velho, Rondônia, 78900-000, Brazil. [36]Instituto Nacional de Pesquisas da Amazonia, Petrópolis, Manaus - AM, 69067-375, Brazil. [37]Universidade Federal do Mato Grosso, Boa Esperança, Cuiabá - MT, 78060-900, Brazil. [38]Department of Biology, Trinity University, San Antonio, TX 78212, USA. [39]Life Sciences and Environment, Technology and Environment of Mahajanga, University of Mahajanga, Mahajanga, 401, Madagascar. [40]New York University, New York City, NY 10012, USA. [41]Washington University in St. Louis, St. Louis, MO 63130, USA. [42]Keeling Center for Comparative Medicine and Research, MD Anderson Cancer Center, Houston, TX 77030, USA. [43]Yale University, New Haven, CT 06520, USA. [44]Universidad Nacional de Formosa, Argentina Fundacion ECO, Formosa, Argentina. [45]Arizona State University, Tempe, AZ 85281, USA. [46]Guinea Worm Eradication Program, The Carter Center Ethiopia, PoB 16316, Addis Ababa 1000, Ethiopia. [47]State Key Laboratory of Genetic Resources and Evolution, Kunming Institute of Zoology, Chinese Academy of Sciences, Kunming, Yunnan 650223, China. [48]Center for Evolutionary & Organismal Biology, Zhejiang University School of Medicine, Hangzhou 310058, China. [49]Villum Center for Biodiversity Genomics, Section for Ecology and Evolution, Department of Biology, University of Copenhagen, DK-2100 Copenhagen, Denmark. [50]State Key Laboratory of Genetic Resources and Evolution, Kunming Institute of Zoology, Chinese Academy of Sciences, Kunming, Yunnan 650223, China. [51]Liangzhu Laboratory, Zhejiang University Medical Center, 1369 West Wenyi Road, Hangzhou 311121, China. [52]Women's Hospital, School of Medicine, Zhejiang University, 1 Xueshi Road, Shangcheng District, Hangzhou 310006, China. [53]Tanzania Wildlife Research Institute (TAWIRI), Head Office, P.O. Box 661, Arusha, Tanzania. [54]Institute of International Animal Health/One Health, Friedrich-Loeffler-Institut, Federal Research Institute for Animal Health, 17493 Greifswald - Insei Riems, Germany. [55]Department of Environmental Ecology, Faculty of Environmental Sciences, University of Science and Central Institute for Natural Resources and Environmental Studies, Vietnam National University, Hanoi 100000, Vietnam. [56]Catalan Institution of Research and Advanced Studies (ICREA), Passeig de Lluís Companys, 23, 08010 Barcelona, Spain. [57]Department of Zoology, State Museum of Natural History Stuttgart, 70191 Stuttgart, Germany. [58]Institut Català de Paleontologia Miquel Crusafont, Universitat Autònoma de Barcelona, Edifici ICTA-ICP, c/ Columnes s/n, 08193 Cerdanyola del Vallès, Barcelona, Spain. [59]Centre for Genomic Regulation (CRG), The Barcelona Institute of Science and Technology, Av. Doctor Aiguader, N88, 08003 Barcelona, Spain. [60]BarcelonaBeta Brain Research Center, Pasqual Maragall Foundation, C. Wellington 30, 08005 Barcelona, Spain. [61]Cuc Phuong Commune, Nho Quan District, Ninh Binh Province 430000, Vietnam. [62]Genome Institute of Singapore (GIS), Agency for Science, Technology and Research (A*STAR), 60 Biopolis Street, Genome, Singapore 138672, Republic of Singapore. [63]Mandai Nature, 80 Mandai Lake Road, Singapore 729826, Republic of Singapore. [64]SingHealth Duke-NUS Institute of Precision Medicine (PRISM), Singapore 168582, Republic of Singapore. [65]Cancer and Stem Cell Biology Program, Duke-NUS Medical School, Singapore 168582, Republic of Singapore. [66]SingHealth Duke-NUS Genomic Medicine Centre, Singapore 168582, Republic of Singapore. [67]Department of Natural Sciences, National Museums Scotland, Chambers Street, Edinburgh EH1 1JF, UK. [68]School of Geosciences, University of Edinburgh, Drummond Street, Edinburgh EH8 9XP, UK. [69]Cognitive Ethology Laboratory, Germany Primate Center, Leibniz Institute for Primate Research, 37077 Göttingen, Germany. [70]Department of Primate Cognition, Georg-August-Universität Göttingen, 37077 Göttingen, Germany. [71]Leibniz Science Campus Primate Cognition, 37077 Göttingen, Germany. [72]Universitat Pompeu Fabra, Pg. Luís Companys 23, 08010 Barcelona, Spain. [73]Department of Anthropology & Archaeology, University of Calgary, 2500 University Dr NW, Calgary, AB T2N 1N4, Canada. [74]Department of Medical Genetics, 3330 Hospital Drive NW, HMRB 202, Calgary, AB T2N 4N1, Canada. [75]Alberta Children's Hospital Research Institute, University of Calgary, 2500 University Dr NW, Calgary, AB T2N 1N4, Canada. [76]Institute of Ecology and Evolution, School of Biological Sciences, University of Edinburgh, Edinburgh EH8 9XP, UK. [77]Gene Bank of Primates and Primate Genetics Laboratory, German Primate Center, Leibniz Institute for Primate Research, Kellnerweg 4, 37077 Göttingen, Germany. [78]Department of Genetics, Yale School of Medicine, New Haven, CT 06520, USA. [79]Analytic and Translational Genetics Unit, Department of Medicine, Massachusetts General Hospital and Harvard Medical School, Boston, MA 02115, USA. [80]Center for Genomic Medicine, Massachusetts General Hospital, Boston, MA 02114, USA. [81]Toyota Technological Institute at Chicago, Chicago, IL 60637, USA.

***Corresponding authors. Email: tomas.marques@upf.edu; jr13@bcm.edu; kfarh@illumina.com** †These authors contributed equally to this work. ‡Current address: Seer, Inc., Redwood City, CA, 94065, USA. §Current address: Department of Clinical Science, College of Veterinary Medicine, North Carolina State University, Raleigh, NC, 27606, USA. ¶Current address: Wisconsin National Primate Research Center, Madison, WA, 53715, USA.

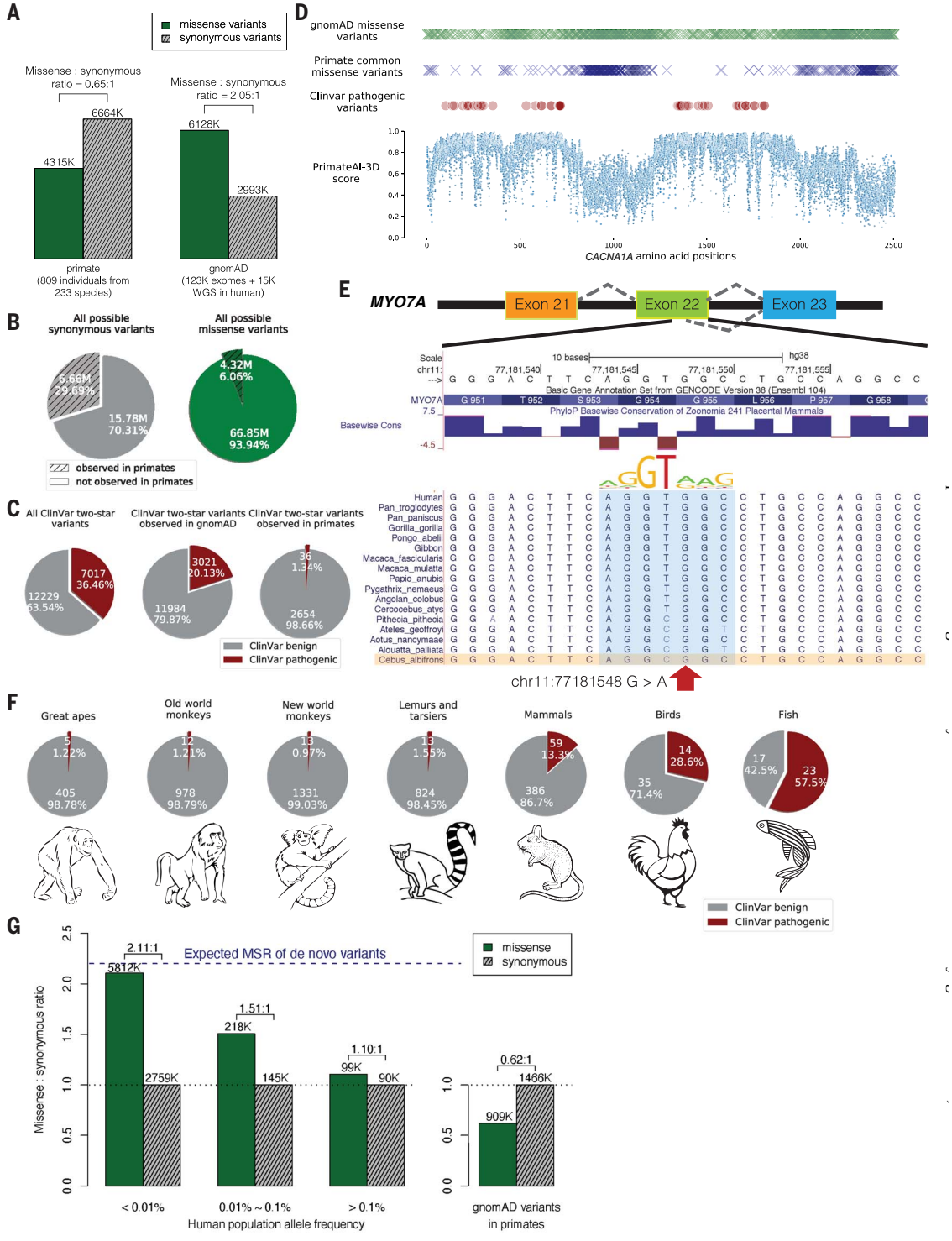


Fig. 1. Common primate variants are largely benign in humans. (**A**) Counts of missense (solid green) and synonymous (shaded gray) variants from primates compared with the gnomAD database. Missense:synonymous counts and ratios are displayed above each bar. (**B**) Fractions of all possible human synonymous (gray) and missense variants (green) observed in primates. (**C**) Counts of benign (gray) and pathogenic (red) missense variants with two-star review status or above in the overall ClinVar database (left pie chart), compared with ClinVar variants observed in gnomAD (middle), and compared with ClinVar variants observed in primates (right). Conflicting benign and pathogenic annotations and variants interpreted only with uncertain significance were excluded. (**D**) Observed gnomAD (green) or primate (blue) missense variants in each amino acid position in the *CACNA1A* gene. Red circles represent the positions of annotated ClinVar pathogenic missense variants. Bottom scatterplot shows PrimateAI-3D predicted pathogenicity scores for all possible missense substitutions along the gene. (**E**) Multiple sequence alignment showing the ClinVar pathogenic variant chr11:77181548 G>A (red arrow) creating a cryptic splice site in human sequence (extended splice motif, blue). This variant is tolerated in *Cebus Albifrons* and other species with a G>C synonymous change in the adjacent nucleotide that stops the splice motif from forming. (**F**) Pie charts showing the fraction of benign (gray) and pathogenic (red) missense variants with ClinVar two-star review status or above in great apes, Old World monkeys, New World monkeys, lemurs/tarsiers, mammals, chicken, and zebrafish. (**G**) Missense:synonymous ratios (MSR) across the human allele frequency spectrum, with MSR of human variants seen in primates shown for comparison. The blue dashed line represents the expected missense:synonymous ratio of de novo variants. Colors and legend are the same as (A).

effect of the variant should also increase until common variants in more-distant species could no longer be reliably counted on as benign in humans. We examined variation in each major branch of the primate tree as well as variation from mammals (mouse, rat, cow, dog), chicken, and zebrafish and evaluated their pathogenicity in ClinVar (Fig. 1F). Common variants from species throughout the primate lineage, including more-distant branches such as lemurs and tarsiers, varied from 98.6 to 99% benign in the human ClinVar database, but this dropped to 87% for placental mammals and 71% for chicken. The high fraction of variants that are pathogenic in humans yet tolerated as common variants in more distant vertebrates indicates that selection on orthologous variants diverges substantially in distantly related

species as a consequence of changes in the surrounding sequence context and other differences in species' biology (fig. S5).

We have made the primate population variant database, which contains more than 4.3 million likely benign missense variants, publicly available at https://primad.basespace.illumina.com as a reference for the genomics community. Overall, this resource is over 50 times larger than ClinVar in terms of number of annotated missense variants and consists almost entirely of variants of previously unknown significance. Most primate variants are rare or absent in the human population, with 98% of these variants at allele frequency <0.01% (fig. S6). This makes it challenging to establish their pathogenicity through other means, because even the largest sequencing laboratories would be unlikely to observe any given variant in more than one unrelated patient. Despite their rarity, the subset of human variants that appear in primates have a low missense:synonymous ratio consistent with being depleted of deleterious missense variants (Fig. 1G). This contrasts with the high missense:synonymous ratio for rare human variants in the overall gnomAD cohort, which approaches the 2.2:1 ratio expected for random de novo mutations in the absence of selective constraint (*47*). At higher allele frequencies, natural selection has had more time to purge deleterious missense variants, allowing the human missense:synonymous ratio to start to converge toward the ratio observed for the subset of human variants that are present in other primates.

Gene-level selective constraint in humans versus nonhuman primates

The primate variant resource makes it possible to compare natural selection acting on individual genes across the primate lineage and identify human-specific evolutionary differences. Because the current primate cohort only contains an average of 3 to 4 individuals per species, we focused on comparing selective constraint in human genes versus primates as a whole. We found that the missense:synonymous ratios of individual genes were well-correlated between humans and primates (Spearman r = 0.637) (Fig. 2A), indicating that genes that were depleted for deleterious missense mutations in humans were also consistently depleted throughout the primate lineage. Moreover, the missense:synonymous ratios of both human and primate genes correlated similarly well with the probability of genes being loss of function intolerant (pLI) (Spearman correlation −0.534 and −0.489, respectively) (*28*). Had there been substantial divergence between humans and primates, pLI, an independent metric derived from human protein-truncating variation, would have been expected to show much clearer agreement with human missense:synonymous ratios than primate.

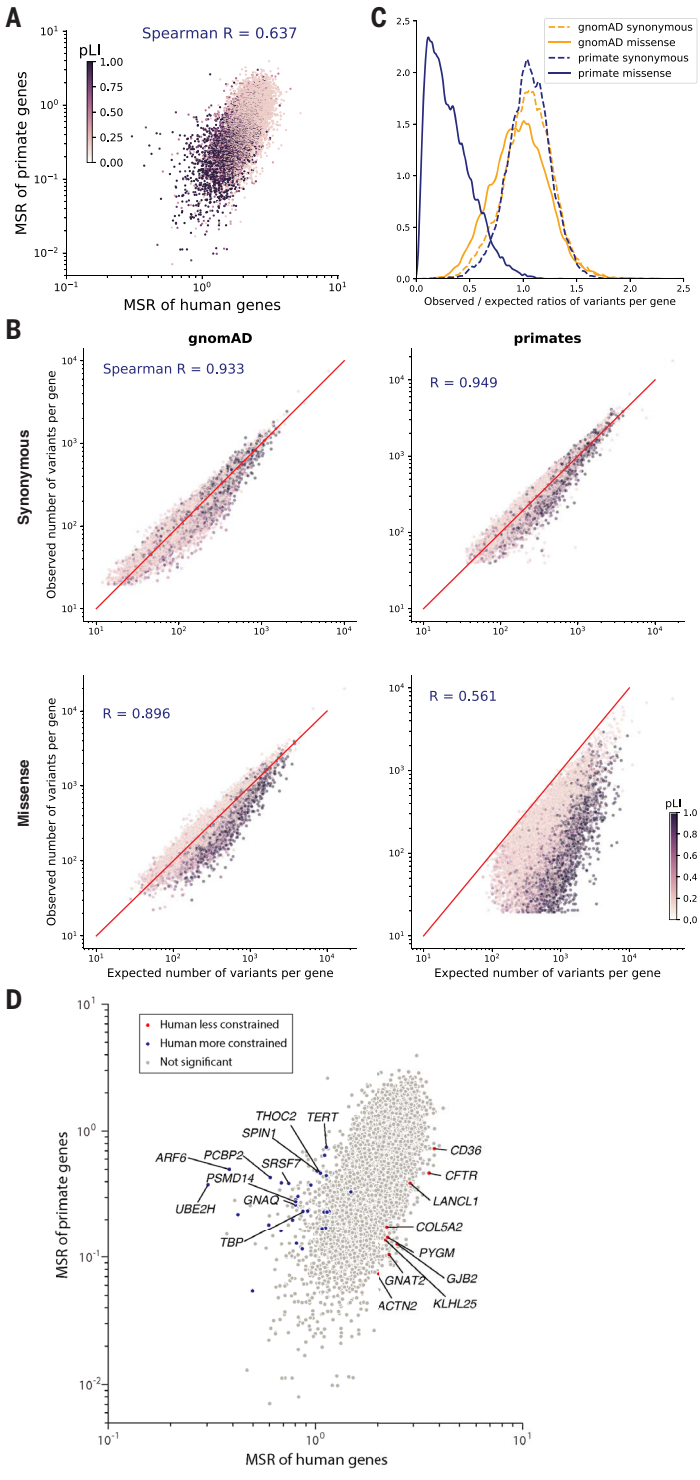


Fig. 2. Selective constraint of primate genes compared with humans. (**A**) Scatter plot of missense:synonymous ratios between primate and human genes. Each gene is colored by its pLI score, with darker points showing haploinsufficient genes. (**B**) Observed and expected counts of synonymous (top) and missense (bottom) variants per gene in gnomAD (left) and primates (right). Genes are colored by their pLI scores. (**C**) Distributions of observed and expected ratios of synonymous (dashed lines) and missense (solid lines) variants for all genes. Results for primate genes (orange) and gnomAD genes (blue) are shown. (**D**) Scatter plot of missense:synonymous ratios between primate and human genes. Highlighted points are genes that are under significantly stronger (blue) or weaker (red) constraint in humans compared with nonhuman primates under both methods (Benjamini-Hochberg FDR < 0.05) and gray points show nonsignificant genes. The top 10 genes with the largest effect sizes in either direction are labeled.

To measure the selective constraint on each gene, we calculated the observed versus expected number of variants per gene, using trinucleotide mutation rates to model the expected probability of observing each variant (fig. S7) (*28*, *29*). We modeled each primate species separately to account for differences in genetic diversity and the number of individuals sampled per species. The expected and observed counts of synonymous variants were highly correlated in both the gnomAD and primate cohorts, indicating that our model accurately captured the background distribution of neutral mutations (Fig. 2B; Spearman correlation 0.933 and 0.949, respectively). By contrast, for missense variants the expected and observed counts per gene diverged substantially (Spearman correlation 0.896 and 0.561 for humans and primates, respectively), due to depletion of deleterious missense variants by natural selection in highly constrained genes (for example, high pLI genes). The most highly constrained genes were almost completely scrubbed of common missense variants in the primate cohort, whereas rare missense variants in the gnomAD cohort were depleted to a more modest extent because of the large sample size of gnomAD (Fig. 2C).

We next aimed to identify genes whose selective constraint was different in humans compared with the rest of the primate lineage, a task made difficult by differences in diversity, allele frequency, and sample size between the human and primate cohorts (*34*, *48*, *49*). To this end, we developed two orthogonal strategies and took the intersection of genes identified under both approaches. First, we used population genetic modeling (*34*, *50*, *51*) to estimate the average selection coefficient, s, ranging from 0 (benign) to 1 (severely pathogenic) of missense mutations in each gene, using a model of recent human population growth (figs. S7 and S8). We fit a single value of s per gene across nonhuman primate species and identified genes that differed between $s_{primate}$ and s_{human} using a likelihood ratio test, which we validated using population simulations (fig. S9). In a second approach, we fit a curve approximating the relationship between human and primate missense:synonymous ratios using a Poisson generalized linear mixed model (*52*) and identified genes in which the observed human missense:synonymous ratio deviated from what would have been expected given the gene's missense:synonymous ratio in primates (fig. S10). We also adjusted for gene length to account for shorter genes having more variability in their missense:synonymous ratio measurements than longer genes. The two methods were broadly concordant, with a Spearman correlation of 0.80 between the genes' effect sizes in the two tests. Estimates of selection coefficients and observed and expected counts for each gene in humans and primate are provided in table S2.

In total, we found 39 genes in which selective constraint differed significantly between humans and other primates under both methods [Benjamini-Hochberg FDR < 0.05 (*53*); Fig. 2D]. The top three genes in which s_{human} decreased the most relative to $s_{primate}$ were *CFTR*, *GJB2*, and *CD36*, autosomal recessive disease genes for cystic fibrosis (*54*), hereditary deafness (*55*), and platelet glycoprotein deficiency (*56*), respectively. All three genes are known for deleterious mutations that are unusually common in local geographic human populations (*57*–*60*), suggesting that they may be experiencing reduced selection due to heterozygote advantage that protects against specific environmental pathogens (*60*–*64*). On the other end of the spectrum, *TERT*, known for its role in maintaining telomere length (*65*, *66*), was among the top genes in which s_{human} increased the most relative to $s_{primate}$. Humans have adapted to a much longer life span compared with other primate species, which have a median life span of 20 to 30 years, suggesting that increased selection on *TERT* may have occurred as part of human adaption toward extended longevity. We note that with the current size of the primate cohort, it is not possible to distinguish whether the increased selection on *TERT* occurred only in humans, or if it is part of a gradual trend toward extended longevity that began earlier in the great ape lineage, which also have longer life spans relative to other primates (~40 years). Expanding the primate cohort by sequencing more individuals per species would improve detection of additional species-specific and lineage-specific evolutionary adaptations and shed light on the evolutionary path that led to the present human condition.

PrimateAI-3D, a deep learning network for classifying protein-altering variants

We constructed PrimateAI-3D, a semisupervised 3D convolutional neural network for variant pathogenicity prediction, which we trained using 4.5 million common missense variants with likely benign consequence (Fig. 3A). In a departure from prior deep learning architectures that operated on linear sequences (*17*, *67*), we voxelized the 3D structure of the protein at 2 Å resolution (figs. S11 and S12) and used 3D convolutions to enable the network to recognize key structural regions that may not be apparent from sequence alone (Fig. 3A). As an example, we show PrimateAI-3D predictions for *STK11* (Fig. 3B), the tumor suppressor gene responsible for Peutz-Jeghers hereditary polyposis syndrome (*68*–*71*), with each amino acid position colored by the average PrimateAI-3D score at that position. Common primate variants used for training and annotated ClinVar pathogenic variants from separate parts of the linear sequence form distinct clusters in 3D space. Although ClinVar variants are shown for illustration, it should be noted that the network was not trained on either human-engineered features or annotated variants from clinical variant databases, thereby avoiding potential human biases in variant annotation. Rather, it learns to infer pathogenicity based on the local enrichment or depletion of common primate variants, taking only the protein's multiple sequence alignment and 3D structure as inputs.

PrimateAI-3D can use protein structures from either experimental sources or computational prediction (*72*–*76*); we used AlphaFold DB (*72*, *73*) and HHpred (*74*) predicted structures for the broadest coverage across human genes. For training data, we incorporated all common missense variants from the 233 nonhuman primate species (*17*) and common human missense variants (allele frequency > 0.1% across populations) in gnomAD (*28*, *29*), TOPMed (*77*, *78*), and UK Biobank (UKBB) (*79*, *80*), resulting in a total of 4.5 million unique missense variants of likely benign consequence. This dataset covers 6.34% of all possible human missense variants and is over 50 times larger than the current ClinVar database (79,381 missense variants after excluding variants of uncertain significance and those with conflicting annotations), greatly enlarging the training dataset available for machine learning approaches. Because the training dataset consists only of variants labeled as benign, we created a control set of randomly selected variants that were matched to the common variants by trinucleotide mutation rate and trained PrimateAI-3D to separate common variants from matched controls as a semisupervised learning task.

In parallel with the variant classification task, we generated amino acid substitution probabilities for each position in the protein by masking the residue and using the sequence context to predict the missing amino acid, borrowing from language model architectures that are trained to predict missing words in sentences (*81*, *82*). We trained both a 3D convolutional "fill-in-the-blank" model, which tasked the network with predicting the missing amino acid in a gap in the voxelized 3D protein structure, and separately, a language model using the transformer architecture to predict the missing amino acid using the surrounding multiple sequence alignment as context (*83*). We implemented these models as additional loss functions to further refine the PrimateAI-3D predictions (fig. S13). We also trained a variational autoencoder (*67*) on multiple sequence alignments and found that it performed comparably to our transformer architecture (fig. S14). Hence, we incorporated the average of their predictions in the loss function, which performed better than either alone.

We evaluated PrimateAI-3D and 15 other published machine learning methods (*67*, *84*)

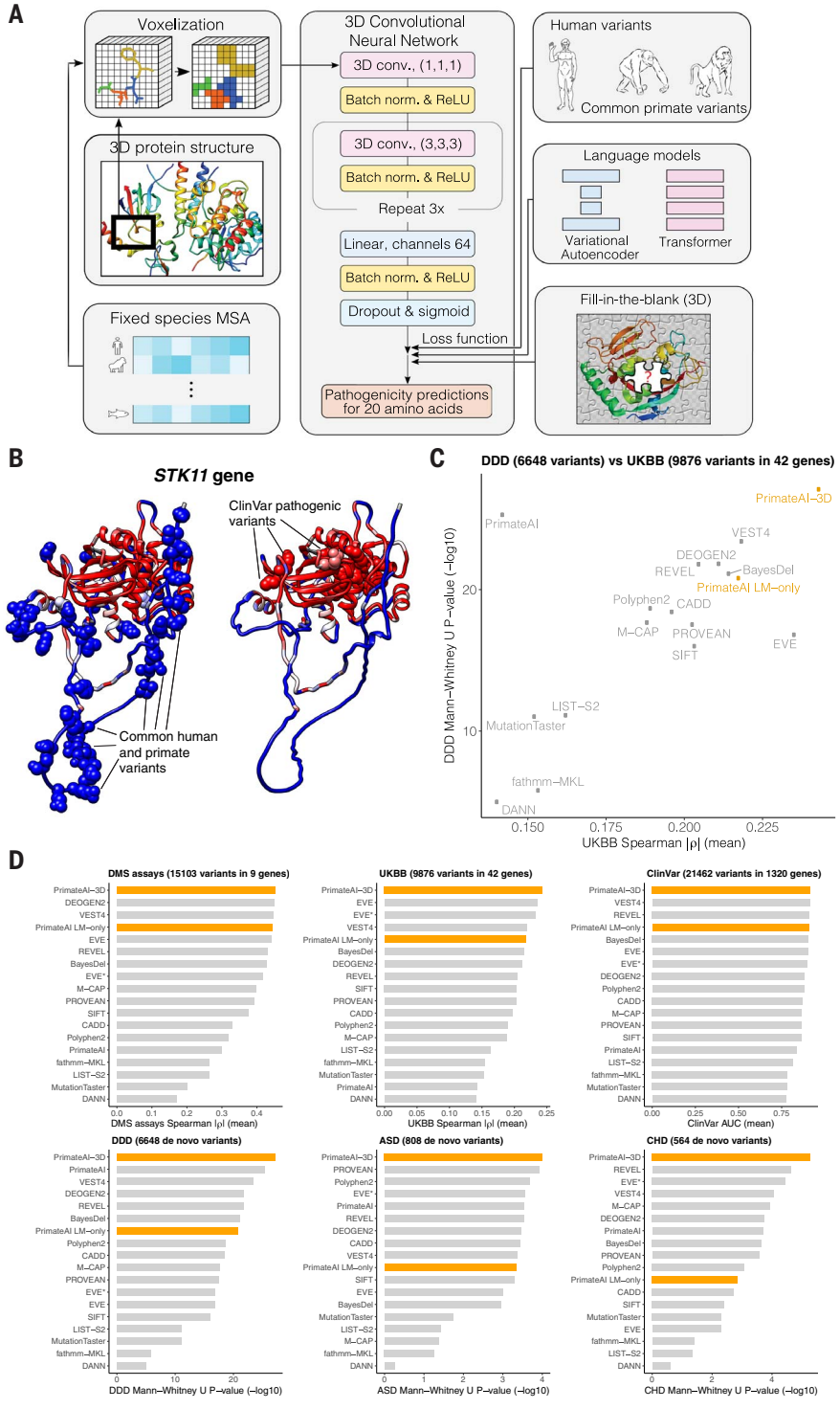


Fig. 3. PrimateAI-3D architecture and variant classification performance. (**A**) PrimateAI-3D workflow. Human protein structures and multiple sequence alignments are voxelized (left) as input to a 3D convolutional neural network that predicts pathogenicity of all possible point mutations of a target residue (middle). The network is trained using a loss function with three components (right): common human and primate variants; fill-in-the-blank of a protein structure; score ranks from language models. (**B**) Protein structure of the *STK11* gene, colored by PrimateAI-3D pathogenicity prediction scores (blue, benign; red, pathogenic). Spheres indicate residues with common human and primate variants (left) or residues with pathogenic mutations from ClinVar (right). For spheres, the color corresponds to the pathogenicity score of only the variant. For other residues, pathogenicity scores are averaged over all variants at that site. (**C**) Scatterplot shows performance of methods that predict missense variant pathogenicity in two clinical benchmarks (DDD and UKBB). Datasets are a subset of variants for which all methods have predictions. (**D**) Six barplots show method performance for six testing datasets (DMS assays, UKBB, ClinVar, DDD, ASD, and CHD).

on their ability to distinguish between benign and pathogenic variants along six different axes (Fig. 3, C and D, and fig. S15): predicting the effects of rare missense variants on quantitative clinical phenotypes in a cohort of 200,643 individuals from the UKBB; distinguishing missense de novo mutations (DNM) seen in 31,058 patients with neurodevelopmental disorders (DDD) (*85*–*87*) from de novo missense mutations in 2555 healthy controls (*88*–*93*); distinguishing de novo missense mutations seen in 4295 patients with autism spectrum disorders (ASD) (*88*–*94*) from de novo missense mutations in the shared set of 2555 healthy controls; distinguishing de novo missense mutations seen in 2871 patients with congenital heart disease (CHD) (*95*) from de novo missense mutations in the shared set of 2555 healthy controls; separating annotated ClinVar benign and pathogenic variants (ClinVar) (*4*); and average correlation with in vitro deep mutational scan (DMS) experimental assays across nine genes (*96*–*105*). Our set of clinical benchmarks is the most comprehensive to date and has a particular focus on rigorously testing the performance of classifiers on large patient cohorts across a diverse range of real-world clinical settings (table S3).

For the UKBB benchmark, we analyzed 200,643 individuals with both exome sequencing data and broad clinical phenotyping and identified 42 genes in which the presence of rare missense variants was associated with changes in a quantitative clinical phenotype controlling for confounders such as population stratification, age, sex, and medications (table S4). These gene-phenotype associations included diverse clinical lab measurements such as low-density lipoprotein (LDL) cholesterol (increased by rare missense variants in *LDLR*, decreased by variants in *PCSK9*), blood glucose (increased by variants in *GCK*), and platelet count (increased by variants in *JAK2*, decreased by variants in *GP1BB*), as well as other quantitative phenotypes such as standing height (increased by variants in *ZFAT*) (table S4). To test each classifier's ability to distinguish between pathogenic and benign missense variants, we measured the correlation between pathogenicity prediction score and quantitative phenotype for patients carrying rare missense variants in each of these genes. We report the average correlation across all gene-phenotype pairs for each classifier, taking the absolute value of the correlation because these genes may be associated with either increase or decrease in the quantitative clinical phenotype.

The DDD, ASD, and CHD cohorts are among the largest published trio-sequencing studies to date and consist of thousands of families with a child with rare genetic disease and their unaffected parents. In each cohort, we cataloged de novo missense mutations that appeared

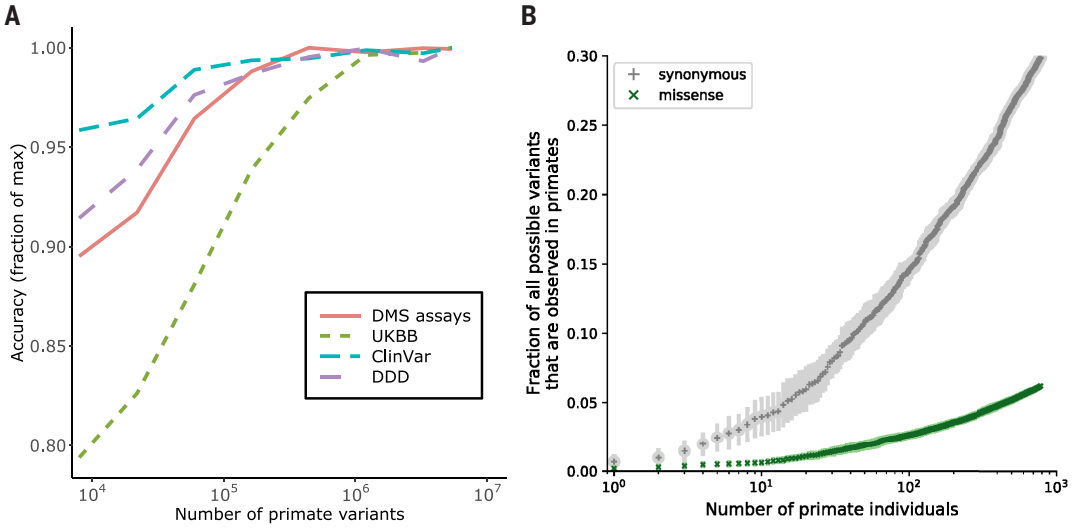


Fig. 4. Impact of training dataset size on classification accuracy. (**A**) Improved performance of PrimateAI-3D with increasing number of common human and primate variants in the training dataset (*x*-axis). Performance of each dataset (*y*-axis) was divided by the maximum performance observed across all training dataset sizes. (**B**) Cumulative fractions of all possible human synonymous (gray) and missense (green) variants observed as common variants in 234 primate species, including humans (allele frequency > 0.1%). Each point shows the average of 10 permutations, calculated with a different random ordering of the list of primate species each time.

in affected probands but were absent in their parents, as well as de novo missense mutations that appeared in a set of shared healthy controls. We evaluated the ability of each classifier to separate the de novo missense mutations that appear in cases versus controls on the basis of their prediction scores, using the Mann-Whitney U test to measure performance.

PrimateAI-3D outperformed all other classifiers at distinguishing pathogenic from benign variants in the four patient cohorts we tested (UKBB, DDD, ASD, CHD); it was also the top performer at separating pathogenic from benign variants in the ClinVar annotation database and had the highest average correlation with the deep mutational scan assays (Fig. 3D and fig. S15). After PrimateAI-3D there was no clear runner-up, with second place occupied by six different classifiers in the six different benchmarks. We observed a moderate correlation between the performance of different classifiers in UKBB and DDD (Spearman r = 0.556; Fig. 3C), which are the two largest clinical cohorts and therefore likely the most robust for benchmarking (with 200,643 and 33,613 patients, respectively), but outside of PrimateAI-3D, strong performance of a classifier on one task had limited generalizability to other tasks. Our results underscore the importance of validating machine learning classifiers along multiple dimensions, particularly in large real-world cohorts, to avoid overgeneralizing a classifier's performance based upon a notable showing along a single axis.

PrimateAI-3D's top-ranked performance at separating benign and pathogenic missense variants in ClinVar was unexpected, as the other machine learning classifiers (with the exception of EVE) were trained either directly on ClinVar or on other variant annotation databases with a high degree of content overlap. Because they are primarily based on variants described in the literature, clinical variant databases are subject to ascertainment bias (*12*, *106*, *107*), which may have contributed to supervised classifiers picking up on tendencies of human variant annotation that are unrelated to the task of separating benign from pathogenic variants (figs. S16, S17, and S18). Given the challenges with human annotation, we also investigated whether PrimateAI-3D could assist in revising incorrectly labeled ClinVar variants, by comparing annotations in the current ClinVar database and those from a September 2017 snapshot. Disagreement between PrimateAI-3D and the 2017 version of ClinVar was highly predictive of future revision and the odds of revision increased with PrimateAI-3D confidence (fig. S19). Among variants with the 10% most confident PrimateAI-3D predictions, the odds of revision were elevated by a factor of 10 if PrimateAI-3D was in disagreement with the ClinVar label ($P < 10^{-14}$).

The performance of PrimateAI-3D on clinical variant benchmarks scaled directly with training dataset size, indicating that additional primate sequencing data will be the key to unlocking further gains (Fig. 4 and fig. S20). The current primate cohort already covers 30% of all possible synonymous variants in the human genome, despite containing only 809 individuals from 233 species (Fig. 4B). By increasing the number of species and the number of individuals sequenced per species, we expect to saturate most of the remaining tolerated substitutions in the human genome (fig. S21), including both coding and noncoding variation, leaving the remaining deleterious variants to be deduced by a process of elimination.

Discovery of candidate disease genes for neurodevelopmental disorders

We applied PrimateAI-3D to improve statistical power for discovering candidate disease genes that are enriched for pathogenic de novo mutations in the neurodevelopmental disorders cohort (fig. S22). De novo missense mutations from affected individuals in the DDD cohort (*87*) were enriched 1.36-fold above expectation, based on estimates of background mutation rate using trinucleotide context (*47*). We selected a PrimateAI-3D classification threshold of 0.821, which called an equal number of pathogenic missense mutations (n = 7,238) as the excess of de novo missense mutations in the cohort (Fig. 5A). Stratifying missense mutations by this threshold increased enrichment of pathogenic de novo missense mutations to 2.0-fold, substantially increasing statistical power for disease gene discovery in the cohort (Fig. 5B).

By applying PrimateAI-3D to prioritize pathogenic missense variants, we identified 290 genes associated with intellectual disability at genome-wide significance ($P < 6.4 \times 10^{-7}$) (Table 1), of which 272 were previously discovered genes that either appeared in the Genomics England intellectual disability gene panel (*108*) or were already identified in the prior study (*109*) without stratifying missense variants (table S5). We excluded two genes, *BMPR2* and *RYR1*, as borderline significant genes that already had well-annotated nonneurological phenotypes. Further clinical studies are needed to independently validate this list of candidate genes and understand their range of phenotypic effects.

Discussion

Our results demonstrate the successful pairing of primate population sequencing with state-of-the-art deep learning models to make meaningful progress toward solving variants of uncertain significance. Primate population sequencing and large-scale human sequencing are likely to fill complementary roles in advancing clinical understanding of human

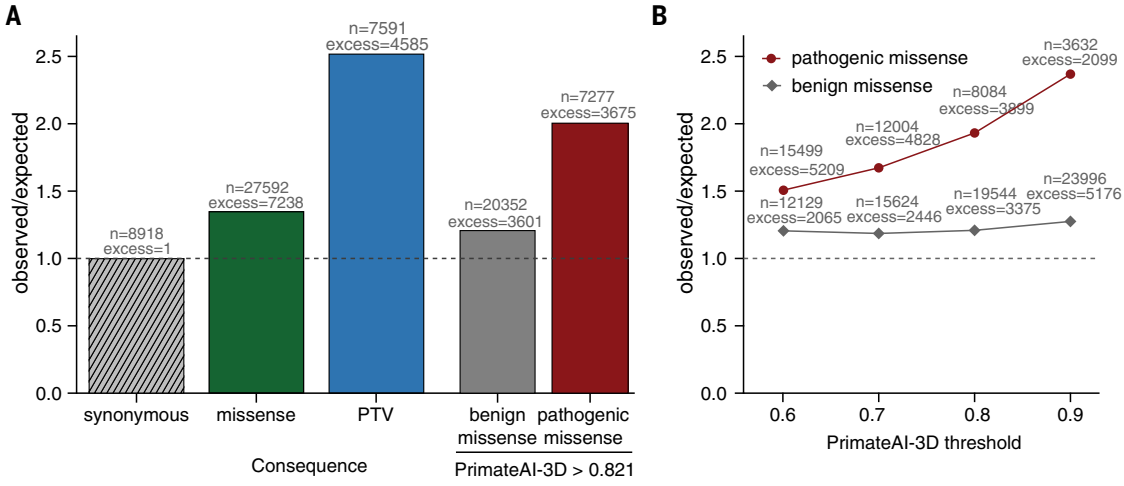


Fig. 5. Enrichment of de novo mutations in the neurodevelopmental disorder cohort over expectation. (**A**) Enrichment of DNMs from Kaplanis *et al.* (*87*) across all genes. Enrichment ratios are given for synonymous, all missense, and protein-truncating variants (PTV), along with missense split by PrimateAI-3D score into benign (<0.821) and pathogenic (>0.821). (**B**) Enrichment of benign and pathogenic missense above expectation at varying PrimateAI-3D thresholds for classifying pathogenic missense.

Table 1. Additional genes discovered in intellectual disability. Genes achieving the genome-wide significance ($P < 6.4 \times 10^{-7}$) are shown when considering only missense de novo mutations with PrimateAI-3D scores ≥0.821. Counts of protein-truncating and missense DNMs are provided. *P* values for gene enrichment are shown when the statistical test was run only with missense mutations with PrimateAI-3D score ≥0.821 and when it was repeated for all missense mutations.

		Missense		*P* value	
HGNC symbol	**Protein-truncating variants**	**PrimateAI-3D score ≥0.821**	**All missense**	**PrimateAI-3D score ≥0.821**	**All missense**
AP1G1	2	4	5	4.1×10^{-7}	5.9×10^{-5}
ATP2B2	1	9	11	2.1×10^{-7}	1.4×10^{-3}
CELF2	2	4	4	1.2×10^{-7}	6.7×10^{-5}
MAP4K4	2	6	7	3.9×10^{-7}	5.0×10^{-4}
MED13	3	6	9	6.6×10^{-8}	3.5×10^{-5}
MFN2	0	6	8	3.4×10^{-7}	1.0×10^{-5}
NR4A2	2	4	5	3.7×10^{-7}	3.3×10^{-5}
PIP5K1C	0	8	9	2.8×10^{-8}	4.9×10^{-4}
RAB5C	2	4	5	8.6×10^{-8}	1.5×10^{-5}
SPOP	1	4	6	4.1×10^{-7}	1.7×10^{-6}
SPTBN2	1	10	16	3.9×10^{-7}	4.5×10^{-3}
XPO1	1	7	7	5.0×10^{-7}	7.2×10^{-4}
EIF4A2	2	4	4	1.7×10^{-7}	2.1×10^{-4}
LMBRD2	0	3	4	6.0×10^{-7}	1.3×10^{-4}
MARK2	4	3	5	2.3×10^{-7}	3.8×10^{-5}
NOTCH1	4	6	17	4.1×10^{-7}	1.3×10^{-6}

genetic variants. From the perspective of acquiring additional benign variants to train PrimateAI-3D, humans are not suitable, as the discovery of common human variants (>0.1% allele frequency) plateaus at ~100,000 missense variants after only a few hundred individuals (*17*), and further population sequencing into the millions mainly contributes rare variants that cannot be ruled out for deleterious consequence. By contrast, because these rare human variants have not been thoroughly filtered by natural selection, they preserve the potential to exert highly penetrant phenotypic effects, making them indispensable for discovering new gene-phenotype relationships in large population sequencing and biobank studies. Fittingly, classifiers trained on common primate variants may accelerate these target discovery efforts by helping to differentiate between benign and pathogenic rare variation.

The genetic diversity found in the 520 known nonhuman primate species is the result of ongoing natural experiments on genetic variation that have been running uninterrupted for millions of years. Today, more than 60% of primate species on Earth are threatened with extinction in the next decade as a result of man-made factors (*31*). We must decide whether to act now to preserve these irreplaceable species, which act as a mirror for understanding our genomes and ourselves, and are each valuable in their own right, or bear witness to the conclusion of many of these experiments.

Materials and methods

Primate polymorphism data

We aggregated high-coverage whole genomes of 809 primate individuals across 233 primate species, including 703 newly sequenced samples and 106 previously sequenced samples from the Great Ape Genome project (*19*). Samples that passed quality evaluation were then aligned to 32 high-quality primate reference genomes (*110*) and mapped to the GRCh38 human genome build.

We developed a random forest (RF) classifier to identify false positive variant calls and errors resulting from ambiguity in the species mapping. In addition, we removed variants that fell in primate codons that did not match the human codon at that position, as well as those residing in primate transcripts with likely annotation errors. We also devised quality metrics based on the distribution of RF scores and Hardy-Weinberg equilibrium, and developed a unique mapping filter to exclude variants in regions of nonunique mapping between primate species.

Identifying differential selection between humans and primates through population modeling

We first established a neutral background distribution of mutation rates per gene for each primate species by fitting the Poisson Random Field model to the segregating synonymous variants in each species. The observed number of segregating synonymous sites is a Poisson random variable, with the mean determined by mutation rate, demography, and sample size (*34*). For simplicity, we assumed an equilibrium (i.e., constant) demography for all species besides humans; for humans, we used Moments (*51*) to find a best-fitting demographic history based on the folded site frequency spectrum of synonymous sites. We adopted a Gamma distributed prior on mutation rates, which also accounts for the impact of GC content on mutation rate. We optimized the prior parameters through maximum likelihood and computed the posterior distribution of the mutation rate per gene.

The number of segregating nonsynonymous sites is modeled as a Poisson random variable similar to synonymous sites with additional selection parameters. We assumed that every nonsynonymous mutation in a gene shares the same population-scaled selection coefficient γ_{ig}. To explicitly estimate the selection coefficient of each gene per species, we devised a two-step procedure analogous to an expectation–maximization algorithm to control for differences in population size across species.

To identify genes in which human constraint is different from nonhuman primate selection, we developed a likelihood ratio test to test whether population-scaled selection coefficients are significantly different between humans and other primates. We then assessed whether our population genetic modeling improved the correlation of selection estimates of our primate data with previous gene-constraint metrics in humans, including pLI (*28*) and s_het (*111*). To validate the performance of our model, we performed population genetic simulations.

Poisson generalized linear mixed modeling of selection between humans and primates

In addition to the population genetics model described above, we also applied an orthogonal approach to detect differences in selection between humans and primates based on missense: synonymous ratios. We fit a Poisson generalized linear mixed model (GLMM) to the pooled polymorphic synonymous and missense mutations across all primates to estimate the depletion of missense variants in each gene. Then, we fit a second Poisson GLMM to the human data, controlling for the primate depletion estimates, and compared the pooled primate MSR with the human MSR for each gene.

PrimateAI-3D model

PrimateAI-3D is a 3D convolutional neural network that uses protein structures and multiple sequence alignments (MSA) to predict the pathogenicity of human missense variants. To generate the input for a 3D convolutional neural network, we voxelized the protein structure and evolutionary conservation in the region surrounding the missense variant. The network was trained to optimize three objectives: distinction between benign and unknown human variants; prediction of a masked amino acid at the variant site; per-gene variant ranks based on protein language models.

Protein structures and multiple sequence alignments

For 341 species, we used vertebrate and mammal MSAs from UCSC Multiz100 (*112*, *113*) and Zoonomia (*23*). Another 251 species appeared in Uniprot for at least 75% of all human proteins (*114*). For each protein, alignments from all 341+251=592 species were merged. Human protein structures were taken from AlphaFold DB (June 2021) (*73*). Proteins that did not sequence-match exactly to our hg38 proteins (2590; 13.5%) were homology modeled using HHpred (*74*) and Modeller (*115*).

Protein voxelization and voxel features

A regular sized 3D grid of 7×7×7 voxels, each spanning 2Å×2Å×2Å, was centered at the Cα atom of the residue containing the target variant (fig. S11). For each voxel, we provided a vector of distances between its center and the nearest Cα and Cβ atoms of each amino acid type (fig. S11; details in Supplementary Text section 1). We also provided additional voxel features including the pLDDT confidence metric from AlphaFold DB (fig. S12), and the evolutionary profile, consisting of each amino acid's frequency at the corresponding position in the 592 species alignment.

Model architecture

The first layers of the PrimateAI-3D model reduce the voxel tensor to a 64-vector through repeated valid-padded 3D convolutions with a kernel size of 3×3×3. A final hidden dense layer transforms this 64-length vector into a 20-length vector, corresponding to one output unit per amino acid at that position. The model was trained simultaneously using multiple loss functions to optimize the following complementary aspects of pathogenicity:

Benign primate variants

Using 4.5 million benign missense variants from primates, we sampled the same number of unknown variants from the set of all possible human missense variants, with the distribution of mutational probabilities matching the benign set, based on a trinucleotide mutation rate model. Variants for the same protein position were combined in a 20-length vector (benign: 0, unknown: 1) which was the target label for the network. We used mean squared error (MSE) as the loss function for non-missing labels and ignored missing labels.

3D fill-in-the-blank

We removed all atoms of a target residue before voxelization, discarding any information about the residue from the input tensor to the network. The network was then trained to predict a 20-length vector, labeled 0 (benign) for amino acids that occur at the target site in any of the 592 species and 1 (pathogenic) otherwise. All human protein positions with at least one possible missense variant were included in this dataset.

Variant ranks from language models

For each gene, we took the average pathogenicity ranking from two protein language models, PrimateAI language model (PrimateAI LM, described below) and our reimplementation of the EVE variational autoencoder algorithm which we extended to all human proteins (EVE*) (*67*). We calculated the pairwise logistic rank loss as described in Pasumarthi *et al.* (*116*).

PrimateAI language model

The PrimateAI language model (PrimateAI LM) is a MSA transformer (*83*) for fill-in-the-blank residue classification, which was trained end-to-end on MSAs of UniRef-50 proteins (*115*, *117*) to minimize an unsupervised masked language modelling (MLM) objective (*81*). Our model requires ~50× less computation for training than previous MSA transformers as a result of several improvements in architecture and training (fig. S9).

Model training procedure

Each batch had the same number of samples from each of the three variant datasets (~33 with a batch size of 100). For the language model ranks dataset, all 33 samples had to come from the same protein. The number of times a protein was chosen for a batch was proportional to the length of the protein. In order to make our model robust against protein orientations, we randomly rotated the protein atomic coordinates in 3D before voxelizing a variant.

Model evaluation

We compared performance of our model and other models (*84*) on variants for which all models had scores. Deep mutational scanning assays were available for 9 human genes: Amyloid-beta (*102*), *YAP1* (*96*), *MSH2* (*98*), *SYUA* (*101*), *VKOR1* (*97*), *PTEN* (*99*, *100*), *BRCA1* (*104*), *TP53* (*103*), and *ADRB2* (*105*). For each assay and prediction model, we calculated the absolute Spearman rank correlation between prediction and assay scores. The UKBB dataset (*79*, *80*) contains 42 gene-phenotype pairs which were significantly associated by rare variant burden testing using all rare missense variants, without applying missense pathogenicity prioritization. The evaluation was the same as with DMS assays, except that correlations were calculated from the quantitative phenotypes of individuals carrying the variant, instead of the assay score for the variant. For ClinVar (*4*), we filtered to high-quality 2-star variants and evaluated model performance by calculating per-gene area under the receiver operating characteristic curve (AUC). For the rare disease cohorts, we collected de novo missense mutations from patients with developmental disorders (*85*–*87*), autism spectrum disorders (*88*–*94*) or congenital heart disorders (*95*). For all three datasets, we compared against DNMs from healthy controls (*88*–*93*). We applied the Mann-Whitney U test to measure how well each model's prediction scores could distinguish patient variants from control variants.

REFERENCES AND NOTES

1. D. G. MacArthur *et al*., Guidelines for investigating causality of sequence variants in human disease. *Nature* **508**, 469–476 (2014). doi: 10.1038/nature13127; pmid: 24759409
2. R. L. Nussbaum, H. L. Rehm; ClinGen, ClinGen and Genetic Testing. *N. Engl. J. Med.* **373**, 1379 (2015). pmid: 26430707
3. H. L. Rehm *et al*., ClinGen—The Clinical Genome Resource. *N. Engl. J. Med.* **372**, 2235–2242 (2015). doi: 10.1056/NEJMsr1406261; pmid: 26014595
4. M. J. Landrum *et al*., ClinVar: Public archive of interpretations of clinically relevant variants. *Nucleic Acids Res.* **44**, D862–D868 (2016). doi: 10.1093/nar/gkv1222; pmid: 26582918
5. X. Liu, C. Wu, C. Li, E. Boerwinkle, dbNSFP v3.0: A One-Stop Database of Functional Predictions and Annotations for Human Nonsynonymous and Splice-Site SNVs. *Hum. Mutat.* **37**, 235–241 (2016). doi: 10.1002/humu.22932; pmid: 26555599
6. P. D. Stenson *et al*., The Human Gene Mutation Database: Building a comprehensive mutation repository for clinical and molecular genetics, diagnostic testing and personalized genomic medicine. *Hum. Genet.* **133**, 1–9 (2014). doi: 10.1007/s00439-013-1358-4; pmid: 24077912
7. H. L. Rehm, Evolving health care through personal genomics. *Nat. Rev. Genet.* **18**, 259–267 (2017). doi: 10.1038/nrg.2016.162; pmid: 28138143
8. N. Whiffin *et al*., Using high-resolution variant frequencies to empower clinical genome interpretation. *Genet. Med.* **19**, 1151–1158 (2017). doi: 10.1038/gim.2017.26; pmid: 28518168
9. S. M. Caspar *et al*., Clinical sequencing: From raw data to diagnosis with lifetime value. *Clin. Genet.* **93**, 508–519 (2018). doi: 10.1111/cge.13190; pmid: 29206278
10. Y. Yang *et al*., Molecular findings among patients referred for clinical whole-exome sequencing. *JAMA* **312**, 1870–1879 (2014). doi: 10.1001/jama.2014.14601; pmid: 25326635
11. J. A. SoRelle, D. M. Thodeson, S. Arnold, G. Gotway, J. Y. Park, Clinical Utility of Reinterpreting Previously Reported Genomic Epilepsy Test Results for Pediatric Patients. *JAMA Pediatr.* **173**, e182302 (2019). doi: 10.1001/jamapediatrics.2018.2302; pmid: 30398534
12. N. Shah *et al*., Identification of Misclassified ClinVar Variants via Disease Population Prevalence. *Am. J. Hum. Genet.* **102**, 609–619 (2018). doi: 10.1016/j.ajhg.2018.02.019; pmid: 29625023
13. O. Campuzano *et al*., Reanalysis and reclassification of rare genetic variants associated with inherited arrhythmogenic syndromes. *EBioMedicine* **54**, 102732 (2020). doi: 10.1016/j.ebiom.2020.102732; pmid: 32268277
14. S. Richards *et al*., Standards and guidelines for the interpretation of sequence variants: A joint consensus recommendation of the American College of Medical Genetics and Genomics and the Association for Molecular Pathology. *Genet. Med.* **17**, 405–424 (2015). doi: 10.1038/gim.2015.30; pmid: 25741868
15. Y. E. Kim, C. S. Ki, M. A. Jang, Challenges and Considerations in Sequence Variant Interpretation for Mendelian Disorders. *Ann. Lab. Med.* **39**, 421–429 (2019). doi: 10.3343/alm.2019.39.5.421; pmid: 31037860
16. M. Slatkin, A population-genetic test of founder effects and implications for Ashkenazi Jewish diseases. *Am. J. Hum. Genet.* **75**, 282–293 (2004). doi: 10.1086/423146; pmid: 15208782
17. L. Sundaram *et al*., Predicting the clinical impact of human mutation with deep neural networks. *Nat. Genet.* **50**, 1161–1170 (2018). doi: 10.1038/s41588-018-0167-z; pmid: 30038395
18. Chimpanzee Sequencing and Analysis Consortium, Initial sequence of the chimpanzee genome and comparison with the human genome. *Nature* **437**, 69–87 (2005). doi: 10.1038/nature04072; pmid: 16136131
19. J. Prado-Martinez *et al*., Great ape genetic diversity and population history. *Nature* **499**, 471–475 (2013). doi: 10.1038/nature12228; pmid: 23823723
20. Z. Fan *et al*., Ancient hybridization and admixture in macaques (genus Macaca) inferred from whole genome sequences. *Mol. Phylogenet. Evol.* **127**, 376–386 (2018). doi: 10.1016/j.ympev.2018.03.038; pmid: 29614345
21. Z. Liu *et al*., Genomic Mechanisms of Physiological and Morphological Adaptations of Limestone Langurs to Karst Habitats. *Mol. Biol. Evol.* **37**, 952–968 (2020). doi: 10.1093/molbev/msz301; pmid: 31846031
22. L. Wang *et al*., A high-quality genome assembly for the endangered golden snub-nosed monkey (Rhinopithecus roxellana). *Gigascience* **8**, giz098 (2019). doi: 10.1093/gigascience/giz098; pmid: 31437279
23. Zoonomia Consortium, A comparative genomics multitool for scientific discovery and conservation. *Nature* **587**, 240–245 (2020). doi: 10.1038/s41586-020-2876-6; pmid: 33177664
24. B. J. Evans *et al*., Speciation over the edge: Gene flow among non-human primate species across a formidable biogeographic barrier. *R. Soc. Open Sci.* **4**, 170351 (2017). doi: 10.1098/rsos.170351; pmid: 29134059
25. L. Yu *et al*., Genomic analysis of snub-nosed monkeys (Rhinopithecus) identifies genes and processes related to high-altitude adaptation. *Nat. Genet.* **48**, 947–952 (2016). doi: 10.1038/ng.3615; pmid: 27399969
26. N. Osada, K. Matsudaira, Y. Hamada, S. Malaivijitnond, Testing sex-biased admixture origin of macaque species using autosomal and X-chromosomal genomic sequences. *Genome Biol. Evol.* **13**, evaa209 (2021). doi: 10.1093/gbe/evaa209; pmid: 33045051
27. A. B. Rylands, R. A. Mittermeier, *Primate Behavioral Ecology*. (Routledge, 2021), ed. 6, pp. 407–428.
28. M. Lek *et al*., Analysis of protein-coding genetic variation in 60,706 humans. *Nature* **536**, 285–291 (2016). doi: 10.1038/nature19057; pmid: 27535533
29. K. J. Karczewski *et al*., The mutational constraint spectrum quantified from variation in 141,456 humans. *Nature* **581**, 434–443 (2020). doi: 10.1038/s41586-020-2308-7; pmid: 32461654
30. E. M. Leffler *et al*., Revisiting an old riddle: What determines genetic diversity levels within species? *PLOS Biol.* **10**, e1001388 (2012). doi: 10.1371/journal.pbio.1001388; pmid: 22984349
31. A. Estrada *et al*., Impending extinction crisis of the world's primates: Why primates matter. *Sci. Adv.* **3**, e1600946 (2017). doi: 10.1126/sciadv.1600946; pmid: 28116351
32. T. Ohta, Slightly deleterious mutant substitutions in evolution. *Nature* **246**, 96–98 (1973). doi: 10.1038/246096a0; pmid: 4585855
33. D. E. Reich, E. S. Lander, On the allelic spectrum of human disease. *Trends Genet.* **17**, 502–510 (2001). doi: 10.1016/S0168-9525(01)02410-6; pmid: 11525833
34. S. A. Sawyer, D. L. Hartl, Population genetics of polymorphism and divergence. *Genetics* **132**, 1161–1176 (1992). doi: 10.1093/genetics/132.4.1161; pmid: 1459433
35. A. Eyre-Walker, P. D. Keightley, The distribution of fitness effects of new mutations. *Nat. Rev. Genet.* **8**, 610–618 (2007). doi: 10.1038/nrg2146; pmid: 17637733
36. W. Fu *et al*., Analysis of 6,515 exomes reveals the recent origin of most human protein-coding variants. *Nature* **493**, 216–220 (2013). doi: 10.1038/nature11690; pmid: 23201682
37. Y. B. Simons, M. C. Turchin, J. K. Pritchard, G. Sella, The deleterious mutation load is insensitive to recent population history. *Nat. Genet.* **46**, 220–224 (2014). doi: 10.1038/ng.2896; pmid: 24509481
38. R. Do *et al*., No evidence that selection has been less effective at removing deleterious mutations in Europeans than in Africans. *Nat. Genet.* **47**, 126–131 (2015). doi: 10.1038/ng.3186; pmid: 25581429
39. P. K. Albers, G. McVean, Dating genomic variants and shared ancestry in population-scale sequencing data. *PLOS Biol.* **18**, e3000586 (2020). doi: 10.1371/journal.pbio.3000586; pmid: 31951611
40. I. Mathieson, G. McVean, Demography and the age of rare variants. *PLOS Genet.* **10**, e1004528 (2014). doi: 10.1371/journal.pgen.1004528; pmid: 25101869
41. L. Damaj *et al*., CACNA1A haploinsufficiency causes cognitive impairment, autism and epileptic encephalopathy with mild cerebellar symptoms. *Eur. J. Hum. Genet.* **23**, 1505–1512 (2015). doi: 10.1038/ejhg.2015.21; pmid: 25735478
42. K. Reinson *et al*., Biallelic CACNA1A mutations cause early onset epileptic encephalopathy with progressive cerebral, cerebellar, and optic nerve atrophy. *Am. J. Med. Genet. A.* **170**, 2173–2176 (2016). doi: 10.1002/ajmg.a.37678; pmid: 27250579
43. A. Bentivegna *et al*., Rubinstein-Taybi Syndrome: Spectrum of CREBBP mutations in Italian patients. *BMC Med. Genet.* **7**, 77 (2006). doi: 10.1186/1471-2350-7-77; pmid: 17052327
44. M. Stef *et al*., Spectrum of CREBBP gene dosage anomalies in Rubinstein-Taybi syndrome patients. *Eur. J. Hum. Genet.* **15**, 843–847 (2007). doi: 10.1038/sj.ejhg.5201847; pmid: 17473832
45. A. S. Kondrashov, S. Sunyaev, F. A. Kondrashov, Dobzhansky-Muller incompatibilities in protein evolution. *Proc. Natl. Acad. Sci. U.S.A.* **99**, 14878–14883 (2002). doi: 10.1073/pnas.232565499; pmid: 12403824
46. D. M. Jordan *et al*., Identification of cis-suppression of human disease mutations by comparative genomics. *Nature* **524**, 225–229 (2015). doi: 10.1038/nature14497; pmid: 26123021
47. K. E. Samocha *et al*., A framework for the interpretation of de novo mutation in human disease. *Nat. Genet.* **46**, 944–950 (2014). doi: 10.1038/ng.3050; pmid: 25086666
48. C. D. Bustamante, J. Wakeley, S. Sawyer, D. L. Hartl, Directional selection and the site-frequency spectrum. *Genetics* **159**, 1779–1788 (2001). doi: 10.1093/genetics/159.4.1779; pmid: 11779814
49. X. Huang *et al*., Inferring genome-wide correlations of mutation fitness effects between populations. *Molecular Biology and Evolution*. **38**, 4588–4602 (2021). doi: 10.1093/genetics/159.4.1779; pmid: 11779814
50. R. N. Gutenkunst, R. D. Hernandez, S. H. Williamson, C. D. Bustamante, Inferring the joint demographic history of multiple populations from multidimensional SNP frequency data. *PLOS Genet.* **5**, e1000695 (2009). doi: 10.1371/journal.pgen.1000695; pmid: 19851460
51. J. Jouganous, W. Long, A. P. Ragsdale, S. Gravel, Inferring the Joint Demographic History of Multiple Populations: Beyond the Diffusion Approximation. *Genetics* **206**, 1549–1567 (2017). doi: 10.1534/genetics.117.200493; pmid: 28495960
52. D. Bates, M. Mächler, B. Bolker, S. Walker, Fitting Linear Mixed-Effects Models Using lme4. *J. Stat. Softw.* **67**, 1–48 (2015). doi: 10.18637/jss.v067.i01
53. Y. Benjamini, Y. Hochberg, Controlling the False Discovery Rate: A Practical and Powerful Approach to Multiple Testing. *J. R. Stat. Soc. B* **57**, 289–300 (1995). doi: 10.1111/j.2517-6161.1995.tb02031.x
54. R. K. Rowntree, A. Harris, The phenotypic consequences of CFTR mutations. *Ann. Hum. Genet.* **67**, 471–485 (2003). doi: 10.1046/j.1469-1809.2003.00028.x; pmid: 12940920
55. S. A. Wilcox *et al*., High frequency hearing loss correlated with mutations in the GJB2 gene. *Hum. Genet.* **106**, 399–405 (2000). doi: 10.1007/s004390000273; pmid: 10830906

56. H. Shu *et al*., The role of CD36 in cardiovascular disease. *Cardiovasc. Res.* (2020). doi: 10.1002/humu.10041; pmid: 33210138
57. J. L. Bobadilla, M. Macek Jr., J. P. Fine, P. M. Farrell, Cystic fibrosis: A worldwide analysis of CFTR mutations—correlation with incidence data and application to screening. *Hum. Mutat.* **19**, 575–606 (2002). doi: 10.1002/humu.10041; pmid: 12007216
58. M. H. Chaleshtori *et al*., High carrier frequency of the GJB2 mutation (35delG) in the north of Iran. *Int. J. Pediatr. Otorhinolaryngol.* **71**, 863–867 (2007). doi: 10.1016/j.ijporl.2007.02.005; pmid: 17428550
59. J. Liu *et al*., Distribution of CD36 deficiency in different Chinese ethnic groups. *Hum. Immunol.* **81**, 366–371 (2020). doi: 10.1016/j.humimm.2020.05.004; pmid: 32487483
60. T. J. Aitman *et al*., Malaria susceptibility and CD36 mutation. *Nature* **405**, 1015–1016 (2000). doi: 10.1038/35016636; pmid: 10890433
61. J. E. Common, W.-L. Di, D. Davies, D. P. Kelsell, Further evidence for heterozygote advantage of GJB2 deafness mutations: A link with cell survival. *J. Med. Genet.* **41**, 573–575 (2004). doi: 10.1136/jmg.2003.017632; pmid: 15235031
62. P. D'Adamo *et al*., Does epidermal thickening explain GJB2 high carrier frequency and heterozygote advantage? *Eur. J. Hum. Genet.* **17**, 284–286 (2009). doi: 10.1038/ejhg.2008.225; pmid: 19050724
63. S. A. Schroeder, D. M. Gaughan, M. Swift, Protection against bronchial asthma by CFTR delta F508 mutation: A heterozygote advantage in cystic fibrosis. *Nat. Med.* **1**, 703–705 (1995). doi: 10.1038/nm0795-703; pmid: 7585155
64. G. B. Pier *et al*., Salmonella typhi uses CFTR to enter intestinal epithelial cells. *Nature* **393**, 79–82 (1998). doi: 10.1038/30006; pmid: 9590693
65. S. E. Bojesen *et al*., Multiple independent variants at the TERT locus are associated with telomere length and risks of breast and ovarian cancer. *Nat. Genet.* **45**, 371–384, 384e1–2 (2013). doi: 10.1038/ng.2566; pmid: 23535731
66. B. Heidenreich, R. Kumar, TERT promoter mutations in telomere biology. *Mutat. Res. Rev. Mutat. Res.* **771**, 15–31 (2017). doi: 10.1016/j.mrrev.2016.11.002; pmid: 28342451
67. J. Frazer *et al*., Disease variant prediction with deep generative models of evolutionary data. *Nature* **599**, 91–95 (2021). doi: 10.1038/s41586-021-04043-8; pmid: 34707284
68. H. D. Chae, C. H. Jeon, Peutz-Jeghers syndrome with germline mutation of STK11. *Ann. Surg. Treat. Res.* **86**, 325–330 (2014). doi: 10.4174/astr.2014.86.6.325; pmid: 24949325
69. I. Hernan *et al*., De novo germline mutation in the serine-threonine kinase STK11/LKB1 gene associated with Peutz-Jeghers syndrome. *Clin. Genet.* **66**, 58–62 (2004). doi: 10.1111/j.0009-9163.2004.00266.x; pmid: 15200509
70. C. Nakanishi *et al*., Germline mutation of the LKB1/STK11 gene with loss of the normal allele in an aggressive breast cancer of Peutz-Jeghers syndrome. *Oncology* **67**, 476–479 (2004). doi: 10.1159/000082933; pmid: 15714005
71. H. R. Yang, J. S. Ko, J. K. Seo, Germline mutation analysis of STK11 gene using direct sequencing and multiplex ligation-dependent probe amplification assay in Korean children with Peutz-Jeghers syndrome. *Dig. Dis. Sci.* **55**, 3458–3465 (2010). doi: 10.1007/s10620-010-1194-5; pmid: 20393878
72. J. Jumper *et al*., Highly accurate protein structure prediction with AlphaFold. *Nature* **596**, 583–589 (2021). doi: 10.1038/s41586-021-03819-2; pmid: 34265844
73. M. Varadi *et al*., AlphaFold Protein Structure Database: Massively expanding the structural coverage of protein-sequence space with high-accuracy models. *Nucleic Acids Res.* (2021). doi: 10.1093/nar/gkab1061; pmid: 34791371
74. J. Söding, A. Biegert, A. N. Lupas, The HHpred interactive server for protein homology detection and structure prediction. *Nucleic Acids Res.* **33**, W244-8 (2005). doi: 10.1093/nar/gki408; pmid: 15980461
75. M. Källberg *et al*., Template-based protein structure modeling using the RaptorX web server. *Nat. Protoc.* **7**, 1511–1522 (2012). doi: 10.1038/nprot.2012.085; pmid: 22814390
76. S. Wang, W. Li, S. Liu, J. Xu, RaptorX-Property: A web server for protein structure property prediction. *Nucleic Acids Res.* **44**, W430-5 (2016). doi: 10.1093/nar/gkw306; pmid: 27112573
77. D. J. Burgess, The TOPMed genomic resource for human health. *Nat. Rev. Genet.* **22**, 200 (2021). doi: 10.1038/s41576-021-00343-x; pmid: 33654294
78. D. Taliun *et al*., Sequencing of 53,831 diverse genomes from the NHLBI TOPMed Program. *Nature* **590**, 290–299 (2021). doi: 10.1038/s41586-021-03205-y; pmid: 33568819
79. C. Bycroft *et al*., The UK Biobank resource with deep phenotyping and genomic data. *Nature* **562**, 203–209 (2018). doi: 10.1038/s41586-018-0579-z; pmid: 30305743
80. C. Sudlow *et al*., UK biobank: An open access resource for identifying the causes of a wide range of complex diseases of middle and old age. *PLOS Med.* **12**, e1001779 (2015). doi: 10.1371/journal.pmed.1001779; pmid: 25826379
81. J. Devlin, M.-W. Chang, K. Lee, K. Toutanova, BERT: Pre-training of Deep Bidirectional Transformers for Language Understanding in *Proceedings of the 2019 Conference of the North American Chapter of the Association for Computational Linguistics: Human Language Technologies, Volume 1 (Long and Short Papers)* (Association for Computational Linguistics, 2019), pp. 4171–4186.
82. Y. You *et al*., in *International Conference on Learning Representations*. (2020).
83. R. M. Rao, J. Liu, R. Verkuil, J. Meier, J. Canny, P. Abbeel, T. Sercu, A. Rives, MSA Transformer in *Proceedings of the 38th International Conference on Machine Learning*, pp. 8844–8856 (2021).
84. X. Liu, C. Li, C. Mou, Y. Dong, Y. Tu, dbNSFP v4: A comprehensive database of transcript-specific functional predictions and annotations for human nonsynonymous and splice-site SNVs. *Genome Med.* **12**, 103 (2020). doi: 10.1186/s13073-020-00803-9; pmid: 33261662
85. Deciphering Developmental Disorders Study, Large-scale discovery of novel genetic causes of developmental disorders. *Nature* **519**, 223–228 (2015). doi: 10.1038/nature14135
86. Deciphering Developmental Disorders Study,, Prevalence and architecture of de novo mutations in developmental disorders. *Nature* **542**, 433–438 (2017). doi: 10.1038/nature21062
87. J. Kaplanis *et al*., Evidence for 28 genetic disorders discovered by combining healthcare and research data. *Nature* **586**, 757–762 (2020). doi: 10.1038/s41586-020-2832-5; pmid: 33057194
88. J. Y. An *et al*., Genome-wide de novo risk score implicates promoter variation in autism spectrum disorder. *Science* **362**, eaat6576 (2018). doi: 10.1126/science.aat6576; pmid: 30545852
89. S. De Rubeis *et al*., Synaptic, transcriptional and chromatin genes disrupted in autism. *Nature* **515**, 209–215 (2014). doi: 10.1038/nature13772; pmid: 25363760
90. I. Iossifov *et al*., The contribution of de novo coding mutations to autism spectrum disorder. *Nature* **515**, 216–221 (2014). doi: 10.1038/nature13908; pmid: 25363768
91. I. Iossifov *et al*., De novo gene disruptions in children on the autistic spectrum. *Neuron* **74**, 285–299 (2012). doi: 10.1016/j.neuron.2012.04.009; pmid: 22542183
92. S. J. Sanders *et al*., Insights into Autism Spectrum Disorder Genomic Architecture and Biology from 71 Risk Loci. *Neuron* **87**, 1215–1233 (2015). doi: 10.1016/j.neuron.2015.09.016; pmid: 26402605
93. S. J. Sanders *et al*., De novo mutations revealed by whole-exome sequencing are strongly associated with autism. *Nature* **485**, 237–241 (2012). doi: 10.1038/nature10945; pmid: 22495306
94. B. J. O'Roak *et al*., Sporadic autism exomes reveal a highly interconnected protein network of de novo mutations. *Nature* **485**, 246–250 (2012). doi: 10.1038/nature10989; pmid: 22495309
95. S. C. Jin *et al*., Contribution of rare inherited and de novo variants in 2,871 congenital heart disease probands. *Nat. Genet.* **49**, 1593–1601 (2017). doi: 10.1038/ng.3970; pmid: 28991257
96. C. L. Araya *et al*., A fundamental protein property, thermodynamic stability, revealed solely from large-scale measurements of protein function. *Proc. Natl. Acad. Sci. U.S.A.* **109**, 16858–16863 (2012). doi: 10.1073/pnas.1209751109; pmid: 23035249
97. M. A. Chiasson *et al*., Multiplexed measurement of variant abundance and activity reveals VKOR topology, active site and human variant impact. *eLife* **9**, e58026 (2020). doi: 10.7554/eLife.58026; pmid: 32870157
98. X. Jia *et al*., Massively parallel functional testing of MSH2 missense variants conferring Lynch syndrome risk. *Am. J. Hum. Genet.* **108**, 163–175 (2021). doi: 10.1016/j.ajhg.2020.12.003; pmid: 33357406
99. K. A. Matreyek *et al*., Multiplex assessment of protein variant abundance by massively parallel sequencing. *Nat. Genet.* **50**, 874–882 (2018). doi: 10.1038/s41588-018-0122-z; pmid: 29785012
100. T. L. Mighell, S. Evans-Dutson, B. J. O'Roak, A Saturation Mutagenesis Approach to Understanding PTEN Lipid Phosphatase Activity and Genotype-Phenotype Relationships. *Am. J. Hum. Genet.* **102**, 943–955 (2018). doi: 10.1016/j.ajhg.2018.03.018; pmid: 29706350
101. R. W. Newberry, J. T. Leong, E. D. Chow, M. Kampmann, W. F. DeGrado, Deep mutational scanning reveals the structural basis for α-synuclein activity. *Nat. Chem. Biol.* **16**, 653–659 (2020). doi: 10.1038/s41589-020-0480-6; pmid: 32152544
102. M. Seuma, A. J. Faure, M. Badia, B. Lehner, B. Bolognesi, The genetic landscape for amyloid beta fibril nucleation accurately discriminates familial Alzheimer's disease mutations. *eLife* **10**, e63364 (2021). doi: 10.7554/eLife.63364; pmid: 33522485
103. A. O. Giacomelli *et al*., Mutational processes shape the landscape of TP53 mutations in human cancer. *Nat. Genet.* **50**, 1381–1387 (2018). doi: 10.1038/s41588-018-0204-y; pmid: 30224644
104. L. M. Starita *et al*., Massively Parallel Functional Analysis of BRCA1 RING Domain Variants. *Genetics* **200**, 413–422 (2015). doi: 10.1534/genetics.115.175802; pmid: 25823446
105. E. M. Jones *et al*., Structural and functional characterization of G protein–coupled receptors with deep mutational scanning. *eLife* **9**, e54895 (2020). doi: 10.7554/eLife.54895; pmid: 33084570
106. C. E. G. Amorim *et al*., The population genetics of human disease: The case of recessive, lethal mutations. *PLOS Genet.* **13**, e1006915 (2017). doi: 10.1371/journal.pgen.1006915; pmid: 28957316
107. B. Quintáns, A. Ordóñez-Ugalde, P. Cacheiro, A. Carracedo, M. J. Sobrido, Medical genomics: The intricate path from genetic variant identification to clinical interpretation. *Appl. Transl. Genomics* **3**, 60–67 (2014). doi: 10.1016/j.atg.2014.06.001; pmid: 27284505
108. A. R. Martin *et al*., PanelApp crowdsources expert knowledge to establish consensus diagnostic gene panels. *Nat. Genet.* **51**, 1560–1565 (2019). doi: 10.1038/s41588-019-0528-2; pmid: 31676867
109. A. Thormann *et al*., Flexible and scalable diagnostic filtering of genomic variants using G2P with Ensembl VEP. *Nat. Commun.* **10**, 2373 (2019). doi: 10.1038/s41467-019-10016-3; pmid: 31147538
110. L. F. Kuderna *et al*., A global catalog of whole-genome diversity from 233 primate species bioRxiv 2023.05.02.538995 [Preprint] (2023); doi: 10.1101/2023.05.02.538995
111. C. A. Cassa *et al*., Estimating the selective effects of heterozygous protein-truncating variants from human exome data. *Nat. Genet.* **49**, 806–810 (2017). doi: 10.1038/ng.3831; pmid: 28369035
112. C. Tyner *et al*., The UCSC Genome Browser database: 2017 update. *Nucleic Acids Res.* **45**, D626–D634 (2017). pmid: 27899642
113. W. J. Kent *et al*., The human genome browser at UCSC. *Genome Res.* **12**, 996–1006 (2002). doi: 10.1101/gr.229102; pmid: 12045153
114. B. E. Suzek, Y. Wang, H. Huang, P. B. McGarvey, C. H. Wu; UniProt Consortium, UniRef clusters: A comprehensive and scalable alternative for improving sequence similarity searches. *Bioinformatics* **31**, 926–932 (2015). doi: 10.1093/bioinformatics/btu739; pmid: 25398609
115. A. Sali, T. L. Blundell, Comparative protein modelling by satisfaction of spatial restraints. *J. Mol. Biol.* **234**, 779–815 (1993). doi: 10.1006/jmbi.1993.1626; pmid: 8254673
116. R. K. Pasumarthi *et al*., TF-Ranking: Scalable TensorFlow Library for Learning-to-Rank. *Proceedings of the 25th ACM SIGKDD International Conference on Knowledge Discovery and Data Mining*, 2970–2978 (2019).
117. B. E. Suzek, H. Huang, P. McGarvey, R. Mazumder, C. H. Wu, UniRef: Comprehensive and non-redundant UniProt reference clusters. *Bioinformatics* **23**, 1282–1288 (2007). doi: 10.1093/bioinformatics/btm098; pmid: 17379688

ACKNOWLEDGMENTS

We thank D. MacArthur, Y. Song, and M. Daly for helpful discussions and the gnomAD team at the Broad Institute for their assistance with the website. **Funding:** L.F.K.K. was supported by an EMBO STF 8286 (to L.F.K.K.). R.R. was supported by an NIH training grant NIH T32 GM007748. M.K. was supported by

"la Caixa" Foundation (ID 100010434 to M.K.), fellowship code LCF/BQ/PR19/11700002 (to M.K.), and the Vienna Science and Technology Fund (WWTF) [10.47379/VRG20001] (to M.K.). J.D.O. was supported by "la Caixa" Foundation (ID 100010434) and the European Union's Horizon 2020 research and innovation programme under the Marie Skłodowska-Curie grant agreement 847648. The fellowship code is LCF/BQ/PI20/11760004. F.E.S. has received funding from the European Union's Horizon 2020 research and innovation programme under the Marie Skodowska-Curie grant agreement No 801505. F.E.S. also received funds from the Conselho Nacional de Desenvolvimento Científico e Tecnológico (CNPq) (Process nos.: 303286/2014-8, 303579/2014-5, 200502/2015-8, 302140/2020-4, 300365/2021-7, 301407/2021-5, 301925/2021-6,; the International Primatological Society (Conservation grant), The Rufford Foundation (14861-1, 23117-2, 38786-B), the Margot Marsh Biodiversity Foundation (SMA-CCO-G0023, SMA-CCOG0037), and Primate Conservation Inc. (#1713 and #1689). The Mamirauá Institute for Sustainable Development received funds from the Gordon and Betty Moore Foundation (grant 5344 to J.V.A. and F.E.S.) Fieldwork for samples collected in the Brazilian Amazon was funded by grants from Conselho Nacional de Desenvolvimento Científico e Tecnológico (CNPq/SISBIOTA Program 563348/2010-0 to I.P.F.), Fundação de Amparo à Pesquisa do Estado do Amazonas (FAPEAM/SISBIOTA 2317/2011 to I.P.F.), and Coordenação de Aperfeiçoamento de Pessoal de Nível Superior (CAPES AUX 3261/2013) to I.P.F. Sampling of nonhuman primates in Tanzania was funded by the German Research Foundation (KN1097/3-1 to S.K. and RO3055/2-1 to C.R.) and by the US National Science Foundation (BNS83-03506 to J.P.C.) No animals in Tanzania were sampled purposely for this study. Details of the original study on *Treponema pallidum* infection can be requested from S.K. Sampling of baboons in Zambia was funded by US NSF grant BCS-1029451 to J.P.C., C.J.J., and J.R. The research reported in this manuscript was also funded by the Vietnamese Ministry of Science and Technology's Program 562 (grant ĐTĐL.CN-64/19). A.N.C. is supported by I+D+i project PID2021-127792NB-I00 funded by MCIN/AEI/10.13039/501100011033 (FEDER Una manera de hacer Europa)" and by "Unidad de Excelencia María de Maeztu", funded by the AEI (CEX2018-000792-M) and Departament de Recerca i Universitats de la Generalitat de Catalunya (GRC 2021 SGR 0467). A.D.M. was supported by the National Sciences and Engineering Research Council of Canada and Canada Research Chairs program. The authors thank the Veterinary and Zoology staff at Wildlife Reserves Singapore for their help in obtaining the tissue samples, as well as the Lee Kong Chian Natural History Museum for storage and provision of the tissue samples. We thank H. Doddapaneni, D. M. Muzny, and M. C. Gingras for their support of sequencing at the Baylor College of Medicine Human Genome Sequencing Center. We greatly appreciate the support of R. Gibbs, director of HGSC, for this project and thank the Baylor College of Medicine for internal funding. T.M.B. is supported by funding from the European Research Council (ERC) under the European Union's Horizon 2020 research and innovation programme (grant agreement 864203 to T.M.B.), PID2021-126004NB-100 (MICIIN/FEDER, UE) and Secretaria d'Universitats i Recerca and CERCA Programme del Departament d'Economia i Coneixement de la Generalitat de Catalunya (GRC 2021 SGR 00177). H.L.R. receives funding from Illumina, Inc to support rare disease gene discovery and diagnosis. M.C.J, D.d.V. I.G., R.M.D.B., and J.P.B. were supported by a UKRI NERC standard grant (NE/T000341/1). We thank P. Karanth (IISc) and H. N. Kumara (SACON) for collecting and providing us with some of the samples from India. S.M.A. was supported by a BINC fellowship from the Department of Biotechnology (DBT), India. We acknowledge the support provided by the Council of Scientific and Industrial Research (CSIR), India, to G.U. for the sequencing at the Centre for Cellular and Molecular Biology (CCMB), India. We acknowledge the Duke Lemur Center for collecting primate samples. This is Duke Lemur Center publication #1560. Samples from Amazônia, Brazil, were accessed under SisGen no. A8F3D55. *Aotus azarae* samples from Argentina were obtained with grant support to E.F.D. from the Zoological Society of San Diego, the Wenner-Gren Foundation, the L.S.B. Leakey Foundation, the National Geographic Society, the US National Science Foundation (NSF-BCS-0621020, 1232349, 1503753, 1848954; NSF-RAPID-1219368, NSF-FAIN-1952072; NSF-DDIG-1540255; NSF-REU 0837921, 0924352, 1026991) and the US National Institute on Aging (NIA- P30 AG012836-19, NICHD R24 HD-044964-11). E.F.D. thanks the Ministry of Production and the Environment of Formosa Province in Argentina for the research presented here. J.H.S. was supported in part by the NIH under award number P40OD024628 - SPF Baboon Research Resource. This research is supported by the National Research Foundation Singapore under its National Precision Medicine Programme (NPM) Phase II Funding (MOH-000588 to P.T. and W.K.L.) and administered by the Singapore Ministry of Health's National Medical Research Council. J.R. is also a Core Scientist at the Wisconsin National Primate Research Center, Univ. of Wisconsin, Madison. K.G. was supported by the Swedish Research Council VR (2020-03398). We acknowledge the institutional support of the Spanish Ministry of Science and Innovation through the Instituto de Salud Carlos III and the 2014–2020 Smart Growth Operating Program, to the EMBL partnership and institutional cofinancing with the European Regional Development Fund (MINECO/FEDER, BIO2015-71792-P). We also acknowledge the support of the Centro de Excelencia Severo Ochoa, and the Generalitat de Catalunya through the Departament de Salut, Departament d'Empresa i Coneixement and the CERCA Programme to the institute. The research reported in this manuscript was also funded by the Vietnamese Ministry of Science and Technology's Program 562 (grant no. ĐTĐL.CN-64/19) to M.D.L..

Author contributions: H.G., T.H., J.E., J.G.S., J.M., M.S.B., Y.Y., A.S.D.D., P.P.F., L.F.K.K., L.S., Y.W., A.A., Y.F., S.C., S.B., G.L., R.R., D.B., F.A., and K.F. performed the analysis and wrote the manuscript. M.C.J., M.K., J.D.O., S.M., A.V., J.B., M.R., F.E.S., L.A., J.B., M.G., D.dV., I.G., R.A.H., M.R., A.J., I.S.C., J.E.H., C.H., D.J., P.F., F.R.dM., F.B., H.B., I.S., I.F., J.V.dA., M.M., M.N.F.dS., M.T., R.R., T.H., N.A., C.J.R., A.Z., C.J.J., J.P.C., G.W., C.A., J.H.S., E.F.D., S.K., F.S., D.W., L.Z., Y.S., G.Z., J.D.K., S.K., M.D.L., E.L., S.M., A.N., T.B., T.N., C.C.K., J.L., P.T., W.K.L., A.C.K., D.Z., I.G., A.M., K.G., M.H.S., R.M.D.B., G.U., C.R., J.P.B. contributed the primate samples and sequencing data. M.L., S.S., A.O.D., H.L.R., J.X., J.R., T.M.B., and K.F. supervised the work. **Competing interests:** Employees of Illumina, Inc. are indicated in the list of author affiliations. Serafim Batzoglou is currently affiliated with Seer, Inc. Heidi L. Rehm receives funding to support rare disease research and tool development from Illumina, Inc. and Microsoft, Inc. Patents related to this work are (1) title: Deep convolutional neural networks to predict variant pathogenicity using three-dimensional (3D) protein structures, filing number US 17/232,056, authors: Tobias Hamp, Kai-How Farh, Hong Gao; (2) title: Transfer learning-based use of protein contact maps for variant pathogenicity prediction, filing No.: US 17/876,481, authors: Chen Chen, Hong Gao, Laksshman Sundaram, Kai-How Farh; (3) title: Multi-channel protein voxelization to predict variant pathogenicity using deep convolutional neural networks, filing number US 17/703,935, authors: Tobias Hamp, Kai-How Farh, Hong Gao;(4) title: Transformer language model for variant pathogenicity, filing number US 17/975,536 and US 17/975,547, authors: Jeffrey Ede, Tobias Hamp, Anastasia Dietrich, Yibing Wu, Kai-How Farh. (5) title: Identifying genes with differential selective constraint between humans and non-human primates, filing number US 63/294,820, authors: H. G., J. G. Schraiber, K.-H. Farh. **Data and materials availability:** All sequencing data have been deposited at the European Nucleotide Archive under the accession number PRJEB49549. Primate variants and PrimateAI-3D prediction scores are available with a noncommercial license upon request and are displayed on https://primad.basespace.illumina.com. The source code of PrimateAI-3D is accessible via https://github.com/Illumina/PrimateAI-3D and is also archived at https://doi.org/10.5281/zenodo.7738731. To reduce problems with circularity that have become a concern for the field, the authors explicitly request that the prediction scores from the method not be incorporated as a component of other classifiers and instead ask that interested parties employ the provided source code and data to directly train and improve upon their own deep learning models. **License information:** Copyright © 2023 the authors, some rights reserved; exclusive licensee American Association for the Advancement of Science. No claim to original US government works. https://www.sciencemag.org/about/science-licenses-journal-article-reuse

SUPPLEMENTARY MATERIALS

science.org/doi/10.1126/science.abn8197
Materials and Methods
Supplementary Text
Figs. S1 to S28
Tables S1 to S6
References (*118*–*161*)
MDAR Reproducibility Checklist

View/request a protocol for this paper from *Bio-protocol*.

Submitted 31 December 2021; accepted 22 March 2023
10.1126/science.abn8197

RESEARCH ARTICLE SUMMARY

PRIMATE GENOMES

Rare penetrant mutations confer severe risk of common diseases

Petko P. Fiziev†, Jeremy McRae†, Jacob C. Ulirsch, Jacqueline S. Dron, Tobias Hamp, Yanshen Yang, Pierrick Wainschtein, Zijian Ni, Joshua G. Schraiber, Hong Gao, Dylan Cable, Yair Field, Francois Aguet, Marc Fasnacht, Ahmed Metwally, Jeffrey Rogers, Tomas Marques-Bonet, Heidi L. Rehm, Anne O'Donnell-Luria, Amit V. Khera, Kyle Kai-How Farh*

INTRODUCTION: Genome-wide association studies (GWASs) have identified thousands of common genetic variants that are predictive of common disease susceptibility, but these variants individually have mild effects on disease owing to the effects of natural selection. By contrast, rare genetic variants can have large effects on common disease risk, but their use in genetic risk prediction has been limited to date owing to the difficulty of distinguishing pathogenic from benign variants and estimating the magnitude of their effects.

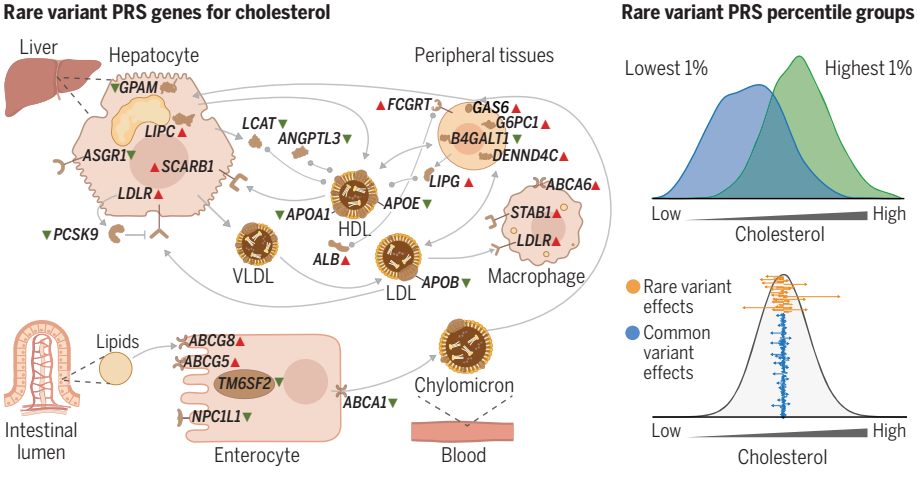
RATIONALE: PrimateAI-3D is a three-dimensional convolutional neural network for missense variant–effect prediction, which was trained with common genetic variants from the population sequencing of 233 primate species. By applying this method to estimate the pathogenicity of rare coding variants in 454,712 UK Biobank individuals, we aimed to improve rare-variant association tests and genetic risk prediction for common diseases and complex traits.

RESULTS: We performed rare-variant burden tests for 90 well-powered, clinically relevant phenotypes in the UK Biobank exome dataset. Stratifying missense variants with PrimateAI-3D greatly improved gene discovery, revealing 73% more significant gene-phenotype associations (false discovery rate <0.05) compared with not using PrimateAI-3D. When benchmarked against prior studies, gene-phenotype pairs identified with our method were better supported by orthogonal genetic evidence from GWAS and genes from related Mendelian disorders. In addition, PrimateAI-3D scores showed the strongest correlation among existing variant interpretation algorithms for predicting the quantitative effects of rare variants on continuous clinical phenotypes.

Having validated our method for finding gene-phenotype relationships, we next constructed a rare-variant polygenic risk score (PRS) model by combining the rare-variant genes for each phenotype, weighting variants by their PrimateAI-3D prediction score and the direction and effect size of each associated gene. For comparison, we constructed common-variant PRS models and evaluated the performance of the two models for genetic risk prediction in a withheld-test subset of the cohort. Although common variants better explained overall population variance, rare-variant PRSs had more power at the ends of the distribution to identify individuals at the greatest risk for disease, and thus may be more relevant for population genetic screening and risk management. By contrast to common-variant PRS models derived from European populations that show poor generalization to non-Europeans, rare-variant PRSs were substantially more portable to different cohorts and ancestry groups that were not seen during model training. Moreover, because they incorporate orthogonal information from nonoverlapping sets of variants, we combined rare- and common-variant PRS models into a unified model and observed further improvement in genetic risk prediction for common diseases.

To understand the extent by which rare-variant PRSs can be expected to improve with increases in discovery cohort size, we repeated our analyses in down-sampled subsets of the UK Biobank cohort. We found that the number of genes contributing to the rare-variant PRS increased linearly, with no signs of plateauing at a half-million exomes. Newly discovered rare-variant genes were strongly enriched at GWAS loci, forming allelic series with effect sizes that were ~10-fold larger on average than the respective common GWAS variant. Among well-powered GWAS loci that could be unambiguously assigned to a single gene, the majority showed subthreshold signal on the rare-variant burden test, indicating that rare penetrant variants exist at a large fraction of GWAS loci and can be incorporated into the rare-variant PRS with further advances in cohort size and variant effect prediction.

CONCLUSION: Understanding the impact of rare variants in common diseases is of prime interest for both precision medicine and the discovery of drug targets. By leveraging advances in variant effect prediction, we have demonstrated major improvements in rare-variant burden testing and genetic risk prediction. Notably, we observed that nearly all individuals carried at least one rare penetrant variant for the phenotypes we examined, demonstrating the utility of personal genome sequencing for otherwise healthy individuals in the general population. ■



Polygenic contribution of rare genetic variants to complex human traits, shown for serum cholesterol as a representative example. (Left) Rare-variant burden tests capture the direction and effect sizes of genes in known lipid biosynthesis pathways. (Top right) When used in a rare-variant polygenic risk score, individuals at opposite ends of the PRS separate into high- and low-cholesterol groups. (Bottom right) Rare variants in these genes have larger effects compared with common variants identified by GWAS and are strongly predictive of individuals who are phenotypic outliers.

The list of author affiliations is available in the full article online.
*Corresponding author. Email: kfarh@illumina.com
†These authors contributed equally to this work
Cite this article as P. P. Fiziev *et al.*, *Science* **380**, eabo1131 (2023). DOI: 10.1126/science.abo1131

READ THE FULL ARTICLE AT
https://doi.org/10.1126/science.abo1131

RESEARCH ARTICLE

PRIMATE GENOMES

Rare penetrant mutations confer severe risk of common diseases

Petko P. Fiziev[1]†, Jeremy McRae[1]†, Jacob C. Ulirsch[1], Jacqueline S. Dron[2,3], Tobias Hamp[1], Yanshen Yang[1], Pierrick Wainschtein[1,4], Zijian Ni[5], Joshua G. Schraiber[1], Hong Gao[1], Dylan Cable[6], Yair Field[1], Francois Aguet[1], Marc Fasnacht[1], Ahmed Metwally[1], Jeffrey Rogers[7,8], Tomas Marques-Bonet[9,10,11,12], Heidi L. Rehm[2,3,13], Anne O'Donnell-Luria[3,13,14], Amit V. Khera[2,3,15], Kyle Kai-How Farh[1]*

We examined 454,712 exomes for genes associated with a wide spectrum of complex traits and common diseases and observed that rare, penetrant mutations in genes implicated by genome-wide association studies confer ~10-fold larger effects than common variants in the same genes. Consequently, an individual at the phenotypic extreme and at the greatest risk for severe, early-onset disease is better identified by a few rare penetrant variants than by the collective action of many common variants with weak effects. By combining rare variants across phenotype-associated genes into a unified genetic risk model, we demonstrate superior portability across diverse global populations compared with common-variant polygenic risk scores, greatly improving the clinical utility of genetic-based risk prediction.

Genome-wide association studies (GWASs) have convincingly identified tens of thousands of common variants that underlie complex human traits and diseases (*1*), although several key challenges remain. First, pinpointing which genes these predominately noncoding variants affect is nontrivial, hindering biological insight into disease mechanisms. Second, individual common variants have modest effects on disease risk, which results in weak aggregate predictors with limited clinical utility and portability between populations (*2*–*4*). In contrast to GWASs, rare coding variant studies directly link perturbed gene function to specific phenotypes. For individuals with cancer or rare genetic diseases, analysis of whole-exome sequencing (WES) routinely uncovers rare, highly penetrant variants that can substantially alter the course of clinical management (*5*–*8*) and drive treatment decisions (*9*, *10*). However, in the context of common diseases, the role of rare coding variants has not been established to the same extent owing to a lack of methods for accurately predicting variant function and insufficient cohort sizes.

Recent large-scale genome and exome sequencing studies of the general population have revealed that the average person carries dozens of potentially deleterious rare variants that have arisen through recent germline mutation (*11*). These studies provide the opportunity to move beyond rare genetic disease and examine the impact of medium- to large-effect rare coding variants on a comprehensive set of complex human traits and diseases. In practice, individually rare variants are often combined into burden tests to more powerfully discover genes underlying these phenotypes, but these tests are limited by our ability to distinguish pathogenic from benign variants. In this study, we show that our recently developed method PrimateAI-3D (*12*), a three-dimensional (3D) convolutional neural network trained on common genetic variants from 233 primate species, accurately quantifies missense variant pathogenicity, resulting in improved gene discovery across 454,712 individuals in the UK Biobank (*13*–*15*). We then show how rare variants in these genes can be combined into a unified genetic risk score, which has distinct advantages over common-variant polygenic risk scores, offering a glimpse into the potential utility of personal genome sequencing for the general population.

[1]Artificial Intelligence Laboratory, Illumina, Inc., San Diego, CA 92122, USA. [2]Center for Genomic Medicine, Massachusetts General Hospital, Boston, MA 02114, USA. [3]Program in Medical and Population Genetics, Broad Institute of MIT and Harvard, Cambridge, MA 02142, USA. [4]Institute for Molecular Bioscience, University of Queensland, Brisbane, Queensland, Australia. [5]Department of Statistics, University of Wisconsin–Madison, Madison, WI 53706, USA. [6]Department of Electrical Engineering and Computer Science, Massachusetts Institute of Technology (MIT), Cambridge, MA 02142, USA. [7]Human Genome Sequencing Center and Department of Molecular and Human Genetics, Baylor College of Medicine, Houston, TX 77030, USA. [8]Wisconsin National Primate Research Center, University of Wisconsin–Madison, Madison, WI 53715, USA. [9]Institute of Evolutionary Biology (UPF-CSIC), 08003 Barcelona, Spain. [10]Catalan Institution of Research and Advanced Studies (ICREA), 08010 Barcelona, Spain. [11]CNAG-CRG, Centre for Genomic Regulation (CRG), Barcelona Institute of Science and Technology (BIST), 08003 Barcelona, Spain. [12]Institut Català de Paleontologia Miquel Crusafont, Universitat Autònoma de Barcelona, 08193 Barcelona, Spain. [13]Analytic and Translational Genetics Unit, Department of Medicine, Massachusetts General Hospital, Boston, MA 02114, USA. [14]Division of Genetics and Genomics, Boston Children's Hospital, Boston, MA 02115, USA. [15]Verve Therapeutics, Cambridge, MA 02215, USA.
*Corresponding author. Email: kfarh@illumina.com
†These authors contributed equally to this work.

PrimateAI-3D empowers gene discovery in rare-variant association tests

To identify genes underlying complex human traits and diseases, we performed rare-variant burden tests for 90 well-powered, nonredundant clinical and quantitative phenotypes, including both medical diagnoses and commonly measured laboratory tests, for 454,712 individuals in the UK Biobank who underwent WES (tables S1 to S3) (*16*). Using an allele frequency (AF) threshold of 0.1%, we detected 1841 gene-phenotype associations with loss-of-function (LoF) variants, 1510 associations with missense variants, and 3035 associations combining missense and LoF variants (average of 33.7 per phenotype) at a false discovery rate (FDR) of 5% (Fig. 1A). When we applied PrimateAI-3D (*12*) to classify pathogenic and benign missense variants, we improved gene discovery by 73%, identifying 1285 more gene-phenotype associations at the same FDR (Fig. 1A, fig. S1, and table S4). As a negative control, we repeated the test considering rare synonymous variants but detected only 28 gene-phenotype associations. Taken together, these results show that our rare-variant tests are well calibrated and that PrimateAI-3D pathogenicity predictions improve gene discovery.

We undertook several additional approaches to validate our gene-phenotype associations and to compare them to prior efforts. First, we investigated the strength of support from common-variant studies for the gene-phenotype pairs identified by our approach. After performing matched GWASs for the 90 phenotypes (table S5) (*16*), we observed that 70% of the 3035 gene-phenotype pairs had a significant GWAS variant ($P < 5 \times 10^{-8}$) within 1 megabase of the transcription start site. Next, we compared our results to a recent rare-variant association study in the same UK Biobank cohort (*17*) (Fig. 1B). Backman *et al.* used a burden test which included all LoF variants but permitted only missense variants predicted to be deleterious by five commonly used missense pathogenicity classifiers (*18*). For matched phenotypes and significance thresholds (*16*), we identified 23% more gene-phenotype pairs (table S6). Gene-phenotype pairs identified exclusively in the present study were more enriched for genes implicated by matching GWASs and overlapped more with genes in related Mendelian diseases (Fig. 1C and table S7), which supports their relevance to complex-trait biology. Third, we benchmarked PrimateAI-3D against 15 other pathogenicity classifiers by integrating them into our burden testing pipeline. Again, gene-phenotype pairs detected exclusively by PrimateAI-3D had consistently higher enrichments for GWAS genes for the same trait compared with any other method (fig. S2). Finally, we assessed how well each classifier could predict the effect size of individual variants on phenotype across 62

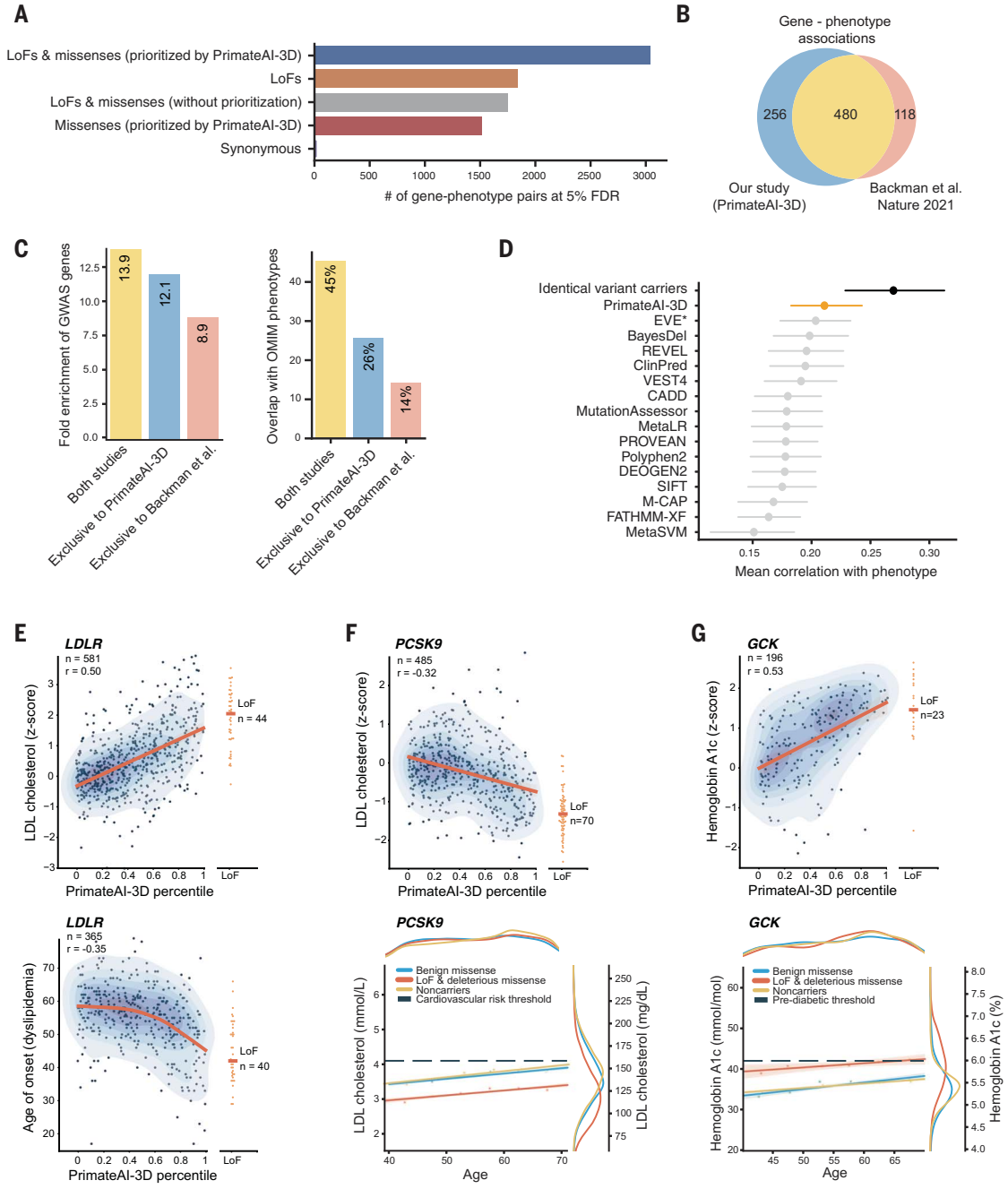


Fig. 1. PrimateAI-3D identifies rare deleterious variants that affect disease severity and age of onset. (**A**) Total number of significant gene-phenotype associations (FDR < 5%) identified across 90 phenotypes for rare-variant burden tests with different inclusion criteria for variants. As a negative control, the number of significant genotype-phenotype associations for a burden test with only synonymous variants is also shown. (**B**) Comparison of the current study with a recent study of rare variants in the UK Biobank (*17*) on the number of gene-phenotype associations detected exclusively by one or both studies for the same traits and matched significance thresholds. (**C**) Comparison of rare-variant genes discovered in this study versus the previous study (*17*) with orthogonal genetic evidence. (Left) Fold enrichment of rare-variant genes at common-variant GWAS loci, matched for the same phenotypes. (Right) Percentage of rare-variant genes overlapping with OMIM genes matched for related phenotypes. (**D**) Performance of different variant pathogenicity classifiers (see methods) at predicting variant effects on quantitative phenotypes. Spearman correlations between pathogenicity scores and phenotype values on a set of 62 gene-phenotype pairs are shown. The phenotypic correlation between individuals carrying an identical missense variant is shown in black as an upper bound for classifier performance. Dots and error bars represent mean ± 95% confidence interval. (**E**) (Top) Positive correlation of LDL cholesterol concentrations (*y* axis) with PrimateAI-3D scores (*x* axis) for rare missense variants in *LDLR*. (Bottom) PrimateAI-3D score is predictive of age of onset for dyslipidemia in carriers of rare missense variants in *LDLR*. (**F**) (Top) Negative correlation of LDL cholesterol concentrations with PrimateAI-3D scores for rare missense variants in *PCSK9*, a down-regulator of *LDLR*. (Bottom) LDL cholesterol concentrations increase with age at a similar rate regardless of carrier status, but carriers of prioritized rare variants have lower LDL concentrations across all ages. (**G**) (Top) Positive correlation of HbA1c concentrations with PrimateAI-3D scores for rare missense variants in *GCK*. (Bottom) HbA1c concentrations increase with age at a similar rate regardless of carrier status, but carriers of rare deleterious variants reach prediabetic thresholds earlier in their lives on average. Deleterious and benign missense variants are defined as variants with PrimateAI-3D score >0.5 and <0.5, respectively. For (E), (F), and (G), red, blue, or yellow lines show regression models fitted to the data.

gene-phenotype pairs detected without variant prioritization (table S8) (*16*) and again observed that PrimateAI-3D outperformed all other methods (median Wilcoxon $P = 8 \times 10^{-7}$) (Fig. 1D and fig. S3).

Having comprehensively validated our use of PrimateAI-3D for rare-variant burden testing, we explored the correlations we observed between PrimateAI-3D scores, clinical laboratory measurements, and ages of onset for common diseases. In general, we observed a linear relationship with the quantitative measurements and an inverse correlation with age of disease onset (table S9). We focus on the examples of *LDLR* and *PCSK9* with low-density lipoprotein (LDL) cholesterol levels and *GCK* with glycated hemoglobin A1c (HbA1c) to demonstrate these general findings (Fig. 1, E to G). Overall, 1307 individuals (0.3%) carried rare, potentially deleterious missense variants in the *LDLR* gene in which pathogenic mutations can cause familial hypercholesterolemia and early-onset cardiovascular disease (*19*, *20*). PrimateAI-3D scores of missense variants in *LDLR* were significantly correlated with LDL levels (Spearman $\rho = 0.50$, $P = 8 \times 10^{-38}$) (*16*). Individuals with variants that had scores near 0 had LDL cholesterol levels indistinguishable from noncarriers, whereas those with scores near 1 had elevated LDL cholesterol levels similar to LoF variant carriers (Fig. 1E, upper panel). Among individuals who received a clinical diagnosis of dyslipidemia, PrimateAI-3D scores correlated inversely with age of diagnosis (Spearman $\rho = -0.35$, $P = 3 \times 10^{-12}$). The most deleterious missense variants advanced age of disease onset by ~15 years, similar to that observed for LoF carriers (Fig. 1E, lower panel).

We next examined rare variants in the *PCSK9* gene, a target of cholesterol-lowering medications (*21*). Rare missense variants with high PrimateAI-3D scores in *PCSK9* were correlated with decreased LDL cholesterol levels (Spearman $\rho = -0.32$, $P = 3 \times 10^{-13}$) and acted in the opposite direction of deleterious *LDLR* variants (Fig. 1F, upper panel). LDL cholesterol levels increased with age at a similar rate (0.2 mmol/liter per decade of normal aging) regardless of *PCSK9* carrier status, but individuals carrying prioritized rare variants in *PCSK9* had an average of 0.6 mmol/liter–lower LDL cholesterol levels at any given age (Fig. 1F, lower panel). Consequently, fewer of these carriers had moderate-to-severe hypercholesterolemia (LDL cholesterol > 4.1 mmol/liter or 160 mg/dl) or elevated cardiovascular disease risk (*22*), whereas those that did manifested these symptoms later in life.

We also observed similar relationships between rare deleterious variants in *GCK* and HbA1c, a proxy for blood glucose levels and a diagnostic laboratory marker for type 2 diabetes (prediabetes HbA1c > 42 mmol/mol, diabetes HbA1c > 48 mmol/mol) (Fig. 1G) (*23*). Analogous to LDL cholesterol, HbA1c levels increased with age, matching the steep rise of diabetes prevalence with age observed in epidemiological studies (*24*). Rare deleterious variants in *GCK* elevated HbA1c levels by an average of 5.1 mmol/mol relative to benign variant carriers and noncarriers, which was 4.6-fold higher than the average rise in HbA1c levels per decade of normal aging. Correspondingly, this increased the fraction of individuals with diabetes between ages 40 and 50 from 3.8% to 24.8% (6.6-fold increase) for carriers of rare deleterious variants. Our results across clinically relevant phenotypes such as LDL cholesterol and HbA1c demonstrate the utility of PrimateAI-3D to distinguish pathogenic from benign variants and highlight the capacity of rare high-penetrance variants to accelerate or delay the age of onset of common diseases by decades.

Rare-variant polygenic risk scores identify individuals most at risk for common diseases

Recent exponential human population growth has created an abundance of rare variants through naturally occurring mutations without providing adequate time for selection to remove those with deleterious consequences (*25*, *26*). In the UK Biobank cohort, we observed that each person carries an average of 2.96 rare deleterious missense variants and 0.97 rare LoF variants within one or more of the genes identified from our burden test. Consistent with models of negative selection (*16*, *27*, *28*), we find that rare variants exerted far greater per-allele effects on human phenotypes than common variants across a subset of 893 genes implicated by both rare- and common-variant studies, with rare deleterious variants having on average an 11.2-fold larger effect than common GWAS variants at the same loci (Fig. 2A and fig. S4). Within each allele frequency bin, LoF variants had the highest per-allele effects, followed by missense variants (PrimateAI-3D > 0.8) and cryptic splice variants (SpliceAI score > 0.2) (*29*). Benign missense (PrimateAI-3D < 0.2) and synonymous variants had nearly null per-allele effects on phenotype, even as singletons. Given the high overall prevalence and strong effect sizes of rare deleterious variants in the predominately healthy UK Biobank cohort, we reasoned that a single polygenic score combining these variants may effectively identify individuals at high risk for complex disease.

Existing polygenic risk score (PRS) models of common disease largely omit rare variants because of challenges in interpreting variants of uncertain significance (VUS) and estimating the magnitude of variant effects (*30*). Here we propose a complementary, rare-variant PRS model, based on a weighted sum of rare deleterious variants from multiple phenotype-associated genes, using PrimateAI-3D for variant effect estimation. To construct the model, we first split the UK Biobank cohort into training and testing subsets and then fit a linear model to each phenotype on the rare variants (AF < 0.1%) in associated genes, weighted by PrimateAI-3D–predicted effect size (table S10) (*16*). For comparison, we also constructed common-variant (AF > 1%) PRS models by performing GWAS on the training dataset and applying the method of clumping and thresholding (table S11) (*31*).

We illustrate the components of the rare-variant PRS model using total cholesterol levels as a representative example and show that it identifies the complex network of genes, cell types, and pathways that underpin lipid metabolism (Fig. 2B). Rare deleterious variants in the 31 associated genes that contribute to the rare-variant PRS model shifted cholesterol levels by ~0.38 mmol/liter on average, 10-fold the average effect size of the 563 variants in the common-variant PRS model (0.040 mmol/liter) (Table 1). Out of these 31 genes, 25 were previously known to play central roles in lipid homeostasis (*32*): from absorption of cholesterol through intestinal enterocytes (*ABCG5*) (*33*), to regulation of serum LDL concentrations (*PCSK9*) (*34*), to comprising key components of lipoproteins (*APOB*) (*35*), to lipid scavenging in macrophages (*STAB1*) (*36*). Beyond identifying genes pertinent to cholesterol metabolism, the direction of effect for these rare deleterious variants was consistent with each gene's known role in the pathway. Notably, many of the genes that produce downregulatory effects on cholesterol levels are therapeutic targets that offer alternatives to statin-based cholesterol reduction for cardiovascular disease, such as *PCSK9* and *NPC1L1* inhibitors (*37*, *38*). Whereas the average chance of an individual carrying a rare deleterious variant for any given gene was only 0.4%, when summed across all 31 genes, one in eight individuals carried a rare, high-penetrance variant for cholesterol.

We sought to evaluate the predictive power of the rare-variant PRS and the corresponding common-variant PRS, as well as a combination of the two methods, on the 10% of UK Biobank individuals that had been withheld for testing. Across 78 quantitative phenotypes, the unified PRS performed best with an average Pearson correlation of 0.307 (Fig. 2C and fig. S5), compared with 0.058 and 0.303 for the rare-variant and common-variant PRSs, respectively. Consistent with the correlations, the average phenotypic variance explained was 10.4, 0.4, and 10.1%, respectively. We also evaluated rare-variant PRS models constructed using 15 other variant pathogenicity classifiers and observed that PRSs based on PrimateAI-3D outperformed all other methods (Fig. 2D), underscoring the importance of accurate pathogenicity prediction to rare-variant PRS performance. Overall, these observations are consistent with those of previous studies that have demonstrated that, in aggregate, rare

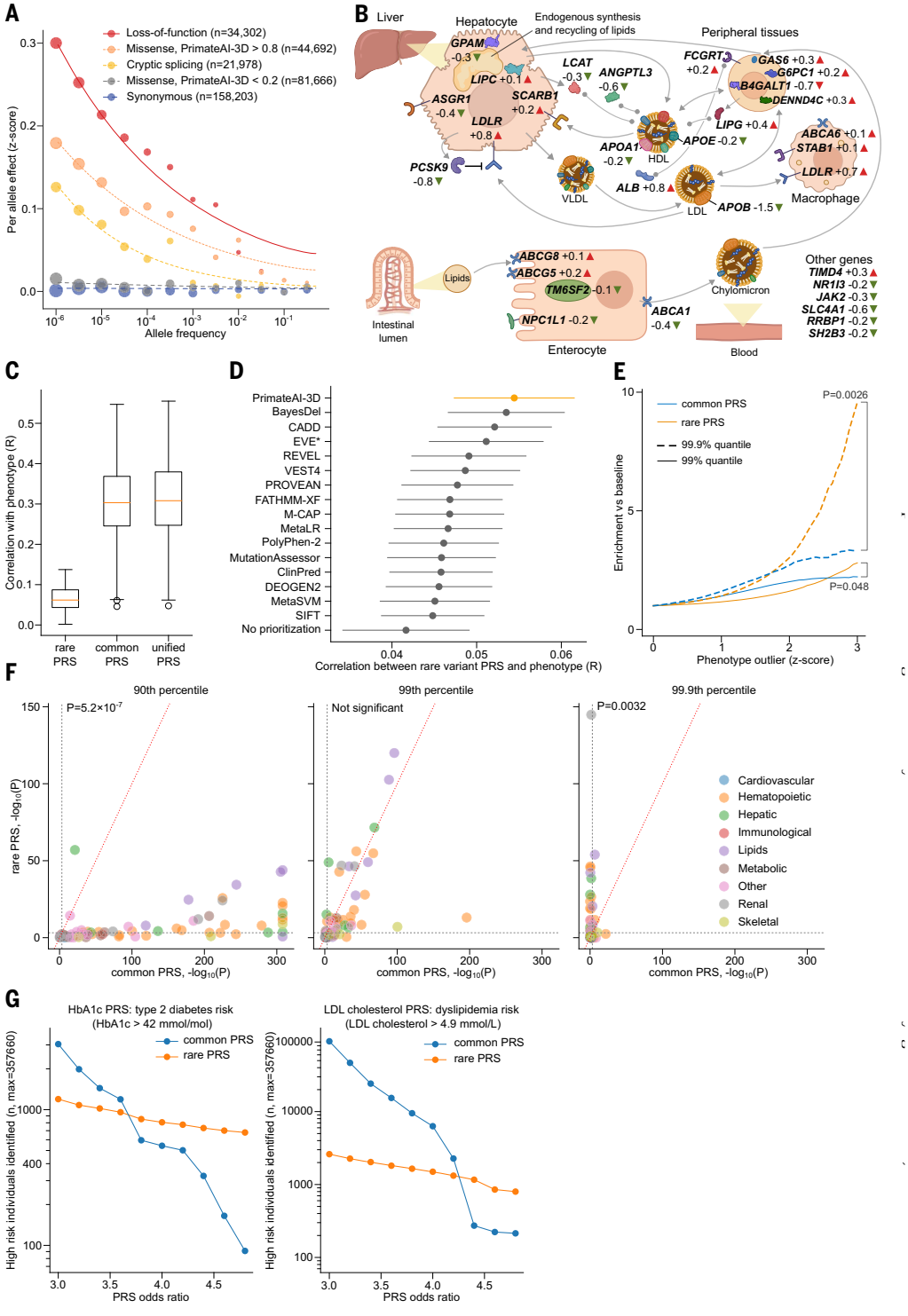


Fig. 2. Comparison of polygenic risk scores (PRSs) from common and rare variants. (**A**) Relationship between variant effect size and allele frequency for different pathogenicity classes of variants. Synonymous variants are shown as negative controls. Dot sizes are proportional to the cube root of the number of variants in each group. Regression fits between the allelic effect size and minor allele frequency are represented by curves for each pathogenicity class, calculated with the equation $\beta = \sigma[2p(1-p)]^{-a/2}$, where β is the per-allele effect, p is the minor allele frequency, and σ and a are parameters for selective constraint. (**B**) Illustration of the cholesterol pathway. Genes in the rare-variant PRS model are superimposed. For each gene, values indicate effect sizes in standardized units (see materials and methods), and triangles indicate direction of effect. (**C**) Comparison of the performance of rare-variant PRS, common-variant PRS, and a unified PRS across 78 phenotypes in the withheld UK Biobank test set. Pearson correlations between PRS predictions and phenotypes are shown. (**D**) Comparison of rare-variant PRSs constructed with different pathogenicity classifiers (see methods). Mean absolute Pearson correlations between PRS and phenotypes are shown. Dots and error bars represent mean ± 95% confidence intervals. (**E**) Enrichment of outlier PRS scores in individuals who are phenotype outliers. Phenotype-outlier individuals were defined as exceeding a certain z-score cutoff (x axis), and the y axis shows the enrichment of outlier PRS scores in phenotype-outlier individuals versus the baseline population, aggregated across 78 phenotypes. (**F**) Comparison of the performance of common-variant PRS (x axis) versus rare-variant PRS (y axis) at identifying individuals at the 90th, 99th, and 99.9th percentiles (left, middle, and right graphs) for 78 quantitative phenotypes. Dashed horizontal and vertical lines represent Bonferroni corrected significance thresholds. Lines of equivalence are represented by dashed diagonal red lines. (**G**) Number of individuals at high clinical risk for type 2 diabetes (left) and dyslipidemia (right), identified by rare- and common-variant PRSs at varying risk thresholds (x axis). Rare-variant PRSs identified more individuals at higher risk (>3.8 higher odds for type 2 diabetes, and >4.4 higher odds for dyslipidemia) than common-variant PRSs.

variants explain less genetic heritability than common variants (*39*).

Although rare-variant PRSs underperformed for average phenotype predictions, we reasoned that they may outperform common-variant PRSs for identifying individuals at phenotypic extremes, which is more relevant for clinical screening and risk management. Indeed, individuals with an outlier phenotype (z-score ≥ 3) were 10-fold more likely than the overall population to have a rare-variant PRS score in the 0.1st or 99.9th percentile, compared with threefold for common-variant PRS (P = 0.0026) (Fig. 2E and fig. S6). Across 78 phenotypes, rare-variant PRSs significantly outperformed common-variant PRSs at identifying individuals with outlier phenotypes at the 99.9th percentile (P = 0.0032), had comparable performance at the 99th percentile (difference not significant), and underperformed at the 90th percentile (P = 5.2 × 10^{-7}) (Fig. 2F

Table 1. Comparison of effect sizes and frequencies for common PRS variants and rare PRS genes used for normalized cholesterol concentrations. Chrom., chromosome; freq., frequency.

Common PRS variants							Rare PRS genes			
Chrom.	Position (GRCh37)	Major allele	Minor allele	Allele freq.	Effect size (*z* score)	*P* value	Gene	Aggregate allele freq.	Effect size (*z* score)	*P* value
1	109415445	C	G	0.012	−0.071	1.2×10^{-10}	*ABCA1*	0.009	−0.377	6.8×10^{-110}
8	59393273	A	G	0.336	0.040	5.0×10^{-111}	*ABCA6*	0.009	0.105	3.6×10^{-8}
8	74894748	G	A	0.321	−0.016	1.3×10^{-18}	*ABCG5*	0.009	0.168	4.8×10^{-23}
14	74250100	C	T	0.275	−0.014	3.8×10^{-12}	*ABCG8*	0.006	0.137	1.6×10^{-8}
17	38244153	G	A	0.334	0.016	1.6×10^{-19}	*ALB*	0.0004	0.827	1.1×10^{-26}
7	18091019	A	G	0.199	0.015	2.3×10^{-10}	*ANGPTL3*	0.003	−0.641	1.5×10^{-119}
10	65255514	CA	C	0.440	0.012	1.0×10^{-15}	*APOA1*	0.003	−0.235	9.6×10^{-12}
19	10948031	A	G	0.178	−0.079	5.3×10^{-198}	*APOB*	0.002	−1.455	$<2.3 \times 10^{-308}$
6	161111700	T	C	0.015	0.185	2.2×10^{-77}	*APOE*	0.004	−0.183	1.5×10^{-10}
19	11192226	C	T	0.060	0.236	$<2.3 \times 10^{-308}$	*ASGR1*	0.001	−0.37	4.5×10^{-15}
7	75899085	C	T	0.144	0.021	4.5×10^{-13}	*B4GALT1*	0.0002	−0.74	6.9×10^{-7}
20	62909520	A	G	0.199	0.018	6.6×10^{-11}	*DENND4C*	0.002	0.274	1.9×10^{-11}
19	45319631	A	G	0.046	−0.417	2.3×10^{-308}	*FCGRT*	0.002	0.239	4.1×10^{-8}
16	79504057	A	G	0.245	0.017	1.4×10^{-14}	*G6PC1*	0.003	0.18	2.5×10^{-8}
20	62696024	T	C	0.495	−0.013	4.5×10^{-16}	*GAS6*	0.001	0.268	2.2×10^{-6}
19	11257169	T	C	0.228	−0.083	1.6×10^{-215}	*GPAM*	0.002	−0.25	4.0×10^{-8}
13	74735830	T	C	0.499	−0.017	2.8×10^{-33}	*JAK2*	0.002	−0.34	3.9×10^{-17}
3	69810294	G	T	0.349	−0.017	1.4×10^{-22}	*LCAT*	0.002	−0.347	2.8×10^{-26}
17	65259726	G	A	0.477	0.012	2.2×10^{-18}	*LDLR*	0.003	0.814	1.2×10^{-186}
1	109427458	G	A	0.030	−0.052	4.2×10^{-14}	*LIPC*	0.009	0.111	2.9×10^{-9}
5	156369171	C	T	0.347	−0.045	9.0×10^{-148}	*LIPG*	0.001	0.36	1.0×10^{-13}
1	220970593	T	G	0.314	−0.036	8.0×10^{-85}	*NPC1L1*	0.013	−0.153	1.6×10^{-26}
2	118535808	T	C	0.082	−0.042	1.9×10^{-25}	*NR1I3*	0.002	−0.21	2.0×10^{-7}
6	26093141	A	G	0.078	−0.060	1.0×10^{-47}	*PCSK9*	0.005	−0.812	1.9×10^{-284}
20	47724665	CA	C	0.304	0.014	3.8×10^{-14}	*RRBP1*	0.002	−0.247	2.6×10^{-7}
4	40036216	CA	C	0.071	−0.024	1.1×10^{-7}	*SCARB1*	0.007	0.19	6.9×10^{-21}
10	17255095	A	G	0.418	0.019	2.6×10^{-35}	*SH2B3*	0.004	−0.154	1.4×10^{-6}
. . .							*SLC4A1*	0.0002	−0.606	1.9×10^{-7}
. . .							*STAB1*	0.011	0.108	4.4×10^{-11}
536 variants omitted							*TIMD4*	0.002	0.302	9.2×10^{-13}
							TM6SF2	0.005	−0.158	2.7×10^{-11}

and fig. S7). Empirically, the prevalence of many complex human diseases is below 1%, including Parkinson's disease (0.3%) (*40*), multiple sclerosis (0.3%) (*41*), myocardial infarction before age 40 (0.6%) (*42*), and type 1 diabetes (0.2%) (*43*), which supports the relevance of these outlier phenotype thresholds for evaluating clinical risk prediction models.

For two diseases, type 2 diabetes and dyslipidemia, we evaluated the ability of common and rare PRS models to identify individuals exceeding predefined diagnostic clinical thresholds (HbA1c > 42 mmol/mol and LDL cholesterol > 4.9 mmol/liter respectively) (Fig. 2G). Up until approximately fourfold-increased odds of disease, the common-variant PRS identified more at-risk individuals, whereas after this threshold, the rare-variant PRS overtook the common-variant PRS. Because the rare- and common-variant PRS models use nonoverlapping sets of variants, combining them into a unified model enables the identification of significantly more individuals at high-disease risk (odds ratio ≥ 4×) than common-variant PRSs alone (type 2 diabetes, 1912 versus 542, $P = 1.4 \times 10^{-178}$; dyslipidemia, 7858 versus 6306, $P = 1.2 \times 10^{-39}$). Taken together, these findings suggest that incorporating rare variants into PRSs can outperform common-variant PRSs for identifying outlier individuals (*30*, *44*) who are most likely to require treatment or to suffer severe, early-onset manifestations of disease and for whom preventive screening would be most impactful (*45*, *46*). Moreover, the ability to point to a single penetrant variant as the primary cause of the phenotype may increase the potential clinical actionability of rare deleterious variants with respect to prognosis, management, and therapeutic interventions (*47*).

Portability of rare-variant PRSs and validation in an independent, multiancestry cohort

Common-variant PRS models derived from European populations have poor portability in non-European populations, which may contribute to future health disparities once adopted into clinical practice (*4*). Even when applied to populations with similar ancestry, common-variant PRSs have decreased performance owing to differences between the cohorts used for training and testing (*48*, *49*). We thus set out to evaluate the robustness of our rare-variant PRSs across independent cohorts and ancestries. We first applied 16 rare-variant PRS models, which had been trained on UK Biobank European-ancestry individuals, to predict quantitative phenotypes in 20,708 European individuals from the Massachusetts General Brigham Biobank (MGB; table S12) (*50*). Across 16 phenotypes, the average predictive performance of the rare-variant PRS model was similar in the two cohorts (Pearson's $r = 0.53$), with a median phenotype correlation of 0.078 between the rare-variant PRS and the UK Biobank withheld-test cohort, compared with 0.084 for the MGB cohort

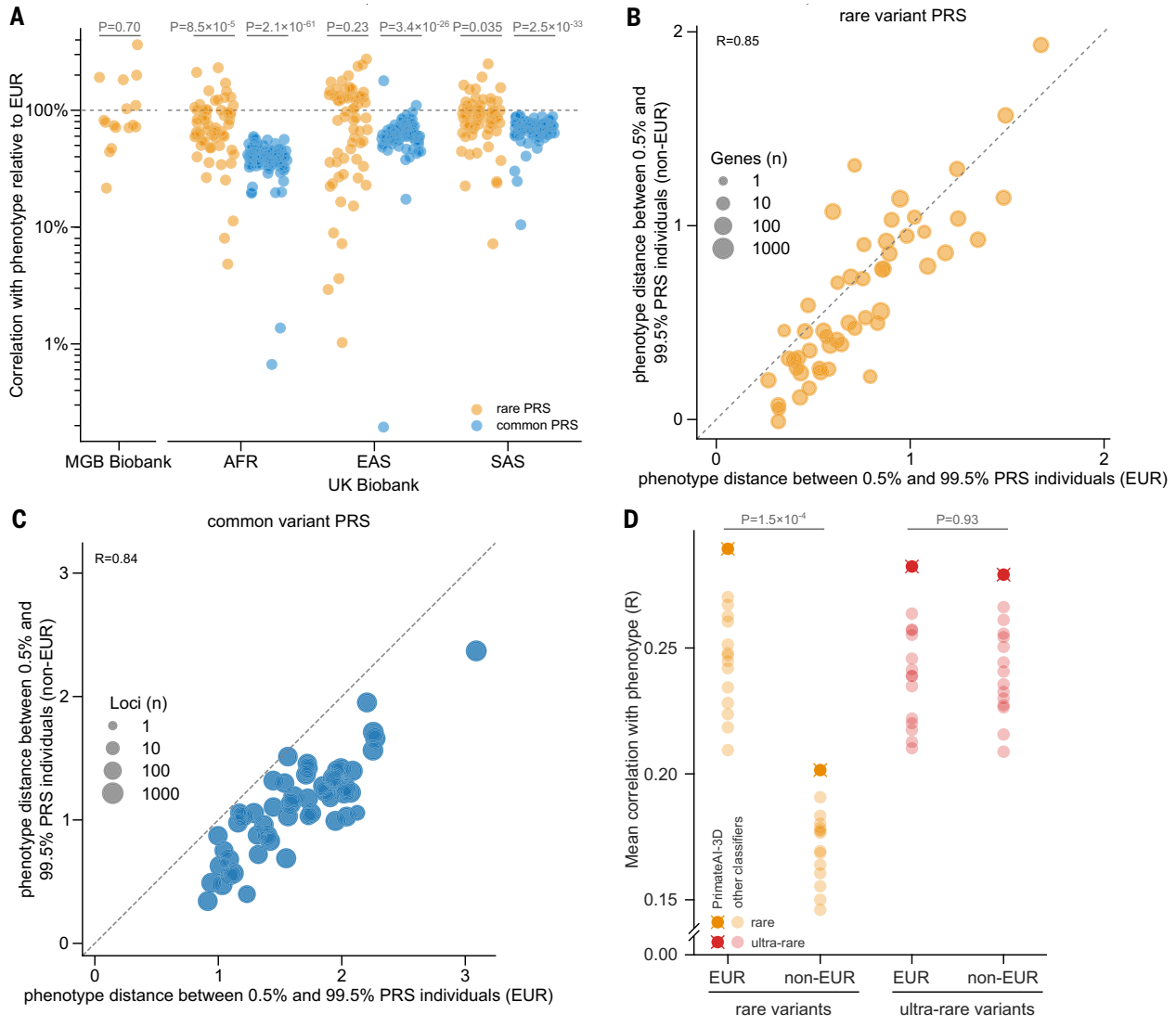


Fig. 3. Validation of rare-variant PRS performance in diverse human populations. (**A**) Performance of rare- and common-variant PRSs derived from UK Biobank Europeans (EUR), measured in the MGB cohort (left) and in UK Biobank non-Europeans (non-EUR) stratified by ancestry (right) (AFR, African; EAS, East Asian; SAS, South Asian). Performance is shown relative to held-out European individuals in the UK Biobank. *P*-values indicate whether the difference in performance versus held-out Europeans is significant. (**B**) Mean phenotype distance between UK Biobank EUR (*x* axis) and UK Biobank non-EUR (*y* axis) individuals is shown for 52 matching traits. The phenotypic distance is calculated by comparing individuals with low (<0.5%) and high (>99.5%) rare-variant PRS percentiles. The Pearson correlation is reported. A line of equivalence is represented by the gray diagonal dashed line. (**C**) Same as (B), but showing the results for common-variant PRSs. (**D**) Performance of PrimateAI-3D variant effect predictions stratified by ancestry and allele frequency for 49 gene-phenotype pairs. Correlation of predicted variant effects with observed phenotypes is shown on the *y* axis. Rare variants have AF < 0.1% in each population. Ultrarare variants are absent from TOPMed, and non-EUR ultrarare variants are singletons (AC = 1), whereas EUR ultrarare variants have allele frequencies less than or equal to those of the non-EUR singletons. *P* values are shown for comparisons across ancestries with PrimateAI-3D. The performance of other variant classifiers is also shown for context.

(Fig. 3A). Notably, the rare-variant PRS models achieved approximately equal performance in the two cohorts despite 43% of the rare deleterious variants in the MGB cohort never appearing in the UK Biobank cohort that was used for model training. Thus, unlike common-variant PRSs, rare-variant PRSs appear largely portable across cohorts with similar ancestry.

We next evaluated the performance of our rare- and common-variant PRS models, which had been trained only on individuals of European ancestry, in individuals of non-European ancestry from the UK Biobank and MGB. As a control, we ensured that the number of variants used per person in the rare-variant PRS was closely matched for different ancestries by applying ancestry-specific allele frequency filters (AF < 0.1%) (fig. S8) and verified that the resulting PRS distributions were similar across ancestries (fig. S9). Consistent with previous reports, the median common-variant PRS correlation with phenotype was 84% lower in individuals with African ancestry ($P = 2.1 \times 10^{-61}$), 62% lower in individuals with East Asian ancestry ($P = 3.4 \times 10^{-26}$), and 51% lower in individuals with South Asian ancestry ($P = 2.5 \times 10^{-33}$) relative to the correlation in individuals with European ancestry (Fig. 3A). By contrast, the rare-variant PRS correlation was substantially more portable with smaller reductions in median correlation of 54%, 14%, and 23%, respectively. To assess the portability of the rare-variant PRS on a more clinically relevant task, we selected individuals with PRS scores at the upper and lower ends of the

phenotype distribution (top or bottom 0.5%) and observed that the average phenotype differences between the two groups were similar for Europeans and non-Europeans in both the UK Biobank withheld-test cohort (Pearson's $r = 0.85$; Fig. 3B) and the MGB cohort (Pearson's $r = 0.88$; fig. S10). Overall, rare-variant PRS models trained in Europeans performed better when tested in non-Europeans than Europeans for 14 out of 52 phenotypes, compared with the common-variant PRS models, which performed worse when tested in non-Europeans for all 52 phenotypes (Fig. 3C).

Although rare-variant PRSs appear to generalize better across ancestries than common-variant PRSs, their average performance still decreases in non-European populations. However, this appears to be distinct from the portability issues experienced by the common-variant PRS, where causal-variant identification remains difficult because of linkage disequilibrium. We hypothesized that the current European bias is due primarily to more accurate allele frequency estimates within the more numerous European individuals in the cohort and in current population databases, resulting in the inadvertent inclusion of common non-European variants into the rare-variant PRS that dilute its performance. To test this hypothesis, we restricted our evaluation to ultrarare variants (seen only once in the UK Biobank and absent from the TOPMed allele frequency database) to minimize common-variant leakage. We found that PrimateAI-3D variant-effect size predictions were equally accurate in European and non-European ultrarare variants (difference not significant; Fig. 3D) but were significantly less accurate for non-European variants at the default allele frequency threshold of 0.1% ($P = 1.5 \times 10^{-4}$ with PrimateAI-3D). As further indication that these issues are independent of variant effect prediction, we show that rare-variant PRSs derived with only LoF variants (without PrimateAI-3D) displayed similarly decreased performance in non-European individuals (fig. S11A), and that the European bias could be reduced by using L_1 regularization to limit overfitting (fig. S11B). Similar challenges have been reported for rare genetic disease diagnosis in non-European populations (*51*, *52*), where inaccurate allele frequency estimates make it difficult to preclude ancestry-specific common variants as potential causes of disease. Therefore, as population allele frequency panels become more accurate and globally inclusive, we expect that the portability of rare-variant PRSs will continue to improve.

The convergence of common- and rare-variant genes forecasts future improvements in rare-variant PRSs

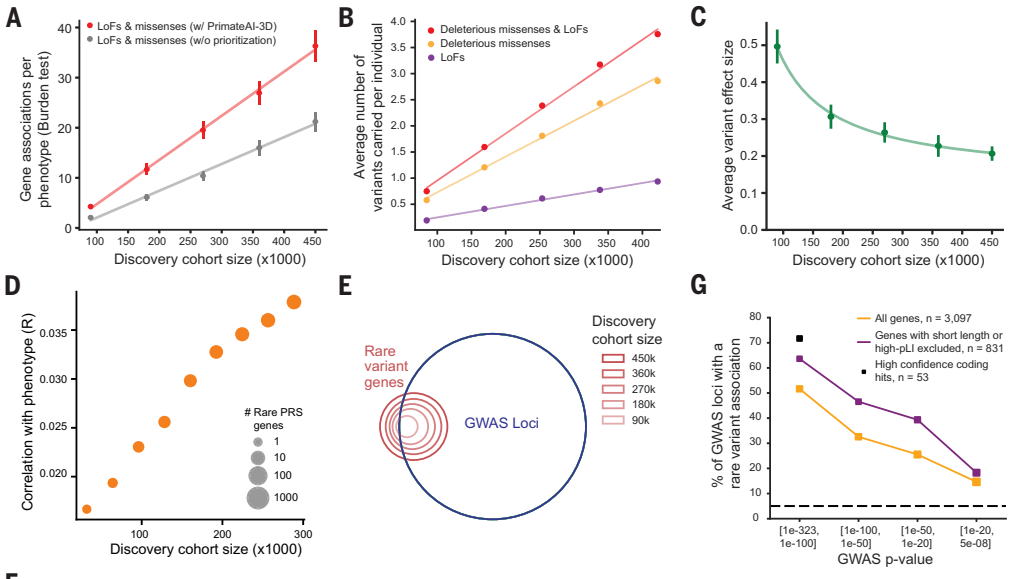
Looking forward, we explored how much the performance of rare-variant PRS approaches is expected to improve as exome sample sizes increase, focusing first on our ability to identify additional exome-wide significant genes (FDR <5%). We performed association tests in down-sampled subsets of the UK Biobank cohort and observed that the number of significant associations increased linearly with sample size for both rare-variant burden tests (FDR <5%) and common-variant GWAS loci ($P < 5 \times 10^{-8}$) (Fig. 4A and fig. S12). On average, PrimateAI-3D enabled discovery of the same number of exome-wide significant genes using 1.8-fold–smaller cohort sizes compared with when missense prioritization was not applied. Consistent with the improved detection of phenotype-associated genes, we observed a linear increase in the number of variants carried by each individual that could be included in the rare-variant PRS model (Fig. 4B). At the full cohort size, we found that 97% of individuals carried a rare penetrant variant in one or more of the associated genes for the 90 clinical and quantitative phenotypes in the study (fig. S13). Although effect sizes were lower in newly identified genes (Fig. 4C), rare-variant PRS performance improved steadily, with each doubling of discovery cohort size corresponding to an 88% improvement in variance explained (Fig. 4D and fig. S14).

Our forecasting analyses suggest that rare-variant PRSs will continue to meaningfully improve as cohort sizes increase, with newly discovered genes preferentially enriched at GWAS loci (Fig. 4E), consistent with recent work showing convergent biological pathways behind both rare- and common-variant heritability (*39*). The observed overlap of common-variant GWAS hits and rare-variant burden test genes was highly phenotype specific (Fig. 4F and figs. S15 and S16) and was not explained by linkage disequilibrium, because we regressed out the effects of significant GWAS variants and population structure before applying the rare-variant burden tests. Focusing on a subset of well-powered GWAS loci that could be unambiguously mapped to a single protein-coding gene (*16*), we found that 64% of common-variant GWAS genes showed significant association in the rare-variant burden test ($P < 0.05$; Fig. 4G). The fraction of genes with rare-variant signal declined for weaker GWAS hits ($P = 3 \times 10^{-37}$), as well as for genes under strong evolutionary selection ($P = 5 \times 10^{-4}$) (*53*), reflecting reduced statistical power to detect enrichments in genes that either have weak phenotypic effects, or that have been depleted of deleterious variants by selective constraint. Similarly, we observed that shorter genes, with consequently fewer variants, were also less likely to be significant in the rare-variant burden test ($P = 7 \times 10^{-6}$). Although we found that only 186 (6%) out of 3097 unambiguously GWAS-implicated genes reached the stringent exome-wide significance threshold for inclusion in the rare-variant PRS (FDR < 5%), 625 (20%) were nominally significant on the burden test at a P-value threshold of < 0.05, indicating that rare-variant associations are likely to be discovered at these genes with larger cohort sizes. Our empirical studies of the convergence of common- and rare-variant associations suggest that allelic series underlie most of the genes implicated in human pathophysiology and can be leveraged in ever-growing sequencing cohorts to improve rare-variant PRS performance.

Discussion

Understanding the role of rare penetrant variants in common diseases is of prime interest to both precision medicine (*5*–*7*) and targeted drug development (*21*, *54*, *55*). In this study, we leverage PrimateAI-3D's state-of-the-art predictions to model the quantitative effects of each variant on multiple phenotypes, uncovering the role played by rare penetrant variants in common human diseases and complex traits. We demonstrate the complementary utility of common and rare variants for predicting the risk of human diseases, observing that common variants explain a higher proportion of total population variance, whereas rare variants more readily identify outlier individuals at the greatest risk for severe, early-onset disease (*45*, *46*). Our results establish that the personal genome of an otherwise healthy individual is not quiescent with limited actionable potential (*56*) but instead carries a substantial burden of rare consequential variants, the clinical utility of which will be more fully realized as variant interpretation improves and discovery cohort sizes increase.

At present, the two greatest barriers to the clinical adoption of common-variant PRS models for use in precision medicine are their limited generalizability between populations with different ancestries and their weak discriminatory capability to identify individuals at high risk for disease (*57*). Specifically, the inclusion of predominately noncoding variants with small effects that are noncausal, but disease-associated owing to linkage disequilibrium, substantially impairs common-variant PRS performance (*58*, *59*). In comparison, our rare-variant PRS models are anchored on PrimateAI-3D's predictions of missense variant–effect size and are largely uninfluenced by the effects of ancestry, because the PrimateAI-3D model was derived from common variants in 236 species of nonhuman primates. This gives rare-variant PRS models an advantage over common-variant PRS models at generalizing to cohorts and human populations that were not seen during training, providing more globally equitable health outcomes than current genetic studies, which are predominantly European. Ultimately, rare-variant PRSs can be combined with common-variant PRSs into a unified risk



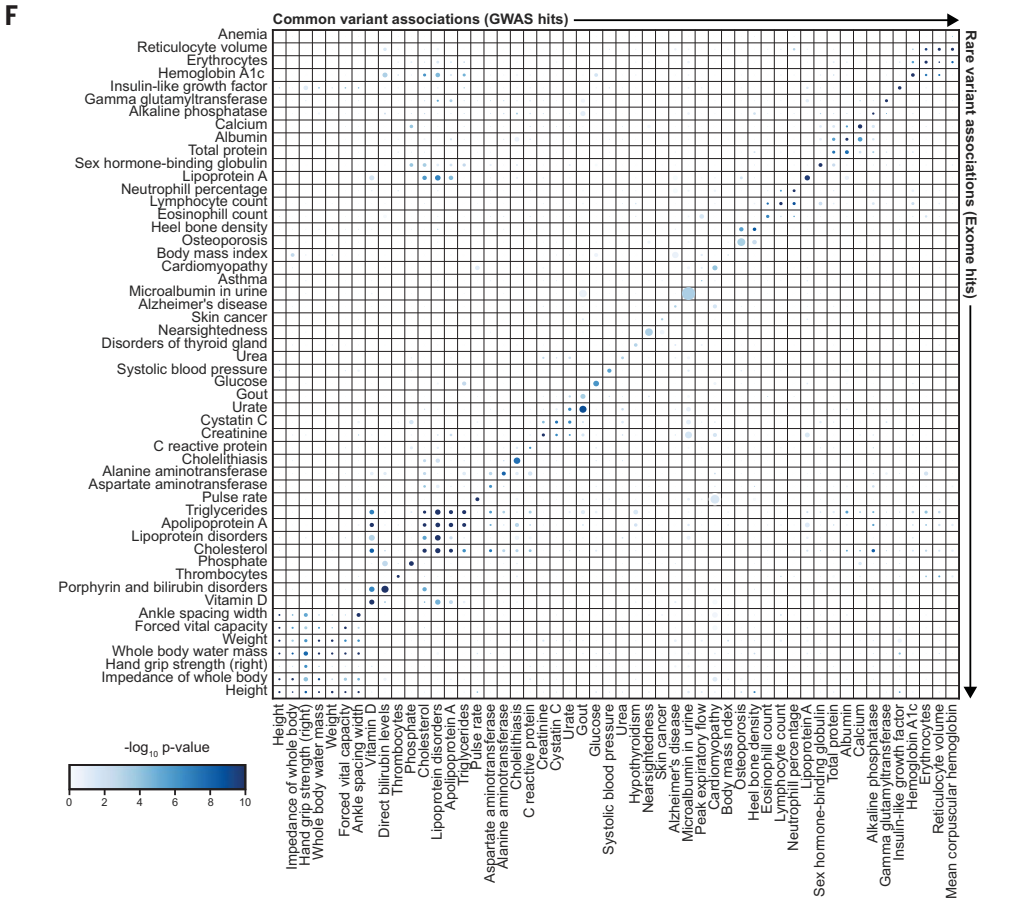


Fig. 4. Forecasting the growth of rare-variant associations with increasing cohort size. (**A**) Number of significant (FDR <0.05) genes identified per phenotype with rare-variant burden tests as a function of the discovery cohort size in thousands of individuals. Missense prioritization with PrimateAI-3D substantially increased the number of genes detected at all cohort sizes. Dots and bars represent mean ± standard error. (**B**) Number of rare deleterious variants identified per individual as a function of the discovery cohort size. (**C**) Average per-variant absolute effect size for newly associated genes (FDR < 0.05) at each discovery cohort size. The fit from the regression $y = a/x + b$ is shown. Dots and error bars represent mean ± standard error. (**D**) Rare-variant PRS performance increases with increasing discovery cohort size. Median correlation between the PRSs and the phenotype is shown on the *y* axis. The number of genes included in the PRS is represented by the size of each point. (**E**) Venn diagram showing the overlap of rare-variant genes with common-variant GWAS loci as a function of discovery cohort size. (**F**) A nonsymmetrical heatmap showing the phenotype-specific overlap of common- and rare-variant associations. Each point shows the statistical significance of the overlap between common-variant GWAS genes associated with the *x* axis phenotype and rare-variant genes associated with the *y* axis phenotype. The size of the points represents the magnitude of the enrichment, whereas the color represents the *P* value. (**G**) Percentage of unambiguously mapped GWAS genes with rare-variant associations (nominal *P* value ≤ 0.05) stratified by GWAS significance thresholds. Results are shown for all genes (orange) and after excluding genes that are less likely to show rare-variant signal (purple) because of short length (<2 kb coding sequence) or strong selective constraint (pLI > 0.99, probability of being loss-of-function intolerant). High-confidence coding hits are defined as having a lead variant with GWAS *P* value < 10^{-100} with strong linkage disequilibrium ($r^2 \geq 0.9$) to a coding variant in the associated gene. The dashed line represents the background FDR.

model to significantly improve the identification of individuals from the general population who are at increased risk for common diseases.

Although the rare-variant PRS models presented in this work show promise for accurate identification of high-risk individuals across diverse human populations, our study has several limitations. At present, rare-variant PRS models have limited power; we are only capable of robustly estimating variant effects for well-powered genes, finding 217 GWAS loci but only 34 rare-variant genes on average per trait. We empirically forecast that the exact causal genes underlying most of these GWAS loci will be uncovered by rare-variant studies with larger cohort sizes and advances in variant interpretation algorithms (*60*). Second, although interpretation of variants of uncertain significance remains a challenge, recent advances that apply deep learning (*12*, *61*), high-throughput experimental assays (*62*), and variant information from closely related primate species (*63*) have each demonstrated promise toward solving variant interpretation on a genome-wide scale. Third, although we observed improved portability across ancestries for rare-variant polygenic prediction, more

accurate allele frequency resources for global populations will further shrink the discrepancies in performance across populations. Indeed, systematic efforts to catalog rare variation in non-European populations are ongoing (*64, 65*) and will likely precede well-powered common-variant GWAS studies in diverse global populations (*66*). Finally, although we only evaluated rare-coding or splice-altering variants, improved noncoding variant prediction coupled with larger sample sizes would likely reveal the pervasive phenotypic impacts of rare penetrant variants in each person, with transformative implications for the utility of clinical whole-genome sequencing in the general population.

Methods summary

Datasets

We analyzed data from unrelated individuals in the UK Biobank, all of whom had genotypes obtained from microarrays and 454,712 of whom had genotypes available from exome sequencing. The work described in this manuscript was approved by the UK Biobank under application no. 33751. In addition, we performed validation experiments with 20,708 individuals from the MGB Biobank.

Phenotype processing

Quantitative traits were standardized by inverse rank normal-transformation and adjusted for medication usage and further covariates including age, sex, ancestry, diet, and others. Binary traits were adjusted for age, age^2, sex, age × sex, age^2 × sex and ancestry.

Common-variant associations

GWAS were performed with common variants (AF > 1%) in individuals of European ancestry in the UK Biobank and causal gene sets were derived by linkage disequilibrium between independent GWAS significant variants ($P < 5 \times 10^{-8}$) and coding variants, splicing variants or expression quantitative trait loci (eQTLs) in nearby genes or by proximity with local transcription start sites.

Rare-variant associations

Burden tests were performed with rare variants (AF < 0.1%) on individuals from all ethnicities by searching for combinations of allele frequencies and missense pathogenicity scores per gene and further calibrating via permutations to maximize significance prior to FDR correction. Significant gene-phenotype pairs were reported at 5% FDR after correction for multiple hypothesis testing across all autosomal protein coding genes in the human genome and across all tested traits. Rare-variant results generated in this study were compared with results from a recent well-powered rare-variant analysis in the UK Biobank (*17*) by examining the overlap of significant genes, along with the enrichment of GWAS and clinically relevant genes. Multiple missense classifiers were considered for pathogenicity prediction in the burden tests, including BayesDel (*67*), CADD (*68*), ClinPred (*69*), DEOGEN2, EVE* (*61*), FATHMM-XF (*70*), M-CAP (*71*), MetaLR (*72*), MetaSVM (*72*), MutationAssessor (*73*), Polyphen-2 (*74*), PrimateAI-3D (*12*), PROVEAN (*75*), REVEL (*76*), SIFT (*77*), and VEST4 (*78*). Scores for the EVE-style variational autoencoder (EVE*) were generated by reimplementing the method. The different classifiers were compared via Spearman correlation with the average phenotype values of the carriers of each qualifying missense variant in high-confidence associated gene-phenotype pairs.

Polygenic risk scores

PRS models were constructed from GWAS and burden test results from training datasets. Common-variant (AF >1%) PRS models were constructed by applying the method of clumping and thresholding (*31*). By contrast, rare-variant PRS models were constructed by fitting linear models to each phenotype on the rare variants (AF < 0.1%) in significantly associated genes, weighted by predicted missense pathogenicity. A unified PRS model was also constructed, which summed the rare- and common-variant PRS models per individual. As with the burden test results, rare-variant PRS performance was evaluated using PrimateAI-3D and other classifiers across 78 traits. The overlap of individuals at phenotypic and PRS extremes was examined to further elucidate PRS performance. For two traits, HbA1c and LDL cholesterol, clinical risk prediction was assessed, since clinically diagnostic thresholds could distinguish cases from controls. PRS portability was assessed in two ways - first between cohorts, by applying models constructed in the UK Biobank to the MGB Biobank, and second between ancestries, by comparing the performance between different ancestry groups in the UK Biobank.

Forecasting analysis

Growth projections of rare- and common-variant associations, PRS performance, and overlap of significantly associated genes from rare and common variants were made from randomly down-sampled data ranging from 20% to 100% of the whole UK Biobank exome cohort with 20% increments. Full materials and methods are available in the supplementary materials (*16*).

REFERENCES AND NOTES

1. A. Buniello *et al*., The NHGRI-EBI GWAS Catalog of published genome-wide association studies, targeted arrays and summary statistics 2019. *Nucleic Acids Res.* **47**, D1005–D1012 (2019). doi: 10.1093/nar/gky1120; pmid: 30445434
2. T. A. Manolio *et al*., Finding the missing heritability of complex diseases. *Nature* **461**, 747–753 (2009). doi: 10.1038/nature08494; pmid: 19812666
3. Y. Ding *et al*., Large uncertainty in individual polygenic risk score estimation impacts PRS-based risk stratification. *Nat. Genet.* **54**, 30–39 (2022). doi: 10.1038/s41588-021-00961-5; pmid: 34931067
4. A. R. Martin *et al*., Clinical use of current polygenic risk scores may exacerbate health disparities. *Nat. Genet.* **51**, 584–591 (2019). doi: 10.1038/s41588-019-0379-x; pmid: 30926966
5. R. Henderson, M. O'Kane, V. McGilligan, S. Watterson, The genetics and screening of familial hypercholesterolaemia. *J. Biomed. Sci.* **23**, 39 (2016). doi: 10.1186/s12929-016-0256-1; pmid: 27084339
6. K. B. Kuchenbaecker *et al*., Risks of Breast, Ovarian, and Contralateral Breast Cancer for BRCA1 and BRCA2 Mutation Carriers. *JAMA* **317**, 2402–2416 (2017). doi: 10.1001/jama.2017.7112; pmid: 28632866
7. S. A. Cohen, C. C. Pritchard, G. P. Jarvik, Lynch Syndrome: From Screening to Diagnosis to Treatment in the Era of Modern Molecular Oncology. *Annu. Rev. Genomics Hum. Genet.* **20**, 293–307 (2019). doi: 10.1146/annurev-genom-083118-015406; pmid: 30848956
8. A. R. Kim *et al*., Functional Selectivity in Cytokine Signaling Revealed Through a Pathogenic EPO Mutation. *Cell* **168**, 1053–1064.e15 (2017). doi: 10.1016/j.cell.2017.02.026; pmid: 28283061
9. K. L. Smith, C. Isaacs, BRCA mutation testing in determining breast cancer therapy. *Cancer J.* **17**, 492–499 (2011). doi: 10.1097/PPO.0b013e318238f579; pmid: 22157293
10. M. Delvecchio, C. Pastore, P. Giordano, Treatment Options for MODY Patients: A Systematic Review of Literature. *Diabetes Ther.* **11**, 1667–1685 (2020). doi: 10.1007/s13300-020-00864-4; pmid: 32583173
11. K. J. Karczewski *et al*., The mutational constraint spectrum quantified from variation in 141,456 humans. *Nature* **581**, 434–443 (2020). doi: 10.1038/s41586-020-2308-7; pmid: 32461654
12. H. Gao *et al*., The landscape of tolerated genetic variation in humans and primates. *Science* **380**, eabn8197 (2023). doi: 10.1126/science.abn8197
13. C. Bycroft *et al*., The UK Biobank resource with deep phenotyping and genomic data. *Nature* **562**, 203–209 (2018). doi: 10.1038/s41586-018-0579-z; pmid: 30305743
14. D. Taliun *et al*., Sequencing of 53,831 diverse genomes from the NHLBI TOPMed Program. *Nature* **590**, 290–299 (2021). doi: 10.1038/s41586-021-03205-y; pmid: 33568819
15. J. C. Denny *et al*., The "All of Us" Research Program. *N. Engl. J. Med.* **381**, 668–676 (2019). doi: 10.1056/NEJMsr1809937; pmid: 31412182
16. See supplementary materials.
17. J. D. Backman *et al*., Exome sequencing and analysis of 454,787 UK Biobank participants. *Nature* **599**, 628–634 (2021). doi: 10.1038/s41586-021-04103-z; pmid: 34662886
18. J. Mbatchou *et al*., Computationally efficient whole-genome regression for quantitative and binary traits. *Nat. Genet.* **53**, 1097–1103 (2021). doi: 10.1038/s41588-021-00870-7; pmid: 34017140
19. J. L. Goldstein, M. S. Brown, Binding and degradation of low density lipoproteins by cultured human fibroblasts. Comparison of cells from a normal subject and from a patient with homozygous familial hypercholesterolemia. *J. Biol. Chem.* **249**, 5153–5162 (1974). doi: 10.1016/S0021-9258(19)42341-7; pmid: 4368448
20. M. S. Brown, J. L. Goldstein, Expression of the familial hypercholesterolemia gene in heterozygotes: Mechanism for a dominant disorder in man. *Science* **185**, 61–63 (1974). doi: 10.1126/science.185.4145.61; pmid: 4366052
21. M. S. Sabatine, PCSK9 inhibitors: Clinical evidence and implementation. *Nat. Rev. Cardiol.* **16**, 155–165 (2019). doi: 10.1038/s41569-018-0107-8; pmid: 30420622
22. S. M. Grundy *et al*., 2018 AHA/ACC/AACVPR/AAPA/ABC/ACPM/ADA/AGS/APhA/ASPC/NLA/PCNA Guideline on the Management of Blood Cholesterol: A Report of the American College of Cardiology/American Heart Association Task Force on Clinical Practice Guidelines. *Circulation* **139**, e1082–e1143 (2019). pmid: 30586774
23. American Diabetes Association, 2. Classification and Diagnosis of Diabetes: Standards of Medical Care in Diabetes—2019. *Diabetes Care* **42**, S13–S28 (2019). doi: 10.2337/dc19-S002; pmid: 30559228
24. C. C. Cowie, S. S. Casagrande, L. S. Geiss, "Prevalence and Incidence of Type 2 Diabetes and Prediabetes" in *Diabetes in America*, C. C. Cowie *et al*., Eds. (National Institutes of Health, ed. 3, 2018).
25. W. Fu *et al*., Analysis of 6,515 exomes reveals the recent origin of most human protein-coding variants. *Nature* **493**, 216–220 (2013). doi: 10.1038/nature11690; pmid: 23201682
26. G. V. Kryukov, L. A. Pennacchio, S. R. Sunyaev, Most rare missense alleles are deleterious in humans: Implications for

complex disease and association studies. *Am. J. Hum. Genet.* **80**, 727–739 (2007). doi: 10.1086/513473; pmid: 17357078
27. J. Zeng *et al*., Signatures of negative selection in the genetic architecture of human complex traits. *Nat. Genet.* **50**, 746–753 (2018). doi: 10.1038/s41588-018-0101-4; pmid: 29662166
28. A. P. Schoech *et al*., Quantification of frequency-dependent genetic architectures in 25 UK Biobank traits reveals action of negative selection. *Nat. Commun.* **10**, 790 (2019). doi: 10.1038/s41467-019-08424-6; pmid: 30770844
29. K. Jaganathan *et al*., Predicting Splicing from Primary Sequence with Deep Learning. *Cell* **176**, 535–548.e24 (2019). doi: 10.1016/j.cell.2018.12.015; pmid: 30661751
30. A. V. Khera *et al*., Genome-wide polygenic scores for common diseases identify individuals with risk equivalent to monogenic mutations. *Nat. Genet.* **50**, 1219–1224 (2018). doi: 10.1038/s41588-018-0183-z; pmid: 30104762
31. S. M. Purcell *et al*., Common polygenic variation contributes to risk of schizophrenia and bipolar disorder. *Nature* **460**, 748–752 (2009). doi: 10.1038/nature08185; pmid: 19571811
32. J. Luo, H. Yang, B.-L. Song, Mechanisms and regulation of cholesterol homeostasis. *Nat. Rev. Mol. Cell Biol.* **21**, 225–245 (2020). doi: 10.1038/s41580-019-0190-7; pmid: 31848472
33. K. E. Berge *et al*., Accumulation of dietary cholesterol in sitosterolemia caused by mutations in adjacent ABC transporters. *Science* **290**, 1771–1775 (2000). doi: 10.1126/science.290.5497.1771; pmid: 11099417
34. J. D. Horton, J. C. Cohen, H. H. Hobbs, Molecular biology of PCSK9: Its role in LDL metabolism. *Trends Biochem. Sci.* **32**, 71–77 (2007). doi: 10.1016/j.tibs.2006.12.008; pmid: 17215125
35. J. Behbodikhah *et al*., Apolipoprotein B and Cardiovascular Disease: Biomarker and Potential Therapeutic Target. *Metabolites* **11**, 690 (2021). doi: 10.3390/metabo11100690; pmid: 34677405
36. J. E. Nahon *et al*., Hematopoietic Stabilin-1 deficiency does not influence atherosclerosis susceptibility in LDL receptor knockout mice. *Atherosclerosis* **281**, 47–55 (2019). doi: 10.1016/j.atherosclerosis.2018.12.020; pmid: 30658191
37. J. J. P. Kastelein *et al*., ODYSSEY FH I and FH II: 78 week results with alirocumab treatment in 735 patients with heterozygous familial hypercholesterolaemia. *Eur. Heart J.* **36**, 2996–3003 (2015). doi: 10.1093/eurheartj/ehv370; pmid: 26330422
38. M. Van Heek *et al*.., In vivo metabolism-based discovery of a potent cholesterol absorption inhibitor, SCH58235, in the rat and rhesus monkey through the identification of the active metabolites of SCH48461. *J. Pharmacol. Exp. Ther.* **283**, 157–163 (1997). pmid: 9336320
39. D. J. Weiner, A. Nadig, K. A. Jagadeesh, K. K. Dey, B. M. Neale, E. B. Robinson, K. J. Karczewski, L. J. O'Connor, Polygenic architecture of rare coding variation across 400,000 exomes. medRxiv 2022.07.06.22277335 [Preprint] (2022) [cited 2023]. doi: 10.1101/2022.07.06.22277335
40. C. Marras *et al*., Prevalence of Parkinson's disease across North America. *NPJ Parkinsons Dis.* **4**, 21 (2018). doi: 10.1038/s41531-018-0058-0; pmid: 30003140
41. M. T. Wallin *et al*., The prevalence of MS in the United States: A population-based estimate using health claims data. *Neurology* **92**, e1029–e1040 (2019). doi: 10.1212/WNL.0000000000007035; pmid: 30770430
42. A. Gupta *et al*., Trends in acute myocardial infarction in young patients and differences by sex and race, 2001 to 2010. *J. Am. Coll. Cardiol.* **64**, 337–345 (2014). doi: 10.1016/j.jacc.2014.04.054; pmid: 25060366
43. J. M. Lawrence *et al*., Trends in Prevalence of Type 1 and Type 2 Diabetes in Children and Adolescents in the US, 2001-2017. *JAMA* **326**, 717–727 (2021). doi: 10.1001/jama.2021.11165; pmid: 34427600
44. A. V. Khera *et al*., Polygenic Prediction of Weight and Obesity Trajectories from Birth to Adulthood. *Cell* **177**, 587–596.e9 (2019). doi: 10.1016/j.cell.2019.03.028; pmid: 31002795
45. B. G. Nordestgaard *et al*., Familial hypercholesterolaemia is underdiagnosed and undertreated in the general population: guidance for clinicians to prevent coronary heart disease: consensus statement of the European Atherosclerosis Society. *Eur. Heart J.* **34**, 3478–3490 (2013). doi: 10.1093/eurheartj/eht273; pmid: 23956253
46. G. Thanabalasingham, K. R. Owen, Diagnosis and management of maturity onset diabetes of the young (MODY). *BMJ* **343** (oct19 3), d6044 (2011). doi: 10.1136/bmj.d6044; pmid: 22012810
47. A. Markham, Evinacumab: First Approval. *Drugs* **81**, 1101–1105 (2021). doi: 10.1007/s40265-021-01516-y; pmid: 34003472
48. D. Curtis, Polygenic risk score for schizophrenia is more strongly associated with ancestry than with schizophrenia. *Psychiatr. Genet.* **28**, 85–89 (2018). doi: 10.1097/YPG.0000000000000206; pmid: 30160659
49. C. Márquez-Luna, S. Gazal, P.-R. Loh, S. S. Kim, N. Furlotte, A. Auton, A. L. Price, 23andMe Research Team, LDpred-funct: incorporating functional priors improves polygenic prediction accuracy in UK Biobank and 23andMe data sets. bioRxiv 375337 [Preprint] (2018) [cited 2023]. doi: 10.1101/375337
50. E. W. Karlson, N. T. Boutin, A. G. Hoffnagle, N. L. Allen, Building the Partners HealthCare Biobank at Partners Personalized Medicine: Informed Consent, Return of Research Results, Recruitment Lessons and Operational Considerations. *J. Pers. Med.* **6**, 2 (2016). doi: 10.3390/jpm6010002; pmid: 26784234
51. E. M. Scott *et al*., Characterization of Greater Middle Eastern genetic variation for enhanced disease gene discovery. *Nat. Genet.* **48**, 1071–1076 (2016). doi: 10.1038/ng.3592; pmid: 27428751
52. N. Shah *et al*., Identification of Misclassified ClinVar Variants via Disease Population Prevalence. *Am. J. Hum. Genet.* **102**, 609–619 (2018). doi: 10.1016/j.ajhg.2018.02.019; pmid: 29625023
53. M. Lek *et al*., Analysis of protein-coding genetic variation in 60,706 humans. *Nature* **536**, 285–291 (2016). doi: 10.1038/nature19057; pmid: 27535533
54. B. Kaufman *et al*., Olaparib monotherapy in patients with advanced cancer and a germ-line BRCA1/2 mutation: An open-label phase II study. *J. Clin. Oncol.* **31** (15_suppl), 11024–11024 (2013). doi: 10.1200/jco.2013.31.15_suppl.11024
55. C. P. Cannon *et al*., Ezetimibe Added to Statin Therapy after Acute Coronary Syndromes. *N. Engl. J. Med.* **372**, 2387–2397 (2015). doi: 10.1056/NEJMoa1410489; pmid: 26039521
56. J. P. Evans, B. C. Powell, J. S. Berg, Finding the Rare Pathogenic Variants in a Human Genome. *JAMA* **317**, 1904–1905 (2017). doi: 10.1001/jama.2017.0432; pmid: 28492888
57. N. J. Schork, S. S. Murray, K. A. Frazer, E. J. Topol, Common vs. rare allele hypotheses for complex diseases. *Curr. Opin. Genet. Dev.* **19**, 212–219 (2009). doi: 10.1016/j.gde.2009.04.010; pmid: 19481926
58. H. Shi *et al*., Population-specific causal disease effect sizes in functionally important regions impacted by selection. *Nat. Commun.* **12**, 1098 (2021). doi: 10.1038/s41467-021-21286-1; pmid: 33597505
59. S. L. Spain, J. C. Barrett, Strategies for fine-mapping complex traits. *Hum. Mol. Genet.* **24** (R1), R111–R119 (2015). doi: 10.1093/hmg/ddv260; pmid: 26157023
60. P. M. Visscher *et al*., 10 Years of GWAS Discovery: Biology, Function, and Translation. *Am. J. Hum. Genet.* **101**, 5–22 (2017). doi: 10.1016/j.ajhg.2017.06.005; pmid: 28686856
61. J. Frazer *et al*., Disease variant prediction with deep generative models of evolutionary data. *Nature* **599**, 91–95 (2021). doi: 10.1038/s41586-021-04043-8; pmid: 34707284
62. G. M. Findlay *et al*., Accurate classification of BRCA1 variants with saturation genome editing. *Nature* **562**, 217–222 (2018). doi: 10.1038/s41586-018-0461-z; pmid: 30209399
63. L. Sundaram *et al*., Predicting the clinical impact of human mutation with deep neural networks. *Nat. Genet.* **50**, 1161–1170 (2018). doi: 10.1038/s41588-018-0167-z; pmid: 30038395
64. C. Rotimi *et al*., Enabling the genomic revolution in Africa. *Science* **344**, 1346–1348 (2014). doi: 10.1126/science.1251546
65. J. D. Wall *et al*., The GenomeAsia 100K Project enables genetic discoveries across Asia. *Nature* **576**, 106–111 (2019). doi: 10.1038/s41586-019-1793-z; pmid: 31802016
66. M. C. Mills, C. Rahal, The GWAS Diversity Monitor tracks diversity by disease in real time. *Nat. Genet.* **52**, 242–243 (2020). doi: 10.1038/s41588-020-0580-y; pmid: 32139905
67. B.-J. Feng, PERCH: A Unified Framework for Disease Gene Prioritization. *Hum. Mutat.* **38**, 243–251 (2017). doi: 10.1002/humu.23158; pmid: 27995669
68. P. Rentzsch, M. Schubach, J. Shendure, M. Kircher, CADD-Splice-improving genome-wide variant effect prediction using deep learning-derived splice scores. *Genome Med.* **13**, 31 (2021). doi: 10.1186/s13073-021-00835-9; pmid: 33618777
69. N. Alirezaie, K. D. Kernohan, T. Hartley, J. Majewski, T. D. Hocking, ClinPred: Prediction Tool to Identify Disease-Relevant Nonsynonymous Single-Nucleotide Variants. *Am. J. Hum. Genet.* **103**, 474–483 (2018). doi: 10.1016/j.ajhg.2018.08.005; pmid: 30220433
70. M. F. Rogers *et al*., FATHMM-XF: Accurate prediction of pathogenic point mutations via extended features. *Bioinformatics* **34**, 511–513 (2018). doi: 10.1093/bioinformatics/btx536; pmid: 28968714
71. K. A. Jagadeesh *et al*., M-CAP eliminates a majority of variants of uncertain significance in clinical exomes at high sensitivity. *Nat. Genet.* **48**, 1581–1586 (2016). doi: 10.1038/ng.3703; pmid: 27776117
72. C. Dong *et al*., Comparison and integration of deleteriousness prediction methods for nonsynonymous SNVs in whole exome sequencing studies. *Hum. Mol. Genet.* **24**, 2125–2137 (2015). doi: 10.1093/hmg/ddu733; pmid: 25552646
73. B. Reva, Y. Antipin, C. Sander, Predicting the functional impact of protein mutations: Application to cancer genomics. *Nucleic Acids Res.* **39**, e118–e118 (2011). doi: 10.1093/nar/gkr407; pmid: 21727090
74. I. A. Adzhubei *et al*., A method and server for predicting damaging missense mutations. *Nat. Methods* **7**, 248–249 (2010). doi: 10.1038/nmeth0410-248; pmid: 20354512
75. Y. Choi, G. E. Sims, S. Murphy, J. R. Miller, A. P. Chan, Predicting the functional effect of amino acid substitutions and indels. *PLOS ONE* **7**, e46688 (2012). doi: 10.1371/journal.pone.0046688; pmid: 23056405
76. N. M. Ioannidis *et al*., REVEL: An Ensemble Method for Predicting the Pathogenicity of Rare Missense Variants. *Am. J. Hum. Genet.* **99**, 877–885 (2016). doi: 10.1016/j.ajhg.2016.08.016; pmid: 27666373
77. N.-L. Sim *et al*., SIFT web server: Predicting effects of amino acid substitutions on proteins. *Nucleic Acids Res.* **40** (W1), W452-7 (2012). doi: 10.1093/nar/gks539; pmid: 22689647
78. H. Carter, C. Douville, P. D. Stenson, D. N. Cooper, R. Karchin, Identifying Mendelian disease genes with the variant effect scoring tool. *BMC Genomics* **14** (Suppl 3), S3 (2013). doi: 10.1186/1471-2164-14-S3-S3; pmid: 23819870
79. P. Fiziev, Burden tests and rare variant analyses, Zenodo (2023); https://doi.org/10.5281/zenodo.7738728.
80. J. McRae, Rare variant polygenic risk score, Zenodo (2023); https://doi.org/10.5281/zenodo.7738720.

ACKNOWLEDGMENTS

We thank D. MacArthur, J. Pritchard, M. Rivas, N. Ersaro, and I. Mitra for helpful discussions, and the participants and investigators in the UK Biobank (Resource Application Number 33751) and MGB studies (protocol 2018P001236) who made this work possible. **Funding:** T.M.B. is supported by funding from the European Research Council (ERC) under the European Union's Horizon 2020 research and innovation programme (grant agreement no. 864203), PID2021-126004NB-100 (MICIIN/FEDER, UE) and Secretaria d'Universitats i Recerca, and CERCA Programme del Departament d'Economia i Coneixement de la Generalitat de Catalunya (GRC 2021 SGR 00177). **Author contributions:** P.P.F., J.M., J.C.U., J.S.D., T.H., Y.Y., P.W., Z.N., J.G.S., H.G., A.M., D.C., F.A., M.F., Y.F, and K.K.-H.F. performed the analysis and wrote the manuscript. J.R., T.M.B., H.L.R., A.O.L., A.V.K., and K.F. supervised the work. **Competing interests:** H.L.R. receives funding from Illumina, Inc. and Microsoft Corporation to support rare disease gene discovery and diagnosis. A.V.K. is an employee of Verve Therapeutics, Inc., has served as a scientific advisor to Amgen Inc., Novartis AG, Silence Therapeutics PLC, Korro Bio, Inc., Veritas International SL, Color Health, Inc., Third Rock Ventures, Illumina Inc., Ambry Genetics Corporation, and Foresite Labs. A.V.K. holds equity in Verve Therapeutics, Inc., Color Health, Inc., and Foresite Labs. Employees of Illumina, Inc. are indicated in the list of author affiliations. Patents related to this work are (i) "Covariate correction including drug use from temporal data"; filing no. 63/351317; P. Fiziev, J. McRae, and K.-H. Farh; (ii) "Optimized burden test based on nested *t* tests that maximize separation between carriers and non-carriers"; filing no. 63/351283; P. Fiziev, J. McRae, and K.-H. Farh; (iii) "Rare variant polygenic risk scores"; filing no. 63/351299; P. Fiziev, J. McRae, and K.-H. Farh; and (iv) "Transformer language model for variant pathogenicity"; filing no. US 17/975,536 and US 17/975,547; J. Ede, T. Hamp, A. Dietrich, Y. Wu, and K.-H. Farh. **Data and materials availability:** PrimateAI-3D prediction scores are available with a non-commercial license upon request and are displayed at https://primad.basespace.illumina.com. Source code is available at https://github.com/Illumina/PrimateAI-3D, with archived versions of the rare variant burden test and polygenic score at (*79*) and (*80*). **License information:** Copyright © 2023 the authors, some rights reserved; exclusive licensee American Association for the Advancement of Science. No claim to original US government works. https://www.science.org/about/science-licenses-journal-article-reuse

SUPPLEMENTARY MATERIALS

science.org/doi/10.1126/science.abo1131
Materials and Methods
Figs. S1 to S16
Tables S1 to S12
References (*81*–*89*)

View/request a protocol for this paper from *Bio-protocol*.

Submitted 14 January 2022; resubmitted 18 January 2023
Accepted 16 March 2023
10.1126/science.abo1131

EDITORIAL

It matters who does science

Scientific research is a social process that occurs over time with many minds contributing. But the public has been taught that scientific insight occurs when old white guys with facial hair get hit on the head with an apple or go running out of bathtubs shouting "Eureka!" That's not how it works, and it never has been. Rather, scientists work in teams, and those teams share findings with other scientists who often disagree, and then make more refinements. Then those findings are placed in the scientific record for even more scientists to examine and produce further adjustments. Eventually, theories become knowledge. All along the way, these scientists are conspicuously and magnificently human—with all the assets and flaws that humans possess. And that means that who those individuals are, and the backgrounds they bring to their work, have a profound influence on the quality of the end result.

It has somehow become a controversial idea to acknowledge that scientists are actual people. For some, the notion that scientists are subject to human error and frailty weakens science in the public eye. But scientists shouldn't be afraid to acknowledge their humanity. Individual scientists are always going to make a mistake eventually, and the objective truth that they claim to be espousing is always going to be revised. When this happens, the public understandably loses trust. The solution to this problem is doing the hard work of explaining how scientific consensus is reached—and that this process corrects for the human errors in the long run.

> "...scientists shouldn't be afraid to acknowledge their humanity."

A raging debate has set in over whether the backgrounds and identities of scientists change the outcomes of research. One view is that objective truth is absolute and therefore not subject to human influences. "The science speaks for itself" is usually the mantra in this camp. But the history and philosophy of science argue strongly to the contrary. For example, Charles Darwin made major contributions to the most important idea in biology, but his book *The Descent of Man* contained many incorrect assertions about race and gender that reflected his adherence to prevalent social ideas of his time. Thankfully, evolution didn't become knowledge the day Darwin proposed it, and it was refined over the decades by many points of view. More recently, pulse oximeters that measure blood oxygen levels were found to be ineffective for dark skin because they were initially developed for white patients. These examples—and countless more in between—reveal how much work needs to be done to strengthen the scientific community and the public understanding of the process.

A monolithic group of scientists will bring many of the same preconceived notions to their work. But a group of many backgrounds will bring different points of view that decrease the chance that one prevailing set of views will bias the outcome. This means that scientific consensus can be reached faster and with greater reliability. It also means that the applications and implications will be more just for all. How is this a threat to scientific rigor and the merit of discoveries? Unfortunately, we're nowhere close to achieving these goals. Science has had enormous trouble building a workforce that reflects the public it serves. And now, numerous state governments are trying to make it more difficult, if not impossible, at the public universities in their states, and even within the scientific community, there are efforts to derail the idea that it matters who does science.

The soundbite "trust the science" has been circulating recently. This framing is unfortunate. Because "the science" in this context is usually a snapshot of ideas or facts in a particular moment—and often from the perspective of a small number of people (or even one person). It would have been better to use a phrase like "trust the scientific process," which would imply that science is what we know now, the product of the work of many people over time, and principles that have reached consensus in the scientific community through established processes of peer review and transparent disclosure.

Scientists should embrace their humanity rather than pretending that they are a bunch of automatons who instantly reach perfectly objective conclusions. That will be more work both in terms of ensuring that science represents that humanity and in explaining how it all works to the public. But in return, society will get better and more just science, and it will allow scientists to immerse themselves in the glorious, messy process of always striving for a greater understanding of the truth*.

–H. Holden Thorp



H. Holden Thorp
Editor-in-Chief,
Science journals.
hthorp@aaas.org;
@hholdenthorp

PHOTO: CAMERON DAVIDSON

*The text was previously posted as a blog at https://www.science.org/content/blog-post/it-matters-who-does-science.

10.1126/science.adi9021

NEWS



IN BRIEF

Edited by **Katie Langin**

WATER POLICY

U.S. wetland protections curtailed

In a decision that reduces federal protections for wetlands, the U.S. Supreme Court last week narrowed the definition of marshy areas covered by the Clean Water Act. A five-justice majority led by Justice Samuel Alito ruled the law applies only to wetlands that have a "continuous surface connection" to nearby regulated waters, rejecting an approach currently used by federal agencies that wetlands require only a "significant nexus." Four justices led by Justice Brett Kavanaugh argued the new standard is too narrow, ignores the law's intent to protect wetlands "adjacent" to waterways, and will undermine efforts to prevent pollution and habitat destruction. Researchers filed amicus briefs in favor of the current standard; some estimate the ruling will end federal regulation of some 18 million hectares of wetlands, or about half of the previously protected area. Many scientists blasted the decision, saying it ignores the complexity of wetland hydrology. President Joe Biden said it "defies the science."

Wetlands without a surface connection to other waters will lose protection.

Defining Long Covid

COVID-19 | A team of scientists says it has nailed down the major symptoms of Long Covid, a condition that has disabled millions of people who were infected with SARS-CoV-2. Analyzing reports from about 2000 people with Long Covid, as well as more than 7000 without—most of whom were also previously infected by the coronavirus—the researchers identified 12 key symptoms, including brain fog, postexertional fatigue, chest pain, and dizziness. Other studies have reported similar findings, but this one, which was published last week in *The Journal of the American Medical Association*, aims to develop a standardized definition and proposes a points system to help doctors accurately diagnose the syndrome. The work is part of RECOVER, a $1.15 billion Long Covid project funded by the U.S. National Institutes of Health.

UAE plans asteroid mission

PLANETARY SCIENCE | The United Arab Emirates (UAE) announced this week it will build a spacecraft to explore seven asteroids located between Mars and Jupiter. Scheduled to launch in 2028, this will be the UAE's second planetary mission, following the success of its Hope spacecraft, currently in orbit around Mars. The new spacecraft, the MBR Explorer—named after Dubai's ruler Sheikh Mohammed bin Rashid Al Maktoum—will end its tour in 2034 by deploying a small lander at Justitia, an odd reddish asteroid that may be covered in organic substances. The UAE is building the MBR Explorer in collaboration with planetary scientists at the University of Colorado Boulder.

WHO urges food fortification

HEALTH POLICY | The World Health Organization (WHO) adopted a resolution on 29 May urging member countries to fortify staple foods with folic acid to prevent conditions such as spina bifida, which is caused by a lack of the key vitamin in the first weeks of pregnancy. The resolution, which was adopted unanimously, noted that the benefits of folic acid fortification are backed by scientific evidence. Only 69 of WHO's 194 member

> “In this country, we know much more about fearing Black people than the fears of Black people.”
>
> **Stanford University social psychologist Jennifer Eberhardt** on NPR. Eberhardt and her colleagues published a study this week examining the fears of Black drivers who were stopped by the police in a U.S. city.

countries—including Australia, Canada, the United States, and Colombia—currently mandate folic acid fortification. The resolution also calls for countries to consider fortifying foods with iodine, zinc, calcium, iron, and vitamins A and D to prevent conditions such as anemia, blindness, and rickets.

X-rays probe lone atoms

MATERIALS SCIENCE | For a century, scientists have studied materials by measuring the x-rays they absorb. Now, researchers have applied absorption spectroscopy to individual atoms, they report this week in *Nature*. The team positioned a metal tip a few atoms wide less than 1 nanometer above organic molecules that contained iron and terbium atoms. Then they bathed the sample in x-rays, which excited the metals' electrons. When the tip was hovering directly over a metal atom, excited electrons popped from the atom to the tip while others flowed in from the gold surface below to replace them. By tracking how the flow of electrons varied with the x-rays' energy, the team determined the ionization state of the metal atoms and how they were bonded to other atoms in the molecules.

COVID-19 study under fire

RESEARCH INTEGRITY | A study on the effects of the malaria drug hydroxychloroquine and the antibiotic azithromycin in COVID-19 patients, led by the controversial French microbiologist Didier Raoult, is drawing criticism from medical groups. In an open letter published in *Le Monde* on 28 May, 16 French medical societies and research organizations slammed it as “the largest known unauthorized clinical trial to date” and urged authorities to take action. The 30,000 patient study prescribed drugs long after they had been shown to be ineffective and didn't adhere to regulations, critics wrote. French authorities say the study will be included in an ongoing investigation of research at the University Hospital Institute Méditerranée Infection, where Raoult served as director until stepping down in September 2022. Raoult denies that the study flouted regulations, saying it was a retrospective analysis of patient data, not a clinical trial.

Bad software doomed Moon probe

LUNAR SCIENCE | The crash of a Japanese lunar lander on 25 April resulted from a software glitch that miscalculated the craft's altitude, causing it to exhaust its fuel and fall roughly 5 kilometers to the surface of the Moon, the probe's developer announced last week. The Japanese company, called ispace, hoped its Hakuto-R Mission 1 would be the first successful commercial landing on the Moon. Company officials said the problem should be fixed in time to keep missions planned for 2024 and 2025 on schedule.

Gene-edited crops draw scrutiny

AGRICULTURE | The U.S. Environmental Protection Agency announced on 25 May that it will require companies to submit data on crops that have been gene edited to resist pests before they go to market. Until now, the agency required evaluation only of transgenic crops, containing genes from other organisms. Gene-edited crops will be exempt from a detailed review if the changes could have been achieved through conventional breeding. But the American Seed Trade Association says the extra paperwork will still be burdensome.

MARINE SCIENCE

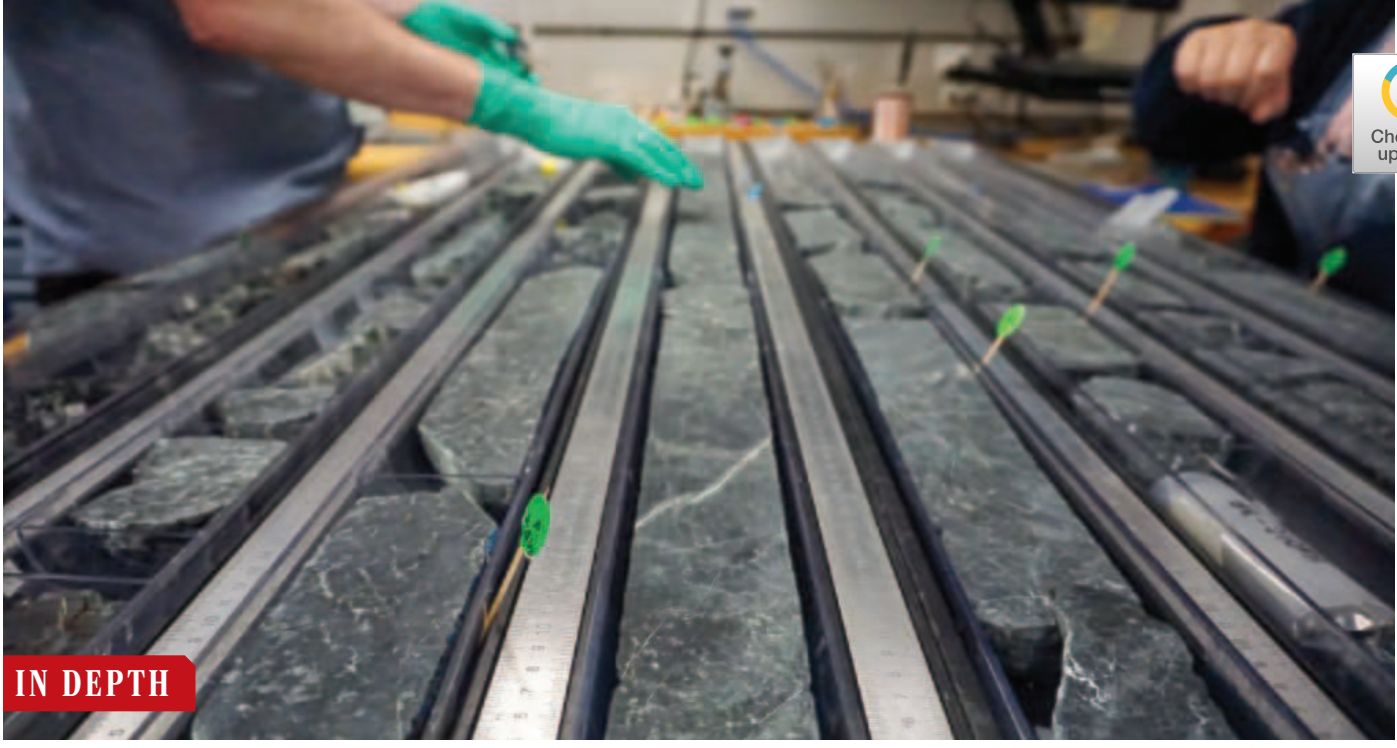
Biodiversity tallied as deep-sea mining looms

The Clarion-Clipperton Zone, a deep-sea region in the eastern Pacific Ocean that is twice the size of Argentina and is threatened by commercial mining, is home to more than 5000 benthic species, but only 436 have been fully described and named. Scientists reported the tally in *Current Biology* last week after analyzing 100,000 records of specimens collected during research cruises. Most of the unnamed species are crustaceans and marine worms. The zone is littered with naturally occurring polymetallic nodules, which contain nickel, cobalt, and other elements that are in high demand for electric vehicles. The International Seabed Authority has approved 17 mining exploration contracts in the region and expects to release regulations for deep-sea mining next month.



This anemone lives in a deep-sea region rich in valuable metals.

PHOTO: SMARTEX PROJECT/NATURAL ENVIRONMENT RESEARCH COUNCIL/SMARTEXCCZ.ORG



IN DEPTH

Researchers have collected an unprecedented amount of peridotite, a kind of mantle rock, from below the sea floor.

EARTH SCIENCE

Ocean drillers exhume a bounty of mantle rocks

Deep cores fulfill 60-year-old quest and could yield science bonanza

By **Paul Voosen**

In 1961, geologists off the Pacific coast of Mexico embarked on a daring journey to a foreign land—the planet's interior. From a ship, they aimed to drill through the thin veneer of Earth's crust and grab a sample of the mantle, the 2900-kilometer-thick layer of dense rock that fuels volcanic eruptions and makes up most of the planet's mass. The drill only got a couple hundred meters below the seabed before the project foundered under spiraling costs. But the quest—one of geology's holy grails—remained.

Researchers onboard the *JOIDES Resolution*, the flagship of the International Ocean Discovery Program (IODP), said last month that they have finally succeeded. Drilling below the seabed in the mid–Atlantic Ocean, they have collected a core of rock more than 1 kilometer long, consisting largely of peridotite, a kind of upper mantle rock. Although it's not clear how pristine and unaltered the samples are, it is certain the cylinders of gray-green rock present an unparalleled new record, says Susan Lang, a biogeochemist at the Woods Hole Oceanographic Institution and a co-lead of the cruise. "These are the types of rock we've been hoping to recover for a long time."

Researchers on land are eagerly following the ship's daily scientific logs as it continues to drill, says Jessica Warren, a mantle geochemist at the University of Delaware. "Getting down to this really fresh stuff has been a dream for decades and decades," she says. "We're finally going to see the Wizard of Oz."

The samples can help answer a host of questions, says Johan Lissenberg, an igneous petrologist from Cardiff University onboard the ship. They can provide direct evidence for how ocean crust differs in composition from the upper mantle and better estimates of elemental abundances in the planet's primary reservoir of rock. The samples of mantle will also help researchers understand how magma melts out of the mantle and rises through the crust to drive volcanism, Lissenberg says. "This could be a whole step forward for understanding magmatism—and the global composition of the bulk Earth."

The 1961 project, called Project Mohole, was the first of a handful of unsuccessful attempts to reach the mantle. It was named after the Mohorovičić discontinuity, or "Moho," a geophysical boundary defined by a sudden spike in the speed of seismic waves where the crust, a mélange of rocks crystallized out of mantle melt and altered by water, gives way to the more homogeneous mantle. The Moho lies some 35 kilometers below thick continental crust. But it is only about 7 kilometers below ocean crust. And it is shallower still at the drilling site of the *JOIDES Resolution* at the Mid-Atlantic Ridge, where the North American and Eurasian tectonic plates are being stretched apart, forcing the mantle upward.

Recovering a long mantle core was not the primary goal of the cruise, which is probing the Atlantis Massif, an underwater mountain, for clues to the origin of life. The massif rocks contain lots of olivine, a mineral that reacts with water in a process called serpentinization. The reactions generate hydrogen, which serves as an energy source for microbial life at the "Lost City," a nearby complex of ocean-bottom mineral chimneys deposited by gushers of superheated water.

It's long been theorized that life could have originated in such settings, which are rich in organic molecules. The cruise aimed to deepen a previously drilled 1.4-kilometer-deep hole, pushing to a depth too hot for life, where organic compounds that might have provided the raw material for the earliest life might lurk. But progress was slow.

So the ship returned to another site near Lost City, where shallow cores drilled in 2015 had found what appeared to be mantle rocks highly altered by seawater. After punching through a horizontal fault near the seabed, "the drilling just went so magi-

cally well," says Andrew McCaig, a geologist at the University of Leeds and the cruise's other chief scientist. The only hiccup came when the recovered peridotite rocks contained veins of asbestos, prompting increased safety protocols.

There's still some room for debate about whether the rocks are a true sample of the mantle, says Donna Blackman, a geophysicist at the University of California, Santa Cruz. The seismic speedup at the Moho is thought to reflect the lack of water or calcium and aluminum minerals in mantle rocks. Because the samples still show some influence of seawater, Blackman says she might classify them as deep crust. "But the petrology is interesting and special regardless," she says. And as the team continues drilling into deeper rocks, Lissenberg says, "They're getting fresher."

Indeed, it appears the team is already sampling mantle rock that has never melted into magma, which then cools and crystallizes into different kinds of crustal rocks, says Vincent Salters, a geochemist at Florida State University. By capturing the source rock, he says, researchers should be able to learn how magma melts, flows, and separates—clues to the workings of volcanoes worldwide.

The rocks could also answer other basic questions, such as how much the lavas collected at midocean ridges—which are often taken as a stand-in for the mantle—differ from the mantle itself, says James Day, a geochemist at the Scripps Institution of Oceanography. The abundance of radioactive elements in the rocks could improve estimates of how much heat the mantle produces as a whole, driving the deep convective motions that are the engine of plate tectonics. And their physical strength can inform studies of how earthquakes fracture and propagate in the upper mantle. The cores could also help clarify how well the mantle is mixed, reincorporating ingredients from the continental crust that is drawn back into Earth's interior at deep ocean trenches. "There's so much more to this than understanding a little piece of ocean floor," Day says.

Research on the rocks has already begun in labs onboard the *JOIDES Resolution*, and eventually the cores will be available at IODP repositories for all. But for all the excitement over the rock samples, the moment is bittersweet: The expedition may be one of the last for the ship. In March, the National Science Foundation (NSF) announced that, because of cost increases and a lack of a deal with its international collaborators, it will end its operating contract for the ship in September 2024.

The ship is in great condition and could continue until 2028, says Anthony Koppers, an associate vice president at Oregon State University and a leader in the IODP community. There's still a slim possibility that the U.S. Congress will fund an extension, he says. But NSF has no plan yet to develop a successor ship. And the other two big contributors to IODP, Europe and Japan, are moving on. This month, they announced the creation of IODP^3, a new global drilling program that will make heavy use of Japan's drill ship, the D/V *Chikyū*, which in the past has operated mostly in waters near Japan.

This was Lang's first cruise on the *JOIDES Resolution*, and she was astonished by the capabilities of its labs and the knowledge of its technical staff. The success they're having testifies to their decades of experience probing beneath the ocean floor, she says. "It's so unfortunate that something like this is going to be lost." ■



PHOTO: GABRIEL TAGLIARO/IODP

Drilling was conducted aboard the *JOIDES Resolution*, a U.S. ship slated to be retired next year.

SCIENCE POLICY

U.S. debt deal clouds funding hopes

Civilian programs take a back seat to defense in averting default

By **Jeffrey Mervis**

An agreement struck last weekend between President Joe Biden and House Speaker Kevin McCarthy (R–CA) to avoid a U.S. government default has reassured jittery financial markets. But its formula for holding federal spending flat for 2 years means science agencies will have to compete against all other civilian programs to win any increases from Congress.

Such a zero-sum game would mark a return to the rules under which Congress operated for a decade ending in 2021, which limited but did not halt growth in research spending. Some research advocates predict it will be hard to win any sizable increases for science given everything else the government must fund.

"I think we're looking at a status quo budget for FY [fiscal year] 2024," says Matthew Hourihan of the Federation of American Scientists. "And when you factor in inflation, that means a real cut for most programs."

The 27 May agreement would allow the U.S. government to continue to borrow money for its operations after 5 June, when it is expected to reach the current debt ceiling of $31.4 trillion. The deal strikes a compromise between Republican demands for deep, sustained cuts in federal spending in return for raising the ceiling and Biden's effort to protect federal programs. It would essentially hold the pot of money that funds all nondefense discretionary spending at its current level of $638 billion in FY 2024, which begins 1 October, rather than the 7% increase Biden has requested. Defense spending would match his request by growing 3%.

The 2024 number for civilian programs, although flat, allows for some new spending by including tens of billions of dollars appropriated this year but not yet used. The unspent funds include money to beef up tax collections and pay for COVID-19 pandemic relief. But Biden was able to protect $5 billion allocated for Project Next Gen, which

cally well," says Andrew McCaig, a geologist at the University of Leeds and the cruise's other chief scientist. The only hiccup came when the recovered peridotite rocks contained veins of asbestos, prompting increased safety protocols.

There's still some room for debate about whether the rocks are a true sample of the mantle, says Donna Blackman, a geophysicist at the University of California, Santa Cruz. The seismic speedup at the Moho is thought to reflect the lack of water or calcium and aluminum minerals in mantle rocks. Because the samples still show some influence of seawater, Blackman says she might classify them as deep crust. "But the petrology is interesting and special regardless," she says. And as the team continues drilling into deeper rocks, Lissenberg says, "They're getting fresher."

Indeed, it appears the team is already sampling mantle rock that has never melted into magma, which then cools and crystallizes into different kinds of crustal rocks, says Vincent Salters, a geochemist at Florida State University. By capturing the source rock, he says, researchers should be able to learn how magma melts, flows, and separates—clues to the workings of volcanoes worldwide.

The rocks could also answer other basic questions, such as how much the lavas collected at midocean ridges—which are often taken as a stand-in for the mantle—differ from the mantle itself, says James Day, a geochemist at the Scripps Institution of Oceanography. The abundance of radioactive elements in the rocks could improve estimates of how much heat the mantle produces as a whole, driving the deep convective motions that are the engine of plate tectonics. And their physical strength can inform studies of how earthquakes fracture and propagate in the upper mantle. The cores could also help clarify how well the mantle is mixed, reincorporating ingredients from the continental crust that is drawn back into Earth's interior at deep ocean trenches. "There's so much more to this than understanding a little piece of ocean floor," Day says.

Research on the rocks has already begun in labs onboard the *JOIDES Resolution*, and eventually the cores will be available at IODP repositories for all. But for all the excitement over the rock samples, the moment is bittersweet: The expedition may be one of the last for the ship. In March, the National Science Foundation (NSF) announced that, because of cost increases and a lack of a deal with its international collaborators, it will end its operating contract for the ship in September 2024.

The ship is in great condition and could continue until 2028, says Anthony Koppers, an associate vice president at Oregon State University and a leader in the IODP community. There's still a slim possibility that the U.S. Congress will fund an extension, he says. But NSF has no plan yet to develop a successor ship. And the other two big contributors to IODP, Europe and Japan, are moving on. This month, they announced the creation of IODP^3, a new global drilling program that will make heavy use of Japan's drill ship, the D/V *Chikyū*, which in the past has operated mostly in waters near Japan.

This was Lang's first cruise on the *JOIDES Resolution*, and she was astonished by the capabilities of its labs and the knowledge of its technical staff. The success they're having testifies to their decades of experience probing beneath the ocean floor, she says. "It's so unfortunate that something like this is going to be lost." ■



PHOTO: GABRIEL TAGLIARO/IODP

Drilling was conducted aboard the *JOIDES Resolution*, a U.S. ship slated to be retired next year.

SCIENCE POLICY

U.S. debt deal clouds funding hopes

Civilian programs take a back seat to defense in averting default

By **Jeffrey Mervis**

An agreement struck last weekend between President Joe Biden and House Speaker Kevin McCarthy (R–CA) to avoid a U.S. government default has reassured jittery financial markets. But its formula for holding federal spending flat for 2 years means science agencies will have to compete against all other civilian programs to win any increases from Congress.

Such a zero-sum game would mark a return to the rules under which Congress operated for a decade ending in 2021, which limited but did not halt growth in research spending. Some research advocates predict it will be hard to win any sizable increases for science given everything else the government must fund.

"I think we're looking at a status quo budget for FY [fiscal year] 2024," says Matthew Hourihan of the Federation of American Scientists. "And when you factor in inflation, that means a real cut for most programs."

The 27 May agreement would allow the U.S. government to continue to borrow money for its operations after 5 June, when it is expected to reach the current debt ceiling of $31.4 trillion. The deal strikes a compromise between Republican demands for deep, sustained cuts in federal spending in return for raising the ceiling and Biden's effort to protect federal programs. It would essentially hold the pot of money that funds all nondefense discretionary spending at its current level of $638 billion in FY 2024, which begins 1 October, rather than the 7% increase Biden has requested. Defense spending would match his request by growing 3%.

The 2024 number for civilian programs, although flat, allows for some new spending by including tens of billions of dollars appropriated this year but not yet used. The unspent funds include money to beef up tax collections and pay for COVID-19 pandemic relief. But Biden was able to protect $5 billion allocated for Project Next Gen, which



President Joe Biden (right) and House Speaker Kevin McCarthy (R–CA) negotiated a deal on the debt ceiling that could squeeze science spending.

will develop improved coronavirus vaccines and drugs.

The negotiators are presenting the agreement as a victory, but hard-liners in both parties are dismayed by their side's concessions. If approved by the House of Representatives and the Senate, the 99-page bill would delay imposing any new ceiling until January 2025, taking default off the political agenda until after the presidential election in November 2024.

For scientists, the real drama will occur this year, as Congress works out the details of government spending in FY 2024. Those negotiations will pit Biden's request for healthy increases at several federal research agencies against a push by Republicans, who control the House but not the Senate, to reverse 2 years of sizable growth in federal research budgets after the previous budget cap was lifted.

"It's in the hands of the appropriators now," says Jennifer Zeitzer of the Federation of American Societies for Experimental Biology, referring to the members sitting on the committee that writes spending bills for every federal agency. "Flat funding makes it more challenging, but it's too soon to say how much more."

Recent increases for research were part of the trillions of dollars in new government spending in laws passed by Congress since Biden took office in January 2021. The legislation includes landmark measures to rebuild the nation's infrastructure, bolster the U.S. semiconductor industry, and combat climate change.

This week's agreement would halt that rising tide. To boost research spending even modestly in FY 2024, Congress would have to reallocate some of what's been targeted for thousands of other discretionary, civilian programs across the government. (More than half of all federal spending goes to mandatory payouts such as Social Security, Medicare, and interest on federal borrowing, accounts that fall outside the annual allocation.)

Civilian and military spending would continue to be constrained in FY 2025, rising by only 1% over 2024 levels. (Republicans had initially sought to impose a decade's worth of tight caps before settling for 2 years.) The agreement also contains a clause requiring a 1% cut in overall discretionary spending if Congress misses its 1 October deadline to pass a full-year budget and temporarily freezes spending. That penalty would be removed, however, if Congress later passes a more detailed spending plan in either year.

Science agencies with the most ambitious plans have the most to lose from the proposed 2-year spending restrictions. For example, Biden's 2024 budget request to Congress, submitted in March, includes a 19% increase, to $11.3 billion, for the National Science Foundation (NSF).

A high priority is NSF's new technology directorate, designed to translate basic research findings into new technologies and businesses. Congress itself had aimed even higher, adopting a 5-year spending blueprint for NSF in the 2022 CHIPS and Science Act to strengthen the U.S. semiconductor industry and related fields that would have allowed NSF's budget to reach $15.6 billion in 2024.

"A flat 2024 budget leaves a 2-year, $7 billion gap with CHIPS," Hourihan notes. "Those levels were always aspirational, but under the new agreement we're barely trying."

Biomedical researchers are also worried about the impact of a flat budget. They were hoping to do much better than the 2% increase ($920 million) Biden requested in 2024 for the National Institutes of Health (NIH), half of which would go to the National Cancer Institute.

"That was a terrible number, and we've been making the case this spring for a bigger increase," Zeitzer says. Biden is also seeking $1 billion more for the new Advanced Research Projects Agency for Health, which this year received $1.5 billion.

The Department of Energy's science programs are slated for big increases under the CHIPS act, with Biden's 2024 request for an 8% increase as a down payment. But energy lobbyists say winning that $680 million boost, which included a large hike for industry partnerships to accelerate progress in fusion energy, will now be a stretch.

Several of NASA's science missions also need a big increase to stay on course. So a tight budget could trigger a political fight pitting the Biden administration's priorities on climate missions against congressional support for planetary exploration. A flat NASA science budget could result in delays to one or more missions.

As *Science* went to press, Congress was expected to vote on the agreement with the House going first as early as 31 May. Legislators hoped to pass the measure in time to avert a default.

Once the agreement is in place, science advocates say the time to press their case will come after Congress divvies up the total amount available for discretionary spending among the 12 appropriations subcommittees, a step that could happen before the 4 July recess.

"Once we see those numbers, we'll have a much clearer picture of what FY 2024 will look like," Zeitzer says. "So I think it's still possible for NIH to do much better." ■

BIOMEDICINE

NIH cracks down on clinical trials reporting

Agency says it has brought more than 200 investigators into compliance since July 2022

By **Meredith Wadman**

Last year, the U.S. National Institutes of Health (NIH) delivered a stern warning to two in-house clinical researchers who had broken an important rule. They had failed to submit the results of two clinical trials they had overseen to ClinicalTrials.gov, a database meant to inform the public about human studies and their results. The reporting requirement has often been ignored, but this time the agency took an unprecedented step: It told the scientists it wouldn't approve any more of their research until they fell in line.

After that warning and other agency actions, the pair complied, well after the 1-year deadline.

The episode, described in a Government Accountability Office (GAO) report published in April, adds to other, systematic changes NIH has recently undertaken to ensure that the more than $6 billion in clinical trials it funds annually, along with their results, are visible to scientists, physicians, patients, and ultimately taxpayers. Transparency advocates say the tougher stance is beginning to pay off. For example, GAO reported that between July and November 2022, the agency brought 235 extramural researchers into compliance with registration and reporting requirements.

"We really do like some of the changes that the NIH has made. We think that that's a really great start," says Navya Dasari, a lawyer who until recently headed efforts by the nonprofit activist group Universities Allied for Essential Medicines to increase transparency of clinical trial results. Candice Wright, lead author of the GAO report, says NIH "should be ensuring compliance [with the policy]. It exists for a reason."

Under a 2007 law, sponsors running many clinical trials of drugs and devices—including those funded by NIH—are required to register them on ClinicalTrials.gov within 21 days of enrolling the first volunteer. The results generally must be submitted to ClinicalTrials.gov within 1 year of when key data are collected on the last participant. The law directs NIH to shut down funding to any institution whose researchers are not up to date.

But NIH has done little to enforce the requirements, even after it put in place a new policy in 2017 that expanded them to cover all NIH-funded trials and media reports began to throw a spotlight on problems.

As recently as August 2022, the U.S. Department of Health and Human Services's Office of the Inspector General found that just 35 of 72 NIH-funded clinical trials due to report their results in 2019 and 2020 had done so in a timely manner—and that 25 had not submitted them at all.

NIH has recently taken steps to bring those numbers up. They include having both the funding institute and the Office of Extramural Research contact tardy investigators to bring them into compliance. And GAO noted that extramural investigators are now required to show NIH proof of trial registration and results reporting before filing the annual progress reports necessary to receive their grant's next year of funding.



Many investigators at NIH's Clinical Center have been slow to post their trial results in a federal database.

Michael Lauer, NIH's extramural research chief, credited the agency's changes when he gave updated numbers for 530 extramural trials required to report results in 2020, 2021, and 2022. In a March blog post, he reported that fully 96% of these trials had reported results to ClinicalTrials.gov. Only 37% had met the 1-year deadline, however, and in 2022 the median for tardiness was 400 days.

"Clearly, we still need to improve, and we are committed to taking this challenge head on," Lauer wrote on the blog. "Moving forward, you will see increased communication from us and, if needed, enforcement actions to get us to where we need to be."

NIH's critics say the agency still needs to do more. The GAO report also found that 16% to 18% of trials are registered late—a number that did not budge from 2019 through 2022. (The numbers are worse for pediatric trials, a recent study reported.) The tardy performances included NIH's own institutes, led by the National Cancer Institute, where 81 trials were registered late in that period.

Deborah Zarin, who directed ClinicalTrials.gov from 2005 to 2018, argues that trial registration and results reporting is as important as getting a research volunteer's informed consent to participate in a study. "What if I told you that 18% of trials had not obtained informed consent? You'd probably be appalled," says Zarin, who is now at Harvard University and Brigham and Women's Hospital. She and others note that the information is needed for many reasons, from making sure two research groups don't repeat the same trial to revealing failed trials that often aren't published so others can steer away from those approaches.

Till Bruckner, a policy analyst who founded TranspariMED, a campaign aimed at ending evidence distortion in medicine, calls NIH's recent actions "an improvement."

But Bruckner thinks NIH should pull funding from entire institutions that have a track record of poor compliance with the requirements. "If NIH would just once crack down properly on institutions, not only on individuals, that would send such a strong signal that going forward, 95% of the problem would be solved." ■

PHOTO: NATIONAL INSTITUTES OF HEALTH



Researchers have used data that track the use of pesticides and other farm chemicals at the county level in a wide array of health and environmental studies.

ENVIRONMENTAL SCIENCE

Scientists protest changes to U.S. pesticide data

Move to reduce scope and frequency of U.S. Geological Survey database sparks concern

By **Virginia Gewin**

Last year, Alan Kolok, an ecotoxicologist at the University of Idaho, published a study that found the incidence of cancer in counties across 11 western U.S. states was correlated with the use of farm chemicals called fumigants, which kill soil pests. The fine-grained analysis was feasible, he says, because a U.S. government database made timely, county-level statistics on pesticide use publicly available.

Now, Kolok is one of many scientists concerned that changes to the National Pesticide Use Maps database will make it far less useful to scientists. Last month, he joined more than 250 researchers and dozens of public health and environmental groups in urging the U.S. Geological Survey (USGS), which oversees the database, to reconsider moves to reduce the number of chemicals it tracks and to release updates less frequently.

The agency says the changes are being driven, in part, by budget constraints and a desire to align the pesticide survey with its other research programs. But in an open letter to USGS, critics say the changes endanger a database that provides "vital information and tracks trends that are not available anywhere else."

The USGS data have played a role in more than 500 peer-reviewed studies, the letter notes, including highly cited works on the impact of pesticides on public health, water quality, and ecosystems. Instead of reducing the database's scope and frequency, the critics say USGS should be expanding it in order better track the estimated 540 million kilograms of pesticides used annually in the United States. "We need credible sources of data to be able to study and understand what this widespread pesticide use means to the health of people and the environment," the letter states.

At its height, the USGS database, which dates to 1992, tracked the shifting use of more than 400 chemicals to control insects, fungi, weeds, and other pests. Each year, the agency typically released preliminary maps documenting pesticide use 2 years prior. To make the maps, agency staff combined farm data on pesticide use on specific crops—purchased from Kynetec, a company based in the United Kingdom—with crop acreage data from the U.S. Department of Agriculture.

In recent years, however, USGS has narrowed its approach. The most recent data release, which covered 2018 and 2019, included only 72 compounds that USGS judged to be especially important because of their widespread use and toxicity. In a statement, the agency said the shorter list aligns the survey with "the list of pesticides that USGS routinely collects data on for water quality purposes."

On 25 May, the agency said there are no immediate plans to expand the list. It also

said that, from now on, it would not release the preliminary data every year. Instead, USGS expects to release its next full report, covering 2018 to 2022, in late 2024; reports will be published every 5 years starting in 2029. The schedule change could save the agency roughly $100,000 each year.

Many scientists aren't happy with those decisions. "This plan to just keep the program running on life support does not reflect how important it is," says Nathan Donley, a senior scientist at the nonprofit Center for Biological Diversity. Having to wait 5 years for data, he argues, will make it impossible for researchers to detect trends and potential problems early and address them quickly. The data are "basically just a history lesson at that point," he says. "What's the point … if you're going make it harder for the public to use the data in any meaningful way?"

Others say the agency should be tracking more pesticides, not fewer. "There are literally hundreds of active ingredients and thousands of products that are applied on croplands," notes Christy Morrissey, an ecotoxicologist at the University of Saskatchewan who studies pesticide impacts on birds and insects. Researchers say USGS should not only restore its original tracking list—which included antibiotics such as oxytetracycline and streptomycin—but also add any new farm chemicals approved by the Environmental Protection Agency (EPA). "The most widespread pollutants today aren't necessarily going to be the most widespread in 5 or 10 years," says Donley, who notes that EPA approves about five new products each year.

Some scientists also want USGS to restart efforts to track one of the fastest growing uses of pesticides: seed coatings that protect against, for example, plant diseases or nematodes. Kynetec stopped tracking chemicals used to coat seeds in 2014 because surveys were deemed too complicated to conduct accurately. One result is that researchers are now unable to track the full extent of neonicotinoids, controversial chemicals that have been linked to dwindling bee populations. (In January, researchers published a paper in the *Proceedings of the National Academy of Sciences* that relied on USGS data from 2008 to 2014, when it still included coated seeds. The study concluded that neonicotinoids had harmed populations of the western bumble bee.)

As *Science* went to press, neither USGS nor its parent agency, the Department of the Interior, had formally responded to the scientists' pleas. ■

Virginia Gewin is a journalist in Portland, Oregon.

GENETICS

Primate genomes offer new view of human health and our past

Sequencing efforts may also aid primate conservation

By **Elizabeth Pennisi**

Humans have long seen themselves mirrored in other primates, with apes' social behavior and cognitive abilities shedding light on our own. Now, two international teams have stared deeper into the mirror. By sequencing the genomes of more than 200 nonhuman primates, from palm-size mouse lemurs to 200-kilogram gorillas, they have come up with clues to human health and disease, and to the origin of our species.

The genomes and their analyses, reported this week in *Science* and *Science Advances*, represent a massive effort involving more than 100 researchers from about 20 countries who braved logistical challenges and bureaucratic gauntlets to collect blood samples from some 800 wild and captive primates. The resulting data show how knowing a primate's genetic diversity could improve the odds of saving highly endangered species.

But our own species could also benefit. One team used the genomes to train a machine learning tool that could assess whether human genetic variants are likely to cause disease. And both explored the complexity of primates' evolution, shedding light on our own. "This massive sample will ultimately spark new and unexpected research directly relevant to human origins," says Luis Darcy Verde Arregoitia, a mammalogist at the Mexico Institute of Ecology who was not involved with either group.

> **"This massive sample will ultimately spark new and unexpected research directly relevant to human origins."**
> **Luis Darcy Verde Arregoitia**, Mexico Institute of Ecology

The bigger of the two genome efforts was spearheaded not by a primatologist or evolutionary biologist, but a clinical geneticist at the DNA-sequencing company Illumina. For Kyle Farh, like many in medicine, the genomics revolution has been a source of frustration as well as hope. Human gene sequencing has turned up myriad variants of individual genes that might explain diseases or treatments. But human genetics alone often can't tell whether a variant is medically relevant.

Farh thought he could find more clarity by searching for analogous variants in other primate species. "We recognized that data from our own species was insufficient." After testing the idea with the primate genomes available several years ago, in 2019 he reached out to evolutionary geneticist Tomas Marques-Bonet from the Institute of Evolutionary Biology in Barcelona, Spain, and primate geneticist Jeffrey Rogers at Baylor College of Medicine with a proposal. If they could come up with blood samples from multiple members of many of the world's 500-plus primates, Illumina would help fund the DNA sequencing.

The ambition was staggering, say some scientists outside the project. "It takes an enormous amount of time, effort, and government permits to obtain genetic samples of wild pri mates," says Paul Garber, a biological anthropologist emeritus at the University of Illinois Urbana-Champaign. And it's even more difficult for species classified as threatened—which more than 60% of nonhuman primates are.

Undaunted, Marques-Bonet signed up researchers around the world. "It was an amazing opportunity to expand the scope of my research interests," recalls ecologist Jean Boubli, who grew up and worked in Brazil before setting up a U.K. lab at the University of Salford. He contributed samples for 77 South American species, most obtained during his 30 years of exploring and living in the Amazon, collaborating with local scientists, museums, and zoos.

Getting blood samples from anesthetized or restrained wild primates in zoos or captive breeding centers was often challenging, says another contributor, Govindhaswamy Umapathy. A conservation biologist at the Centre for Cellular and Molecular Biology, Umapathy traveled from state to state in India to lobby forest managers and local officials for access to

said that, from now on, it would not release the preliminary data every year. Instead, USGS expects to release its next full report, covering 2018 to 2022, in late 2024; reports will be published every 5 years starting in 2029. The schedule change could save the agency roughly $100,000 each year.

Many scientists aren't happy with those decisions. "This plan to just keep the program running on life support does not reflect how important it is," says Nathan Donley, a senior scientist at the nonprofit Center for Biological Diversity. Having to wait 5 years for data, he argues, will make it impossible for researchers to detect trends and potential problems early and address them quickly. The data are "basically just a history lesson at that point," he says. "What's the point … if you're going make it harder for the public to use the data in any meaningful way?"

Others say the agency should be tracking more pesticides, not fewer. "There are literally hundreds of active ingredients and thousands of products that are applied on croplands," notes Christy Morrissey, an ecotoxicologist at the University of Saskatchewan who studies pesticide impacts on birds and insects. Researchers say USGS should not only restore its original tracking list—which included antibiotics such as oxytetracycline and streptomycin—but also add any new farm chemicals approved by the Environmental Protection Agency (EPA). "The most widespread pollutants today aren't necessarily going to be the most widespread in 5 or 10 years," says Donley, who notes that EPA approves about five new products each year.

Some scientists also want USGS to restart efforts to track one of the fastest growing uses of pesticides: seed coatings that protect against, for example, plant diseases or nematodes. Kynetec stopped tracking chemicals used to coat seeds in 2014 because surveys were deemed too complicated to conduct accurately. One result is that researchers are now unable to track the full extent of neonicotinoids, controversial chemicals that have been linked to dwindling bee populations. (In January, researchers published a paper in the *Proceedings of the National Academy of Sciences* that relied on USGS data from 2008 to 2014, when it still included coated seeds. The study concluded that neonicotinoids had harmed populations of the western bumble bee.)

As *Science* went to press, neither USGS nor its parent agency, the Department of the Interior, had formally responded to the scientists' pleas. ■

Virginia Gewin is a journalist in Portland, Oregon.

GENETICS

Primate genomes offer new view of human health and our past

Sequencing efforts may also aid primate conservation

By **Elizabeth Pennisi**

Humans have long seen themselves mirrored in other primates, with apes' social behavior and cognitive abilities shedding light on our own. Now, two international teams have stared deeper into the mirror. By sequencing the genomes of more than 200 nonhuman primates, from palm-size mouse lemurs to 200-kilogram gorillas, they have come up with clues to human health and disease, and to the origin of our species.

The genomes and their analyses, reported this week in *Science* and *Science Advances*, represent a massive effort involving more than 100 researchers from about 20 countries who braved logistical challenges and bureaucratic gauntlets to collect blood samples from some 800 wild and captive primates. The resulting data show how knowing a primate's genetic diversity could improve the odds of saving highly endangered species.

But our own species could also benefit. One team used the genomes to train a machine learning tool that could assess whether human genetic variants are likely to cause disease. And both explored the complexity of primates' evolution, shedding light on our own. "This massive sample will ultimately spark new and unexpected research directly relevant to human origins," says Luis Darcy Verde Arregoitia, a mammalogist at the Mexico Institute of Ecology who was not involved with either group.

> **"This massive sample will ultimately spark new and unexpected research directly relevant to human origins."**
> **Luis Darcy Verde Arregoitia**, Mexico Institute of Ecology

The bigger of the two genome efforts was spearheaded not by a primatologist or evolutionary biologist, but a clinical geneticist at the DNA-sequencing company Illumina. For Kyle Farh, like many in medicine, the genomics revolution has been a source of frustration as well as hope. Human gene sequencing has turned up myriad variants of individual genes that might explain diseases or treatments. But human genetics alone often can't tell whether a variant is medically relevant.

Farh thought he could find more clarity by searching for analogous variants in other primate species. "We recognized that data from our own species was insufficient." After testing the idea with the primate genomes available several years ago, in 2019 he reached out to evolutionary geneticist Tomas Marques-Bonet from the Institute of Evolutionary Biology in Barcelona, Spain, and primate geneticist Jeffrey Rogers at Baylor College of Medicine with a proposal. If they could come up with blood samples from multiple members of many of the world's 500-plus primates, Illumina would help fund the DNA sequencing.

The ambition was staggering, say some scientists outside the project. "It takes an enormous amount of time, effort, and government permits to obtain genetic samples of wild pri mates," says Paul Garber, a biological anthropologist emeritus at the University of Illinois Urbana-Champaign. And it's even more difficult for species classified as threatened—which more than 60% of nonhuman primates are.

Undaunted, Marques-Bonet signed up researchers around the world. "It was an amazing opportunity to expand the scope of my research interests," recalls ecologist Jean Boubli, who grew up and worked in Brazil before setting up a U.K. lab at the University of Salford. He contributed samples for 77 South American species, most obtained during his 30 years of exploring and living in the Amazon, collaborating with local scientists, museums, and zoos.

Getting blood samples from anesthetized or restrained wild primates in zoos or captive breeding centers was often challenging, says another contributor, Govindhaswamy Umapathy. A conservation biologist at the Centre for Cellular and Molecular Biology, Umapathy traveled from state to state in India to lobby forest managers and local officials for access to

gibbons, lorises, macaques, and lemurs.

Led by Marques-Bonet's postdoc Lukas Kuderna, now at Illumina, the consortium sequenced 703 individuals of 211 species using "short-read" technology in which DNA is first broken into small bits. The new data joined 106 already sequenced genomes from 29 additional primate species and a set of new genomes for 27 other primate species. Those genomes came from the second consortium, co-led by Dong-Dong Wu, a geneticist at the Chinese Academy of Sciences's Kunming Institute of Zoology, which used a technique that read longer stretches of DNA.

With their data and the other primate genomes, Wu and his colleagues honed the family tree for this group of mammals and identified unexpected genomic rearrangements—duplicated or inverted regions of chromosomes, for example—that distinguished primates living in different environments, such as tropical rainforest and semidesert. Further study may reveal whether the shuffling helped those species adapt to the various conditions.

The trove of primate genomes allowed Farh, Rogers, Marques-Bonet, and colleagues to go hunting for single nucleotide polymorphisms (SNPs), individual DNA base variations within or between species that may change the proteins encoded by genes or alter a gene's activity. They found 4.3 million that altered a protein's amino acid sequence. "The initial presentations took my breath away," recalls Amanda Melin, a biological anthropologist at the University of Calgary who provided samples of Costa Rican primates. "The scale of it was really staggering."

On the assumption that a human SNP with commonly observed counterparts in primates probably doesn't cause disease, Farh exonerated many human variants. His team also used the "benign" primate SNPs to train a neural network, called Primate AI-3D. With AlphaFold, a protein-structure prediction tool based on artificial intelligence (AI), as its scaffold, his program builds 3D models of each protein. Based on the benign SNPs, it identifies regions where changes to the protein's structure would not disrupt its function. Conversely, changes in other regions were more likely to cause problems.

He then applied the AI to predict the potential harm of human SNPs. And when he and colleagues matched those predictions with a database of human base changes that had been tentatively linked to diseases, they concluded 6% of the SNPs are likely innocent. "I was a bit skeptical" at first, says Kaitlin Samocha, a geneticist at Massachusetts General Hospital. But, "This resource is a great way to 'rule out' a variant as being damaging and does move the needle on our ability to interpret protein-altering variation."

The team also used the primate-trained AI to do the opposite: Identify harmful genes. They applied it to the health records and gene variant data of 454,712 people in the UK BioBank to find SNPs likely to play a role in 90 human health concerns. "It allows us to identify which genes are potential drug targets," Farh says.



Tarsiers like this one were among hundreds of primates whose DNA was sequenced.

Neil Risch, a geneticist at the University of California, San Francisco, says other researchers will need to vet the AI predictions. But he does think these primate genomes "are treasured samples."

Evolutionary biologists agree. Already the genomes have revealed an important role in evolution for hybridization, once thought to be rare. In one *Science* paper, Wu and his colleagues show that the critically endangered gray snub-nosed monkey, which is endemic to mountains in south-central China, arose after the golden snub-nosed monkey mated with the ancestors of two other species in that genus, *Rhinopithecus*. Moreover, one of the three groups of macaques arose through hybridization between the other two, about 3.5 million years ago, they report in *Science Advances*.

The other consortium, led by Rogers, also found signs of rampant hybridization in the DNA of 225 wild baboons from multiple species, which conservation biologist Julius Keyyu at the Tanzania Wildlife Research Institute helped obtain and analyze. "This work provides a potential analog to recent human evolution," notes Eleanor Scerri, an evolutionary archaeologist at the Max Planck Institute of Geo anthropology. Increasing evidence shows that intermingling once occurred among various hominids—Neanderthals, modern humans, Denisovans, and maybe others—tens of thousands of years ago.

The primates that are delivering these insights are themselves under threat from habitat destruction and other human activity. But a surprising finding from the studies could aid efforts to save them. Normally a population crash in a species also narrows its genetic diversity, thanks to inbreeding among the survivors. Yet all but 15 primate species sequenced by the team still had relatively high genetic diversity—higher than humans. That was true even in extremely endangered ones such as the northern sportive lemur (*Lepilemur septentrionalis*) of which only 40 are known to exist, all within 12 square kilometers of Madagascar.

This suggests the primates' population crashes, some likely caused by human habitat destruction, were so recent that there hasn't been time for inbreeding to lower the species' diversity. "The population declines are so rapid that genetics does not manage to catch up with it," says Katerina Guschanski, an evolutionary biologist at the University of Edinburgh and Uppsala University.

Umapathy and others say the finding is encouraging, because higher diversity should make species more resilient. As animal ecologist Fabiano Melo from Viçosa Federal University, who collaborates with Boubli, points out, "It means that we still have time to revert this situation." ■



The U.S. Geological Survey is funding mapping of metamorphic rocks in eastern Alaska that are likely to hold a number of critical minerals, including rare earths.

PHOTO: ADRIAN BENDER/U.S. GEOLOGICAL SURVEY

TREASURE HUNT

The first U.S. nationwide geological survey in a generation could reveal badly needed supplies of critical minerals

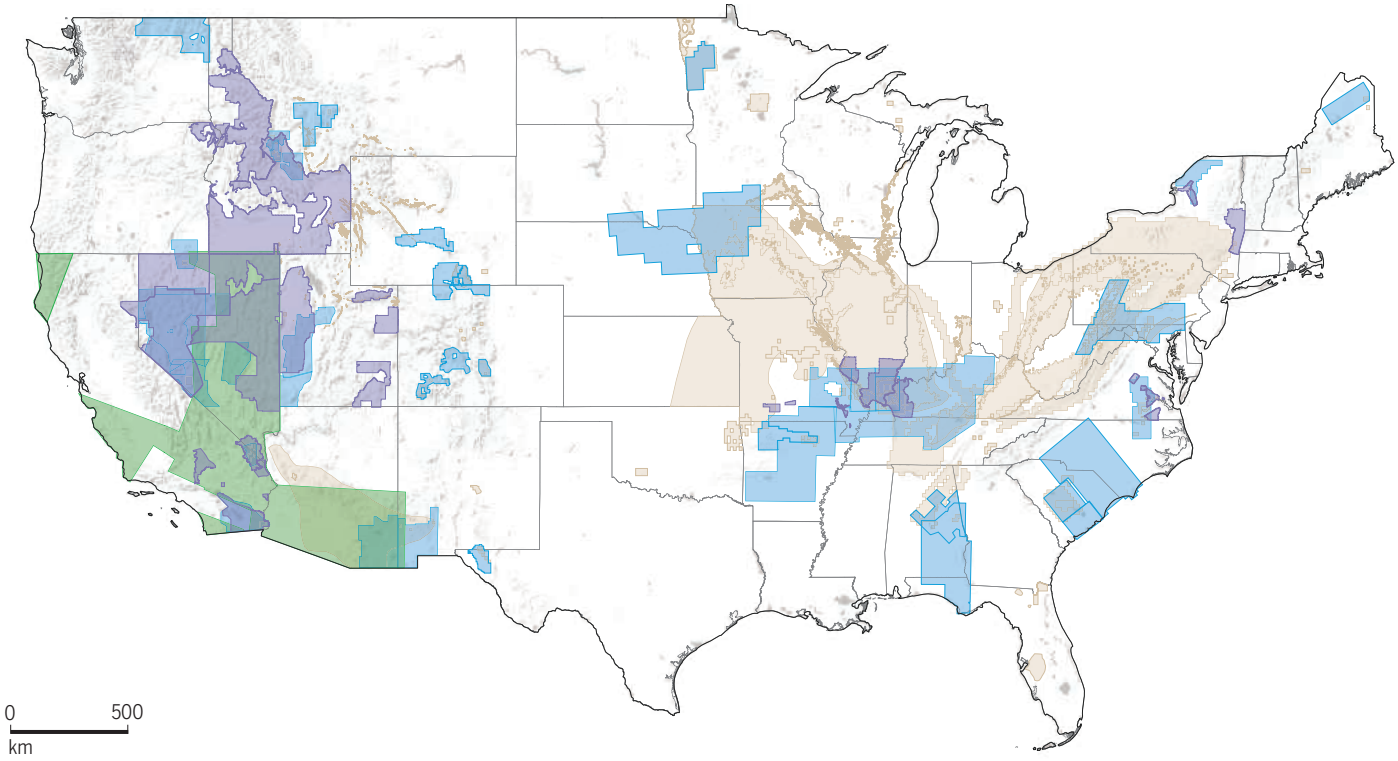
By **Paul Voosen**

From the air, Maine is a uniform sea of green: Forests cover 90% of the state. But beneath the foliage and the dirt lies an array of geological terrains that is far more diverse, built from the relics of volcanic islands that collided with North America hundreds of millions of years ago.

Two years ago, sensor-laden aircraft began to survey these geochemically rich terrains for precious minerals. Researchers spotted an anomalous signal streaming out of Pennington Mountain, 50 kilometers from the Canadian border. State geologists bushwhacked through the paper mill–bound pine forests, taking rock samples. They eventually uncovered deposits containing billions of dollars' worth of zirconium, niobium, and other elements that are critical in electronics, defense, and renewable energy technologies. "It was a perfect discovery," says John Slack, an emeritus scientist at the U.S. Geological Survey (USGS) who worked on the Maine find. He expects more like it.

Hunting high and low

Armed with a $320 million boost from Congress, the U.S. Geological Survey is funding airborne and field campaigns to identify rocks likely to hold minerals critical for renewable energy and electronics, like lithium and rare earth elements. The campaign, called the Earth Mapping Resources Initiative (Earth MRI), is the first major assessment of the country's mineral wealth in nearly half a century. It is deploying different techniques depending on the geology of each region.



Geophysics
Low-flying aircraft outfitted with magnetometers can survey iron-bearing rocks hidden in the shallow earth. Gamma ray spectrometers hunt for the radioactive signature of rare earth elements.

Lidar
Earth MRI is helping complete a high-resolution topographic map using airborne laser altimeters, or lidar. These data are essential for geological mapping and can reveal the surface expression of ancient landforms.

Hyperspectral
In the arid West, where trees don't block the view, flights using a NASA hyperspectral instrument will hunt for the signature of minerals in hundreds of channels of reflected light.

Ground-based
The agency is sponsoring field mapping campaigns by state geologists. It is also funding broader geochemical surveys and studies of mineral resources left in old mine waste piles.

"We think there's potential throughout the Appalachians."

Few topics draw more bipartisan support in Washington, D.C., than the need for the United States to find reliable sources of "critical minerals," a collection of 50 mined substances that now come mostly from other countries, including some that are unfriendly or unstable. The list, created by USGS at the direction of Congress, contains not only the 17 rare earth elements produced mostly in China, but also less exotic materials such as zinc, used to produce steel, and cobalt, used in electric car batteries. "These commodities are necessary for everything," says Sarah Ryker, USGS's associate director for energy and minerals. "They're also a flashpoint for conflict."

But last decade, when lawmakers began to ask USGS about U.S. supplies, the response was unsettling: The agency didn't even know where to look. For decades, companies had been moving mining operations abroad, in part to avoid relatively stringent U.S. environmental regulations. The basic exploration needed to identify mineral resources and spur corporate interest had languished. The last nationwide survey, a quest for uranium, ended in the 1980s. Ryker says the U.S. is "undermapped" compared with most developed countries, including Australia, Canada, and even Ireland. "We're at an embarrassing point."

To start filling in this knowledge void, USGS in 2019 began what it calls the Earth Mapping Resources Initiative, or Earth MRI. With a modest $10 million annual budget, the agency began working with state geological surveys to digitize data and commission fieldwork to map the most promising terrain in fine detail.

Then, in 2021, the Bipartisan Infrastructure Law directed $320 million into the program—nearly one-third of the entire USGS budget—to be spent over 5 years. That spending has already enabled hundreds of survey flights, and it is opening a golden age for economic geology. It is also a boon for basic science—filling in gaps in geologic history, identifying unknown earthquake faults, and revealing geothermal systems. "We're seeing a renaissance throughout the whole country," says Virginia McLemore, an economic geologist at the New Mexico Bureau of Geology and Mineral Resources. "I've been training all my life to get to this point."

The discoveries could spur a rash of mining, and environmentalists are wary. If USGS spots promising ore systems, companies will have to show that they can develop them safely and with minimal environmental impact, says Melissa Barbanell, director of U.S.-international engagement at the World Resources Institute, an environmental nonprofit. "It can never be zero harm," she says. "But how can we minimize the harm and keep it to the mine itself?"

Mining companies, meanwhile, are embracing Earth MRI. Donald Hicks, a geophysicist at global mining giant Rio Tinto, which has dozens of operations worldwide but only a few in the U.S., says he has encouraged fellow miners to collaborate and share data with the program. Rio Tinto even funded some USGS flights in Montana, in re-



In Nevada, a helicopter towing an induction coil measures subsurface electrical resistance (top left) and a researcher calibrates data collected by an airborne hyperspectral sensor (right). In Maine, geologists carry sensors to chart rocks' radioactivity (bottom left).

PHOTOS: (CLOCKWISE FROM TOP LEFT) BRETT ROBINSON/XCALIBUR MULTIPHYSICS VIA U.S. GEOLOGICAL SURVEY; USGS; ANJI SHAH/USGS

turn for 1 year's exclusive access to the data. "Having this high-quality, large-scale data in the public domain will drive new ideas and new discoveries," Hicks says.

FOR MOST OF THE HISTORY of mining, the origin story of a mineral lode was beside the point. Prospectors found it and miners dug it up. But by now, most of the obvious finds are gone, says Anne McCafferty, a USGS geophysicist. "The low-hanging fruit has been picked."

This scarcity has pushed Earth MRI into adopting a "mineral systems" approach, first pioneered in Australia, that attempts to predict where critical minerals might be found based on the processes that form them. For example, a search for rare earth minerals might begin by looking for an unusual kind of carbon-rich rock called a carbonatite, which often contains pockets of rare earths formed when it crystallized out of lava. Or geologists might seek out clay-rich rocks or sediments that can capture concentrations of the rare earths after water erodes them from a source rock. Prospectors would also look for signs that these ore rocks were preserved across the eons.

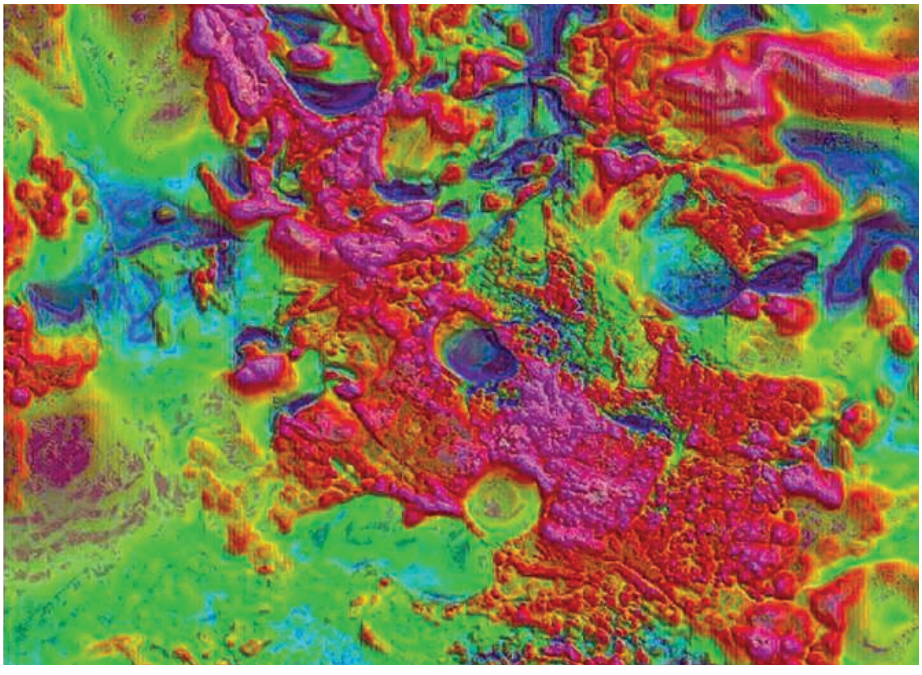
To assemble these telltale rock histories, USGS scientists need to integrate a variety of information sources. Some already exist: large-scale geological maps based on decades of fieldwork, and surveys of the deep structure of rock formations based on the reflections of seismic waves from artificial or natural earthquakes.

Earth MRI's airborne surveys, with flights just 100 meters above the surface, will add much more detail and inform a new generation of sharper geologic maps. One tool affixed to the aircraft is a magnetometer, which detects rocks rich in iron and other magnetic minerals—often a clue that they hold critical minerals. Another is a gamma ray spectrometer, which like a Geiger counter can capture the radiation emitted by thorium, uranium, and potassium. Those elements frequent the same volcanic rocks as rare earth minerals and are often incorporated into their crystal structures. Other aircraft carry laser altimeters that can map surface relief to reveal geologic history. And a pioneering "hyperspectral" instrument developed by NASA can identify minerals exposed on the surface based on the specific wavelengths of light they absorb. In the combined data, "You can see all the geology underneath," says Anjana Shah, the USGS geophysicist leading the agency's East Coast airborne surveys. "It's a very powerful way of understanding the Earth."

In early forays, Earth MRI aircraft crisscrossed North and South Carolina, tracing the ancient roots of the landscape. Hidden beneath the states' tobacco farms are fossilized beaches that mark shorelines left during the warm periods between past ice ages, when sea levels were higher than today. Laser altimeter maps capturing subtle relief bloom with those shorelines and the paleorivers that dissected them, says Kathleen Farrell, a geomorphologist at the North Carolina Geological Survey. "There's a lot more coastal plain than anyone thought."

The ancient beaches hold deposits of

black sands, eroded from mountains and deposited by rivers, that are rich in heavy elements. By combining the new airborne data collected by Shah with field mapping and boreholes drilled to sample the deep sediments, Farrell and her colleagues hope to learn how the Carolina sands originated. They want to know how the coastal plains were assembled over time, why the heavy sands formed only during certain periods, and where upriver those sands came from. The answers should help guide geologists to new heavy metal deposits; similar sites in northern Florida are among the few commercial sources of titanium in the U.S.



Magnetic anomalies (red) beneath southeastern Missouri reveal iron oxide deposits formed 1.4 billion years ago.

The airborne campaigns in South Carolina will have another benefit, Shah adds: They flew over Charleston, collecting magnetic data that, by identifying shifts and offsets in subsurface rocks, reveal the hidden seismic faults that ruptured in 1886 in an earthquake as large as magnitude 7. Such a quake, if it struck again today, would cause billions of dollars in damage.

This year, an Earth MRI survey covering parts of Missouri, Kentucky, Tennessee, Arkansas, Illinois, and Indiana will probe another mysterious seismic zone. Buried under kilometers of sediment lurks the Reelfoot Rift, a gash in the continent's bedrock likely created some 750 million years ago when the Rodinia supercontinent began to crack apart. In 1811 and 1812, faults tied to this rift caused the New Madrid earthquakes, the largest to ever strike the U.S. east of the Rocky Mountains. But despite the potential hazard, the fault zone remains poorly understood.

The Reelfoot and nearby bedrock deformations not only create hazards; they also create opportunities for minerals to form. The rifts provided conduits for magma to well up much later in geologic time, when Africa collided with North America to form the Appalachian Mountains. This magma is thought to have expelled gases that flowed into limestones, chemically altering them. One result is the fluorspar district of southern Illinois, which once produced a majority of the country's fluorite—used to smelt steel and create hydrofluoric acid.

Those magma injections could have played a role in creating Hicks Dome, which rises 1 kilometer above the Illinois countryside and is the closest thing the state has to a volcano. Jared Freiburg, critical minerals chief for the Illinois State Geological Survey, calls it "a crazy magmatic cryptovolcanic explosive structure." It pops out as a magnetic anomaly in USGS airborne data, and cores drilled from the dome are rich in rare earth minerals. Geochemical tracers from the cores hint that deposits deeper in the dome were formed from carbonatites—the unusual volcanic rocks associated with the world's best rare earth deposits. "It's like a kitchen sink of critical minerals there," McCafferty says.

The midcontinent surveys could also help geologists assess another resource: natural hydrogen, a clean-burning fuel. Currently, all hydrogen is manufactured, but some researchers believe, contrary to conventional wisdom, that Earth produces and traps vast stores of the gas (*Science*, 17 February, p. 630). The iron-rich volcanic rocks of the Reelfoot are exactly the kind that could produce hydrogen. Yaoguo Li, a geophysicist at the Colorado School of Mines, is developing a Department of Energy (DOE) grant proposal to prospect for hydrogen source rocks with the USGS data. "We have not done anything yet," he says. "But I can see there's so much we can do."

Besides identifying resources to extract, the surveys could pay other dividends. They are pinpointing the steel casings of abandoned oil and gas wells that often leak greenhouse gases. They will help identify porous rock reservoirs, bounded by faults, that could hold carbon dioxide captured from smokestacks, keeping it out of the atmosphere. And they could also map variations in the radioactive rocks that emit radon gas, a health hazard.

THESE DAYS, no mineral may be more critical than the lithium, used in cellphone and electric car batteries, that moves an ever-increasing number of the world's electrons. Yet only one lithium mine exists in the U.S., in Nevada, and its raw lithium is sent abroad for processing. The state has potential to hold much, much more, and could become an international lithium "epicenter," says James Faulds, Nevada's state geologist.

Lithium is often found in igneous rocks—magma that crystallized in the crust or lava that cooled on the surface. Many of the known lithium deposits are in the state's north, in the McDermitt caldera, a volcanic crater formed 16 million years ago by the deep-Earth hot spot currently fueling Yellowstone. Rainwater falling within the caldera or hot water from below has concentrated lithium within caldera clay deposits to levels not seen elsewhere, in other eruptions of the Yellowstone hot spot. "Why did this mineralization happen?" asks Carolina Muñoz-Saez, a geologist at the University of Nevada, Reno. She and her collaborators are studying the geochemistry of the lithium and the clays to find out whether the element was formed and concentrated during the eruption itself by superheated water or whether the concentration came later, as water infiltrated the caldera's ash-rich rocks. The answer could lead the geologists to other, equally rich deposits.

Earth MRI has already shown that lithium prospectors need not stick to calderas. Field geologists have found rocks that seem to be rich in lithium in basins bounded by tectonically uplifted blocks of crust. Nevada, famous for its "basin and range" topography, has a lot of places like that, Faulds says. Even better, the basins tend to host systems of hot brine, a potential source of geothermal power—one reason DOE is funding surveys in the state, says Jonathan Glen, a USGS geophysicist.



Mountain Pass in California is the only U.S. mine producing rare earth elements. The U.S. Geological Survey hopes Earth MRI will encourage more mining.

Just south of Nevada, DOE has similarly invested in USGS flights over California's Salton Sea, which is being stretched apart by the movement of the Northern American and Pacific tectonic plates, leaving the crust thin and hot. "Temperatures are really high," Glen says. "There's huge geothermal potential." Beyond mapping potential lithium deposits and geothermal sites, the surveys have also found new faults at the southern end of the San Andreas, and what appear to be buried volcanoes beneath the Salton Sea. "This is brand new stuff," Glen says. "We didn't know any of this."

Those insights come from magnetometer, radiometric, and laser altimeter flights. But Earth MRI is also planning hyperspectral surveys that will scan the treeless, arid surface for pay dirt. Lithium and rare earth elements, for example, have strong spectral reflections; and other signatures can reveal the iron or clay minerals associated with lithium or other minerals. Beyond prospecting, the data will be valuable for spotting volcanic hazards. Those include rocks on the flanks of volcanoes that have been altered into soft clays by melting snow and heat, says Bernard Hubbard, a remote-sensing geologist at USGS. "Those become unstable—and then they collapse."

BESIDES IDENTIFYING the rock formations likely to hold mineral deposits, Earth MRI has accelerated USGS efforts to detect valuable resources left behind in tailings from defunct copper or iron mines. Last decade, Shah spotted the distinctive radioactive signatures of rare earths in such piles in Mineville, a hamlet in New York. With state geological agencies, USGS is compiling a national database of mine waste sites, along with methods for researchers to assess the waste's mineral potential. "What's the point of digging another hole in the ground if you can remine the rocks?" asks Darcy McPhee, Earth MRI's program coordinator at USGS.

Those lingering tailings piles are a reminder of the environmental damage mining can do. For decades, the U.S. avoided environmental debates over mining by outsourcing it to other countries. The new consensus is that work should happen here, Ryker says. "But that means we have to deal with the conflict." The survey will reveal new resources. But the rest is up to us, she says. "How much should we develop? That's a much more complicated question."



The mineral stibnite is the ore for antimony, used in batteries.

Those questions are now unfolding, state by state. In Nevada, lithium prospecting is booming, spurred by the Inflation Reduction Act's mandate that electric cars must use some U.S.-sourced minerals for buyers to get a tax credit. But in Maine, legislators enacted a strict mining law in 2017, when the state's largest landowner, the Canadian forestry company J.D. Irving, considered exploiting reserves of gold, silver, and copper found on its lands. Following the discovery of rare earth deposits at Pennington Mountain and lithium elsewhere in the state, lawmakers are now considering amending the law to allow some responsible mining.

Given the demands of green technology and the imperative to lower carbon emissions, many environmental groups are softening their stance on critical-mineral mining, Barbanell says. This exploitation doesn't have to go on forever, she adds. Unlike coal, which must be mined indefinitely as it's burned, the minerals used for batteries and wind turbines can almost always be recycled—as long as policymakers push for their reuse.

Slack would also welcome some mining. He retired to Maine for its natural splendor, but until recycling can cover society's needs, critical mineral exploitation needs to happen somewhere. "We cannot have a low carbon future and green tech without mining," he says. "It's not an option. It's a necessity. It's essential." ■

PHOTOS: (TOP TO BOTTOM) TMY350/WIKIMEDIA COMMONS; NIKI WINTZER/USGS



ANTHROPOLOGY

Embodying measurement

Measuring with body parts is a handy and persistent cross-cultural phenomenon

By **Stephen Chrisomalis**

Humans use multiple culturally-specific cognitive strategies for managing social and technical challenges. Measurement, the correlation of some target to some comparator or unit, is cross-culturally universal and has a deep history (*1*). Ethnographic and historical analyses have documented these strategies for individual societies, but generalizing across languages and cultures is still an incomplete task. On page 948 of this issue, Kaaronen *et al.* (*2*) show that body-based measuring is both common worldwide and builds on embodied cognitive properties that make such practices highly suitable for many measuring problems. Rather than considering standardized measures such as the metric system as superior, the authors argue that body-based measurement is often advantageous when solving human problems at human scales. Assessing 186 societies, past and present, they show that body-based measuring is globally prevalent because it is readily available to users, ergonomically adaptive, and linked to local knowledge, language, and tasks.

Body-based measurement is one of a suite of cognitive technologies for representing, notating, and evaluating the world. Other related cognitive technologies include numerical notations (*3*), finger-counting (*4*), arithmetical devices (*5*), coinage (*6*), and writing systems (*7*). They may involve artifacts, the body, or even, as in the case of number words or color terms, be principally linguistic. Cognitive technologies are interesting because they organize thought, by structuring otherwise nebulous domains, and behavior, by affording practices that would otherwise be challenging. Crucially, cognitive technologies are cultural—socially shared, not simply one-off solutions by a single individual. Although they may not be formally standardized, cognitive technologies produce a common lexicon for cooperative activities such as trade and craft production. They are embodied in individuals and embedded in language within and across communities.

Kaaronen *et al.* use the Human Relations Area Files (HRAF) database of cultural materials classified by subject to show that in a wide range of societies, body-based measuring systems persisted long after standardized measures were introduced into various regions. This is because, for tasks involving the body, body-based measurements are the best solution to ergonomic and technical problems.

Because many of the problems that humans face are similar, and because human brains and bodies are similar, some robust generalizations about cognitive technologies can be made. For instance, the worldwide predominance of decimal numeral words is clearly related to the hands with their 10 fingers (*8*). However, because there is no one perfect way to measure a length, and no one way to count on one's fingers, cognitive technologies tend to sit in that interesting space between total cultural particularity and universality. Many linguistic and cultural phenomena have only a few "stable engineering solutions satisfying multiple design constraints" (*9*, p. 429). For example, there are only five basic structural principles underlying the world's >100 numerical notations (such as the Roman numerals, Inka khipu, and modern Indo-Arabic positional systems), even though others are easily imaginable (*3*). Far greater diversity has been observed in the world's systems for counting using the fingers and the body than might be expected (*4*). Such diversity in cognitive technologies does not mean that anything can arise or that searches for patterns should be abandoned. Instead, it should compel future ethnographic and historical case studies into how people make decisions about which technologies they employ.

Cognitive technologies provide a social and material structure on which to build conceptual representations. In Japan, day names and month names are commonly mapped onto the joints of the hand, creating a blended "material anchor" that provides a "handy" tool for computing the day of the week of any date (*10*). This might lead to a form of extended cognition in which the brain is seen as a necessary but insufficient part of a cognitive system (*11*). However, hands and fingers are not tools until they are conceptualized as tools by their users, their capacities are linked to a socially recognized problem, and a workable solution such as the span (the width of an open palm) or cubit (the length between fingertips and elbow) is developed and shared. In turn, these technologies can be internalized so that they can work even in the absence of the object itself. Once trained, users of arithmetical tools such as the Chinese *suan pan* and Japanese *soroban* can perform arithmetic using a "mental abacus," a representation of an artifact that serves in lieu of the object itself, either on its own or supported by gesture (*12*).

The study of cognitive technologies in experimental conditions often suffers from the problem that the populations being studied are overly Western, educated, industrialized, rich, and democratic (WEIRD) (*13*). But an additional problem is that analyses might be biased toward modern societies. It should not be presumed that the cognitive technologies of the past are identical to those of

Department of Anthropology, Wayne State University, Detroit, MI, USA. Email: chrisomalis@wayne.edu

An ancient Greek metrological relief from the mid-fifth century BCE, depicting, when complete, a Greek fathom (orguia) of 209 cm and a foot (above the arm) of 29.6 cm, matching known measures of the period to idealized body parts.

the present. Even though human bodies are similar to those of the past, human technical and social needs are potentially quite different. Thus, it is important to understand how information was structured, not only in the fraction of human existence that can be observed most directly but also in ancient and premodern societies throughout the world. Datasets such as HRAF, used by Kaaronen *et al.*, are skewed toward ethnographically known societies from the 19th and 20th centuries. Future studies must employ cognitive cross-cultural research that is sensitive to how technologies change across time (diachronically), not merely synchronic patterns in the modern world.

Caution should also be exercised when investigating any cognitive technology to avoid assuming either that it is universal or that, if present, its function is universal. In a Eurocentric framework, it is easy to assume that lexical structures such as color terms or number words are essential tools for processing the information that the world provides. But there is evidence to suggest that neither of these are as universal as was once assumed. Powerful combinations of ethnographic, experimental, and linguistic evidence reveal that the correlation between color technology (such as painting and dyeing) and the complexity of the color lexicon is neither simple nor predictable across social scale (*14*). Body-based measures, similarly, are not some vestige or a cultural-evolutionary precursor, but have survived and thrived despite the presence of other forms of standardized measures, because they continue to be useful for societies and the individuals within them. ■

REFERENCES AND NOTES

1. K. Cooperrider, D. Gentner, *Cognition* **191**, 103942 (2019).
2. R. O. Kaaronen *et al.*, *Science* **380**, 948 (2023).
3. S. Chrisomalis, *Reckonings: Numerals, Cognition, and History* (MIT, 2020).
4. A. Bender, S. Beller, *Cognition* **124**, 156 (2012).
5. M. C. Frank, D. Barner, *J. Exp. Psychol. Gen.* **141**, 134 (2012).
6. B. Pavlek, J. Winters, O. Morin, *J. Anthropol. Archaeol.* **56**, 101103 (2019).
7. P. Kelly, J. Winters, H. Miton, O. Morin, *Curr. Anthropol.* **62**, 669 (2021).
8. C. Everett, *Numbers and the Making of Us* (Harvard Univ. Press, 2017).
9. N. Evans, S. C. Levinson, *Behav. Brain Sci.* **32**, 429 (2009).
10. E. Hutchins, *J. Pragmatics* **37**, 1555 (2005).
11. A. Clark, D. Chalmers, *Analysis* **58**, 7 (1998).
12. N. B. Brooks, D. Barner, M. Frank, S. Goldin-Meadow, *Cogn. Sci.* **42**, 554 (2018).
13. J. Henrich, S. J. Heine, A. Norenzayan, *Behav. Brain Sci.* **33**, 61 (2010).
14. E. Wnuk, A. Verkerk, S. C. Levinson, A. Majid, *Cognition* **229**, 105223 (2022).

10.1126/science.adi2352

MATERIALS SCIENCE

Improving glass nanostructure fabrication

A new method offers high-resolution three-dimensional printing and low-temperature firing

By **Paolo Colombo**[1,2] *and* **Giorgia Franchin**[1]

Ceramics, glass ceramics, and glasses have a combination of properties that no other classes of materials (polymers and metals) display. For example, they have high chemical durability, hardness, bending strength, electrical resistivity, and transparency (for glasses). However, they are conventionally produced by sintering (consolidation of powder compacts by heating below melting point) or by high-temperature processing leading to a melt that is shaped and cooled to form a solid object. These forming processes require high temperatures and are limited by the minimum feature size achievable in a component. On page 960 of this issue, Bauer *et al.* (*1*) report that a photocurable polyhedral oligomeric silsesquioxane (POSS) liquid precursor blended with a suitable acrylic oligomer and a photoinitiator allows the fabrication of highly transparent silica glass nano- and microstructures with high resolution using two-photon polymerization (TPP) followed by firing at low temperature.

Alternative approaches to the high-temperature fabrication of ceramic and glass bulk components are based on the use of organic-inorganic precursors that can be converted to ceramics or glasses, after shaping, by a low-temperature heat treatment (i.e., 500° to 1000°C). They include sol-gel precursors (*2*) and preceramic polymers (*3*), which are either liquid or easily soluble in common solvents. Molecular sol-gel precursors enable a wide range of mainly metal oxide materials to be obtained. Preceramic polymers offer a more limited compositional range of just silicon- or boron-containing materials, but their polymeric nature allows high processability. In both cases, a fully inorganic material can be produced by thermally eliminating residual organic moieties and/or completing condensation reactions to form a network made up of, for example, metal-oxygen bonds. Depending on the composition, the organic-inorganic shaped body is transformed into a fully ceramic or glass material at low temperature, which allows cost and environmental benefits, shorter processing times, and enhanced compatibility with other materials when fabricating multicomponent devices.

TPP is a volumetric additive manufacturing technology relying on the localized absorption of radiation for selective cross-linking of a photocurable material with submicrometer resolution. Attempts at producing silica-based structures using TPP demonstrated that it is possible to obtain defect-free glass components at a scale of a few hundred micrometers (*4*) or nanometers (*5*) by using photocurable systems containing colloidal silica particles. However, high-temperature sintering, either 1300° or 1100°C, was necessary to achieve properties similar to those of pure silica glass (fused silica). The presence of colloidal particles complicates the three-dimensional (3D) printing process that is used to shape the material owing to scattering, which limits the resolution of the printed features. An all-liquid, particle-free precursor system, such as the one proposed by Bauer *et al.*, does not suffer from these drawbacks. However, efforts to process sol-gel solutions by TPP have mostly concentrated on producing only unfired parts—thus developing organic-inorganic components (*6*) that do not have the range of favorable properties of an inorganic glass or ceramic.

Using preceramic polymers, such as siloxanes, silicon oxycarbide (SiOC) parts were produced, although at a slightly lower resolution than that reported by Bauer *et al.* and lacking transparency owing to the presence of residual free carbon in the glass structure (*7–9*). These siloxane precursors contain a large amount of carbon-containing moieties that renders them poorly suited to the fabrication of pure, transparent silica glass bodies because the exothermal oxidation occurring when firing them in air typically leads to the formation of microcracks. In a similar approach to that of Bauer *et al.*, a precondensed liquid silicone resin to which a silane acrylate was chemically bonded enabled a low-carbon–containing liquid precursor to be obtained that was photocurable and printable by TPP (*10*). This was converted to silica glass

[1]Department of Industrial Engineering, University of Padova, Padova, Italy. [2]Department of Materials Science and Engineering, The Pennsylvania State University, University Park, PA, USA. Email: paolo.colombo@unipd.it

An ancient Greek metrological relief from the mid-fifth century BCE, depicting, when complete, a Greek fathom (orguia) of 209 cm and a foot (above the arm) of 29.6 cm, matching known measures of the period to idealized body parts.

the present. Even though human bodies are similar to those of the past, human technical and social needs are potentially quite different. Thus, it is important to understand how information was structured, not only in the fraction of human existence that can be observed most directly but also in ancient and premodern societies throughout the world. Datasets such as HRAF, used by Kaaronen *et al.*, are skewed toward ethnographically known societies from the 19th and 20th centuries. Future studies must employ cognitive cross-cultural research that is sensitive to how technologies change across time (diachronically), not merely synchronic patterns in the modern world.

Caution should also be exercised when investigating any cognitive technology to avoid assuming either that it is universal or that, if present, its function is universal. In a Eurocentric framework, it is easy to assume that lexical structures such as color terms or number words are essential tools for processing the information that the world provides. But there is evidence to suggest that neither of these are as universal as was once assumed. Powerful combinations of ethnographic, experimental, and linguistic evidence reveal that the correlation between color technology (such as painting and dyeing) and the complexity of the color lexicon is neither simple nor predictable across social scale (*14*). Body-based measures, similarly, are not some vestige or a cultural-evolutionary precursor, but have survived and thrived despite the presence of other forms of standardized measures, because they continue to be useful for societies and the individuals within them. ■

REFERENCES AND NOTES

1. K. Cooperrider, D. Gentner, *Cognition* **191**, 103942 (2019).
2. R. O. Kaaronen *et al.*, *Science* **380**, 948 (2023).
3. S. Chrisomalis, *Reckonings: Numerals, Cognition, and History* (MIT, 2020).
4. A. Bender, S. Beller, *Cognition* **124**, 156 (2012).
5. M. C. Frank, D. Barner, *J. Exp. Psychol. Gen.* **141**, 134 (2012).
6. B. Pavlek, J. Winters, O. Morin, *J. Anthropol. Archaeol.* **56**, 101103 (2019).
7. P. Kelly, J. Winters, H. Miton, O. Morin, *Curr. Anthropol.* **62**, 669 (2021).
8. C. Everett, *Numbers and the Making of Us* (Harvard Univ. Press, 2017).
9. N. Evans, S. C. Levinson, *Behav. Brain Sci.* **32**, 429 (2009).
10. E. Hutchins, *J. Pragmatics* **37**, 1555 (2005).
11. A. Clark, D. Chalmers, *Analysis* **58**, 7 (1998).
12. N. B. Brooks, D. Barner, M. Frank, S. Goldin-Meadow, *Cogn. Sci.* **42**, 554 (2018).
13. J. Henrich, S. J. Heine, A. Norenzayan, *Behav. Brain Sci.* **33**, 61 (2010).
14. E. Wnuk, A. Verkerk, S. C. Levinson, A. Majid, *Cognition* **229**, 105223 (2022).

10.1126/science.adi2352

MATERIALS SCIENCE

Improving glass nanostructure fabrication

A new method offers high-resolution three-dimensional printing and low-temperature firing

By **Paolo Colombo**[1,2] *and* **Giorgia Franchin**[1]

Ceramics, glass ceramics, and glasses have a combination of properties that no other classes of materials (polymers and metals) display. For example, they have high chemical durability, hardness, bending strength, electrical resistivity, and transparency (for glasses). However, they are conventionally produced by sintering (consolidation of powder compacts by heating below melting point) or by high-temperature processing leading to a melt that is shaped and cooled to form a solid object. These forming processes require high temperatures and are limited by the minimum feature size achievable in a component. On page 960 of this issue, Bauer *et al.* (*1*) report that a photocurable polyhedral oligomeric silsesquioxane (POSS) liquid precursor blended with a suitable acrylic oligomer and a photoinitiator allows the fabrication of highly transparent silica glass nano- and microstructures with high resolution using two-photon polymerization (TPP) followed by firing at low temperature.

Alternative approaches to the high-temperature fabrication of ceramic and glass bulk components are based on the use of organic-inorganic precursors that can be converted to ceramics or glasses, after shaping, by a low-temperature heat treatment (i.e., 500° to 1000°C). They include sol-gel precursors (*2*) and preceramic polymers (*3*), which are either liquid or easily soluble in common solvents. Molecular sol-gel precursors enable a wide range of mainly metal oxide materials to be obtained. Preceramic polymers offer a more limited compositional range of just silicon- or boron-containing materials, but their polymeric nature allows high processability. In both cases, a fully inorganic material can be produced by thermally eliminating residual organic moieties and/or completing condensation reactions to form a network made up of, for example, metal-oxygen bonds. Depending on the composition, the organic-inorganic shaped body is transformed into a fully ceramic or glass material at low temperature, which allows cost and environmental benefits, shorter processing times, and enhanced compatibility with other materials when fabricating multicomponent devices.

TPP is a volumetric additive manufacturing technology relying on the localized absorption of radiation for selective cross-linking of a photocurable material with submicrometer resolution. Attempts at producing silica-based structures using TPP demonstrated that it is possible to obtain defect-free glass components at a scale of a few hundred micrometers (*4*) or nanometers (*5*) by using photocurable systems containing colloidal silica particles. However, high-temperature sintering, either 1300° or 1100°C, was necessary to achieve properties similar to those of pure silica glass (fused silica). The presence of colloidal particles complicates the three-dimensional (3D) printing process that is used to shape the material owing to scattering, which limits the resolution of the printed features. An all-liquid, particle-free precursor system, such as the one proposed by Bauer *et al.*, does not suffer from these drawbacks. However, efforts to process sol-gel solutions by TPP have mostly concentrated on producing only unfired parts—thus developing organic-inorganic components (*6*) that do not have the range of favorable properties of an inorganic glass or ceramic.

Using preceramic polymers, such as siloxanes, silicon oxycarbide (SiOC) parts were produced, although at a slightly lower resolution than that reported by Bauer *et al.* and lacking transparency owing to the presence of residual free carbon in the glass structure (*7–9*). These siloxane precursors contain a large amount of carbon-containing moieties that renders them poorly suited to the fabrication of pure, transparent silica glass bodies because the exothermal oxidation occurring when firing them in air typically leads to the formation of microcracks. In a similar approach to that of Bauer *et al.*, a precondensed liquid silicone resin to which a silane acrylate was chemically bonded enabled a low-carbon–containing liquid precursor to be obtained that was photocurable and printable by TPP (*10*). This was converted to silica glass

[1]Department of Industrial Engineering, University of Padova, Padova, Italy. [2]Department of Materials Science and Engineering, The Pennsylvania State University, University Park, PA, USA. Email: paolo.colombo@unipd.it

micro-optic components after firing in air at 600° to 1000°C, with a refractive index for the material heated at 600°C similar to that of fused silica. However, heating to 1000°C led to a further ~4% shrinkage, indicating that the material was not yet fully dense. Bauer *et al.* developed a photocurable blend based on a POSS that achieved ~100-nm resolution with TPP and demonstrated that, owing to its densely packed cage structure, a heat treatment at 650°C allowed characteristics that were virtually indistinguishable from those of fused silica. Notably, the transparency of the printed parts enabled fabrication of micro-optical elements with high smoothness and optical performance.

TPP is already used to generate micro-optical elements with unlimited design freedom compared with conventional techniques. However, its commercial application has so far been limited to polymers. The results of Bauer *et al.* pave the way for implementing glass micro-optics for more demanding temperatures and environments. Furthermore, the increased durability would also benefit the field of microfluidics. Glass microfluidic devices are a necessity when aggressive, reactive, and flammable fluids have to be injected (often at high pressures and temperatures), such as for the investigation of carbon dioxide (CO_2) sequestration and hydrocarbon recovery operations. The current multistep fabrication processes are complex and involve the use of chemically reactive plasma (reactive ion etching) or liquid chemicals (wet etching) to selectively remove the material from a glass wafer. TPP can be a simpler, more sustainable alternative, and it opens up new 3D designs that are impossible with current techniques.

The limited firing temperature requirement of the approach demonstrated by Bauer *et al.* allows in principle for the fabrication of miniaturized devices (e.g., individual microlenses or arrays) directly onto substrates, such as optical fibers and chips, which could enable process automation and high precision. However, the considerable linear shrinkage (by ~40%) that occurs upon heat treatment might limit the coupling with different materials. ■

REFERENCES AND NOTES

1. J. Bauer, C. Crook, T. Baldacchini, *Science* **380**, 960 (2023).
2. C. J. Brinker, G. W. Scherer, *Sol-Gel Science: The Physics and Chemistry of Sol-Gel Processing* (Academic Press, 1990).
3. P. Colombo, G. Mera, R. Riedel, G. D. Sorarù, *J. Am. Ceram. Soc.* **93**, 1805 (2010).
4. F. Kotz *et al.*, *Adv. Mater.* **33**, 2006341 (2021).
5. X. Wen *et al.*, *Nat. Mater.* **20**, 1506 (2021).
6. Z.-P. Liu *et al.*, *Appl. Phys. Lett.* **97**, 211105 (2010).
7. L. Brigo *et al.*, *Adv. Sci.* **5**, 1800937 (2018).
8. J. Bauer *et al.*, *Matter* **1**, 1547 (2019).
9. G. Konstantinou *et al.*, *Addit. Manuf.* **35**, 101343 (2020).
10. Z. Hong, P. Ye, D. A. Loy, R. Liang, *Optica* **8**, 904 (2021).

10.1126/science.adi2747

NEUROSCIENCE

A super Sonic circadian synchronizer

Sonic Hedgehog signaling and primary cilia control the core mammalian circadian clock

By **Dong Won Kim**[1,2] *and* **Seth Blackshaw**[3,4,5,6,7]

Virtually all mammalian physiological functions fall under the control of an internal circadian rhythm, or body clock. This circadian rhythm is governed by master neural networks in the hypothalamus that synchronize the activity of peripheral clocks in cells throughout the body (*1*). Environmental perturbations that are a regular part of modern life, such as artificial light and international travel, can disrupt circadian rhythms, leading to adverse consequences for mental and physical health (*2*). On page 972 of this issue, Tu *et al.* (*3*) report that primary cilia–mediated Sonic Hedgehog (SHH) signaling allows cells in the master circadian clock to maintain synchronization and control circadian rhythmicity in mice, identifying an unexpected functional role for this developmental regulator.

The master circadian pacemaker responsible for regulating our daily rhythms is located in the suprachiasmatic nucleus (SCN) in the anterior hypothalamus. The cells that make up this pacemaker maintain intercellular coupling of molecular circadian rhythms, ensuring synchrony of SCN neurons. Robust clocks keep time using redundant mechanisms, and the SCN is no exception. Signals that promote cellular synchrony include paracrine signaling by fast neurotransmitters and multiple neuropeptides as well as gap junction–dependent electrical coupling (*4*). This cellular synchrony ensures the robust output of the central clock and renders it resistant to signals that reset peripheral clocks.

Primary cilia are elongated organelles that are expressed on the surface of many cell types, including neurons. They act as mechanosensors and also function as organizing centers for transducing a broad range of extracellular signals. Receptors and signal transduction proteins are transported between the base and tip of the cilium by intraflagellar transport (IFT) (*5*), leading to the assembly of multiprotein complexes that contain receptors for many secreted factors. These include Smoothened (SMO) co-receptors for SHH signaling during development, as well as many G protein–coupled receptors (*6*). The assembly of primary cilia is regulated by the cell cycle during development, and defects in cilia assembly lead to a range of syndromic human genetic disorders called ciliopathies (*7*).

Tu *et al.* demonstrate that primary cilia–dependent SHH signaling in adult SCN neuronal populations expressing the neuropeptide neuromedin S (NMS^+) plays a critical role in regulating circadian rhythms by maintaining intercellular coupling of cellular oscillators. These NMS^+ neurons, which are crucial for SCN synchrony (*8*), exhibit circadian phase–dependent changes in cilia number and length, unlike other tissues. Selective deletion of IFT genes in NMS^+ neurons led to rapid light-induced shifts in molecular rhythms, accelerated activity shifts in jet lag–like conditions, and reduced intercellular coupling in the SCN. These findings mirror disruptions in neuropeptide signaling or NMS^+ neuronal function. Tu *et al.* found that these defects in circadian rhythmicity upon disruption of primary cilia in NMS^+ neurons are, at least in part, due to defects in SHH signaling. SHH signaling activated by SMO in the cilia of NMS^+ neurons exhibits circadian rhythmicity. Blocking SHH signaling in NMS^+ neurons phenocopied the cellular, molecular, and behavioral defects that are observed after the disruption of IFT genes. Crucially, all SHH-dependent effects on circadian clock function were dependent on the expression of IFT genes (see the figure).

The demonstration of a central role for SHH signaling in controlling central clock function in mice is surprising because SHH has been almost exclusively studied in the context of development. SHH is essential

[1]Danish Research Institute of Translational Neuroscience (DANDRITE), Nordic EMBL Partnership for Molecular Medicine, Aarhus University, Aarhus, Denmark. [2]Department of Biomedicine, Aarhus University, Aarhus, Denmark. [3]Solomon H. Snyder Department of Neuroscience, Johns Hopkins University School of Medicine, Baltimore, MD, USA. [4]Department of Ophthalmology, Johns Hopkins University School of Medicine, Baltimore, MD, USA. [5]Department of Neurology, Johns Hopkins University School of Medicine, Baltimore, MD, USA. [6]Institute for Cell Engineering, Johns Hopkins University School of Medicine, Baltimore, MD, USA. [7]Kavli Neuroscience Discovery Institute, Johns Hopkins University School of Medicine, Baltimore, MD, USA. Email: sblack@jhmi.edu

micro-optic components after firing in air at 600° to 1000°C, with a refractive index for the material heated at 600°C similar to that of fused silica. However, heating to 1000°C led to a further ~4% shrinkage, indicating that the material was not yet fully dense. Bauer *et al.* developed a photocurable blend based on a POSS that achieved ~100-nm resolution with TPP and demonstrated that, owing to its densely packed cage structure, a heat treatment at 650°C allowed characteristics that were virtually indistinguishable from those of fused silica. Notably, the transparency of the printed parts enabled fabrication of micro-optical elements with high smoothness and optical performance.

TPP is already used to generate micro-optical elements with unlimited design freedom compared with conventional techniques. However, its commercial application has so far been limited to polymers. The results of Bauer *et al.* pave the way for implementing glass micro-optics for more demanding temperatures and environments. Furthermore, the increased durability would also benefit the field of microfluidics. Glass microfluidic devices are a necessity when aggressive, reactive, and flammable fluids have to be injected (often at high pressures and temperatures), such as for the investigation of carbon dioxide (CO_2) sequestration and hydrocarbon recovery operations. The current multistep fabrication processes are complex and involve the use of chemically reactive plasma (reactive ion etching) or liquid chemicals (wet etching) to selectively remove the material from a glass wafer. TPP can be a simpler, more sustainable alternative, and it opens up new 3D designs that are impossible with current techniques.

The limited firing temperature requirement of the approach demonstrated by Bauer *et al.* allows in principle for the fabrication of miniaturized devices (e.g., individual microlenses or arrays) directly onto substrates, such as optical fibers and chips, which could enable process automation and high precision. However, the considerable linear shrinkage (by ~40%) that occurs upon heat treatment might limit the coupling with different materials. ■

REFERENCES AND NOTES

1. J. Bauer, C. Crook, T. Baldacchini, *Science* **380**, 960 (2023).
2. C. J. Brinker, G. W. Scherer, *Sol-Gel Science: The Physics and Chemistry of Sol-Gel Processing* (Academic Press, 1990).
3. P. Colombo, G. Mera, R. Riedel, G. D. Sorarù, *J. Am. Ceram. Soc.* **93**, 1805 (2010).
4. F. Kotz *et al.*, *Adv. Mater.* **33**, 2006341 (2021).
5. X. Wen *et al.*, *Nat. Mater.* **20**, 1506 (2021).
6. Z.-P. Liu *et al.*, *Appl. Phys. Lett.* **97**, 211105 (2010).
7. L. Brigo *et al.*, *Adv. Sci.* **5**, 1800937 (2018).
8. J. Bauer *et al.*, *Matter* **1**, 1547 (2019).
9. G. Konstantinou *et al.*, *Addit. Manuf.* **35**, 101343 (2020).
10. Z. Hong, P. Ye, D. A. Loy, R. Liang, *Optica* **8**, 904 (2021).

10.1126/science.adi2747

NEUROSCIENCE

A super Sonic circadian synchronizer

Sonic Hedgehog signaling and primary cilia control the core mammalian circadian clock

By **Dong Won Kim**[1,2] *and* **Seth Blackshaw**[3,4,5,6,7]

Virtually all mammalian physiological functions fall under the control of an internal circadian rhythm, or body clock. This circadian rhythm is governed by master neural networks in the hypothalamus that synchronize the activity of peripheral clocks in cells throughout the body (*1*). Environmental perturbations that are a regular part of modern life, such as artificial light and international travel, can disrupt circadian rhythms, leading to adverse consequences for mental and physical health (*2*). On page 972 of this issue, Tu *et al.* (*3*) report that primary cilia–mediated Sonic Hedgehog (SHH) signaling allows cells in the master circadian clock to maintain synchronization and control circadian rhythmicity in mice, identifying an unexpected functional role for this developmental regulator.

The master circadian pacemaker responsible for regulating our daily rhythms is located in the suprachiasmatic nucleus (SCN) in the anterior hypothalamus. The cells that make up this pacemaker maintain intercellular coupling of molecular circadian rhythms, ensuring synchrony of SCN neurons. Robust clocks keep time using redundant mechanisms, and the SCN is no exception. Signals that promote cellular synchrony include paracrine signaling by fast neurotransmitters and multiple neuropeptides as well as gap junction–dependent electrical coupling (*4*). This cellular synchrony ensures the robust output of the central clock and renders it resistant to signals that reset peripheral clocks.

Primary cilia are elongated organelles that are expressed on the surface of many cell types, including neurons. They act as mechanosensors and also function as organizing centers for transducing a broad range of extracellular signals. Receptors and signal transduction proteins are transported between the base and tip of the cilium by intraflagellar transport (IFT) (*5*), leading to the assembly of multiprotein complexes that contain receptors for many secreted factors. These include Smoothened (SMO) co-receptors for SHH signaling during development, as well as many G protein–coupled receptors (*6*). The assembly of primary cilia is regulated by the cell cycle during development, and defects in cilia assembly lead to a range of syndromic human genetic disorders called ciliopathies (*7*).

Tu *et al.* demonstrate that primary cilia–dependent SHH signaling in adult SCN neuronal populations expressing the neuropeptide neuromedin S (NMS^+) plays a critical role in regulating circadian rhythms by maintaining intercellular coupling of cellular oscillators. These NMS^+ neurons, which are crucial for SCN synchrony (*8*), exhibit circadian phase–dependent changes in cilia number and length, unlike other tissues. Selective deletion of IFT genes in NMS^+ neurons led to rapid light-induced shifts in molecular rhythms, accelerated activity shifts in jet lag–like conditions, and reduced intercellular coupling in the SCN. These findings mirror disruptions in neuropeptide signaling or NMS^+ neuronal function. Tu *et al.* found that these defects in circadian rhythmicity upon disruption of primary cilia in NMS^+ neurons are, at least in part, due to defects in SHH signaling. SHH signaling activated by SMO in the cilia of NMS^+ neurons exhibits circadian rhythmicity. Blocking SHH signaling in NMS^+ neurons phenocopied the cellular, molecular, and behavioral defects that are observed after the disruption of IFT genes. Crucially, all SHH-dependent effects on circadian clock function were dependent on the expression of IFT genes (see the figure).

The demonstration of a central role for SHH signaling in controlling central clock function in mice is surprising because SHH has been almost exclusively studied in the context of development. SHH is essential

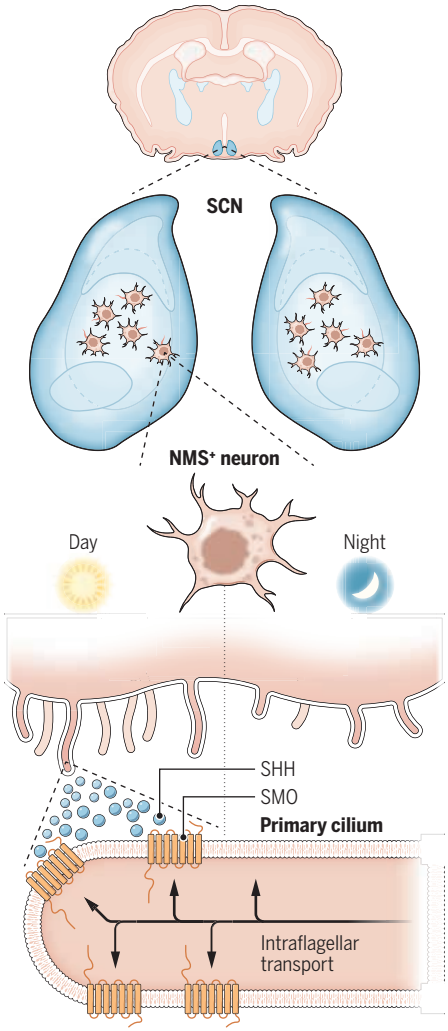
[1]Danish Research Institute of Translational Neuroscience (DANDRITE), Nordic EMBL Partnership for Molecular Medicine, Aarhus University, Aarhus, Denmark. [2]Department of Biomedicine, Aarhus University, Aarhus, Denmark. [3]Solomon H. Snyder Department of Neuroscience, Johns Hopkins University School of Medicine, Baltimore, MD, USA. [4]Department of Ophthalmology, Johns Hopkins University School of Medicine, Baltimore, MD, USA. [5]Department of Neurology, Johns Hopkins University School of Medicine, Baltimore, MD, USA. [6]Institute for Cell Engineering, Johns Hopkins University School of Medicine, Baltimore, MD, USA. [7]Kavli Neuroscience Discovery Institute, Johns Hopkins University School of Medicine, Baltimore, MD, USA. Email: sblack@jhmi.edu

for the development and specification of many brain structures during embryogenesis, including the SCN (*9*), and it also regulates axonal targeting, dendrite formation, and synaptogenesis (*10*). An ongoing role for SHH signaling in the adult SCN raises several important questions. It is unclear what cells are the relevant source of SHH or how its synthesis and release are regulated. Primary cilia regulate many other classes of extracellular signaling—such as Notch, Wnt, Hippo, and mammalian target of rapamycin (mTOR) pathways—often through receptor-independent mechanisms. Thus, it is unclear whether other extrinsic factors might contribute to controlling SCN function. Additionally, the study of Tu *et al.* suggests that at least a subset of ciliopathy patients may show circadian defects that resemble those seen in IFT mutant mice. Because ciliopathies are syndromic and often present with blindness and intellectual disability (*11*), these more obvious phenotypes may have masked defects in clock function that should be readily detectable with appropriate behavioral studies.

Although components of the SHH signaling pathway are expressed in mature neurons (*12*), the study of Tu *et al.* provides convincing evidence that SHH actively regulates neuronal activity independently of its well-characterized developmental functions. This suggests that SHH signaling may be more broadly important in controlling neuronal function and identifies potential mechanisms by which ciliopathies could disrupt brain function. However, this discovery raises some important caveats about the potentially exciting translational applications. In the study of Tu *et al.*, pharmacological antagonists of SHH reduce coupling among SCN neurons and render them susceptible to rapid resetting by light, whereas SHH agonists enhance cellular synchronization in mice. Although this suggests that drugs targeting SHH signaling could be relevant to conditions ranging from travel-induced jet lag to aging-related sleep disorders (*13*, *14*), it also raises the possibility of broad and unexpected side effects. Therefore, caution must be exercised in the development and application of SHH-targeting drugs. Nonetheless, the work of Tu *et al.* provides critical new insight into how central clock function is regulated and demonstrates an unexpected role for a key regulator of brain development in controlling neuronal function in adults. ■

Regulating cilia signaling throughout the day

The master circadian pacemaker in the suprachiasmatic nucleus (SCN) contains neuromedin S–expressing (NMS^+) neurons that have primary cilia. The number and length of these cilia change throughout the day, which alters Sonic Hedgehog (SHH) signaling through Smoothened (SMO) co-receptors expressed on the cilia. When this signaling is disrupted, the cellular oscillators in the SCN become uncoupled, which affects circadian rhythmicity in mice.



GRAPHIC: A. FISHER/*SCIENCE*

REFERENCES AND NOTES

1. A. Patke, M. W. Young, S. Axelrod, *Nat. Rev. Mol. Cell Biol.* **21**, 67 (2020).
2. A. B. Fishbein, K. L. Knutson, P. C. Zee, *J. Clin. Invest.* **131**, e148286 (2021).
3. H.-Q. Tu *et al.*, *Science* **380**, 972 (2023).
4. M. H. Hastings, E. S. Maywood, M. Brancaccio, *Nat. Rev. Neurosci.* **19**, 453 (2018).
5. W. Wang *et al.*, *Front. Cell Dev. Biol.* **9**, 661350 (2021).
6. G. Wheway, L. Nazlamova, J. T. Hancock, *Front. Cell Dev. Biol.* **6**, 8 (2018).
7. J. F. Reiter, M. R. Leroux, *Nat. Rev. Mol. Cell Biol.* **18**, 533 (2017).
8. I. T. Lee *et al.*, *Neuron* **85**, 1086 (2015).
9. T. Shimogori *et al.*, *Nat. Neurosci.* **13**, 767 (2010).
10. Y. H. Belgacem, A. M. Hamilton, S. Shim, K. A. Spencer, L. N. Borodinsky, *J. Dev. Biol.* **4**, 35 (2016).
11. X.-R. Yang, M. D. Benson, I. M. MacDonald, A. M. Innes, *Am. J. Med. Genet. C Semin. Med. Genet.* **184**, 538 (2020).
12. E. Traiffort, D. Charytoniuk, L. Watroba, H. Faure, N. Sales, M. Ruat, *Eur. J. Neurosci.* **11**, 3199 (1999).
13. J. Mattis, A. Sehgal, *Trends Endocrinol. Metab.* **27**, 192 (2016).
14. J. Arendt, *Drugs* **78**, 1419 (2018).

10.1126/science.adi3177

HUMAN GENETICS

Genetic heart–brain connections

Multiorgan imaging unveils the intertwined nature of the human heart and brain

By **Julia Sacher**[1,2] *and* **A. Veronica Witte**[1,2]

Big brain-mapping initiatives such as UK Biobank (*1*), NeuroCharge (*2*), and Enigma (*3*) are transforming the methods used to explore neuroscience. However, the focus on imaging the brain as a singular entity often ignores the intricate interplay with the rest of the body. On page 934 of this issue, Zhao *et al.* (*4*) delve into multiorgan magnetic resonance imaging (MRI) data from over 40,000 individuals to examine the connection between heart traits and measures of brain structure and function. They identify multiple genetic links between distinct aspects of cardiovascular function and brain health. By offering a multidimensional analysis of heart-brain connections, this study could contribute to the development of personalized disease risk prediction.

Zhao *et al.* used deep machine learning, a type of artificial intelligence (AI), to analyze cardiac MRI phenotypes. This approach allows for advanced complex modeling of health-related and disease-related metrics. They extracted 82 cardiac and aortic traits, such as mass, area, volume, wall thickness and pumping efficiency, that correlated with clinical markers of heart anatomy, function, and health (*5*). Specific heart traits covaried with specific MRI-derived brain traits. For example, greater myocardial wall thickness was associated with larger subcortical brain volumes, and smaller distal aortic area was associated with differences in (pre)frontal and hippocampal volumes, and with lower global and regional measures of white matter microstructural coherence (see the figure). In addition, Zhao *et al.* reported heritability and genome-wide associations for the heart traits, which included loci associated with complex body and brain traits

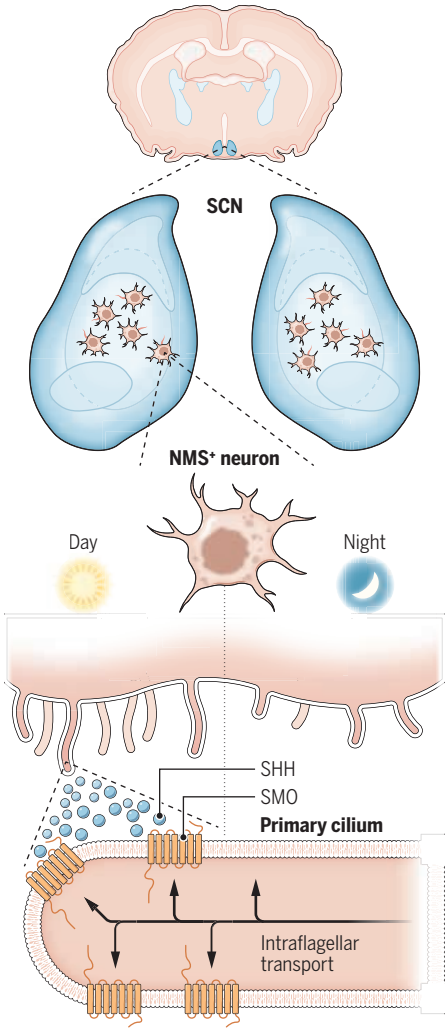
[1]Cognitive Neurology, University of Leipzig Medical Center, Leipzig, Germany. [2]Department of Neurology, Max Planck Institute for Human Cognitive and Brain Sciences, Leipzig, Germany. Email: julia.sacher@medizin.uni-leipzig.de; veronica.witte@medizin.uni-leipzig.de

for the development and specification of many brain structures during embryogenesis, including the SCN (*9*), and it also regulates axonal targeting, dendrite formation, and synaptogenesis (*10*). An ongoing role for SHH signaling in the adult SCN raises several important questions. It is unclear what cells are the relevant source of SHH or how its synthesis and release are regulated. Primary cilia regulate many other classes of extracellular signaling—such as Notch, Wnt, Hippo, and mammalian target of rapamycin (mTOR) pathways—often through receptor-independent mechanisms. Thus, it is unclear whether other extrinsic factors might contribute to controlling SCN function. Additionally, the study of Tu *et al.* suggests that at least a subset of ciliopathy patients may show circadian defects that resemble those seen in IFT mutant mice. Because ciliopathies are syndromic and often present with blindness and intellectual disability (*11*), these more obvious phenotypes may have masked defects in clock function that should be readily detectable with appropriate behavioral studies.

Although components of the SHH signaling pathway are expressed in mature neurons (*12*), the study of Tu *et al.* provides convincing evidence that SHH actively regulates neuronal activity independently of its well-characterized developmental functions. This suggests that SHH signaling may be more broadly important in controlling neuronal function and identifies potential mechanisms by which ciliopathies could disrupt brain function. However, this discovery raises some important caveats about the potentially exciting translational applications. In the study of Tu *et al.*, pharmacological antagonists of SHH reduce coupling among SCN neurons and render them susceptible to rapid resetting by light, whereas SHH agonists enhance cellular synchronization in mice. Although this suggests that drugs targeting SHH signaling could be relevant to conditions ranging from travel-induced jet lag to aging-related sleep disorders (*13*, *14*), it also raises the possibility of broad and unexpected side effects. Therefore, caution must be exercised in the development and application of SHH-targeting drugs. Nonetheless, the work of Tu *et al.* provides critical new insight into how central clock function is regulated and demonstrates an unexpected role for a key regulator of brain development in controlling neuronal function in adults. ■

Regulating cilia signaling throughout the day

The master circadian pacemaker in the suprachiasmatic nucleus (SCN) contains neuromedin S–expressing (NMS$^+$) neurons that have primary cilia. The number and length of these cilia change throughout the day, which alters Sonic Hedgehog (SHH) signaling through Smoothened (SMO) co-receptors expressed on the cilia. When this signaling is disrupted, the cellular oscillators in the SCN become uncoupled, which affects circadian rhythmicity in mice.



GRAPHIC: A. FISHER/*SCIENCE*

REFERENCES AND NOTES

1. A. Patke, M. W. Young, S. Axelrod, *Nat. Rev. Mol. Cell Biol.* **21**, 67 (2020).
2. A. B. Fishbein, K. L. Knutson, P. C. Zee, *J. Clin. Invest.* **131**, e148286 (2021).
3. H.-Q. Tu *et al.*, *Science* **380**, 972 (2023).
4. M. H. Hastings, E. S. Maywood, M. Brancaccio, *Nat. Rev. Neurosci.* **19**, 453 (2018).
5. W. Wang *et al.*, *Front. Cell Dev. Biol.* **9**, 661350 (2021).
6. G. Wheway, L. Nazlamova, J. T. Hancock, *Front. Cell Dev. Biol.* **6**, 8 (2018).
7. J. F. Reiter, M. R. Leroux, *Nat. Rev. Mol. Cell Biol.* **18**, 533 (2017).
8. I. T. Lee *et al.*, *Neuron* **85**, 1086 (2015).
9. T. Shimogori *et al.*, *Nat. Neurosci.* **13**, 767 (2010).
10. Y. H. Belgacem, A. M. Hamilton, S. Shim, K. A. Spencer, L. N. Borodinsky, *J. Dev. Biol.* **4**, 35 (2016).
11. X.-R. Yang, M. D. Benson, I. M. MacDonald, A. M. Innes, *Am. J. Med. Genet. C Semin. Med. Genet.* **184**, 538 (2020).
12. E. Traiffort, D. Charytoniuk, L. Watroba, H. Faure, N. Sales, M. Ruat, *Eur. J. Neurosci.* **11**, 3199 (1999).
13. J. Mattis, A. Sehgal, *Trends Endocrinol. Metab.* **27**, 192 (2016).
14. J. Arendt, *Drugs* **78**, 1419 (2018).

10.1126/science.adi3177

HUMAN GENETICS

Genetic heart–brain connections

Multiorgan imaging unveils the intertwined nature of the human heart and brain

By **Julia Sacher**[1,2] *and* **A. Veronica Witte**[1,2]

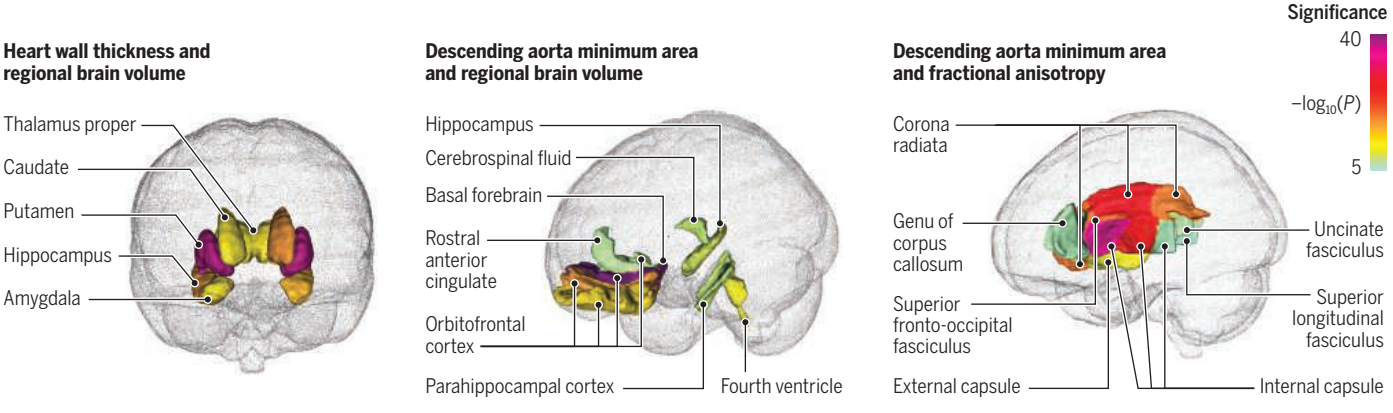
Big brain-mapping initiatives such as UK Biobank (*1*), NeuroCharge (*2*), and Enigma (*3*) are transforming the methods used to explore neuroscience. However, the focus on imaging the brain as a singular entity often ignores the intricate interplay with the rest of the body. On page 934 of this issue, Zhao *et al.* (*4*) delve into multiorgan magnetic resonance imaging (MRI) data from over 40,000 individuals to examine the connection between heart traits and measures of brain structure and function. They identify multiple genetic links between distinct aspects of cardiovascular function and brain health. By offering a multidimensional analysis of heart-brain connections, this study could contribute to the development of personalized disease risk prediction.

Zhao *et al.* used deep machine learning, a type of artificial intelligence (AI), to analyze cardiac MRI phenotypes. This approach allows for advanced complex modeling of health-related and disease-related metrics. They extracted 82 cardiac and aortic traits, such as mass, area, volume, wall thickness and pumping efficiency, that correlated with clinical markers of heart anatomy, function, and health (*5*). Specific heart traits covaried with specific MRI-derived brain traits. For example, greater myocardial wall thickness was associated with larger subcortical brain volumes, and smaller distal aortic area was associated with differences in (pre)frontal and hippocampal volumes, and with lower global and regional measures of white matter microstructural coherence (see the figure). In addition, Zhao *et al.* reported heritability and genome-wide associations for the heart traits, which included loci associated with complex body and brain traits

[1]Cognitive Neurology, University of Leipzig Medical Center, Leipzig, Germany. [2]Department of Neurology, Max Planck Institute for Human Cognitive and Brain Sciences, Leipzig, Germany. Email: julia.sacher@medizin.uni-leipzig.de; veronica.witte@medizin.uni-leipzig.de

Brain features correlate with heart traits

Brain regions in which magnetic resonance imaging features showed statistically significant associations with heart morphology are color-coded according to the degree of significance. (Left) Thicker muscle walls of the heart were associated with larger gray matter volumes of subcortical regions including the thalamus, caudate, putamen, hippocampus, and amygdala. (Middle) The size of the distal aortic area was associated with gray matter volume of the prefrontal cortex and hippocampus. (Right) A smaller distal aortic area was associated with higher fractional anisotropy, a measure of the coherence of connecting fiber tracts, in major white matter tracts including the corpus callosum, corona radiata, and uncinate fasciculus.



and diseases such as stroke, dementia, Parkinson's disease, schizophrenia, bipolar disorder, and eating disorders.

Zhao *et al.* also leveraged known genetic underpinnings of disease to test for a causal relationship between heart and brain traits. They found that neurological diseases were significantly more common among participants with genetic risk of specific aortic traits than in participants without those risk alleles. Similarly, changes to left ventricular radial strain (heart pump efficiency) were more common among participants carrying genetic variants associated with risk of sleep apnea than noncarriers. On the basis of their findings, Zhao *et al.* propose distinct, reciprocal pathways between heart and brain function and suggest that these pathways could be exploited to provide biomarkers of disease risk and progression. However, several methodological and conceptual challenges will need to be addressed in future studies.

Multivariate analyses such as those of Zhao *et al.* involve a myriad of data points and nearly endless possible combinations of variables, which means that establishing meaningful relationships can be complicated by confounders, negligible effect sizes, and multiple testing (*6*). Zhao *et al.* enhanced the reliability of their reported results in several ways: They took into consideration a well-thought-out set of possible confounders, applied rigorous thresholds to define statistical significance, and ran replication analyses in a separate dataset. Future studies will need to use computational analysis to gauge the relative level of support that data offer for competing hypotheses (*7*), thus overcoming some of the limitations.

The fine-grained analysis of cardiac MRI data by Zhao *et al.* was possible because of their use of vision-inspired AI. Recent advances in such methods could revolutionize medical image analysis by predicting an individual's diagnosis with unprecedented accuracy (*8*). Therefore, future studies could make further use of cardiac and brain MRI datasets by training AI algorithms to predict disease progression from raw or preprocessed images, perhaps in combination with phenotypic data. However, whether the neural networks underlying these AI predictions rely on biologically meaningful features of the images and not, for example, on image artifacts, unknown data manipulation, or acquisition bias is often not clear. This limitation might explain a lack of clinical implementation so far, but explainable AI tools (*9*) can help solve these issues.

Unfortunately, AI tools often reflect the discriminative nature of society against specific groups such as non-white individuals and women. The reason for AI biases lies in the information used to train them. Although an estimated 14% of UK residents have non-white ancestry, the vast majority of UK Biobank participants are white. The main analysis by Zhao *et al.* only included participants of white ancestry, which has been the default for many genetic studies. This means that an opportunity to sample all available variance is missed. Application of AI tools without inclusive action will continue to exacerbate race and gender bias in biomedical sciences and likely result in a reinforcement of health disadvantages for most of the world's population—namely those who are not of Western, educated, industrialized, rich, and democratic (WEIRD) origin.

Commendably, Zhao *et al.* report sex-stratified analyses, showing that the strength of some heart–brain correlations differed between females and males. Given sex differences in cardiovascular and neurodegenerative diseases, including worse outcome after stroke and higher rates of Alzheimer's disease in females (*10*, *11*), these kinds of analyses are essential. Future studies, however, should investigate the effect of gender as a social construct on the heart–brain relationship.

For many common noncommunicable diseases, the first subclinical signs of disease precede the onset of severe symptoms by several decades. Therefore, leveraging multiorgan imaging data with genetic information to improve individualized detection of early biomarkers for cardiovascular and brain disease could provide an opportunity for highly effective intervention. True advances, however, will only be possible if previously underserved communities are not left out. ■

REFERENCES AND NOTES

1. T. J. Littlejohns *et al.*, *Nat. Commun.* **11**, 2624 (2020).
2. C. L. Satizabal *et al.*, *Nat. Genet.* **51**, 1624 (2019).
3. P. M. Thompson *et al.*, *Transl. Psychiatry* **10**, 100 (2020).
4. B. Zhao *et al.*, *Science* **380**, 934 (2023).
5. W. Bai *et al.*, *Nat. Med.* **26**, 1654 (2020).
6. D. Colquhoun, *R. Soc. Open Sci.* **4**, 171085 (2017).
7. R. Van de Schoot *et al.*, *Nat. Rev. Methods Primers* **1**, 1 (2021).
8. X. Liu *et al.*, *Lancet Digit. Health* **1**, e271 (2019).
9. S. M. Hofmann *et al.*, *Neuroimage* **261**, 119504 (2022).
10. K. M. Rexrode *et al.*, *Circ. Res.* **130**, 512 (2022).
11. M. T. Ferretti *et al.*, *Nat. Rev. Neurol.* **14**, 457 (2018).

ACKNOWLEDGMENTS

The authors were supported by grants from the German Research Foundation (209933838 CRC1052-03 A1) and collaborative research grant "Brain-Hatch" from the Max Planck Society and the Medical Faculty, University Clinic Leipzig.

10.1126/science.adi2392

POLICY FORUM

REGULATION

Reforming regulation with an eye toward equity

The Biden administration seeks to change how agencies weigh the effects of regulation

By **Robert W. Hahn**[1,2]

In many jurisdictions around the world, a primary way that scientific and technical knowledge and expertise can influence society is through government regulation. Government agencies regularly conduct technical analyses of proposed regulations, which can influence whether and how a regulation is implemented. In the United States, the Biden administration recently proposed some of the most dramatic attempts to modernize US federal regulatory analysis in decades. These reforms, which are broadly consistent with the president's objectives of promoting equity and addressing climate change, could substantially change how regulatory oversight is performed at the federal level and how benefits and costs are calculated. Although mostly in draft form [and open for public comments (*1*)], these reforms, if implemented, could have lasting effects on how regulation affects economic growth, on the winners and losers from regulatory activity, and on how the United States and other countries respond to long-term challenges—notably, climate change.

Since 1981, US federal regulatory oversight has required weighing the benefits and costs of major federal regulations, typically focused on environmental, health, and safety regulation. The presidential executive orders that have governed regulatory oversight across all administrations during this period share some common themes. For example, they ask that both costs and benefits be monetized by using standard economic techniques. Furthermore, the executive orders generally ask agencies to evaluate and select the regulatory alternative that maximizes net benefits (defined as the difference between benefits and costs) subject to various concerns such as legal feasibility and equity. The orders also generally recognize that not all benefits and costs can be quantified and ask for a discussion of unquantifiable benefits and costs when they may be important.

[1]Smith School of Enterprise and the Environment, Oxford University, Oxford, UK. [2]Department of Engineering and Public Policy, Carnegie Mellon University, Pittsburgh, PA, USA. Email: robert.hahn@smithschool.ox.ac.uk.

The orders have been influenced by economic principles. Economists generally agree that government regulation can have an important impact on growth and the well-being of consumers. There is also agreement that benefit-cost analysis can be a useful tool for informing regulatory decision-making, especially for large regulations involving billions of dollars of society's resources (*2*). The annual cost of the regulations that are reviewed has been estimated to be in the hundreds of billions of dollars, with benefits estimated to be a similar order of magnitude.

THE PROPOSED REFORMS

The Biden administration has shown a strong interest in modernizing regulatory oversight, having issued a memo on this topic on the president's first day in office (*1*). The current proposal to modernize the regulatory review process would retain an important role for benefit-cost analysis but would place much greater importance on identifying the winners and losers from regulatory activity (and how much they won or lost) than had previous administrations.

There are five key changes that the administration is considering or in the process of implementing, two of them contained in the executive order "Modernizing Regulatory Review" and three proposed changes to "Circular A-4," which is a draft technical document from the Office of Management and Budget (OMB) that provides guidelines to agencies on how they should do benefit-cost analysis (*1*). The reason for separating these changes is that executive orders are typically reviewed by each new administration. By contrast, the last time Circular A-4 was modified was in 2003.

The two big changes in the executive order relate to broader public participation, and the dollar cutoff point for when a formal benefit-cost analysis is required. First, the executive order attempts to encourage greater public participation to promote inclusive regulatory policy (*1*). This change can be interpreted as building on attempts by earlier administrations to be more inclusive. For example, the Clinton executive order calls for maximizing consultation involving the public and state, local, and tribal officials. It is not clear how the Biden administration will build on such efforts or whether it will succeed. Researchers have an opportunity to help shape and study the effectiveness of this process (*3*). It appears that these efforts will be targeted toward underserved communities. The administration may also want to think about targeting general consumers, who may not be well represented because the costs of regulation on consumers may not be substantial on a per person basis but may be substantial in the aggregate.

Second, the executive order changes the threshold for a "significant" regulation requiring formal benefit-cost analysis from a $100 million annual economic impact to $200 million. This change reflects an update for inflation and economic growth that has occurred and is unlikely to be controversial. It may help OMB and regulatory agencies focus their resources on the most important regulations.

There are three big changes in Circular A-4 on how agencies should do benefit-cost analyses. These concern who should be counted in a benefit-cost analysis; how different groups, such as high-income and low-income groups, should be weighed; and what discount rate should be used to compare future benefits and costs with current benefits and costs (*1*).

First, there is a substantial change concerning who should be counted in a benefit-cost analysis. There has been widespread agreement that US citizens and residents of the country should be counted in a benefit-cost analysis being reviewed by OMB. This is because such policies are supposed to advance US interests in the sense of increasing net benefits for US consumers. The draft of Circular A-4 expands this idea to include all citizens of the world in some contexts. For example, if it could be argued that US action on climate change would promote greater international cooperation, this could provide a rationale for counting net benefits to all citizens of the world, rather than focusing on benefits and costs to US residents and citizens. Although this provides a plausible rationale for considering all citizens of the world, Circular A-4 does not appear to consider the possibility that when the US does

more to provide a global public good, such as the reduction of greenhouse gas emissions, other countries may do less.

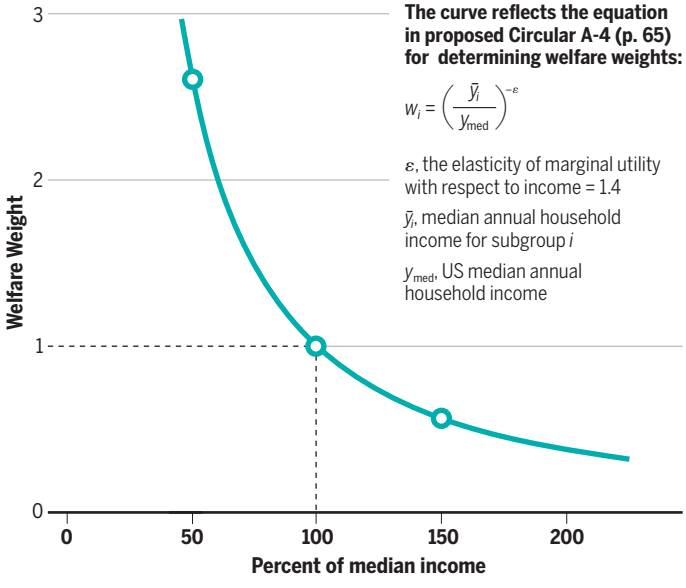
Although the Circular A-4 draft does not require agencies to take a global perspective, the impact could be considerable if they did. For example, consider the social cost of carbon, which is the value of reducing a ton of carbon in the atmosphere. The US social cost of carbon has been estimated to be about 10% of the global social cost of carbon (*4*). This suggests that the choice of using a global or domestic social cost of carbon in benefit-cost analyses for regulatory activities could make a big difference in selecting policies that maximize net benefits (*5*, *6*).

Second, the administration proposes to make a quantitative change to promote equity. It notes that a low-income person may get more satisfaction or happiness from an additional dollar than a high-income person. Thus, different welfare weights might be applied to these individuals in measuring costs and benefits (*7*). The application of such welfare weights is becoming more widely used in both academic research and policy circles, but it is not yet broadly applied (*8*). Part of the problem lies in agreeing on what the precise weights should be. The proposed change would be consistent with what was discussed in earlier policy documents that govern regulation outside of the United States, such as the "Green Book" in the UK (*9*).

What is different in the US context is that OMB introduces a formula to compute welfare weights. Although OMB does not require that agencies use this formula, their choosing to do so could have a big impact on policies that are selected. According to OMB's guidance, the welfare weight varies as a percent of median annual household income, with the welfare weight decreasing as income increases (see the figure). The welfare weight at the median annual household income, which in the United States is about $71,000, is set to 1. A family that has an income of 50% of the median would count 2.6 times as much as the median family in the benefit-cost analysis. By contrast, a family that has an income 50% more than the median would count 57% as much as the median family in the analysis. In the extreme case in which a family has zero income, the welfare weight is infinite, which defies common sense.

Introducing these welfare weights could justify regulations whose primary focus is the redistribution of wealth. For example, transferring a dollar from a group that is 150% above the median income to one that is 50% below the median would result in net benefits of $2.03 ($2.60 minus $0.57). Moreover, using this weighting can lead to a different ordering of the net benefits of programs compared with a standard benefit-cost analysis, which uses a welfare weight of one for all groups. In the context of climate change, applying such weights while also expanding analysis to consider benefits accruing to those outside the United States would imply that the net benefits to low-income developing countries would be weighted more highly than net benefits accruing to US citizens. Such a weighting scheme, although it may align with what many consider a just approach to addressing historical impacts of US actions on the rest of the world, could nonetheless raise political concerns.

Welfare weight increases as income decreases



Third, the recommended discount rate, which converts estimates of future monetized benefits and costs into current benefits and costs, is set substantially lower. The 2003 version of Circular A-4 advised using discount rates of 3 and 7%, with 7% suggested for the base case. The 3% number was estimated on the basis of the real rate of return on US long-term government debt. Following the same approach used to estimate the original 3% number, but using the last 30 years of data, the draft Circular A-4 suggests using a real discount rate of 1.7%. [The draft Circular A-4 also suggests accounting for the impacts of a regulation on capital formation by using a different, and more economically defensible, approach to measuring impacts than was used in the 2003 Circular A-4 (*10*)]. To see how this change might matter, consider a $1 benefit that accrues in 10 years from an investment. With a 1.7% rate, that dollar would be worth $0.84 today; at a 3% rate, that dollar would be worth $0.74 today; and at a 7% rate, that dollar would be worth $0.51 today. The lower the discount rate, the more the future benefits will be worth in today's dollars, meaning projects or regulations that deliver those future benefits will look more attractive. Because nearly all regulations have upfront costs and deliver benefits over time, the upshot of this proposed change is to make regulation look more attractive in terms of a benefit-cost test. This is particularly true for issues, such as climate change, in which benefit streams accrue over a long time period and may increase over time. For example, a lower discount rate would tend to increase the social cost of carbon, which would make regulations that reduce carbon dioxide emissions or store carbon dioxide more attractive.

The impacts of the five key changes listed above are difficult to gauge. Assuming that they are implemented, in the short term agencies are likely to place more efforts in meeting with the intended beneficiaries of regulation. We are likely to see more efforts aimed at distributional analysis, which up to this point has been the exception rather than the rule (*11*, *12*). This could lead to better-informed regulation because decision-makers may use more disaggregated information on the benefits and costs of particular regulations. We will also likely see the passage of more stringent regulations tamping down on greenhouse gas emissions because of the use of lower discount rates. However, there will inevitably be trade-offs. It is likely that this administration will trade-off narrow efficiency objectives (defined in terms of a traditional benefit-cost test) against broader concerns with redistribution because of its focus on equity. Over a decade or two, it is difficult to know which of these reforms will last. According to history, reforms in Circular A-4 may be more durable.

HOW RESEARCHERS CAN HELP

There are many ways in which academics might support the effort to modernize reg-

ulatory review. A good place to start is the basic policy framework. There has been a "benefit-cost analysis consensus" among economists in the sense of using benefit-cost analysis as a key input, if not the key input, in regulatory decision-making (*2*). It is worth asking, as the Biden administration does, whether other issues such as equity should be included and, if so, how. For example, should equity analyses be kept separate from standard benefit-cost analyses? In the current proposal, equity concerns could be included in benefit-cost analyses through the use of equity weights but can also be addressed separately with their own measures. Separating equity analyses has the advantage of retaining a clear benchmark for comparison for the benefit-cost analysis while providing potentially useful information for decision-makers on potential winners and losers from a policy.

The current regulatory proposals would evaluate equity impacts at the level of an individual regulation, but this may not be the best approach from a societal point of view. One might argue with respect to income groups that ideally, it would be better to evaluate the distributional impacts of regulation for all regulations passed in a given year, or even consider the distributional impacts of all government policies (such as taxes, subsidies, and regulation). "Losers" on some policies may be "winners" on others; thus, reviewing equity impacts at the level of individual policies could mean that regulatory interventions achieve lower net benefits (as measured with conventional benefit-cost analysis) than they would if the distributional impacts of such interventions were considered at a higher level of aggregation (an overall smaller "pie" with the same level of redistribution).

Another area relates to modeling how policy gets made. Totally absent from the OMB discussion is the notion that agencies are not disinterested players in the policy process [Breyer suggests that agencies may have "tunnel vision" (*13*)]. For example, agencies may have a tendency to overstate benefits or understate costs for policies that they prefer, and existing oversight procedures may not adequately reduce such bias. One indirect way of countering this bias, albeit crude, might be to raise the discount rate that is required for projects to pass a benefit-cost test. My point is not to advocate for this policy but to note that a political economy framing of the regulatory problem could lead to different policy prescriptions.

Last, the regulatory oversight policy framework for the past several decades has divided federal regulations into two categories: those that get serious scrutiny and those that do not (based on the threshold proposed to be raised from $100 million to $200 million). An alternative framing, and one used by the UK and the European Union, is to suggest that analysis should be proportional to the size and importance of the issue. This "principle of proportionality" offers a different way of approaching regulatory oversight that is more finely tuned than the current approach. It implicitly recognizes that a cutoff is arbitrary and that several different levels of effort may be appropriate for different types of regulations. This could include no analysis, a "back-of-the-envelope" benefit-cost analysis, or a more formal analysis that is reviewed by the Office of Information and Regulatory Affairs within the OMB.

"There is an important role that academics can play in shaping and evaluating these reforms."

In addition to rethinking policy frameworks, academics can help in several areas related to policy implementation. There is a growing literature that evaluates how benefit-cost analysis for regulations has been implemented by government agencies. The research shows that agencies do not always implement such analyses in accord with OMB directives. Part of the problem may lie with resources. This is important because the equity analysis that OMB is requesting under the Biden proposals will require additional resources.

Even if agencies do have adequate resources, there is a question of how to make the best use of them to influence the regulatory policy process. Some critics of the use of benefit-cost analysis have argued, for example, that such analysis is often done too late or simply used to justify agency or administration decisions after the fact. If true, this would suggest that early consultations between the regulatory agency and OMB that rely on a preliminary benefit-cost analysis could lead to better policy outcomes. Such consultations could help ensure that benefit-cost analysis plays a more prominent role in actual decision-making.

Academics can help evaluate such challenges with implementation and make suggestions for improvement. Consider three examples. One relates to reproducibility. Many of the results for benefit-cost analysis of federal regulations are not easily reproduced. If there were interest, the government could provide resources along with guidance about how this could be done, including how to address concerns about data privacy and confidentiality. This could lead to a more transparent process for public policy-making that holds decision-makers more accountable (*14*). A second example relates to helping with equity analysis (*15*). Decision-makers currently have very limited reliable information on how low-income consumers and high-income consumers respond to different regulations, such as electric vehicle subsidies, and thus the benefits of interventions by subgroup. They also have very limited information on how the cost of regulation is apportioned among different groups. Last, scholars do not have a good understanding of the actual impact of regulatory oversight on real-world policy outcomes. There is a working presumption that regulatory oversight makes a difference, but exactly how and why are not well understood.

It remains to be seen how the suite of proposed reforms will be implemented. Likely policy outcomes in the short term include a greater focus on equity and more regulations aimed at addressing climate change. If the discount rate changes endure, they could favor policy interventions with benefits over longer time horizons, such as those affecting climate change. There is an important role that academics can play in shaping and evaluating these reforms. ■

REFERENCES AND NOTES

1. The White House, Modernizing regulatory review, memorandum, 20 January 2021; https://www.whitehouse.gov/omb/information-regulatory-affairs/modernizing-regulatory-review.
2. K. J. Arrow *et al.*, *Science* **272**, 221 (1996).
3. J. V. Lavery, *Science* **361**, 554 (2018).
4. W. Nordhaus, *J. Assoc. Environ. Resour. Econ.* **1**, 273 (2014).
5. A. Fraas *et al.*, *Science* **351**, 569 (2016).
6. R. L. Revesz *et al.*, *Rev. Environ. Econ. Policy* **11**, 172 (2017).
7. M. D. Adler, *Measuring Social Welfare* (Oxford Univ. Press, 2019).
8. D. Anthoff, C. Hepburn, R. S. J. Tol, *Ecol. Econ.* **68**, 836 (2009).
9. HM Treasury, *The Green Book: Central Government Guidance on Appraisal and Evaluation* (Stationery Office, 2003).
10. R. G. Newell, W. A. Pizer, B. C. Prest, "The shadow price of capital: Accounting for capital displacement in benefit–cost analysis," Working paper no. 23-07 (Resources for the Future, 2023).
11. L. A. Robinson, J. K. Hammitt, R. J. Zeckhauser, *Rev. Environ. Econ. Policy* **10**, 308 (2016).
12. C. Cecot, R. W. Hahn, *Regul. Govern.* 10.1111/rego.12508 (2022).
13. S. Breyer, *Breaking the Vicious Circle: Toward Effective Risk Regulation* (Harvard Univ. Press, 1995).
14. F. Hoces de la Guardia, S. Grant, E. Miguel, *Sci. Public Policy* **48**, 154 (2021).
15. A. Levinson, *J. Assoc. Environ. Resour. Econ.* **6** (S1), S7 (2019).

ACKNOWLEDGMENTS

The author thanks J. Akesson, D. Anthoff, C. Cecot, N. Hendren, C. Hepburn, S. Katzen, A. McGartland, R. Metcalfe, and R. Stavins for helpful comments, and B. Harrison, C. Hutchinson, and J. K. Ong for valuable research assistance.

10.1126/science.adi6279



INSIGHTS

BOOKS *et al.*

REVIEW ROUNDUP

Summer reading 2023

Indigenous narratives inform an ecologist's ode to the octopus. An underappreciated form of communication takes center stage in a linguist's life's work. A much-maligned party drug gains respect as a therapeutic agent. From a fictional glimpse into the lives of hysteria patients in 19th-century Paris, to a fascinating history of California's dwindling redwoods, to a soul-searching account of a voyage to Antarctica, the books on this year's summer reading list invite careful reflection on topics ranging from physics to codebreaking. Read on for reviews written by alumni of the AAAS Mass Media Science & Engineering Fellows program of nine books with strong science themes set to publish this summer. **—Valerie Thompson**

In a Flight of Starlings

Reviewed by **Robert Frederick**[1]

In his latest book, *In a Flight of Starlings*, Nobel Prize–winning physicist Giorgio Parisi sets himself a task that he admits is possible but not easy: to convey both scientific results and, more importantly, how scientists create them. His overall goal is to highlight how science and society are intertwined, a coproduction, shaping and being shaped by one another.

Historically, this task has not always been so challenging. For centuries, readers of the Royal Society's *Philosophical Transactions*, the world's longest-running scientific journal, were encouraged to replicate experiments for themselves, thereby enacting the publisher's motto, *Nullius in verba* ("Take nobody's word for it"). As science became more specialized and experiments became more complicated, however, the need for a new system emerged. In the 1830s, the Royal Society introduced the peer-review process.

Unfortunately, Parisi writes, this process has led some scientists and science communicators to overemphasize results, avoiding the more difficult task of explaining the underlying evidence and analysis, while also failing to stress science's inherent uncertainty. As a result, when new evidence contradicts previously peer-reviewed findings, public trust in the scientific enterprise wanes. That distrust, in turn, can lead to science denialism and disastrous consequences.

The book's opening chapter on Parisi's experience studying the collective behavior of airborne flocks of starlings is an accessible tale of trial and error, scientific and technological advances, surprise and delight. Why a theoretical physicist spent decades studying these birds is answered by the next few chapters: Parisi did not specialize, despite receiving advice to do so from fellow CERN physicist Martinus "Tini" Veltman, who was doing his own Nobel Prize–winning work at the time. Parisi argues that it was because he studied many things simultaneously that he made connections among different fields that led to new discoveries.

The book's subsequent chapters require considerably more patience. In chapter 5, for example, readers might struggle to understand the mathematical modification that Parisi used to develop his theory about spin glasses, the work for which he won a Nobel Prize in Physics in 2021.

Parisi writes that his Nobel Prize–



winning discovery happened by accident: He was researching a mathematical tool that he planned to apply to an unrelated problem, encountered a conceptual error that led the tool to produce incoherent results, reworked the math himself, and discovered the spin glass equations. Indeed, several of Parisi's memorable anecdotes bring to mind Louis Pasteur's famous quote about how chance favors the prepared mind.

With humility, Parisi also shares stories of how his preparation and intuition have sometimes failed him. He devotes an entire chapter, for example, to recounting how a series of missteps in 1973 led him to shelve an idea rather than spend "a moment's thought" pursuing alternative hypotheses. A few months later, three other scientists had that same thought and coauthored a paper that would go on to win them a Nobel Prize in 2004.

Although Parisi's stated goal is to address a wide audience, this book speaks directly to fellow scientists and to anyone who communicates science. We must communicate both results and methods, Parisi maintains, all while sharing science's "beauty, importance, and cultural value," lest we share in the responsibility for encouraging science denialism.

In a Flight of Starlings: The Wonders of Complex Systems, *Giorgio Parisi*, Penguin Press, 2023, 144 pp.

I Feel Love

Reviewed by **Elie Dolgin**[2]

On a sunny September morning in 1975, two university students, Carl Resnikoff and Judith Gips, boarded a ferry in San Francisco Bay. Each swallowed a small capsule filled with a crystalline white powder. Their afternoon was soon filled with laughter, waves of euphoria, and a profound sense of compassion for each other and all of humanity. The pair were the first people identified by name to have taken 3,4-methylenedioxymethamphetamine—a drug better known as MDMA, molly, ecstasy, or simply "E."

Millions of others have since "rolled" on MDMA. The drug initially gained popularity among practitioners of psychedelic-assisted psychotherapy, before being discovered by young partygoers in the nightclub and rave scenes. Governments around the world then cracked down on the compound, leading to the rise of an underground drug trade fueled by a chemistry whiz who synthesized kilograms of near-pure MDMA out of a converted laboratory in southern Brazil. The stash was sold by a priest turned MDMA kingpin who, before serving a 7-year sentence for drug dealing, donated thousands of pills (which were then sold for cash) to help fund animal toxicity studies intended to demonstrate MDMA's safety.

Science journalist Rachel Nuwer recounts all this and more in her new book, *I Feel Love*, which details the complex and fascinating saga of how MDMA, a once obscure chemical, went on to become a beloved party drug, a controversial therapy tool, and a powerful symbol of the human desire for connection. While the stories and figures she describes may not share the same level of public recognition as those surrounding "Bicycle Day"—the anniversary of chemist Albert Hofmann's first intentional LSD trip—they are no less captivating. And as regulatory approval nears—pharmaceutical-grade MDMA will soon be available in Australia as a treatment for posttraumatic stress disorder, with authorizations in other countries expected soon—the need for an improved understanding and public awareness of the drug's potential effects on the brain has never been more urgent.

Much of the terrain that Nuwer treads was previously explored in Michael Pollan's 2018 bestseller, *How to Change Your Mind*, which delved into the science, culture, and history of "classical" psychedelics such as LSD and psilocybin. That influential treatise helped raise mainstream consciousness about the therapeutic potential of these substances and marked a turning point in the rise of today's psychedelic renaissance. But as Nuwer writes, "MDMA has its own distinct history and compelling cast of characters, its own unique neurological mechanisms and potential for both ill and good."

I Feel Love thus serves as something

of an unofficial sequel to Pollan's literary landmark, filling in details about a therapeutically promising drug left out of that earlier narrative. Scientifically, it picks up where Pollan left off, highlighting years of additional research into how psychedelics rewire the brain so as to create a renewed state of childlike openness and suggestibility, while also underscoring clinical data demonstrating the safety and efficacy of MDMA as a treatment for everything from alcoholism to social anxiety disorder.

As MDMA stands poised to become a cornerstone of mental health treatment, readers must ask themselves: Are they ready to roll?

I Feel Love: MDMA and the Quest for Connection in a Fractured World, *Rachel Nuwer*, Bloomsbury, 2023, 384 pp.



The octopus is featured in Indigenous stories and cultural items, such as this textile crafted by a Kuna Indian artist.

Many Things Under a Rock

Reviewed by **Dan Blustein**[3]

What has seven arms, can shape-shift to match a tuft of algae, and neutralizes a live clam by drilling a hole in its shell and injecting paralyzing saliva? If you guessed a male octopus that just lost an arm to a cannibalistic female after a failed mating attempt, you would be correct!

Many Things Under a Rock, by ecologist David Scheel, includes numerous such dramatic and captivating octopus factoids, but it also presents an accessible and nuanced exploration of the lives of these intriguing invertebrates. The book's careful scientific observation, contextualized with modern and historical accounts of the species from Western and Native peoples, is an engaging read and a refreshing break from the seemingly steady stream of "sharktopus" thrillers with which we have been presented in recent years.

Scheel, a cephalopod researcher, quickly garners the reader's trust with his meticulous description of octopuses in the lab and in the wild. We follow along as Scheel's perspective shifts from an initial fear of these mysterious creatures, driven by legends of gigantic octopuses wrestling with divers, to one of nuanced respect. He details his transformation into an octopus expert as the book progresses, recounting expeditions to the frigid depths of the northern Pacific and to southern Australian clam beds as he searched for clues about how different octopus species interact with their environment, predators, prey, and each other.

Exploring the octopus requires a multidisciplinary approach, to which Scheel commits as he weaves together Western evolutionary history, behavior, ecology, and neuroscience with Indigenous ways of knowing. He illustrates the connections between octopus biology and Native Alaskan octopus histories, for example, by revealing how variations in Indigenous language seem to reflect octopus natural history. The root "am-" in the Inuit word for octopus, "amikuk," means "skin", he reveals—a seeming reference to the key evolutionary adaptation differentiating octopus from more-ancient mollusks: the loss of an external shell and the emergence of skin that enables swimming.

Warming waters have driven transient octopus population booms in Japan and England throughout the past 150 years, a phenomenon that is also reflected in various Indigenous histories. Scheel connects these histories by discussing how communities have made sense of local changes in octopus abundance.

A few of the book's descriptions of octopus actions and anatomy may be too detailed for nonexperts, but such instances are infrequent and further reinforce Scheel's precise attention to detail in recounting his field observations. Scheel also references a range of scientific studies throughout the text, including some very recent work, although readers must rely on a notes section at the end rather than in-text citations to learn more about this research.

The word for "octopus" in Eyak—a language native to Southcentral Alaska—is "tse-le:x-guh," which translates literally as "many things under a rock." The book's title is thus a descriptor, not only of an octopus's eight arms sheltered by a protective rock but also the many mysteries left to unravel about these extraordinary creatures.

Many Things Under a Rock: The Mysteries of Octopuses, *David Scheel*, Norton, 2023, 320 pp.

The Hidden History of Code-Breaking

Reviewed by **Francisco J. Guerrero**[4]

Chock-full of code puzzles for readers to solve, Sinclair McKay's *The Hidden History of Code-Breaking* is an interactive exploration of the seemingly never-ending arms race between codemakers and codebreakers. The book's strengths include its focus on the motivations behind code creation and the individuals who created some of history's most well-known codes. McKay writes, for example, about the serendipitous moment Samuel Morse first conceived of the dots, dashes, and spaces that would become Morse code while on board a transatlantic ship. Like vessels crossing the ocean, Morse imagined words going on a similar journey, carried by short electrical impulses along very long wires. McKay also highlights the stories of individuals who used their intelligence, persistence, and creativity to crack codes that stumped others for years. This latter group includes Alan Turing, whose Bletchley Park team eventually cracked the Enigma code used by the Nazis during World War II.

McKay's writing is clear and engaging, making complex concepts and theories accessible to readers without oversimplifying them. In chapter 12, for example, he balances technical details and storytelling masterfully while exploring the Human Genome Project. Here, complex ideas such as gene sequencing are woven skillfully into tales about solving the mystery of what makes us human.

The book touches on various fields, including linguistics, math, history, archaeology, literature, biology, and politics, and demonstrates how codebreaking has influenced these fields throughout history,

offering a rich and insightful perspective for readers interested in the intersection of these fields. In chapter 5, for example, McKay explores the role of human relationships in the evolution of codes and ciphers, noting how secret lovers have long encoded messages in poetry, songs, and other romantic expressions to arrange specific dates and encounters.

Shortcomings include the fact that the puzzles presented for readers to solve throughout the book are of varying and inconsistent difficulty, a few contain inherent language and cultural biases that may not be accessible to all readers, and the instructions to solve them are not always clear. Furthermore, the book's focus on historical military and government codes may not appeal to all readers, especially those inclined toward modern cryptography applications. The book could also have benefited from more detailed explanations or images of some codes and artifacts. For example, McKay's description of the Phaistos disc would have been clearer if accompanied by a pictorial diagram.

Despite these weaknesses, *The Hidden History of Code-Breaking* is a worthwhile introduction to the world of codes and ciphers that offers a glimpse into the fascinating realm of encryption and how codes have been used throughout history. Its puzzles and historical trivia would make for interesting summer travel companions.

The Hidden History of Code-Breaking: The Secret World of Cyphers, Uncrackable Codes, and Elusive Encryptions, *Sinclair McKay*, Pegasus, 2023, 400 pp.

Thinking with Your Hands

Reviewed by **Lisa Aziz-Zadeh**[5]

How does gesture influence thinking? What does it reveal about language and conceptual learning? How can we use it to teach, parent, and heal? These are among the many questions Susan Goldin-Meadow discusses in her thorough and powerful book, *Thinking with Your Hands*. The volume synthesizes the author's 50+ years of expertise in gesture research, for which, among other awards and accolades, she won election into the National Academy of Sciences in 2020 and was the recipient of the prestigious David E. Rumelhart Prize in 2021.

In the book's first chapter, Goldin-Meadow discusses how gesture can reveal whether a child is ready to learn a new concept. She and her colleagues found, for example, that children will sometimes provide a wrong answer to a mathematical question while simultaneously revealing through gesture that they understand the underlying concept, a mismatch that can be used as a sign that the child is on the cusp of learning the idea being taught. But educators must be attuned to gesture to maximize this learning stage—not recognizing the gesture–speech mismatch is a loss of a teachable moment, she argues.

Meanwhile, in chapter 4, Goldin-Meadow reveals that children who are not taught language—for example, deaf children whose hearing parents do not use sign language—will often develop language spontaneously. By studying the so-called "homesign" gestures made by such children, researchers have determined that humans can develop certain language features on their own—for example, creating gesture sentences that are hierarchically structured. Other aspects of language, however, such as the use of the passive voice, need to be learned. Interestingly, mathematical reasoning appears to require more person-to-person teaching than does language; apparently not all abstract concepts are similar in their amenability to self-invention.

After discussing how gesture can be used to improve teaching, parenting, and rehabilitation, Goldin-Meadow questions whether mediums that do not reveal gesture—auditory recordings, for example, or live or recorded videos that restrict gesture space—should be admissible in judicial hearings. Laboratory studies indicate that an interviewer's gestures might introduce biases in a witness's memory and, simultaneously, that a witness's gestures may reveal more information than their speech alone.

It is at this point that the true power of this book emerges: Having convinced the reader to accept the importance and impact of gesture, Goldwin-Meadow urges us to question its broader societal implications. That she might bring a lay audience this far in their appreciation of the vital but often overlooked impact of gesture on interpersonal communication is a triumph of this book.



PHOTO: G-STOCK STUDIO

Gestures can convey information that speech cannot, making them critical features of communication.

Thinking with Your Hands: The Surprising Science Behind How Gestures Shape Our Thoughts, *Susan Goldin-Meadow*, Basic Books, 2023, 272 pp.

The Madwomen of Paris

Reviewed by **Stephani Sutherland**[6]

The Madwomen of Paris by Jennifer Cody Epstein tells the fictional story of Laure, a young woman living in Paris in the late 19th century who has been orphaned, separated from her sister, and, like so many real women of that time, institutionalized with hysteria at the Salpêtrière asylum. There, Laure recovers and—with few other choices as a penniless young woman—stays on to work as a nursemaid to other hysterical patients. Her determination to be reunited with her sister is complicated by the arrival of a mysterious new patient, Josephine, who has clearly undergone a serious trauma but has no memory of what has happened to her.

Josephine becomes a "star patient" of the asylum's head doctor, Jean-Martin Charcot, who hypnotizes his hysterical patients to study the disease, often in front of a packed public audience. Under hypnosis, patients are subjected to all sorts of humiliations, including sexual assault. Those who behave badly receive "hydrotherapy," which consists of being sprayed with a strong hose, or are thrown into the "softs" (padded cells). The worst fate, it seems, is to be assigned to the "lunacy" wing of the hospital, where patients' sanity is believed to be beyond repair. Josephine is placed under Laure's care, and together they survive the horrific conditions of the asylum and unravel the mystery of Josephine's past.

Readers are informed up front that "Though inspired by a real place (the Salpêtrière asylum, now a teaching hospital in Paris), real events, and real historical figures, *The Madwomen of Paris* is a work of fiction." But a key character of the book, Charcot, was a real person, sometimes referred to as the "father of neurology." In addition to studying hysteria, the real Charcot connected pathophysiology with the symptoms of neurological diseases, allowing him to make the first diagnoses of multiple sclerosis and amyotrophic lateral sclerosis, among

other diseases. Josephine, too, is based in part on a real "star" patient—Augustine Gleizes—the author explains in a note.

The book's blend of fact and fiction may leave readers with questions about which parts of the story reflect reality and which do not. For example, were the conditions truly as terrible for institutionalized women at that time as the book describes? Cody Epstein notes that she has "done what historical novelists can happily (if perhaps uncomfortably for some) do, shifting and omitting some events and chronologies, and entirely inventing others."

Other unanswered questions may inspire further reading. Hysteria is no longer recognized as a medical disorder, for example, so what really afflicted the patients in the asylum?

In any case, Cody Epstein has achieved her goal of immersing readers in the "stranger-than-fiction universe" of late-19th-century Paris. At a time when women's reproductive rights are under threat and people with unexplained medical conditions are routinely gaslit, *The Madwomen of Paris* provides a fascinating look back at a condition with modern-day resonance.

The Madwomen of Paris: A Novel, *Jennifer Cody Epstein*, Ballantine Books, 2023, 336 pp.

Life on Other Planets

Reviewed by **Clare Fieseler**[7]

Aomawa Shields is many things: daughter of musicians, boarding school star, trained actor, sometimes astronomer, and a person with a deeply curious mind. Her 2015 TED talk "How we'll find life on other planets" propelled her to internet fame and inspired the title of her new memoir, *Life on Other Planets*. But Shields should not be defined by her alien-seeking research. As she puts it: "I am a champion of interdisciplinarity."

Shields's powerfully personal book tells the story of a Black woman with two passions finding her place in the world. After a failed first start as an astrophysics PhD student, Shields pursued professional acting for a decade. She eventually returned to the stars—and graduate school—restarting a career as an astrobiologist and, later, professor. Her journey is filled with self-doubt and serious soul-searching, but here's what is clear: Modern science is still built for the easily defined worker. As a scientist-turned-journalist myself, I said "yes" out loud multiple times as I read how hard it was for Shields to be an interdisciplinarian and career-pivoter.

In *Life on Other Planets*, Shields makes a stand against a kind of unbridled scientific success that comes at any cost. Hers is a story of applying to the US astronaut program three times, rejected each time and wiser for it. The time away from her daughter would not have been worth it, she realized. She normalizes a view of the scientific career that is always changing. Goals will—and should—evolve as we learn more about ourselves and the objects we study.

In one moving scene, Shields describes her elation at being invited to lunch by Ann Druyan, Carl Sagan's widow and writing partner, where Shields receives a warm embrace and mutual respect from "the most important person" in Sagan's life. Shields and Sagan are the closest of kindred spirits, sharing a propensity for polymathy and a passion for science communication. As a Black woman, the obstacles Shields encountered ascending to a Sagan-like professional position feel unfair. She describes her experiences in touching detail, but she does not interrogate the external societal structures that continue to serve as obstacles for women and people of color, not to mention polymaths.

What, if anything, should change so that the life of an astronomer-slash-actor is not so arduous? The book should be a warning to the scientific community that, still today, pays lip service to STEAM (science, technology, engineering, arts, and mathematics) while leaving behind the people who do that work: scientific artists and artistic scientists.

Imagining the reader as someone compelled by the cosmos, like herself, Shields gets to the root of it: "What do I want for you? I want you to look up and be amazed. I want you to feel supported, less lonely and afraid, a part of rather than apart from." We may or may not be alone in the Universe, but Shields makes a case for togetherness, with each other and within ourselves.



Aomawa Shields stands in front of the Arecibo Observatory in Puerto Rico in 1996.

Life on Other Planets: A Memoir of Finding My Place in the Universe, *Aomawa Shields*, Viking, 2023, 352 pp.

The Ghost Forest

Reviewed by **Bridget Alex**[8]

Evolving some 200 million years ago, redwood trees survived the rupturing of Pangea, the meteor that offed the dinosaurs, and innumerable natural catastrophes and climate swings. Individual trees have attained heights of more than 350 feet, trunks with 30-feet diameters, and 3000th birthdays.

In the mid-19th century, these primordial giants flourished in a 2-million-acre forest that stretched along California's coast from the Bay Area to the Oregon border. Today, just 4% of this land harbors coast (or California) redwoods. The trees' evolutionary cousin, the giant sequoia, ekes by in scattered groves of the Sierra Nevada. *The Ghost Forest* explores how and why the world's tallest trees were logged nearly to extinction in less than two centuries.

Greg King is an authoritative guide for this journey, highlights of which include extractive capitalism, specious regulations, and shady dealings. A journalist and environmental activist, he also enters the plot as a protagonist who led campaigns in the 1980s and 1990s to save declining old-growth forests. The book interweaves King's experiences from the front lines of eco-activism with his decades of archival research into the forces behind redwood decimation.

The history unfolds in three eras. During the late 1800s, private companies illegally acquired lands inhabited by coast redwoods. After World War I, loggers liquidated these forests and sold the prized timber to make

[1]The reviewer is at the Global Virus Network, Baltimore, MD 21201, USA. Email: ref@gvn.org [2]The reviewer is a science journalist in Somerville, MA, USA. Email: elie@eliedolgin.com [3]The reviewer is at the Department of Psychology, Acadia University, Wolfville, NS B4P 2R6, Canada. Email: dan@danblu.com [4]The reviewer is at the Department of Forest Engineering, Resources, and Management, Oregon State University, Corvallis, OR 97333, USA. Email: francisco.guerrero@oregonstate.edu [5]The reviewer is at the Department of Psychology, University of Southern California, Los Angeles, CA 90089, USA. Email: lazizzad@usc.edu [6]The reviewer is a freelance writer based in Claremont, CA, USA. Email: sutherland@nasw.org [7]The reviewer is at the National Museum of Natural History, Smithsonian Institution, Washington, DC 20013, USA, and *The Post and Courier*, Charleston, SC 29403, USA. Email: clare.fieseler@gmail.com [8]The reviewer is at the Department of Human Evolutionary Biology, Harvard University, Cambridge, MA 02138, USA. Email: balex@harvard.edu [9]The reviewer is at the Department of Earth and Environmental Sciences, Columbia University, New York, NY 10027, USA. Email: ehc2150@columbia.edu



Logging and disingenuous conservation efforts have substantially reduced populations of California redwoods (*Sequoia sempervirens*).

PHOTO: DOUG GIMESY

water and oil pipes, railway ties, shingles, telephone poles, and other infrastructure for the growing country. Near the end of the 20th century, corporations profited once more from the swindled land when they sold redwood stands back to the government.

The book triumphs as a comprehensive accounting of events and entities that ushered in this irreplaceable loss. Synthesizing decades of sleuthing, King reveals unexpected culprits such as the Save the Redwoods League—an organization created by business titans wanting to protect scenic redwood stands so the public would be placated but logging could continue out of sight. He also tactfully grapples with vile redwood protectors: Eugenicists and Nazi supporters considered the trees to be "apex species" worthy of life.

For casual readers, some portions will drag as King names historical individuals and companies that figure only briefly and situates tree groves within California watershed geography. The text also becomes oversaturated with superlatives for redwood size, forest acres, and timber planks and payouts—but how else does one describe astronomical profits made from felling vast swaths of the world's tallest trees?

Patient readers will be rewarded because the pace quickens to that of a page-turner when King recounts tales of harrowing activism in the 1980s and 1990s. Suffering arrests, death threats, and FBI infiltrators, he and colleagues staged heroic protests, once even scaling the Golden Gate Bridge.

Although set in the past, the book is urgently of-the-moment. Early perpetrators of what is now called "greenwashing," corporate leaders hatched the Save the Redwoods League at Bohemian Grove, the elite resort recently in headlines because of Supreme Court Justice Clarence Thomas's visits, for example. More broadly, the systems of power and wealth that targeted the redwoods and their protectors continue to inflict violence on Earth's defenders worldwide. If the trends of global warming and deforestation hold steady, *The Ghost Forest* may eventually read as a prequel to the ghost planet.

The Ghost Forest: Racists, Radicals, and Real Estate in the California Redwoods, *Greg King*, PublicAffairs, 2023, 480 pp.

The Quickening

Reviewed by **Elizabeth Case**[9]

In *The Quickening*, Elizabeth Rush takes readers to the precipice of the climate crisis. Aboard the *Nathaniel B. Palmer*, an American icebreaker, Rush and a crew of scientists, journalists, and support staff set bow and stern in front of Thwaites Glacier for the first time in history, sampling water in unnamed bays; collecting sediments, shells, and bones; and sending submarines under the glacier to photograph evidence of past rates of glacial retreat.

The Quickening is framed as a play in four acts. The cast consists of the scientists, crew, two other journalists, and the glacier (although, interestingly, not Rush herself). Interspersed between Rush's monologues, her shipmates tell stories about their births, the reasons they do the work they do, and the lessons they learn from it. The glacier, of course, never speaks directly. Instead, it calves, groans, and creaks—communiques left open to our interpretation.

Rush's descriptions of the ice and ocean transport readers to the ship's bridge. The first iceberg she sees is "dove gray," "whipped meringue," "a milky-aquamarine spire," and "the pearly luster of kyanite." Later, between floes, "where the nearly frozen water shows," she recalls "a turquoise so deep it torques all it touches into something new."

The Quickening is an intensely personal story—a memoir that is also an act of processing as Rush works through her decision to have a child as the climate crisis looms. The book's title references the sensation a mother experiences when a baby first moves in utero—a nod not just to Rush's own efforts to become pregnant but also to the moment scientists noticed that Thwaites had begun to respond to climate change.

As a scientist, I have also traveled to Thwaites. I am planning to go again this year. And because, as Rush points out, no pregnant people are allowed to work in or around Antarctica, each year I go is another year my partner and I must wait to start a family, another year of uncertainty about whether the desire for a child is selfish, biological, logical, or loving. *The Quickening* helped me orient these questions, although, of course, it could not answer them.

I did wonder about the sense of agency Rush grants to Thwaites and whether it undermines humankind's responsibility for the planet's future. At one point, she asks, "Will Miami even exist in one hundred years?" and answers, "Thwaites will decide." Rush is referring to how much sea level rise Thwaites will contribute as it melts. But it is us—and really a small subset of us—who will decide. We may already have, if the glacier has already begun unstably collapsing.

This response aside, *The Quickening* is a poignant, necessary addition to the body of Antarctic literature, one that centers—without glorifying—motherhood, uncertainty, community, vulnerability, and beauty in a rapidly melting world.

The Quickening: Creation and Community at the Ends of the Earth, *Elizabeth Rush*, Milkweed Editions, 2023, 424 pp.

10.1126/science.adi7361



LETTERS

Shanghai Tower received a green building certifica
but no label in China currently assesses the
carbon generated by a building throughout its lifespan.

guidelines for energy efficiency evaluation and labeling of civil buildings" (2008); http://www.gov.cn/govweb/gzdt/2008-07/05/content_1036757.htm [in Chinese].
6. "Beijing 2022 Winter Olympics has become the first 'carbon neutral' Winter Olympics to date," *CCTV* (2022); https://news.cctv.com/2022/02/18/ARTI5afFeKSxFQCbxdtOBbir220218.shtml [in Chinese].
7. "Zhu Yingxin: Exploring the 'China scheme' of green building for carbon neutralization," *Surging News* (2022); https://m.thepaper.cn/baijiahao_18153458 [in Chinese].
8. Z. Xiong, X. Shen, Q. Wu, Q. Guo, H. Sun, *Int. J. Electric. Pow. Energ. Syst.* **151**, 109148 (2023).
9. N. Alaux *et al.*, *J. Clean. Product.* **382**, 135278 (2023).
10. M. K. Ansah *et al.*, *Sci. Tot. Environ.* **821**, 153442 (2022).
11. "How to build low-carbon buildings? Look at the green wisdom contained in ancient Chinese architecture," *Surging News* (2021); https://baijiahao.baidu.com/s?id=1701688054930361850&wfr=spider&for=pc [in Chinese].
12. "ASHRAE publishes first zero net energy and zero net carbon standard," ASHRAE (2023).

10.1126/science.adi0397

Edited by **Jennifer Sills**

Improve energy-efficient construction in China

In the past few decades, China's construction industry has undergone a swift expansion, increasing its energy use and carbon emissions (*1*). In an effort to meet climate goals (*2*), China has formulated guidelines to minimize carbon emissions in new development (*3*). However, the construction industry lacks effective regulatory standards and assessments to ensure energy efficiency.

When inspecting the carbon impact of construction, the Chinese government primarily refers to the Green Building Evaluation Standard and the Technical Guidelines for Energy Efficiency Evaluation and Labeling of Civil Buildings, which comprehensively assess variables such as resource management, land planning, and building features (such as air conditioning units, light and sound impacts, and green spaces) (*4*, *5*). However, these standards rely on outdated baselines. For instance, the 2022 Beijing Winter Olympics have been hailed as the first Olympics in history to achieve carbon neutrality (*6*), but the construction of the Olympic venues adhered to 2014 regulations for green buildings (*7*). Since 2014, carbon mitigation strategies have improved, and lower emission options could have been used for energy systems, construction materials, and operational strategies (*8*, *9*).

The current standards also lack a framework for monitoring and appraising the carbon footprint throughout the entire lifecycle of buildings. The impact of new infrastructure includes not only design and construction but also the emissions produced while it is in use—in some cases spanning decades—and its demolition and disposal (*10*). Many projects in China now claim to qualify as "low-carbon construction" (*11*) (a more efficient classification than "green construction") by citing energy-saving technologies used during limited stages, such as construction or operation. To accurately classify projects as low carbon emitters, China needs a comprehensive evaluation system.

To maximize the use of low-carbon construction equipment, materials, and methods, the central government should standardize the design and construction of energy-efficient buildings. Local governments and relevant agencies should rigorously review project applications, strengthen construction quality monitoring, and increase the frequency of spot checks during the building operation phase. Finally, an evaluation system that determines the carbon emissions over the entire lifespan of new infrastructure, similar to the US Evaluation System for Zero Net Carbon Building Performance (*12*), should inform development decisions.

Xinbo Xu and Zhiwei Lian*
Department of Architecture, Shanghai Jiao Tong University, Shanghai 200240, China.
*Corresponding author. Email: zwlian@sjtu.edu.cn

REFERENCES AND NOTES

1. "Report: China's urban building carbon emissions show a decreasing distribution from north to south and from east to west," *Guangming Net* (2023); https://m.gmw.cn/baijia/2023-01/05/1303244808.html [in Chinese].
2. "Xi Jinping's report to the 20th National Congress of the Communist Party of China," *Xinhua* (2022); http://www.gov.cn/xinwen/2022-10/25/content_5721685.htm [in Chinese].
3. Y.-M. Wei *et al.*, *Engineering* **14**, 52 (2022).
4. Ministry of Housing and Urban-Rural Development, "Notice on national standard for comments on the national standard 'green building evaluation standard (partially revised draft for comment)'" (2023); https://www.mohurd.gov.cn/gongkai/zhengce/zhengcefilelib/202302/20230223_770428.html [in Chinese].
5. Ministry of Housing and Urban-Rural Development, "Notice on printing and distributing the technical

Researchers need better access to US Census data

The US Census Bureau decided to adopt a differential privacy framework by adding noise to the 2020 Census data to improve the confidentiality of individual Census responses (*1*). To protect the collected data, random noise was added to the tabulated statistics, and the data and noise were stored together in a Noisy Measurement File (NMF). The NMF is critical for understanding biases in the Census data and for performing valid statistical inferences, as it potentially allows data users to adjust for the noise in their analyses. However, in 2021, the Census Bureau released only the final tabulated statistics that were produced after postprocessing the NMF (*1*). This postprocessing ensured the final published data met data consistency requirements (such as nonnegative population counts), but it may have also introduced systematic biases (*2*–*7*). The Census Bureau must provide data users access to the NMF in usable form to facilitate the wide array of use cases for Census data.

In April, after public requests (*2*, *8*), the Census Bureau released a demonstration NMF based on the 2010 Census data (*9*). It plans to release the NMF for the 2020 Census later this year (*10*). Unfortunately, the current NMF release is difficult to process and is unlikely to be useful for most Census data users (*11*).

To help users work with the NMF, the Census Bureau should host an unnested, labeled version on the Census website with Application Programming Interface access so researchers can more easily access and analyze data. Centralized NMF documentation

should be made available that explains the high-level structure of the NMF and its relation to published decennial statistics and tabulation geographies. Aggregation specifications should link raw noisy measurements to traditional tabulation statistics to facilitate statistical analysis. An additional version of the NMF for which these aggregations have already been performed should also be made available, so that each tabulation has a single estimate. Detailed geographic information for the NMF, including shapefiles and geography assignment files that describe the relationship between traditional tabulation geographies and NMF geographies, will also help analysts.

Census data serve as the backbone for a substantial number of scientific analyses and policy decisions. Producing a more accessible and useful NMF will benefit researchers and facilitate more accurate and applicable conclusions without compromising the confidentiality of individual Census responses.

Cory McCartan[1], Tyler Simko[2], Kosuke Imai[1,2]*
[1]Department of Statistics, Harvard University, Cambridge, MA, USA. [2]Department of Government, Harvard University, Cambridge, MA, USA.
*Corresponding author. Email: imai@harvard.edu

REFERENCES AND NOTES

1. J. Abowd *et al.*, *Harvard Data Sci. Rev.* (Special Issue 2) 10.1162/99608f92.529e3cb9 (2022).
2. C. Dwork, R. Greenwood, G. King, "Letter to U.S. Census Bureau: Request for release of 'noisy measurements file' by September 30 along with redistricting data products" (2021).
3. C. T. Kenny *et al.*, *Sci. Adv.* **7**, 1 (2021).
4. National Congress of American Indians, "Letter to Dr. Ron S. Jarmin from Dante Desiderio, Chief Executive Officer" (2021).
5. JASON, "Consistency of data products and formal privacy methods for the 2020 Census (jsr21-02, January 11, 2022)," Tech. Rep., The MITRE Corporation (2022).
6. C. T. Kenny *et al.*, *Harvard Data Sci. Rev.* (Special Issue 2) 10.1162/99608f92.abc2c765 (2023).
7. J. Scariano, I. Youngs, "Balancing utility versus privacy in the 2020 Census: Sentiments from data users" 10.2139/ssrn.4089888 (2022).
8. Phillips v. Census Bureau, 1:2022cv09304, US District Court for the Southern District of New York (2022).
9. J. Abowd *et al.*, "2010 Census production settings redistricting data (P.L. 94-171) Demonstration Noisy Measurement File" (2023).
10. US Census Bureau, "Press Release CB23-CN.03: Census Bureau announces schedule updates for 2020 Census data products" (2023).
11. C. McCartan, T. Simko, K. Imai, "Making differential privacy work for Census data users" arXiv:2305.07208 (2023).

10.1126/science.adi7004

Chile's road plans threaten ancient forests

During the United Nations Biodiversity Conference (COP15) in December 2022, nearly 200 countries, including Chile, agreed to halt biodiversity loss by 2030 and to take urgent actions to stop the extinction of endangered species. Despite this commitment, the Chilean government is pushing for the construction of a road that would cross the Alerce Costero National Park (*1*), an area of global importance for biodiversity conservation (*2*) and home to the endangered conifer *Fitzroya cupressoides* (*3*). Throughout the world, roads threaten biodiversity and ecosystem functions (*4*). Before pushing this project ahead, Chile should consider the likelihood that the road will undermine the country's progress toward international environmental commitments.

Fitzroya, which grows exclusively in Chile and Argentina, is one of the longest-living tree species on Earth (*5*, *6*). *Fitzroya* forests are among the forests that sequester the most carbon worldwide, and they provide critical ecosystem services and a wealth of historical and environmental information (*7*). *Fitzroya* populations face a high risk of extinction after centuries of overexploitation and burning (*7*) and, more recently, as a result of climate change (*3*).

The Alerce Costero National Park is the only area that protects a genetically unique *Fitzroya* population and the last remnants of species-rich Valdivian temperate rainforests from the Coastal range (*8*, *9*). Building a road through this vulnerable ecosystem would increase the risk of invasion by alien species, facilitate illegal logging, and greatly increase the probability of extensive wildfires in the park (*4*). More than 90% of wildfires occur within 1 km of roads in Chile (*10*).

Chile's proposed road completely ignores the COP15 agreement. The government must honor its commitments and prioritize the protection of the country's most endangered species. The global biodiversity crisis and the unprecedented high risk of species extinction (*11*) call for timely and concrete actions. The preservation of roadless areas is critical to the goals of reducing extinction risks and protecting 30% of the planet.

Rocío Urrutia-Jalabert[1,2,3]*, Jonathan Barichivich[3,4,5], Álvaro G. Gutiérrez[3,6,7], Alejandro Miranda[2,8]
[1]Departamento de Ciencias Naturales y Tecnología, Universidad de Aysén, Coyhaique, Chile. [2]Centro de Ciencia del Clima y la Resiliencia, CR2, Santiago, Chile. [3]Corporación Alerce, Valdivia, Chile. [4]Laboratoire des Sciences du Climat et de l'Environnement (LSCE), LSCE/IPSL, CEA-CNRS-UVSQ, Université Paris-Saclay, Gif-sur-Yvette, France. [5]Instituto de Geografía, Pontificia Universidad Católica de Valparaíso, Valparaíso, Chile. [6]Departamento de Ciencias Ambientales y Recursos Naturales Renovables, Facultad de Ciencias Agronómicas, Universidad de Chile, Santiago, Chile. [7]Instituto de Ecología y Biodiversidad, Santiago, Chile. [8]Laboratorio de Ecología del Paisaje y Conservación, Departamento de Ciencias Forestales, Universidad de La Frontera, Temuco, Chile.
*Corresponding author.
Email: rocio.urrutia@uaysen.cl

REFERENCES AND NOTES

1. Ministerio de Obras Públicas, "Ficha del Proyecto: Conservación Ruta T-720, Cruce T-60 (Las Ventanas) Alerce Costero Cruce T-450 (Corral)" (2023) [in Spanish].
2. R. A. Mittermeier, W. R. Turner, F. W. Larsen, T. M. Brooks, C. Gascon, in *Biodiversity Hotspots; Distribution and Protection of Conservation Priority Areas*, F. Zachos, J. Habel, Eds. (Springer-Verlag, 2011), pp. 3–22.
3. J. F. Perez-Quezada *et al.*, *J. Geophys. Res. Biogeosci.* **128**, e2022JG007258 (2023).
4. P. L. Ibisch *et al.*, *Science* **354**, 1423 (2016).
5. A. Lara, R. Villalba, *Science* **260**, 1104 (1993).
6. G. Popkin, *Science* 10.1126/science.add1051 (2022).
7. M. E. González *et al.*, *Front. For. Glob. Change* **5**, 10.3389/ffgc.2022.960429 (2022).
8. T. R. Allnutt *et al.*, *Mol. Ecol.* **8**, 975 (1999).
9. C. Smith-Ramírez, F. Squeo, Eds., *Biodiversidad y Ecología de los Bosques Costeros, Second Edition* (Editorial Universidad de Los Lagos, Osorno, Chile, 2019).
10. J. Carrasco *et al.*, *J. Environ. Manag.* **297**, 113428 (2021).
11. E. S. Brondizio, J. Settele, S. Díaz, H. T. Ngo, Eds., "Global assessment report on biodiversity and ecosystem services of the Intergovernmental Science-Policy Platform on Biodiversity and Ecosystem Services" (IPBES, 2019).

10.1126/science.adi0228

TECHNICAL COMMENT ABSTRACTS

Comment on "Policy impacts of statistical uncertainty and privacy"

Yifan Cui *et al.*

Steed *et al.* illustrate the crucial impact that the quality of official statistical data products may exert on policy decisions. We underscore the importance of conducting principled quality assessment of official statistical data products. We observe that the quality assessment procedure employed by Steed *et al.* needs improvement, due to the inadmissibility of the estimator used and the inconsistent probability model it induces on the joint space of the estimator and the observed data. We propose alternative statistical methods to conduct principled quality assessments for official statistical data products.

Full text: dx.doi.org/10.1126/science.adf9724

Response to Comment on "Policy impacts of statistical uncertainty and privacy"

Ryan Steed *et al.*

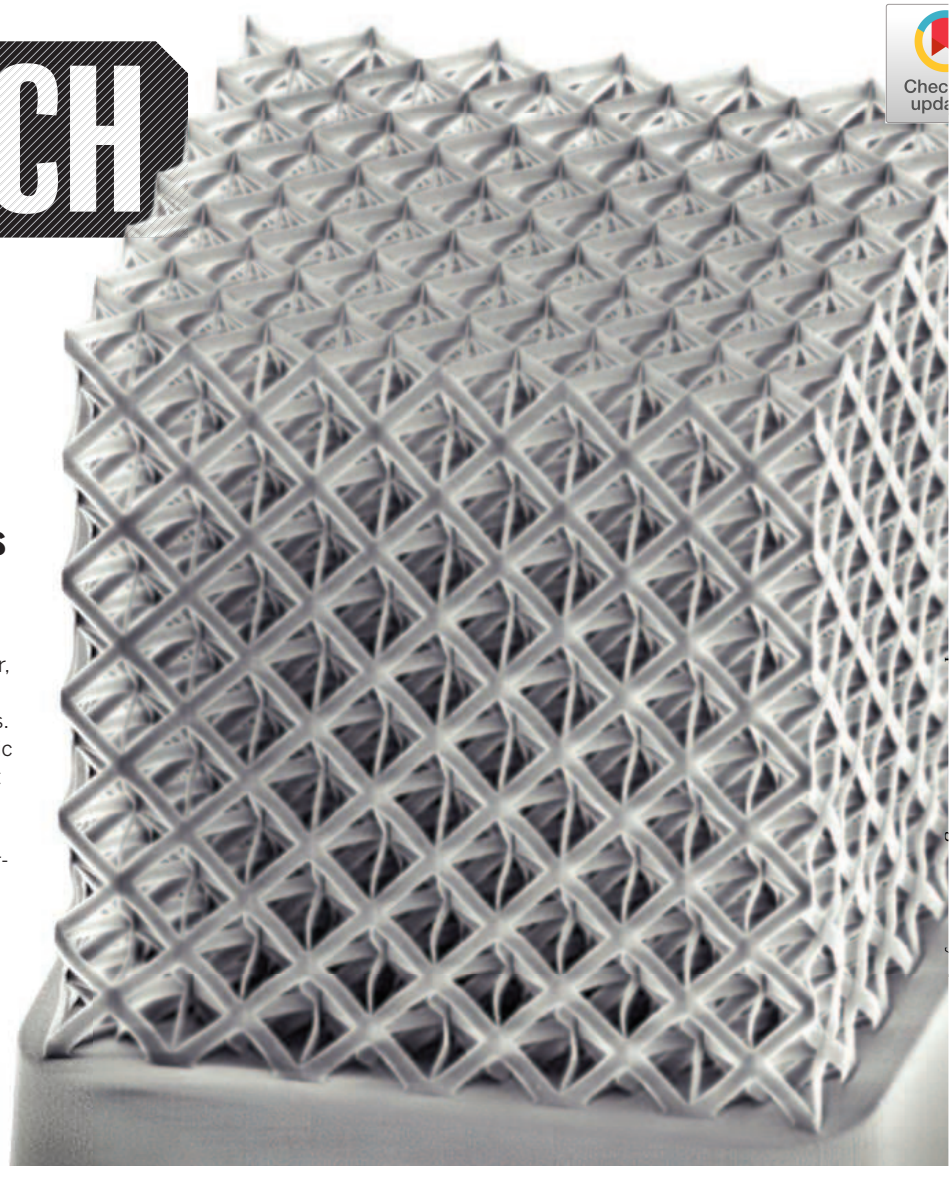
Cui *et al.* propose a valuable improvement to our method of estimating lost entitlements due to data error. Because we don't have access to the unknown, "true" number of children in poverty, our paper simulates data error by drawing counterfactual estimates from a normal distribution around the official, published poverty estimates, which we use to calculate lost entitlements relative to the official allocation of funds. But, if we make the more realistic assumption that the published estimates are themselves normally distributed around the "true" number of children in poverty, Cui *et al.*'s proposed framework allows us to reliably estimate lost entitlements relative to the unknown, ideal allocation of funds—what districts would have received if we knew the "true" number of children in poverty.

Full text: dx.doi.org/10.1126/science.adh2297

RESEARCH

IN *SCIENCE* JOURNALS

Edited by **Michael Funk**



A fused silica lattice created by 3D printing

PHOTO: COOPER *ET AL.*

3D PRINTING

A cool path for making glass

Printing glass with additive manufacturing techniques could provide access to new materials and structures for many applications. However, one key limitation to this is the high temperature usually required to cure glass. Bauer *et al*. used a hybrid organic-inorganic polymer resin as a feedstock material that requires a much lower temperature for curing (see the Perspective by Colombo and Franchin). The ability to form transparent, fused silica at only 650°C opens up different uses for the material. The glass produced has excellent spatial resolution, optical quality, and mechanical properties. —BG

Science, abq3037, this issue p. 960; see also adi2747, p. 895

MATERIALS SCIENCE

Self-healing, self-aligning polymers

One advantage of using soft materials for robotic devices is that there is greater scope for self-healing, but a challenge for multilayer devices is to ensure realignment after damage. Cooper *et al*. present a method for healing multilayered and functional polymer materials by showing how a combination of dynamic hydrogen-bonding interactions and phase separation between different polymeric building blocks can be leveraged to achieve simultaneous autonomous realignment and healing of multilayered polymer films. This approach can restore both the mechanical and functional properties of complex polymer composites and even enables underwater self-assembly. —MSL

Science, adh0619, this issue p. 935

ANTHROPOLOGY

A hand's breadth

For as long as humans have produced things, there have been reasons to measure. Early measurements made use of what people had at hand—parts of their bodies—to create relatively standardized measurements. Kaaronen *et al*. looked at the development and use of body-based measurements across more than 180 cultures (see the Perspective by Chrisomalis) and found that such measures occur across cultures and commonly form the base of measurement systems. In many cultures, standardized measurement systems have replaced body-based ones, but these do persist and are sometimes superior to standard measurement, especially when the goal is to build something for use by a specific person. —SNV

Science, adf1936, this issue p. 948; see also adi2352, p. 894

APTAMER DESIGN

Step by step

Developing highly selective aptamers, folded RNA or DNA oligonucleotides that bind to ligands, is a challenge because the sequence space is difficult to explore efficiently, nucleotides have limited chemical functionality, and methods for predicting RNA structure are not very accurate. Yang *et al*. developed an approach for sequential optimization of aptamers by modifying the target molecule with various functional groups. To design a sensor for the amino acid leucine, they used multiple derivatives to isolate aptamers with high affinity and selectivity. They then used a stepwise approach based on substructure to generate an aptamer for the antifungal drug voriconazole. —MAF

Science, abn9859, this issue p. 942

BIOSENSING

Miniaturized wireless tracking

Minimally invasive medical procedures often require cameras or markers to track locations within the body. However, there are places that cables cannot reach, and there are challenges with imaging into deep tissues or trying to limit exposure to harmful radiation. Gleich *et al*. developed an innovative platform for magnetic tracking and sensing applications using magneto-mechanical resonators (MMRs). In theory and experiments, the authors showed that MMRs can outperform existing technologies such as radiofrequency markers in terms of sensitivity. They also demonstrate sensing applications (position and orientation, pressure, and temperature) and provide examples of spatial tracking in three dimensions. —MSL

Science, adf5451, this issue p. 966

ULTRAFAST DYNAMICS

The view from rhodium

The capacity of metals such as rhodium and palladium to cleave carbon–hydrogen bonds facilitates numerous useful chemical reactions. Fundamental studies of the underlying dynamics at the metal center have often relied indirectly on shifts in the vibrational frequency of a spectator carbon monoxide ligand as the reaction with hydrocarbons ensues. Jay *et al*. used x-ray spectroscopy to study the ultrafast evolution of rhodium's electronic state directly as the metal bound and then broke a carbon–hydrogen bond in octane. —JSY

Science, adf8042, this issue p. 955

PHYSIOLOGY

A neurotrophin to maintain liver mass

In the healthy liver, a subset of hepatocytes proliferates to ensure a defined organ size. Trinh *et al*. explored how hepatocyte proliferation is supported by pericytes known as hepatic stellate cells (also see the Focus by Schoenberger and Tchorz). Hepatic stellate cell ablation in adult mice caused the liver to shrink over time because the hepatocytes stopped proliferating, leading to gradual tissue loss. Hepatic stellate cells were a source of the growth factor neurotrophin-3, which drove hepatocyte proliferation in vitro and in hepatic stellate cell–depleted mice by stimulating the receptor TrkB. —AMV

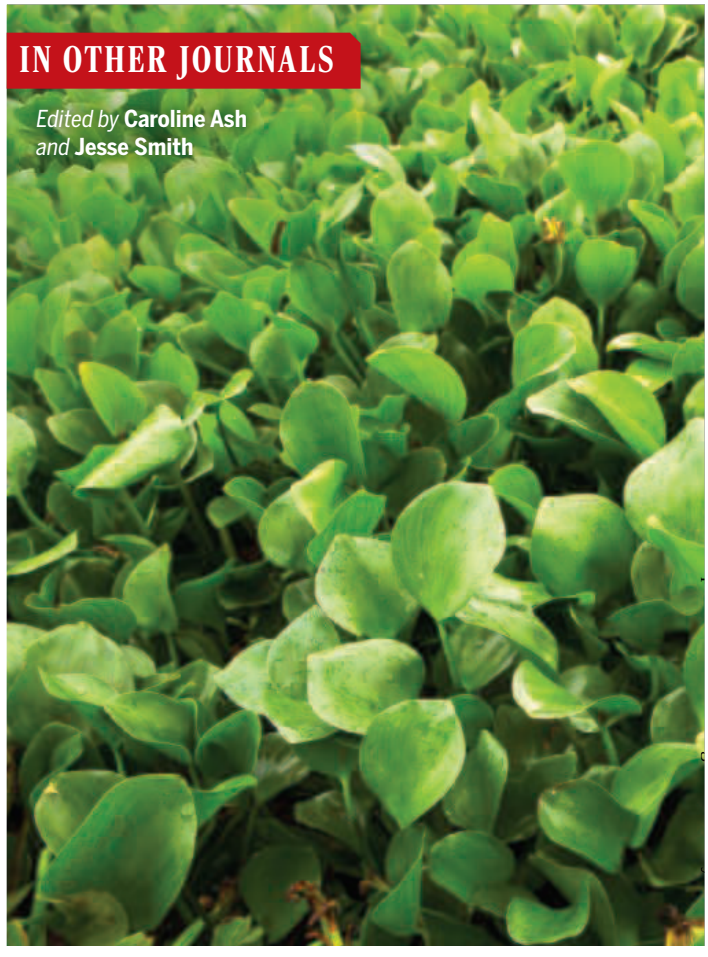
Sci. Signal. (2023)
10.1126/scisignal.adf6696,
10.1126/scisignal.adh5460

T CELLS

T cells contribute to psoriasis

Psoriasis is a chronic inflammatory skin disorder that can be triggered by infection with group A *Streptococcus* (GAS). It is known that GAS-induced immune responses can promote psoriasis, but how T cells are involved in the pathogenesis is unclear. CD1a is a cell surface protein that presents lipid antigens to T cells and is known to be linked to psoriasis. Chen *et al*. studied peripheral blood and skin samples from human participants, identifying a CD1a-restricted, GAS-responsive population of T cells with diverse functionalities. These cells were expanded in patients with psoriasis and were also reactive to the self-antigen lysophosphatidylcholine, which is increased in inflammatory conditions. Skin inflammation was exacerbated after GAS infection in transgenic mice expressing human CD1a. These findings demonstrate that clonal expansion of CD1a-restricted T cells induced by GAS infection can drive autoreactivity in psoriasis. —HMI

Sci. Immunol. (2023)
10.1126/sciimmunol.add9232



METABOLISM

A search for cholesterol genes

Despite substantial progress in understanding coronary artery disease, it remains one of the top causes of death, and cholesterol metabolism plays a major role in its progression. In some cases, genetic variants that alter the uptake of low-density lipoprotein (LDL) cholesterol, the "bad" type, have been characterized and even targeted with specific therapies, but these are only found in small numbers of patients. Hamilton *et al*. combined genome-scale CRISPR screening, mouse experiments, and analysis of human data from the UK Biobank to identify the hundreds of genes and some pathways involved in LDL metabolism, helping to identify potential targets for future therapeutic development. —YN

Cell Genom. (2023)
10.1016/j.xgen.2023.100304

HOST DEFENSE

CDC key to broad antibacterial immunity?

CD4 T cells play an important role in immune defense against the bacterial pathogen *Streptococcus pneumoniae* (pneumococcus), but the antigens that they recognize are not well understood. Ciacchi *et al.* report the existence of a highly immunogenic epitope derived from the pneumococcal cholesterol-dependent cytolysin (CDC) and the virulence factor pneumolysin (Ply). A polyclonal repertoire of αβ CD4 T cells from the majority of blood donors tested recognizes the $Ply_{427–444}$ undecapeptide in the context of broadly expressed human leukocyte antigen allotypes. Moreover, $Ply_{427–444}$–specific CD4 T cells can also recognize CDCs from a wide range of other bacterial species, suggesting that this conserved epitope might be a productive target for vaccines

ALSO IN *SCIENCE* JOURNALS

Edited by **Michael Funk**

HUMAN GENETICS

Heart-brain connections and genetics

It is known that cardiovascular disorders correlate with some neurological and psychiatric conditions, but it is not always clear what the connections are and whether they are caused by an innate predisposition or by the stress induced by having a medical condition. To detangle these questions, Zhao *et al*. examined imaging and genetic data from tens of thousands of participants in the UK Biobank and BioBank Japan (see the Perspective by Sacher and Witte). Through this large-scale analysis, the authors uncovered correlations between structure and function of both the heart and the brain, such as links between specific features of cardiac imaging and neuropsychiatric disorders. The authors also used Mendelian randomization to demonstrate shared genetic influences on both the brain and the heart. —YN

Science, abn6598, this issue p. 934; see also adi2392, p. 897

CIRCADIAN RHYTHMS

Controlling clock-neuron coupling

Coordination of physiology with daily rhythms is regulated by the neurons of the suprachiasmatic nucleus (SCN), the central pacemaker of the biological clock. Tu *et al*. describe a signaling mechanism at cilia in these neurons that keeps the individual cells of the SCN synchronized (see the Perspective by Kim and Blackshaw). The length and abundance of primary cilia in SCN neurons oscillated with daily light-dark cycles. Cilia organize signaling by the morphogen Sonic Hedgehog (SHH), and regulation of the expression of this gene was required for synchrony of the SCN cells. In mice exposed to an altered light cycle to induce experimental jet lag, disrupting SHH signaling allowed the animals to adjust more quickly to the altered environment. —LBR

Science, abm1962, this issue p. 972; see also adi3177, p. 896

THALASSEMIA

Linking blood and bone in beta-thalassemia

Why beta-thalassemia results in bone defects in some patients is unclear. Aprile *et al*. now show that the elevated erythropoietin seen in beta-thalassemia results in increased fibroblast growth factor-23 (FGF23) in the bone and bone marrow, which can produce bone defects. A small peptide inhibiting FGF23 both restored the bone marrow hematopoietic stem cell niche and rescued bone defects in a mouse model. This study thus ties the blood and bone together in beta-thalassemia and demonstrates an avenue to target their pathological interaction. —CAC

Sci. Transl. Med. (2023) 10.1126/scitranslmed.abq3679

CHEMISTRY

Using electrons to replace metals

Aryl-aryl cross-couplings are critical to the efficient synthesis of pharmaceuticals, electronic materials, and fine chemicals. These reactions are typically performed with metal catalysts that carry expensive ligands. Abe and Shirakawa found an exciting alternative that uses light to generate electrons that act as catalysts for the coupling under mild conditions, thus bypassing the need for the metal catalysts. —MG

Sci. Adv. (2023) 10.1126/sciadv.adh3544

PRIMATE GENOMES

A global primate resource

Primates are a widely distributed and variable group. Characterizing primate evolution and variation not only allows us to better understand and conserve species, many of which are highly threatened, but will also help us to better understand ourselves. Kuderna *et al*. present high-coverage genome-sequence data across all 16 primate families and 86% of species. The authors used these data to create a new phylogeny, explore relationships between population size and mutation rate, measure levels of threat, and identify missense mutations as they relate to those found in our own species. —SNV

Science, abn7829, this issue p. 906

PRIMATE GENOMES

Understanding primate evolution

Although humans think of ourselves as unique among animals—and we are in many ways—we are fundamentally one species among hundreds of others in the primate lineage. Thus, as we learn about evolution and adaptation across this group, we also learn about ourselves at both basal and derived levels. Shao *et al*. looked across 50 primate genomes in a comparative phylogenetic framework to resolve patterns of gene evolution, selection, and adaptation. They identified thousands of genes under selection that contribute to the phenotypic shaping of this varied lineage. Many of the innovations that they identified occurred in the ancestral lineage, meaning that they are widely shared across the group. —SNV

Science, abn6919, this issue p. 913

PRIMATE GENOMES

Primate histories

The process of speciation among populations is not instantaneous. Within genomes of related species, some regions will not show evidence of difference for a long time after ecological speciation has occurred, a process called incomplete lineage sorting (ILS). By accounting for ILS across primates, Rivas-González *et al*. were able to produce a primate phylogeny that agrees with fossil estimates (unlike past attempts). Patterns of ILS allow for estimates of ancestral population sizes and the impacts of selection and disease resistance within this group. —SNV

Science, abn4409, this issue p. 925

PRIMATE GENOMES

Two make one

Hybridization can occur between closely related species, but the offspring often have reduced fitness, suggesting that such interbreeding is an evolutionary dead-end. Despite this general impression, hybridization does sometimes lead to viable, or even more fit, offspring. In such cases, reproductive preference or reinforcement can lead to the divergence of a hybrid lineage. Wu *et al*. used genome sequences from a group of monkey species in the *Rhinopithecus* genus and found clear evidence that the gray snub-nosed monkey is derived from hybridization between the golden snub-nosed monkey and the ancestor of two extant *Rhinopithecus* species. The unusual coat color seen in the gray snub-nosed monkey is caused by this mixing. —SNV

Science, abl4997, this issue p. 926

PRIMATE GENOMES

Shaped by the cold

The evolution of sociality is perennially fascinating to humans as highly social creatures, but understanding how such complex behavior emerged is challenging. Qi *et al*. looked across the colobine group of monkeys, which show varying levels of sociality, using fossils, genomics, ecology, and biogeography to reveal the drivers of and mechanisms underlying social evolution. They found that adaptation to cold climates led to both behavioral and genetic

changes, which in some groups furthered social complexities such as prolonged maternal care and reduced male-male aggression. —SNV

Science, abl8621, this issue p. 927

PRIMATE GENOMES

A complex history

It has been increasingly recognized that hybridization is not a rare anomaly that occurs at species range edges but can be integral to the process of speciation. One group of species that has been identified as having a history of hybridization is that containing the genus *Papio*, the baboons. Sørensen *et al.* used high-coverage whole-genome sequencing to reveal the evolutionary history of the six overlapping baboon species and found evidence of repeated admixture, including a population derived from three distinct lineages. Understanding such evolutionary complexity in baboons can shed light on how this process occurs more widely. —SNV

Science, abn8153, this issue p. 928

PRIMATE GENOMES

Finding benign variants across species

As genomic analysis of human patients has become more common, many different genetic variants have been found. Unfortunately, it is difficult to know which are directly associated with disease, especially for rare variants. To help address this gap in knowledge, Gao *et al.* collected gene-sequencing data from hundreds of nonhuman primates across 233 different species. Using these primates' genomes, the authors mapped out common gene variants that were preserved by natural selection and were not pathogenic. On the basis of these data, the authors built a deep learning network that can be applied to help identify benign genetic variants in human patients based on their similarity to those seen in nonhuman primates. —YN

Science, abn8197, this issue p. 929

PRIMATE GENOMES

Primate genomes help with human genes

Large-scale genetic studies of human participants typically identify numerous gene variants that correlate with various traits and diseases. Unfortunately, it is difficult to determine which of these are biologically relevant and which ones are only correlated because of their chromosomal location near relevant genes. To clarify which gene variants are truly pathogenic, Fiziev *et al.* combined data from multiple large human biobanks with information derived from 233 nonhuman primate species. The authors delineated rare pathogenic variants with strong effects and more common ones with weaker effects and demonstrated that the former generally confer a greater risk of severe or early-onset disease. —YN

Science, abo1131, this issue p. 930

BIOSENSING

Miniaturized wireless tracking

Minimally invasive medical procedures often require cameras or markers to track locations within the body. However, there are places that cables cannot reach, and there are challenges with imaging into deep tissues or trying to limit exposure to harmful radiation. Gleich *et al*. developed an innovative platform for magnetic tracking and sensing applications using magneto-mechanical resonators (MMRs). In theory and experiments, the authors showed that MMRs can outperform existing technologies such as radiofrequency markers in terms of sensitivity. They also demonstrate sensing applications (position and orientation, pressure, and temperature) and provide examples of spatial tracking in three dimensions. —MSL

Science, adf5451, this issue p. 966

ULTRAFAST DYNAMICS

The view from rhodium

The capacity of metals such as rhodium and palladium to cleave carbon–hydrogen bonds facilitates numerous useful chemical reactions. Fundamental studies of the underlying dynamics at the metal center have often relied indirectly on shifts in the vibrational frequency of a spectator carbon monoxide ligand as the reaction with hydrocarbons ensues. Jay *et al*. used x-ray spectroscopy to study the ultrafast evolution of rhodium's electronic state directly as the metal bound and then broke a carbon–hydrogen bond in octane. —JSY

Science, adf8042, this issue p. 955

PHYSIOLOGY

A neurotrophin to maintain liver mass

In the healthy liver, a subset of hepatocytes proliferates to ensure a defined organ size. Trinh *et al*. explored how hepatocyte proliferation is supported by pericytes known as hepatic stellate cells (also see the Focus by Schoenberger and Tchorz). Hepatic stellate cell ablation in adult mice caused the liver to shrink over time because the hepatocytes stopped proliferating, leading to gradual tissue loss. Hepatic stellate cells were a source of the growth factor neurotrophin-3, which drove hepatocyte proliferation in vitro and in hepatic stellate cell–depleted mice by stimulating the receptor TrkB. —AMV

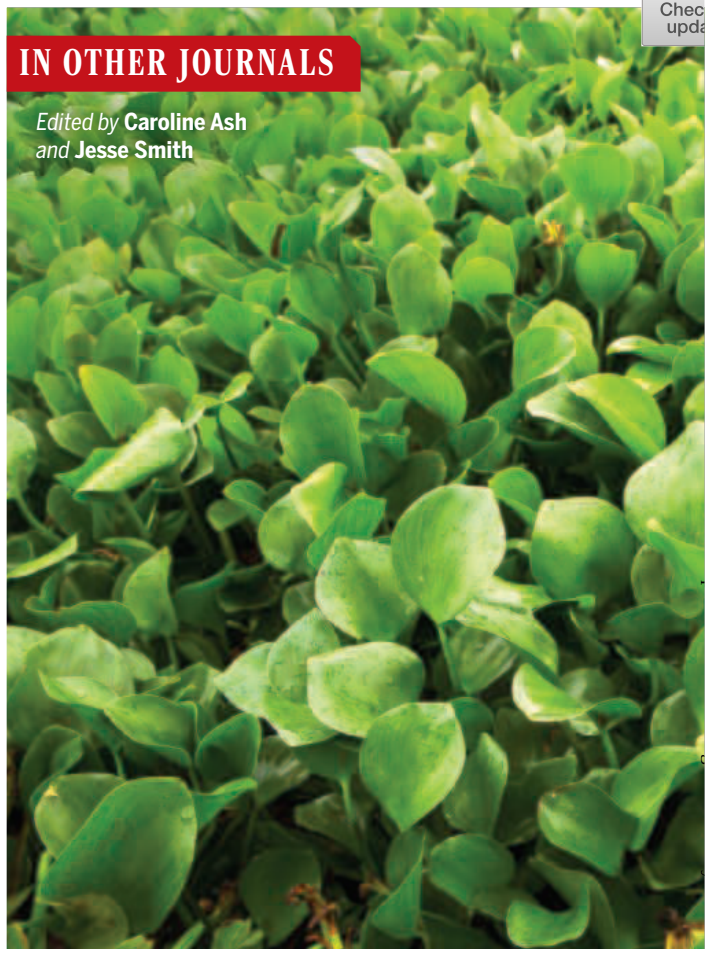
Sci. Signal. (2023)
10.1126/scisignal.adf6696,
10.1126/scisignal.adh5460

T CELLS

T cells contribute to psoriasis

Psoriasis is a chronic inflammatory skin disorder that can be triggered by infection with group A *Streptococcus* (GAS). It is known that GAS-induced immune responses can promote psoriasis, but how T cells are involved in the pathogenesis is unclear. CD1a is a cell surface protein that presents lipid antigens to T cells and is known to be linked to psoriasis. Chen *et al*. studied peripheral blood and skin samples from human participants, identifying a CD1a-restricted, GAS-responsive population of T cells with diverse functionalities. These cells were expanded in patients with psoriasis and were also reactive to the self-antigen lysophosphatidylcholine, which is increased in inflammatory conditions. Skin inflammation was exacerbated after GAS infection in transgenic mice expressing human CD1a. These findings demonstrate that clonal expansion of CD1a-restricted T cells induced by GAS infection can drive autoreactivity in psoriasis. —HMI

Sci. Immunol. (2023)
10.1126/sciimmunol.add9232



METABOLISM

A search for cholesterol genes

Despite substantial progress in understanding coronary artery disease, it remains one of the top causes of death, and cholesterol metabolism plays a major role in its progression. In some cases, genetic variants that alter the uptake of low-density lipoprotein (LDL) cholesterol, the "bad" type, have been characterized and even targeted with specific therapies, but these are only found in small numbers of patients. Hamilton *et al*. combined genome-scale CRISPR screening, mouse experiments, and analysis of human data from the UK Biobank to identify the hundreds of genes and some pathways involved in LDL metabolism, helping to identify potential targets for future therapeutic development. —YN

Cell Genom. (2023)
10.1016/j.xgen.2023.100304

HOST DEFENSE

CDC key to broad antibacterial immunity?

CD4 T cells play an important role in immune defense against the bacterial pathogen *Streptococcus pneumoniae* (pneumococcus), but the antigens that they recognize are not well understood. Ciacchi *et al.* report the existence of a highly immunogenic epitope derived from the pneumococcal cholesterol-dependent cytolysin (CDC) and the virulence factor pneumolysin (Ply). A polyclonal repertoire of αβ CD4 T cells from the majority of blood donors tested recognizes the $Ply_{427–444}$ undecapeptide in the context of broadly expressed human leukocyte antigen allotypes. Moreover, $Ply_{427–444}$–specific CD4 T cells can also recognize CDCs from a wide range of other bacterial species, suggesting that this conserved epitope might be a productive target for vaccines



BIOLOGICAL INVASION

High costs of invasive species

A subset of the myriad species that people have introduced into new regions become "invasive," with outsized effects on ecosystems and human health, food production, and livelihoods. However, the costs associated with biological invasions may be underrecognized because their impacts often take a long time to appear and accumulate. Turbelin *et al.* compared the costs of damage associated with invasive species against those of natural hazards, including storms, drought, fires, floods, and earthquakes, both globally and within the United States. At both scales, storms incurred the highest costs, but the total costs of invasive species were similar to or greater than those of other types of natural hazards—and are increasing over time. —BEL

Perspect. Ecol. Conserv. (2023) 10.1016/j.pecon.2023.03.002

Invasive species such as water hyacinth, pictured here, have high economic costs.

and immunotherapies against many different bacterial diseases. —STS

Immunity (2023) 10.1016/j.immuni.2023.03.020

VASCULAR DEVELOPMENT

Imaging vascular remodeling of skin

An organized vascular system is imperative for proper organ development and function. The mouse skin provides a unique platform with which to visualize vascular network maturation and adult homeostatic states at single-cell resolution. Kam *et al*. sought to understand the principles of vascular network maturation using intravital imaging to spatiotemporally track and manipulate skin blood vessels and endothelial cells (ECs) in vivo. In neonates, vessel regression drives capillary network expansion through EC migration. In adults, ECs become positionally stable, and the coordination of their collective rearrangements maintains vessel integrity. Adult, but not neonatal, ECs preferentially survive damage through a self-repair mechanism of damaged plasma membranes that prevents vessel regression. Thus, adult ECs prioritize self-repair and vessel maintenance more than those in the neonatal vasculature, in which vessels are expendable. —SMH

Cell (2023) 10.1016/j.cell.2023.04.017

SCIENTIFIC WORKFORCE

Parity in physics starts in high school

Over the past two decades, the number of undergraduate physics degrees awarded to women in the United States has held steady at just 20%. Research shows that the decision to study physics is influenced by cultural associations and complex social dynamics about "who does physics." Potvin *et al.* examined the effect of physics lessons with counternarratives, discourses that provide perspectives of those who have been marginalized, on high school students' future physics career intentions. Their results showed that female students and students from minoritized racial or ethnic groups who had been exposed to the counternarratives were more likely to think that they had a possible future in physics, demonstrating that high school classrooms can be an effective place to have equity discussions surrounding science participation. —MMc

Phys. Rev. Phys. Educ. Res. (2023) 10.1103/PhysRevPhysEducRes.19.010126

2D MATERIALS

A magnet with a twist

The properties of layered two-dimensional magnets depend strongly on the number of layers and the way they are stacked on top of each other. For instance, the material CrI_3, which orders ferromagnetically in monolayer form, can have ferromagnetic or antiferromagnetic interlayer coupling depending on whether the stacking is rhombohedral or monoclinic. Natural bilayers have monoclinic stacking, resulting in antiferromagnetic coupling and no overall magnetization. Xie *et al.* studied what happens when two such bilayers are twisted with respect to each other by a small angle. Using magneto-optical measurements, the researchers observed a nonzero overall magnetization and signatures of noncollinear spins that peaked at the twist angle of 1.1°. Future studies will be needed to visualize the spin texture directly. —JSt

Nat. Phys. (2023) 10.1038/s41567-023-02061-z

QUANTUM COMPUTING

A quantum route to solving graphs

Graph theory is a branch of mathematics in which practical problems such as optimization, networking, and operational research can be mapped geometrically. The time and resources required to find solutions to such problems can grow exponentially with the problem size and quickly become unsolvable on classical computers. Deng *et al.* demonstrate the application of the intermediate-sized optical quantum computer "Jiuzhang" to solve two difficult graph theory problems: random search and simulated annealing. Their boson sampling strategy looks at the expectation probabilities of a number of single photons making their way through a scattering matrix formed of complex photonic circuits representing the graphs. With increasing system size, such a quantum approach is likely to present a computational advantage over classical algorithms. —ISO

Phys. Rev. Lett. (2023) 10.1103/PhysRevLett.130.190601

RESEARCH ARTICLE SUMMARY

HUMAN GENETICS

Heart-brain connections: Phenotypic and genetic insights from magnetic resonance images

Bingxin Zhao, Tengfei Li, Zirui Fan, Yue Yang, Juan Shu, Xiaochen Yang, Xifeng Wang, Tianyou Luo, Jiarui Tang, Di Xiong, Zhenyi Wu, Bingxuan Li, Jie Chen, Yue Shan, Chalmer Tomlinson, Ziliang Zhu, Yun Li, Jason L. Stein, Hongtu Zhu*

INTRODUCTION: There is increasing evidence pointing to a close relationship between heart health and brain health, with cardiovascular diseases potentially leading to brain diseases such as stroke, dementia, and cognitive impairment. Magnetic resonance imaging (MRI) is a valuable tool that can be used to assess both the heart and brain, generating biomarkers and endophenotypes for various clinical outcomes. However, although recent large-scale analyses have been conducted on heart and brain MRI-derived traits separately, few studies have explored the potential for multiorgan MRI to examine heart-brain connections and identify shared genetic effects. The structural and functional links between the heart and the brain remain unclear.

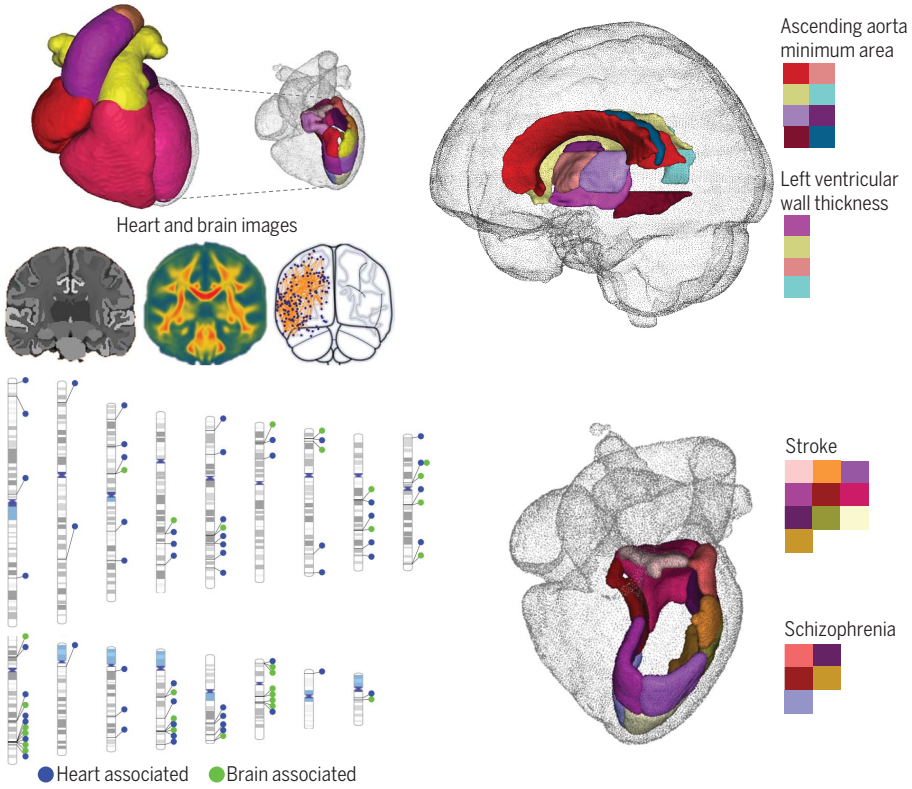
RATIONALE: Using multiorgan MRI and genetic data from >40,000 subjects, we aimed to quantify interorgan connections between the heart and brain and identify the underlying genetic variants. Specifically, we analyzed 82 cardiac and aortic MRI-derived traits across six categories: left and right ventricles, left and right atria, and ascending and descending aortas, as well as 458 brain MRI traits that measu
structure and function.

RESULTS: After controlling for various covariates, we found that heart MRI traits were clearly associated with the brain across all imaging modalities studied. We observed multiple patterns of association for brain gray matter morphometry, white matter microstructure, and functional networks. For example, we found that the left ventricle of the heart showed the strongest correlations with microstructure metrics of cerebral white matter tracts, suggesting that adverse heart features were associated with poorer white matter microstructure.

Our genome-wide association analysis of heart MRI traits identified 80 associated genomic loci ($P < 6.09 \times 10^{-10}$). We performed sex-specific analysis and found that the genetic effects on heart structure and function were highly consistent between both sexes. Further, we conducted a systematic search of previously reported genetic results in these genomic loci and found that heart MRI traits had shared genetic influences and colocalized with heart and brain diseases and complex traits.

We identified genetic correlations between heart MRI traits and various brain complex traits and diseases such as stroke, eating disorders, schizophrenia, cognitive function, and mental health traits. For example, adverse myocardial wall thickness condition was positively genetically correlated with stroke. We further used two-sample Mendelian randomization to explore causal genetic links between the heart and brain, and our findings suggest that adverse heart features have genetic causal effects on several brain diseases such as psychiatric disorders and depression.

CONCLUSION: This study deepened our understanding of heart-brain links and their genetic basis. We observed that MRI measurements of the two organs were associated with each other, and this was independent of a wide variety of body measures, shared risk factors, and imaging confounders. We also uncovered genetic colocalizations and correlations between heart structure and function and brain clinical end points, suggesting that adverse heart metrics may have implications for brain abnormalities and the risk of brain diseases. By understanding human health from a multiorgan perspective, we may be able to improve disease risk prediction and prevention and mitigate the negative effects of one organ disease on other organs that may be at risk. ■



Heart-brain connections revealed by multiorgan imaging genetics. Top left: Quantifying the heart and brain structure and function in MRI. Top right: Examples of associations between heart MRI traits and brain white matter tracts. Bottom left: Genomic loci associated with heart MRI traits that overlapped with traits and disorders of the heart and/or brain. Bottom right: Selected genetic correlations between heart MRI traits and brain disorders.

The list of author affiliations is available in the full article online.
*Corresponding author. Email: htzhu@email.unc.edu
Cite this article as B. Zhao *et al.*, *Science* **380**, eabn6598 (2023). DOI: 10.1126/science.abn6598

READ THE FULL ARTICLE AT
https://doi.org/10.1126/science.abn6598

RESEARCH ARTICLE

HUMAN GENETICS

Heart-brain connections: Phenotypic and genetic insights from magnetic resonance images

Bingxin Zhao[1,2], Tengfei Li[3,4], Zirui Fan[1,2], Yue Yang[5], Juan Shu[2], Xiaochen Yang[2], Xifeng Wang[5], Tianyou Luo[5], Jiarui Tang[5], Di Xiong[5], Zhenyi Wu[2], Bingxuan Li[6], Jie Chen[5], Yue Shan[5], Chalmer Tomlinson[5], Ziliang Zhu[5], Yun Li[5,7], Jason L. Stein[7,8], Hongtu Zhu[4,5,7,9,10]*

Cardiovascular health interacts with cognitive and mental health in complex ways, yet little is known about the phenotypic and genetic links of heart-brain systems. We quantified heart-brain connections using multiorgan magnetic resonance imaging (MRI) data from more than 40,000 subjects. Heart MRI traits displayed numerous association patterns with brain gray matter morphometry, white matter microstructure, and functional networks. We identified 80 associated genomic loci ($P < 6.09 \times 10^{-10}$) for heart MRI traits, which shared genetic influences with cardiovascular and brain diseases. Genetic correlations were observed between heart MRI traits and brain-related traits and disorders. Mendelian randomization suggests that heart conditions may causally contribute to brain disorders. Our results advance a multiorgan perspective on human health by revealing heart-brain connections and shared genetic influences.

A growing amount of evidence suggests close interplays between heart health and brain health (fig. S1). Cardiovascular diseases may provide a pathophysiological background for several brain diseases, including stroke (*1*), dementia (*2*), cerebral small vessel disease (*3*), and cognitive impairment (*4*, *5*). For example, atrial fibrillation has been linked to an increased incidence of dementia (*6*) and silent cerebral damage (*7*) even in stroke-free cohorts (*8*). It has been consistently observed that heart failure is associated with cognitive impairment and eventually dementia (*9*), likely because of the reduced cerebral perfusion caused by the failing heart (*10*). Conversely, mental disorders and negative psychological factors may contribute substantially to the initiation and progression of cardiovascular diseases (*11*–*13*). Patients with mental illnesses such as schizophrenia, bipolar disorder, epilepsy, or depression show an increased incidence of cardiovascular diseases (*14*–*17*). Acute mental stress may cause a higher risk of atherosclerosis because of stress-induced vascular inflammation and leukocyte migration (*18*). Primarily because of the lack of data, almost all prior studies on heart-brain interactions and associated risk factors (*19*–*25*) have focused on one (or a few) specific diseases or used small samples. Therefore, the overall picture of the structural and functional links between the heart and the brain remains unclear.

In heart and brain diseases, magnetic resonance imaging (MRI)–derived traits are well-established endophenotypes. Cardiovascular magnetic resonance imaging (CMR) has been widely used to assess cardiac structure and function, yielding insights into the risk and pathological status of cardiovascular diseases (*26*–*28*). Brain MRI modalities provide detailed information about brain structure and function (*29*). Clinical applications of brain MRI have revealed the associated brain abnormalities that accompany multiple neurological and neuropsychiatric disorders (*30*–*32*). Moreover, twin and family studies have shown that CMR and brain MRI traits are moderately to highly heritable (*33*–*35*). For example, the left ventricular mass (LVM) has a heritability estimate >0.8 (*34*). Most brain structural MRI traits are highly heritable (heritability ranges from 0.6 to 0.8) (*36*), and the heritability of brain functional connectivity is usually between 0.2 and 0.6 (*37*). A few recent genome-wide association studies (GWASs) have been separately conducted on CMR (*38*–*43*) and brain MRI traits (*44*–*51*). For example, several large-scale efforts have been made to discover genetic variants associated with brain structures; examples include ENIGMA (*31*), Neuro-CHARGE (*52*), and IMAGEN (*53*). Although MRI has been widely used in clinical research and genetic mapping, few studies have used multiorgan MRI to examine heart-brain connections and identify the shared genetic signatures of the heart and the brain.

In the present study, we investigated heart-brain connections using multiorgan imaging data obtained from >40,000 subjects in the UK Biobank (UKB) study (*54*). By using a recently developed heart segmentation and feature extraction pipeline (*55*–*57*), we generated 82 CMR traits from the raw short-axis, long-axis, and aortic cine images. These CMR traits included global measures of four cardiac chambers, the left ventricle (LV), right ventricle (RV), left atrium (LA), and right atrium (RA), and two aortic sections, the ascending aorta (AAo) and the descending aorta (DAo), as well as regional (*58*) phenotypes of the LV myocardial wall thickness and strain [table S1 and supplementary text (*59*)]. Then, we identified the relationships between the 82 CMR traits and a wide variety of the brain MRI traits discovered from multimodality images (*60*), including structural MRI (164 traits), diffusion MRI (110 traits), resting functional MRI (resting fMRI) (92 global traits and >60,000 regional traits), and task fMRI (92 global traits and >60,000 regional traits). These brain MRI traits provided fine details of brain structural morphometry (*45*, *61*) (regional brain volumes and cortical thickness traits), brain structural connectivity (*47*, *62*) [diffusion tensor imaging (DTI) invariant measures of white matter tracts], and brain intrinsic and extrinsic functional organizations (*49*, *63*, *64*) (functional activity and connectivity at rest and during a task) (table S2). To evaluate the genetic determinates underlying heart-brain connections, we performed GWASs for the 82 CMR traits to uncover the genetic architecture of the heart and aorta. Compared with existing GWASs of CMR traits (*38*–*43*), our study used a much broader group of cardiac and aortic traits, allowing us to identify the shared genetic components with a wide variety of brain-related complex traits and disorders. For example, (*42*) mainly focused on nine measures of the right heart, (*38*) analyzed six LV traits, and (*43*) studied three traits of diastolic function. Figure 1 provides an overview of the study design and analyses. The GWAS results of 82 CMR traits can be explored and are freely available through the heart imaging genetics knowledge portal (Heart-KP) at http://heartkp.org/.

Phenotypic heart-brain connections

To verify that the 82 CMR traits are well defined and biologically meaningful, we first examined their reproducibility using the repeat scans obtained from the UKB repeat imaging visit (n = 2903; average time between visits, 2 years). For each trait, we calculated the intraclass correlation (ICC) between two observations from all revisited individuals. The average ICC was 0.653 (range = 0.369 to 0.970; table S1).

[1]Department of Statistics and Data Science, University of Pennsylvania, Philadelphia, PA 19104, USA. [2]Department of Statistics, Purdue University, West Lafayette, IN 47907, USA. [3]Department of Radiology, University of North Carolina at Chapel Hill, Chapel Hill, NC 27599, USA. [4]Biomedical Research Imaging Center, School of Medicine, University of North Carolina at Chapel Hill, Chapel Hill, NC 27599, USA. [5]Department of Biostatistics, University of North Carolina at Chapel Hill, Chapel Hill, NC 27599, USA. [6]Department of Computer Science, Purdue University, West Lafayette, IN 47907, USA. [7]Department of Genetics, University of North Carolina at Chapel Hill, Chapel Hill, NC 27599, USA. [8]UNC Neuroscience Center, University of North Carolina at Chapel Hill, Chapel Hill, NC 27599, USA. [9]Department of Computer Science, University of North Carolina at Chapel Hill, Chapel Hill, NC 27599, USA. [10]Department of Statistics and Operations Research, University of North Carolina at Chapel Hill, Chapel Hill, NC 27599, USA.
*Corresponding author. Email: htzhu@email.unc.edu

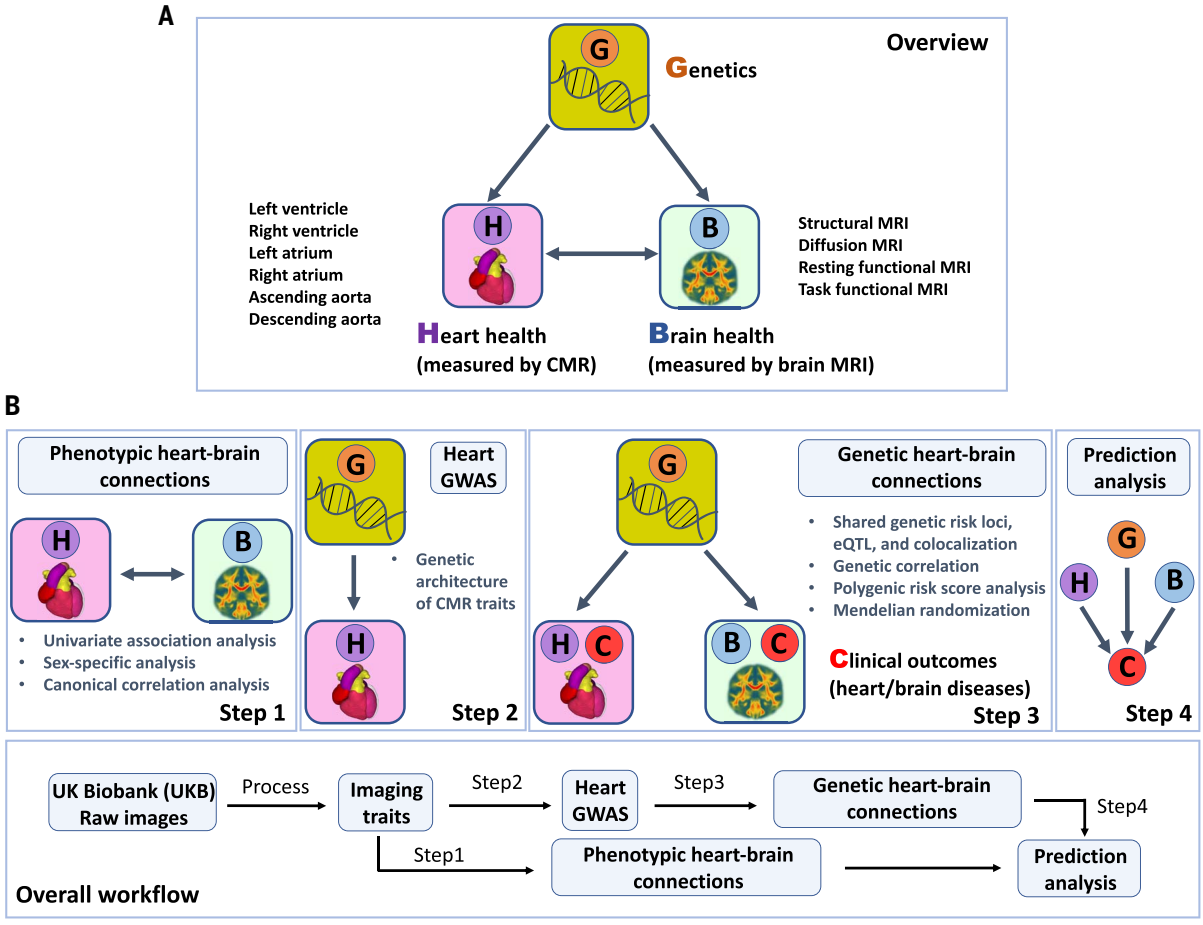


Fig. 1. Overview of the study design and analyses. (**A**) Overview of the study. We used CMR and brain MRI traits as endophenotypes to explore the phenotypic and genetic connections between the heart and the brain. (**B**) Description of the overall workflow and the key analyses involved in each step.

Some volumetric traits had very high ICC (>0.9), including the LV end-diastolic volume (LVEDV), LVM, RV end-diastolic volume (RVEDV), RV end-systolic volume (RVESV), AAo maximum area, AAo minimum area, DAo maximum area, DAo minimum area, and global myocardial wall thickness. The ejection fraction [such as the LV ejection fraction (LVEF)] and distensibility traits (e.g., the DAo distensibility) had the lowest ICC among all volumetric traits (mean = 0.574 and 0.519, respectively). In addition, the average ICC was 0.760 for the 17 wall thickness traits, 0.532 for the seven longitudinal peak strains, 0.569 for the 17 circumferential strains, and 0.516 for the 17 radial strains. Additionally, we examined the changes in 82 CMR traits over a 2-year period and were able to replicate the direction of most of the aging effects (per 7.5 years) described in (*55*) [table S1 and supplementary text (*59*)]. Overall, these results suggest that the extracted CMR traits have moderate to high within-subject reliability and can consistently delineate the cardiac and aortic structure and function.

We examined the associations between CMR traits and brain MRI traits in UKB individuals of white British ancestry (n = 31,152; see the materials and methods for a list of adjusted covariates). At the Bonferroni significance level ($P < 1.33 \times 10^{-6}$), CMR traits were associated with a wide variety of brain MRI traits, including regional brain volumes, cortical thickness, DTI parameters, and resting and task fMRI traits (Fig. 2A, fig. S2, and table S3). Among the 4193 Bonferroni-significant associations in our discovery sample, 1574 were significant at the nominal level (0.05) in a holdout independent validation dataset (n = 5316) with concordant association signs (figs. S3 to S5). For example, global wall thickness was positively associated with the volumes of multiple subcortical brain structures (fig. S2B). Particularly, both left and right putamen volumes were associated with at least 10 wall thickness traits (fig. S4). Subcortical regions across both brain hemispheres showed consistent association patterns, potentially highlighting the robustness of these correlations. Additional examples of replicated associations can be found in the supplementary text (*59*).

CMR traits were also correlated with brain structural and functional connectivity. For example, fractional anisotropy (FA) and mean diffusivity (MD) are two robust measures of brain structural connectivity and white matter microstructure, with higher FA and lower MD values typically signifying better white matter integrity (*65*). The FA values of several white matter tracts consistently showed negative associations with aortic areas (e.g., AAo and DAo minimum areas), LV traits (e.g., LVM, LVEDV, and wall thickness traits), and LA minimum volume (LAV_{min}). Moreover, these CMR traits exhibited consistent positive associations with MD values (Fig. 2, B and C, and fig. S6). For resting fMRI, both mean functional connectivity and mean amplitude (i.e., functional activity) traits were negatively associated with volumetric measures of the four cardiac chambers, such as the LV cardiac output (LVCO), RV ejection fraction (RVEF), LA stroke volume (LASV), and RA ejection fraction (RAEF) (fig. S7). By contrast, positive correlations were widely observed for wall thickness traits, longitudinal strains, and peak circumferential strains. The task fMRI traits showed similar patterns (fig. S8). To further discover fine-grained details of CMR connections with brain functions, we examined pairwise associations between 82 CMR traits and 64,620 high-resolution functional connectivity traits (*49*) in resting fMRI.

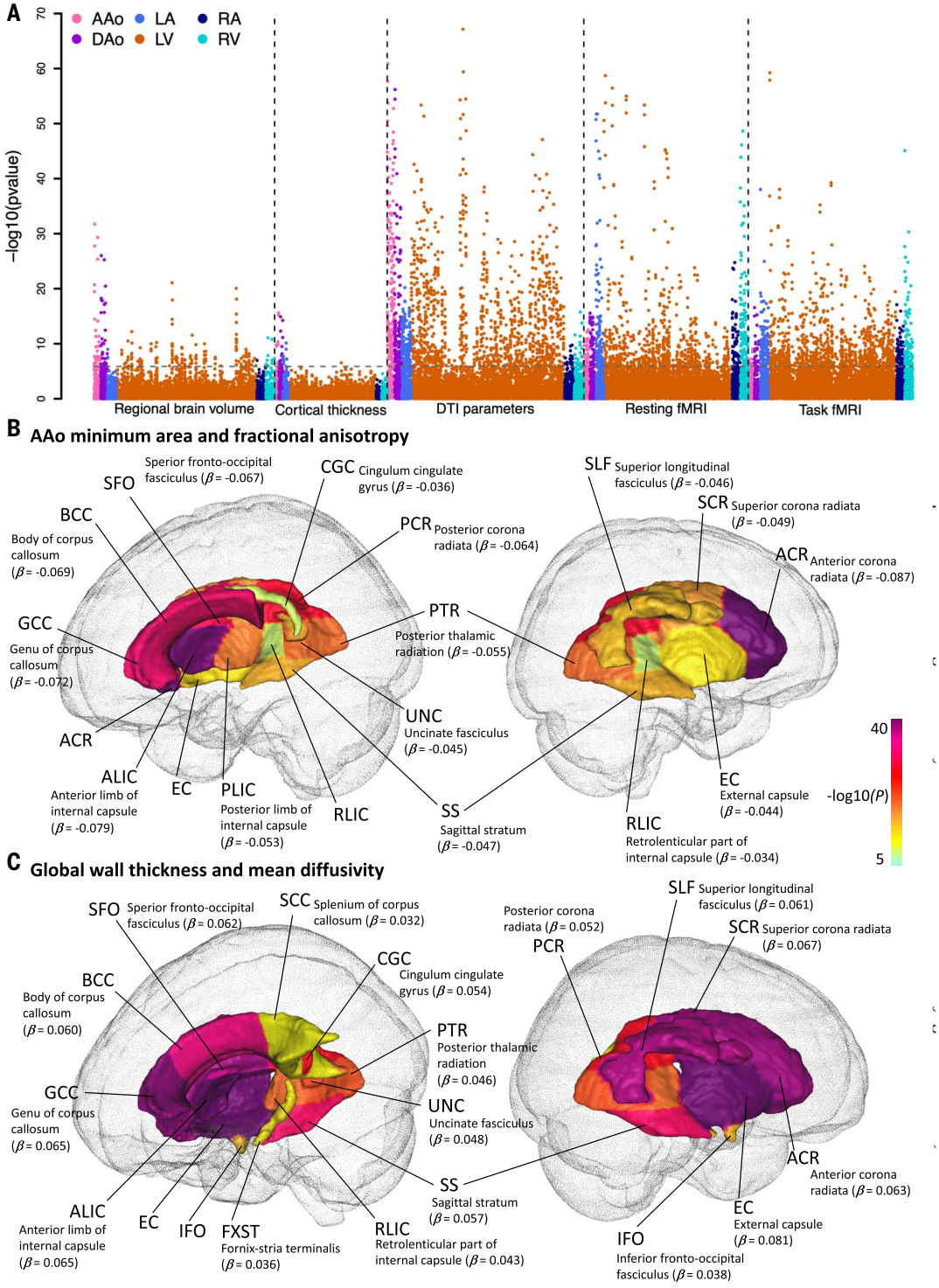


Fig. 2. Phenotypic heart-brain associations. (**A**) The −log10 (*P* value) of phenotypic correlations between 82 CMR traits and five groups of brain MRI traits, including 101 regional brain volumes, 63 cortical thickness traits, 110 DTI parameters, 92 resting fMRI traits, and 92 task fMRI traits. The dashed line indicates the Bonferroni significance level ($P < 1.33 \times 10^{-6}$). Each CMR trait category is labeled with a different color. (**B**) Significant correlations ($P < 1.33 \times 10^{-6}$) between fractional anisotropy values of white matter tracts and AAo minimum area. (**C**) Significant correlations ($P < 1.33 \times 10^{-6}$) between mean diffusivity values of white matter tracts and global myocardial wall thickness at end diastole (global wall thickness).

Bonferroni-significant associations ($P < 7.15 \times 10^{-8}$) were observed across the functional connectivity of the whole brain, with specific patterns emerging across different functional areas and networks (fig. S9, A and B). For example, the somatomotor network and its connectivity with the secondary visual network were associated with multiple CMR traits. Specifically, positive somatomotor associations were observed in the LVM, RVESV, RA minimum volume (RAV_{min}), global peak circumferential strain, and global wall thickness (figs. S9C and S10 to S13), and negative correlations were observed in all four ejection fraction traits [RVEF, LA ejection fraction (LAEF), RAEF, and LVEF] and LVCO (figs. S9D and S14 to S17). Additional examples can be found in the supplementary text (*59*) (figs. S18 to S28). Furthermore, we performed the above phenotypic association analyses separately for males and females (figs. S29 to S32), used canonical correlation analysis (CCA) (*66*) to investigate the multivariate associations between CMR traits and various groups of brain MRI traits, and examined the influence of environmental factors and biomarkers on the underlying mechanisms of heart-brain interactions [figs. S33 to S35, table S4, and supplementary text (*59*)].

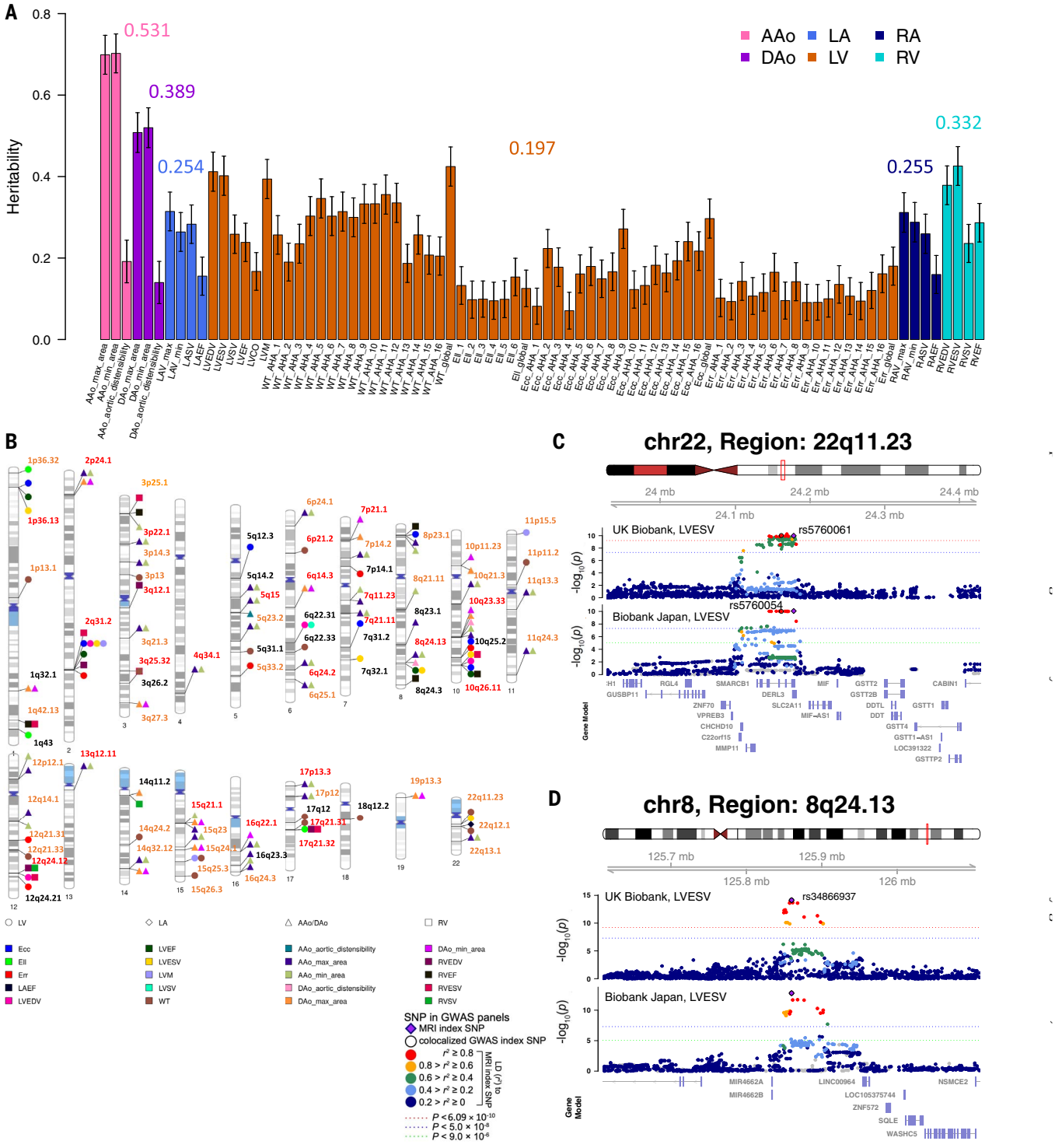


Fig. 3. Genetics of CMR traits in the UKB. (**A**) SNP heritability of 82 CMR traits across the six categories. The *x* axis displays the short names of CMR traits; see table S1 for the full names of these traits. The average heritability of each category is labeled. (**B**) Ideogram of 80 genomic regions associated with CMR traits ($P < 6.09 \times 10^{-10}$). Red and brown name labels denote genomic regions that have been replicated in the validation dataset after applying Bonferroni correction and at a nominal level, respectively. (**C**) LVESV was associated with the 22q11.23 region in both the UKB (index variant rs5760061) and BBJ (index variant rs5760054) studies. (**D**) LVESV was associated with the 8q24.13 region in both the UKB and BBJ studies (shared index variant rs34866937).

Heritability and the associated genetic loci of 82 CMR traits

We estimated the single-nucleotide polymorphism (SNP) heritability for the 82 CMR traits using UKB individuals of white British ancestry (*67*) (n = 31,875). The mean heritability (h^2) was 22.9% for the 82 traits (range = 7.07 to 70.2%; Fig. 3A), all of which remained significant after adjusting for multiple testing using the Benjamini-Hochberg procedure to control the false discovery rate (FDR) at the 0.05 level ($P < 1.09 \times 10^{-3}$) (table S5). The h^2 of the AAo/DAo maximum areas and AAo/DAo minimum areas was >50%. Among cardiac traits, the global wall thickness, RVESV, RVEDV, LV end-systolic

volume (LVESV), LVEDV, and LVM had the highest heritability (h^2 > 37.8%). A sex-specific heritability analysis was conducted separately for females and males, and the heritability estimates for both sexes were similar (mean h^2 = 24.8 versus 22.6%, correlation = 0.910, P = 0.332; fig. S36).

We next performed GWASs for the 82 CMR traits using this white British cohort (n = 31,875). All Manhattan and QQ plots can be browsed through the server on Heart-KP. The intercepts of linkage disequilibrium (LD) score regression (LDSC) (*68*) were all close to one, suggesting no genomic inflation of test statistics caused by confounding factors (mean intercept = 0.99986; range = 0.982 to 1.019). At the significance level 6.09×10^{-10} ($5 \times 10^{-8}/82$, that is, the standard GWAS significance threshold, additionally Bonferroni adjusted for the 82 traits), we identified independent (LD r^2 < 0.1) significant associations in 80 genomic regions (cytogenetic bands) for 49 CMR traits, including 35 for LV, 35 for AAo, 14 for DAo, 11 for RV, and 1 for LA (Fig. 3B and table S6). Detailed interpretations of these identified regions can be found below. These genetic effects on CMR traits were highly consistent in the sex-specific GWASs, in which males and females were analyzed separately (correlation = 0.944; P = 0.739; fig. S37). In the supplementary text (*59*), we further demonstrate that these CMR traits exhibited a highly polygenic genetic architecture and shared heritability with brain MRI traits, particularly with DTI parameters measuring white matter microstructure (figs. S38 and S39 and table S7).

To replicate the identified loci, we performed separate GWASs using holdout datasets in the UKB study that were independent from our discovery dataset. First, we repeated GWASs on a European dataset with 8252 subjects (see the materials and methods). For the 243 independent (LD r^2 < 0.1) CMR-variant associations in the 80 genomic regions, 56 (23.04%, in 25 regions) passed the Bonferroni significance level (2.06×10^{-4}, 0.05/243) in this European validation GWAS, and 178 (73.25%, in 61 regions) passed the nominal significance level (0.05) (Fig. 3B and table S8). All 178 associations had concordant directions in the two independent GWASs, and the correlation of their genetic effects was 0.963 (fig. S40). These results show a high degree of generalizability of our GWAS findings among European cohorts. We also performed GWAS on two non-European UKB validation datasets: the UKB Asian (UKBA, n = 500) and UKB Black (UKBBL, n = 271). One association between 8q24.3 and the RVEF passed the Bonferroni significance level ($P = 8.281 \times 10^{-5}$) in UKBA, and 14 more regions passed the nominal significance level. For UKBBL, 12 regions passed the nominal significance level, and none of them survived the Bonferroni significance level, which may be partially caused by the small sample size of this non-European GWAS. Additionally, we evaluated the ancestry-specific effects using Asian GWAS summary statistics of three CMR traits [analogous to the LVEDV, LVESV, and LVEF (*41*)], which were generated from 19,000 subjects in the BioBank Japan (BBJ) study (*69*). At the stringent GWAS 1.666×10^{-8} ($5 \times 10^{-8}/3$) threshold, BBJ CMR traits identified independent (LD r^2 < 0.1) significant associations in 22q11.23, 8q24.13, and 10q22.2. Of the three regions, 22q11.23 and 8q24.13 were among the 80 regions that were discovered in the UKB white British cohort. These two regions were significantly associated with the LVSEV in both the UKB and the BBJ studies (Fig. 3, C and D). The 10q22.2 had a small P value in the UKB GWAS ($P = 1.58 \times 10^{-9}$), but did not survive the 6.09×10^{-10} threshold.

Finally, we constructed polygenic risk scores (PRSs) using lassosum (*70*) to evaluate the out-of-sample prediction power of the discovery GWAS results (see the materials and methods). Among the 82 CMR traits, 75 had significant PRS at the FDR 5% level (P range = 4.47×10^{-125} to 3.74×10^{-2}; table S9). The highest incremental R^2 value (after adjusting for the effects of covariates) was observed on the AAo minimum area and the AAo maximum area (7.20 and 7.04%, respectively). To evaluate the cross-population performance, PRS was also constructed on UKB white British discovery GWAS data using BBJ GWAS summary statistics of the LVEDV, LVESV, and LVEF. We found that the PRSs of these three traits were all significant in the UKB (P range = 1.58×10^{-11} to 8.13×10^{-7}; R^2 range = 3.90×10^{-4} to 1.35×10^{-3}). The prediction accuracy was lower than that in the above within European prediction analysis (R^2 range = 7.72×10^{-3} to 9.67×10^{-3}), which may be explained by the smaller training GWAS sample size in the BBJ study and population differences between the UKB and BBJ cohorts.

Pleiotropy of genetic variants across body systems

To identify the shared genetic effects between CMR traits and complex traits, we performed association lookups for independent (LD r^2 < 0.1) significant variants (and variants in their LD, $r^2 \geq 0.6$, $P < 6.09 \times 10^{-10}$) detected in our UKB white British GWAS. In the National Human Genome Research Institute–European Bioinformatics Institute (NHGRI-EBI) GWAS catalog (*71*), our results tagged variants that have been linked to a wide range of traits and diseases, including heart diseases, heart structure and function, blood pressure, lipid traits, blood traits, diabetes, stroke, neurological and neuropsychiatric disorders, psychological traits, cognitive traits, lung function, parental longevity, smoking, and drinking. To evaluate whether two associated genetic signals were consistent with the shared causal variant, we applied the Bayesian colocalization analysis (*72*) for CMR traits and selected phenotypes with publicly available GWAS summary statistics. Evidence of pairwise colocalization was defined as having a posterior probability of the shared causal variant hypothesis (PPH4) > 0.8 (*72*, *73*). Many shared genetic variants were found to be expression quantitative trait loci (eQTLs) in a recent large-scale eQTL meta-analysis of brain (*74*) and blood tissues (*75*). The traits with shared genetic effects are presented in table S10, with selected pairs shown in Fig. 4 and figs. S41 to S108. Table S11 summarizes the results of colocalization and eQTL analyses. Below, we highlight genetic overlaps between CMR traits and complex traits and diseases of the heart and brain, as well as other clinical outcomes.

First, we replicated 27 genomic regions that have been previously linked to cardiac and aortic traits, such as fractional shortening and LV internal dimension (fig. S41). There were 21 regions associated with heart rate and electrocardiographic traits (e.g., QRS duration; figs. S42 to S46) and six regions with aortic measures (e.g., thoracic aortic aneurysms and dissections; figs. S47 and S48). In addition, 30 regions had shared associations (LD $r^2 \geq$ 0.6) with cardiovascular diseases, including 12 regions with coronary artery disease (*76*) (figs. S49 and S50), nine regions with atrial fibrillation (*77*) (Fig. 4A and figs. S51 to S55), and five regions with hypertension (*78*) (figs. S56 to S58). Other heart diseases included abdominal aortic aneurysm (*79*) (figs. S47 and S59), mitral valve prolapse (*80*) (fig. S46), and idiopathic dilated cardiomyopathy (*81*) (figs. S60 and S61). There was widespread evidence of colocalization on many loci (PPH4 > 0.899). Additionally, 41 of the 80 genomic regions were associated with blood pressure traits such as diastolic or systolic blood pressure, pulse pressure, and mean arterial pressure (Fig. 4B and figs. S62 to S81). CMR traits were in LD ($r^2 \geq 0.6$) with various cardiovascular and blood biochemistry biomarkers such as lipid traits (figs. S50, S56, S67, and S82), red blood cell count, blood protein levels, red cell distribution width, and plateletcrit (figs. S83 to S87).

We found genetic pleiotropy between CMR traits and multiple brain-related complex traits and disorders. In the 6p21.2, 7p21.1, and 12q24.12 regions, CMR traits were in LD ($r^2 \geq 0.6$) with stroke (*82*) (e.g., ischemic stroke, large artery stroke, and small-vessel ischemic stroke), intracranial aneurysm (*83*), and moyamoya disease (*84*) (Fig. 4, A and B, and fig. S50). The index variants of 7p21.1 (rs2107595) and 12q24.12 (rs597808) were eQTLs of *TWIST1* and *ALDH2* in human brain tissues (*74*), suggesting that these CMR-associated variants were known to affect gene expression in human brain. *TWIST1* was associated with cerebral vasculature defects (*85*), and there was a higher level of *ALDH2*

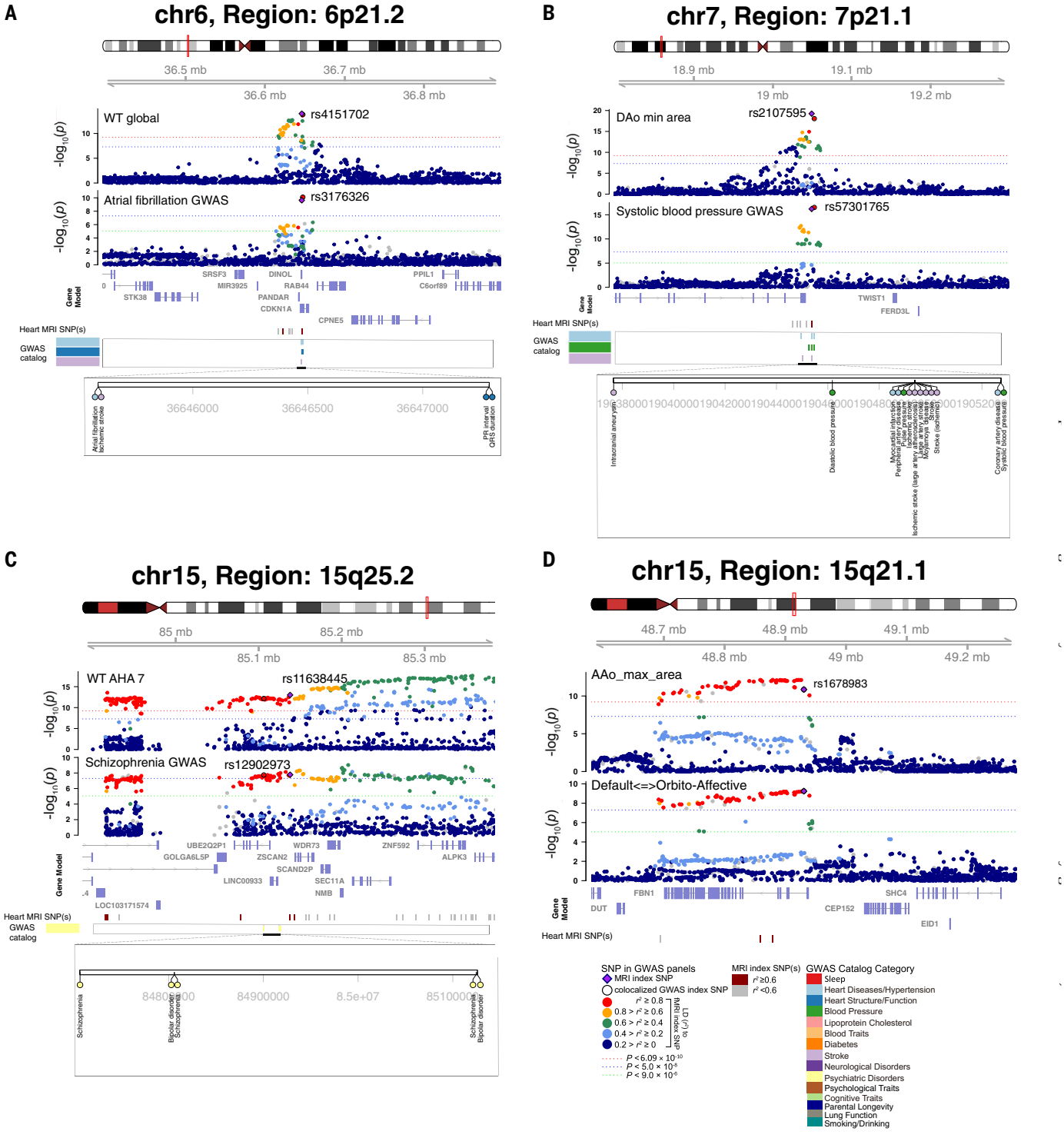


Fig. 4. Selected genetic loci associated with both CMR trait and other complex traits and diseases. (**A**) In 6p21.2, we observed colocalization between the global myocardial wall thickness (WT) at end-diastole (WT global, index variant rs4151702) and atrial fibrillation (index variant rs3176326). The posterior probability of Bayesian colocalization analysis for the shared causal variant hypothesis (PPH4) is 0.997. In this region, the WT global was also in LD ($r^2 \geq 0.6$) with ischemic stroke. (**B**) In 7p21.1, we observed colocalization between the DAo minimum area (DAo min area, index variant rs2107595) and systolic blood pressure (index variant rs57301765, PPH4 = 0.998). In this region, the DAo min area was also in LD with stroke, intracranial aneurysm, coronary artery disease, and moyamoya disease. (**C**) In 15q25.2, we observed colocalization between the regional myocardial wall thickness at end-diastole (WT AHA 7, index variant rs11638445) and schizophrenia (index variant rs12902973, PPH4 = 0.922). In this region, the WT AHA 7 was also in LD with bipolar disorder. AHA 7, American Heart Association (AHA) region 7. (**D**) We illustrated the colocalization between the AAo maximum area (AAo max area) and functional connectivity between the default mode and orbito-affective networks (shared index variant rs1678983) in 15q21.1 (PPH4 = 0.964).

activity in the putamen and temporal cortex of patients with Alzheimer's disease (*86*). CMR traits were also in LD ($r^2 \geq 0.6$) with neurodegenerative and neuropsychiatric disorders such as Parkinson's disease (*87*) and Alzheimer's disease (*88*) (fig. S88), hippocampal sclerosis of aging (*89*) (fig. S74), schizophrenia (*90*) (Fig. 4C and fig. S49), bipolar disorder (*91*) (Fig. 4C and figs. S82 and S89), and eating disorders (*92*) (fig. S90). In addition, CMR traits were in LD ($r^2 \geq 0.6$) with mental health traits such as neuroticism, depressive symptoms, subjective well-being, and risk-taking tendency (figs. S88 and S91 to S93).

For cognitive traits and education, we tagged 17q21.31, 11p11.2, and 11q13.3 with cognitive function and educational attainment (figs. S88, S93, and S94); 7q32.1 with reading disability (fig. S95); and 12q24.12 with reaction time (fig. S50). We also found shared associations (LD $r^2 \geq 0.6$) in five regions with DTI parameters (*47*) (figs. S96 to S100); four regions with regional brain volumes (*45*) (figs. S101 to S104); and five regions with fMRI traits (*49*) (Fig. 4D and figs. S105 to S108). The colocalization analysis revealed that CMR traits shared causal genetic variants with these phenotypes, such as 15q25.2 with schizophrenia, 15q21.1 with functional connectivity, as well as 11q24.3 and 12q24.12 with white matter microstructure (PPH4 > 0.809). There is substantial evidence supporting the interplay between cardiovascular health and these brain traits and diseases. For example, people with better heart health have better cognitive abilities (*93*) and lower risk for brain disorders such as stroke and Alzheimer's disease (*94*). In addition, mental health disorders may result in biological processes and behaviors that are associated with cardiovascular diseases (*11*, *95*). Our findings indicate that cardiovascular conditions share substantial genetic components with brain diseases, mental health traits, and cognitive functions, suggesting a potential genetic basis for heart-brain connections.

Genetic overlaps with other diseases and complex traits were also observed. For example, RVEDV was in LD ($r^2 \geq 0.6$) with type 1 diabetes (*96*) and type 2 diabetes (*97*, *98*) in the 12q24.12 region (fig. S50). CMR traits were in LD ($r^2 \geq 0.6$) in 11 regions with lung conditions such as asthma (*99*) (fig. S82), idiopathic pulmonary fibrosis (*100*), interstitial lung disease (*101*) (fig. S88), and lung function (figs. S60, S64, S67, and S77). We also found shared genetic associations (LD $r^2 \geq 0.6$) with smoking (figs. S50, S82, and S93) and alcohol consumption and alcohol use disorder (figs. S49, S88, and S93).

Genetic correlations with brain disorders and complex traits

First, we examined genetic correlations among 82 CMR traits using cross-trait LDSC (*102*). Strong genetic correlations were observed within and between categories of CMR traits (fig. S109 and table S12). For example, RVEDV was genetically correlated with other RV traits, including RV stroke volume (RVSV), RVESV, and RVEF. The RVEDV was also correlated with CMR traits from other categories, such as AAo maximum area and DAo maximum area, LASV and RA stroke volume (RASV), as well as LVEDV, LVESV, LVM, and LVEF. In addition, we found a strong relationship between phenotypic and genetic correlations among all CMR traits ($\beta = 0.781$, $P < 2 \times 10^{-16}$).

Next, we examined the genetic correlations between 82 CMR traits and 60 complex traits and diseases. At the FDR 5% level (82 × 60 tests), the CMR traits were associated with heart diseases, lung function, cardiovascular risk factors, and brain-related complex traits and diseases (table S12). For example, hypertension had clear genetic correlations with aortic traits and LV traits (Fig. 5A). The strongest correlation between LV traits and hypertension was found in wall thickness traits ($P < 2.43 \times 10^{-9}$), which were also associated with coronary artery disease, type 2 diabetes, and stroke (Fig. 5B). In addition, atrial fibrillation was significantly associated with aortic, LA, and RA traits ($P < 6.66 \times 10^{-4}$), suggesting that atrial fibrillation might have a higher genetic similarity with LA and RA traits than with LV and RV traits.

In both schizophrenia and bipolar disorder, we observed genetic correlations with multiple LV traits (Fig. 5C). Specifically, LVCO, LVEF, radial strains, and wall thickness traits showed positive genetic correlations with schizophrenia and/or bipolar disorder. By contrast, peak circumferential strains had negative genetic correlations with the two brain disorders. Additionally, anorexia nervosa (an eating disorder) was genetically associated with LAV_{min} and LAEF, whereas cognitive traits and neuroticism were mainly associated with right heart traits (RA and RV traits) (Fig. 5, D and E). For example, intelligence, cognitive function, and numerical reasoning were genetically correlated with RA volumes. Lung functions (FEV and FVC) had genetic correlations with multiple CMR traits, with longitudinal strains showing the strongest correlations. There were more associations with other complex traits analyzed in previous GWAS, such as smoking, PR interval, blood pressure, education, risky behaviors, and lipid traits (fig. S110A). We also found high genetic correlations with four previously reported LV traits (*41*) (genetic correlation > 0.847, $P < 6.44 \times 10^{-201}$) (fig. S110B). Additionally, we built PRS for 82 CMR traits and examined their associations with 276 phenotypes available in the UKB study. The PRS analysis produced genetic association patterns similar to those from the LDSC analysis. More details and interpretations are available in the supplementary text (*59*) (figs. S111 and S112 and table S13).

Causal heart-brain relationships detected by Mendelian randomization

In light of the widespread genetic correlations between the heart and brain, we examined their underlying causal genetic links using the 82 CMR traits with Mendelian randomization (MR) (*103*).

We investigated 11 well-powered ($n > 20{,}000$) brain-related clinical outcomes from the FinnGen database (*104*) and six neuropsychiatric disorders from the Psychiatric Genomics Consortium (*105*). We also evaluated nine cognitive and mental health traits such as intelligence and neuroticism (see the materials and methods).

Most of the MR findings indicated genetic causal effects from the heart to the brain (table S14 and fig. S113). We identified causal genetic links underlying heart health and neuropsychiatric disorders. Specifically, multiple genetic causal effects of wall thickness traits, DAo minimum area, and LVESV to psychiatric diseases and mental health traits were identified at the FDR 5% level ($P < 1.68 \times 10^{-4}$), such as the cross disorders [five major psychiatric disorders (*106*)], bipolar disorder, and depression (Fig. 6). The presence of heart conditions may adversely affect attitude and mood, which may ultimately lead to mental health problems such as depression and other psychiatric disorders (*107*). For example, hypertrophic cardiomyopathy is associated with an increased risk of mood disorders (*108*). Heart muscle thickening makes it more difficult for the heart to pump blood, and when oxygen to the brain is reduced, mental health issues may develop (*109*). We also observed causal genetic effects of wall thickness traits on neuroticism, for which the phenotypic association has been identified (*55*). Moreover, AAo minimum area and AAo maximum area were causally linked to multiple FinnGen diseases of the nervous system, such as neurological diseases, sleep apnea, and episodic and paroxysmal disorders. Conversely, we identified several causal relationships in which brain disorders were the exposure and CMR traits were the outcome; most of these were from sleep apnea to radial strains. In previous studies, the reduction in radial strain has been found in patients with moderate to severe obstructive sleep apnea (*110*), and our results demonstrate that this association may have a causal genetic component.

Biological and gene-level analyses

We performed gene-level association testing using GWAS summary statistics of the 82 CMR traits with MAGMA (*111*). We identified 163 significant genes for 48 CMR traits ($P < 3.24 \times 10^{-8}$, Bonferroni adjusted for 82 traits) (table S15). Next, we mapped significant variants ($P < 6.09 \times 10^{-10}$) to genes by combining evidence

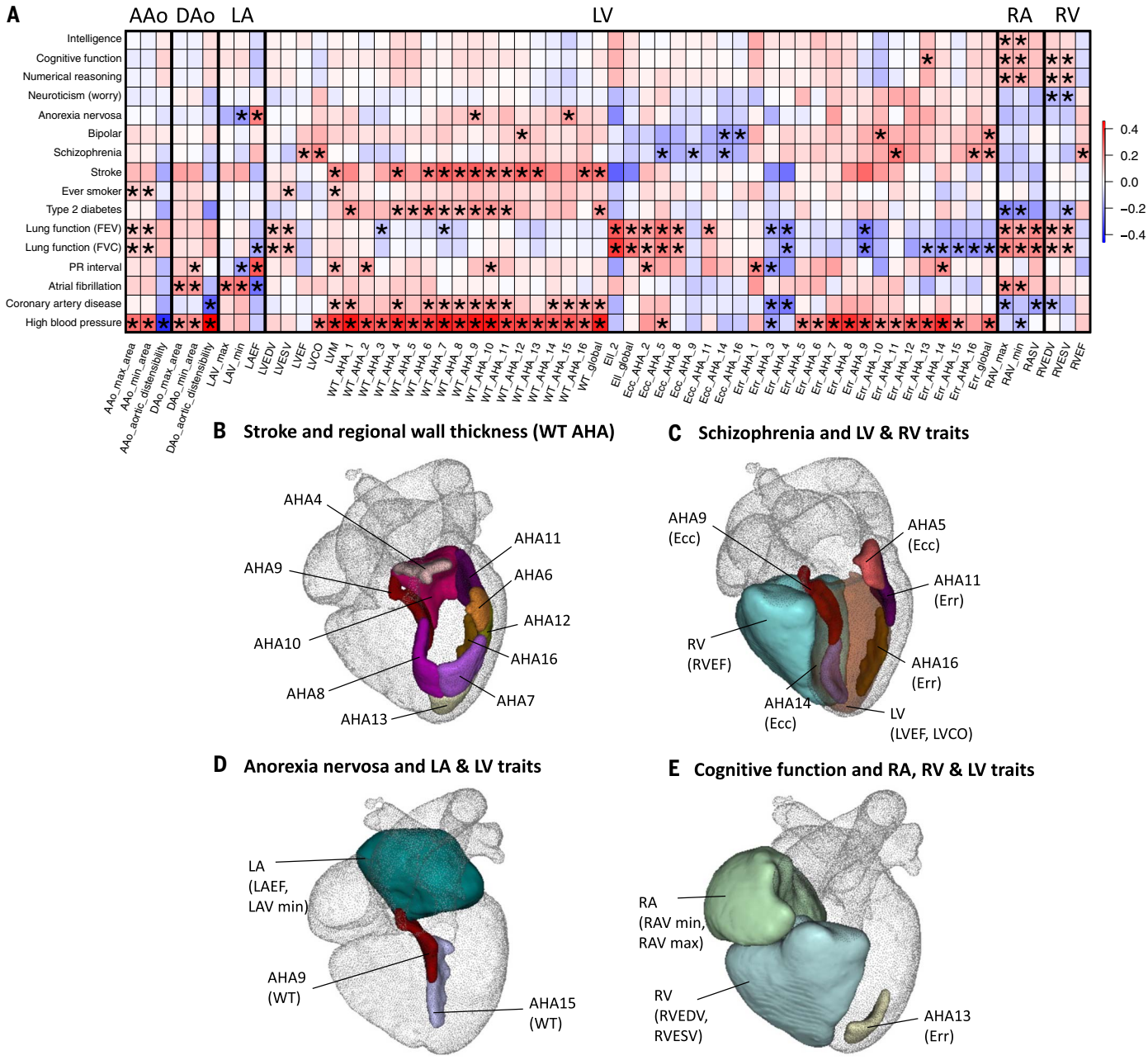


Fig. 5. Genetic correlations between CMR traits and other complex traits and diseases. (**A**) We illustrated selected genetic correlations between CMR traits (*x* axis) and complex traits and diseases (*y* axis). The asterisks highlight genetic correlations that have passed multiple testing adjustments using the Benjamini-Hochberg procedure to control the FDR at the 5% level. (**B** to **E**) Illustration of CMR traits that exhibited genetic correlations with stroke (B), schizophrenia (C), anorexia nervosa (D), and cognitive function (E).

of physical position, eQTL association, and three-dimensional chromatin (Hi-C) interaction using FUMA (*112*). We found 585 mapped genes, 440 of which were not identified in MAGMA (table S16). Moreover, 91 MAGMA or FUMA-identified genes had a high probability of being loss-of-function intolerant (*113*) (pLI > 0.98), indicating significant enrichment of intolerance of loss-of-function variation among these CMR-associated genes ($P = 1.68 \times 10^{-4}$). We conducted MAGMA gene-set analysis to prioritize enriched biological pathways and performed partitioned heritability analyses (*114*) to identify tissues and cell types (*115*) in which genetic variation contributed to differences in CMR traits [fig. S114, table S17, and supplementary text (*59*)].

Ten genes were targets for 32 cardiovascular system drugs (*116*), such as 15 calcium channel blockers [anatomical therapeutic chemical (ATC) code: C08] to lower blood pressure, five cardiac glycosides (ATC code: C01A) to treat heart failure and irregular heartbeats, and three antiarrhythmics (ATC code: C01B) to treat heart rhythm disorders (table S18). Three of these genes, *CACNA1I*, *ESR1*, and *CYP2C9*, and four more CMR-associated genes, *ALDH2*, *HDAC9*, *NPSR1*, and *TRPA1*, were targets for 11 nervous system drugs, including four antiepileptic drugs (ATC code: N03A) and two drugs for addictive disorders (ATC code: N07B). Some drug target genes have known biological functions in both the heart and the brain. For example, *ALDH2* plays a role in clearance of toxic aldehydes, which is an important mechanism related to myocardial and cerebral



Fig. 6. Genetic causal effects of CMR traits on psychiatric disorders. We illustrated selected significant ($P < 1.68 \times 10^{-4}$) causal genetic links from CMR traits (exposure) to psychiatric disorders (outcome) after adjusting for multiple testing using the Benjamini-Hochberg procedure to control the FDR at the 5% level. Category, the category of CMR traits; #IVs, the number of genetic variants used as instrumental variables. Different Mendelian randomization methods and their regression coefficients are labeled with different colors. See table S14 for data resources of psychiatric disorders.

ischemia–reperfusion injury (*117*). Therefore, *ALDH2* has been proposed to be a protective target for heart and brain diseases and dysfunctions triggered by ischemic injury and related risk factors (*118*, *119*).

Finally, we conducted complex trait and disease prediction using both genetic and multi-organ MRI data. We found that integrating genetic PRS, CMR traits, and brain MRI traits could enhance the prediction of multisystem diseases (e.g., diabetes) compared with using only one data type [figs. S115 and 116, tables S19 and S20, and supplementary text (*59*)].

Discussion

The intertwined connections between heart and brain health are gaining increasing attention. This study quantified the heart-brain associations using CMR and brain MRI data from >40,000 individuals in one study cohort (UKB). After accounting for various body measurements, shared risk factors, and imaging confounders, we discovered that CMR traits were associated with specific brain regions, white matter tracts, and functional networks. For example, LV traits and aortic areas were connected to white matter microstructure, with FA and MD values exhibiting opposite directions. Univariate analysis and CCA indicated that aortic traits were associated with basal forebrain volumes in both the left and right hemispheres. The basal forebrain cholinergic system, which is the primary cholinergic output of the central nervous system, is crucial in cognitive decline and dementia (*120*, *121*). Reduced basal forebrain volume and vascular dysregulation are early predictors of Alzheimer's disease pathology (*122*, *123*). Moreover, several CMR traits, including LVM and ejection fraction measures, were associated with the somatomotor, auditory, and default mode networks in resting fMRI. The CMR associations with the default mode and other networks were generally in opposite directions. Increased LVM and reduced ejection fraction traits are associated with a higher risk of cardiac diseases (*55*). Our findings suggest that abnormal functional connectivity within these networks could potentially act as an early biomarker of brain dysfunction associated with adverse cardiac conditions. Overall, our research indicates that there are associations between multimodal MRI measurements of the heart and brain, hinting at

potential connections between cardiovascular and neurological health.

We used multiorgan imaging data to identify genetic variations that can affect both the heart and brain. Comprehending the genetic pleiotropies and the intricate directional and bidirectional interactions of human organs is a complex task (*11*). Our study provides evidence of causal genetic effects between CMR traits and brain disorders through MR analysis. Because CMR traits are endophenotypes of various cardiovascular diseases (e.g., hypertension and hypertensive diseases), these findings suggest that early intervention in heart conditions and the management of cardiac risk may have a positive impact on brain health. Numerous studies have examined the cognitive and neuropsychiatric effects of antihypertensive medications, such as β-blockers and calcium channel blockers (*124*, *125*), and some recent studies reported their beneficial effects on psychiatric and neurological disorders. For example, in a meta-analysis of 209 studies, antihypertensive medications were found to reduce dementia risk by 21% (*126*). Brain-penetrant calcium channel blockers were associated with a lower incidence of neuropsychiatric disorders (*127*). The CMR and brain MRI traits prioritized in our heart-brain analyses could be helpful in identifying potential therapeutic targets and evaluating the therapeutic potential (or side effects) of existing antihypertensive drugs and heart disease medications for mental health and neurodegenerative disorders.

To mitigate the confounding effects of body size, our analyses have adjusted for a wide range of variables collected by the UKB study, including height, weight, whole-body fat free mass, waist-to-hip ratio, body surface area, and nonlinear high-order terms (*128*). However, unobserved biological interactions and environmental factors may still confound the identified heart-brain connections. The concept of large-scale multiorgan imaging genetics analysis is relatively new, and future research using additional data resources, such as long-term longitudinal data and large-scale omics data from multiple organs, may provide further insights into the shared biology between the brain and heart. In addition, our analyses faced challenges because of the use of different brain MRI traits generated from multiple imaging modalities. For example, previous studies have shown that lower FA and higher MD of white matter are associated with accelerated brain aging, indicating reduced microstructural coherence with aging (*129*). Resting functional connectivity strength has also been often found to be lower in the aging brain (*130*). In our analyses, certain CMR traits correlated with distinct categories of brain MRI traits in contrasting directions. For example, higher wall thickness was linked to larger subcortical regional brain volumes in structural MRI, lower FA in diffusion MRI, and mostly stronger functional connectivity strength in resting fMRI of cortical brain areas. These findings may suggest that white matter and gray matter are differentially associated with certain heart functions. However, potential confounding factors cannot be completely ruled out, because the MRI traits were from different areas of the brain and extracted using different brain maps and processing procedures. To better establish and investigate these patterns, future studies could incorporate new brain MRI traits, such as microstructure measures in gray matter brain regions, and produce diffusion MRI and fMRI traits in the same brain atlas, allowing for a more comprehensive analysis of the structural and functional relationships between the heart and the brain.

In this study, imaging data were mainly from individuals of European ancestry. Comparing UKB GWAS results with those of BBJ, we found both similarities and differences for genetic influences on CMR traits. For example, participants in UKB and BBJ had similar genetic effects on cardiac conditions at 22q11.23 and 8q24.13, but only the BBJ cohort showed genetic effects at 10q22.2. There was also a reduction in PRS performance in the BBJ-UKB prediction compared with the prediction analysis within the UKB study. Furthermore, the UKB study is well known for its "healthy volunteer" selection bias and may not be an ideal representation of the general European population (*131*). It can be expected that some of the genetic components that underlie heart-brain connections may be population specific or UKB specific. More open and large-scale imaging datasets (*132*) collected from global populations may help to identify causal variants associated with CMR traits in globally diverse populations and quantify population-specific heterogeneity of genetic effects. These new data will also enable the development of a better picture of neurological-cardiac interactions and allow researchers to examine the reproducibility of scientific findings.

This paper specifically focuses on heart-brain connections. Because of the large amount of data collected in the UKB study, it is also possible to study the relationships between the brain and other human organs and systems (*133*). For example, increasing evidence supports the gut-brain axis, which involves complex interactions between the central nervous system and the enteric nervous system (*134*). Patients with inflammatory bowel disease (e.g., Crohn's disease) show a higher risk of mental disorders such as depression and anxiety (*135*). Multisystem analysis using biobank-scale data may provide insights for interorgan pathophysiological mechanisms and guide the prevention and early detection of brain diseases.

Methods summary

Our study aimed to explore the connection between the heart and brain by analyzing multiorgan imaging data obtained from >40,000 subjects. We used recently developed pipelines for cardiac and aortic MRI (*55*–*57*) to generate imaging traits for four cardiac chambers, LV, LA, RV, and RA, and two aortic sections, AAo and DAo. Moreover, we extracted various imaging traits from multiple brain MRI modalities, including structural MRI (*47*), diffusion MRI (*49*), and resting-state and task-based fMRI (*51*). We then performed phenotypic and genetic analyses on these multiorgan imaging traits to examine the relationship between the heart and brain.

We performed a discovery-replication analysis to assess pairwise phenotypic associations between heart and brain imaging traits while controlling for various covariates such as body size (*128*), shared risk factors, and imaging confounders. Additionally, we conducted separate univariate analyses of structural and functional connection patterns for both female and male subjects. To better understand the relationship between CMR traits and different brain MRI modalities, we used CCA (*66*) to examine multivariate associations.

We used data from UKB individuals of British ancestry to estimate the SNP heritability of 82 CMR traits (*67*) and performed GWAS using linear mixed-effect models implemented in fastGWA (*136*). To ensure the robustness of our findings, we conducted separate GWASs with independent holdout datasets to replicate the identified loci. We also conducted sex-specific SNP heritability and GWAS analyses to compare the genetic effects on CMR traits between males and females. Additionally, we generated PRS (*70*) to assess the proportion of variation in CMR traits that could be predicted by genetic variants in European and non-European testing cohorts. To investigate gene-level associations, we used MAGMA (*95*), and we mapped GWAS signals to genes using functional genomic information in FUMA (*38*).

We used GWAS results of CMR traits to uncover the genetic overlaps with other complex traits and diseases previously identified in GWASs, including our brain MRI traits and those catalogued in the NHGRI-EBI GWAS database (*71*). We applied Bayesian colocalization analysis (*72*) to examine the presence of shared causal genetic variants underlying genetic pleiotropy. Additionally, we used cross-trait LDSC (*102*) to estimate genome-wide genetic correlations between CMR traits and other complex traits and diseases.

We further investigated genetic associations by examining the relationship between PRS of CMR traits and phenotypes collected in the UKB study. We also used additional data resources, such as FinnGen (*104*), which provided GWAS results on brain-related clinical

outcomes, to conduct a two-sample MR analysis (*103*) to investigate the genetic causal relationships between CMR traits and brain disorders. Additionally, we evaluated the predictive ability of CMR traits for complex traits and diseases in the UKB study, and improved prediction accuracy by integrating genetic PRS, CMR traits, and brain MRI traits.

REFERENCES AND NOTES

1. H. Gardener, C. B. Wright, T. Rundek, R. L. Sacco, Brain health and shared risk factors for dementia and stroke. *Nat. Rev. Neurol.* **11**, 651–657 (2015). doi: 10.1038/nrneurol.2015.195; pmid: 26481296
2. I. J. Broce *et al*., Dissecting the genetic relationship between cardiovascular risk factors and Alzheimer's disease. *Acta Neuropathol.* **137**, 209–226 (2019). doi: 10.1007/s00401-018-1928-6; pmid: 30413934
3. A. Papadopoulos *et al*., Left ventricular hypertrophy and cerebral small vessel disease: A systematic review and meta-analysis. *J. Stroke* **22**, 206–224 (2020). doi: 10.5853/jos.2019.03335; pmid: 32635685
4. P. Abete *et al*., Cognitive impairment and cardiovascular diseases in the elderly. A heart-brain continuum hypothesis. *Ageing Res. Rev.* **18**, 41–52 (2014). doi: 10.1016/j.arr.2014.07.003; pmid: 25107566
5. F. Moroni *et al*., Cardiovascular disease and brain health: Focus on white matter hyperintensities. *Int. J. Cardiol. Heart Vasc.* **19**, 63–69 (2018). doi: 10.1016/j.ijcha.2018.04.006; pmid: 29946567
6. C. S. Kwok, Y. K. Loke, R. Hale, J. F. Potter, P. K. Myint, Atrial fibrillation and incidence of dementia: A systematic review and meta-analysis. *Neurology* **76**, 914–922 (2011). doi: 10.1212/WNL.0b013e31820f2e38; pmid: 21383328
7. A. Kobayashi, M. Iguchi, S. Shimizu, S. Uchiyama, Silent cerebral infarcts and cerebral white matter lesions in patients with nonvalvular atrial fibrillation. *J. Stroke Cerebrovasc. Dis.* **21**, 310–317 (2012). doi: 10.1016/j.jstrokecerebrovasdis.2010.09.004; pmid: 21111632
8. D. Kim *et al*., Risk of dementia in stroke-free patients diagnosed with atrial fibrillation: Data from a population-based cohort. *Eur. Heart J.* **40**, 2313–2323 (2019). doi: 10.1093/eurheartj/ehz386; pmid: 31212315
9. R. L. Vogels, P. Scheltens, J. M. Schroeder-Tanka, H. C. Weinstein, Cognitive impairment in heart failure: A systematic review of the literature. *Eur. J. Heart Fail.* **9**, 440–449 (2007). doi: 10.1016/j.ejheart.2006.11.001; pmid: 17174152
10. L. Meng, W. Hou, J. Chui, R. Han, A. W. Gelb, Cardiac output and cerebral blood flow: The integrated regulation of brain perfusion in adult humans. *Anesthesiology* **123**, 1198–1208 (2015). doi: 10.1097/ALN.0000000000000872; pmid: 26402848
11. G. N. Levine *et al*., Psychological health, well-being, and the mind-heart-body connection: A scientific statement from the American Heart Association. *Circulation* **143**, e763–e783 (2021). doi: 10.1161/CIR.0000000000000947; pmid: 33486973
12. D. S. Krantz, M. M. Burg, Current perspective on mental stress-induced myocardial ischemia. *Psychosom. Med.* **76**, 168–170 (2014). doi: 10.1097/PSY.0000000000000054; pmid: 24677165
13. S. S. Abisse, R. Lampert, M. Burg, R. Soufer, V. Shusterman, Cardiac repolarization instability during psychological stress in patients with ventricular arrhythmias. *J. Electrocardiol.* **44**, 678–683 (2011). doi: 10.1016/j.jelectrocard.2011.07.019; pmid: 21920534
14. R. Jindal, E. M. MacKenzie, G. B. Baker, V. K. Yeragani, Cardiac risk and schizophrenia. *J. Psychiatry Neurosci.* **30**, 393–395 (2005). pmid: 16327872
15. R. E. Nielsen, J. Banner, S. E. Jensen, Cardiovascular disease in patients with severe mental illness. *Nat. Rev. Cardiol.* **18**, 136–145 (2021). doi: 10.1038/s41569-020-00463-7; pmid: 33128044
16. A. Tawakol *et al*., Relation between resting amygdalar activity and cardiovascular events: A longitudinal and cohort study. *Lancet* **389**, 834–845 (2017). doi: 10.1016/S0140-6736(16)31714-7; pmid: 28088338
17. R. L. Verrier, T. D. Pang, B. D. Nearing, S. C. Schachter, The Epileptic Heart: Concept and clinical evidence. *Epilepsy Behav.* **105**, 106946 (2020). doi: 10.1016/j.yebeh.2020.106946; pmid: 32109857
18. J. Hinterdobler *et al*., Acute mental stress drives vascular inflammation and promotes plaque destabilization in mouse atherosclerosis. *Eur. Heart J.* **42**, 4077–4088 (2021). doi: 10.1093/eurheartj/ehab371; pmid: 34279021
19. S. R. Cox *et al*., Associations between vascular risk factors and brain MRI indices in UK Biobank. *Eur. Heart J.* **40**, 2290–2300 (2019). doi: 10.1093/eurheartj/ehz100; pmid: 30854560
20. M. T. Jensen *et al*., Changes in cardiac morphology and function in individuals with diabetes mellitus: The UK Biobank cardiovascular magnetic resonance substudy. *Circ. Cardiovasc. Imaging* **12**, e009476 (2019). doi: 10.1161/CIRCIMAGING.119.009476; pmid: 31522551
21. S. Subramaniapillai *et al*., Sex- and age-specific associations between cardiometabolic risk and white matter brain age in the UK Biobank cohort. *Hum. Brain Mapp.* **43**, 3759–3774 (2022). doi: 10.1002/hbm.25882; pmid: 35460147
22. A. G. de Lange *et al*., Multimodal brain-age prediction and cardiovascular risk: The Whitehall II MRI sub-study. *Neuroimage* **222**, 117292 (2020). doi: 10.1016/j.neuroimage.2020.117292; pmid: 32835819
23. M. Babo-Rebelo, C. G. Richter, C. Tallon-Baudry, Neural responses to heartbeats in the default network encode the self in spontaneous thoughts. *J. Neurosci.* **36**, 7829–7840 (2016). doi: 10.1523/JNEUROSCI.0262-16.2016; pmid: 27466329
24. S. J. Markovic *et al*., Investigating the link between later-life brain volume and cardiorespiratory fitness after mild traumatic brain injury exposure. *Gerontology* **69**, 201–211 (2023). doi: 10.1159/000526297; pmid: 36174542
25. F. Raimondo *et al*., Brain-heart interactions reveal consciousness in noncommunicating patients. *Ann. Neurol.* **82**, 578–591 (2017). doi: 10.1002/ana.25045; pmid: 28892566
26. S. E. Petersen *et al*., UK Biobank's cardiovascular magnetic resonance protocol. *J. Cardiovasc. Magn. Reson.* **18**, 8 (2016). doi: 10.1186/s12968-016-0227-4
27. T. J. Littlejohns, C. Sudlow, N. E. Allen, R. Collins, Opportunities for cardiovascular research. *Eur. Heart J.* **40**, 1158–1166 (2019). doi: 10.1093/eurheartj/ehx254; pmid: 28531320
28. Z. Raisi-Estabragh, N. C. Harvey, S. Neubauer, S. E. Petersen, Cardiovascular magnetic resonance imaging in the UK Biobank: A major international health research resource. *Eur. Heart J. Cardiovasc. Imaging* **22**, 251–258 (2021). doi: 10.1093/ehjci/jeaa297; pmid: 33164079
29. K. L. Miller *et al*., Multimodal population brain imaging in the UK Biobank prospective epidemiological study. *Nat. Neurosci.* **19**, 1523–1536 (2016). doi: 10.1038/nn.4393; pmid: 27643430
30. M. H. Lee, C. D. Smyser, J. S. Shimony, Resting-state fMRI: A review of methods and clinical applications. *AJNR Am. J. Neuroradiol.* **34**, 1866–1872 (2013). doi: 10.3174/ajnr.A3263; pmid: 22936095
31. P. M. Thompson *et al*., ENIGMA and global neuroscience: A decade of large-scale studies of the brain in health and disease across more than 40 countries. *Transl. Psychiatry* **10**, 100 (2020). doi: 10.1038/s41398-020-0705-1; pmid: 32198361
32. G. B. Frisoni, N. C. Fox, C. R. Jack Jr., P. Scheltens, P. M. Thompson, The clinical use of structural MRI in Alzheimer disease. *Nat. Rev. Neurol.* **6**, 67–77 (2010). doi: 10.1038/nrneurol.2009.215; pmid: 20139996
33. G. L. Colclough *et al*., The heritability of multi-modal connectivity in human brain activity. *eLife* **6**, e20178 (2017). doi: 10.7554/eLife.20178; pmid: 28745584
34. C. A. Busjahn *et al*., Heritability of left ventricular and papillary muscle heart size: A twin study with cardiac magnetic resonance imaging. *Eur. Heart J.* **30**, 1643–1647 (2009). doi: 10.1093/eurheartj/ehp142; pmid: 19406865
35. K.-L. Chien, H.-C. Hsu, T.-C. Su, M.-F. Chen, Y.-T. Lee, Heritability and major gene effects on left ventricular mass in the Chinese population: A family study. *BMC Cardiovasc. Disord.* **6**, 37 (2006). doi: 10.1186/1471-2261-6-37; pmid: 16945138
36. A. G. Jansen, S. E. Mous, T. White, D. Posthuma, T. J. Polderman, What twin studies tell us about the heritability of brain development, morphology, and function: A review. *Neuropsychol. Rev.* **25**, 27–46 (2015). doi: 10.1007/s11065-015-9278-9; pmid: 25672928
37. H. Foo *et al*., Genetic influence on ageing-related changes in resting-state brain functional networks in healthy adults: A systematic review. *Neurosci. Biobehav. Rev.* **113**, 98–110 (2020). doi: 10.1016/j.neubiorev.2020.03.011; pmid: 32169413
38. N. Aung *et al*., Genome-wide analysis of left ventricular image-derived phenotypes identifies fourteen loci associated with cardiac morphogenesis and heart failure development. *Circulation* **140**, 1318–1330 (2019). doi: 10.1161/CIRCULATIONAHA.119.041161; pmid: 31554410
39. A. Córdova-Palomera *et al*., Cardiac imaging of aortic valve area from 34,287 UK Biobank participants reveals novel genetic associations and shared genetic comorbidity with multiple disease phenotypes. *Circ. Genom. Precis. Med.* **13**, e003014 (2020). doi: 10.1161/CIRCGEN.120.003014; pmid: 33125279
40. H. V. Meyer *et al*., Genetic and functional insights into the fractal structure of the heart. *Nature* **584**, 589–594 (2020). doi: 10.1038/s41586-020-2635-8; pmid: 32814899
41. J. P. Pirruccello *et al*., Analysis of cardiac magnetic resonance imaging in 36,000 individuals yields genetic insights into dilated cardiomyopathy. *Nat. Commun.* **11**, 2254 (2020). doi: 10.1038/s41467-020-15823-7; pmid: 32382064
42. J. P. Pirruccello *et al*., Genetic analysis of right heart structure and function in 40,000 people. *Nat. Genet.* **54**, 792–803 (2022). doi: 10.1038/s41588-022-01090-3; pmid: 35697867
43. M. Thanaj *et al*., Genetic and environmental determinants of diastolic heart function. *Nat. Cardiovasc. Res.* **1**, 361–371 (2022). doi: 10.1038/s44161-022-00048-2; pmid: 35479509
44. L. T. Elliott *et al*., Genome-wide association studies of brain imaging phenotypes in UK Biobank. *Nature* **562**, 210–216 (2018). doi: 10.1038/s41586-018-0571-7; pmid: 30305740
45. B. Zhao *et al*., Genome-wide association analysis of 19,629 individuals identifies variants influencing regional brain volumes and refines their genetic co-architecture with cognitive and mental health traits. *Nat. Genet.* **51**, 1637–1644 (2019). doi: 10.1038/s41588-019-0516-6; pmid: 31676860
46. S. M. Smith *et al*., An expanded set of genome-wide association studies of brain imaging phenotypes in UK Biobank. *Nat. Neurosci.* **24**, 737–745 (2021). doi: 10.1038/s41593-021-00826-4; pmid: 33875891
47. B. Zhao *et al*., Common genetic variation influencing human white matter microstructure. *Science* **372**, eabf3736 (2021). doi: 10.1126/science.abf3736; pmid: 34140357
48. K. L. Grasby *et al*., The genetic architecture of the human cerebral cortex. *Science* **367**, eaay6690 (2020). doi: 10.1126/science.aay6690; pmid: 32193296
49. B. Zhao *et al*., Genetic influences on the intrinsic and extrinsic functional organizations of the cerebral cortex. *medRxiv*, 2021.2007. 2027.21261187 (2021). doi: 10.1101/2021.07.27.21261187
50. E. Hofer *et al*., Genetic correlations and genome-wide associations of cortical structure in general population samples of 22,824 adults. *Nat. Commun.* **11**, 4796 (2020). doi: 10.1038/s41467-020-18367-y; pmid: 32963231
51. C. L. Satizabal *et al*., Genetic architecture of subcortical brain structures in 38,851 individuals. *Nat. Genet.* **51**, 1624–1636 (2019). doi: 10.1038/s41588-019-0511-y; pmid: 31636452
52. B. M. Psaty *et al*., Cohorts for Heart and Aging Research in Genomic Epidemiology (CHARGE) Consortium: Design of prospective meta-analyses of genome-wide association studies from 5 cohorts. *Circ. Cardiovasc. Genet.* **2**, 73–80 (2009). doi: 10.1161/CIRCGENETICS.108.829747; pmid: 20031568
53. L. Mascarell Maričić *et al*., The IMAGEN study: A decade of imaging genetics in adolescents. *Mol. Psychiatry* **25**, 2648–2671 (2020). doi: 10.1038/s41380-020-0822-5; pmid: 32601453
54. T. J. Littlejohns *et al*., The UK Biobank imaging enhancement of 100,000 participants: Rationale, data collection, management and future directions. *Nat. Commun.* **11**, 2624 (2020). doi: 10.1038/s41467-020-15948-9; pmid: 32457287
55. W. Bai *et al*., A population-based phenome-wide association study of cardiac and aortic structure and function. *Nat. Med.* **26**, 1654–1662 (2020). doi: 10.1038/s41591-020-1009-y; pmid: 32839619
56. W. Bai *et al*., Automated cardiovascular magnetic resonance image analysis with fully convolutional networks. *J. Cardiovasc. Magn. Reson.* **20**, 65 (2018). doi: 10.1186/s12968-018-0471-x; pmid: 30217194
57. W. Bai, H. Suzuki, C. Qin, G. Tarroni, O. Oktay, P. M. Matthews, D. Rueckert, "Recurrent neural networks for aortic image sequence segmentation with sparse annotations," in: A. Frangi, J. Schnabel, C. Davatzikos, C. Alberola-López, G. Fichtinger, Eds. *Medical Image Computing and Computer Assisted Intervention – MICCAI 2018* (Springer, 2018), vol. 11073 of *MICCAI 2018 Lecture Notes in Computer Science*, pp. 586–594.

58. M. D. Cerqueira *et al*., Standardized myocardial segmentation and nomenclature for tomographic imaging of the heart. A statement for healthcare professionals from the Cardiac Imaging Committee of the Council on Clinical Cardiology of the American Heart Association. *Circulation* **105**, 539–542 (2002). doi: 10.1161/hc0402.102975; pmid: 11815441
59. Supplementary materials are available online.
60. F. Alfaro-Almagro *et al*., Image processing and Quality Control for the first 10,000 brain imaging datasets from UK Biobank. *Neuroimage* **166**, 400–424 (2018). doi: 10.1016/j.neuroimage.2017.10.034; pmid: 29079522
61. B. B. Avants *et al*., A reproducible evaluation of ANTs similarity metric performance in brain image registration. *Neuroimage* **54**, 2033–2044 (2011). doi: 10.1016/j.neuroimage.2010.09.025; pmid: 20851191
62. S. Mori *et al*., Stereotaxic white matter atlas based on diffusion tensor imaging in an ICBM template. *Neuroimage* **40**, 570–582 (2008). doi: 10.1016/j.neuroimage.2007.12.035; pmid: 18255316
63. M. F. Glasser *et al*., A multi-modal parcellation of human cerebral cortex. *Nature* **536**, 171–178 (2016). doi: 10.1038/nature18933; pmid: 27437579
64. J. L. Ji *et al*., Mapping the human brain's cortical-subcortical functional network organization. *Neuroimage* **185**, 35–57 (2019). doi: 10.1016/j.neuroimage.2018.10.006; pmid: 30291974
65. I. J. Bennett, D. J. Madden, C. J. Vaidya, D. V. Howard, J. H. Howard Jr., Age-related differences in multiple measures of white matter integrity: A diffusion tensor imaging study of healthy aging. *Hum. Brain Mapp.* **31**, 378–390 (2010). pmid: 19662658
66. S. M. Smith *et al*., A positive-negative mode of population covariation links brain connectivity, demographics and behavior. *Nat. Neurosci.* **18**, 1565–1567 (2015). doi: 10.1038/nn.4125; pmid: 26414616
67. J. Yang, S. H. Lee, M. E. Goddard, P. M. Visscher, GCTA: A tool for genome-wide complex trait analysis. *Am. J. Hum. Genet.* **88**, 76–82 (2011). doi: 10.1016/j.ajhg.2010.11.011; pmid: 21167468
68. B. K. Bulik-Sullivan *et al*., LD Score regression distinguishes confounding from polygenicity in genome-wide association studies. *Nat. Genet.* **47**, 291–295 (2015). doi: 10.1038/ng.3211; pmid: 25642630
69. M. Kanai *et al*., Genetic analysis of quantitative traits in the Japanese population links cell types to complex human diseases. *Nat. Genet.* **50**, 390–400 (2018). doi: 10.1038/s41588-018-0047-6; pmid: 29403010
70. T. S. H. Mak, R. M. Porsch, S. W. Choi, X. Zhou, P. C. Sham, Polygenic scores via penalized regression on summary statistics. *Genet. Epidemiol.* **41**, 469–480 (2017). doi: 10.1002/gepi.22050; pmid: 28480976
71. A. Buniello *et al*., The NHGRI-EBI GWAS Catalog of published genome-wide association studies, targeted arrays and summary statistics 2019. *Nucleic Acids Res.* **47** (D1), D1005–D1012 (2019). doi: 10.1093/nar/gky1120; pmid: 30445434
72. C. Giambartolomei *et al*., Bayesian test for colocalisation between pairs of genetic association studies using summary statistics. *PLOS Genet.* **10**, e1004383 (2014). doi: 10.1371/journal.pgen.1004383; pmid: 24830394
73. N. K. Kibinge, C. L. Relton, T. R. Gaunt, T. G. Richardson, Characterizing the causal pathway for genetic variants associated with neurological phenotypes using human brain-derived proteome data. *Am. J. Hum. Genet.* **106**, 885–892 (2020). doi: 10.1016/j.ajhg.2020.04.007; pmid: 32413284
74. N. de Klein *et al*., Brain expression quantitative trait locus and network analyses reveal downstream effects and putative drivers for brain-related diseases. *Nat. Genet.* **55**, 377–388 (2023). doi: 10.1038/s41588-023-01300-6; pmid: 36823318
75. U. Võsa *et al*., Large-scale cis- and trans-eQTL analyses identify thousands of genetic loci and polygenic scores that regulate blood gene expression. *Nat. Genet.* **53**, 1300–1310 (2021). doi: 10.1038/s41588-021-00913-z; pmid: 34475573
76. C. P. Nelson *et al*., Association analyses based on false discovery rate implicate new loci for coronary artery disease. *Nat. Genet.* **49**, 1385–1391 (2017). doi: 10.1038/ng.3913; pmid: 28714975
77. C. Roselli *et al*., Multi-ethnic genome-wide association study for atrial fibrillation. *Nat. Genet.* **50**, 1225–1233 (2018). doi: 10.1038/s41588-018-0133-9; pmid: 29892015
78. F. Takeuchi *et al*., Interethnic analyses of blood pressure loci in populations of East Asian and European descent. *Nat. Commun.* **9**, 5052 (2018). doi: 10.1038/s41467-018-07345-0; pmid: 30487518
79. G. T. Jones *et al*., Meta-analysis of genome-wide association studies for abdominal aortic aneurysm identifies four new disease-specific risk loci. *Circ. Res.* **120**, 341–353 (2017). doi: 10.1161/CIRCRESAHA.116.308765; pmid: 27899403
80. C. Dina *et al*., Genetic association analyses highlight biological pathways underlying mitral valve prolapse. *Nat. Genet.* **47**, 1206–1211 (2015). doi: 10.1038/ng.3383; pmid: 26301497
81. E. Villard *et al*., A genome-wide association study identifies two loci associated with heart failure due to dilated cardiomyopathy. *Eur. Heart J.* **32**, 1065–1076 (2011). doi: 10.1093/eurheartj/ehr105; pmid: 21459883
82. R. Malik *et al*., Multiancestry genome-wide association study of 520,000 subjects identifies 32 loci associated with stroke and stroke subtypes. *Nat. Genet.* **50**, 524–537 (2018). doi: 10.1038/s41588-018-0058-3; pmid: 29531354
83. T. Foroud *et al*., Genome-wide association study of intracranial aneurysm identifies a new association on chromosome 7. *Stroke* **45**, 3194–3199 (2014). doi: 10.1161/STROKEAHA.114.006096; pmid: 25256182
84. L. Duan *et al*., Novel susceptibility loci for moyamoya disease revealed by a genome-wide association study. *Stroke* **49**, 11–18 (2018). doi: 10.1161/STROKEAHA.117.017430; pmid: 29273593
85. M. A. Tischfield *et al*., Cerebral vein malformations result from loss of Twist1 expression and BMP signaling from skull progenitor cells and dura. *Dev. Cell* **42**, 445–461.e5 (2017). doi: 10.1016/j.devcel.2017.07.027; pmid: 28844842
86. Y. D'Souza, A. Elharram, R. Soon-Shiong, R. D. Andrew, B. M. Bennett, Characterization of Aldh2 (-/-) mice as an age-related model of cognitive impairment and Alzheimer's disease. *Mol. Brain* **8**, 27 (2015). doi: 10.1186/s13041-015-0117-y; pmid: 25910195
87. J. Simón-Sánchez *et al*., Genome-wide association study reveals genetic risk underlying Parkinson's disease. *Nat. Genet.* **41**, 1308–1312 (2009). doi: 10.1038/ng.487; pmid: 19915575
88. M. I. Kamboh *et al*., Genome-wide association study of Alzheimer's disease. *Transl. Psychiatry* **2**, e117 (2012). doi: 10.1038/tp.2012.45; pmid: 22832961
89. P. T. Nelson *et al*., ABCC9 gene polymorphism is associated with hippocampal sclerosis of aging pathology. *Acta Neuropathol.* **127**, 825–843 (2014). doi: 10.1007/s00401-014-1282-2; pmid: 24770881
90. A. F. Pardiñas *et al*., Common schizophrenia alleles are enriched in mutation-intolerant genes and in regions under strong background selection. *Nat. Genet.* **50**, 381–389 (2018). doi: 10.1038/s41588-018-0059-2; pmid: 29483656
91. L. Hou *et al*., Genome-wide association study of 40,000 individuals identifies two novel loci associated with bipolar disorder. *Hum. Mol. Genet.* **25**, 3383–3394 (2016). doi: 10.1093/hmg/ddw181; pmid: 27329760
92. T. D. Wade *et al*., Genetic variants associated with disordered eating. *Int. J. Eat. Disord.* **46**, 594–608 (2013). doi: 10.1002/eat.22133; pmid: 23568457
93. Z. Raisi-Estabragh *et al*., Associations of cognitive performance with cardiovascular magnetic resonance phenotypes in the UK Biobank. *Eur. Heart J. Cardiovasc. Imaging* **23**, 663–672 (2022). doi: 10.1093/ehjci/jeab075; pmid: 33987659
94. R. F. Gottesman *et al*., Associations between midlife vascular risk factors and 25-year incident dementia in the Atherosclerosis Risk in Communities (ARIC) cohort. *JAMA Neurol.* **74**, 1246–1254 (2017). doi: 10.1001/jamaneurol.2017.1658; pmid: 28783817
95. V. Vaccarino *et al*., Brain-heart connections in stress and cardiovascular disease: Implications for the cardiac patient. *Atherosclerosis* **328**, 74–82 (2021). doi: 10.1016/j.atherosclerosis.2021.05.020; pmid: 34102426
96. J. C. Barrett *et al*., Genome-wide association study and meta-analysis find that over 40 loci affect risk of type 1 diabetes. *Nat. Genet.* **41**, 703–707 (2009). doi: 10.1038/ng.381; pmid: 19430480
97. D. L. Cousminer *et al*., First genome-wide association study of latent autoimmune diabetes in adults reveals novel insights linking immune and metabolic diabetes. *Diabetes Care* **41**, 2396–2403 (2018). doi: 10.2337/dc18-1032; pmid: 30254083
98. A. Mahajan *et al*., Multi-ancestry genetic study of type 2 diabetes highlights the power of diverse populations for discovery and translation. *Nat. Genet.* **54**, 560–572 (2022). doi: 10.1038/s41588-022-01058-3; pmid: 35551307
99. F. Demenais *et al*., Multiancestry association study identifies new asthma risk loci that colocalize with immune-cell enhancer marks. *Nat. Genet.* **50**, 42–53 (2018). doi: 10.1038/s41588-017-0014-7; pmid: 29273806
100. I. Noth *et al*., Genetic variants associated with idiopathic pulmonary fibrosis susceptibility and mortality: A genome-wide association study. *Lancet Respir. Med.* **1**, 309–317 (2013). doi: 10.1016/S2213-2600(13)70045-6; pmid: 24429156
101. T. E. Fingerlin *et al*., Genome-wide association study identifies multiple susceptibility loci for pulmonary fibrosis. *Nat. Genet.* **45**, 613–620 (2013). doi: 10.1038/ng.2609; pmid: 23583980
102. B. Bulik-Sullivan *et al*., An atlas of genetic correlations across human diseases and traits. *Nat. Genet.* **47**, 1236–1241 (2015). doi: 10.1038/ng.3406; pmid: 26414676
103. S. Burgess, F. Dudbridge, S. G. Thompson, Combining information on multiple instrumental variables in Mendelian randomization: Comparison of allele score and summarized data methods. *Stat. Med.* **35**, 1880–1906 (2016). doi: 10.1002/sim.6835; pmid: 26661904
104. M. I. Kurki *et al*., FinnGen provides genetic insights from a well-phenotyped isolated population. *Nature* **613**, 508–518 (2023). doi: 10.1038/s41586-022-05473-8; pmid: 36653562
105. P. F. Sullivan *et al*., Psychiatric genomics: An update and an agenda. *Am. J. Psychiatry* **175**, 15–27 (2018). doi: 10.1176/appi.ajp.2017.17030283; pmid: 28969442
106. Cross-Disorder Group of the Psychiatric Genomics Consortium, Identification of risk loci with shared effects on five major psychiatric disorders: A genome-wide analysis. *Lancet* **381**, 1371–1379 (2013). doi: 10.1016/S0140-6736(12)62129-1; pmid: 23453885
107. A. K. Dhar, D. A. Barton, Depression and the link with cardiovascular disease. *Front. Psychiatry* **7**, 33 (2016). doi: 10.3389/fpsyt.2016.00033; pmid: 27047396
108. H. L. Hu *et al*., Association between depression and clinical outcomes in patients with hypertrophic cardiomyopathy. *J. Am. Heart Assoc.* **10**, e019071 (2021). doi: 10.1161/JAHA.120.019071; pmid: 33834850
109. J. F. Morgan, A. C. O'Donoghue, W. J. McKenna, M. M. Schmidt, Psychiatric disorders in hypertrophic cardiomyopathy. *Gen. Hosp. Psychiatry* **30**, 49–54 (2008). doi: 10.1016/j.genhosppsych.2007.09.005; pmid: 18164940
110. C. Cuspidi, M. Tadic, Obstructive sleep apnea and left ventricular strain: Useful tool or fancy gadget? *J. Clin. Hypertens. (Greenwich)* **22**, 120–122 (2020). doi: 10.1111/jch.13787; pmid: 31891443
111. C. A. de Leeuw, J. M. Mooij, T. Heskes, D. Posthuma, MAGMA: Generalized gene-set analysis of GWAS data. *PLOS Comput. Biol.* **11**, e1004219 (2015). doi: 10.1371/journal.pcbi.1004219; pmid: 25885710
112. K. Watanabe, E. Taskesen, A. van Bochoven, D. Posthuma, Functional mapping and annotation of genetic associations with FUMA. *Nat. Commun.* **8**, 1826 (2017). doi: 10.1038/s41467-017-01261-5; pmid: 29184056
113. M. Lek *et al*., Analysis of protein-coding genetic variation in 60,706 humans. *Nature* **536**, 285–291 (2016). doi: 10.1038/nature19057; pmid: 27535533
114. H. K. Finucane *et al*., Partitioning heritability by functional annotation using genome-wide association summary statistics. *Nat. Genet.* **47**, 1228–1235 (2015). doi: 10.1038/ng.3404; pmid: 26414678
115. A. Kundaje *et al*., Integrative analysis of 111 reference human epigenomes. *Nature* **518**, 317–330 (2015). doi: 10.1038/nature14248; pmid: 25693563
116. Q. Wang *et al*., A Bayesian framework that integrates multi-omics data and gene networks predicts risk genes from schizophrenia GWAS data. *Nat. Neurosci.* **22**, 691–699 (2019). doi: 10.1038/s41593-019-0382-7; pmid: 30988527
117. X.-J. Luo, B. Liu, Q.-L. Ma, J. Peng, Mitochondrial aldehyde dehydrogenase, a potential drug target for protection of heart and brain from ischemia/reperfusion injury. *Curr. Drug Targets* **15**, 948–955 (2014). doi: 10.2174/1389450115666140828142401; pmid: 25163552
118. J. Pang, J. Wang, Y. Zhang, F. Xu, Y. Chen, Targeting acetaldehyde dehydrogenase 2 (ALDH2) in heart failure-Recent insights and perspectives. *Biochim. Biophys. Acta Mol. Basis Dis.* **1863**, 1933–1941 (2017). doi: 10.1016/j.bbadis.2016.10.004; pmid: 27742538
119. C.-H. Chen, J. C. B. Ferreira, E. R. Gross, D. Mochly-Rosen, Targeting aldehyde dehydrogenase 2: New therapeutic opportunities. *Physiol. Rev.* **94**, 1–34 (2014). doi: 10.1152/physrev.00017.2013; pmid: 24382882

120. E. C. Ballinger, M. Ananth, D. A. Talmage, L. W. Role, Basal forebrain cholinergic circuits and signaling in cognition and cognitive decline. *Neuron* **91**, 1199–1218 (2016). doi: 10.1016/j.neuron.2016.09.006; pmid: 27657448
121. C. Geula *et al*., Basal forebrain cholinergic system in the dementias: Vulnerability, resilience, and resistance. *J. Neurochem.* **158**, 1394–1411 (2021). doi: 10.1111/jnc.15471; pmid: 34272732
122. Y. Iturria-Medina, R. C. Sotero, P. J. Toussaint, J. M. Mateos-Pérez, A. C. Evans; Alzheimer's Disease Neuroimaging Initiative, Early role of vascular dysregulation on late-onset Alzheimer's disease based on multifactorial data-driven analysis. *Nat. Commun.* **7**, 11934 (2016). doi: 10.1038/ncomms11934; pmid: 27327500
123. T. W. Schmitz, R. Nathan Spreng; Alzheimer's Disease Neuroimaging Initiative, Basal forebrain degeneration precedes and predicts the cortical spread of Alzheimer's pathology. *Nat. Commun.* **7**, 13249 (2016). doi: 10.1038/ncomms13249; pmid: 27811848
124. J. C. Huffman, T. A. Stern, Neuropsychiatric consequences of cardiovascular medications. *Dialogues Clin. Neurosci.* **9**, 29–45 (2007). doi: 10.31887/DCNS.2007.9.1/jchuffman; pmid: 17506224
125. M. Stuhec, J. Keuschler, J. Serra-Mestres, M. Isetta, Effects of different antihypertensive medication groups on cognitive function in older patients: A systematic review. *Eur. Psychiatry* **46**, 1–15 (2017). doi: 10.1016/j.eurpsy.2017.07.015; pmid: 28992530
126. Y.-N. Ou *et al*., Blood pressure and risks of cognitive impairment and dementia: A systematic review and meta-analysis of 209 prospective studies. *Hypertension* **76**, 217–225 (2020). doi: 10.1161/HYPERTENSIONAHA.120.14993; pmid: 32450739
127. L. Colbourne, P. J. Harrison, Brain-penetrant calcium channel blockers are associated with a reduced incidence of neuropsychiatric disorders. *Mol. Psychiatry* **27**, 3904–3912 (2022). doi: 10.1038/s41380-022-01615-6; pmid: 35618884
128. G. de Simone, M. Galderisi, Allometric normalization of cardiac measures: Producing better, but imperfect, accuracy. *J. Am. Soc. Echocardiogr.* **27**, 1275–1278 (2014). doi: 10.1016/j.echo.2014.10.006; pmid: 25479898
129. A. L. Alexander, J. E. Lee, M. Lazar, A. S. Field, Diffusion tensor imaging of the brain. *Neurotherapeutics* **4**, 316–329 (2007). doi: 10.1016/j.nurt.2007.05.011; pmid: 17599699
130. L. K. Ferreira, G. F. Busatto, Resting-state functional connectivity in normal brain aging. *Neurosci. Biobehav. Rev.* **37**, 384–400 (2013). doi: 10.1016/j.neubiorev.2013.01.017; pmid: 23333262
131. A. Fry *et al*., Comparison of sociodemographic and health-related characteristics of UK Biobank participants with those of the general population. *Am. J. Epidemiol.* **186**, 1026–1034 (2017). doi: 10.1093/aje/kwx246; pmid: 28641372
132. A. R. Laird, Large, open datasets for human connectomics research: Considerations for reproducible and responsible data use. *Neuroimage* **244**, 118579 (2021). doi: 10.1016/j.neuroimage.2021.118579; pmid: 34536537
133. C. McCracken *et al*., Multiorgan imaging demonstrates the heart-brain-liver axis in UK Biobank participants. *Nat. Commun.* **13**, 7839 (2022). doi: 10.1038/s41467-022-35321-2; pmid: 36543768
134. M. Carabotti, A. Scirocco, M. A. Maselli, C. Severi, The gut-brain axis: Interactions between enteric microbiota, central and enteric nervous systems. *Ann. Gastroenterol.* **28**, 203–209 (2015). pmid: 25830558
135. B. Barberio, M. Zamani, C. J. Black, E. V. Savarino, A. C. Ford, Prevalence of symptoms of anxiety and depression in patients with inflammatory bowel disease: A systematic review and meta-analysis. *Lancet Gastroenterol. Hepatol.* **6**, 359–370 (2021). doi: 10.1016/S2468-1253(21)00014-5; pmid: 33721557
136. L. Jiang *et al*., A resource-efficient tool for mixed model association analysis of large-scale data. *Nat. Genet.* **51**, 1749–1755 (2019). doi: 10.1038/s41588-019-0530-8; pmid: 31768069
137. Analysis code for: B. Zhao *et al*., Heart-brain connections: phenotypic and genetic insights from magnetic resonance images, Zenodo (2023); https://zenodo.org/record/7799207.
138. GWAS summary statistics for: B. Zhao *et al*., Heart-brain connections: phenotypic and genetic insights from magnetic resonance images, Zenodo (2023); https://zenodo.org/record/7239166.

ACKNOWLEDGMENTS

We thank the individuals represented in the UKB for their participation and the research teams for their work in collecting, processing, and disseminating these datasets for analysis; the research computing groups at the University of North Carolina at Chapel Hill, Purdue University, and the Wharton School of the University of Pennsylvania for providing computational resources and support that have contributed to these research results; and all of the authors and databases that made GWAS and eQTL summary-level data publicly available. **Funding:** This research was partially supported by National Institutes of Health (grant MH086633 to H.Z., grant MH116527 to T.F.L., and grant R56 AG079291 to Y.L.; startup funding from Purdue University Department of Statistics (B.Z.); and the UNC Intellectual and Developmental Disabilities Research Center (Eunice Kennedy Shriver National Institute of Child Health and Human Development grant P50 HD103573 to Y.L.). This research was conducted using the UKB resource (application no. 22783), which is subject to a data transfer agreement. **Author contributions:** B.Z. designed the study. B.Z., T.F.L., Z.F., Y.Y., J.S., X.Y., X.W., T.Y.L., J.T., D.X., Z.W., and B.L. analyzed the data. TF.L., Y.Y., J.T., X.W., D.X., T.Y.L., J.C., Y.S., C.T., and Z.Z. processed heart imaging data and undertook quantity controls. H.Z., J.L.S., and Y.L. provided feedback on the study design and results interpretation. B.Z. wrote the manuscript with contributions from J.S. and X.Y. and feedback from all authors. **Competing interests:** Chalmer Tomlinson is currently an employee at Janssen R&D of Johnson & Johnson, Raritan, NJ, USA. The remaining authors declare that no competing interests. **Data and materials availability:** We made use of publicly available software and tools. Our analysis code is freely available at Zenodo (*137*). The code for heart image analysis can be found at https://github.com/baiwenjia/ukbb_cardiac. The code for CCA can be found at https://www.fmrib.ox.ac.uk/datasets/HCP-CCA/. Our GWAS summary statistics of 82 CMR traits have been shared on Zenodo (*138*) and at Heart-KP (http://heartkp.org/). The GWAS summary statistics of brain MRI traits can be freely downloaded at BIG-KP https://bigkp.org/. The individual-level UKB data used in this study can be obtained from https://www.ukbiobank.ac.uk/. **License information:** Copyright © 2023 the authors, some rights reserved; exclusive licensee American Association for the Advancement of Science. No claim to original US government works. https://www.science.org/about/science-licenses-journal-article-reuse

SUPPLEMENTARY MATERIALS

science.org/doi/10.1126/science.abn6598
Materials and Methods
Supplementary Text
Figs. S1 to S117
Tables S1 to S20
References (*139–156*)
MDAR Reproducibility Checklist

View/request a protocol for this paper from *Bio-protocol*.

Submitted 10 December 2021; resubmitted 17 November 2022
Accepted 11 April 2023
10.1126/science.abn6598

RESEARCH ARTICLE

MATERIALS SCIENCE

Autonomous alignment and healing in multilayer soft electronics using immiscible dynamic polymers

Christopher B. Cooper[1]†, Samuel E. Root[1]†, Lukas Michalek[1], Shuai Wu[2], Jian-Cheng Lai[1], Muhammad Khatib[1], Solomon T. Oyakhire[1], Renee Zhao[2], Jian Qin[1], Zhenan Bao[1]*

Self-healing soft electronic and robotic devices can, like human skin, recover autonomously from damage. While current devices use a single type of dynamic polymer for all functional layers to ensure strong interlayer adhesion, this approach requires manual layer alignment. In this study, we used two dynamic polymers, which have immiscible backbones but identical dynamic bonds, to maintain interlayer adhesion while enabling autonomous realignment during healing. These dynamic polymers exhibit a weakly interpenetrating and adhesive interface, whose width is tunable. When multilayered polymer films are misaligned after damage, these structures autonomously realign during healing to minimize interfacial free energy. We fabricated devices with conductive, dielectric, and magnetic particles that functionally heal after damage, enabling thin-film pressure sensors, magnetically assembled soft robots, and underwater circuit assembly.

Self-healing allows soft electronic devices to recover from various forms of damage, such as punctures, scratches, and slices, to improve device robustness and lifetime. Previous work has demonstrated self-healing polymers that use a range of dynamic bonds, such as hydrogen bonding (*1*–*3*), metal-ligand coordination (*4*–*6*), or dynamic covalent bonds (*7*). These polymers are generally insulating, thus, to make functional electronic devices, they are embedded with conductive or dielectric materials (e.g., particles, nanowires, nanotubes, flakes, etc.) to achieve the desired bulk electrical properties while retaining the soft mechanical properties of the self-healing polymer matrix. These self-healing composites can recover not only their original mechanical properties upon healing but also their electrical conductivity (*8*).

Many self-healing devices have been reported, including aquatic skin, field-effect transistors, light-emitting capacitors, battery-based sensors, and advanced multifunctional sensing platforms (*9*–*11*). As the complexity of devices has increased, it has become necessary for self-healing to simultaneously occur between multiple layers with different functions. This concept was shown for an electronic skin that integrated multiple functional components, but thick layers and careful manual alignment were needed to ensure functional self-healing between all layers (*8*). A similar problem was encountered for self-healing transistors, which saw a decreased drain current by almost one order of magnitude, owing to imperfect alignment of the source and drain electrodes (*12*).

Self-healing devices have required manual alignment after damage to properly align different functional components, which is impractical for thin devices (<~100 μm) (*10*). When the fractured surfaces of a multilayered device are brought back into contact, even slightly misaligned layers can limit functional recovery. This issue stems from the use of only a single type of self-healing polymer throughout the device. Although using the same polymer for all functional components ensures strong interlayer adhesion, there is no selectivity during healing between different functional components to drive realignment.

We demonstrate a multilayered self-healing device composed of a pair of self-healing polymers with identical dynamic bonds but immiscible polymer backbones. When misaligned after damage, these multilayer structures have composition gradients that drive directional chain diffusion to enable autonomous realignment. Moreover, the similar dynamic bonds between the polymers enable strong interfacial adhesion between the otherwise immiscible layers. We prepared conductive and insulating composites to form thin-film pressure sensors, magnetically assembled soft robots, and underwater circuits, which readily self-heal after mechanical damage. The minimal interlayer diffusion between the polymers also prevents diffusion of the embedded particles, which preserves each layer's electronic function and prevents damage-induced mixing.

[1]Department of Chemical Engineering, Stanford University, Stanford, CA 94305, USA. [2]Department of Mechanical Engineering, Stanford University, Stanford, CA 94305, USA.
*Corresponding author. Email: zbao@stanford.edu
†These authors contributed equally to this work.

Molecular design of immiscible dynamic polymers

We selected polydimethylsiloxane (PDMS) and polypropylene glycol (PPG) as model immiscible backbone polymers because they are flexible, amorphous polymers with low glass transition temperatures ($T_{g,PDMS}$ = −125°C and $T_{g,PPG}$ = −75°C) and different bulk surface free energies ($\gamma_{PDMS} \approx 21$ mJ/m^2 and $\gamma_{PPG} \approx 31$ mJ/m^2) (*13*, *14*). To minimize the effect of film microstructure on self-healing properties, we incorporated a combination of bisurea bonds formed from both 4,4′-methylene bis(phenyl isocyanate) (MPU) and isophorone diisocyanate (IU) into each polymer, which has been shown to produce amorphous, self-healing films without nanoscale aggregation (*1*, *15*–*17*). The strong directional binding of the MPU units incorporate elasticity into the network, while the weaker binding interactions of the IU units provide a stress-dissipation mechanism to improve bulk toughness and prevent formation of microstructures. For both synthesized polymers, we tuned the MPU:IU ratio and the average backbone molecular weight (M_b) to achieve healing dynamics between 30° and 100°C with solid-like properties at room temperature, which are necessary for device fabrication and stability. The PDMS-based polymer, hereafter referred to as PDMS-HB, has an average M_b of 5 kDa for the PDMS backbone repeat units, an MPU:IU molar ratio of 0.3:0.7, and an overall number-averaged molecular weight (M_n) of 46 kDa [dispersity ($Đ$) ~ 1.5]. The PPG-based polymer, hereafter referred to as PPG-HB, has an average M_b of 0.75 kDa for the PPG backbone repeat units, an MPU:IU ratio of 0.5:0.5, and an M_n of 10 kDa ($Đ$ ~ 1.7) (Fig. 1, A and B, and table S1).

We confirmed the lack of larger microstructures by small-angle x-ray scattering (SAXS), which gave characteristic domain spacings of between 6 and 9 nm (Fig. 1C and table S1). Moreover, both polymers exhibit a crossover between the storage and loss modulus between 75° and 85°C (Fig. 1D and table S1) and glass transition temperatures well below room temperature ($T_{g,PDMS\text{-}HB}$ < −80°C, $T_{g,PPG\text{-}HB}$ = −35°C; fig. S1), which enables experimentally accessible healing dynamics. PPG-HB has less than one-fifth the M_b of PDMS-HB but similar mechanical and thermal properties, which is consistent with previous work that has found that polyethers destabilize hydrogen bond formation and require higher density to achieve a given mechanical property (*2*). The difference in surface energies between PDMS-HB (23 mJ/m^3) and PPG-HB (44 mJ/m^3) was experimentally confirmed by contact angle measurements (fig. S2 and tables S1 and S2) (*18*).

We characterized the self-healing behavior of PDMS-HB and PPG-HB by adapting a recently reported technique, wherein disks of polymer are healed on a parallel plate rheometer with a contact area defined by a polytetrafluroethylene (PTFE) sheet with a hole (Fig. 1E) (*2*, *19*). After annealing, the plates were pulled apart at a constant rate to generate stress-displacement curves, similar to those obtained

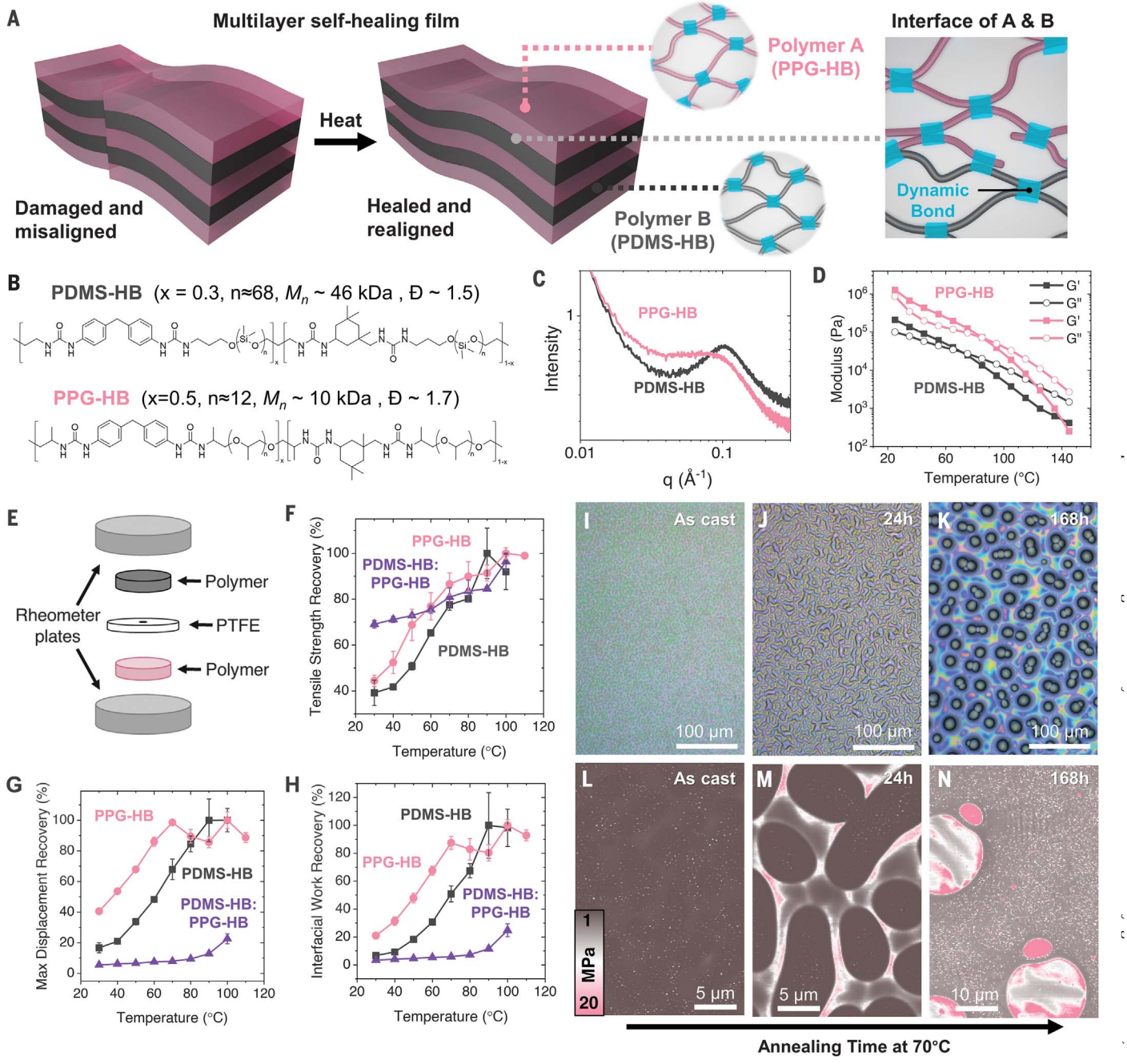


Fig. 1. Design and characterization of a pair of dynamic polymers—PDMS-HB and PPG-HB—with immiscible backbones and identical hydrogen bonding units. (**A**) Schematic showing the principle of surface tension–mediated realignment and healing of a fractured multilayer laminate. The difference in surface energy between the two polymer backbones (type A and type B) drives realignment, while the dynamic bonds in both polymers promote interlayer adhesion for device performance. (**B**) Chemical structures of the two immiscible dynamic polymers used in this study, PDMS-HB and PPG-HB. x, mole fraction of MPU; n, average number of monomers in the backbone segment between dynamic bonds. (**C**) SAXS curves showing the amorphous structure of PDMS-HB (black) and PPG-HB (pink) with domain sizes of ~6 to 9 nm. (**D**) Rheological characteristics of PDMS-HB (black) and PPG-HB (pink) showing the crossover between the storage modulus (G′, solid squares) and loss modulus (G″, open circles) around 75° to 85°C. This crossover point corresponds to the onset of flow in the bulk materials. (**E**) Schematic of the experimental setup of the self- or interfacial healing between two polymers. The recovery in tensile strength (**F**), max displacement (**G**), and interfacial work (**H**) for self-healed PDMS-HB (black squares), self-healed PPG-HB (pink circles), and PDMS-HB healed with PPG-HB (purple triangles). Each point is averaged over three samples, with a healing time of 30 min at the specified temperature. Optical microscope images of a spin-coated film of PDMS-HB and PPG-HB (50 wt %) immediately after casting (**I**) and after annealing at 70°C for 24 hours (**J**) and 168 hours (**K**), and the corresponding AFM nanomechanical images (**L** to **N**). Phase separation increases with increased annealing time. The modulus of neat PDMS-HB and PPG-HB measured by AFM are 1 and 20 MPa, respectively, suggesting that the pink regions are PPG-rich.

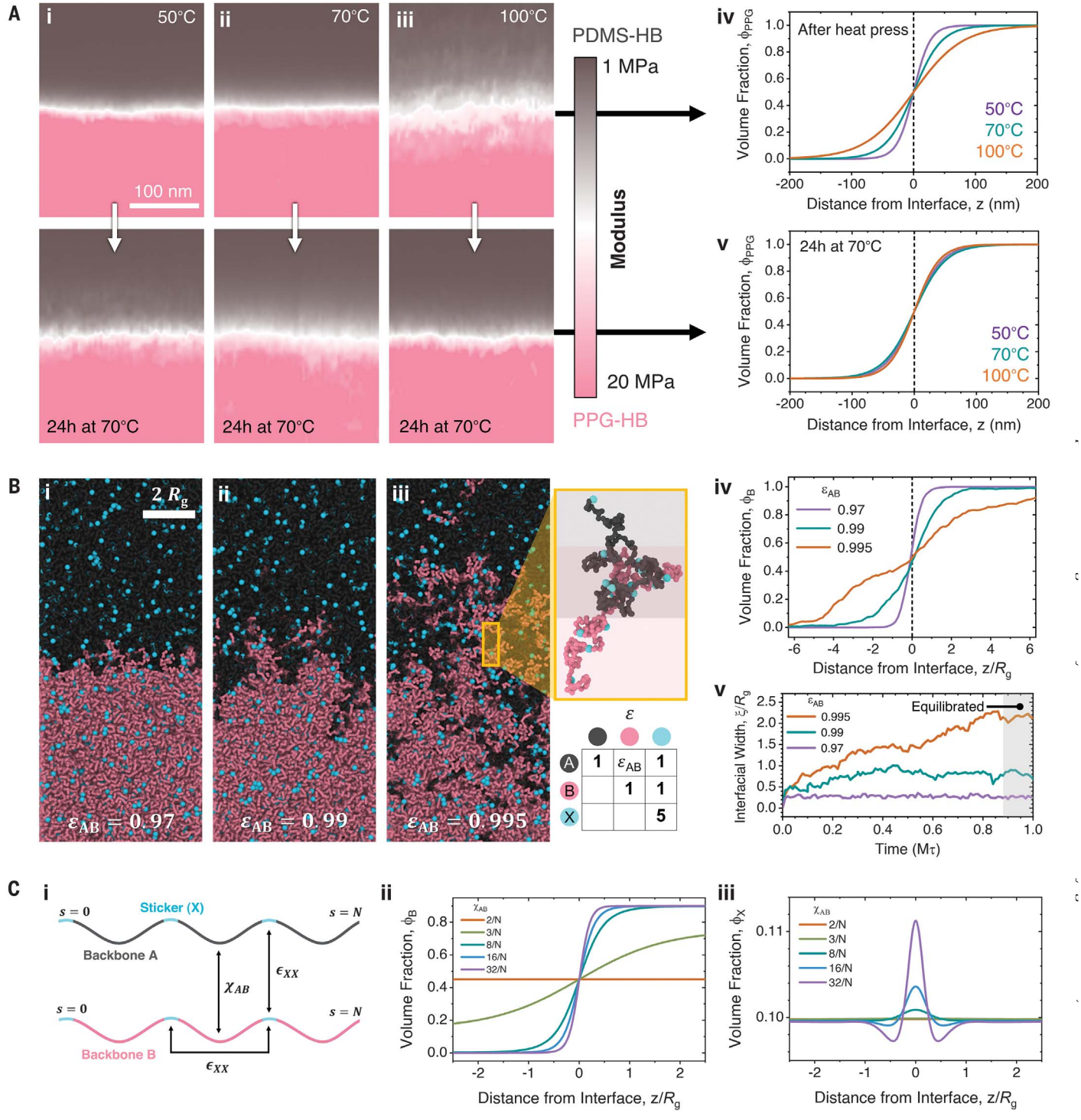


Fig. 2. The interface between two immiscible dynamic polymer networks with identical dynamic bonds. (**A**) AFM characterization of the modulus gradient across the interfaces of bilayer films prepared by gently hot pressing (~20 kPa) at (i) 50°C, (ii) 70°C, and (iii) 100°C, before (top) and after (bottom) annealing for 24 hours at 70°C. The higher-modulus region corresponds to pure PPG-HB (pink), and the lower-modulus region corresponds to pure PDMS-HB (dark gray). Fitted interfacial profiles obtained from the AFM images (iv) immediately after hot pressing and (v) after annealing for 24 hours at 70°C, showing that the interfaces are at thermodynamic equilibrium. (**B**) Coarse-grained molecular dynamics simulation snapshots for equilibrated interfaces with (i) ϵ_{AB} = 0.97, (ii) ϵ_{AB} = 0.99, and (iii) ϵ_{AB} = 0.995. Inset shows chains at the interface with two different polymer backbones (A beads, black; B beads, pink) and identical dynamic bonds (X beads, blue). Table gives the relative energetic attraction between different bead types. (iv) Fitted interfacial profiles obtained from the equilibrated simulations. (v) Dynamics of the fitted interfacial width during simulation while approaching equilibrium. (**C**) (i) Schematic of the field-theoretic model, showing two polymer backbones (A, gray; B, pink) with a repulsive χ_{AB} interaction, an identical dynamic bond (X, blue) with an attractive ϵ_{XX} interaction, and a chain length of N. (ii) Interfacial profiles predicted by the field-theoretic model for different values of χ_{AB} normalized by chain length: 2/N (orange), 3/N (green), 8/N (teal), 16/N (blue), and 32/N (purple). (iii) Sticker volume fraction across the interface for the same χ_{AB} values, showing that dynamic bonds cluster at the interface with increasing χ_{AB}.

on an extensometer (figs. S3 and S4). We repeated this process for different temperatures in 10°C steps and monitored healing by tracking the recovery in the tensile strength (Fig. 1F), the max displacement (Fig. 1G), and the interfacial work (i.e., the area under the stress-displacement curve; Fig. 1H) as a function of healing temperature (fig. S3). In all cases, we observed a plateau at higher temperatures indicative of full healing. Both PDMS-HB and PPG-HB were fully healed after 30 min at ~80° to 90°C, consistent with their terminal flow onset temperatures (Fig. 1D and table S1). These results are also consistent with experimental work on interfacial healing of metallosupramolecular polymers as well as theoretical and computational predictions (*20*–*22*).

We next evaluated the interfacial healing between PDMS-HB and PPG-HB, which have identical dynamic bonds but immiscible polymer backbones. The self-healing of two polymeric interfaces involves wetting between the two-dimensional (2D) interfaces and then creation of a 3D interphase that propagates with macromolecular diffusion and possibly polymer reentanglement to restore bulk properties (*23*). Neumann *et al*. found that for self-healing of metallosupramolecular polymers, full healing was achieved only when the 3D interphase reached widths on the order of ~100 nm (*20*). We hypothesized that the use of similar dynamic bonds would enable wetting and adhesion of the 2D interface, while the difference in surface free energies between PDMS-HB and PPG-HB would limit the width of a 3D interphase, approaching the limiting case of two fully immiscible polymer blends (*24*, *25*). Compared with the self-healing cases, the PDMS-HB:PPG-HB interface exhibited reduced healing, even at 100°C, when both samples exhibit rapid dynamics and liquid-like behavior. The tensile strength recovered almost immediately to ~70% of the PDMS-HB pristine interface, indicative of good wetting between the surfaces. However, both the max displacement and interfacial work recoveries remained lower (<20%) than the healed samples with two pieces of identical polymers (Fig. 1, F to H).

These results suggest that healing between the samples is thermodynamically restricted because of a lack of macromolecular diffusion across the interface. To further test this hypothesis, we spin-coated a film of PDMS-HB and PPG-HB (50 wt % blend) from a homogeneous solution and then annealed the sample at 70°C for various lengths of time. Optical microscope images (Fig. 1, I to K) and atomic force microscopy (AFM) images (Fig. 1, L to N) showed increasing phase separation with increased annealing, with coarsening occurring across all measured length scales. These observations suggest that PDMS-HB and PPG-HB are thermodynamically immiscible and explain the limited healing observed between the two polymers. In addition, we measured interfacial healing between PDMS-HB and PPG-HB at 70°C for longer healing times and showed that minimal additional healing occurred (fig. S5). This finding implies that increased healing at higher temperatures (Fig. 1, F to H) arises not from faster polymer dynamics but rather from increased miscibility.

Interface between two immiscible dynamic polymers

To further test this hypothesis, we characterized the interface between PDMS-HB and PPG-HB through a combination of experiments, simulation, and theory. We laminated two layers of PDMS-HB and PPG-HB together by gently hot pressing (~20 kPa of pressure; fig. S6) at different temperatures and then measured cut interfaces by AFM before and after annealing at 70°C (*26*, *27*). Tracking changes in the modulus revealed an interface between PDMS-HB and PPG-HB (Fig. 2A), whose width we measured quantitatively by fitting to a sigmoidal function (Eq. 1), analogous to the analytic solution by Helfand and Tagami for the interface between two immiscible polymers (*24*)

$$\phi(z) = \frac{1}{1 + e^{-(z - z_0)/\xi}} \quad (1)$$

$\phi(z)$ is the volume fraction of one polymer as a function of position, z_0 is the location of the interface, and ξ is a measure of the interfacial width. The fitted interfacial widths (ξ) increased with increasing hot-pressing temperature with values of 13 ± 1, 23 ± 1, and 39 ± 1 nm for 50°, 70°, and 100°C hot-pressed films, respectively (Fig. 2A and fig. S7). However, if subsequently annealed at the same temperature, all films exhibited similar interfacial widths (Fig. 2A and fig. S7) of 23 ± 1, 26 ± 2, and 20 ± 1 nm for the initially 50°, 70°, and 100°C hot-pressed films, respectively. These observations suggest that the interfaces are at thermodynamic equilibrium during hot pressing and annealing. Moreover, these interfaces were all measured at room temperature, without rapid quenching, which means that the interfacial width (and thus the interlayer adhesion) can be programmed at a specific temperature and then locked in place by cooling the chains into a kinetically trapped state. To demonstrate this concept, we performed an interfacial healing experiment at 100°C for 30 min with an additional annealing step at 70°C for 30 min (fig. S8). Consistent with the decreased interfacial width measured after annealing, the interfacial work between the two polymers decreased with the additional annealing step.

We also estimated the interdiffusion depth of PDMS-HB into bulk PPG-HB by performing x-ray photoelectron spectroscopy (XPS) on interfaces healed for 30 min at 70° and 100°C and then mechanically separated at room temperature. We saw a clear decrease in the Si/C ratio with increased sputtering, which allowed us to estimate the molar fraction of PDMS-HB as a function of depth from the interface (figs. S9 and S10). This yielded an interfacial width (ξ) of 7 nm at 100°C and 2 nm at 70°C. The increased interfacial width at higher temperature matches the trend observed through AFM.

We next sought to model this process in a general manner by conducting coarse-grained molecular dynamics simulations of the interface between two identical polymers containing identical dynamic bonds but immiscible backbones (Fig. 2B) (*28*, *29*). We periodically spaced dynamic bonding beads along the polymer backbone with increased interaction energy ($\varepsilon_R = 5\varepsilon$) relative to the backbone beads ($\varepsilon_P = 1\varepsilon$). Following previous simulations of homopolymers, immiscibility of the backbones was introduced by decreasing the interaction energy between distinct backbone beads from $\varepsilon_{AB} = 1\varepsilon$ (self-healing) to $\varepsilon_{AB} = 0.95\varepsilon$ (entirely immiscible) (*30*). Independently prepared slabs of the two polymer species were brought together in the melt state and allowed to interdiffuse over time until the interface reached a thermodynamic equilibrium (Fig. 2B). Throughout the simulation, the interfacial width was tracked as a function of time by fitting Eq. 1 to the extracted density profiles (Fig. 2B). Consistent with experiments, we observed a sigmoidal density profile and that the equilibrium interfacial width (measured as a correlation length by fitting to Eq. 1) decreased with increasing backbone immiscibility.

Finally, we developed a field-theoretic description of the interface between two immiscible polymer backbones (denoted by A or B monomers) with the same dynamic bonding units (denoted by X monomers). The model predicts the monomer density profiles for an incompressible melt of AX and BX block copolymers of the same chain length N, whose interactions are dominated by a pairwise, repulsive χ parameter between A and B monomers (χ_{AB}) and a pairwise, attractive parameter between X monomers (ϵ_{XX}) (Fig. 2C). With increasing χ_{AB}, analogous to decreasing temperature in experiments, we observed a decrease in the interfacial width between the polymers (Fig. 2C). In addition, we also observed an increase in sticker clustering at the AX-BX interface with increasing χ_{AB} (Fig. 2C), where stickers at the interface reduced the system free energy by minimizing the number of A-B contacts. This is further supported by the fact that the density profiles are almost independent of ϵ_{XX} (fig. S11).

The combination of experiments, simulation, and theory suggest that with increasing temperature, the interface between two immiscible dynamic polymers is governed by a decreasing

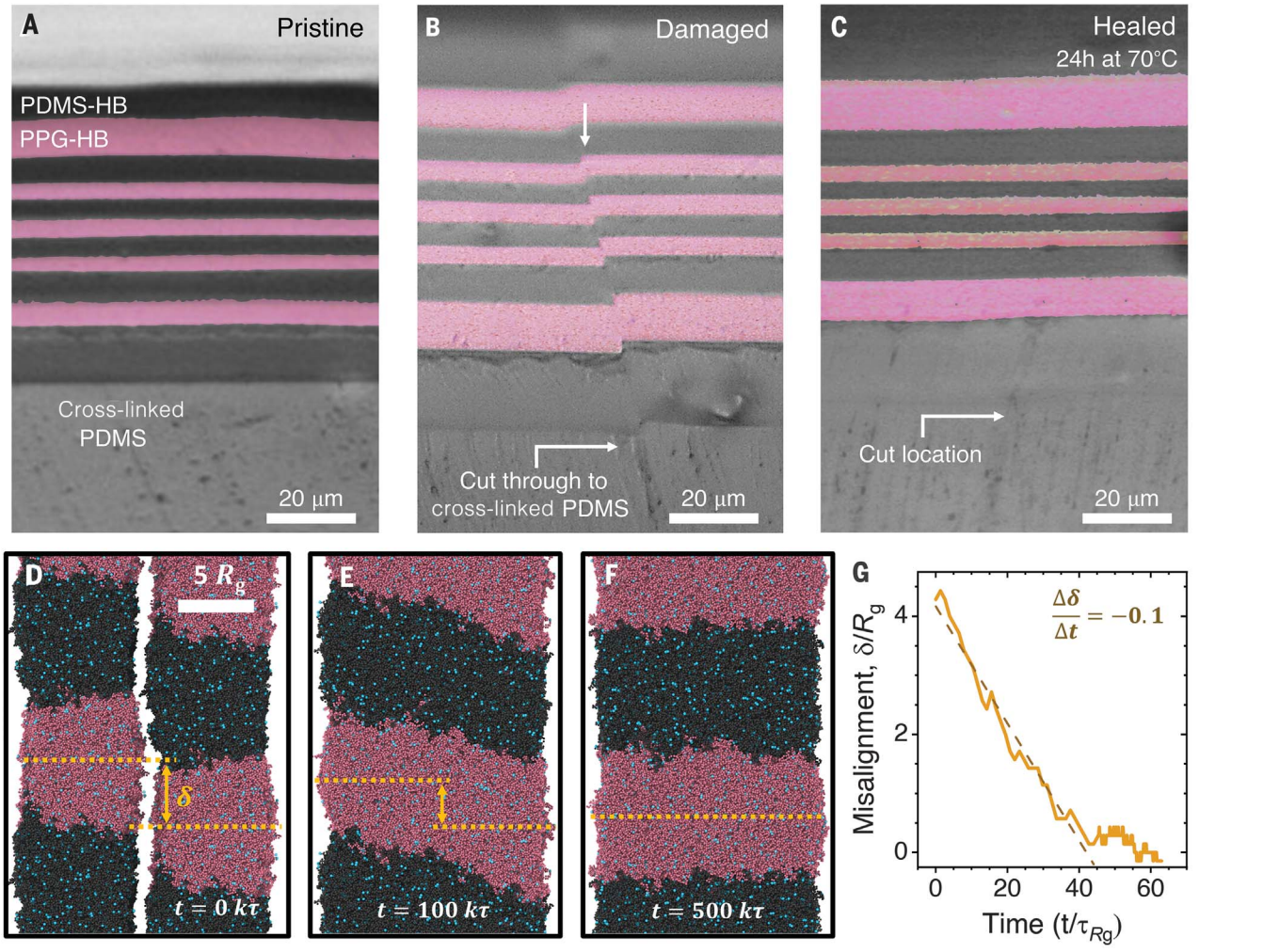


Fig. 3. Autonomous alignment and healing between immiscible dynamic polymers in a multilayered film. Cross-sectional optical microscope images of (**A**) the pristine hot-pressed multilayer laminate, (**B**) the damaged and misaligned laminate, and (**C**) the healed and realigned laminate after annealing for 24 hours at 70°C. A small amount of blue dye was added to PPG-HB for optical contrast, which appears pink in dark-field images at higher magnifications. The cross-linked PDMS substrate (bottom layer) was unable to heal and marks the damage site. (**D** to **F**) Simulation snapshots showing how an initially misaligned and separated laminate aligns and heals over time. (**G**) Misalignment distance (δ), normalized by the chain R_g, decreases linearly with simulation time, normalized by the time to diffuse one chain $R_g(\tau_{R_g})$, until alignment is achieved. The slope of −0.1 corresponds to a realignment rate of $0.1R_g$ per τ_{R_g}.

χ parameter (χ_{AB}) between the polymer backbones, which increases the interfacial width. In addition, dynamic bonds cluster at the interface to reduce contacts between the immiscible backbones. When normalized by estimated radius of gyration, R_g, values for PDMS-HB and PPG-HB (~6 and ~3 nm, respectively, assuming homopolymers with similar M_n), the interfacial widths measured experimentally by AFM are larger than those observed in simulations or predicted by theory (*31*). However, the normalized interfacial widths obtained by XPS are well within the observed values. We attribute the larger interfacial widths measured by AFM to finite tip-size broadening during the indentation measurement but note that the important qualitative trends remain consistent across experiments, simulation, and theory (*32*). Moreover, the consistency between experiments, simulation, and theory suggests that these models could be used to screen polymer backbones and dynamic bonding linkers for desirable mechanical and healing properties.

Autonomous alignment and healing of multilayered polymer films

We next tested the healing of multilayer films of PDMS-HB and PPG-HB. We hypothesized that the reduced interfacial healing between the polymers would enable autonomous realignment of the films after damage. Taking advantage of the immiscibility of PDMS-HB and PPG-HB, we stacked alternating films with a thickness of ~100 μm and hot pressed them to a final film with a thickness of ~70 μm and 11 alternating layers, with individual thicknesses ranging from 3 to 15 μm (Fig. 3A). The resulting film was placed on a cross-linked PDMS substrate and then cut in half. Figure 3B shows the misalignment between the alternating layers as well as the cut extending into the cross-linked PDMS substrate. During healing, the layers autonomously realigned and reformed sharp and alternating interfaces between the PDMS-HB and PPG-HB (Fig. 3C). The misaligned cut in the cross-linked PDMS (which was not able to self-heal) remains visible. When the same type of dynamic polymer was used for both layers, autonomous realignment during healing was not observed (fig. S12).

The phenomenon of autonomous realignment and healing in multilayer structures was also observed in our coarse-grained simulation model. In the simulation, polymer surfaces

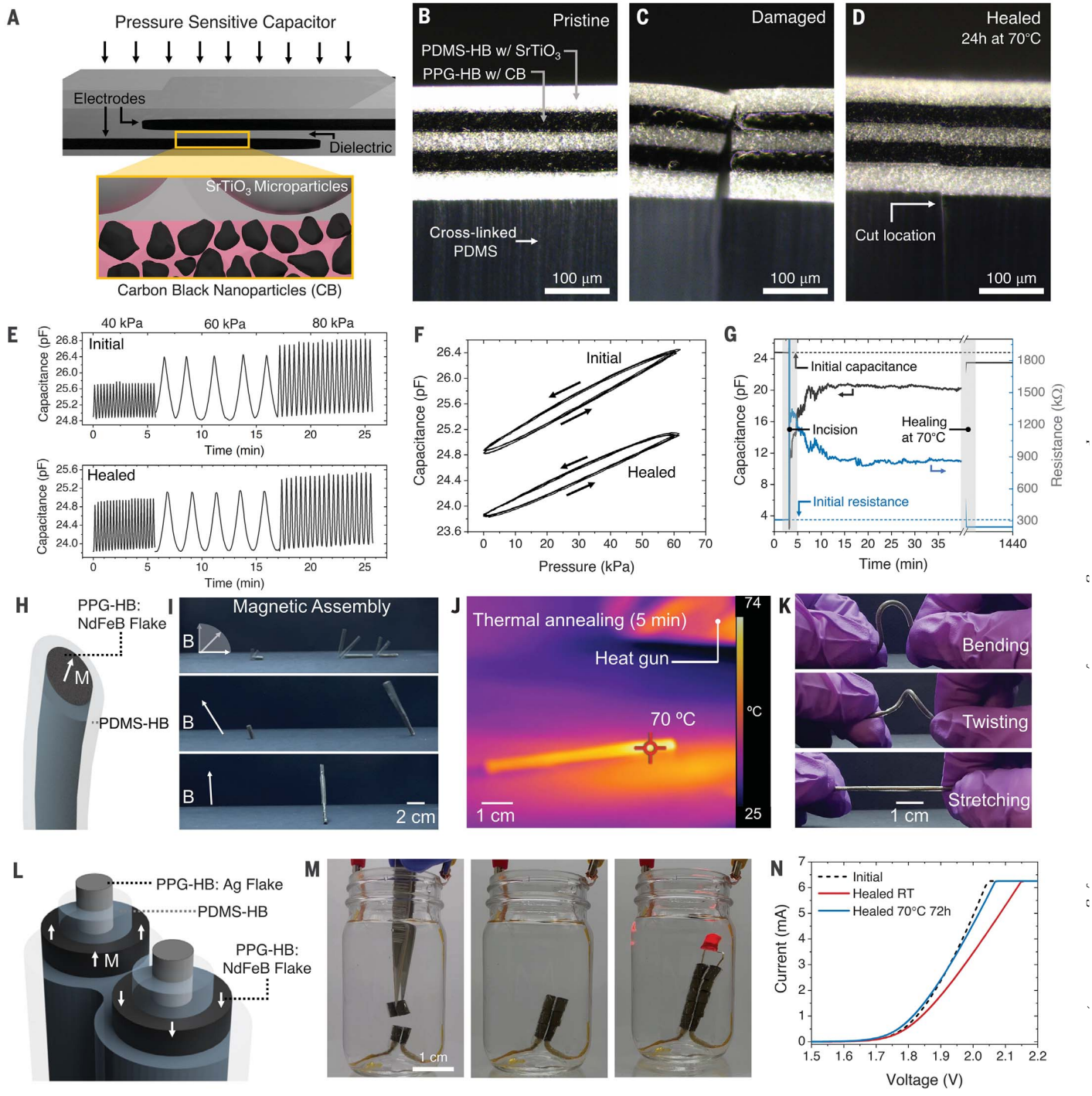


Fig. 4. Demonstration of functional layer recognition and healing in soft electronic devices based on dynamic polymer composites. (**A**) Schematic of a pressure sensitive capacitor with electrodes made from a PPG-HB:carbon black 4:1 weight ratio composite, and dielectric layers made from a PDMS-HB: $SrTiO_3$ 4:1 weight ratio composite. Dark-field optical images of the cross sections of the initial capacitor (**B**), the capacitor after fracture showing layer misalignment (**C**), and the healed device after realignment during annealing for 24 hours at 70°C (**D**). (**E**) Initial (top) and healed (bottom) pressure-sensing performance as a time series. Capacitance was monitored while cyclically applying pressures ranging from 0 to 80 kPa. (**F**) Capacitance versus pressure showing the linear dependence of the capacitance on pressure, with minimal change in drift and hysteresis between the initial (top) and healed (bottom) sensor. (**G**) Series capacitance and resistance as the device is cut and healed at room temperature, and after annealing at 70°C. (**H**) Schematic of core-shell magnetic fibers made from a PPG-HB:NdFeB flake 1:4 weight ratio composite and PDMS-HB. (**I**) Magnetic assembly of the core-shell fibers. (**J**) Thermal welding of the assembled fiber at 70°C for 5 min with a heat gun. (**K**) Images of the welded device bending, twisting, and stretching to show mechanical robustness. (**L**) Schematic of double core-shell fibers with separate electrically conductive (PPG-HB:Ag flake 1:1 weight ratio composite) and magnetic (PPG-HB:NdFeB flake 1:4 weight ratio composite) layers with PDMS-HB shells. (**M**) Images of the underwater circuit assembly of the LED. (**N**) Current–voltage sweeps of the initial device (dashed black), after room temperature underwater healing (solid red), and after annealing at 70°C for 72 hours (solid blue).

fused together with an initial misalignment (denoted δ) and then selectively interdiffused and steadily realigned until reaching complete alignment (Fig. 3, D to G, and fig. S13). The correspondence between simulation and experiment suggests that this phenomenon can be generalized to other pairs of polymers to simultaneously achieve strong interlayer adhesion and selective interlayer healing.

Demonstration of functional healing for soft electronics

To demonstrate that the use of alternating layers of immiscible dynamic polymers could promote alignment during the healing of a thin (~10 to 100 μm) multilayered electronic device, we investigated the functional healing of a pressure-sensitive capacitor (Fig. 4A). The capacitor was made from alternating layers of homogeneous composites of PDMS-HB embedded with dielectric strontium titanate ($SrTiO_3$) microparticles (20 wt %) and PPG-HB embedded with conductive carbon black nanoparticles (20 wt %). Figure 4, B to D, shows microscope images of a cross section of the parallel plate capacitor in the pristine, damaged, and healed states. Even when misaligned after damage, the multilayer capacitor realigned during healing and recovered its sensing capability, exhibiting quantitatively similar pressure-sensing performance when subjected to the same cyclic loading conditions (Fig. 4, E and F). We also monitored the change in the series capacitance and resistance immediately after damage (Fig. 4G). Only a partial recovery of the capacitance was observed at room temperature, and microscope images of the edge of the device showed misaligned layers (Fig. 4C). However, after heating, the layers almost completely realigned (Fig. 4D), and the device recovered 96% of its initial capacitance. Mechanical recovery was also confirmed by manually applying a tensile force to the sample, resulting in fracture of the underlying substrate while maintaining integrity of the healed layers (fig. S14).

As an additional demonstration of the utility of this pair of selectively weldable dynamic polymers, we fabricated core-shell fiber structures with composites containing magnetic NdFeB microflakes (~10 μm, 80 wt %) embedded in PPG-HB as the core material and PDMS-HB as the shell material (Fig. 4H). These fibers are magnetized along their longitudinal directions with an impulse magnetizer (1.5 T). When cut into pieces, the fibers' motion could be controlled with an external magnetic field to achieve rigid body rotations for reassembling without any manual alignment. When close in distance, these fibers exhibited a magnetic attractive force that induced a contact pressure to promote selective welding of the layers (Fig. 4I and movie S1). After thermal welding at 70°C, the magnetically assembled fibers could withstand bending, twisting, and stretching deformations (Fig. 4, J and K). In contrast to single-component magnetic self-healing, which achieves macroscopic assembly of pieces but lacks the precision for microscopic alignment, this work shows that we can simultaneously employ two alignment mechanisms: magnetically guided macroscopic alignment and interfacial-tension mediated microscopic alignment (*33*–*36*).

Building on this demonstration, we fabricated multilayered magnetic wires with a conductive core, an insulating shell, a magnetized layer, and an outer encapsulating shell (Fig. 4L). Two wires with opposite magnetic orientation were assembled to make a light-emitting diode (LED) circuit. Upon cutting the wires into four pieces, the circuit could be reassembled by adding the components into a glass vial filled with water, where the magnetic forces guided the assembly of the wire to achieve almost instantaneous electrical healing, illuminating an LED (Fig. 4M, fig. S15, and movie S2). The magnetic forces guided the alignment of the two terminals of the LED in the correct orientation with respect to the voltage source (+3 V) and ground. Comparison of current–voltage sweeps showed comparable turn-on voltages before and after healing (Fig. 4N), with full mechanical and electrical healing achieved after thermal annealing at 70°C for 72 hours.

In this study, we achieved autonomous alignment during the self-healing of multilayered soft electronic devices by using two immiscible dynamic polymers, whose different backbones enabled interfacial tension-mediated realignment after damage. We used the same dynamic bond in both polymers to maintain strong interlayer adhesion required for a stretchable device. The interfacial width between the polymers, which subsequently determines the interlayer adhesion, can be programmed by annealing temperature. Simulation and theory results suggest that this design concept can be readily extended to other molecular systems. We fabricated thin-film healable pressure sensors, magnetically assembled and welded structures, and self-healable underwater circuits that autonomously realign during healing to demonstrate the capabilities of this approach.

REFERENCES AND NOTES

1. J. Kang *et al*., *Adv. Mater.* **30**, e1706846 (2018).
2. Y. Yanagisawa, Y. Nan, K. Okuro, T. Aida, *Science* **359**, 72–76 (2018).
3. P. Cordier, F. Tournilhac, C. Soulié-Ziakovic, L. Leibler, *Nature* **451**, 977–980 (2008).
4. C.-H. Li *et al*., *Nat. Chem.* **8**, 618–624 (2016).
5. Y.-L. Rao *et al*., *J. Am. Chem. Soc.* **138**, 6020–6027 (2016).
6. S. C. Grindy *et al*., *Nat. Mater.* **14**, 1210–1216 (2015).
7. R. J. Wojtecki, M. A. Meador, S. J. Rowan, *Nat. Mater.* **10**, 14–27 (2011).
8. D. Son *et al*., *Nat. Nanotechnol.* **13**, 1057–1065 (2018).
9. M. Khatib, O. Zohar, W. Saliba, H. Haick, *Adv. Mater.* **32**, e2000246 (2020).
10. M. Khatib, O. Zohar, H. Haick, *Adv. Mater.* **33**, e2004190 (2021).
11. Y. J. Tan *et al*., *Nat. Mater.* **19**, 182–188 (2020).
12. M. Khatib *et al*., *Small* **15**, e1803939 (2019).
13. G. Wypych, in *Handbook of Polymers* (ChemTec Publishing, ed. 2, 2016), pp. 340–344.
14. G. Wypych, in *Handbook of Polymers* (ChemTec Publishing, ed. 2, 2016), pp. 517–519.
15. D. Döhler *et al*., *ACS Appl. Polym. Mater.* **2**, 4127–4139 (2020).
16. C. B. Cooper *et al*., *J. Am. Chem. Soc.* **142**, 16814–16824 (2020).
17. C. B. Cooper *et al*., *ACS Cent. Sci.* **7**, 1657–1667 (2021).
18. A. Faghihnejad *et al*., *Adv. Funct. Mater.* **24**, 2322–2333 (2014).
19. Y. Fujisawa, A. Asano, Y. Itoh, T. Aida, *J. Am. Chem. Soc.* **143**, 15279–15285 (2021).
20. L. N. Neumann *et al*., *Sci. Adv.* **7**, eabe4154 (2021).
21. E. B. Stukalin, L.-H. Cai, N. A. Kumar, L. Leibler, M. Rubinstein, *Macromolecules* **46**, 7525–7541 (2013).
22. Z. Shen, H. Ye, Q. Wang, M. Kröger, Y. Li, *Macromolecules* **54**, 5053–5064 (2021).
23. R. P. Wool, K. M. O'Connor, *J. Appl. Phys.* **52**, 5953–5963 (1981).
24. E. Helfand, Y. Tagami, *J. Polym. Sci. B* **9**, 741–746 (1971).
25. G. H. Fredrickson, *The Equilibrium Theory of Inhomogeneous Polymers*, vol. 134 of International Series of Monographs on Physics (Oxford Univ. Press, 2006).
26. C. He, S. Shi, X. Wu, T. P. Russell, D. Wang, *J. Am. Chem. Soc.* **140**, 6793–6796 (2018).
27. K. Hu *et al*., *Macromolecules* **52**, 9759–9765 (2019).
28. A. Stukowski, *Model. Simul. Mater. Sci. Eng.* **18**, 015012 (2009).
29. A. P. Thompson *et al*., *Comput. Phys. Commun.* **271**, 108171 (2022).
30. T. Ge, G. S. Grest, M. O. Robbins, *ACS Macro Lett.* **2**, 882–886 (2013).
31. L. J. Fetters, D. J. Lohse, D. Richter, T. A. Witten, A. Zirkel, *Macromolecules* **27**, 4639–4647 (1994).
32. Q. D. Nguyen, K.-H. Chung, *Ultramicroscopy* **202**, 1–9 (2019).
33. A. J. Bandodkar *et al*., *Sci. Adv.* **2**, e1601465 (2016).
34. X. Kuang *et al*., *Adv. Mater.* **33**, e2102113 (2021).
35. S. Wu *et al*., *ACS Appl. Mater. Interfaces* **11**, 41649–41658 (2019).
36. Q. Ze *et al*., *Adv. Mater.* **32**, e1906657 (2020).

ACKNOWLEDGMENTS

Funding: This work was supported by Army Research Office Materials Design Program, grant W911NF-21-1-0092 (Z.B.); National Science Foundation Career Award CMMI-2145601 (R.Z.); National Science Foundation Award CMMI-2142789 (R.Z.); Department of Defense, National Defense Science & Engineering Graduate Fellowship Program (C.B.C.); Walter Benjamin Fellowship Program, Deutsche Forschungsgemeinschaft DFG 456522816 (L.M.); and TomKat Center Fellowship for Translational Research at Stanford University (S.T.O.). Part of this work was performed at the Stanford Nano Shared Facilities (SNSF), supported by the National Science Foundation under award ECCS-1542152. Use of the Stanford Synchrotron Radiation Lightsource, SLAC National Accelerator Laboratory, for SAXS experiments was supported by the US Department of Energy, Office of Science, Office of Basic Energy Sciences, under contract DE-AC02-76SF00515. This work used Expanse computing resources at the San Diego Supercomputer Center through allocation MAT220035 from the Advanced Cyberinfrastructure Coordination Ecosystem: Services & Support (ACCESS) program, which is supported by National Science Foundation grants 2138259, 2138286, 2138307, 2137603, and 2138296. **Author contributions:** Conceptualization: C.B.C., S.E.R., and Z.B. Methodology: C.B.C., S.E.R., L.M., and J.Q. Investigation: C.B.C., S.E.R., L.M., S.W., J.-C.L., M.K., and S.T.O. Visualization: C.B.C., S.E.R., and Z.B. Writing – original draft: C.B.C., S.E.R., and Z.B. Writing – review & editing: C.B.C., S.E.R., L.M., S.W., J.-C.L., M.K., S.T.O., R.Z., J.Q., and Z.B. Supervision: Z.B., J.Q., and R.Z. **Competing interests:** A US provisional patent on this work (serial number 63/440,656) was filed on 23 January 2023 by Z.B., C.B.C., and S.E.R. The authors declare that they have no other competing interests. **Data and materials availability:** All data are available in the main text or the supplementary materials. **License information:** Copyright © 2023 the authors, some rights reserved; exclusive licensee American Association for the Advancement of Science. No claim to original US government works. https://www.science.org/about/science-licenses-journal-article-reuse

SUPPLEMENTARY MATERIALS

science.org/doi/10.1126/science.adh0619
Materials and Methods
Supplementary Text
Figs. S1 to S15
Tables S1 and S2
References
Movies S1 and S2

Submitted 14 February 2023; accepted 14 April 2023
10.1126/science.adh0619

APTAMER DESIGN

A functional group–guided approach to aptamers for small molecules

Kyungae Yang[1]*, Noelle M. Mitchell[2], Saswata Banerjee[1], Zhenzhuang Cheng[1], Steven Taylor[1], Aleksandra M. Kostic[1]†, Isabel Wong[1], Sairaj Sajjath[1]‡, Yameng Zhang[1]§, Jacob Stevens[1], Sumit Mohan[3], Donald W. Landry[1], Tilla S. Worgall[4], Anne M. Andrews[2,5], Milan N. Stojanovic[1,6]*

Aptameric receptors are important biosensor components, yet our ability to identify them depends on the target structures. We analyzed the contributions of individual functional groups on small molecules to binding within 27 target-aptamer pairs, identifying potential hindrances to receptor isolation—for example, negative cooperativity between sterically hindered functional groups. To increase the probability of aptamer isolation for important targets, such as leucine and voriconazole, for which multiple previous selection attempts failed, we designed tailored strategies focused on overcoming individual structural barriers to successful selections. This approach enables us to move beyond standardized protocols into functional group–guided searches, relying on sequences common to receptors for targets and their analogs to serve as anchors in regions of vast oligonucleotide spaces wherein useful reagents are likely to be found.

Aptamers are oligonucleotide-based receptors isolated from random libraries through cycles of enrichment based on target affinity coupled to amplifications (*1*–*4*). Aptamers can be selected for a variety of small molecules for which antibodies cannot—that is, targets ignored by the immune system even when conjugated to carrier proteins, such as neurotransmitters (*5*) and amino acids (*6*, *7*). Once available, aptamers can be readily engineered into various sensor formats (*3*, *4*), including for use as fluorescent (*8*), electrochemical (*9*), or electronic biosensors (*10*).

One of the main obstacles to the broad application of aptamers in biosensing is a lack of aptamers with appropriate affinities for many important low-molecular-weight targets (*3*, *4*). For example, we were repeatedly unable to isolate DNA aptamers for two clinically important molecules, the amino acid leucine (Leu, **1**) and the antifungal agent voriconazole (**2**) (Fig. 1A). Aptamers to detect blood leucine levels could be used to rapidly clarify false positives during newborn screening for maple syrup urine disease (MSUD) (*6*, *11*). We have sought to expand on our success with vancomycin sensing (*12*) and to isolate receptors that could be used for voriconazole therapeutic monitoring (*13*). Our attempts were variations of selections based on target-induced stem closure (Fig. 1B) (*14*, *15*). In this approach, oligonucleotide libraries with internal random 36-nucleotide oligomer (36-mer) regions are immobilized through 5′-primer regions that hybridize with tethered capture sequences. Potential aptamers hybridized on columns are released by interactions with unmodified targets in solution, which can stabilize stem formation upon displacement (Fig. 1B).

Our failure to isolate DNA aptamers for leucine was surprising because RNA aptamers had been previously isolated through affinity columns displaying tethered leucine (*16*). Similarly, voriconazole should have been a straightforward target because of its aromatic surfaces and heteroatoms. However, we could neither adapt reported aptamers cross-reactive with the azole class of antifungals (*17*) as sensor components (*8*, *12*), nor could we isolate specific aptamers. These two seemingly unrelated targets, with substantially different molecular weights, share proximate pairs of sterically crowded sp^3 carbons (Fig. 1A), which inspired us to pursue a broader understanding of the general relationships between target structures and outcomes of highly standardized selections. Our aim was to develop a generalizable approach to aptamer isolation that succeeds when other standard methods fail.

Analysis of free energies of oligonucleotide displacement across related targets

We amassed 27 aptamers, 23 of which were newly isolated through this study. These aptamers emerged directly from selections and without further optimization, being identified as the highest-affinity receptors targeting amines, amino acids, and their analogs. In the past, while working with individual aptamers, we focused on aptamer dissociation constants obtained by a fluorescence-quenching assay that reported fluorescently labeled aptamer competition with a quencher-labeled capture oligonucleotide (Fig. 1C and displacement assay rationale, materials and methods); the assay could be adapted to a model of allosteric antagonism to account for partial release upon binding (*18*). To characterize the impact of targets on selection outcomes, we instead needed to compare targets in their abilities to outcompete capture oligonucleotides. Thus, we focused on the equilibrium constant, $^{app}K_D$ (a midpoint response or $X_{50\%}$), of the displacement of oligonucleotide competitor that is used on the affinity column during selection, which is related to the Gibbs free energy of displacement, ΔG_D. In contrast to the free energy of binding, ΔG_B—obtained, for example, by isothermal calorimetry—ΔG_D governs a comprehensive set of equilibria that affects the release of aptamers from the column upon target addition. The difference between ΔG_D and ΔG_B is primarily in the contributions of the capture oligonucleotide present at equilibria.

The targets (table S3) and their aptamers (figs. S4 to S34) were organized in related pairs (Fig. 1D and figs. S41 to S45), with each pair differing by the addition of a single functional group or group transformation—for example, methylamine (**3**) and phenylethylamine (**4**) differ by the addition of a seven-carbon benzyl group (Fig. 1D). We defined $\Delta\Delta G_{GBE}$ as the free-energy difference related to the equilibria positions affecting the relative outcomes of two selections, attributable to the presence of the additional functional group or transformation. We also assumed the portions of ΔG_D that govern equilibria unrelated to either target or capture oligonucleotide binding to be similar across all aptamers and predicted that they would largely cancel each other when subtracting two ΔG_D values within pairs, which allowed us to extract estimates of $\Delta\Delta G_{GBE}$ values (Fig. 1D). Related concepts on contributions to the free energy of binding associated with functional groups are often used for ligand optimization in medicinal chemistry (*19*, *20*), but there a receptor is shared by multiple targets.

Two key assumptions, aside from nearly identical selection conditions, were needed to extend the concept of functional-group free-energy contributions to selections:

First, there are ~10^{21} possible random 36-mers. In selections, we sample only ~10^{14} of these sequences. Thus, in the absence of extraordinary luck, we do not isolate unique receptors, but typical ones (*21*, *22*), which are examples

[1]Department of Medicine, Columbia University Irving Medical Center, New York, NY 10032, USA. [2]Department of Chemistry and Biochemistry and California Nanosystems Institute, University of California, Los Angeles, Los Angeles, CA 90095, USA. [3]Department of Epidemiology, Mailman School of Public Health, New York, NY 10032, USA. [4]Department of Pathology and Cell Biology, Columbia University Irving Medical Center, New York, NY 10032, USA. [5]Department of Psychiatry and Biobehavioral Sciences and Hatos Center for Neuropharmacology, David Geffen School of Medicine, University of California, Los Angeles, Los Angeles, CA 90095, USA. [6]Departments of Biomedical Engineering, Fu Foundation School of Engineering and Applied Science, and Systems Biology, Columbia University Irving Medical Center, New York, NY 10032, USA.
*Corresponding author. Email: ky2231@cumc.columbia.edu (K.Y.); mns18@cumc.columbia.edu (M.N.S.)
†Present address: Rutgers New Jersey Medical School, Newark, NJ 07103, USA.
‡Present address: Robin Chemers Neustein Laboratory of Mammalian Cell Biology and Development, Howard Hughes Medical Institute, The Rockefeller University, New York, NY 10065, USA.
§Present address: Division of Biology and Biological Engineering, California Institute of Technology, Pasadena, CA 91125, USA.

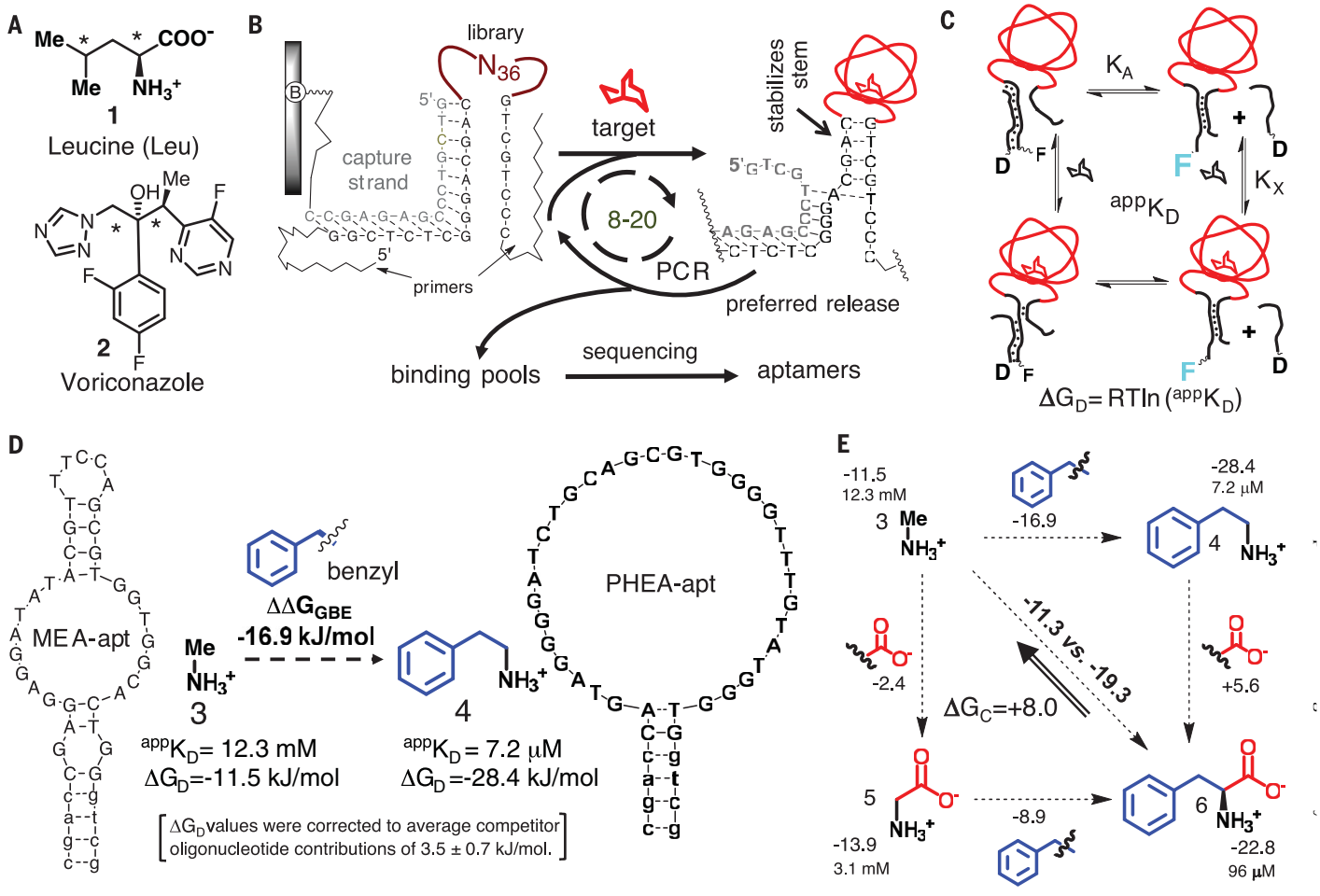


Fig. 1. Target functional-group binding free-energy analysis for aptamers from stem-loop libraries: (**A**) Using standard protocols, we were unable to isolate aptamers for leucine (**1**) and voriconazole (**2**), which have congested pairs of carbons (*). (**B**) Aptamer selection is driven by small-molecule-induced stem closures. An oligonucleotide library with a random loop (N_{36}) is hybridized to the complement (capture strand) of a polymerase chain reaction (PCR) primer. The capture strand is tethered to a column. The column is exposed to target solutions. Sequences that bind the targets and undergo stem stabilization are released, preferentially amplified, and used in the next selection cycle. (**C**) We measured apparent $^{app}K_D$ values for aptamers and from these calculated the free energies of displacement, ΔG_D, on the basis of a fluorescence displacement assay associated with the equilibrium between an aptamer (labeled with fluorescein, F) and a complementary oligonucleotide used for capture in selection (labeled with a quencher, dabcyl, D). The addition of the target leads to concentration-dependent increases in fluorescence through the equilibria shown. K_X and K_A are dissociation constants for a target-aptamer complex without competitor and an aptamer-competitor complex without target, respectively. (**D**) We isolated the contributions of individual functional groups by subtracting individual ΔG_D values of aptamer-target pairs, with these values corrected to account for differences in oligonucleotide quenching. The two targets, methylamine (MEA) (**3**) and phenylethylamine (PHEA) (**4**), differ by a benzyl group. The difference in free energy associated with benzyl group addition is $\Delta\Delta G_{GBE}$ (benzyl). The two aptamers used for this calculation are shown (constant regions in lower case). (**E**) Cooperativity is assessed by double functional group replacement cycles (*24*). The ΔG_D and $^{app}K_D$ (normalized to average impact of oligonucleotide on equilibrium, in kJ/mol) values are shown next to the targets, with $\Delta\Delta G_{GBE}$ values shown next to the fragments. A $\Delta\Delta G_{GBE}$ >0 indicates a decrease in affinity upon adding a functional group; the ΔG_C value (+8.0 kJ/mol) represents the difference between adding functional groups separately (top horizontal and left vertical values) versus at the same time (diagonally), which is interpreted as negative cooperativity when both a benzyl group and a carboxylate are present together in a molecule.

of multiple sequences having similar affinities values broadly distributed over oligonucleotide space. This sparse sampling then allows us to treat the properties of the isolated aptamers, represented here by the "best" aptamer from each selection, as characteristic of the highly standardized selection conditions, libraries, and targets. Because selections for previously identified aptamers differ mostly in their targets, we attribute large changes in the properties of the aptamers to the impact of structural differences between targets—that is, to specific functional groups.

Second, functional group contributions to selections can only be based on well-known noncovalent interactions (*20*, *23*). Thus, as a first approximation, within a set of close analogs, we expect to be able to isolate additive effects. When we observe systematic nonadditivities in thermodynamic cycles—for example, cooperativity (ΔG_C) as estimated through cycles of double replacements of functional groups (*20*, *24*)—we can analyze nonadditivities to generate hypotheses about barriers to aptamer isolation (Fig. 1E). Reciprocally, if correct in our assumptions, after initial selection failures, we can perform functional group analysis of targets to identify possible structural barriers leading to these failures and design selection protocols to improve our chances of isolating aptamers.

We performed the following three tests with the available aptamers to assess these

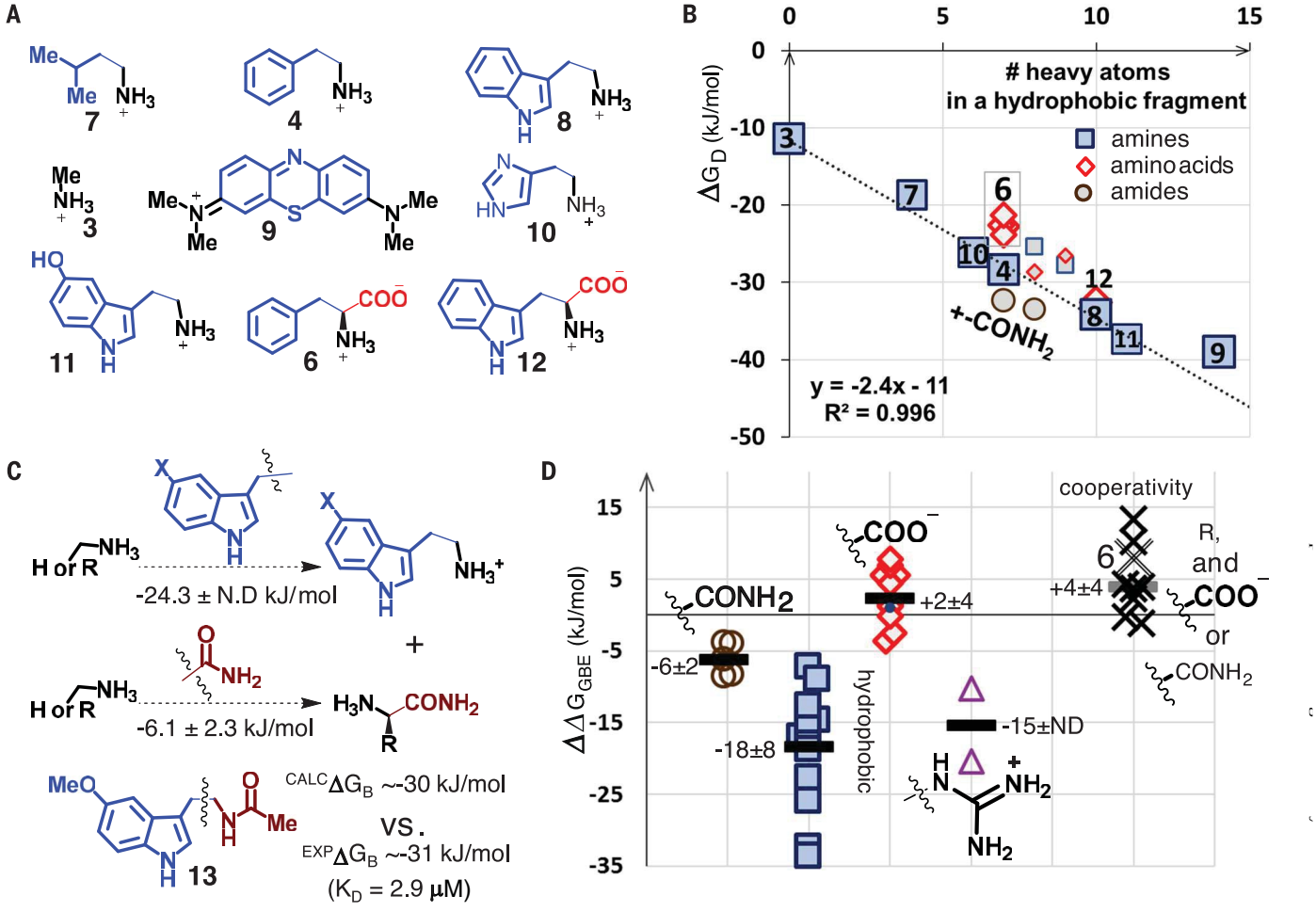


Fig. 2. Analysis of ΔG_D and $\Delta\Delta G_{GBE}$ from a set of 27 aptamers. (**A**) Exemplary targets used to characterize binding optimization to hydrophobic surfaces during selections. (**B**) Regression analysis of target ΔG_D versus number of heavy atoms (other than hydrogen) in aromatic hydrophobic fragments within targets. Hydrophobic and aromatic fragments are shown as blue squares (amines) or red diamonds (amino acids). The regression line, including methylamine and two aromatic amines (**3**, **4**, **8**), was used to estimate the contributions of the hydrophobic surfaces in two aromatic amino acids (**6**, **10**) and a nonaromatic hydrophobic amine related to leucine (**7**). Data for the four aptamers for **6** are shown individually. Methylene blue (**9**) is the target with the highest affinity for the aptamers isolated directly from N_{36} libraries. Two amides ($CONH_2$, brown circles; figs. S26 and S27) have ΔG_D values above the regression line, carboxylates below (diamonds), and histamine (**10**) and serotonin (**11**) are on the regression line. Unmarked data points are for tyramine (fig. S30), tyrosine (fig. S29), dopamine (fig. S33), and L-dopa (fig. S20). R^2, coefficient of determination. (**C**) Additivity of $\Delta\Delta G_{GBE}$ in similar compounds (compare to fig. S46). Using the average $\Delta\Delta G_{GBE}$ values of a pair of planar indole-methylene-containing molecules and five carboxamides, we estimated ΔG_B for the melatonin (**13**) aptamer. H, hydrogen; R, other substituents. (**D**) Distributions of $\Delta\Delta G_{GBE}$ contributions of selected functional groups for carboxylates, carboxamides, guanidiniums, and hydrophobic groups. We show rounded averages (thick lines) and standard deviations in kJ/mol. We also present (black crosses) cooperativities (ΔG_C) assessed through double functional group replacement cycles (Fig. 1E) for groups added to methylamine together with carboxylates and carboxamides to obtain individual amino acids and their amides [figs. S41 to S45; the value for phenylalanine (**6**) is stressed]. All data points in (B) to (D) are results of individual selection experiments, and the uncertainty of this approach can be assessed by four aptamers for phenylalanine (**6**) in (B), which were isolated in four independent selections. ND, not determined, $N < 3$.

assumptions. Although each test individually was limited because of small sample sizes, together, they strongly supported our reasoning. First, we analyzed the four highest-affinity aptamers for phenylalanine from four separate selections and obtained similar ΔG_D values (and estimated ΔG_B values) within <3 kJ of each other (Fig. 2B and table S4). This result is consistent with the affinity of winning aptamers being regularly distributed over oligonucleotide space, thus representing a reproducible property of selections. These findings suggest that large differences in target-related ΔG_D should reflect differences in functional groups and not different selections.

Second, we observed correlations between ΔG_D values and the numbers of heavy (nonhydrogen) atoms in the hydrophobic fragments within related targets (Fig. 2, A and B). The molecule with the largest hydrophobic surface, methylene blue (**9**), yielded the highest affinity of all targets. The correlation between methylamine (**3**) and two planar aromatic amines in our set, **4** and **8**, supports an argument that the applied selection pressure directly optimizes affinity in proportion to hydrophobic surfaces—that is, is based on the functional groups present—and that we can subtract two ΔG_D values to isolate the impact of structural changes. We see indications that functional group–based optimization is general, with methylbutylamine (**7**), histamine (**10**), and serotonin (**11**) being very close to the aromatic amine (**3**, **4**, **8**) regression line, although caution should be exercised not to overinterpret these results without further structural information (*24*).

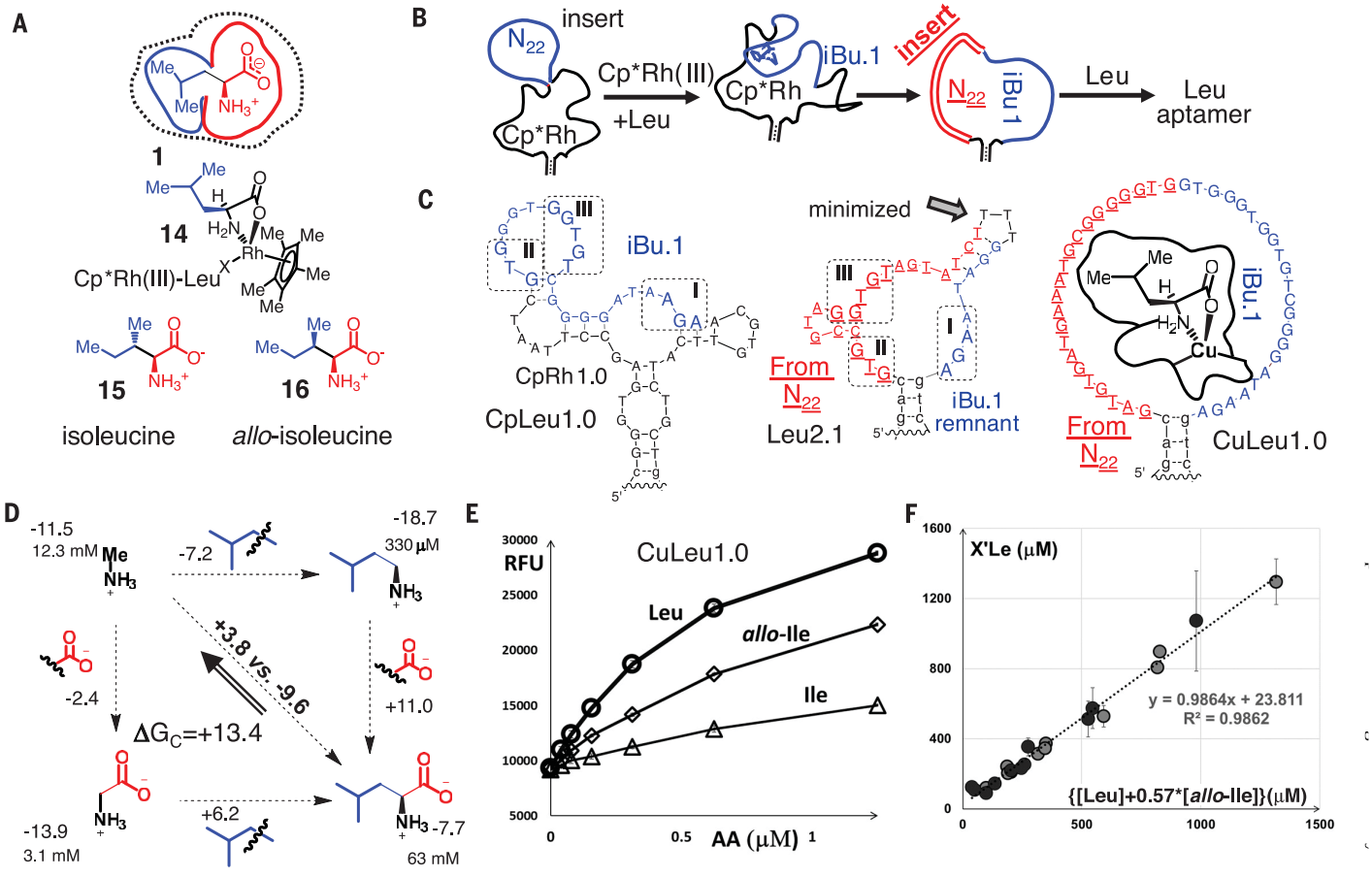


Fig. 3. Multistep functional group–guided approach to high-affinity aptamers for leucine. (**A**) Leucine was split into two fragments, isobutyl and 2-aminoethanoate. We designed a selection to isolate aptamers sequentially to recognize one, then both fragments, thereby reducing the target-related barriers in each step and increasing the probability of finding leucine aptamers. Shown are the complex of leucine and Cp*Rh(III) (**14**) and other amino acids for which we observed challenging aptamer cross-reactivities (**15**, **16**). (**B**) We started with a Cp*Rh(III) aptamer, performing an N_{22} random insertion to form a library used to identify the *i*Bu.1 sequence, which contained motifs important for recognition of the *i*Bu group. We used a second N_{22} library (red) to focus selection pressure on the 2-aminoethoanoate group to arrive at leucine aptamers. (**C**) Secondary structures of the related aptamers CpLeu1.0, Leu2.1 (minimized from Leu2.0, fig. S34), and CuLeu1.0. The inserted *i*Bu1 motif is shown in blue in CpLeu1.0, and carried-over sections of the CpRh1.0 aptamer are shown in black in all three aptamers. The CpLeu1.0 aptamer binds Leu in the presence of Cp*Rh(III), whereas Leu2.1 binds leucine on its own. The CuLeu1.0 aptamer binds Leu in the presence of Cu(II) with high affinity ($^{app}K_D$ ~170 nM). (**D**) Double-functional group replacement cycle, methylamine (**3**) to leucine (**1**). (**E**) Fluorescence versus target concentrations in the presence of 40 µM Cu(II) (displacement assay; compare to Fig. 1C) for CuLeu1.0 and three branched-chain amino acids. RFU, relative fluorescence units; AA, amino acids. (**F**) Preliminary analytical assessment of CuLeu1.0 in mock human serum samples spiked with branched-chain amino acids to mimic values for patients with MSUD (table S5 and fig. S53). The correlation is between measured values [dilution 1:500, 100 µM Cu(II)] of X'Le (the sensor-responsive fraction) versus added values for {[Leu] + 0.57*[*allo*-Ile]}. The high correlation indicates that this sensor is a suitable component of a minimal cross-reactive array for monitoring in patients, although dilution might have to be adjusted depending on the target range. *Allo*-Ile is negligible at birth and during the first several postpartum days (*11*); thus, we also show correlation in the same mock samples but without *allo*-Ile (gray circles indicate mock samples with both Leu and *allo*-Ile; black circles indicate mock samples without *allo*-Ile). Measurements in (E) and (F) are in triplicates with standard deviations shown (too small to be seen in E).

Third, we added average $\Delta\Delta G_{GBE}$ values calculated from two planar indole-containing amines and five primary carboxamides (fig. S46) to obtain a close match with an experimentally determined ΔG_B value for melatonin (**13**), a planar molecule containing an indole and a secondary carboxamide (Fig. 2C; the addition of $\Delta\Delta G_{GBE}$ values leads to ΔG_B). Thus, our protocol simultaneously optimizes the presence of multiple functional groups, and we can use this property to interpret deviations from additivity. Our standard selection protocol (Fig. 1B) depends on target-induced oligonucleotide displacement outcompeting background "noise" in the form of more common processes (*22*, *25*)–here, most dominantly, ligand-independent oligonucleotide release from the column. Then, throughout our protocol, certain combinations of functional groups on targets decrease the overall probability of isolating candidate aptamers, including in the early selection steps, which could be critical for selection success.

We used the aromatic amine (**3**, **4**, **8**) regression line (Fig. 2B) to estimate the impact of additional carboxylates on the ΔG_D values for the aptamer-target complexes of two related aromatic amino acids, phenylalanine (**6**) and tryptophan (**12**), observing that the addition of a carboxyl group is similar to the loss of receptor hydrophobic contacts for between one and two heavy atoms, which is intuitively consistent with the introduction of a polar carboxylate near a primarily hydrophobic pocket. Our analysis of double functional group replacement cycles (Figs. 1E and 2D, and figs. S41 to S45) revealed substantial negative cooperativity while adding negative charge in proximity to mismatched groups, such as hydrophobic residues (in phenylalanine and

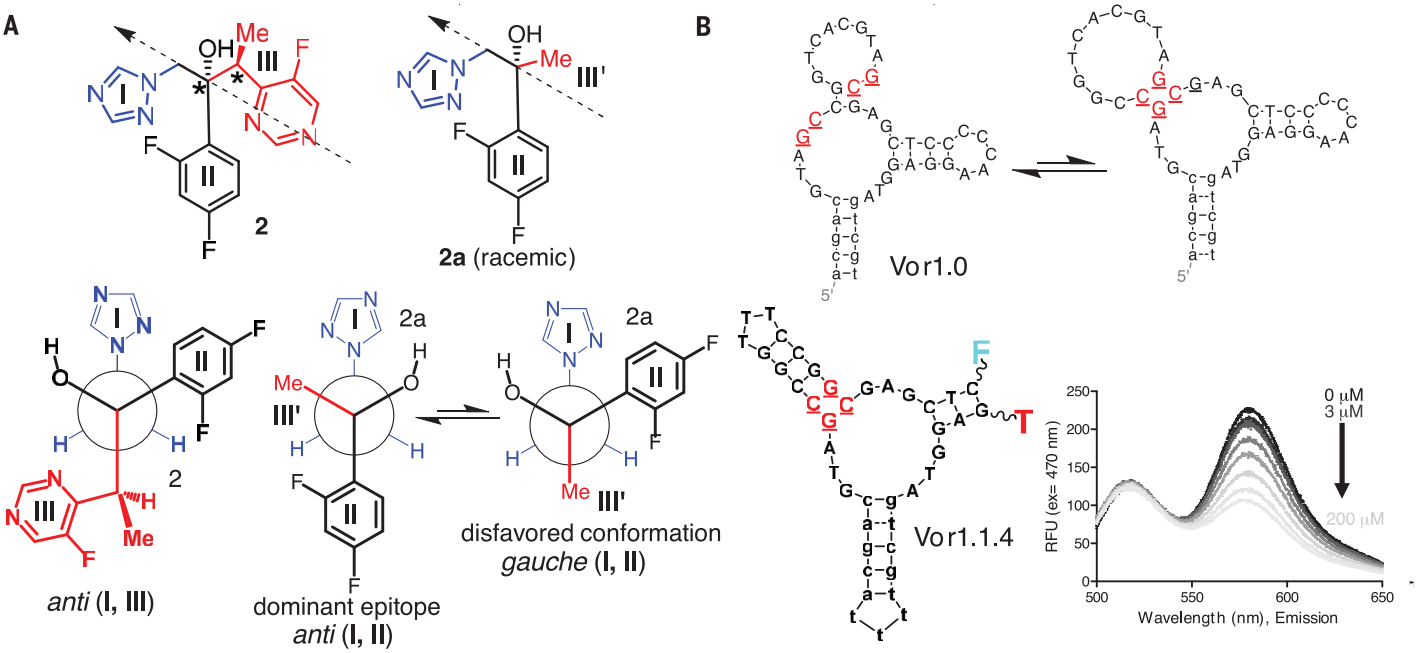


Fig. 4. Selection of voriconazole aptamers using an analog. (**A**) Structure of voriconazole (**2**) with three fragments (I to III) and its analog **2a**, in which fragment III was substituted with a methyl group (III'). The arrows indicate the perspective used to produce the Newman projections below. The *anti* (I, III) conformation is similar to an observed crystal structure (*30*). The voriconazole analog **2a** simplifies the largest fragment (III) and was designed for reduced complexity and as a more suitable target for selection. Here, the *anti* (I, II) conformation is likely to be favored and to be the dominant epitope in selection. (**B**) The aptamer Vor1.0 was isolated in the selection protocol that used **2** and **2a** in parallel. The secondary structure of Vor1.0 is shown as predicted by (top) mFold and (bottom) as an alternative secondary structure, which was subsequently confirmed to be the active sensor structure. Structure switching allows this aptamer to be captured on the column (the upper structure allows capture) during the initial stages of selection (compare to fig. S61). A variant of Vor1.0, Vor1.1.4 (which cannot be captured on the column and thus was not isolated during selection), was turned into a quenching-FRET sensor and responded to both **2** and **2a** [fluorophores: F, fluorescein; T, TAMRA (carboxytetramethylrhodamine)]. By using fluorescence, this sensor detected voriconazole concentrations as low as 3 μM; thus, this oligonucleotide is a candidate for engineering of electrochemical sensors for in vivo monitoring (*12*).

tryptophan). These structural constellations, then, were identified as likely to reduce the probability of aptamer isolation for leucine.

Functional group–guided selections for leucine

We extended our analysis to hypothesize that the two out-of-plane carbons and a carboxylate, all in proximity in leucine, act synergistically to minimize contact surfaces and reduce affinities of typical aptamers, thus allowing competing ligand-independent release mechanisms to dominate and suppress the desired outcomes. To overcome this issue, we separated the selection steps for the alkyl (isobutyryl) and α-amino-carboxylate groups (Fig. 3, A and B). We first implemented a protocol to identify a sequence, *i*Bu.1**,** certain to contain a binding motif for the isobutyl group. We started with a cyclopentadienyl-rhodium(III) [Cp*Rh(III)]–binding aptamer (CpRh1.0) specifically isolated for this purpose, as a temporary placeholder for sequences that interact with the carboxyl and amino groups (*26*). We inserted a random 22-mer region (N_{22}), which would become *i*Bu, into the CpRh1.0, creating a new library (we can screen a complete 22-mer sequence space). From this library, we selected aptamers such as CpLeu1.0, which bound leucine in the presence of the Cp*Rh(III) cofactor. Although we could immediately eliminate CpLeu1.0 from further consideration as a Leu sensor, because of its complex mechanism of interactions with leucine, reflected in a sharp threshold behavior of the fluorescent sensor (compare to fig. S38), we knew that the inserted sequence, *i*Bu, had to contain binding motifs for the Leu side chain.

We then designed a library of 22-mers (N_{22}) with *i*Bu.1 positioned next to the stem. From this library, using elutions with leucine without the cofactor, we identified Leu2.1 (Fig. 3C). The Leu2.1 aptamer had a K_D of almost 10 mM (fig. S28) and an ~4:1 preference for Leu over isoleucine (Ile) (fig. S49). The negative cooperativity (ΔG_C) between the carboxyl and isobutyryl groups was large (>10 kJ/mol), providing an explanation for our initial selection difficulties (Fig. 3D).

We identified homologous regions I to III in CpLeu1.0 and Leu2.1, two of which, II and III in Leu2.1**,** originated from the inserted random region outside of *i*Bu.1. The short Leu2.1 aptamer should have been abundant in any initial pool; furthermore, isolation of motifs II and III in control studies of insertion reselection (fig. S50) indicated that motif I is not absolutely required in Leu aptamers. However, apparently because of its low affinity, Leu2.1 required the prefixed compatible sequences within I to increase the probability of isolation through a reduction in the required sequence length in the newly inserted random region.

The Leu2.1 aptamer had a millimolar target affinity insufficient for the intended application of testing newborns with MSUD (*11*). In addition, Leu2.1 preferred phenylalanine over leucine (fig. S49), which was a dominant problem in our prior selections that used Cp*Rh(III) as the cofactor (fig. S51). Thus, in the last step of the selection, we added an aminophilic Cu(II) (*27*), to improve affinity and selectivity. We hypothesized that Cu(II) would serve as a protecting group neutralizing the effects of the carboxylate through complexation with the 2-aminoethanoate group. Complexation would allow better access of hydrophobic DNA monomer residues to the leucine side chain, improving affinity and selectivity. Consistent with our hypothesis, we identified aptamer CuLeu1.0 as having a 44-mer loop, conserved sections of *i*Bu.1, and high affinity for leucine (K_D ~170 nM; Fig. 3C).

CuLeu1.0 had selectivity for leucine over isoleucine, valine, and phenylalanine, but we

noted strong cross-reactivity with *allo*-isoleucine (*allo*-Ile) (Fig. 3E and Newman projections in fig. S52). The *allo*-isoleucine metabolite was not initially considered in the aptamer counterselections because its concentrations are negligible at birth. Newborn screening is currently performed with mass spectroscopy (*11*), which integrates isobaric species to provide XLe values (where XLe is Leu + Ile + *allo*-Ile + 2OHPro) (where 2OHPro is 2-hydroxyproline). Thus, our aptamer sensor is a candidate for the development of rapid tests to address false positives in MSUD by showing a lack of steady increase in X′Le values in consecutive measurements, with X′Le defined, for example, as [Leu] + 0.57*[*allo*-Ile] (Fig. 3F and fig. S53). After the first few days of life, however, *allo*-Ile concentrations increase, so a monitoring strategy without fully specific aptamers would require a cross-reactive array (*26*, *28*), for which CuLeu1.0 is a suitable component.

The multistep approach with Cu(II) can be generalized to amino acids that display a side chain away from the Cp*Rh(III) complex, such as Ile (compare to CuIle1.1, figs. S54 to S56). This approach would not work for amino acids that carry a chelating group beyond 2-aminoethanoate—for example, glutamate (fig. S57). For comparison, we performed a single-step Leu selection with Cu(II) as the cofactor. We isolated receptors with about fivefold-lower affinities than that of CuLeu1.0. The two most abundant sequences preferred isoleucine or methionine (figs. S58 to S60). These aptamers are also candidates for arrays.

A structure-guided approach to aptamers for voriconazole

Leucine (**1**) is closely related to other amino acids in our target set. By contrast, voriconazole (**2**) is an example of applying a structurally guided approach to unrelated molecules. We initially attributed our voriconazole selection failures to its limited solubility (~200 μM). Nonetheless, selections using a soluble voriconazole phosphate analog also failed. We considered that voriconazole, similarly to leucine, has a sterically crowded structure (Fig. 4A) that forces its fragments (structural subunits) into a propeller-like conformation, as revealed in crystal structures (*30*). This sterically crowded conformation was hypothesized to lead to suboptimal access to hydrophobic surfaces in DNA that are needed to interact with fragments I to III (Fig. 4A). One possible retrosynthetic disconnection (*31*) led to a simplified, less-congested, and readily synthesized alcohol analog, **2a** (Fig. 4A).

Initial attempts starting with **2a** at high concentrations—although introducing voriconazole separately in later cycles—failed, yielding exclusively analog-binding aptamers. Further conformational analysis using Newman projections clarified that **2a** likely presents a dominant epitope during selection in which fragments I and II are positioned *anti*. Conversely, in voriconazole, these structural subunits are *gauche* (Fig. 4A). Inspired by approaches to outflank the immunodominance of epitopes (*32*), we mixed **2** and **2a** at their respective maximal soluble concentrations in the initial selection steps, only gradually phasing out the analog. We hypothesized that this procedure would maximize the probability of release of aptamers that bind similar conformations of the target and its analog, which could be important in the initial rounds of selection. In contrast to previous failures, this change led to two aptamers (figs. S61 and S62) responsive to **2** and **2a** (Fig. 4B), confirming the advantage of adding the analog.

The mechanisms underlying the improved selection strategy for voriconazole are partially unclear because we cannot exclude the possibility that the analog minimizes target aggregation. Nonetheless, the presence of **2a** is certain to improve target-receptor occupancy in the initial cycles, likely buttressing low effective concentrations of monomeric voriconazole in conformations that can elicit aptamers. The isolated aptamers do not bind fluconazole, suggesting they are not class-wide cross-reactive aptamers (*17*, *28*, *29*) and further confirming that stabilizing interactions occur with group III in **2** (Fig. 4A).

Mutagenesis studies indicated that our lead aptamer, Vor1.0, is a destabilized three-way junction (Fig. 4B), which we engineered into a fluorescence resonance energy transfer (FRET) sensor, Vor1.1.4 (Fig. 4B). The latter shows sufficient sensitivity for testing as an electrochemical sensor for in vivo use (*12*). This specific family of voriconazole-binding three-way junctions, despite being common, are eliminated from direct selections by exceptionally poor interactions with capture oligonucleotides, a problem that was prevented in Vor1.0 by structure switching (Fig. 4B and fig. S61). These observations showcase the complex balance between positive and negative selection pressures in selection protocols. Our procedures, as demonstrated through leucine and voriconazole selections, shift selection balance in our favor by addressing probabilistic barriers assigned to crowded (and other nonoptimal) substructures within targets.

Conclusions

In traditional organic synthesis, the functional group abstractions and their reactivities guide us through transformations involving relationships between nuclei and electron clouds (*33*). In our structure-guided aptamer selections, analogous concepts directed random searches through the space of complementary interactions between targets and aptamer receptors. We developed several approaches that can be used in functional group-guided selections. These include insertion reselection, carrying-over and anchoring of partial motifs, the expanded use of metal complexes as "protecting" groups matched to targets, placeholders, cross-linkers, and the synthesis of simpler analogs designed to overcome steric, conformational, or solubility barriers. These approaches can be further studied, optimized, and combined with one another and with traditional protocols (*3*, *4*), organic receptor cofactors (*6*, *34*), and modified bases (*35*), while considering library designs (*25*), to enable isolation of high-quality aptamers and engineering of biosensors for previously inaccessible targets.

There are further topics to which our approach, once systematically expanded, is expected to provide original insights. The first is the question of natural selection of complex functions in the hypothetical, preprotein, RNA world (*36*). Behaving as tinkerers (*37*), we reused simple sequence pieces to find functions requiring more complex sequences, thus expanding the early work on the use of cofactors in RNA catalysis (*38*). Second, the approach that applies structural analysis of ligands to find optimal receptors could be inverted, combined with structural methods and insights from a large set of aptamers to improve our ability to design small-molecule drugs that specifically modulate natural nucleic acid targets (*39*). And third, we provide a substantially expanded set of sequences with confirmed target binding that could be used to improve training sets for computational designs of aptamers (*40*).

REFERENCES AND NOTES

1. A. D. Ellington, J. W. Szostak, *Nature* **346**, 818–822 (1990).
2. C. Tuerk, L. Gold, *Science* **249**, 505–510 (1990).
3. A. Ruscito, M. C. DeRosa, *Front Chem.* **4**, 14 (2016).
4. H. Yu, O. Alkhamis, J. Canoura, Y. Liu, Y. Xiao, *Angew. Chem. Int. Ed.* **60**, 16800–16823 (2021).
5. N. Nakatsuka *et al.*, *Science* **362**, 319–324 (2018).
6. K. A. Yang *et al.*, *Nat. Chem.* **6**, 1003–1008 (2014).
7. K. M. Cheung *et al.*, *ACS Sens.* **4**, 3308–3317 (2019).
8. N. Tejavibulya *et al.*, *iScience* **21**, 328–340 (2019).
9. B. S. Ferguson *et al.*, *Sci. Transl. Med.* **5**, 213ra165 (2013).
10. C. Zhao *et al.*, *Sci. Adv.* **7**, eabj7422 (2021).
11. K. Stroek *et al.*, *JIMD Rep.* **54**, 68–78 (2020).
12. P. Dauphin-Ducharme *et al.*, *ACS Sens.* **4**, 2832–2837 (2019).
13. H. Elewa, E. El-Mekaty, A. El-Bardissy, M. H. H. Ensom, K. J. Wilby, *Clin. Pharmacokinet.* **54**, 1223–1235 (2015).
14. R. Nutiu, Y. Li, *Angew. Chem. Int. Ed.* **44**, 1061–1065 (2005).
15. M. Rajendran, A. D. Ellington, *Anal. Bioanal. Chem.* **390**, 1067–1075 (2008).
16. M. Yarus, *J. Mol. Evol.* **47**, 109–117 (1998).
17. G. R. Wiedman, Y. Zhao, D. S. Perlin, *MSphere* **3**, ee00623–18 (2018).
18. F. J. Ehlert, *Mol. Pharmacol.* **33**, 187–194 (1988).
19. S. M. Free Jr., J. W. Wilson, *J. Med. Chem.* **7**, 395–399 (1964).
20. C. Bissantz, B. Kuhn, M. Stahl, *J. Med. Chem.* **53**, 5061–5084 (2010).
21. J. R. Lorsch, J. W. Szostak, *Acc. Chem. Res.* **29**, 103–110 (1996).
22. S. E. Osborne, A. D. Ellington, *Chem. Rev.* **97**, 349–370 (1997).
23. H. Gohlke, G. Klebe, *Angew. Chem. Int. Ed.* **41**, 2644–2676 (2002).
24. B. Baum *et al.*, *J. Mol. Biol.* **397**, 1042–1054 (2010).
25. J. M. Carothers, S. C. Oestreich, J. H. Davis, J. W. Szostak, *J. Am. Chem. Soc.* **126**, 5130–5137 (2004).
26. A. Buryak, K. Severin, *J. Am. Chem. Soc.* **127**, 3700–3701 (2005).
27. Z. Liu *et al.*, *Chem. Sci.* **9**, 7053–7057 (2018).
28. K.-A. Yang, R. Pei, D. Stefanovic, M. N. Stojanović, *J. Am. Chem. Soc.* **134**, 1642–1647 (2012).

29. W. Yang *et al*., *Nucleic Acids Res.* **47**, e71 (2019).
30. K. Ravikumar, B. Sridhar, K. D. Prasad, A. K. S. Bhujanga Rao, *Acta Crystallogr. Sect. E Struct. Rep. Online* **63**, o565–o567 (2007).
31. E. J. Corey, *The Logic of Chemical Synthesis* (Wiley, 1989).
32. D. Angeletti *et al*., *Proc. Natl. Acad. Sci. U.S.A.* **116**, 13474–13479 (2019).
33. H. Ochiai, *J. Phil.Chem.* **19**, 139–160 (2013).
34. J. C. Manimala, S. L. Wiskur, A. D. Ellington, E. V. Anslyn, *J. Am. Chem. Soc.* **126**, 16515–16519 (2004).
35. F. Pfeiffer *et al*., *Nat. Protoc.* **13**, 1153–1180 (2018).
36. H. Saito, *Nat. Rev. Mol. Cell Biol.* **23**, 582 (2022).
37. F. Jacob, *Science* **196**, 1161–1166 (1977).
38. J. R. Lorsch, J. W. Szostak, *Nature* **371**, 31–36 (1994).
39. K. D. Warner, C. E. Hajdin, K. M. Weeks, *Nat. Rev. Drug Discov.* **17**, 547–558 (2018).
40. W. M. Billings, B. Hedelius, T. Millecam, D. Wingate, D. D. Corte, ProSPr: Democratized implementation of Alphafold protein distance prediction network. bioRxiv 830273 [Preprint] (2019).

ACKNOWLEDGMENTS

We thank B. Solaja, F. Katz, H. Hess, D. Stefanović, S. Rudchenko, A. K. Rinderspacher, C. Boyle, V. Cornish, and J. Loeb for their input during the writing of this manuscript. We thank S. Deng and A. K. Rinderspacher for helping Z. Cheng with the synthesis of analogs and handling of data. M.N.S. and K.Y. thank the Maple Syrup Urine Disease Family Group for inspiration and guidance and K. Strauss and K. Brigatti, Clinic for Special Children, Strasburg, Pennsylvania, for advice on testing and applications of leucine sensors. K.Y. thanks B.-T. Zhang for introducing her to hypernetwork theory, which led to insertion-reselection designs. M.N.S. dedicates the work to his teachers of organic chemistry, Y. Kishi and B. Solaja. **Funding:** The project was supported by the NIH (voriconazole, leucine, other small molecules, and general conceptualization of functional group–based approach, GM138843 to M.N.S.; neurotransmitters, DA045550 to A.M.A.; other small molecules, DK126739 to S.M. and EB022015 to M.N.S.); the NSF (aptamers as inputs to molecular computing, CCF1518715 to M.N.S.; aptamers for planar compounds to use Spiegelmers, 1763632 to M.N.S.); the Defense Threat Reduction Agency (overlapping materials, 16-1-0053 to M.N.S.); the Raymond and Beverly Sackler Center, in Honor of Herbert Pardes, MD, at CUIMC (instrumentation); and the Maple Syrup Urine Disease Family Group gift for studies of receptors that bind leucine. **Author contributions:** K.Y. and M.N.S. conceptualized the approach and designed the experiments; K.Y. isolated all aptamers for amines and amino acids; and S.B. isolated aptamers for two amides, under her supervision. Z.C. synthesized voriconazole analogs. A.M.K. was a high school student supported by the NSF, and I.W. was an undergraduate student on an NSF REU (CCF1518715, 1763632). They both optimized and characterized aptamers. S.S. worked on epinephrine aptamers, and Y.Z. was an undergraduate student who worked on isolating methylene blue aptamers and was supervised by S.T. and K.Y. D.W.L. initiated research on aptamers in general, helped formulate an early version of this manuscript, and suggested experiments. J.S. and S.M. initiated the research on voriconazole aptamers and helped design parameters of initial selection experiments. T.S.W. initiated research on amino acids and ammonia and helped design early selection experiments with these targets. N.M.M. and A.M.A. produced and analyzed isothermal calorimetry data, and A.M.A. also helped define neurotransmitter targets and parameters for selections. M.N.S. is responsible for all free-energy calculations and initially drafted the manuscript. M.N.S., K.Y., N.M.M., and A.M.A. produced the final manuscript form with input and approval from all authors. **Competing interests:** M.N.S., K.Y., T.S.W., A.M.A., S.T., J.S., and S.M. have (and expect) patents and patent applications regarding aptamers, their uses (patent application 20210223240), and sequences (patent application 20190136241), including on the use of cofactors in aptamer selection (patent number 10155940). M.N.S. and T.S.W. have founders' shares of a startup company (Aptatek Biosciences), are on the scientific board, and have expected consulting incomes related to aptamers from companies (M.N.S., Aptatek and Nutromics; T.S.W., Aptatek). K.Y. had consulting income from academic institutions and expects income from a company (Nutromics). **Data and materials availability:** All data needed to evaluate the conclusions in the paper are presented in the paper or the supplementary materials, except high-throughput sequencing data for selections, which are deposited in the Sequence Read Archive of the National Center for Biotechnology Information and can be found using the title of this paper or accession no. PRJNA947642. No original software was created during these studies. **License information:** Copyright © 2023 the authors, some rights reserved; exclusive licensee American Association for the Advancement of Science. No claim to original US government works. https://www.science.org/about/science-licenses-journal-article-reuse

SUPPLEMENTARY MATERIALS

science.org/doi/10.1126/science.abn9859
Materials and Methods
Figs. S1 to S62
Tables S1 to S5
References (*41*–*46*)
MDAR Reproducibility Checklist

View/request a protocol for this paper from *Bio-protocol*.

Submitted 5 January 2022; resubmitted 3 February 2023
Accepted 3 May 2023
10.1126/science.abn9859

ANTHROPOLOGY

Body-based units of measure in cultural evolution

Roope O. Kaaronen[1]*, Mikael A. Manninen[1], Jussi T. Eronen[1,2]

Measurement systems are important drivers of cultural and technological evolution. However, the evolution of measurement is still insufficiently understood. Many early standardized measurement systems evolved from body-based units of measure, such as the cubit and fathom, but researchers have rarely studied how or why body-based measurement has been used. We documented body-based units of measure in 186 cultures, illustrating how body-based measurement is an activity common to cultures around the world. Here, we describe the cultural and technological domains these units are used in. We argue that body-based units have had, and may still have, advantages over standardized systems, such as in the design of ergonomic technologies. This helps explain the persistence of body-based measurement centuries after the first standardized measurement systems emerged.

The ability to measure things is central to human cultures. Throughout the history of human cultural evolution, systems of measurement have been products and drivers of cultural complexity (*1*–*4*). Global industry, technologies, and commerce, as well as science itself, are largely built upon interchangeable units of measure. Standardization systems, such as the International System of Units, permeate the everyday lives of people across the globe. Some might say that modern times are built upon our ability to measure the world. But how does the current system compare with those from the past, and what role has measurement played in the development of human societies?

Worldwide, many early standardized measurement systems are thought to have evolved from body-based units of measure (*3*, *4*). For example, one of the earliest-known standard measures, the royal cubit of Old Kingdom Egypt (around 2700 BCE), evolved from the use of the natural cubit (the distance from one's elbow to the tip of the extended middle finger) (*5*). Harappan measurement systems were influenced by units such as the fingerbreadth (*6*), and various Ancient Mesopotamian measurement systems were abstracted from body-based units such as the foot, cubit, and pace (*4*). Traditional Chinese (*7*), Roman (*8*), Greek (*3*), Aztec (*9*), and Maya (*10*) measurement systems also used body-derived standards for measurement.

A unifying feature of past measurement systems is the use of individually variable body parts as units of measure (*1*, *3*, *4*, *11*). "Body-based units" are here defined as those units that are determined by using components of the human body. We analyzed the use of body-based units of measure in 186 cultures across the world, describing common units and the cultural domains in which they are used. Body-derived yet standardized units of measure, such as the British Imperial foot, are not included in our data, even if the etymology of these units suggests an earlier use as body-based units.

Recent work has suggested that the cultural evolution of measurement can be characterized as a series of stages, starting from practical and gestural comparisons between objects, proceeding through unequal comparisons and initial standardization, and followed by interrelated standardized units that form abstract and complex systems of measurement (*1*). However, these are not historical stages that cultures transition through and leave behind, and units of various types may coexist (*1*). We found that a recurrent pattern in historical and ethnographic data on measurement is that body-based units have persisted alongside standardized measurement systems.

Not all cultures adopted standardized measurement systems to the same extent, and many cultures used body-based units well into the 20th and 21st centuries, hundreds to thousands of years after the first emergence of standardization. In the past, body-based measurement systems have often been described as primitive predecessors of standardized units (*12*). We question this notion and illustrate how body-based measurement systems have offered various problem-solving solutions and adaptive advantages in the evolution of human cultures and technologies (Fig. 1).

Drawing on our ethnographic dataset, we discuss potential cognitive-cultural causes for the long-term persistence of body-based measurement, documenting mechanisms by which body-based units have proven to be successful and competitive with standardized systems.

Results

We documented body-based units in 186 cultures (Fig. 2A). Table 1 lists the most common units. Variations of the fathom, hand span, and cubit are most frequent and exhibit striking similarities between cultures around the world (Fig. 2, B to D). We also found 62 cases of activity-based units of measure. These are units based on bodily activity, such as "a day's tr… by foot" (measure of distance), or "a day's p… ing" (measure of area).

Cultures in our dataset are coded on the basis of their inclusion in the Standard Cross-Cultural Sample (SCCS) to mitigate Galton's problem (see materials and methods for further discussion). In total, our dataset includes evidence of body-based measurement in 99 SCCS cultures (around 53% of all SCCS cultures). The SCCS subset allows us to better estimate the independent use of specific body-based units (Table 1). In the SCCS subset, the fathom (44 observations; 23.7% of all SCCS cultures), hand span (41 and 22%, respectively), and the cubit (40 and 21.5%) are the most frequent body-based units, suggesting that these units appear most commonly in human cultures (their frequency might also be a product of remarkably distant common origins). These estimates are only lower bounds because body-based measurement has often gone undocumented.

In Table 2, we present a typology that describes the behavioral and cultural domains in which body-based units are used. We found body-based units especially common in the design of technologies, which highlights the important role of body-based units in technological evolution. We also document noteworthy use of body-based measurement in trade, agriculture, and rituals. Body-based units are mostly one-dimensional measures of length. However, cases of measuring area, volume (e.g., handfuls), and temperature are also documented.

Body-based units are found on all inhabited continents (Fig. 2A). Our results suggest that cultures around the world use very similar units (Fig. 2, B to D). Body-based units are mostly used in specific contexts, such as the measurement of a particular technology. However, our dataset also documents elaborate, domain-general systems of body-based measurement, such as those used among the Māori, Mara, Siwai, Trobriand, Iban, Katu, Kwakwaka'wakw, and Chuuk cultures.

Figure 3 depicts the temporal distribution of the evidence of body-based measurement per each cultural region in our dataset. We found ample evidence for the use of body-based units in the 20th century. According to global reviews on historical metrology (*3*, *4*), most cultural regions had encountered standardized units of measure prior to the 20th century. Table S1 and Fig. 3 document, for each cultural subregion in our dataset, plausible early dates for the introduction of standardized measurement systems. Our dataset supports the general claim that body-based measurement systems have persisted despite potential access to standardization (Fig. 3).

Definitive claims on culture-specific retention of body-based units are difficult to make

[1]Past Present Sustainability Research Unit, Faculty of Biological and Environmental Sciences, HELSUS, University of Helsinki, FI-00014 Helsinki, Finland. [2]BIOS Research Unit, FI-00170 Helsinki, Finland.
*Corresponding author. Email: roope.kaaronen@helsinki.fi

because the first emergence of standards often pre-dates the categorization of contemporary cultures, and culture-level evidence on encounters with standardized measurement systems is sometimes lacking. However, we surmise that within cultural regions, such contact would often occur; therefore, knowledge of standardization would spread, and in many cases cultures could opt to adopt nearby standard units if they deemed them necessary or superior.

In certain cases, the retention of body-based units is more obvious. For instance, in the Middle East, where some of the first known standardized measurement systems evolved three to five millennia ago (*3*, *4*), body-based units have been documented as late as the 21st century (Fig. 3). Similarly, in various European regions, the first emergence of standards dates to the Roman Republic or Hellenistic Greek eras or even prehistoric times (*13*), but body-based units are still documented from the Middle Ages to the 1900s (table S1 and Fig. 3). In an exemplary case, the Zapotec used body-based units in the mid-to-late 20th century, even though Spanish standards were well-known at the time, and standards such as the *vara* (the rod) were introduced centuries earlier (*14*). The Zapotec have even named some of their body-based units after Spanish standards (*14*). Our dataset documents similar cases of retention in Hawaiian, Turkish, Yup'ik, Palestinian, and Mapuche cultures. Moreover, as discussed below, body-based measurement is still used in some contexts in the industrialized West.

Discussion

From the dataset, we identify four cognitive-cultural mechanisms that help explain why body-based units have been used to begin with, and why they were still often preferred to standardized units up until the recent past.

1. Ergonomic design

Body-based units have the advantage that they provide custom-made ergonomic designs in ways that standardized systems often overlook (Fig. 1). We find references to ergonomic design by body-based units of measure in 25 cultures (Table 2). We take indigenous ergonomics to be an especially favorable domain for the use of body-based units. Erased by the industrial revolution, ergonomics largely reemerged in the Western world only after World War II (*15*).

Illustrative evidence of ergonomic design is found in kayak building. A responsive kayak requires proper positioning of the body. Consequently, no one-size-fits-all design serves all kayakers. Kayaking cultures, including the Yup'ik (*16*) and Greenlandic Inuit (*17*), have used body-based units to correct kayak designs for interpersonal variation. Kayaks were typically designed "by and for their user for the best possible performance" (*18*, p. 5), to ensure

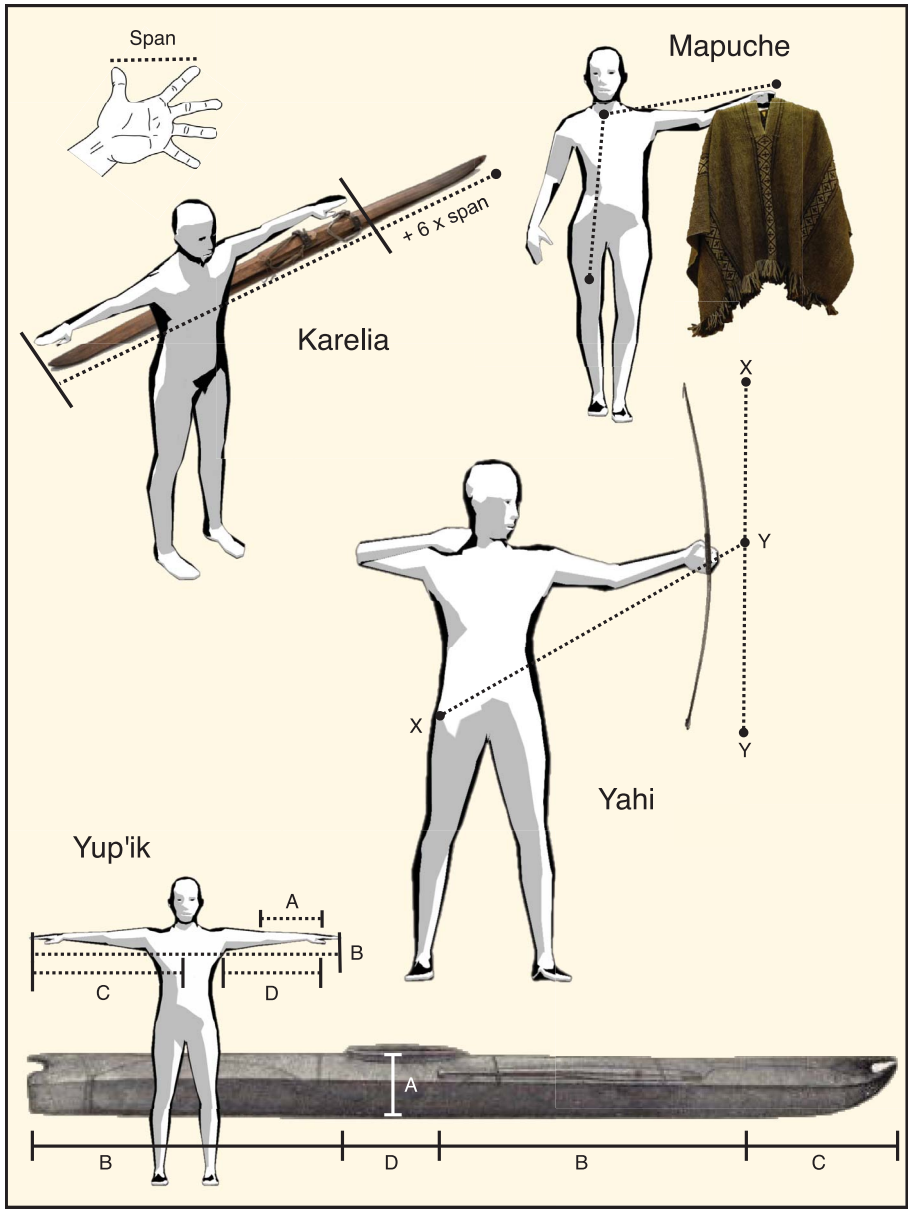


Fig. 1. Examples of objects designed with body-based units. (Top left) Karelian skis, early 1900s. The gliding ski was the user's fathom plus six spans (*36*). (Top right) Mapuche ponchos were measured from the neck to halfway between the waistline and knee and from neck to thumb with arm outstretched (*26*). (Center) Yahi bow, early 1900s. The bow's length was from the opposite hip joint (X) to the tip of the outstretched arm (Y) (*37*). The width below and above the hand grip was four fingers for a powerful bow. (The posture pictured is not a typical Yahi shooting position.) (Bottom) Yup'ik kayak from the Alaskan coast, late 1800s. The kayak's length was two fathoms (B), plus one half-fathom (C), plus the length of the cockpit, which was the length of an arm with a closed fist (D) (*19*). The kayak's height at the cockpit was one cubit with closed fist (A). The kayak's width was two cubits. [Images: Ski: National Museum of Finland (CC-BY 4.0). Poncho: Wikimedia commons (CC BY-SA 2.0), by Pontificia Universidad Católica de Chile. Bow: Internet Archive (identifier: yahiarcherysaxton00poperich). Kayak: Internet Archive (identifier: eskimoberingstrait00nelsrich). Human models: MakeHuman. Hand: Wikimedia commons (FAL 1.3), by J.N.L.]

"perfect fit between the kayak and its maker" (*16*, p. 91). Yup'ik kayaks were designed with various body measures (*16*, *19*) (Fig. 1). Similar methods are used in the design of paddles: A common length for a double-bladed Greenland paddle is the user's fathom plus one cubit, and the blade width is determined by the maximum breadth that one can grip (*17*).

Body-based units have also guided the design of tools such as skis. For example, a Khanty

Table 1. Body parts used for measurement. The fifth column counts the fourth column as a proportion of the total 186 SCCS cultures, describing the percentage of all SCCS cultures in which we have documented each body-based unit of measure. Incidence refers to the number of cultures with the specific unit. The parity in the number of cultures (186) in our dataset and in the SCCS is coincidental.

Unit	Description and variations	Incidence (full dataset) (*N* = 186)	Incidence (SCCS subset) (*N* = 99)	% of total SCCS (*N* = 186)
Fathom (arm span)	Distance between fingertips of outstretched arms. Variations include, e.g., the fathom with closed fists.	85	44	23.7%
Hand span	Distance between the tip of the extended thumb to the tip of one of any four other fingers on an outstretched hand.	81	41	22.0%
Cubit (ell)	The distance from the tip of the elbow to the tip of an extended finger (typically the middle finger). Also sometimes measured to, e.g., the closed fist or wrist, or from elbow crease to fingertips. Other similar forearm-based units are included.	76	40	21.5%
Arm length	Any units based on the length of an arm, typically from tip of outstretched fingers to one of the following: armpit, shoulder, or middle of chest (half-fathom).	66	35	18.8%
Activity-based measures	Units of measure based on physical activity, such as a "day's journey" or "stone's throw" (linear measures) or a "day's worth of plowing" (measure of area).	63	32	17.2%
Finger width	Width of one or multiple fingers (or fingernails), excluding the thumb (see "thumb width").	44	21	11.3%
Hand width	Width of the palm (also known simply as the "palm"). Also includes the width of four fingers or the fist, or the circumference of the palm.	39	16	8.6%
Pace	A pace, step, or stride.	34	19	10.2%
Finger length	Length of any of the four fingers, thumb excluded (see "thumb length"). Includes the length of finger joints and combinations thereof.	34	18	9.7%
Height	A person's height from the sole of the foot to the tip of the head, or to the tip of vertically extended arms. Also includes measures of height to other specified points of the upper body (e.g., navel, eyes, and forehead).	28	16	8.6%
Foot	Inner or outer length of the foot. Also includes foot width.	27	15	8.1%
Handful	Cupped hand (handful) or two cupped hands (double handful), a measure of volume.	26	18	9.7%
Thumb width	The width of the thumb (including nail width).	15	8	4.3%
Fistmele	Width of the fist with an extended thumb (similar to "thumbs-up" gesture).	14	5	2.7%
Thumb length	The length of the thumb or thumb joint(s).	14	7	3.8%
Hand length	The length of a hand, typically from the wrist joint or crease to the tip of the middle finger.	12	7	3.8%
Arm thickness	As thick as the arm (or wrist).	7	5	2.7%
Armful	As much as a person can carry in both arms (a measure of volume), or the circumference that the arms can surround.	7	6	3.2%
Pinch	A small measure for volume measured by pinching the thumb against the tip of a finger (e.g., a "pinch of salt").	7	6	3.2%
Leg length	The distance from the sole of the foot to the knee or hip.	5	2	1.1%
Ring	Measure of circumference made by pinching the tip of a finger to the thumb (similar to the "OK" or "ring" gesture).	5	4	2.2%
Leg thickness	As thick as (any part of) the leg.	3	2	1.1%

ski maker might measure ski width with their outstretched "finger-and-thumb span plus two fingers" and ski length from the ground to their eyebrows (*20*, p. 159). This affords ergonomic balance: Too narrow skis would sink into soft snow, and too wide skis would be cumbersome and carry excessive snow. Sixteenth-century evidence suggests that the length of Saami skis was the height of the user for the kicking ski and the user's height plus the length of their foot for the gliding ski (*21*) (see also the Karelian skis in Fig. 1). In contemporary skiing cultures, it is still commonplace to use one's own height to determine ski and pole length. For repetitive and injury-prone practices such as farming,

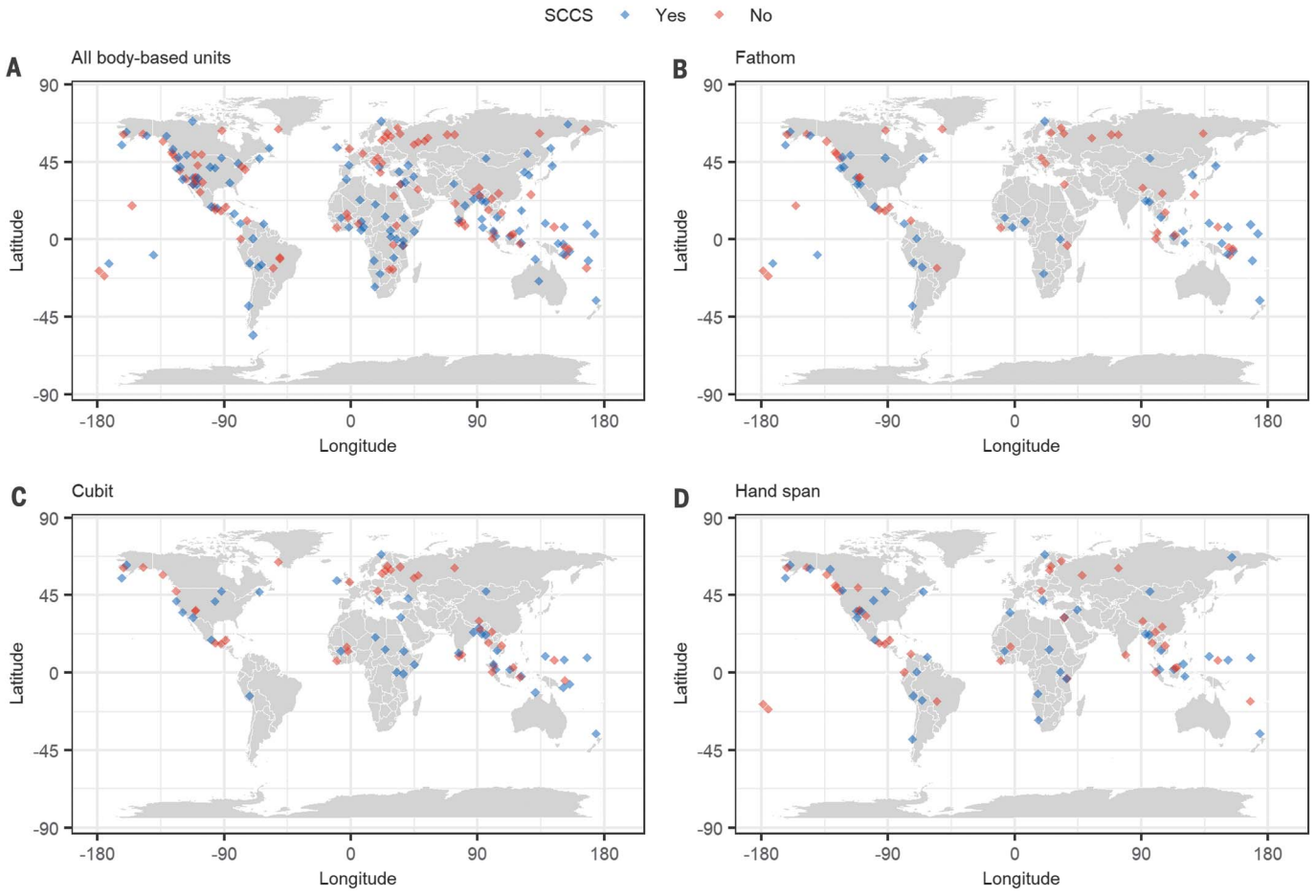


Fig. 2. Cultures in the dataset on a world map. The maps illustrate the widespread practice of body-based measurement. Each diamond represents a culture in the dataset. Cultures included in the SCCS are colored blue, other cultures are colored red. The map in (**A**) depicts the distribution of all documented cultures with body-based units of measure. The other maps illustrate the three most common body-based units in the dataset: the fathom (**B**), cubit (**C**), and hand span (**D**). The locations of cultures are based mostly on eHRAF (Human Relations Area Files) coordinates. Locations are only rough estimates because many cultures and ethnic groups are geographically widespread and/or mobile.

ergonomic tool design is especially important (*14*). Various Zapotec tools were measured with the user's own body measures, such as the Zapotec *vara* (fathom), to ensure that the farmer's tools (e.g., plows and axes) were custom-made and therefore ergonomic (*14*).

Weapons such as bows also require ergonomic design to ensure proper shooting form and draw length. Body-based bow design is found in various North American indigenous cultures. For instance, Ojibwe bow length varied with the stature of the bow's owner, measuring from "the point of the shoulder across the chest to the end of the middle finger of the opposite hand" (*22*, p. 146) (see also Yahi bow design in Fig. 1). Similar design is found in Europe, as documented in Edward IV's orders for every Englishman between 16 and 60 years of age to construct a longbow of their own height plus one fistmele (width of fist with thumb extended) (*23*). Even today, body-based units are being used in archery and bowhunting. A description of Yup'ik spear throwing highlights the importance of an ergonomically sized weapon (*16*, p. 138):

> They can use one *yagneq* (arm span) to measure when they make a *nanerpak* [seal spear]. People use their own body measurements. If a person uses a spear of someone taller than he is, it will be too long for him, and he will throw it differently. But when they make it to size, it can hit the target when thrown.

Custom-tailored clothes and footwear are also made using body-based units. An illustrative example is the case of Mapuche poncho design (Fig. 1). Today, even tailors in commercial economies use body measures to ensure the custom fit of garments.

These findings suggest that body-based units and indigenous ergonomics have played an important, typically overlooked role in the design and evolution of technologies worldwide. Not unlike cultures of today, cultures in the past have struggled with ailments caused by repetitive and intensive activities (*24*), and reducing strain through functional design would have been essential for them.

2. Motor efficiency

Body-based units afford convenient motor routines. For example, measuring slack items such as fishing nets or rope with standard rulers is impractical because they must be outstretched for each partial measurement and can be inconveniently long. By contrast, manual measurement can be conducted with relative ease, using simple motoric procedures. Consider, for example, Samoan methods of measuring three-ply braid (*25*, p. 240):

> [T]he worker measures the braid by holding one end with the left hand and running it through the right as he stretches the arms to full

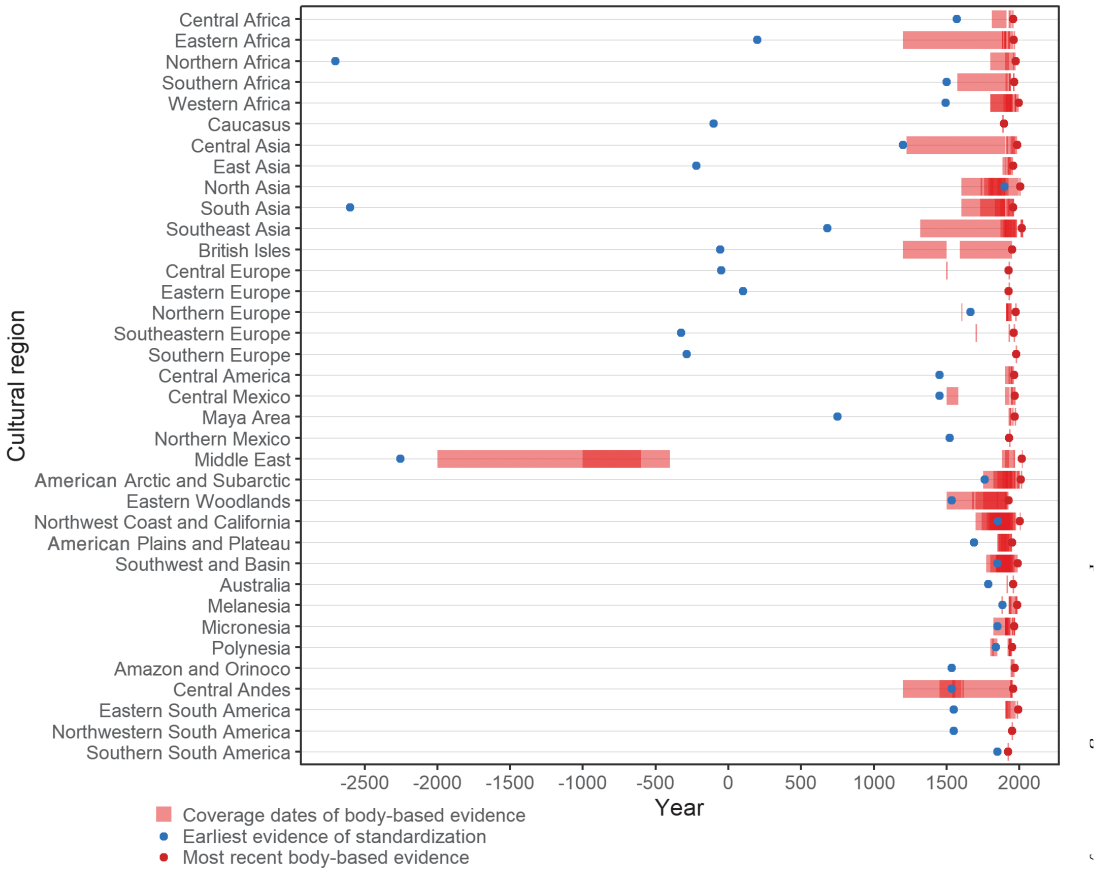


Fig. 3. Timeline of standardization and recorded body-based measurement. For each cultural region in our dataset (based on the HRAF regional categories), we defined the earliest-known case of standardized units of measure (blue points), the coverage dates of ethnographic evidence for body-based measurement (red segments; darker segments indicate greater amounts of evidence), and the most recent evidence for body-based measurement (red points). These dates are defined and described in more detail in table S1.

> length. The full arm span is called a *ngafa*. The right hand holds the farthest point of the first span and draws it into the left hand which seizes the point. The second span is run through and so on until the number of spans or *ngafa* are counted.

Our dataset documents similar techniques of using fathoms to measure nets and ropes around the world. The influence of such practices is still observable today: A standardized fathom is used for measuring water depth in the British Imperial system. A likely explanation for these similarities across cultures is the procedural ease by which the fathom suits the measuring of slack items.

3. Availability

Body-based units have the advantage that their use does not require additional, and often cumbersome, measurement tools. This provides access to easy measurement even for highly mobile populations. Availability is useful even in contexts where standardized measures exist. For example, as one Mapuche informant describes (*26*, p. 93):

> But I do not always have a meter measure handy; I know that my *wima* [the length from Adam's apple to tip of fingers of an outstretched arm] is nearly a meter and I use it.

4. Integration with local knowledge

The use of body-based units, unlike that of standardized units, is often restricted to specific practical tasks. Accordingly, body-based units often account for local information in ways that standardized units overlook. This is especially the case with activity-based units of measure.

For example, the Nicobarese have conveyed canoe trip distances as quantities of young coconut drinks consumed (*27*). Hydration is an especially important factor in the salt water of the Indian Ocean, and it would make practical sense to measure journey distances with required hydration units. In addition, standardized units of length such as nautical miles would not solely account for local variation in currents, weather, and wind conditions, which can all affect physical effort and travel time (and therefore, the amount of hydration required).

Vernacular units may be more sensitive to local conditions, conveying relevant information that standardized measures disregard. For instance, the Ifugao have used the number of rests required as a measure of distance, which is reasonable given that the local mountainous terrain is highly variable, rendering standard linear measures less useful (*28*). Similarly, in some cultures, land is measured in terms of physical activity, such as a day's worth of plowing, which also naturally adjusts for variabilities in terrain quality (*29*). Such measurement units allow adaptation to practical local context in deliberate ways. These findings align with research suggesting that context-specific counting systems can have cognitive and practical advantages (*30*).

Lastly, standardized units of distance may simply not be very useful in everyday local lifeways. Local societies typically know their surroundings very well, so there would be little need for them to measure distances between these points. For example, distances on the Ifaluk Atoll are so short and universally known by locals that "there is little need to discuss them" (*31*, p. 20).

From rules of thumb to standardization

Our data show that body-based units were still used worldwide in the 20th century, close to five millennia after the emergence of the first known standardized units. Our analyses suggest that considerable time lags existed between the regional emergence of standardized units and the use of body-based units (Fig. 3). This may be the result of practical advantages, such as ergonomics and availability.

Table 2. Behavioral and cultural domains in which body-based units of measure are used. The third column describes the incidence of the trait in the full dataset (the number of cultures that the trait appears in). The fourth column describes the number of SCCS cultures in the dataset that are recorded with each trait.

Theme	Description	Incidence (*N* = 186)	Incidence (SCCS subset) (*N* = 99)
	Technological domains		
Garments and cloth	Body-based units are used in the design, measurement, or weaving of garments or cloth. Includes textiles, clothes, footwear, and other wearable items.	44	23
Building	Body-based units are used in the design or construction of buildings or other infrastructure. Includes carpentry.	34	17
Weaponry	Body-based units are used in the design or construction of weapons (e.g., bows and spears).	31	17
Transport	Body-based units are used in the design or construction of transport-related technologies (e.g., kayaks, canoes, boats, skis, equestrian items, and sleds).	24	13
Household	Body-based units are used in the design or construction of other household items, such as mats, pottery, utensils, and looms.	21	12
Fishing tools	Body-based units are used in the context of fishing (also, e.g., crabbing, shellfish, and harvesting), such as the measurement of fishing nets, lines, hooks, and harpoons.	13	9
Agricultural tools	Body-based units are used in the design or construction of agricultural technologies, such as scythes or plows.	5	1
Instrument	Body-based units are used in the design or construction of musical instruments.	3	0
	Other cultural domains		
Trade	Body-based units are used for trade, in markets and barter, or for measuring units of currency.	35	21
Agriculture	Body-based units are used in agriculture (or horticulture), e.g., in measuring cultivated land or agricultural products, or distance between sowed seeds.	29	14
Ritual	Body-based units are used in ritual, ceremonial, religious, burial, or divination purposes.	23	12
Animals	Body-based units are used to measure the size (or value) of livestock and other animals.	9	5
Cooking	Body-based units are used in cooking and the measurement of food items.	6	3
Medicine	Body-based units are used for medical purposes.	3	2
Games	Body-based units are used in the context of games or play.	2	2
	Dimensionality		
Linear	Body-based units measure linear distance (one-dimensional; between two points).	169	90
Area	Body-based units measure area (two-dimensional space).	29	13
Volume	Body-based units measure volume (three-dimensional space).	27	17
	Other		
Ergonomic	Instances where body-based units of measure are mentioned to be used in designing custom-sized (ergonomic) technologies.	25	12
Temperature	Instances where the body is used to measure temperature (e.g., when something is "too hot to touch" or of "body temperature").	2	1

Another potential (not mutually exclusive) explanation for the persistent use of body-based units is cultural inertia. Cultural innovations are often slow to spread, and new formal innovations that require auxiliary technologies and standardization are often delayed in their cultural diffusion. This traction is well documented in histories of measurement (*2*, *32*).

We suggest that pressures for standardization grow mainly in large-scale societies and particularly in intercultural states and commerce. We therefore raise the possibility that the transition from body-based units to standardized ones often spread as a case of "seeing like a state" (*33*) and not only for practical purposes: Standardized measurement systems were cognitive-cultural inventions that enabled seamless statecraft. The early use of standardized units typically revolves around governance and administration (*32*), whereas body-based units are more often used by manual workers and artisans (*14*, *16*). Statecraft-related activities such as intercultural commerce, regulation, and taxation would have demanded standardization and divisibility in ways that body-based units of measure could not deliver. This would also explain why standardized units primarily emerge through the influence of empires and large states (table S1).

Idiosyncratic rules of thumb could not coexist with the demands of mass production. This is evident in industrialist Taylorist principles, which were antagonistic toward "inefficient rule-of-thumb methods" (*34*, p. 16). Even if body-based measurements could serve manual workers, they could not be adapted to the strict

requirements of factory workflows. The move from body-based measurement systems to standardized and abstract systems therefore reflects a larger break in human cultural evolution, one that has seen production systems evolve from local and heterogeneous to global and homogenous. As a consequence, traditional units of measure are endangered in the broader cultural extinction event (*35*) that has followed globalization, industrialization, and colonization.

REFERENCES AND NOTES

1. K. Cooperrider, D. Gentner, *Cognition* **191**, 103942 (2019).
2. A. W. Crosby, *The Measure of Reality: Quantification in Western Europe, 1250-1600* (Cambridge Univ. Press, 1997).
3. J. Gyllenbok, *Encyclopaedia of Historical Metrology, Weights, and Measures* (Springer, 2018), vols. 1–3.
4. S. A. Treese, *History and Measurement of the Base and Derived Units* (Springer, 2018).
5. M. H. Stone, *J. Anthropol.* **2014**, 1–11 (2014).
6. J. M. Kenoyer, in *The Archaeology of Measurement: Comprehending Heaven, Earth and Time in Ancient Societies*, I. Morley, C. Renfrew, Eds. (Cambridge Univ. Press, 2010), pp. 106–121.
7. D. N. Keightley, *East Asian Sci. Technol. Med.* **12**, 18–40 (1995).
8. A. M. Riggsby, in *Oxford Classical Dictionary*, S. Hornblower, A. Spawforth, E. Eidinow, Eds. (2021).
9. J. E. Clark, in *The Archaeology of Measurement: Comprehending Heaven, Earth and Time in Ancient Societies*, I. Morley, C. Renfrew, Eds. (2010), pp. 150–169.
10. P. J. O'Brien, H. D. Christiansen, *Am. Antiq.* **51**, 136–151 (1986).
11. W. Kula, *Measures and Men* (Princeton Univ. Press, 2014).
12. G. T. McCaw, *Empire Survey Review* **5**, 236–259 (1939).
13. A. Teather, A. Chamberlain, M. Parker Pearson, *Br. J. Hist. Math.* **34**, 1–11 (2019).
14. R. J. González, *Zapotec Science: Farming and Food in the Northern Sierra of Oaxaca* (Univ. of Texas Press, 2001).
15. D. Meister, *The History of Human Factors and Ergonomics* (CRC Press, 2018).
16. A. Fienup-Riordan, *Masterworks of Yup'ik Science and Survival: Yuungnaqpiallerput, the Way We Genuinely Live* (Anchorage Museum of History and Art, 2007).
17. J. D. Heath, E. Y. Arima, *Eastern Arctic Kayaks: History, Design, Technique* (Univ. of Alaska Press, 2004).
18. J. Robert-Lamblin, *The Aleut Kayak as Seen By Its Builder and User and the Sea Otter Hunt* (Musée de l'homme, Mus. Nat. d'Histoire Naturell, 1980).
19. J. Lipka, C. Jones, N. Gilsdorf, K. Remick, A. Rickard, *Kayak Design: Scientific Method and Statistical Analysis*, Math in a Cultural Context: Lessons Learned from Yup'ik Eskimo Elders (Univ. of Alaska Fairbanks, 2010).
20. P. D. Jordan, *Technology as Human Social Tradition* (Univ. of California Press, 2014).
21. J. Schefferus, *Lapponia id est, regionis lapponum et gentis nova et verissima descriptio. In qua multa de origine, superstitione, sacris magis, victu, cultu, negotiis lapponum, item animalium, metallorumque indole, quæ in terris eorum proveniunt, hactenus incognita. Produntur, & eiconibus adjectis cum cura illustrantur* (Ex officina Christiani Wolffii typis Joannis Andreae, Francofurti, 1673).
22. F. Densmore, "Chippewa customs" (Bureau of American Ethnology, Bulletin 86, Smithsonian Institution, 1929).
23. T. Hastings, *The British Archer, or, Tracts on Archery* (R. Ackermann, 1831).
24. P. S. Bridges, *Annu. Rev. Anthropol.* **21**, 67–91 (1992).
25. P. H. Buck, "Samoan material culture" (Bulletin 75, Bernice P. Bishop Museum, 1930).
26. M. I. Hilger, *Araucanian Child Life and Its Cultural Background* (Smithsonian Institution, 1957).
27. E. H. Man, *The Nicobar Islands and Their People* (Royal Anthropological Institute of Great Britain and Ireland, 1932).
28. R. F. Barton, *Philippine Pagans: The Autobiographies of Three Ifugaos* (Routledge, 1938).
29. R. Behnke, *The Herders of Cyrenaica: Ecology, Economy, and Kinship among the Bedouin of Eastern Libya* (Univ. of Illinois Press, 1980).
30. S. Beller, A. Bender, *Science* **319**, 213–215 (2008).
31. E. G. Burrows, M. E. Spiro, *An Atoll Culture: Ethnography of Ifaluk in the Central Carolines* (Human Relations Area Files, 1957).
32. J. Vincent, *Beyond Measure: The Hidden History of Measurement from Cubits to Quantum Constants* (W. W. Norton, 2022).
33. J. C. Scott, *Seeing Like a State: How Certain Schemes to Improve the Human Condition Have Failed* (Yale Univ. Press, 1998).
34. F. W. Taylor, *The Principles of Scientific Management* (Harper & Brothers, 1919).
35. H. Zhang, R. Mace, *Evol. Hum. Sci.* **3**, e30 (2021).
36. U. T. Sirelius, *Suomen kansanomaista kulttuuria: esineellisen kansatieteen tuloksia.* (Otava, Helsinki, 1919).
37. T. Kroeber, *Ishi in Two Worlds: A Biography of the Last Wild Indian in North America* (Univ. of California Press, 1961).
38. R. O. Kaaronen, Body-based units of measure in cultural evolution, Open Science Framework (2023); https://doi.org/10.17605/OSF.IO/FEGVR.

ACKNOWLEDGMENTS

We thank members of the Past Present Sustainability Research Unit for valuable feedback during the writing of this article. We also thank three anonymous reviewers. **Funding:** This work was supported by Academy of Finland grant 347305 (R.O.K.), Academy of Finland grant 338558 (J.T.E. and R.O.K.), European Union Horizon 2020 Research and Innovation Programme grant 869471 (J.T.E. and M.A.M.), KONE Foundation grant "Arkistotiedon käyttö ympäristöntutkimuksessa – pohjoisen sosioekologinen ympäristöhistoria työkaluna ympäristömuutosten ymmärtämiseen" (J.T.E. and M.A.M.), and a HELSUS postdoctoral grant (R.O.K.). **Author contributions:** Conceptualization: R.O.K., M.A.M., and J.T.E. Methodology: R.O.K., M.A.M., and J.T.E. Investigation: R.O.K., M.A.M., and J.T.E. Visualization: R.O.K. Funding acquisition: R.O.K., M.A.M., and J.T.E. Project administration: R.O.K. Writing – original draft: R.O.K., M.A.M., and J.T.E. Writing – review and editing: R.O.K., M.A.M., and J.T.E. **Competing interests:** The authors declare no competing interests. **Data and materials availability:** The body-based unit of measure dataset is available at (*38*). Also included is a readme file with instructions for the interpretation of the dataset, as well as the R code used to analyze the data and produce Fig. 2 and Tables 1 and 2. **License information:** Copyright © 2023 the authors, some rights reserved; exclusive licensee American Association for the Advancement of Science. No claim to original US government works. https://www.science.org/about/science-licenses-journal-article-reuse

SUPPLEMENTARY MATERIALS

science.org/doi/10.1126/science.adf1936
Materials and Methods
Table S1
References (*39*–*51*)
MDAR Reproducibility Checklist

Submitted 5 October 2022; accepted 10 April 2023
10.1126/science.adf1936

ULTRAFAST DYNAMICS

Tracking C–H activation with orbital resolution

Raphael M. Jay[1]*†, Ambar Banerjee[1]*†, Torsten Leitner[1]‡, Ru-Pan Wang[2], Jessica Harich[2], Robert Stefanuik[1], Hampus Wikmark[1]§, Michael R. Coates[3], Emma V. Beale[4], Victoria Kabanova[4]¶, Abdullah Kahraman[4]#**, Anna Wach[4,5], Dmitry Ozerov[4], Christopher Arrell[4], Philip J. M. Johnson[4], Camelia N. Borca[4], Claudio Cirelli[4], Camila Bacellar[4], Christopher Milne[6], Nils Huse[2], Grigory Smolentsev[4], Thomas Huthwelker[4], Michael Odelius[3], Philippe Wernet[1]*

Transition metal reactivity toward carbon–hydrogen (C–H) bonds hinges on the interplay of electron donation and withdrawal at the metal center. Manipulating this reactivity in a controlled way is difficult because the hypothesized metal-alkane charge-transfer interactions are challenging to access experimentally. Using time-resolved x-ray spectroscopy, we track the charge-transfer interactions during C–H activation of octane by a cyclopentadienyl rhodium carbonyl complex. Changes in oxidation state as well as valence-orbital energies and character emerge in the data on a femtosecond to nanosecond timescale. The x-ray spectroscopic signatures reflect how alkane-to-metal donation determines metal-alkane complex stability and how metal-to-alkane back-donation facilitates C–H bond cleavage by oxidative addition. The ability to dissect charge-transfer interactions on an orbital level provides opportunities for manipulating C–H reactivity at transition metals.

The transformation of saturated hydrocarbons under mild conditions into more valuable products constitutes a long-standing challenge in chemistry (*1*–*4*). Photoinitiated reactions of transition metal carbonyl complexes with alkanes have long served as fruitful model systems (*5*, *6*), providing detailed insights into the cleavage mechanism of strong C–H bonds at a metal center (*1*, *2*, *4*, *7*). In these systems, photo-induced ligand loss is known to create a highly reactive species with an undercoordinated and electron-deficient metal center (Fig. 1A). The metal then rapidly binds an alkane from solution to form a σ-complex, in which the metal coordinates to one or more C–H σ-bonds. Ultimately, metal insertion between C and H atoms breaks the C–H bond to form a metal alkyl hydride product. The σ-complex intermediates have been extensively studied over the past several decades to probe their molecular structure and mechanistic role (*8*–*20*).

Quantum chemical calculations, in particular, suggest that the metal-alkane bond in σ-complexes is formed by donation of electron density from the occupied C–H σ-orbital into unoccupied metal d-orbitals concomitant with back-donation from occupied metal d-orbitals into the unoccupied antibonding C–H σ*-orbital (*21*–*24*) (similar to, albeit substantially weaker than, metal-carbonyl bonds, as illustrated in Fig. 1B). Both types of interactions simultaneously enhance metal-alkane bonding and weaken the alkane C–H bond. Because it is the balance of back-and-forth charge-transfer via different orbitals that determines whether a σ-complex ultimately proceeds to C–H bond cleavage, dissecting individual charge-transfer interactions could provide orbital-based design principles as a guide for catalyst development. Experimentally, time-resolved infrared (IR) spectroscopy has been instrumental in identifying reaction intermediates in C–H activation (*17*) by probing shifts in infrared marker modes of spectator ligands. Such shifts are the result of changes in spectator-ligand bond strengths induced by changes in the integrated charge-transfer interactions in the complex. Separately accessing donation and back-donation to and from the metal in a σ-complex, however, would be a way to experimentally correlate individual orbital interactions with reactivity toward C–H bond cleavage (*7*).

In this work, we demonstrate a distinct way to experimentally evaluate metal-ligand charge-transfer interactions during C–H activation of metal complexes. Using time-resolved x-ray absorption spectroscopy (XAS) at the metal L-edge (*11*, *25*–*30*), we probe the short-lived reaction intermediates from the vantage point of the reactive metal site to interrogate the decisive charge-transfer interactions that determine the overall reaction. In two ultraviolet (UV)–pump and x-ray–probe experiments at the Swiss Free Electron Laser facility (SwissFEL) and the Swiss Light Source synchrotron radiation facility (SLS), we track σ-complex formation and oxidative addition using $CpRh(CO)_2$ (where Cp is cyclopentadienyl) (*10*, *18*–*20*) in octane solution. The time-resolved Rh L-edge absorption spectra were recorded by collecting the x-ray fluorescence as a function of incident x-ray photon energy around the Rh L_3 absorption edge (Fig. 1C; see supplementary materials for experimental details). As is the case for other 4d transition metal complexes (*27*, *31*, *32*), the Rh L_3-edge transitions can be assigned to excitations of Rh 2p core electrons to unoccupied molecular orbitals (see Fig. 1D). Changes in transition energies reflect changes in orbital energies, whereas oscillator strengths vary with the degree to which Rh 4d and ligand orbitals hybridize. In combination with our calculations, the data provide direct access to back-and-forth charge-transfer interactions along the C–H activation reaction trajectory at the level of individual orbitals.

Time-resolved XAS of C–H activation

The steady-state Rh L_3-edge absorption spectrum of $CpRh(CO)_2$ shown in Fig. 1D exhibits a peak at a photon energy of ~3006 eV that results from excitation of Rh 2p core electrons into the lowest unoccupied molecular orbital (LUMO), the empty 4d-derived orbital of the Rh(I) d^8 ground state configuration. The second peak at ~3007.5 eV is assigned to transitions of Rh 2p electrons into unoccupied orbitals of mainly CO and/or Cp ligand character. Through metal-ligand back-donation, these ligand-derived orbitals acquire Rh 4d character and become accessible by the Rh 2p→d dipole transitions in L_3-edge XAS (*33*).

Upon laser excitation, as seen in the difference spectrum recorded at a pump-probe time delay of 250 fs, a pre-edge peak appears at ~3002.5 eV together with substantial bleaching

Table 1. Mulliken charge and orbital properties of the CpRh(CO)-octane and Rh(acac)(CO)-octane σ-complexes (B3LYP level of theory).

σ-complex	Rh Mulliken charge	LUMO character			
		Rh 4d (%)	Cp or acac (%)	CO (%)	Octane (%)
CpRh(CO)-octane	0.37	39.3	28.8	4.2	6.2
Rh(acac)(CO)-octane	0.46	52.2	15.2	1.5	9.2

[1]Department of Physics and Astronomy, Uppsala University, 751 20 Uppsala, Sweden. [2]Center for Free-Electron Laser Science, Department of Physics, University of Hamburg, 22761 Hamburg, Germany. [3]Department of Physics, Stockholm University, 106 91 Stockholm, Sweden. [4]Paul-Scherrer Institute, CH-5232 Villigen PSI, Switzerland. [5]Institute of Nuclear Physics, Polish Academy of Sciences, PL-31342 Krakow, Poland. [6]European XFEL GmbH, 22869 Schenefeld, Germany.
*Corresponding author. Email: raphael.jay@physics.uu.se (R.M.J.); ambar.banerjee@physics.uu.se (A.B.); philippe.wernet@physics.uu.se (P.W.)
†These authors contributed equally to this work.
‡Present address: MCA Engineering GmbH, 80807 Munich, Germany.
§Present address: Proximion AB, 164 40 Kista, Sweden.
¶Present address: Department of Physics and Astronomy, Uppsala University, 751 20 Uppsala, Sweden.
#Present address: Stanford PULSE Institute, SLAC National Accelerator Laboratory, Stanford University, Menlo Park, CA 94025, USA.
**Present address: Physical Sciences Division, Pacific Northwest National Laboratory, Richland, WA 99352, USA.

of main-edge features (Fig. 1D). The temporal evolution of the pre-edge peak intensity, shown as a time trace in Fig. 1E, is well described by a biexponential decay to a metastable species (reduced χ^2 = 1.11; see supplementary materials for a kinetic model). The two time constants are assigned to CO dissociation from excited states of $CpRh(CO)_2$ within 370 ± 50 fs followed by octane association within 2.0 ± 0.1 ps. These assignments agree with the timescales for ligand substitution in other metal carbonyls from previous femtosecond measurements (*28*, *34*). Our experiment establishes the timescale of formation of the CpRh(CO)-octane σ-complex, and the spectrum at 10 ps in Fig. 1D constitutes a direct fingerprint of how metal-ligand charge-transfer interactions change upon substituting a CO with an alkane ligand. On nanosecond timescales, the disappearance of the σ-complex pre-edge peak (time trace at 3004.4 eV in Fig. 1F) and the simultaneous emergence of a positive absorption feature (time trace at 3006.6 eV in Fig. 1F and transient spectrum at nanosecond delay times in Fig. 1D) reflect how the metal-ligand charge-transfer interactions further change upon C–H activation by oxidative addition.

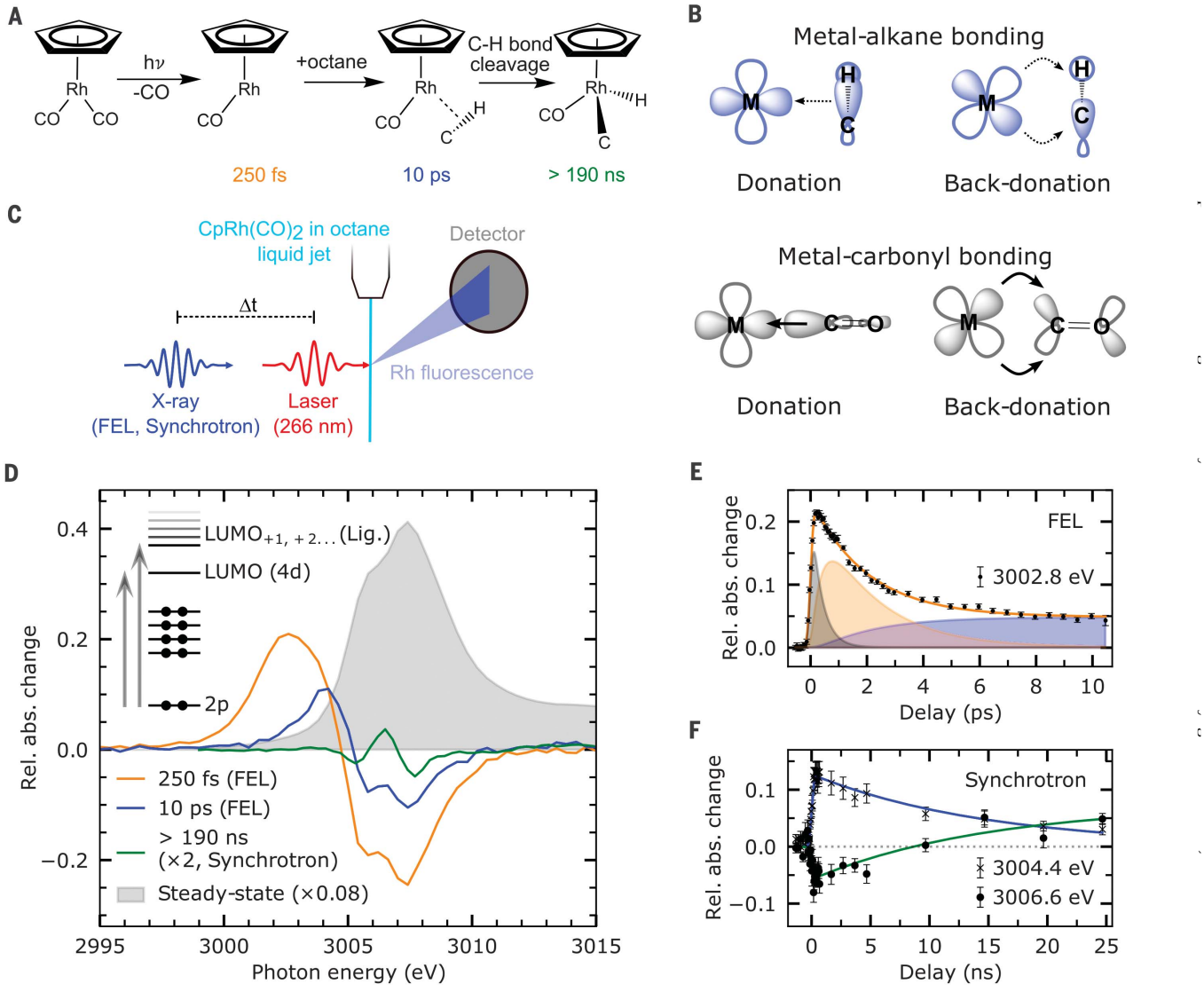


Fig. 1. Mechanistic model and time-resolved XAS of C–H activation by $CpRh(CO)_2$ in octane solution. (**A**) Schematic of C–H activation by $CpRh(CO)_2$ via photoextrusion of CO followed by alkane complexation and oxidative addition. hν, UV photon. (**B**) Orbital-specific metal-ligand charge-transfer interactions for metal-alkane and metal-carbonyl bonds. (**C**) Schematic of the experiment with UV–laser pump pulses triggering the reaction and x-ray pulses probing orbital evolution as a function of time delay between pump and probe pulses. Reaction intermediates and products [as well as ground-state $CpRh(CO)_2$] are characterized by detecting the Rh fluorescence as a measure of the Rh-specific x-ray absorption (see supplementary materials). (**D**) Steady-state and transient Rh L_3-edge absorption spectra at indicated pump-probe time delays as well as a schematic depiction of the L-edge absorption process [difference spectra are plotted relative to the edge-jump of the steady-state spectrum (intensity at 3015 eV), which is normalized to 1; steady-state and difference spectrum at delays >190 ns are scaled for illustration]. Rel. abs., relative absorption. (**E** and **F**) Time traces (intensities versus time delay) measured at indicated x-ray photon energies with (E) femtosecond and (F) picosecond time resolution. In (E), the gray, orange, and purple shaded regions represent the relative populations of the $CpRh(CO)_2$ excited state, the CpRh(CO) fragment, and the CpRh(CO)-octane σ-complex, respectively.

Both time traces are modeled with a single exponential (reduced χ^2 = 1.01), yielding a time constant of 14 ± 2 ns, which is in excellent agreement with the ~14 ns for C–H activation of octane with $CpRh(CO)_2$ from time-resolved IR measurements (*18*).

Comparison with theory

This assignment of the transient x-ray absorption spectra is further validated and detailed by the calculated spectra in Fig. 2A. Because shapes and intensities of the measured spectra are well reproduced, we can robustly assign x-ray transitions to underlying charge-transfer interactions (see supplementary materials for computational details and discussion of deviations between experiment and theory). We use the experiment-theory comparison to extract the orbital correlation diagram shown in Fig. 2B.

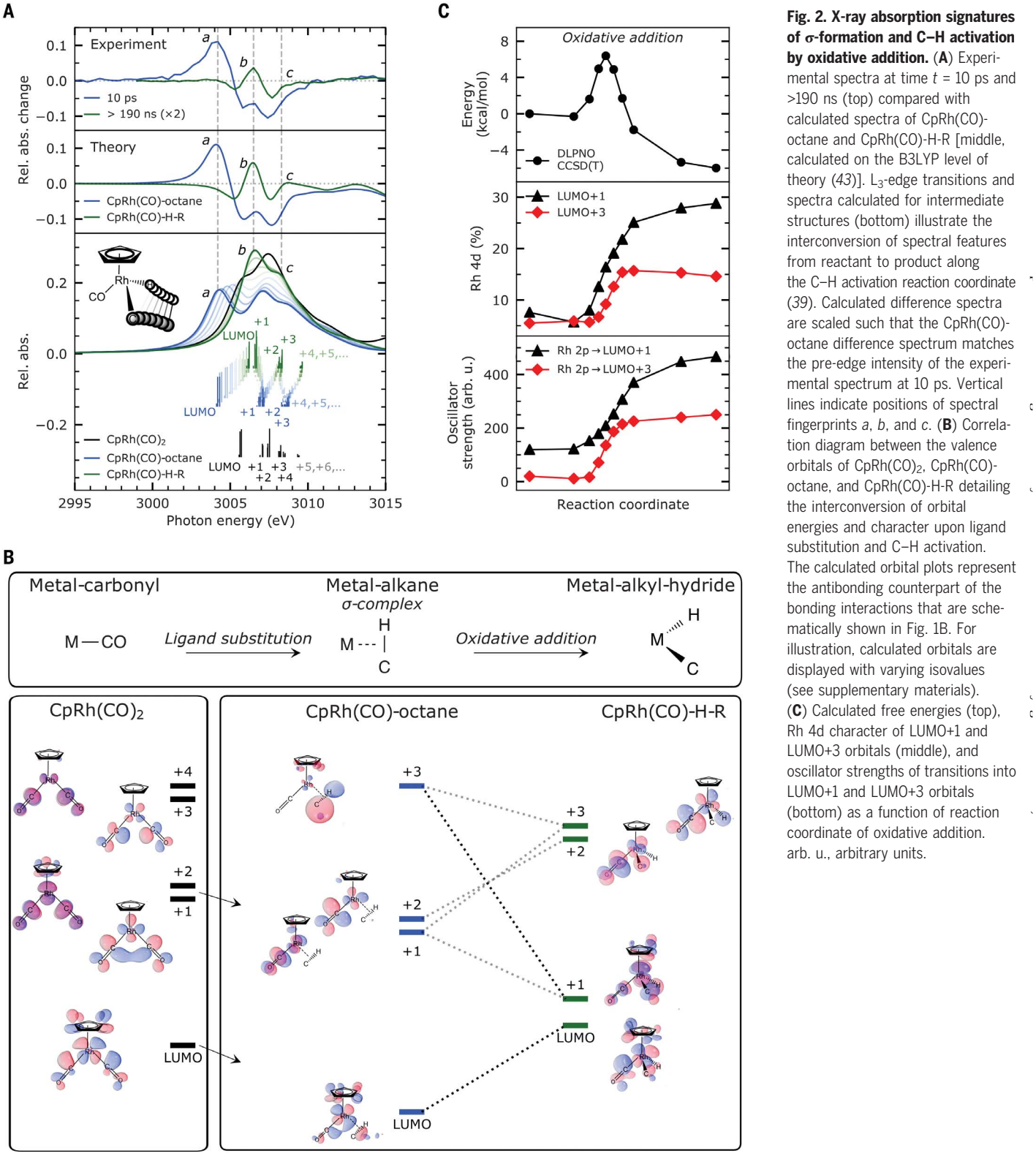


Fig. 2. X-ray absorption signatures of σ-formation and C–H activation by oxidative addition. (**A**) Experimental spectra at time t = 10 ps and >190 ns (top) compared with calculated spectra of CpRh(CO)-octane and CpRh(CO)-H-R [middle, calculated on the B3LYP level of theory (*43*)]. L_3-edge transitions and spectra calculated for intermediate structures (bottom) illustrate the interconversion of spectral features from reactant to product along the C–H activation reaction coordinate (*39*). Calculated difference spectra are scaled such that the CpRh(CO)-octane difference spectrum matches the pre-edge intensity of the experimental spectrum at 10 ps. Vertical lines indicate positions of spectral fingerprints *a*, *b*, and *c*. (**B**) Correlation diagram between the valence orbitals of $CpRh(CO)_2$, CpRh(CO)-octane, and CpRh(CO)-H-R detailing the interconversion of orbital energies and character upon ligand substitution and C–H activation. The calculated orbital plots represent the antibonding counterpart of the bonding interactions that are schematically shown in Fig. 1B. For illustration, calculated orbitals are displayed with varying isovalues (see supplementary materials). (**C**) Calculated free energies (top), Rh 4d character of LUMO+1 and LUMO+3 orbitals (middle), and oscillator strengths of transitions into LUMO+1 and LUMO+3 orbitals (bottom) as a function of reaction coordinate of oxidative addition. arb. u., arbitrary units.

Importantly, this correlation diagram, which is based on robust experimental observations, relates orbital interactions from ligand substitution and σ-complex formation to C–H bond breaking and oxidative addition.

Two major effects in metal-ligand bonding of the CpRh(CO)-octane σ-complex compared with $CpRh(CO)_2$ are reflected in the 10-ps transient spectrum. First, substituting the strong-field CO ligand with the weakly interacting octane stabilizes (decreases the energy of) the Rh 4d-derived LUMO orbital (Fig. 2B). This is directly reflected in a decrease of 2p→LUMO transition energies: The pre-edge peak that is due to 2p→LUMO transitions is shifted to lower energy in the σ-complex (3004.2 eV) compared with $CpRh(CO)_2$ (3006 eV; Fig. 2A). Second, an overall reduced degree of back-donation in the σ-complex compared with $CpRh(CO)_2$ lowers the hybridization of ligand orbitals with Rh 4d orbitals. This diminishes intensities of the Rh 2p transitions to ligand-derived orbitals in the σ-complex and causes the depletion in the main-edge region of 3006 to 3009 eV (Fig. 2A).

For the subsequent C–H bond breaking and oxidative addition step from the σ-complex to the metal alkyl hydride, calculations of the free-energy landscape shown in the top panel of Fig. 2C suggest a barrier of ~7 kcal/mol and an exothermic reaction. The underlying reaction coordinate is constructed from a Nudged-Elastic-Band (NEB)/TPPSh/Def2-TZVP computation (*35*–*37*). Using the geometries of this reaction path scan, the free-energy landscape was computed at the DLPNO-CCSD(T)/Def2-TZVP level of theory (*38*). Although we do not experimentally observe the intermediate structures along the reaction coordinate, the L_3-edge x-ray absorption spectra computed for these structures relate the spectral changes from the σ-complex reactant to the metal alkyl hydride product, which we observe. The key spectral fingerprint regions (denoted as *a*, *b*, and *c* in Fig. 2A) can be assigned to excitations of Rh 2p electrons predominantly into the LUMO, LUMO+1, LUMO+2, and LUMO+3 orbitals (LUMO+4, +5, … are not discussed because they contribute to a negligible degree only). Changes of the features *a* to *c* hence report on the combined transformations of the four lowest unoccupied orbitals upon C–H bond breaking and oxidative addition. As detailed in the following paragraphs, feature *a* reflects changes in metal-alkane orbital overlap as metal-alkane bond distances change, feature *b* reports on the oxidation of the metal, and feature *c* reflects changes in metal-ligand back-donation.

In line with previous work (*39*), our calculated reaction coordinate describes the C–H bond moving toward the Rh center and, at the same time, the C–H bond elongating and breaking until the individual Rh–C and Rh–H bonds are established (see schematic of the reaction coordinate in Fig. 2A, bottom). As a consequence of these atomic rearrangements along the reaction coordinate, the Rh 4d-derived LUMO orbital shifts to higher energies because of increasing orbital overlap with the approaching C–H group with minor changes in hybridization (Fig. 2B and fig. S7). The corresponding increase of 2p→LUMO transition energies is directly observed experimentally by the disappearance of the pre-edge feature *a* in the spectrum upon transformation of the σ-complex to the alkyl hydride product: The 2p→LUMO transitions shift to higher energy and merge with the main edge of the spectrum, thereby contributing to the generation of feature *b* in the spectrum of the CpRh(CO)–H–R alkyl hydride product.

LUMO+1 in the σ-complex is the energetically lowest ligand-derived orbital with dominant CO π* character and with some Rh 4d admixture due to Rh-CO back-donation (see orbital plots in Fig. 2B). Upon oxidative addition, LUMO+1 shifts to slightly lower energy and, importantly, gains considerable Rh 4d character (see calculated Rh 4d character in Fig. 2C). The increase is so substantial that the Rh 4d character becomes the dominating contribution. This can be interpreted as an effective transformation of the former ligand-derived orbital into a second unoccupied Rh 4d-derived orbital (in addition to the LUMO; see orbital plots in Fig. 2B). The increase of Rh 4d character directly scales with an increase of oscillator strength of the Rh 2p→LUMO+1 transitions (Fig. 2C). Feature *b* hence emerges as a strong peak, drawing intensity from both the LUMO+1 transforming into a second unoccupied Rh 4d-derived orbital and the LUMO shifting to higher energy and merging with the main edge (Fig. 2A). The emergence of feature *b* thus reflects the combined electronic-structure effects of C–H bond cleavage (LUMO destabilization) and oxidative addition (LUMO+1 transformation). In particular, the oxidation of the metal center from a Rh(I) (d^8) to a Rh(III) (d^6) configuration is evidenced by the emergence of two unoccupied Rh 4d orbitals.

The increase of the Rh oxidation state substantially destabilizes LUMO+2 (Fig. 2B) and slightly reduces its Rh 4d character (see fig. S7). As the second CO π* orbital, its destabilization thus directly reflects a decrease in back-donation from the oxidized metal onto CO π*. This effect has also been associated with the shift of CO marker modes to higher energy upon C–H activation (*17*), consistent with our results. Finally, LUMO+3 in the σ-complex constitutes the octane C–H σ* orbital, which exhibits weak Rh 4d admixture because of low back-donation from Rh to C–H (orbital plot in Fig. 2B). Back-donation, however, increases as the C–H bond is broken and the covalent Rh–C and Rh–H bonds are formed, as evidenced by the substantial increase in Rh 4d character in LUMO+3 (see Rh 4d character in Fig. 2C and orbital plots in Fig. 2B). Accordingly, the oscillator strengths of Rh 2p→LUMO+3 transitions also strongly increase upon oxidative addition (Fig. 2C). Together with the transitions into LUMO+2 shifting toward higher energies, this causes the formation of the strong peak *c* in the alkyl hydride spectrum, which exhibits an intensity similar

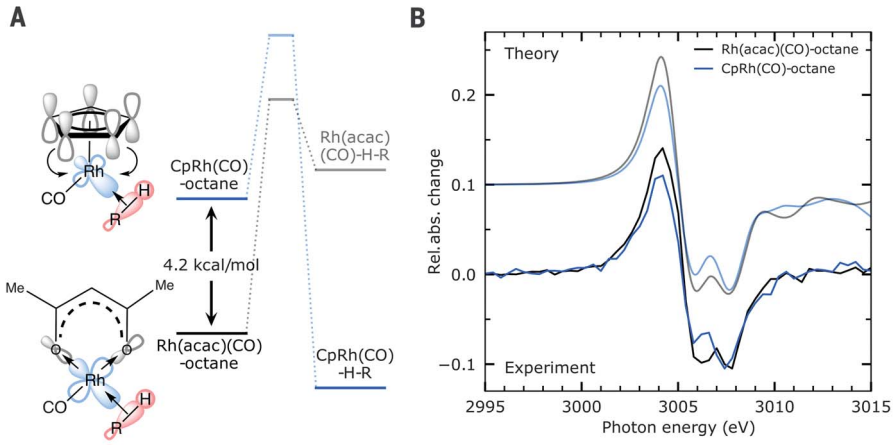


Fig. 3. X-ray orbital view of reactivity modulations in C–H activation by varying the ligand environments in σ-complexes. (**A**) Schematic of the LUMO orbitals of CpRh(CO)-octane and Rh(acac)(CO)-octane with variations in metal-ligand bonding (charge-transfer indicated by arrows) and their effect on the affinity for oxidative addition (calculated free energies). Me, methyl. (**B**) Calculated difference spectra of CpRh(CO)-octane and Rh(acac)(CO)-octane compared with transient difference L_3-edge absorption spectra measured at SwissFEL at a pump-probe delay time of 10 ps. For comparison, the experimental Rh(acac)(CO)-octane spectrum is scaled to match the depletion of the CpRh(CO)-octane. This scaling is validated by the excellent agreement with the calculated spectra, which are shown with the same scaling as in Fig. 2A (see supplementary materials).

to the steady-state spectrum of $CpRh(CO)_2$ and one considerably stronger than that in the σ-complex (Fig. 2A). Experimentally, this is reflected in negligible intensities in the alkyl hydride difference spectrum at the energies of feature *c* compared with the strong bleaching in the transient σ-complex spectrum.

A more stable σ-complex

By experimentally observing individual charge-transfer interactions, we verify the validity of orbital correlation diagrams along C–H activation reactions that were previously derived from quantum chemical calculations alone (*40*). Our approach allows us, in particular, to expand upon established notions of charge-transfer interactions between the metal and the C–H group by experimentally assessing the critical role of additional orbital interactions between the metal and the spectator ligands. We further demonstrate this here by evaluating how different σ-complexes exhibit different reactivities toward C–H activation owing to specific differences in orbital interactions as a result of their different ligand environments. It has previously been shown that replacing the Cp moiety with an acetylacetonate (acac) group leads to a stable σ-complex, which, however, does not proceed to oxidative addition of the C–H bond (*41*). Our calculations shown in Fig. 3A suggest a 4.2 kcal/mol stabilization of the Rh(acac)(CO)-octane with respect to the CpRhCO-octane σ-complex. Together with the endothermic free-energy profile we calculated, this renders the C–H activated product unfavorable. We find the extra stabilization of Rh(acac)(CO)-octane to be predominantly due to a higher donation from the octane onto the Rh center. This stronger donation is favored by the higher charge deficiency at the Rh in the case of the more ionic bond between Rh and the acac group compared with the bond between Rh and Cp (see the Mulliken charges in Table 1).

Our calculations predict this variation in ionicity and the related variation in reactivity for C–H activation to manifest in the x-ray absorption difference spectra of the two σ-complexes as shown in Fig. 3B. Our experiment directly confirms this prediction. In quantitative agreement with theory, the measured spectrum of Rh(acac)(CO)-octane shows a higher pre-edge intensity than CpRh(CO)-octane (Fig. 3B). We find this difference to be due to a higher Rh 4d character in the LUMO (at the expense of a lower hybridization with the acac group; see Table 1), which causes the more intense 2p→LUMO pre-edge transitions in Rh(acac)(CO)-octane. This higher Rh 4d character, which directly correlates with higher Rh ionicity, renders the reaction step to the Rh(acac)(CO)-H-R species endothermic. A more charge-deficient Rh(I) center—in the case of acac, having a lower propensity to be further oxidized to Rh(III)—is consistent with and extends established trends in alkane oxidative addition (*7*). We thus establish a direct measure of how the lower hybridization of Rh 4d with spectator-ligand orbitals in the more ionic bond to the acac ligands modulates reactivity for C–H activation by unfavorably changing the balance of charge-transfer interactions that bind (alkane-to-metal σ-donation) versus those that break the C–H bond (propensity for oxidation via metal-to-alkane back-donation).

Our results demonstrate the value of time-resolved, metal-specific, L-edge x-ray absorption spectroscopy for understanding, on an orbital level, which factors determine reactivity for C–H activation at a metal complex. We anticipate that our approach will be used in the future to systematically screen σ-complexes and alkyl hydride reaction products to provide a distribution of valence orbital energies and character as measures of metal-alkane bond stability and propensity toward C–H activation with oxidative addition and, potentially, other mechanisms (*40*). With C–H activation ranging from nucleophilic to electrophilic, depending on the relative weight of charge donation and back-donation, the here established experimental observables can be used to ascertain where in the range of mechanisms a probed system lies. Such insight can then be used to pin the results from computational studies that correlate valence electronic structure with reactivity. We envision this approach to extend established trends for reactivity (*7*) by providing experimentally verified correlations between metal-ligand charge-transfer interactions and reactivity for orbital-level control of C–H activation.

REFERENCES AND NOTES

1. R. G. Bergman, *Nature* **446**, 391–393 (2007).
2. J. A. Labinger, J. E. Bercaw, *Nature* **417**, 507–514 (2002).
3. B. A. Arndtsen, R. G. Bergman, T. A. Mobley, T. H. Peterson, *Acc. Chem. Res.* **28**, 154–162 (1995).
4. K. I. Goldberg, A. S. Goldman, *Acc. Chem. Res.* **50**, 620–626 (2017).
5. J. K. Hoyano, A. D. McMaster, W. A. G. Graham, *J. Am. Chem. Soc.* **105**, 7190–7191 (1983).
6. A. H. Janowicz, R. G. Bergman, *J. Am. Chem. Soc.* **104**, 352–354 (1982).
7. J. Hartwig, *Organotransition Metal Chemistry: From Bonding to Catalysis* (University Science Books, 2010).
8. C. Hall, R. N. Perutz, *Chem. Rev.* **96**, 3125–3146 (1996).
9. W. D. Jones, *Acc. Chem. Res.* **36**, 140–146 (2003).
10. J. B. Asbury, H. N. Ghosh, J. S. Yeston, R. G. Bergman, T. Lian, *Organometallics* **17**, 3417–3419 (1998).
11. S. A. Bartlett *et al*., *J. Am. Chem. Soc.* **141**, 11471–11480 (2019).
12. D. J. Lawes, S. Geftakis, G. E. Ball, *J. Am. Chem. Soc.* **127**, 4134–4135 (2005).
13. F. M. Chadwick *et al*., *J. Am. Chem. Soc.* **138**, 13369–13378 (2016).
14. S. Geftakis, G. E. Ball, *J. Am. Chem. Soc.* **120**, 9953–9954 (1998).
15. J. D. Watson, L. D. Field, G. E. Ball, *Nat. Chem.* **14**, 801–804 (2022).
16. E. P. Wasserman, C. B. Moore, R. G. Bergman, *Science* **255**, 315–318 (1992).
17. S. E. Bromberg *et al*., *Science* **278**, 260–263 (1997).
18. M. W. George *et al*., *Proc. Natl. Acad. Sci. U.S.A.* **107**, 20178–20183 (2010).
19. A. L. Pitts *et al*., *J. Am. Chem. Soc.* **136**, 8614–8625 (2014).
20. M. C. Asplund *et al*., *J. Am. Chem. Soc.* **124**, 10605–10612 (2002).
21. E. A. Cobar, R. Z. Khaliullin, R. G. Bergman, M. Head-Gordon, *Proc. Natl. Acad. Sci. U.S.A.* **104**, 6963–6968 (2007).
22. J. Y. Saillard, R. Hoffmann, *J. Am. Chem. Soc.* **106**, 2006–2026 (1984).
23. P. E. M. Siegbahn, M. Svensson, *J. Am. Chem. Soc.* **116**, 10124–10128 (1994).
24. D. Balcells, E. Clot, O. Eisenstein, *Chem. Rev.* **110**, 749–823 (2010).
25. R. M. Jay, K. Kunnus, P. Wernet, K. J. Gaffney, *Annu. Rev. Phys. Chem.* **73**, 187–208 (2022).
26. Y. Kim *et al*., *J. Phys. Chem. Lett.* **12**, 12165–12172 (2021).
27. B. E. Van Kuiken *et al*., *J. Phys. Chem. Lett.* **3**, 1695–1700 (2012).
28. P. Wernet *et al*., *Nature* **520**, 78–81 (2015).
29. W. Gawelda *et al*., *J. Am. Chem. Soc.* **128**, 5001–5009 (2006).
30. A. A. Cordones *et al*., *Nat. Commun.* **9**, 1989 (2018).
31. B. E. Van Kuiken *et al*., *J. Phys. Chem. A* **117**, 4444–4454 (2013).
32. F. De Groot, *Coord. Chem. Rev.* **249**, 31–63 (2005).
33. R. K. Hocking *et al*., *J. Am. Chem. Soc.* **128**, 10442–10451 (2006).
34. A. G. Joly, K. A. Nelson, *Chem. Phys.* **152**, 69–82 (1991).
35. V. Ásgeirsson *et al*., *J. Chem. Theory Comput.* **17**, 4929–4945 (2021).
36. J. Tao, J. P. Perdew, V. N. Staroverov, G. E. Scuseria, *Phys. Rev. Lett.* **91**, 146401 (2003).
37. F. Weigend, R. Ahlrichs, *Phys. Chem. Chem. Phys.* **7**, 3297–3305 (2005).
38. Y. Guo *et al*., *J. Chem. Phys.* **148**, 011101 (2018).
39. R. H. Crabtree, E. M. Holt, M. Lavin, S. M. Morehouse, *Inorg. Chem.* **24**, 1986–1992 (1985).
40. D. H. Ess, W. A. GoddardIII, R. A. Periana, *Organometallics* **29**, 6459–6472 (2010).
41. T. P. Dougherty, W. T. Grubbs, E. J. Heilweil, *J. Phys. Chem.* **98**, 9396–9399 (1994).
42. R. M. Jay *et al*., Data for "Tracking C–H activation with orbital resolution." Zenodo (2023); https://doi.org/10.5281/zenodo.7837518.
43. A. D. Becke, *J. Chem. Phys.* **98**, 1372–1377 (1993).

ACKNOWLEDGMENTS

We acknowledge the Paul Scherrer Institut, Villigen, Switzerland, for provision of beamtime at the Alvra beamline of SwissFEL as well as at the PHOENIX beamline of the Swiss Light Source (SLS). We thank R. Wetter and C. Frieh for their excellent technical support. The computations were partly enabled by resources provided by the Swedish National Infrastructure for Computing (SNIC) at UPPMAX, which is partially funded by the Swedish Research Council through grant agreement nos. 2021-22968 and 2022-22975. The computations were also partly enabled by resources provided by the National Academic Infrastructure for Supercomputing in Sweden (NAISS) and the SNIC at the National Supercomputer Centre in Sweden (NSC) and the PDC (Parallelldatorcentrum) Center for High Performance Computing, which are partially funded by the Swedish Research Council through grant agreement nos. 2022-06725 and 2018-05973. **Funding:** A.B. and P.W. acknowledge funding from the Carl Tryggers Foundation (contract CTS 19: 399). P.W. acknowledges funding from the Swedish Research Council (grant agreement no. 2019-04796). J.H. and N.H. acknowledge funding from the Cluster of Excellence "CUI: Advanced Imaging of Matter" of the Deutsche Forschungsgemeinschaft (DFG), EXC 2056, project ID 390715994. R.-P.W. acknowledges funding from the German Ministry of Education and Research (BMBF), project ID 05K19GU2. V.K., A.K., and C.B. acknowledge support from the Swiss National Science Foundation (SNSF) through the NCCR:MUST. A.W. acknowledges the National Science Centre, Poland (NCN), for partial support through grant no. 2019/03/X/ST3/00035. **Author contributions:** R.M.J., A.B., and P.W. originated the project concept. R.M.J., P.J.M.J., C.C., C.B., C.M., N.H., G.S., T.H., and P.W. planned and conceived the experiments. R.M.J., T.L., R.S., R.-P.W., J.H., E.V.B., V.K., A.K., A.W., D.O., C.A., P.J.M.J., C.N.B., C.C., C.B., G.S., T.H., and P.W. executed the experiments. R.M.J., T.L., H.W., C.C., and P.W. analyzed the experimental data. R.M.J., A.B., M.R.C., and M.O. performed the theoretical calculations. R.M.J., A.B., and P.W. wrote the paper

with input from all the authors. **Competing interests:** The authors declare that they have no competing interests. **Data and materials availability:** All data presented in the main text and the supplementary materials are freely available through Zenodo (*42*).
License information: Copyright © 2023 the authors, some rights reserved; exclusive licensee American Association for the Advancement of Science. No claim to original US government works. https://www.science.org/about/science-licenses-journal-article-reuse

SUPPLEMENTARY MATERIALS

science.org/doi/10.1126/science.adf8042
Materials and Methods
Supplementary Text
Figs. S1 to S11
Table S1
References (*44*–*65*)
Movies S1 to S4

Submitted 20 January 2023; accepted 2 May 2023
10.1126/science.adf8042

3D PRINTING

A sinterless, low-temperature route to 3D print nanoscale optical-grade glass

J. Bauer[1,2]*, C. Crook[2], T. Baldacchini[3]

Three-dimensional (3D) printing of silica glass is dominated by techniques that rely on traditional particle sintering. At the nanoscale, this limits their adoption within microsystem technology, which prevents technological breakthroughs. We introduce the sinterless, two-photon polymerization 3D printing of free-form fused silica nanostructures from a polyhedral oligomeric silsesquioxane (POSS) resin. Contrary to particle-loaded sacrificial binders, our POSS resin itself constitutes a continuous silicon-oxygen molecular network that forms transparent fused silica at only 650°C. This temperature is 500°C lower than the sintering temperatures for fusing discrete silica particles to a continuum, which brings silica 3D printing below the melting points of essential microsystem materials. Simultaneously, we achieve a fourfold resolution enhancement, which enables visible light nanophotonics. By demonstrating excellent optical quality, mechanical resilience, ease of processing, and coverable size scale, our material sets a benchmark for micro– and nano–3D printing of inorganic solids.

The three-dimensional (3D) free-form manufacturing of silica glass is dominated by techniques that rely on particle-loaded binders and sintering (*1*–*4*). However, these impose several limitations restricting their adoption within microsystem technology, which prevents major technological breakthroughs.

Silica glass has a softening point of 1100°C, which makes it historically challenging to structure. However, its superior optical transparency and thermal, chemical, and mechanical resilience make it one of the most important materials for modern engineering applications, which include micro-optics (*5*, *6*), photonics (*7*–*9*), microelectromechanical systems (MEMS) (*10*, *11*), and microfluidics and biomedicine (*12*, *13*). Established microsystems synthesis routes (*14*) manufacture silica structures by means of elaborate top-down process sequences, which involve techniques such as 2D mask lithography, thermal oxidation, vapor deposition, and etching, but these processes hardly translate to 3D designs. Recently, the free-form manufacturing of silica glass has greatly advanced. However, the most advanced 3D printing and molding methods (*12*) still rely on melting or particle-sintering steps identical to ancient blowing techniques and established industrial processes.

Nearly unconstrained 3D design freedom at nanometer resolution grants two-photon polymerization (TPP) 3D printing (*15*) the potential to radically transform microsystem technology, which today is largely constrained to planar structures. However, TPP printing is based on the laser exposure of photosensitive materials, which are most commonly polymers with intrinsically variable optical (*16*) and mechanical properties (*17*) and limited environmental stability. TPP facilitates the in situ 3D printing of complexly shaped polymeric free-form micro- and nanostructures (*18*–*20*) directly on microchips. If the same could be achieved with robust silica glass instead of polymer, the technique could realize major breakthroughs within optoelectrical systems such as superior imaging devices (*18*, *21*), optical MEMS (*10*, *11*), and nanophotonic integrated circuits (*19*, *20*), such as for the development of quantum computers (*22*).

Recently, the TPP printing of silica glass has been demonstrated (*2*, *3*); however, these approaches are still based on particle-loaded sacrificial polymer binders with limited applicability. To remove the binder and fuse the silica particles into solid structures, several day-long sintering procedures under vacuum or inert atmosphere at 1100° to 1300°C are required. These temperatures lie above the melting points of many important engineering semiconductors, such as germanium, cadmium telluride, and indium phosphide, which are some of the most efficient materials for solar cells, infrared and fiber optics, lasers, and photodetectors. The same applies to most metals used in electrical circuits. Thus, traditional particle-based silica glass resins are generally not capable of on-chip manufacturing. The only alternative, postprint assembly of microscale components, involves a multitude of challenges (*19*) and can hardly compete with state-of-the-art assembly routes (*14*) that use orders of magnitude higher throughput with 2D and 2.5D techniques. In addition, particle-based TPP resins limit the printing resolution as features approach the length scale of the dispersed particles. The smallest reported free-standing features that are achieved with particle-derived TPP-printed silica are 0.4 μm in size (*3*); the maximum resolution—i.e., the smallest resolvable spacing of several features—is often [illegible] times as large and has not been reported. This spacing is still insufficient for nanophotonic devices for the visible light spectrum, such as metalenses (*21*), 3D bandgap materials (*23*), and invisibility cloaks (*24*). Standard TPP with organic resins can print down to 100-nm-sized features (*15*). Optimized print setups and precursor chemistries can already push below 10 nm (*15*, *25*), smaller than a single nanoparticle of the existing silica-particle TPP resins. Similar limitations may also apply to the achievable surface quality. Ultimately, the development of dispersions from ever smaller particles is limited, and particle-based approaches may not be able to meet the continuously increasing capabilities of TPP processes.

The thermal decomposition of organic and organic-inorganic hybrid polymers is a promising particle-free alternative to manufacture inorganic materials. This approach is currently being widely studied for the TPP fabrication of a range of micro- and nanoscale ceramics. TPP printing and subsequent heat treatment with organic, preceramic, and sol-gel precursors manufactures 3D nanostructures with feature sizes down to <200 nm in glassy carbon (*26*), silicon oxycarbide (*27*, *28*), and titania (*29*), as well as glass ceramics (*30*, *31*), respectively. The latter can also be visibly transparent and have been used to print optical lenses (*31*–*33*), albeit the optical transmission has not been reported. However, the sol-gel approaches are disadvantageous compared with the particle-loaded resins (*2*, *3*) from a processing perspective. They entail tedious preprint preparations, the hardened gel film state imposes printing constraints, and to densify the final material, the TPP-printed templates are also heat treated at 1000° to 1100°C (*30*–*32*).

Polyhedral oligomeric silsesquioxanes (POSSs) (*34*, *35*) are hybrid organic-inorganic polymers composed of cage-like silicon-oxygen frameworks with a general formula ($SiO_{1.5}$) close to that of fused silica. However, POSS polymers have so far not been used to TPP print silica glass. At their corners, the POSS-cage molecules can bond to a large catalog of organic functional groups to enable polymerization into solids with greater resistance to temperature and oxidation than most purely organic polymers. POSS polymers have been studied for their suitability as templating materials for semiconductors within different lithography techniques (*36*–*38*). More recently, epoxy-functionalized POSS resins (*39*) have successfully been applied in TPP printing. However, the reported efforts still focused on the synthesis of temperature-stable hybrid polymers rather than exploiting the POSS material platform as a precursor to manufacture purely inorganic materials. Thermal decomposition of printed parts has been found to form glass ceramics

[1]Institute of Nanotechnology, Karlsruhe Institute of Technology, 76131 Karlsruhe, Germany. [2]Materials Science and Engineering Department, University of California, Irvine, CA 94550, USA. [3]Edwards Lifesciences, Irvine, CA 92614, USA.
*Corresponding author. Email: jens.bauer@kit.edu

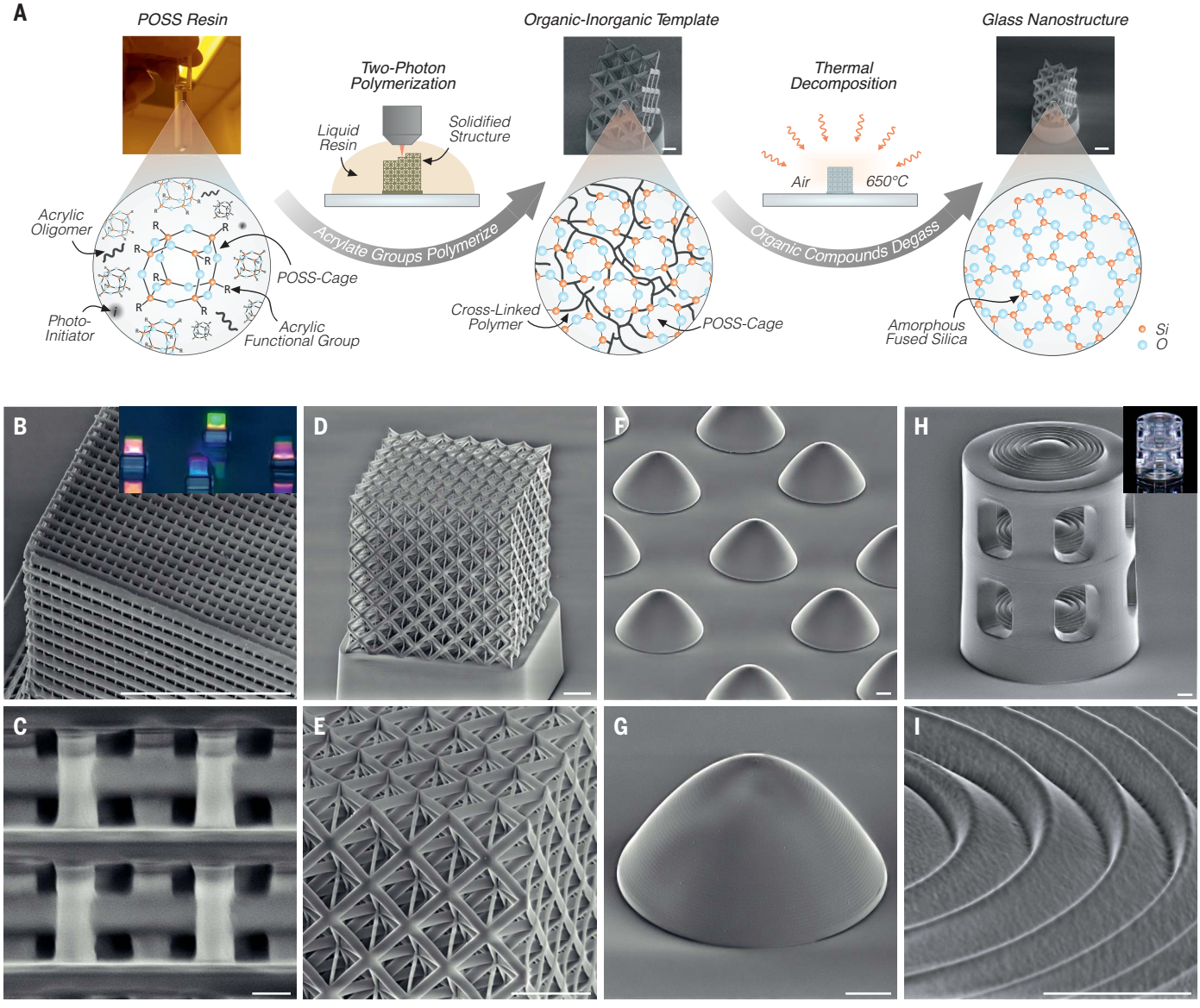


Fig. 1. Fabrication of high-quality fused silica nanostructures from an acrylate-functionalized POSS resin. (**A**) Schematic synthesis through TPP 3D printing and subsequent thermal treatment at 650°C. (**B** to **I**) Micrographs of fused silica structures: (B) woodpile photonic crystal with inset optical true-color blue-violet light reflection (front structure), (C) close-up top view of pattern from 97-nm-wide lines, (D and E) octet nanolattice composed of >5000 beams, (F and G) parabolic microlenses, (H) 150-μm-tall multilens diffractive micro-objective with inset optical micrograph, and (I) close-up view of the nanostructured Fresnel lens element. Scale bar in (C), 100 nm; all other scale bars, 10 μm.

with organic impurities, and no optical properties have been reported (*39*). Like sol-gel precursors, epoxy-functionalized resins also constrain prints because printing is performed within spin-coated gel thin films, which limits structures to low aspect ratios on flat substrates.

We present a sinterless, low-temperature 3D-printing route that fabricates complex transparent fused silica glass nanostructures (Fig. 1). We introduce a particle-free organic-inorganic POSS-glass resin engineered to use acrylate-functionalized POSS chemistry (i) to TPP print high-quality 3D structures in an unconstrained, facile, and reproducible manner and (ii) to convert as-printed polymer templates into high-fidelity, optical-grade SiO_2 nanostructures through low-temperature thermal treatment. We schematically illustrate the composition of our POSS-glass resin, the TPP printing of polymeric templates, and their conversion into fused silica in Fig. 1A.

Resin formulation

Our POSS-glass resin is a negative-tone TPP photoresist composed of three parts, each of which contributes a specific set of functionalities (fig. S1): (i) 89 wt % acrylate-functionalized POSS monomer, (ii) 9 wt % trifunctional acrylic monomer, and (iii) 2 wt % photoinitiator of the α-aminoketone family (*40*). The POSS monomer was the main component, whose POSS-cage cores constituted the silicon-oxygen nanocluster source that enables the SiO_2 conversion. Its acrylic functional groups were essential to achieve high-performance TPP. Acrylate-based resins are the most widely used TPP material class (*41*, *42*) because of their processing ease and wide assortment of functionalities and monomer sizes (*43*). Contrary to epoxy or sol-gel TPP resins, the acrylic reaction kinetics (*44*) allow printing in a liquid state with a high polymerization rate (*45*). However, the rigid structure of POSS monomers generally prevents the formation of sufficiently cross-linked (*15*, *46*) self-supporting

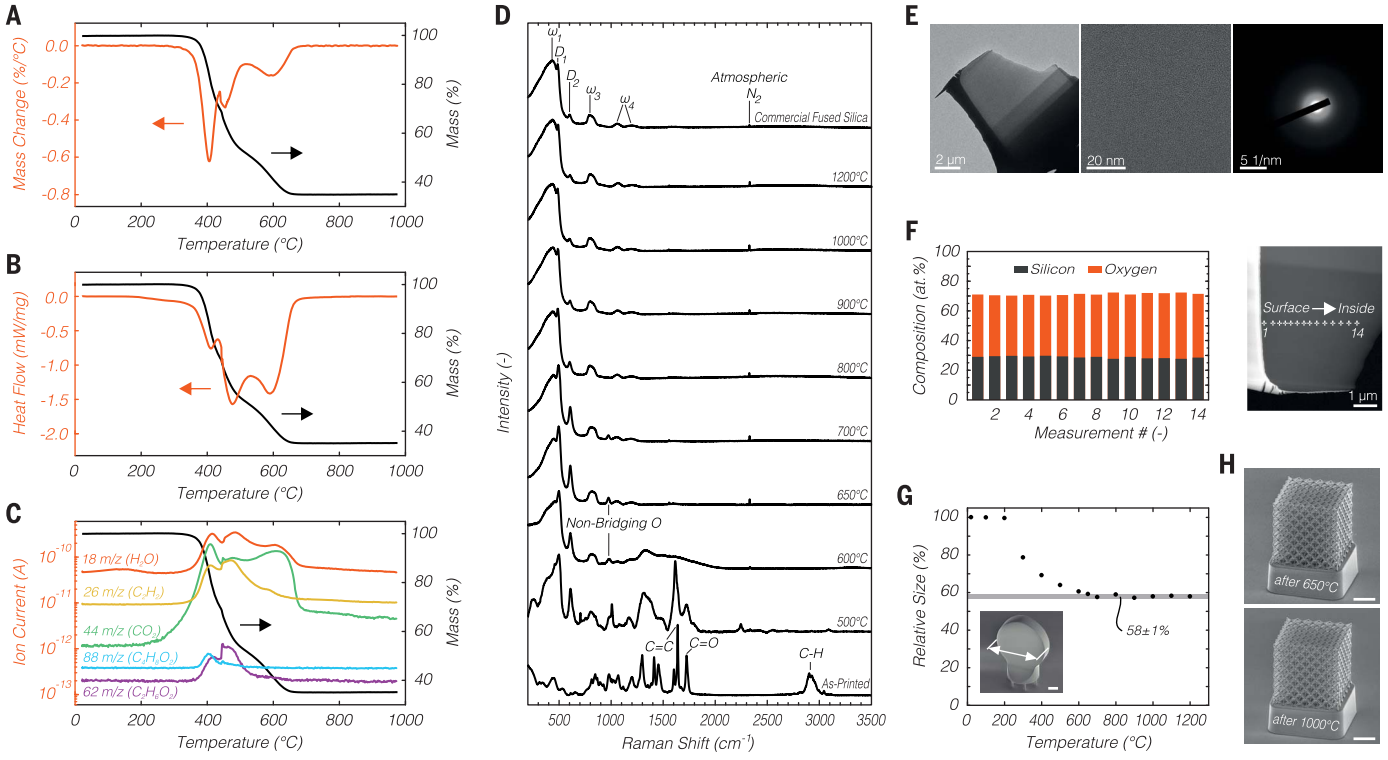


Fig. 2. Materials characterization confirming treatment at 650°C creates pristine fused silica glass. (**A** to **C**) Simultaneous TGA (A), DSC (B), and mass spectrometry (C) illustrate how the polymerized precursor's organic compounds decompose between 350° and 650°C; monitored emissions correspond to the mass/charge ratios (m/z) of the molecular ions of the indicated substances. (**D**) Micro-Raman spectra after treatment at increasing temperatures show the conversion of as-printed templates into fused silica at 650°C. (**E**) Bright-field TEM images and a selected area diffraction pattern confirm a homogeneous amorphous microstructure, free from detectable pores. (**F**) EELS data confirm that the material is composed solely of silicon and oxygen with an atomic ratio closely matching stochiometric SiO_2. (**G**) Measured diameters of disk-shaped specimens (inset) after exposure to increasing temperatures show the linear contraction of as-printed templates as they convert to fused silica; above 650°C, the final POSS glass retains perfect geometrical integrity up to 1200°C, with 58 ± 1% of the as-printed size. (**H**) As-processed fused silica nanolattice before and after high temperature exposure. Scale bars in (G) and (H), 20 µm.

TPP-printed parts. Reported epoxy-POSS TPP resins are limited to 10 to 60 wt % POSS loading (*39*). In our material, the conformational flexibility of the small addition of the long-armed, branched trifunctional acrylate facilitates reproducible TPP printing despite the high POSS loading of 89 wt % and provides important resilience against cracking (*47*). This was key to printing structures with a sufficiently close packing of silicon-oxygen nanoclusters, which successfully converted to dense SiO_2 at low temperatures. Furthermore, the branched trifunctional acrylate's concentration allowed control over the resin's viscosity (*48*). Acting as an eluent modulating the diffusion of radicals and dissolved molecular oxygen, this enabled the resin to print finely resolved features. The chosen photoinitiator induced copolymerization of the resin's acrylic groups through light exposure. We selected it for its efficient radical generation quantum yield, nonlinear absorption, and primary radical reactivities at the excitation wavelength of 780 nm of the TPP system we used (*49*, *50*).

We synthesized the POSS-glass resin by means of a mixing and heating procedure of the above three components (*51*) and obtained a clear, light-yellow liquid that is stable at ambient conditions for several years and readily usable for TPP printing. We optimized the final mixture's compositional ratio to maximize its silicon-oxygen nanocluster content while retaining excellent printability, as confirmed by TPP-printed calibration grids (fig. S2).

Facile fabrication of complex nanostructures

TPP printing of 3D polymer-template structures followed simple standard procedures (*15*) by using a commercial TPP system. Therein, the resin was drop cast onto fused silica or silicon substrates, and the printer's magnification objective was directly immersed in the resin. The objective focused an ultrafast pulsed laser beam into the resin. Within the focal volume, simultaneous absorption of two photons by the photoinitiator molecules results in their homolytic cleavage and the formation of two radicals. These initiated the cross-linking of the monomers' acrylate groups, which transformed the resin into a solid network that was composed of an organic matrix with embedded silicon-oxygen POSS nanoclusters. The 3D structures were printed by in-plane scanning of the focused laser beam by means of galvanometer mirrors and by three-axis motion of the piezoelectric sample stage. In contrast to reported TPP-printed epoxy-functionalized POSS (*39*), preceramic (*29*), and sol-gel (*30*) resins, no pretreatments, restricting immersion oil and spacer layers or similar were required. After printing, a 20-min-long isopropanol alcohol development bath dissolved the remaining uncured resin. The fabricated specimens were either air dried or, for the case of the most delicate structures, supercritically dried to prevent damage from capillary forces.

Moderate thermal treatment (fig. S3) to only 650°C in an air atmosphere converted the as-printed polymer templates to fused silica structures. Accompanied by an isotropic linear contraction of ~40%, the elevated temperature decomposed and degassed the organic compounds, with the atmospheric oxygen removing the remaining elemental carbon. Therein, our POSS templates' densely packed continuous silicon-oxygen molecular networks constituted the crucial feature that circumvents

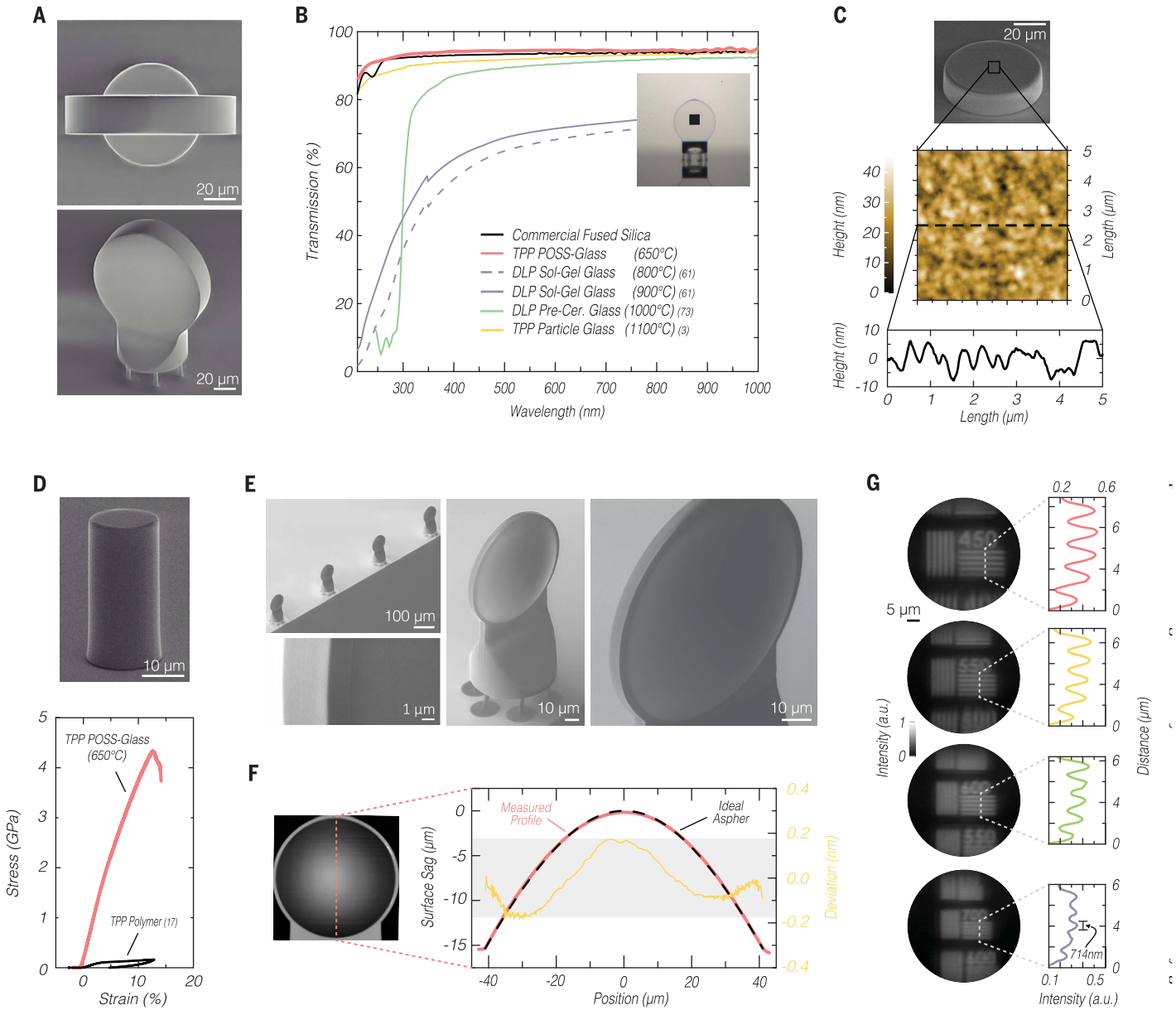


Fig. 3. TPP-printed POSS glass enables the fabrication of high-quality free-form micro-optical elements. (**A**) Free-standing, disk-shaped specimens for optical transmission measurements through UV-Vis-NIR microspectrophotometry. (**B**) Optical transmission data show transparency on par with commercial fused silica and exceeding literature-reported fused silica (*3*, *61*, *73*) from sol-gel, preceramic, and particle precursors, 3D printed through TPP or digital light processing (DLP); indicated temperatures refer to thermal treatments during manufacturing. The inset shows the area where the UV-Vis-NIR signal was collected. (**C**) Atomic force microscopy data from a flat disk show optically smooth surface finish. (**D**) Micropillar and a measured compressive stress-strain curve demonstrating ultrahigh mechanical resilience with 10-fold increased strength and stiffness over TPP-printed polymer (*17*). (**E**) Aspheric aberration–corrected high-precision microlenses as optical device demonstrators. (**F**) Optical profilometry confirms near-ideal accuracy. (**G**) Images formed by the microlenses of a resolution target demonstrate excellent imaging performance; inset contrast intensity profiles show up to 700 lp/mm are resolved. a.u., arbitrary unit.

the extreme temperatures that are otherwise required to sinter discrete silica particles to a continuum (*1*–*3*).

We demonstrate a variety of 3D fused silica glass micro- and nanostructures (Fig. 1, B to I) that outperform the resolution, structure quality, and coverable size scale of previously reported inorganic TPP-printed materials. We fabricated woodpile photonic crystals composed of 97-nm-sized free-standing features (Fig. 1, B and C). This constitutes a fourfold improvement over existing TPP-printed fused silica (*3*) and matches the smallest reported features of inorganic TPP structures (*30*) in general. Moreover, the feature quality we achieved substantially outperforms that of the previously reported comparably resolved structures (*30*). The photonic crystal we synthesized had a rod spacing of 350 nm, which demonstrates the capability to realize nanophotonic structures at wavelengths approaching the ultraviolet (UV) regime (*24*, *52*). The optical micrograph (Fig. 1B, inset) shows the structure reflecting light of a blue-violet color, along with photonic crystals that

adjust colors of longer wavelength by larger rod spacings. Furthermore, we printed pristine nanolattice metamaterials composed of thousands of individual bars (Fig. 1, D and E), smoothly shaped aspherical microlenses (Fig. 1, F and G), and complex mesoscale microobjectives (Fig. 1, H and I) with ~150-μm overall size, which contained diffractive lens elements with nanoscale details. Overall, our POSS-glass process achieved a level of print quality, complexity, and coverable size scale that was previously only realizable with polymeric structures from standard organic resins.

Materials characterization

Our materials characterization confirmed that moderate thermal treatment at only 650°C in air atmosphere successfully converted the POSS resin to pure fused silica. Figure 2 shows the results from combined thermogravimetric analysis (TGA), differential scanning calorimetry (DSC) and mass spectrometry as well as micro-Raman spectroscopy, and transmission electron microscopy (TEM).

Combined TGA, DSC, and mass spectrometry identified the glass conversion of our material to take place between 350° and 650°C (Fig. 2, A to C). The material underwent a total mass loss of ~65%, with three mass derivative peaks at 415°, 480°, and 595°C that correlate with three exothermal peaks of the heat flow data. Each of these peaks corresponded to three consecutive reaction stages that are characteristic of the thermo-oxidative degradation of highly cross-linked acrylic polymers (*53*, *54*). In the first and second stages, these reaction paths include the formation of peroxide groups, followed by random chain scission and volatilization of produced species such as water, carbon dioxide, hydrocarbons, alcohols, and higher-mass species (*53*, *55*). Mass spectrometry of the exhaust gases confirmed this fragmentation as monitored by the molecular ions of acetylene (C_2H_2), 1,2-ethanediol ($C_2H_6O_2$), and methylpropionate ($C_4H_8O_2$). During the first reaction stage, emissions of all the above species were present simultaneously with CO_2 and H_2O. The second stage continued the decomposition; however, no further higher-mass species were formed. In the third and final reaction stage, only CO_2 and H_2O emissions passed through a maximum, with no increase in emissions of monomer-related ions. This indicates the final reaction stage as the complete oxidation of remaining stable hydrocarbon impurities. We confirmed this by a control TGA and DSC experiment in inert atmosphere (fig. S4). The inert decomposition also included the first two reaction stages, which are primarily temperature driven (*54*, *55*); however, it completed without a third stage and formed chars with marked amounts of residual carbon. Above 650°C, neither TGA nor DSC showed any notable further changes, which indicated complete volatilization of all organic constituents and left an inorganic material behind. In general, oxidizing atmospheres accelerated the decomposition processes (*55*). In a pure-oxygen atmosphere, the decomposition of our material completed at ~600°C (fig. S4).

Micro-Raman spectroscopy measurements after thermal treatment at progressively increasing temperatures demonstrated the conversion of as-printed organic-inorganic POSS structures into fused silica (Fig. 2D). As a reference, we provide the spectrum of commercial fused silica. Therein, the ω_1 and ω_3 bands correspond to bending vibration of the $Si(O_{1/2})_4$ tetrahedrons' Si-O-Si bridges, and the ω_4 bands are attributed to the stretching motion of their Si-O bonds (*56*). The D_1 and D_2 lines relate to the symmetric stretching of silicon-oxygen ring molecules (*56*). Distinct from the fused silica signal, the spectrum of as-printed POSS structures was typical of a thermoset, for which the strongest peaks represent the carbon-carbon (1630 cm^{-1}) and carbon-oxygen (1720 cm^{-1}) double bonds, whose intensity ratio can be used to quantify the extent of cross-linking between the acrylic chains (*17*). The signal around 2900 cm^{-1} corresponded to the characteristic aliphatic and aromatic stretching modes of the carbon-hydrogen single bonds (*57*). At 500°C, the organic microstructure had partially disappeared, as demonstrated by the absence of the 2900 cm^{-1} signal. The remaining associated peaks became smaller and notably broadened, which is indicative of increasing disorder. This observation is consistent with the above simultaneous thermal analysis, which confirms the fragmentation and removal of a substantial portion of the material's organic groups in the first two reaction stages. Simultaneously, the typical signal of fused silica below 1000 cm^{-1} began to appear. This shows that the material's silicon-oxygen POSS-cage nanoclusters, which are initially solely connected through the cross-linked organic matrix, directly start to form a continuous inorganic silica network as organic groups decompose and volatilize. Above 600°C, the organic peaks disappeared entirely, and the spectra took the characteristic fused silica shape, which indicated the material had completely transformed into SiO_2 at 650°C. In agreement with the TGA, DSC, and mass spectrometry results, the spectra collected after treatments above 650°C revealed the absence of any further compositional changes and only showed some microstructural reorganization. Between 650° and 800°C, the decreasing intensity of the D_1 and D_2 lines with respect to the ω_1 band indicated the transition of four- and three-membered ring molecules, which may have been inherited from the POSS-cage structure, toward tetrahedrons. The disappearance of the small peak at 972 cm^{-1} above 700°C indicated the elimination of a trace amount of tetrahedral silica with two nonbridging oxygens (*58*). Above 800°C, the spectra of the POSS glass and commercial fused silica were identical, and no further changes were observed up to the maximum temperature tested, 1200°C.

We used TEM to confirm that our POSS glass is pristine SiO_2. We took measurements on a lamella extracted from the center plane of a 10-μm-diameter micropillar. Bright-field TEM micrographs showed a homogeneous amorphous phase without any detectable pores, which we confirmed by selected area diffraction of the interior of the lamella (Fig. 2E). We determined the composition by electron energy loss spectroscopy (EELS) at 14 points along the center axis of the lamella at varying distances from the top surface of the pillar (Fig. 2F). We did not detect impurities, and the material consisted solely of silicon and oxygen, which closely matched stochiometric SiO_2. We measured 29 ± 1 atomic percent (at %) silicon and 71 ± 1 at % oxygen; the typical uncertainties associated with the individual EELS quantifications are on the order of 2 to 4 at % (*59*, *60*).

Although processed at only 650°C, the POSS glass retained perfect geometrical integrity upon high temperature exposure, which is consistent with the demonstrated chemical stability. Dimensional characterizations after exposure to increasing temperatures, from the as-printed polymer-template state up to 1200°C, show the TPP-printed template structures underwent isotropic linear contraction of 42 ± 1% during their thermal conversion. After 650°C, the resulting fused silica retained perfect geometrical integrity up to 1200°C without measurable further shrinkage (Fig. 2G). Correspondingly, even the most delicate nanoarchitectures weathered higher temperatures without any distortion, fusion, or other damage (Fig. 2H).

Despite being processed at considerably lower temperatures, the optical transparency of our 3D-printed POSS glass exceeded that of previously reported additively manufactured forms of fused silica. We conducted UV–visible–near-infrared (UV-Vis-NIR) microspectrophotometry measurements with free-standing, 25-μm-thick disk-shaped specimens that were TPP printed from our POSS-precursor and converted to fused silica at 650°C (Fig. 3A). The POSS glass had excellent optical transmission, on par with commercial fused silica. Across the measurement range from the UV to the NIR spectrum, no absorption bands were present (Fig. 3B). By contrast, the transmission of silica glasses from sol-gel precursors (*61*) that have been 3D printed at the macroscale and processed at 800°C are reportedly limited to ~70% and almost completely opaque in the UV range. Also, the particle-derived TPP-printed fused silica (*3*), sintered at 1100°C, did not quite reach the transmission of the POSS glass. Consistent with the demonstrated

structural thermal stability, exposure to 1000°C did not notably alter the transmission of our material (fig. S5).

The POSS glass further achieves an optically smooth surface finish and ultrahigh mechanical strength. Atomic force microscopy on a flat disk measured a root mean-square (RMS) roughness of 5.5 nm (Fig. 3C). Compression of POSS-glass micropillars treated at 650°C showed elastic-plastic behavior with notable plastic deformability and 4.0 ± 0.2 GPa strength (Fig. 3D). Granted by the small scale, which limits the probability of preexisting flaws, this value is four times as high as the compressive strength of bulk UV-grade fused silica (*62*). Comparably beneficial mechanical behavior has been reported for opaque TPP-derived pyrolytic carbon (*63*, *64*). Treatment at 1000°C was found to further increase the strength of the POSS glass (fig. S6) (*51*). The measured Young's moduli of up to 67 GPa were within the range of common forms of dense fused silica (*65*). Our POSS glass has more than an order of magnitude higher strength and stiffness (*17*) than the state-of-the-art polymers that hold the current benchmark for TPP-printed high-fidelity micro-optics.

Optical device demonstration

We demonstrate our material enables the fabrication of free-form fused silica glass micro-optical elements with excellent optical performance (Fig. 3, E to G). Lens systems for imaging and beam shaping are among the most important micro-optical devices. However, the highest-precision glass microlenses (*66*) have thus far been fabricated by subtractive top-down approaches, which are limited to simple designs that, for example, cannot correct for aberrations. Here, we TPP printed planoconvex fused silica microlenses with an aspheric profile, which was numerically optimized to correct for spherical aberrations. The final POSS-glass lenses, with a base diameter of 82 μm and 15 μm sagittal (sag) height, were treated at 650°C and were of pristine structural quality with finely resolved nanoscale contours and smooth surfaces (Fig. 3E). We conducted optical profilometry measurements (Fig. 3F) to confirm the excellent shape accuracy with a peak-to-valley deviation of the lens profile with respect to the aspheric design of ±175 nm. The measured RMS roughness was 8.1 nm (fig. S7), which translates to an RMS-to-sag ratio of 0.05%. These values are on par with the latest achievements with polymeric TPP-printed lenses (*67*)—which report shape deviations of 0.1 to 0.5 μm and 4- to 15-nm RMS roughness—and within the specifications of the highest-quality commercial glass microlenses fabricated by reactive ion etching or ion exchange techniques, for which RMS/sag ratios of 0.01 to 0.09% are reported (*66*). Optical resolution measurements with a 1951 USAF–type resolution target under white light illumination demonstrated the excellent imaging performance of our microlenses. Figure 3G shows images formed by the microlenses of the target, which we projected onto a complementary metal-oxide semiconductor camera sensor with an optical microscope system. The visible labels indicate the respective pattern elements' number of line pairs per millimeter (lp/mm), and the inset graphs show the measured intensity contrast between adjacent line elements. We were able to resolve up to 700 lp/mm with ~6% remaining contrast with our microlenses, meaning that 714-nm-sized features remained distinguishable. This approximately corresponds to group 9, element 4 of the 1951 USAF target, which notably outperforms previously reported inorganic planoconvex microlenses that were TPP printed from sol-gel precursors (*31*, *33*, *68*), whose resolution capability is reported within groups 4 to 7 of the 1951 USAF target.

Conclusion

The POSS-glass TPP 3D printing route may help redefine the paradigm for the free-form manufacturing of silica glass and overcome the fundamental limitations of the particle-based approaches that have dominated the field. The crucial innovation of our approach lies in the developed POSS resin, which, contrary to a particle-loaded binder, is not sacrificial but itself polymerizes into a continuous silicon-oxygen molecular network. Hence, the material circumvents the extreme temperatures that are otherwise required to sinter discrete silica particles to a continuum (*1*–*4*), which enables conversion to fused silica at only 650°C. By constituting a temperature reduction of ~500°C with respect to the best reported TPP approaches (*2*, *3*), this brings the free-form synthesis of silica glass below the melting points of essential materials for microsystems technology, including silver, copper, gold, and aluminum. This represents a breakthrough that enables the evolution of on-chip 3D printing of transparent matter from state-of-the-art organic polymers to resilient optical-grade fused silica. Similarly, our POSS-glass process breaches the critical resolution limit to realize free-form silica nanophotonic devices in the visible light spectrum (*24*, *52*) while simultaneously being capable of manufacturing hundreds of micrometer-sized high aspect ratio structures. Overall, we achieved attractive combinations of optical quality, mechanical resilience, processing ease, and coverable size scale and set the benchmark for the micro- and nanoscale 3D printing of inorganic solids in general.

The potential fields of application of our POSS glass are widespread, ranging from micro-optics and photonics, MEMS, and microfluidic and biomedical devices to fundamental research. Examples include aging- and environment-resistant ultracompact imaging systems (*18*) for applications from medical endoscopes to consumer electronics; superior-accuracy sensors, whose 3D design today typically limits them to centimeter-sized devices for costly applications, such as deep space missions (*69*); and beam-shaping elements (*19*) for the end faces of diode lasers, which are the basic components for most high-power laser applications but whose output power cannot be sustained by polymers. In fracture mechanics research, fused silica is a model material (*70*); however, specimen geometries are often nontrivial and challenging to manufacture. The design freedom of our POSS-glass process enables us to systematically investigate fracture mechanisms at the smallest scale, which includes metamaterials, such as nanolattices (*71*, *72*).

REFERENCES AND NOTES

1. F. Kotz *et al*., *Nature* **544**, 337–339 (2017).
2. F. Kotz *et al*., *Adv. Mater.* **33**, e2006341 (2021).
3. X. Wen *et al*., *Nat. Mater.* **20**, 1506–1511 (2021).
4. M. Mader *et al*., *Science* **372**, 182–186 (2021).
5. H. Zappe, *Fundamentals of Micro-Optics* (Cambridge Univ. Press, 2010).
6. X. Q. Liu *et al*., *Laser Photonics Rev.* **13**, 1800272 (2019).
7. J. C. Knight, T. A. Birks, P. S. J. Russell, D. M. Atkin, *Opt. Lett.* **21**, 1547–1549 (1996).
8. A. J. Ikushima, T. Fujiwara, K. Saito, *J. Appl. Phys.* **88**, 1201–1213 (2000).
9. A. S. Sinitskii, A. V. Knot'ko, Y. D. Tretyakov, *Solid State Ion.* **172**, 477–479 (2004).
10. M. C. Wu, O. Solgaard, J. E. Ford, *J. Lightwave Technol.* **24**, 4433–4454 (2006).
11. T. Nagourney, S. Singh, B. Shiari, J. Y. Cho, K. Najafi, in *2018 IEEE Micro Electro Mechanical Systems (MEMS)* (IEEE, 2018), pp. 1000–1003.
12. D. Zhang, X. Liu, J. Qiu, *Front. Optoelectron.* **14**, 263–277 (2021).
13. P. Neužil, S. Giselbrecht, K. Länge, T. J. Huang, A. Manz, *Nat. Rev. Drug Discov.* **11**, 620–632 (2012).
14. W. Menz, J. Mohr, O. Paul, *Microsystem Technology* (Wiley, 2001).
15. T. Baldacchini, *Three-Dimensional Microfabrication Using Two-Photon Polymerization* (Elsevier, ed. 2, 2019).
16. M. Schmid, D. Ludescher, H. Giessen, *Opt. Mater. Express* **9**, 4564 (2019).
17. J. Bauer, A. Guell Izard, Y. Zhang, T. Baldacchini, L. Valdevit, *Adv. Mater. Technol.* **4**, 1900146 (2019).
18. T. Gissibl, S. Thiele, A. Herkommer, H. Giessen, *Nat. Photonics* **10**, 554–560 (2016).
19. P.-I. Dietrich *et al*., *Nat. Photon.* **12**, 241–247 (2018).
20. M. Blaicher *et al*., *Light Sci. Appl.* **9**, 71 (2020).
21. F. Balli, M. Sultan, S. K. Lami, J. T. Hastings, *Nat. Commun.* **11**, 3892 (2020).
22. J. Wang, F. Sciarrino, A. Laing, M. G. Thompson, *Nat. Photon.* **14**, 273–284 (2020).
23. G. von Freymann *et al*., *Adv. Funct. Mater.* **20**, 1038–1052 (2010).
24. J. Fischer, T. Ergin, M. Wegener, *Opt. Lett.* **36**, 2059–2061 (2011).
25. Z. Gan, Y. Cao, R. A. Evans, M. Gu, *Nat. Commun.* **4**, 2061 (2013).
26. J. Bauer, A. Schroer, R. Schwaiger, O. Kraft, *Nat. Mater.* **15**, 438–443 (2016).
27. J. Bauer *et al*., *Matter* **1**, 1547–1556 (2019).
28. L. Brigo *et al*., *Adv. Sci.* **5**, 1800937 (2018).
29. A. Vyatskikh, R. C. Ng, B. Edwards, R. M. Briggs, J. R. Greer, *Nano Lett.* **20**, 3513–3520 (2020).
30. D. Gailevičius *et al*., *Nanoscale Horiz.* **4**, 647–651 (2019).
31. Z. Hong, P. Ye, D. A. Loy, R. Liang, *Optica* **8**, 904–910 (2021).
32. D. Gonzalez-Hernandez *et al*., *Photonics* **8**, 577 (2021).

33. Z. Hong, P. Ye, D. A. Loy, R. Liang, *Adv. Sci.* **9**, e2105595 (2022).
34. S. W. Kuo, F. C. Chang, *Prog. Polym. Sci.* **36**, 1649–1696 (2011).
35. J. J. Schwab, J. D. Lichtenhan, *Appl. Organomet. Chem.* **12**, 707–713 (1998).
36. E. Tegou *et al*., *Chem. Mater.* **16**, 2567–2577 (2004).
37. J. H. Moon, J. S. Seo, Y. Xu, S. Yang, *J. Mater. Chem.* **19**, 4687–4691 (2009).
38. Y. Xu, X. Zhu, S. Yang, *ACS Nano* **3**, 3251–3259 (2009).
39. G. Fang, H. Cao, L. Cao, X. Duan, *Adv. Mater. Technol.* **3**, 1700271 (2018).
40. H. F. Gruber, *Prog. Polym. Sci.* **17**, 953–1044 (1992).
41. L. H. Nguyen, M. Straub, M. Gu, *Adv. Funct. Mater.* **15**, 209–216 (2005).
42. T. Baldacchini *et al*., *J. Appl. Phys.* **95**, 6072–6076 (2004).
43. C. Decker, *Acta Polym.* **45**, 333–347 (1994).
44. G. Odian, *Principles of Polymerization* (Wiley, ed. 4, 2004).
45. C. Decker, *Prog. Polym. Sci.* **21**, 593–650 (1996).
46. S. Maruo, J. T. Fourkas, *Laser Photonics Rev.* **2**, 100–111 (2008).
47. Z. Czech, J. Kabatc, M. Bartkowiak, K. Mozelewska, D. Kwiatkowska, *Polymers* **12**, 2617 (2020).
48. T. Zandrini *et al*., *Opt. Mater. Express* **9**, 2601–2616 (2019).
49. Z. Tomova, N. Liaros, S. A. Gutierrez Razo, S. M. Wolf, J. T. Fourkas, *Laser Photonics Rev.* **10**, 849–854 (2016).
50. Q. Hu *et al*., *Addit. Manuf.* **51**, 102575 (2022).
51. Materials and methods are available as supplementary materials online.
52. M. Khorasaninejad *et al*., *Science* **352**, 1190–1194 (2016).
53. A. Goswami, G. Srivastava, A. M. Umarji, G. Madras, *Thermochim. Acta* **547**, 53–61 (2012).
54. L. Li, R. Liang, Y. Li, H. Liu, S. Feng, *J. Colloid Interface Sci.* **406**, 30–36 (2013).
55. V. V. Krongauz, *Thermochim. Acta* **503–504**, 70–84 (2010).
56. K. Mishchik, thesis, Université Jean Monnet - Saint-Etienne (2012).
57. T. Baldacchini, M. Zimmerley, C.-H. Kuo, E. O. Potma, R. Zadoyan, *J. Phys. Chem. B* **113**, 12663–12668 (2009).
58. P. McMillan, *Am. Mineral.* **69**, 622–644 (1984).
59. G. Bertoni, J. Verbeeck, *Ultramicroscopy* **108**, 782–790 (2008).
60. N. Miyajima *et al*., *J. Microsc.* **238**, 200–209 (2010).
61. I. Cooperstein, E. Shukrun, O. Press, A. Kamyshny, S. Magdassi, *ACS Appl. Mater. Interfaces* **10**, 18879–18885 (2018).
62. R. N. Widmer *et al*., *Mater. Des.* **204**, 109670 (2021).
63. A. Albiez, R. Schwaiger, *MRS Adv.* **4**, 133–138 (2019).
64. J. Bauer, M. Sala-Casanovas, M. Amiri, L. Valdevit, *Sci. Adv.* **8**, eabo3080 (2022).
65. S. Bruns, K. E. Johanns, H. U. R. Rehman, G. M. Pharr, K. Durst, *J. Am. Ceram. Soc.* **100**, 1928–1940 (2017).
66. H. Ottevaere *et al*., *J. Opt. A Pure Appl. Opt.* **8**, S407–S429 (2006).
67. L. Siegle, S. Ristok, H. Giessen, *Opt. Express* **31**, 4179–4189 (2023).
68. D. Gonzalez-Hernandez *et al*., *Photonics* **8**, 577 (2021).
69. D. M. Rozelle, in *Proceedings of the 19th AAS/AIAA Space Flight Mechanics Meeting* (AAS/AIAA, 2009), pp. 1157–1178.
70. S. M. Wiederhorn, *J. Am. Ceram. Soc.* **52**, 99–105 (1969).
71. J. Bauer *et al*., *Adv. Mater.* **29**, 1701850 (2017).
72. A. J. D. Shaikeea, H. Cui, M. O'Masta, X. R. Zheng, V. S. Deshpande, *Nat. Mater.* **21**, 297–304 (2022).
73. D. G. Moore, L. Barbera, K. Masania, A. R. Studart, *Nat. Mater.* **19**, 212–217 (2020).

ACKNOWLEDGMENTS

The authors gratefully acknowledge L. Valdevit, T. Aoki, and D. Fishman at the University of California, Irvine for providing laboratory and equipment access, for assistance with EELS characterization, and for enriching discussions, respectively. We are very thankful to J. Burdett and CRAIC Technologies, Inc., for the assistance with conducting microspectrophotometry measurements, as well as to R. Thelen and S. Hengsbach at the Karlsruhe Institute of Technology for their support with the optical profilometry and the image resolution measurements. TEM imaging was performed at the UC Irvine Materials Research Institute (IMRI), which is supported in part by the National Science Foundation through the UC Irvine Materials Research Science and Engineering Center (DMR-2011967). Use of the FEI Quanta 3D FEG dual-beam (SEM/FIB) is funded in part by the National Science Foundation Center for Chemistry at the Space-Time Limit (CHE-0802913). **Funding:** The research has been funded by the Deutsche Forschungsgemeinschaft (DFG; German Research Foundation) (grant BA 5778/2-1), as well as by the German Federal Ministry of Education and Research (BMBF) and the Baden-Württemberg Ministry of Science through the university of excellence measure KIT Future Fields – Young Investigator of the Karlsruhe Institute of Technology (KIT), as part of the Excellence Strategy of the German Federal and State Governments. Additionally, the research was supported by the DFG under Germany's Excellence Strategy through the Excellence Cluster '3D Matter Made to Order' (EXC-2082/1- 390761711). **Author contributions:** J.B. and T.B. conceptualized the research. T.B. and J.B. synthesized the raw material, and J.B. developed the manufacturing process steps. J.B. and C.C. designed the manufactured specimens, and J.B. carried out fabrication efforts. C.C. conducted TEM analyses and the optical lens design and optimization. J.B. performed all other experimental characterizations. J.B., C.C., and T.B. interpreted results, and J.B. wrote the manuscript. **Competing interests:** A patent application has been filed under the serial number 63/339,241 with the US Patent and Trademark office. The authors declare no other competing interests. **Data and materials availability:** All data are available in the main text or the supplementary materials. **License information:** Copyright © 2023 the authors, some rights reserved; exclusive licensee American Association for the Advancement of Science. No claim to original US government works. https://www.science.org/about/science-licenses-journal-article-reuse

SUPPLEMENTARY MATERIALS

science.org/doi/10.1126/science.abq3037
Materials and Methods
Supplementary Text
Figs. S1 to S7
Reference (*74*)

Submitted 30 March 2022; resubmitted 20 March 2023
Accepted 12 April 2023
10.1126/science.abq3037

BIOSENSING

Miniature magneto-mechanical resonators for wireless tracking and sensing

Bernhard Gleich[1], Ingo Schmale[1], Tim Nielsen[1], Jürgen Rahmer[1]*

Sensor miniaturization enables applications such as minimally invasive medical procedures or patient monitoring by providing process feedback in situ. Ideally, miniature sensors should be wireless, inexpensive, and allow for remote detection over sufficient distance by an affordable detection system. We analyze the signal strength of wireless sensors theoretically and derive a simple design of high-signal resonant magneto-mechanical sensors featuring volumes below 1 cubic millimeter. As examples, we demonstrate real-time tracking of position and attitude of a flying bee, navigation of a biopsy needle, tracking of a free-flowing marker, and sensing of pressure and temperature, all in unshielded environments. The achieved sensor size, measurement accuracy, and workspace of ~25 centimeters show the potential for a low-cost wireless tracking and sensing platform for medical and nonmedical applications.

The rise of minimally invasive procedures has created a need for tracking medical instruments inside the human body, which is currently satisfied by cabled electromagnetic trackers (*1*), optical tracking approaches based on cameras (*2*) or optical fibers (*3*), imaging-based markers (*4*), and wireless radiofrequency (RF) markers (*5*). Specific drawbacks of each method, however, limit their general usability. Not all body locations can be reached with a wire, an optical line of sight is usually not available inside the human body, imaging equipment is costly or may use harmful radiation, and wireless RF markers require a minimal size of roughly 10 mm to accommodate an antenna for communication with a detector outside the body (*5*). Another field that suffers from current technology limitations is the data-driven evaluation of physiological parameters (*6*), e.g., for early detection of disease but also for monitoring patients at home to reduce time in the hospital (*7*). In these applications, small low-cost sensors are required to continuously monitor and report physiological parameters not only from the surface (*8*) but also from inside the human body. Based on theoretical insights, we designed a technology platform that can address these needs by combining existing technologies with miniaturized sensors ~1 mm in size. The platform may serve many applications, e.g., the navigation of surgical devices and catheters (*2*), home monitoring of blood pressure (*9*), radiation-free gastric emptying studies (*10*), controlling oral medication adherence (*11*, *12*), monitoring insect behavior (*13*, *14*), or labeling of goods with sensors acting as micro radiofrequency identification (RFID) tags (*15*).

[1]Philips Research, Hamburg, Germany.

*Corresponding author. Email: juergen.rahmer@philips.com

The basic concept of our magneto-mechanical resonator (MMR) is displayed in Fig. 1A. The resonator consists of two spherical NdFeB magnets (*16*), one fixed to the cylindrical housing and the other suspended from a thin filament. The suspended sphere is held in place by the magnets' mutual attractive force, which surpasses the gravitational force by 3 orders of magnitude. The torque exerted by the fixed magnet's field drives the magnetic moments into an antiparallel alignment. To start a rotational oscillation, an external magnetic field pulse is applied whose torque creates an angular deflection of the suspended sphere (movie S1 and Fig. 1A, white double arrow). The oscillation frequency is determined by the restoring torque provided by the fixed sphere and thus depends on the distance between the spheres. The principle of our MMR detection system is described in Fig. 1B. It generates current pulses that are transmitted through electromagnetic coils (Fig. 1C) to excite the MMR oscillation. The oscillating magnetic moment then induces a voltage in these coils which, after amplification, represents the received signal. The low friction in the MMR filament bearing translates into a slow signal decay, so that short excitation periods can alternate with long windows for signal acquisition. Figure 1D displays the voltage induced in one of the 16 receive coils by an MMR resonating at 2.2 kHz. It is repeatedly excited by short pulse trains. Before each re-excitation, the system performs a real-time evaluation of the acquired data to adjust excitation pulse frequency, phase, and amplitude for optimal buildup of the MMR oscillation. The signals obtained from the different coils encode spatial position and orientation of the MMR. Because the planar oscillation of the magnetization vector creates two orthogonal signal components (see supplementary materials), the position and full orientation information, i.e., 6 degrees of freedom (DoF), can be reconstructed using the known spatial sensitivity profiles of the coils.

The signal amplitude distribution over the coils is used for tracking, while the frequency of the MMR signal does not carry spatial information. It can be used to measure a physical parameter that changes distance between the two magnetic spheres and thus modulates the oscillation frequency. Examples are temperature through thermal expansion or pressure through compressible housing. Materials that respond to radiation or certain chemicals enable dosimeters or chemical sensors, respectively.

Results

To highlight the small marker footprint, a bee equipped with an MMR (~1.5 mg) is tracked in real time while walking and flying at distances up to 200 mm from the coil array (Fig. 2 and movies S2 and S3). The raw measurement rate is ~40 Hz and each measurement delivers the bee's momentary position (x, y, z) and attitude (pitch, yaw, roll), i.e., 6-DoF information. According to both the tracking data and camera view, the flying bee achieved velocities up to 600 mm per second.

For demonstrating medical navigation, an MMR is integrated in a stylet that is inserted in a curved biopsy needle (Fig. 3A). Because of the low resonance frequency of 2.2 kHz, the titanium alloy of the needle only weakly attenuates the MMR signal. Therefore, accurate needle tip tracking over the volume of a gelatin phantom (Fig. 3B, diameter 135 mm) is possible, with ~140 mm distance between the needle and coil array. The 6-DoF information enables accurate navigation of the needle toward a target (Fig. 3C and movie S4). Navigation could be fully based on a "roadmap" provided by a medical imaging system whose frame of reference is aligned with the tracking system. No line of sight to the needle tip is required and the camera view has only been included for reference. To simulate tracking of an ingestible marker during gastrointestinal passage, an untethered MMR is localized while flowing through a winding tube phantom (fig. S5 and movie S7).

To demonstrate sensing, a sealed MMR pressure sensor is subjected to pressure changes (Fig. 4). The diffusion-tight metallic housing (Fig. 4A) is compressible, similar to a common aneroid barometer. Sensitivity and measurement range of the sensor can be tuned through the stiffness of the housing. The sensor uses two oscillating spheres to reduce sensitivity to static magnetic background fields. Figure 4B shows the resonance frequency extracted from the measured signal while pressure changes are applied manually using a syringe. For reference, the pressure measured by a commercial pressure sensor is plotted in Fig. 4C, showing that frequency directly represents pressure. A pressure range of 400 mbar (300 mmHg) is

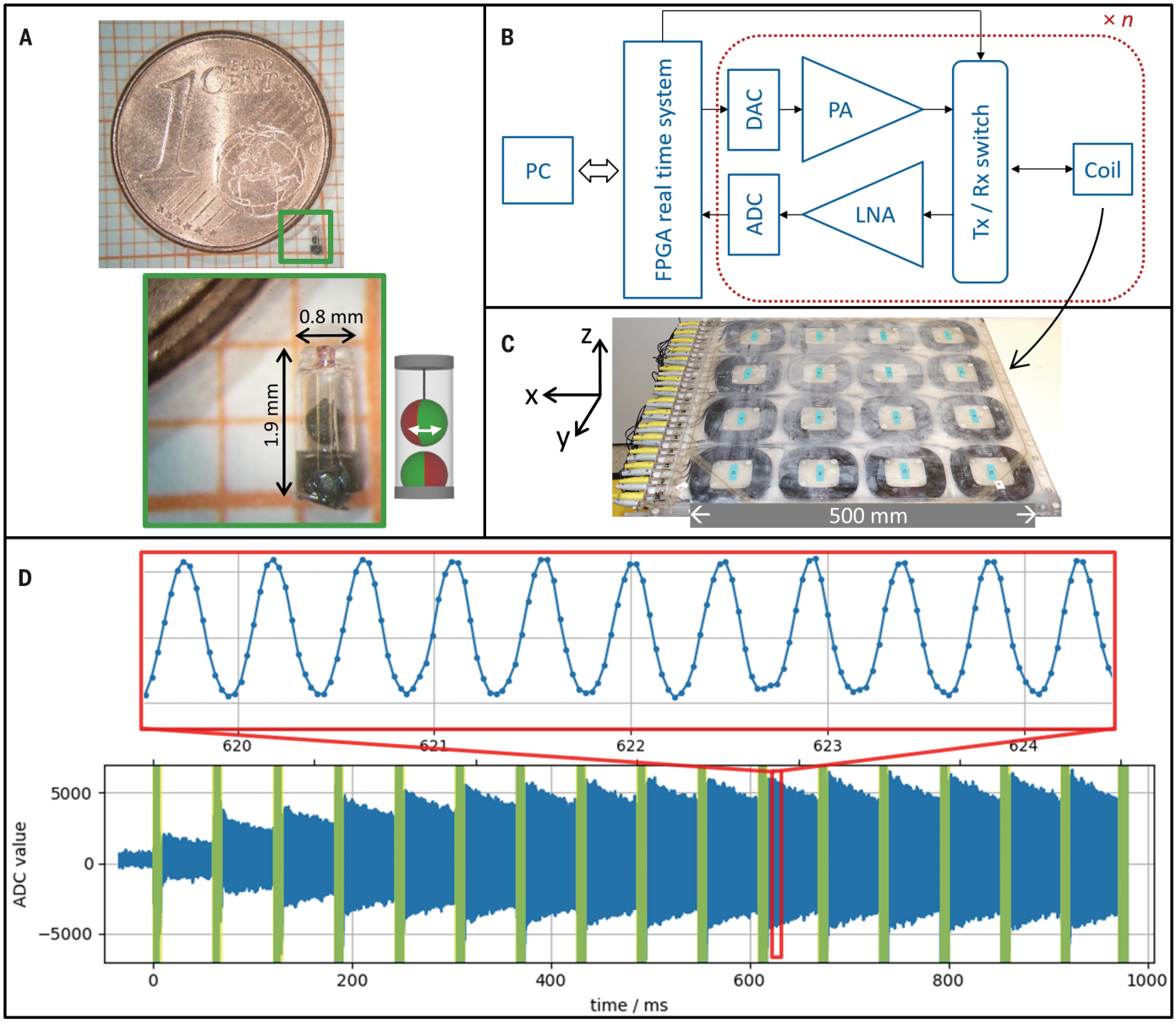


Fig. 1. MMR system components and signal response. (**A**) MMR demonstrator in relation to a coin (1 Euro Cent, diameter 16.25 mm) and sketch of its design. The suspended magnetic sphere (diameter 0.5 mm) can perform a rotational oscillation (white double arrow, see movie S1) about the long axis of the cylinder, which has a volume of 0.96 mm^3. In equilibrium, the spheres have antiparallel alignment (red, magnetic north pole; green, south pole). (**B**) Schematic of transmit and receive (Tx and Rx, respectively) detection system with *n* channels. A field-programmable gate array (FPGA) is used for real-time control of the Tx and Rx data streams. The transmit pulse trains are generated by digital-to-analog converters (DAC) and sent through power amplifiers (PA) to the coils of the array. The receive signals pass through low-noise amplifiers (LNA) to the analog-digital converters (ADC) connected to the FPGA. A switch protects the receive path during application of the excitation pulses. (**C**) 4 × 4 coil array used for MMR excitation and detection of its spatial signal profile. (**D**) Overview and magnification of a typical MMR time signal. Brief excitation windows (overlaid by yellow-green boxes) alternate with receive periods during which signal decays. Starting from equilibrium, excitation pulses are played repeatedly with correct timing to build up the oscillation amplitude over several transmit and receive cycles.

covered, which is sufficient for a blood pressure sensor (*9*) and leaves room for pressure offsets as a result of different geographic altitudes. Sensitivity of the sensor is 0.34 Hz per mbar. Figure S4 and movie S5 show that the tracking marker of the needle navigation experiment can also be used for measuring temperature.

Scaling Laws

The experiments demonstrate MMR tracking and sensing using millimeter-sized devices. This miniaturization was achieved by designing the MMRs for maximal signal. For comparison with existing technology, we compare the signal of MMRs with conventional passive RF circuits. RF circuits are also called LC resonators because the resonant circuit contains an inductor L and a capacitor C, with the inductor acting as an antenna (circuit diagram in fig. S3A) (*5*, *9*). For generating a signal that is detectable during the acquisition phase, MMRs and LC resonators must first be driven to sufficiently high oscillation amplitudes using excitation fields of amplitude B_1 at

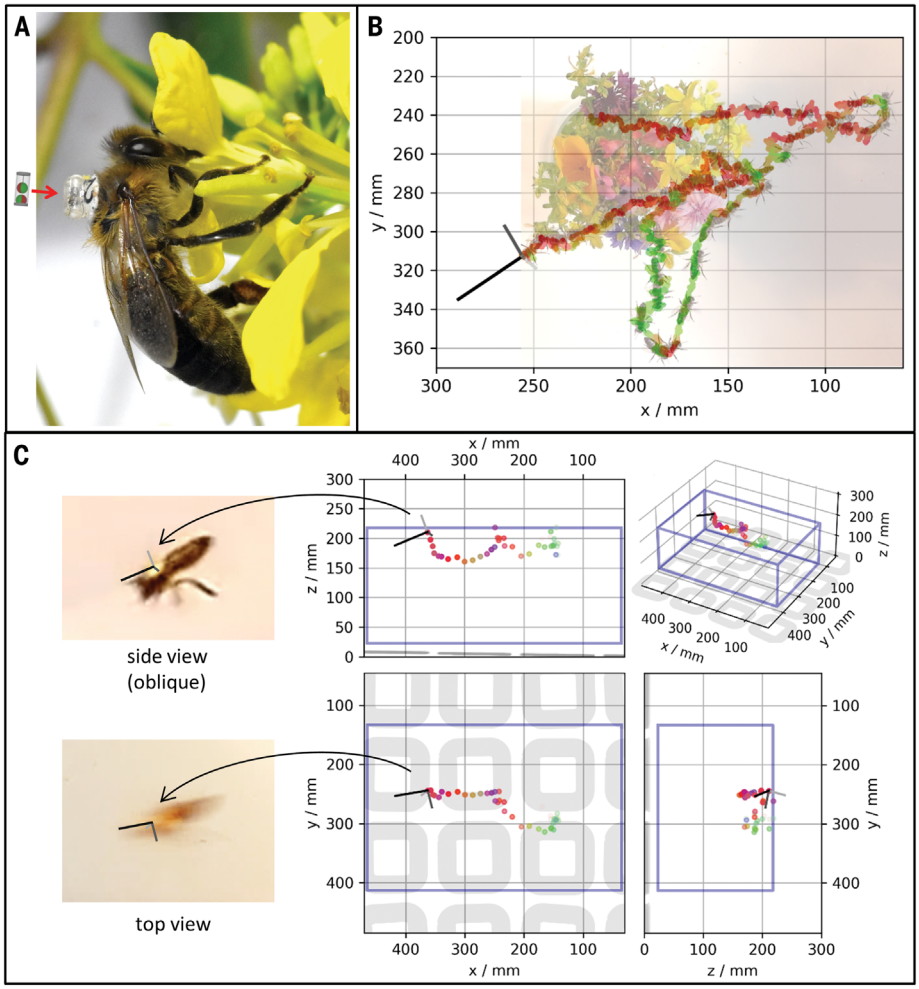


Fig. 2. Bee tracking experiments. (**A**) Honeybee equipped with an MMR marker. (**B**) Tracked path of a bee walking upside down below the transparent lid of a box garnished with a bunch of meadow flowers. The lid is ~20 cm above the planar 4 × 4 coil array used for detection. The path of the bee reconstructed from the MMR signal is plotted with an overlay of images extracted from a video sequence (see movie S2). The black and gray lines indicate the bee's attitude in space for the last displayed measurement, and the previous orientations of the long bee axis (black line) are color coded in the plotted path (red, green, and blue lines indicate bee axis aligned along the *x*, *y*, and *z* directions, respectively). (**C**) Brief segment of a tracking experiment of a flying bee. (Right) The graphs show orthogonal projections of the reconstructed bee positions to visualize the 3D flight path relative to the box (indicated by violet lines). From each measurement, position and attitude of the bee is obtained as shown by the lines plotted at the last position (black, long axis of bee; dark gray, lateral axis; light gray, vertical axis). (Left) Extracted movie frames show the good correlation of the attitude obtained from MMR tracking with the attitude seen by the two cameras.

the device resonance frequency f_0. The dominant limiting factor to the applicable field amplitude is the rate of field change $R = 2\pi f_0 B_1$ that describes the magnitude of field change per time. R determines how much voltage is induced in surrounding materials and is thus restricted by safety limits on touch voltages on metallic surfaces and by physiological limits such as peripheral nerve stimulation and tissue heating (*17*, *18*). To quantify the achievable signal, we introduce a normalized device signal Σ as a function of rate R and radius r of the field generating element in the wireless device.

For MMRs, r is the radius of the oscillating spherical magnet (cf. Figure 5A) and the key finding is the proportionality:

$$\Sigma_{MMR} \propto R^{\frac{1}{3}} r^{\frac{7}{3}} \quad (1)$$

For LC resonators, r is the outer radius of the coil element (cf. Figure 5B) and the device signal scales as:

$$\Sigma_{LC} \propto R\, r^5 \quad (2)$$

The complete formulae and their derivation are found in the supplementary materials.

Figure 5C displays device signals Σ_{MMR} and Σ_{LC} as a function of r for different rates of field change R. In view of safety regulations, a rate of $R \approx 1000$ mT/s at the device position is assumed to be the highest tolerable rate in the frequency range between a few kilohertz and 100 MHz. The combination of this limit with a minimal detectable signal threshold leads to triangular regions in the plots, indicating the signal and size combinations which the respective technology can provide. For LC resonators the triangular operating region is shaded in blue whereas the region for MMR devices is shaded in green. According to the scaling laws, the operating region for the MMRs extends to smaller device sizes. The needle tracking experiment is indicated as "MMR." Because of power limitations of the transmit amplifiers of our detection system, it does not fully exploit the theoretical size reduction potential for this signal level. For comparison, an LC resonator would need to be almost one order of magnitude larger in linear dimension r to reach the same signal level.

For sensing applications, information is encoded in frequency and therefore frequency resolution Δf relates to measurement accuracy. For assessing sensor performance, the device signal Σ must thus be weighted with a quality function ζ coupled to frequency resolution, as described in the methods section. The respective products $\Sigma \cdot \zeta$ are plotted in Fig. 5D, showing that the relative miniaturization potential of MMR technology compared with LC technology is even higher for sensors than for markers.

Discussion and Conclusion

MMR technology enables miniaturization of wireless markers and sensors by ~1 order of magnitude in the linear dimension compared with existing LC resonator technology; the required field generator and detection system have a similar footprint. The marker used in the needle tracking experiment has a length of 1.9 mm whereas an LC-based product with similar workspace has a length of 8 mm (*5*). Commercial miniature RFID tags used in the bee experiments (*13*) have a size similar to that of the MMR but provide so little signal that they can only be detected up to a few millimeters. The MMR pressure sensor has a length of 1.8 mm compared with 11 mm for the coil element of a commercial miniature pressure sensor (*9*).

Miniaturization is enabled by the high MMR signal, which results from several aspects (see eq. S1 in materials and methods): First, the high magnetization of NdFeB permanent magnets (*16*) leads to an efficient energy transfer to and from the MMR. Second, the low dissipation in the filament minimizes energy losses and results in very high quality factors.

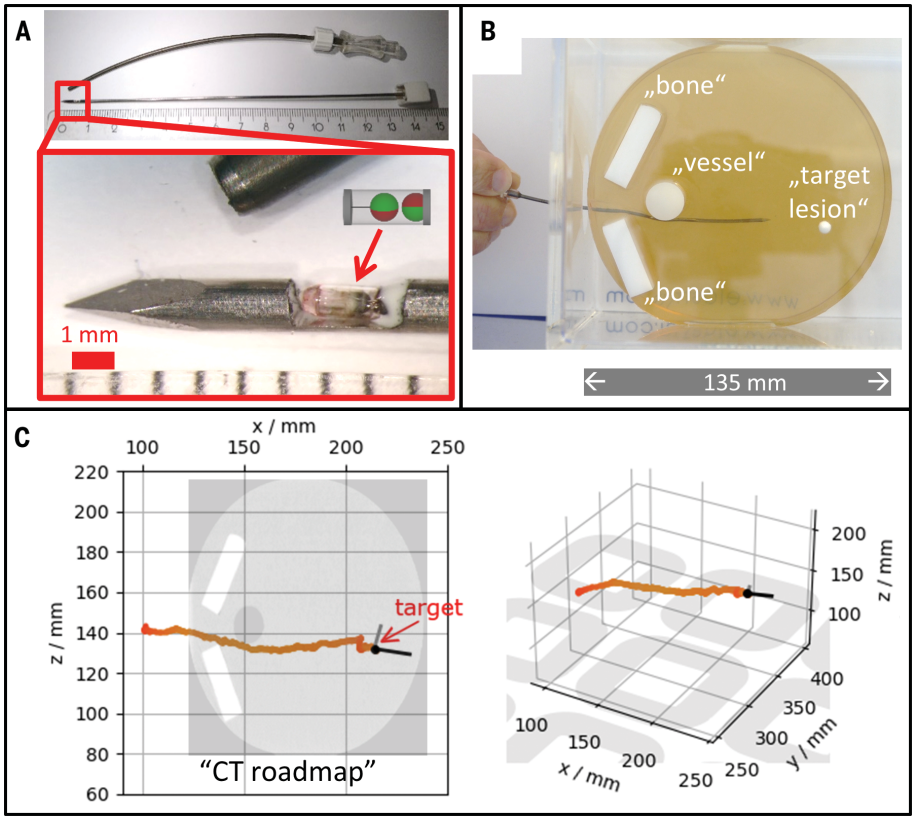


Fig. 3. Curved needle navigation experiment. (**A**) For demonstration, the MMR is glued into a recess cut into a flexible stylet that is inserted into a curved biopsy needle. The diameter of the MMR housing is 0.8 mm, the diameter of the stylet is 1.3 mm, and the outer diameter of the needle is 1.65 mm (16G Birmingham gauge). (**B**) Gelatin phantom simulating a patient. Two “bones” and one “vessel” block direct access to the “target lesion.” (**C**) Projection and oblique view of reconstructed needle path inside the phantom (see movie S4). The black dot marks the needle tip derived from the MMR position and orientation. The black line points along the needle axis and the gray line marks the axial rotation to enable controlled needle rotation. For navigation, a slice of a 3D computed tomography (CT) data set of the phantom has been projected (and is therefore deformed) on the *xz* view. The shaky course of the needle is mainly caused by stick-slip movement of the needle in the rather hard Gelatin phantom material.

Third, the filament bearing allows high angular oscillation amplitudes of the suspended sphere, leading to large magnetization changes that induce high voltages in the detection coils. Fourth, the magnetic restoring torque provided by the second magnet corresponds to a low stiffness or torsion constant that results in a rather low resonance frequency when compared with purely mechanical resonators. When the rate of excitation field change is limited—as is the case in most practical applications—a lower frequency enables higher angular oscillation amplitudes and thus increased signal. Our mathematical derivation shows that frequencies around a few kilohertz are optimal for MMRs, whereas much higher frequencies are optimal for LC resonators. Low frequencies have the benefit of inducing fewer eddy currents in metallic objects or a patient body and thus reduce shielding effects. This is demonstrated in the curved needle experiment, where the MMR is detected inside a metallic needle.

The MMR design also overcomes limitations encountered by magnetic micro-electromechanical systems (MEMS) for wireless actuation and sensing applications (*19*–*21*). MEMS processes are limited to low remanence magnetic materials, and resonators typically use rather stiff mechanical elements resulting in high frequencies but low oscillation amplitudes, leading to low signal. Furthermore, dissipation in mechanical elements is generally higher than in magnetic restoring elements, which limits MEMS quality factors and thus frequency resolution for sensing applications.

The simplicity of MMRs may enable simple manufacturing and low cost. The housing can be made from glass or plastic; the filament and the NdFeB magnets are also inexpensive. The MMR assembly does not require high precision, as the magnetic forces automatically center the oscillating sphere. These benefits combined with the small size of MMRs and their wireless detection distance of ~25 cm (see supplemental materials fig. S6) could improve or enable a wide range of applications.

One potential medical application could be medication adherence control, where an MMR is integrated in a pill whose presence can be detected wirelessly inside a patient’s gastrointestinal (GI) tract. Existing approaches either require detection patches with body contact (*11*) or centimeter-sized electronic pills (*12*). MMR tracking in the GI tract as simulated by the phantom experiment in the supplementary materials (fig. S5 and movie S7) could also deliver dynamic information on gastric emptying (*10*) and bowel motility (*22*). Here, several MMR markers with different resonance frequencies could be operated in parallel to collect information from many locations simultaneously; an advantage over magnetic tracking technologies using larger static magnets (*23*, *24*). A proof-of-principle experiment on simultaneous tracking of 3 MMRs operating at different frequencies is presented in fig. S7 and movie S8. Furthermore, MMR sensing in the GI tract could simultaneously deliver body core temperature (*25*), peristaltic pressure, pH value, or bowel content viscosity. In surgical applications, MMRs could be used for marking tumor tissue to guide excision. Current nonradioactive solutions require larger markers while having a smaller detection distance than MMRs (*26*, *27*). For monitoring and telemedicine solutions, tiny MMR sensors could be operated directly in the blood stream, e.g., for measuring physiological parameters such as blood pressure (*9*) or for functional monitoring of implanted devices, e.g., early detection of clogging in vascular stents.

MMRs could also be added to medical instruments such as needles, catheters, guidewires, or bronchoscopes to simplify in-body navigation (*2*) without the need for imaging, which is costly and often involves harmful x-ray radiation. The magnetic detection mechanism avoids line-of-sight problems of camera-based tracking systems. In addition, wireless MMRs promise simpler integration in devices and better workflow than cable- or fiber-dependent solutions (*3*). Furthermore, position and full orientation information (6 DoF) can be retrieved from a single MMR. With wireless LC resonators (*5*) or conventional wired electromagnetic tracking coils (*28*), at least two markers must be combined to deliver all three angles that determine orientation in space.

MMR technology could also be useful in nonmedical applications, e.g., RFID tagging. Millimeter-sized MMRs could be integrated in products and consumables where current RFID tags are either too large or too limited in detection distance. For identification, differences in resonance frequency, damping constant, magnetic dipole moment, and various nonlinear properties could be used to discern millions of MMRs by their signal response.

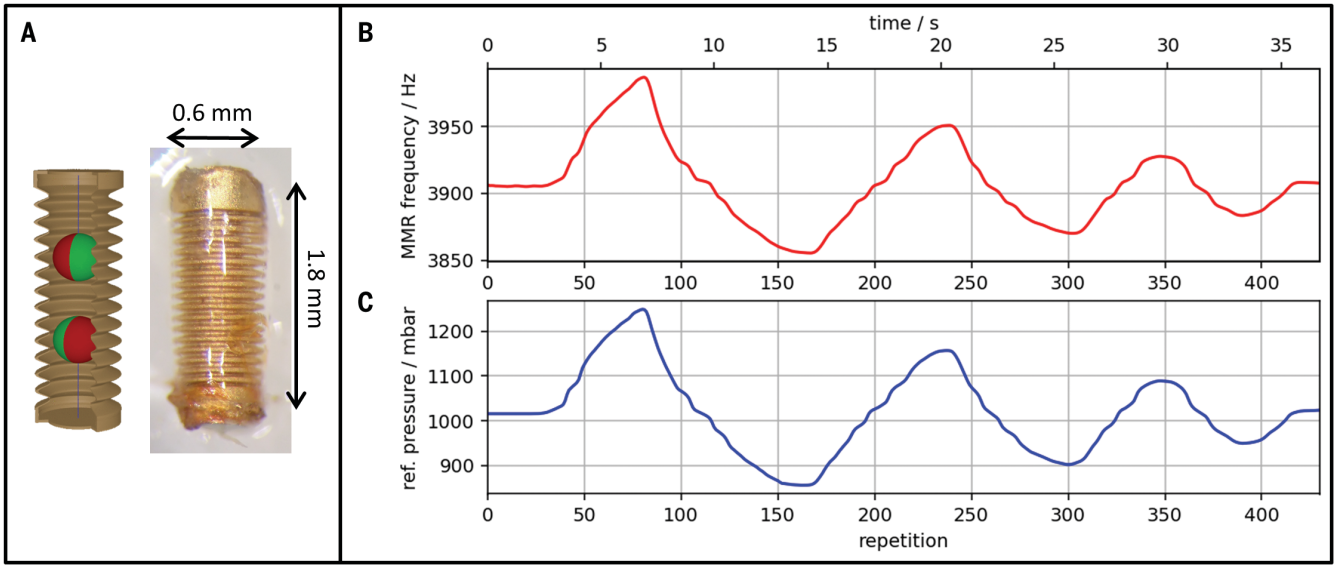


Fig. 4. Pressure sensor design, demonstrator, and measured pressure variation. (**A**) A compressible housing translates outer pressure variations to distance changes between two oscillating spheres. The diffusion-tight metal housing of the demonstrator provides the required stiffness and is coated with silicone rubber for a biocompatible surface. The sensor volume is 0.51 mm^3. (**B**) Application of external pressure using a manually operated syringe changes the resonance frequency of the MMR. Thereby, an increasing pressure reduces the MMR intersphere distance and increases the frequency. The MMR is placed ~70 mm above the coil array. (**C**) For reference, a commercial pressure sensor provides the applied pressure.

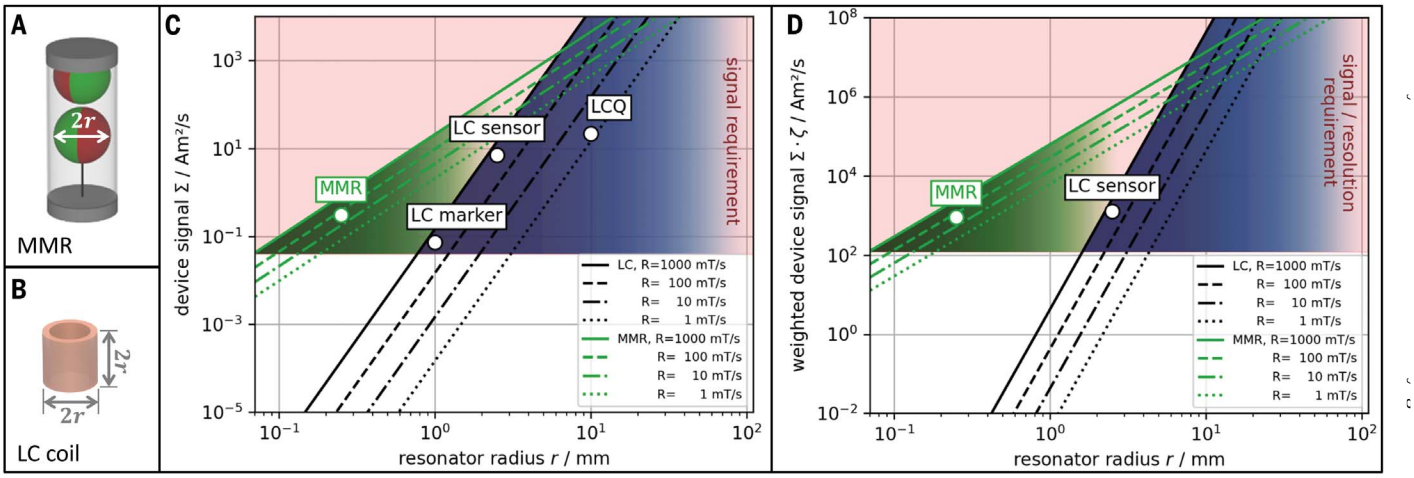


Fig. 5. Signal scaling comparison between MMR and LC-type resonators for marker and sensor applications. For markers, device signal Σ determines tracking performance, whereas for sensors, performance depends on signal Σ multiplied with a quality function ζ that reflects frequency resolution. (**A**) The "resonator radius" *r* corresponds to the radius of the oscillating MMR sphere. (**B**) For LC resonators, *r* is the radius of a cylindrical antenna coil of height 2 *r* and conductor thickness *r*/4. (**C**) Double logarithmic plot of signal Σ from MMRs (green lines) and LC resonators (black lines) for different applied rates of field change *R* (different dash styles). A minimal signal requirement for detecting the devices up to reasonable distances of ~ 20 cm in an unshielded environment is shaded in light red. The blue area indicates where LC resonators can be operated. The green area shows the region only accessible to the MMR technology. The circles annotated with "MMR" and "LCQ" illustrate values of the marker demonstrators (supplementary materials) presented in this work, and "LC marker" and "LC sensor" represent typical values of optimized devices. (**D**) Double logarithmic plot of weighted device signal Σ· ζ. The quality function ζ is a constant factor for MMRs whereas for LC sensors it scales with the squared coil radius. The resulting limited frequency resolution prevents shrinking LC sensor size below a few millimeters.

There are limitations of the MMR technology that may impact certain applications. A general limitation is the achievable signal level versus noise and background signals. Although our demonstrations were performed with millimeter-sized MMRs up to a distance of ~25 cm in an unshielded environment, a potential need for even smaller devices, higher accuracy, or larger workspaces may require advanced background signal subtraction strategies. The system could also be operated in a shielded environment, which would allow miniaturization of the magnetic elements to a few micrometers (*29*). Further limitations are systematic errors caused by nearby ferromagnetic or metallic objects. Stray fields from ferromagnets can shift the MMR resonance frequency and affect sensing accuracy. Eddy currents induced in metals can distort the dynamic magnetic fields and thus affect localization accuracy, an effect shared with wire-bound

electromagnetic tracking (*2*). A limitation for tracking of very fast objects, such as a flying bee, are position and orientation changes occurring within the signal acquisition window.

In conclusion, the presented MMR design enables shrinking wireless markers and sensors to the millimeter range while maintaining sufficient signal and sensitivity for remote detection. Demonstrations of tracking, device navigation, and sensing show the potential for a platform technology that can cover a wide range of applications.

REFERENCES AND NOTES

1. A. M. Franz *et al*., *IEEE Trans. Med. Imaging* **33**, 1702–1725 (2014).
2. A. Sorriento *et al*., *IEEE Rev. Biomed. Eng.* **13**, 212–232 (2020).
3. C. Shi *et al*., *IEEE Trans. Biomed. Eng.* **64**, 1665–1678 (2017).
4. D. Kessel, I. Robertson, T. Sabharwal, *Interventional Radiology: A Survival Guide* (Elsevier, 2011), ed. 3.
5. T. R. Willoughby *et al*., *Int J Radiat Oncol Biol Phys*. **65**, 528–534 (2006).
6. C. Orphanidou, *Biophys. Rev.* **11**, 83–87 (2019).
7. S. P. Radhoe, J. F. Veenis, J. J. Brugts, *Sensors* **21**, 2014 (2021).
8. M. Lin, H. Hu, S. Zhou, S. Xu, *Nat. Rev. Mater.* **7**, 850–869 (2022).
9. W. T. Abraham *et al*., *Am. Heart J.* **161**, 558–566 (2011).
10. J. Keller *et al*., *Nat. Rev. Gastroenterol. Hepatol.* **15**, 291–308 (2018).
11. H. Hafezi *et al*., *IEEE Trans. Biomed. Eng.* **62**, 99–109 (2015).
12. P. R. Chai *et al*., *J. Med. Internet Res.* **19**, e19 (2017).
13. S. Streit, F. Bock, C. W. W. Pirk, J. Tautz, *Zoology* **106**, 169–171 (2003).
14. J. D. Crall *et al*., *Science* **362**, 683–686 (2018).
15. V. Chawla, D. S. Ha, *IEEE Commun. Mag.* **45**, 11–17 (2007).
16. J. J. Croat, J. F. Herbst, R. W. Lee, F. E. Pinkerton, *J. Appl. Phys.* **55**, 2078–2082 (1984).
17. International Commission on Non-Ionizing Radiation Protection (ICNIRP), *Health Phys.* **99**, 818–836 (2010).
18. International Commission on Non-Ionizing Radiation Protection (ICNIRP), *Health Phys.* **118**, 483–524 (2020).
19. O. Cugat, J. Delamare, G. Reyne, *IEEE Trans. Magn.* **39**, 3607–3612 (2003).
20. D. Niarchos, *Sens. Actuators A Phys.* **106**, 255–262 (2003).
21. B. Paden, B. Norling, J. Verkaik, Telemetry method and apparatus using magnetically-driven mems resonant structure (2007), United States Patent US20070236213A1.
22. A. Aburub, M. Fischer, M. Camilleri, J. R. Semler, H. M. Fadda, *Int. J. Pharm.* **544**, 158–164 (2018).
23. W. Andrä *et al*., *Med. Phys.* **32**, 2942–2944 (2005).
24. E. Stathopoulos, V. Schlageter, B. Meyrat, Y. Ribaupierre, P. Kucera, *Neurogastroenterol. Motil.* **17**, 148–154 (2005).
25. A. M. Edwards, N. A. Clark, *Br. J. Sports Med.* **40**, 133–138 (2006).
26. C. McGugin *et al*., *Breast Cancer Res. Treat.* **177**, 735–739 (2019).
27. L. R. Lamb, M. Bahl, M. C. Specht, H. A. D'Alessandro, C. D. Lehman, *AJR Am. J. Roentgenol.* **211**, 940–945 (2018).
28. P. G. Seiler, H. Blattmann, S. Kirsch, R. K. Muench, C. Schilling, *Phys. Med. Biol.* **45**, N103–N110 (2000).
29. M. Liebl *et al*., *Sci. Rep.* **9**, 5014 (2019).
30. B. Gleich, I. Schmale, T. Nielsen, J. Rahmer, Data and Code for Needle Tracking and Temperature Sensing with Miniature Magneto-Mechanical Resonators, Version 1, Zenodo (2023); https://doi.org/10.5281/zenodo.7664908.

ACKNOWLEDGMENTS

The authors thank the Müller family for providing and handling the bees, our students for their contributions, our colleagues for hardware support, medical devices, and CT measurements, the reviewers for their feedback, and the internal project sponsors for their continued backing. **Funding:** none declared. **Author contributions:** Conceptualization: B.G. and J.R. Methodology: B.G., J.R., and T.N. Investigation: J.R., B.G., I.S., and T.N. Evaluation: J.R. and T.N. Visualization: J.R. and B.G. Project administration: J.R. Writing – original draft: J.R. and B.G. Writing – review and editing: B.G., I.S., T.N., and J.R. **Competing interests:** All authors are employees of Philips GmbH Innovative Technologies Research Laboratories Hamburg. Philips has submitted the following patent applications regarding the presented technology: US20220257138, US20220238011, US20220175487, US20210244305, US20200397320, US20200397530, US20200397510, US20200400509. **Data and materials availability:** All data necessary to understand and assess the conclusions are available in the manuscript and the supplementary material. Additional data and evaluation code are accessible online (*30*). **License information:** Copyright © 2023 the authors, some rights reserved; exclusive licensee American Association for the Advancement of Science. No claim to original US government works. https://www.sciencemag.org/about/science-licenses-journal-article-reuse

SUPPLEMENTARY MATERIALS

science.org/doi/10.1126/science.adf5451
Materials and Methods
Supplementary Text
References (*31*–*34*)
Figs. S1 to S8
Movies S1 to S10

View/request a protocol for this paper from *Bio-protocol*.

Submitted 28 October 2022; accepted 3 May 2023
10.1126/science.adf5451

CIRCADIAN RHYTHMS

Rhythmic cilia changes support SCN neuron coherence in circadian clock

Hai-Qing Tu[1]†, Sen Li[1]†, Yu-Ling Xu[1]†, Yu-Cheng Zhang[1]†, Pei-Yao Li[1], Li-Yun Liang[1], Guang-Ping Song[1], Xiao-Xiao Jian[1], Min Wu[1], Zeng-Qing Song[1], Ting-Ting Li[1], Huai-Bin Hu[1], Jin-Feng Yuan[1], Xiao-Lin Shen[1], Jia-Ning Li[1], Qiu-Ying Han[1], Kai Wang[1], Tao Zhang[3], Tao Zhou[1], Ai-Ling Li[1,2], Xue-Min Zhang[1,2]*, Hui-Yan Li[1,2]*

The suprachiasmatic nucleus (SCN) drives circadian clock coherence through intercellular coupling, which is resistant to environmental perturbations. We report that primary cilia are required for intercellular coupling among SCN neurons to maintain the robustness of the internal clock in mice. Cilia in neuromedin S–producing (NMS) neurons exhibit pronounced circadian rhythmicity in abundance and length. Genetic ablation of ciliogenesis in NMS neurons enabled a rapid phase shift of the internal clock under jet-lag conditions. The circadian rhythms of individual neurons in cilia-deficient SCN slices lost their coherence after external perturbations. Rhythmic cilia changes drive oscillations of Sonic Hedgehog (Shh) signaling and clock gene expression. Inactivation of Shh signaling in NMS neurons phenocopied the effects of cilia ablation. Thus, cilia-Shh signaling in the SCN aids intercellular coupling.

All mammals have an internal circadian clock (~24 hours) that regulates daily oscillations in metabolism, physiology, and behavior, such as rest-activity and sleep-wake cycles (*1*). The suprachiasmatic nucleus (SCN) acts as the master circadian pacemaker (*2*, *3*). Its autonomous and coherent oscillatory output signals orchestrate the peripheral clocks in multiple tissues throughout the body (*4*, *5*). Environmental circadian disruptions, such as acute jet lag and long-term shift work, cause temporal unsynchronization between the internal circadian clock and external time cues, leading to physiological stress (*6*, *7*). Circadian disruption has been implicated in tumorigenesis and various psychiatric, neurological, and metabolic diseases, including depression and diabetes (*8*, *9*).

The SCN contains a heterogeneous population of ~20,000 neurons, most of which can individually generate autonomous circadian oscillations (*10*, *11*). These oscillations are driven by autoregulatory transcription-translation feedback loops (TTFLs) of clock genes (*12*, *13*). The function of SCN as the master pacemaker relies on intercellular coupling, a process that synchronizes period and phase among SCN neurons (*14*, *15*). Intercellular coupling enables the SCN to generate robust and coherent oscillations at the population level that are resistant to environmental perturbations (*16*, *17*). Several neurotransmitters, including vasoactive intestinal peptide (VIP), γ-aminobutyric acid (GABA), and arginine vasopression (AVP), function in maintaining this intercellular coupling (*18*–*22*). The release of these neurotransmitters is regulated by clock genes, the transcription of which can be further activated by the neurotransmitters (*23*). Thus, these neurotransmitters and clock genes form a feedforward loop to maintain intercellular coupling in the SCN.

The primary cilium, a sensory organelle nucleated by the mother centriole, functions in mammalian embryonic development (*24*). Defective ciliogenesis results in a series of human disorders collectively known as ciliopathies (*25*, *26*). The primary cilium is also present in adult neurons and regulates glycometabolism (*27*, *28*). We found that in a subset of SCN neurons, cilia exhibit pronounced circadian rhythmicity in abundance and length. We also identified primary cilia as a critical device for intercellular coupling to maintain the circadian clock in the SCN.

Results

Primary cilia in the SCN exhibit circadian rhythmic changes

We examined the distribution of primary cilia in the mouse brain and found that many SCN neurons contained primary cilia (Fig. 1, A and B, and movie S1). Because the SCN is the master circadian pacemaker, we tested whether primary cilia of SCN neurons exhibited oscillatory rhythms during light-dark (LD) and dark-dark (DD) cycles. In mice maintained in LD cycles, both the number and length of primary cilia showed a pronounced circadian rhythmicity, peaking at ZT 0 and reaching a trough at ZT 12 (Fig. 1, C to E), where ZT represents Zeitgeber time used in LD cycles, and ZT 0 and ZT 12 are lights on and lights off, respectively. This oscillation was antiphase to that of the clock gene *Cry1*. Rhythmic oscillations of primary cilia in the SCN were also observed in DD cycles, peaking at CT 0 and reaching a trough at CT 12 (Fig. 1F and fig. S1, A and B), where CT represents circadian time, and CT 0 and CT 12 are subjective dawn and dusk, respectively, indicating that these ciliary oscillations are not driven by light but rather by internal rhythms. We next used a transgenic mouse model expressing ADP ribosylation factor-like guanosine triphosphatase 13B (ARL13B)–mCherry fusion protein to label the axoneme of primary cilia and also observed the diurnal oscillations of ciliary abundance in the SCN during DD cycles (fig. S1C).

Primary cilia in other cerebral regions and peripheral tissues, including the paraventricular nucleus of the hypothalamus (PVN), hippocampus, kidney, and pancreas, lacked circadian rhythmicity (Fig. 1G and fig. S1, D to G). In most cells, ciliary abundance and length are tightly connected to cell cycle progression (*29*). In vivo bromodeoxyuridine incorporation assays showed that almost all of the cells in the SCN were postmitotic neurons (fig. S1H), indicating that the rhythmicity of cilia is not coupled to the cell cycle. Bmal1 is a core component of the mammalian circadian clock, and its deletion expectedly abolished circadian behaviors in mice (*30*, *31*) (fig. S1I). The circadian oscillation of ciliary abundance was lost in Bmal1-deficient mice, indicating that the rhythmicity of cilia is regulated by clock output (Fig. 1H).

To monitor primary cilia in live SCN neurons isolated from postnatal mice, we transduced them with modified baculovirus encoding the mCherry-tagged constitutively ciliary-localized protein 5-hydroxytryptamine receptor 6 (5-HT6), and performed time-lapse imaging. Consistent with the fixed-slice data, primary cilia displayed circadian rhythmic oscillation in length: They took ~12 hours to shorten to the minimum length and regrew to the maximum length during the next 12 hours (movie S2; Fig. 1, I and J; and fig. S1J). The abundance of Cry1 in ciliated cells was lower than that in nonciliated cells (fig. S1, K and L), consistent with our in vivo observations.

Primary cilia confer robustness to the intrinsic circadian clock

The SCN consists of multiple types of neurons, including AVP-expressing neurons, VIP-expressing neurons, and NMS-expressing neurons. NMS neurons represent 40% of all SCN neurons and encompass most VIP- and AVP-expressing neurons (*32*). To identify the cell types of ciliated neurons in the SCN, we crossed *Nms-Cre* or *Vip-Cre* mice with *Rosa-stop-tdTomato* reporter mice to label NMS or VIP neurons. Type III adenylyl cyclase (ACIII) is a prominent marker of primary cilia throughout the brain. As revealed by ACIII staining of SCN coronal sections, we found that 90% of ciliated neurons were NMS neurons and 31%

[1]Nanhu Laboratory, National Center of Biomedical Analysis, Beijing, China. [2]School of Basic Medical Sciences, Fudan University, Shanghai, China. [3]Laboratory Animal Center, Academy of Military Medical Sciences, Beijing, China.
*Corresponding author. Email: hyli@ncba.ac.cn (H-Y.L.); zhangxuemin@cashq.ac.cn (X-M.Z.)
†These authors contributed equally to this work.

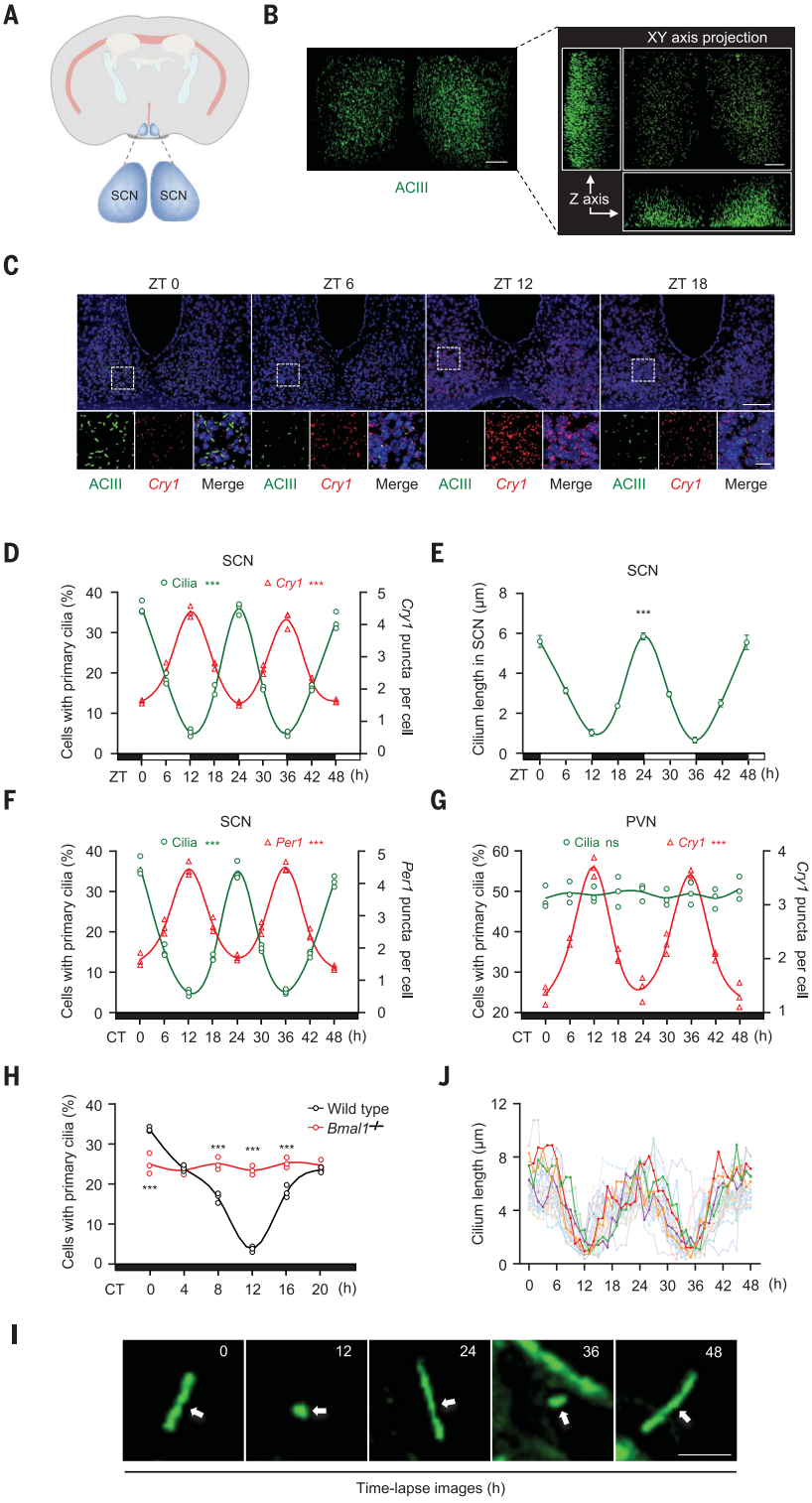


Fig. 1. Primary cilia in the SCN exhibit circadian changes in abundance and length. (**A**) Schematic diagram of the SCN. (**B**) Representative three-dimensional reconstructed projection images of the SCN at 20× magnification of the two-photon imaging. SCN slices were stained with anti-ACIII (primary cilia marker, green). Scale bars, 50 μm. (**C**) Representative images of primary cilia and expression of clock gene *Cry1* in the SCN during the LD cycle. SCN coronal sections were stained with anti-ACIII (green), *Cry1* RNAscope probes (red), and Hoechst (blue). Insets show enlarged views of the boxed regions in the SCN. Scale bars, 100 μm (main image) and 20 μm (magnified region). (**D**) Percentage of cells with primary cilia or *Cry1* RNAscope signals in the SCN determined based on (C). (**E**) Quantitative analysis of the cilium length in (C). (**F**) Percentage of cells with primary cilia or *Per1* RNAscope signals in the SCN quantified during the DD cycle. (**G**) Percentage of cells with primary cilia or *Cry1* RNAscope signals in the PVN determined during the DD cycle. (**H**) Percentage of cells with primary cilia in the SCN for wild-type and *Bmal1*$^{-/-}$ mice during the DD cycle. (**I**) Representative time-lapse images of the primary cilium in SCN neurons for 48 hours. Isolated live SCN neurons from postnatal mice were transduced with modified baculovirus encoding mCherry-tagged 5-HT6. The numbers on the images indicate the time. Arrows indicate primary cilia. Scale bar, 5 μm. (**J**) Quantitative analysis of the cilium length in (I). Each line represents the oscillation of cilium length in an individual neuron. All data are presented as mean ± SEM. Statistics indicate significance by one-way ANOVA with Tukey's correction [(D) to (G)] or two-way ANOVA with Bonferroni correction (H). n = 3 mice per time point. ***P < 0.001; ns, not significant.

were VIP neurons (Fig. 2, A and B, and fig. S2A). We performed double immunostaining using antibodies to ACIII and AVP and found that only 5% of ciliated cells were AVP neurons (Fig. 2, A and B). Thus, primary cilia are mainly present on NMS neurons in the SCN (Fig. 2C).

We disrupted primary cilia specifically in NMS neurons by conditionally deleting *Ift88* or *Ift20*, two genes required for ciliogenesis (*33*–*35*). Primary cilia on SCN neurons were abolished in *Nms-Ift88*$^{-/-}$ or *Nms-Ift20*$^{-/-}$ mice (fig. S2, B to E). By contrast, the numbers of primary cilia in other tissues were comparable between control and *Nms-Ift88*$^{-/-}$ or *Nms-Ift20*$^{-/-}$ mice

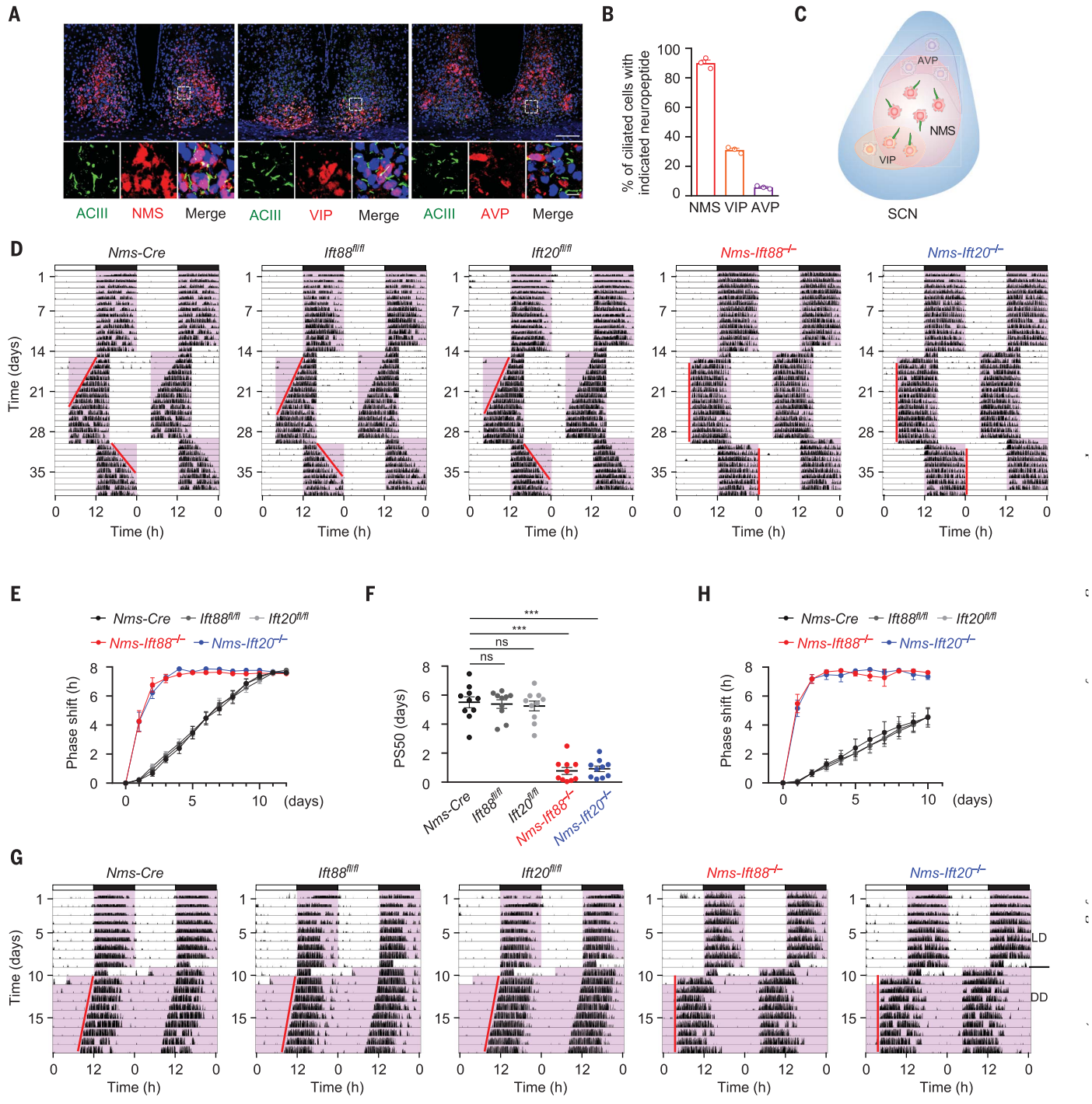


Fig. 2. Primary cilia in NMS neurons confer robustness to the intrinsic circadian clock. (**A**) Representative images of primary cilia in multiple types of SCN neurons. For NMS and VIP neurons, SCN coronal sections from *Nms-tdTomato* or *Vip-tdTomato* mice were stained with antibody to ACIII (green) and Hoechst (blue). For AVP neurons, SCN coronal sections were stained with anti-ACIII (green), anti-AVP (red), and Hoechst (blue). Insets show enlarged views of the boxed regions in the SCN. Scale bars, 100 μm (main image) and 10 μm (magnified region). (**B**) Quantitative analysis of the percentage of ciliated cells with the indicated neuropeptide in (A) (n = 3). (**C**) Distribution diagram of primary cilia in NMS, AVP, and VIP neurons. (**D**) Representative double-plotted actogram of mice under experimental jet-lag conditions. Activity records are double plotted so that 48 hours are represented horizontally. Each 24-hour interval is presented both to the right of and beneath the preceding day. Mice were maintained in LD cycles for 14 days, then the cycle was advanced 8 hours, and 15 days later, the cycle was returned to the original lighting regime. (**E**) Line graphs showing the daily phase shift of wheel-running activities after an 8-hour advance in (D) (n = 10). (**F**) PS_{50} values after an 8-hour advance in (D) (n = 10). (**G**) Representative double-plotted actograms of mice subjected to an 8-hour phase advance on day 1 and released to DD. (**H**) Line graphs showing the daily phase shift of wheel-running activities in (G) (n = 10). For this and subsequent figures, wheeling-running activity is indicated by black markings. White and pink backgrounds indicate lights on and lights off, respectively. The red lines on the actograms indicate the phase of activity onset or offset. All data are presented as mean ± SEM. Statistics indicate significance by one-way ANOVA with Dunnett correction (F). ***P < 0.001; ns, not significant.

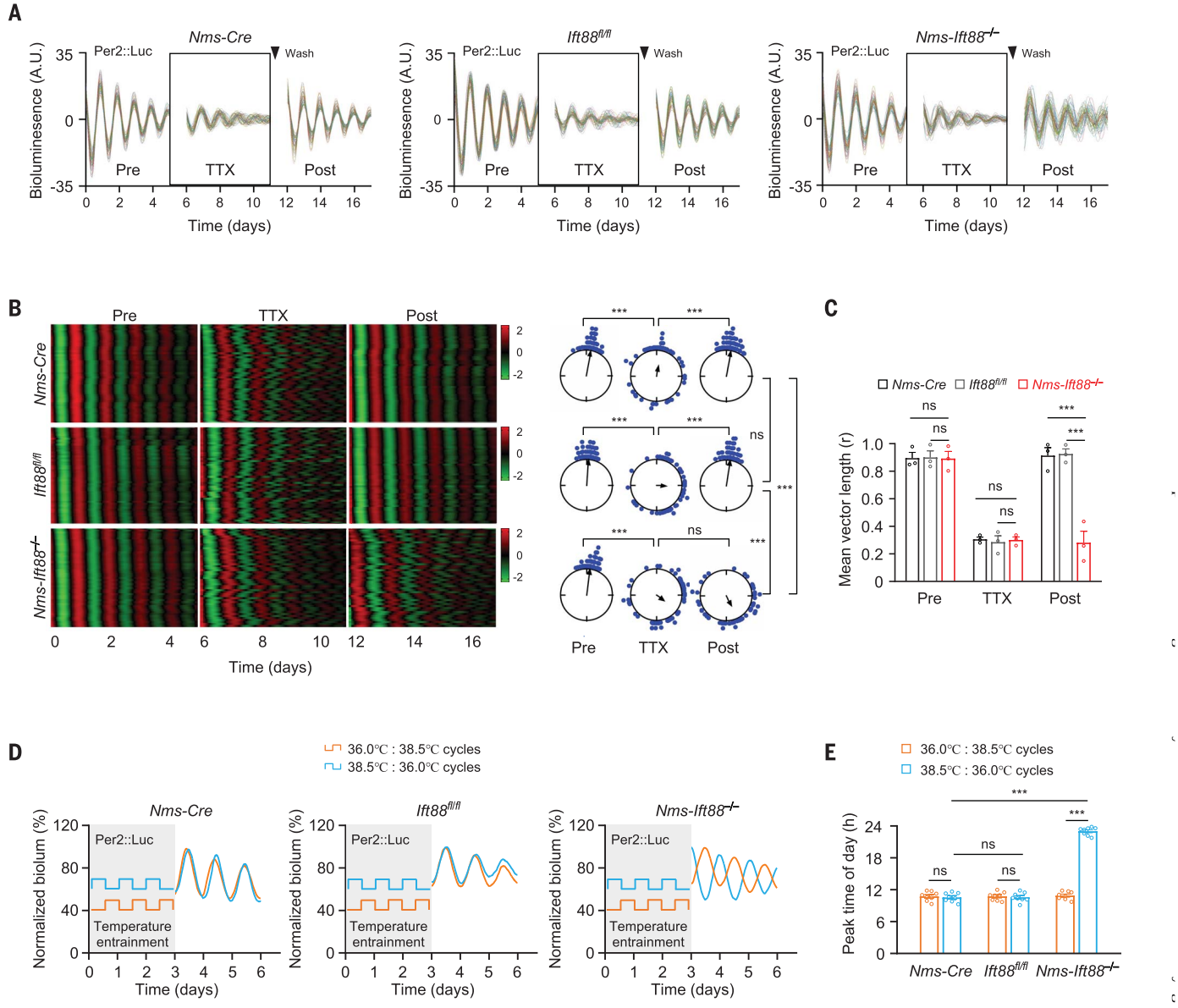


Fig. 3. Primary cilia promote interneuronal coupling in the SCN. (**A**) Representative records of single-cell Per2 bioluminescence in SCN slices under three conditions: pretreatment, TTX treatment, and after washout of TTX (n = 50 cells). Arrows indicate TTX washout by medium changes. (**B**) Left, representative heatmap of Per2 bioluminescence oscillation in (A). Red and green represent high and low bioluminescence intensity, respectively. Right, Rayleigh plots showing the phase distribution of single cells during the third day (midpoint) in (A). Arrows represent mean circular phase, and the length of the arrow represents the strength of synchronization. (**C**) Homogeneity of the single-cell phase from multiple replicate SCN slices evaluated with length of the Rayleigh plot vector in (B) (n = 3). (**D**) Representative records of Per2 bioluminescence rhythms in SCN slices. SCN slices were exposed to 12 hours of 36°C and 12 hours of 38.5°C temperature cycles or oppositely phased temperature cycles for 3 days, and their bioluminescence was then monitored continuously at a constant 36°C. Bioluminescence was normalized to the first peak. (**E**) Quantitative analysis of the peak time of Per2 bioluminescence after the temperature cycles in (D) (n = 8). Data are presented as mean ± SEM. Statistics indicate significance by Watson-Wheeler test (B) or two-way ANOVA with Bonferroni correction [(C) and (E)]. ***P < 0.001; ns, not significant.

(fig. S2, F and G). Deletion of *Ift88* or *Ift20* in NMS neurons did not affect mouse development or the morphology of the SCN (fig. S3).

We also investigated whether primary cilia contribute to the pacemaker function of the SCN by monitoring the locomotor activity of *Nms-Ift88*$^{-/-}$ or *Nms-Ift20*$^{-/-}$ mice, referred to hereafter as SCN$^{\text{cilia-null}}$ mice. Under LD cycles, both control (*Nms-Cre*, *Ift88*$^{\text{fl/fl}}$ and *Ift20*$^{\text{fl/fl}}$) and SCN$^{\text{cilia-null}}$ mice exhibited normal locomotor activity with a wheel-running period of 24 hours (fig. S4A). Under DD cycles, control mice exhibited intrinsic periods of 23.6 ± 0.1 hours (fig. S4, A and B). SCN$^{\text{cilia-null}}$ mice had a moderately elongated intrinsic period: 24.0 ± 0.1 hours for *Nms-Ift88*$^{-/-}$ mice and 23.9 ± 0.1 hours for *Nms-Ift20*$^{-/-}$ mice (fig. S4, A and B).

We further examined the behavior of SCN$^{\text{cilia-null}}$ mice under experimental jet-lag conditions. Mice were maintained in normal LD cycles for 14 days, the cycle was advanced by 8 hours, and 15 days later, the cycle was returned to the original lighting regime. Under LD cycles, both control and SCN$^{\text{cilia-null}}$ mice successfully entrained to the LD schedule. When the lighting cycle was advanced, control mice re-entrained

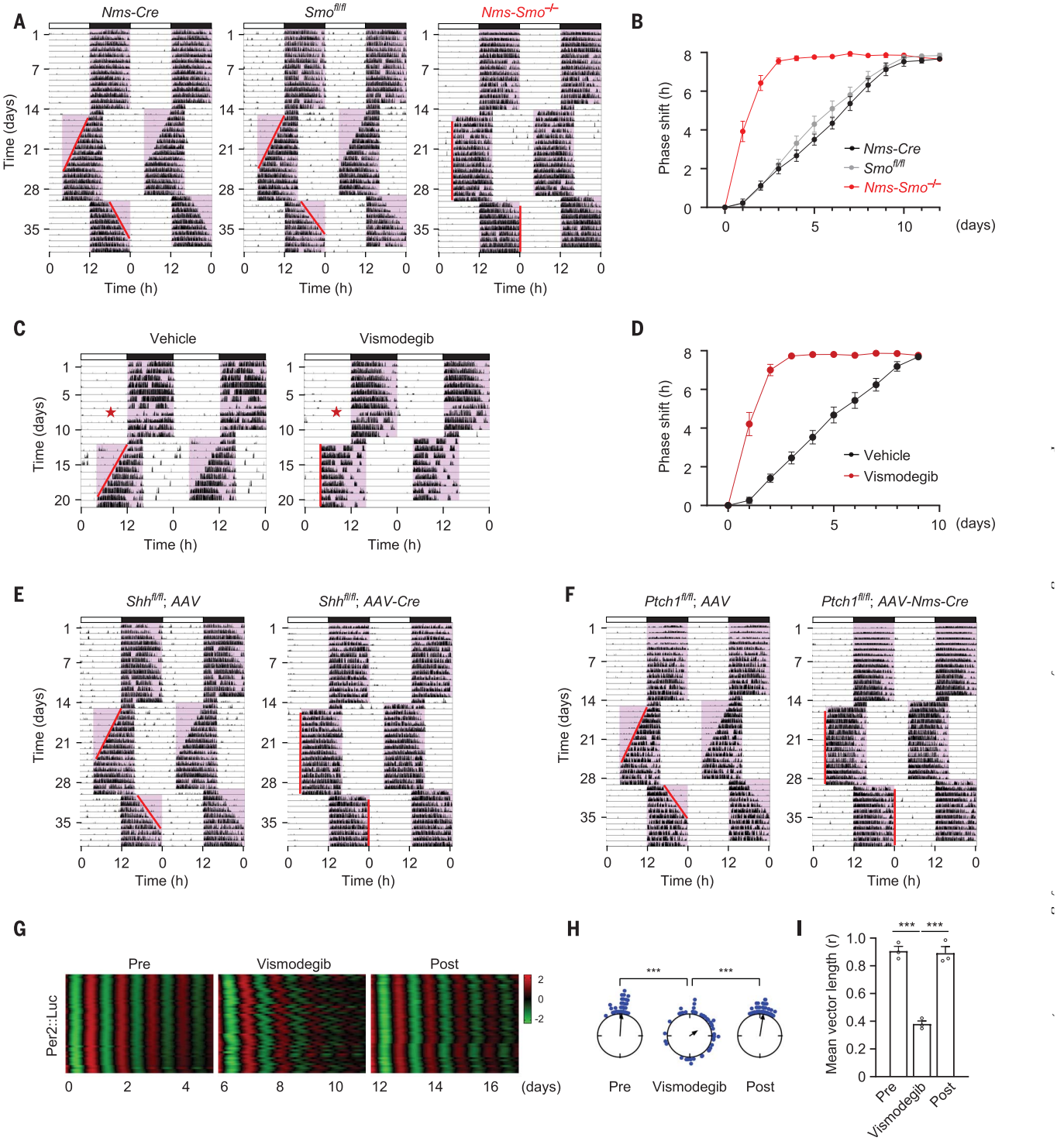


Fig. 4. Hedgehog signaling maintains circadian rhythm in the SCN. (**A**) Representative double-plotted actogram of *Nms-Cre*, *Smo*$^{fl/fl}$, and *Nms-Smo*$^{-/-}$ mice under experimental jet-lag conditions. (**B**) Line graphs showing the daily phase shift of wheel-running activities after an 8-hour advance in (A) (n = 10). (**C**) Representative double-plotted actograms of mice treated with vehicle (left) or 5 mM vismodegib (right) under experimental jet-lag conditions. Vismodegib was applied to the SCN by osmotic minipump. Asterisks indicate time of surgery. Three days after surgery, LD cycles were advanced by 8 hours. (**D**) Line graphs showing the daily phase shift of wheel-running activities after an 8-hour advance in (C) (n = 11 for the vehicle group, n = 12 for the vismodegib group). (**E**) Representative double-plotted actogram of *Shh*$^{fl/fl}$;*AAV* and *Shh*$^{fl/fl}$;*AAV-Cre* mice under experimental jet-lag conditions. (**F**) Representative double-plotted actogram of *Ptch1*$^{fl/fl}$;*AAV* and *Ptch1*$^{fl/fl}$;*AAV-Nms-Cre* mice under experimental jet-lag conditions. (**G**) Heatmap of Per2 bioluminescence oscillation under three conditions: pretreatment, vismodegib treatment, and after washout of vismodegib (n = 50 cells). (**H**) Rayleigh plots of phase distribution of single cells in (G) during the third day. (**I**) Homogeneity of the single-cell phase from three replicate SCN slices was evaluated with length of the Rayleigh plot vector in (G). All data are presented as mean ± SEM. Statistics indicate significance by Watson-Wheeler test (H) or one-way ANOVA with Bonferroni correction (I). ***P < 0.001.

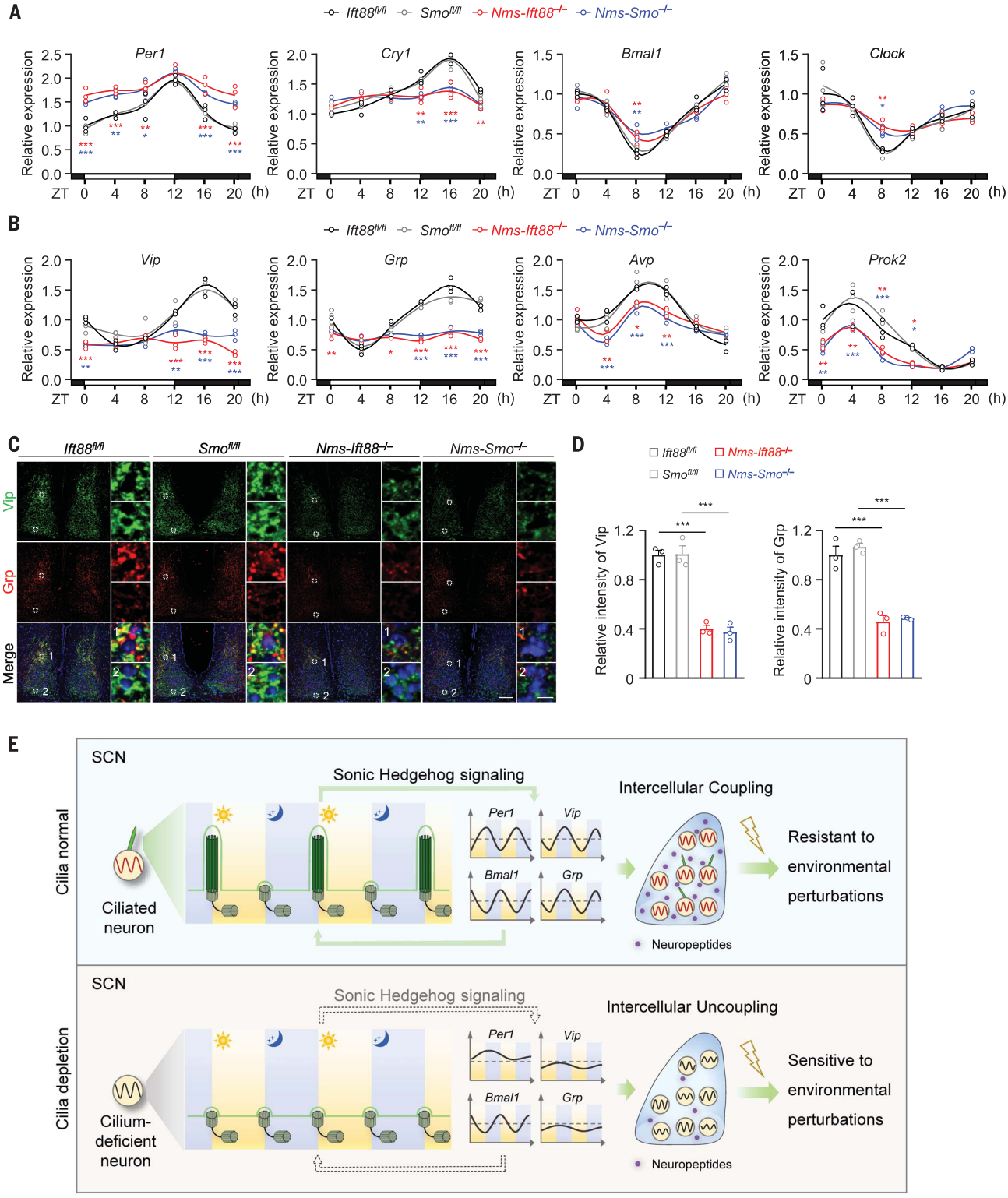


Fig. 5. Ciliary Hedgehog signaling regulates the rhythms of clock genes and neuropeptides. (**A** and **B**) Quantitative real-time polymerase chain reaction (PCR) analysis of core clock genes (A) and neuropeptides (B) in the SCN. The SCN was collected at 4-hour intervals across the LD cycle. (**C**) Representative immunostaining images of Vip and Grp in the dosal and ventral SCN at ZT 20. SCN coronal sections were stained with anti-Vip (green), anti-Grp (red), and Hoechst (blue). Insets show enlarged views of the boxed regions. Scale bars, 100 μm (main image) and 10 μm (magnified region). (**D**) Quantification of the relative intensity of Vip and Grp in (C). (**E**) Summary diagram showing primary cilia in SCN neurons and downstream Hedgehog signaling as critical regulatory mechanisms promoting interneuronal coupling, thereby maintaining SCN network synchrony and circadian rhythms. All data are presented as mean ± SEM. Statistics indicate significance by one-way ANOVA (D) or two-way ANOVA [(A) and (B)] with Bonferroni correction. $n = 3$ independent experiments for *Nms-Ift88*$^{-/-}$ versus *Ift88*$^{fl/fl}$ and *Nms-Smo*$^{-/-}$ versus *Smo*$^{fl/fl}$. $^{*}P < 0.05$, $^{**}P < 0.01$, $^{***}P < 0.001$.

progressively over 9 to 11 days (Fig. 2, D and E). By contrast, $SCN^{cilia\text{-}null}$ mice re-entrained more quickly, and the entrainment was complete within 1 to 3 days (Fig. 2, D and E). We then calculated the time at which half the phase shift was completed (PS_{50}). The PS_{50} value of control mice was about 5.4 days, whereas that of *Nms-Ift88*$^{-/-}$ and *Nms-Ift20*$^{-/-}$ mice was 0.7 ± 0.2 and 0.9 ± 0.2 days, respectively (Fig. 2F). When the cycle was returned to the original lighting regime, control mice re-entrained progressively over several days (Fig. 2D and fig. S4, C and D), whereas $SCN^{cilia\text{-}null}$ mice again re-entrained immediately to the LD cycle. These data indicate that primary cilia in NMS neurons influence the entrainment of circadian rhythms.

Vip-Ift88$^{-/-}$ or *Vip-Ift20*$^{-/-}$ mice also re-entrained more quickly than did control mice (4 to 6 days versus 9 to 11 days) (fig. S5, A to E). However, these mice took more time to be re-entrained than did *Nms-Ift88*$^{-/-}$ or *Nms-Ift20*$^{-/-}$ mice (1 to 3 days), presumably because some ciliated neurons remained in *Vip-Ift88*$^{-/-}$ or *Vip-Ift20*$^{-/-}$ mice (fig. S5, F and G). *Avp-Ift88*$^{-/-}$ or *Avp-Ift20*$^{-/-}$ mice behaved normally under experimental jet-lag conditions, as primary cilia were not affected in these mice (fig. S6). These data further support a specific role of cilia in NMS neurons in circadian rhythm entrainment.

There were no differences between control and $SCN^{cilia\text{-}null}$ mice in the number of *c-Fos*$^{+}$ cells induced by a 30-min light pulse at CT 22 (fig. S7), indicating that the light response of $SCN^{cilia\text{-}null}$ mice was similar to that of control mice. These results demonstrate that $SCN^{cilia\text{-}null}$ mice are more adaptive to phase shifts during LD cycles, suggesting that primary cilia influence resistance to environmental time cues.

To exclude the effect of light on activity of mice, we subjected mice to constant darkness (DD) after an 8-hour phase advance in an LD protocol. Under DD, $SCN^{cilia\text{-}null}$ mice exhibited significant phase advances in the free-running behavior, whereas control mice did not (Fig. 2, G and H). This finding suggests that the immediate adaptation to a new LD cycle in $SCN^{cilia\text{-}null}$ mice is a rapid phase shift of the internal clock, not a masking of the environmental LD cycle.

Primary cilia promote interneuronal coupling in the SCN

SCN neurons rely on intercellular coupling to maintain intrinsic circadian behavior. Intercellular coupling confers robustness to neuronal networks and synchronizes periods of individual cellular oscillators. *Per2::Luciferase* (*Per2::Luc*) transgenic reporter mice can be used to track *Per2* rhythmic expression in single cells ex vivo. To test whether primary cilia are required for intercellular coupling among SCN neurons, we used real-time luciferase luminescence imaging of SCN slices isolated from control (*Nms-Cre* and *Ift88*$^{fl/fl}$) or *Nms-Ift88*$^{-/-}$ mice that expressed the *Per2::Luc* reporter. Circadian rhythmicity of the analyzed SCN cell population was coherent in both control and *Nms-Ift88*$^{-/-}$ slices under normal culture conditions (Fig. 3, A to C). We then applied tetrodotoxin (TTX), a sodium ion channel blocker, to disrupt the intercellular coupling of SCN neurons. TTX disrupted the phase order of both control and *Nms-Ift88*$^{-/-}$ SCN neurons (Fig. 3, A to C). After the washout of TTX, control neurons recovered their coherent phase order, whereas *Nms-Ift88*$^{-/-}$ neurons failed to do so (Fig. 3, A to C; fig. S8; and movies S3 to S5). Thus, primary cilia in NMS neurons appear to promote intercellular coupling.

Intercellular coupling in the SCN is required for resistance to physiological temperature changes (*17*). We therefore tested whether primary cilia in the SCN contributed to the resistance to cyclic temperature entrainment. Control and *Nms-Ift88*$^{-/-}$ SCN slices were exposed to 12 hours of 36°C and 12 hours of 38.5°C temperature cycles (normal body temperature cycles) or oppositely phased temperature cycles for 3 days. Both control and *Nms-Ift88*$^{-/-}$ SCN slices maintained their phases of *Per2* bioluminescence after normal cyclic temperature entrainment. After oppositely phased temperature cycles, the phase of control SCN slices remained unchanged, but the phase of *Nms-Ift88*$^{-/-}$ SCN slices was obviously shifted (Fig. 3, D and E). Thus, the cilia-null SCN was less resistant to cyclic temperature changes. This resistance likely stems from cilia-dependent intercellular coupling in the SCN.

Hedgehog signaling maintains circadian rhythm in the SCN

To investigate how primary cilia in NMS neurons mediate intercellular coupling, we examined the functions of Avp and Vip receptors, two well-known heterotrimeric G–protein coupled receptors (GPCRs) in the SCN (*19*, *20*). Avp and Vip receptors did not localize to cilia, and Vip receptor function remained normal in *Nms-Ift88*$^{-/-}$ mice (fig. S9). The primary cilium is a critical organelle that regulates Sonic Hedgehog (Shh) signaling (*36*–*38*). In a genome-wide screen, inhibition of the Hedgehog pathway resulted in long period length of circadian oscillations in U2OS cells (*39*). *Shh* genes were broadly expressed in SCN neurons (fig. S10, A and B). The addition of Shh could induce the expression of the downstream gene *Gli1* in NMS neurons, and this effect was abolished in *Nms-Ift88*$^{-/-}$ mice (fig. S10, C and D). The expression of *Gli1* and *Ptch1*, two Shh signaling target genes, exhibited rhythmic oscillation in the SCN under both LD and DD conditions (fig. S10E). This rhythmic oscillation was lost in *Nms-Ift88*$^{-/-}$ mice or Bmal1-deficient mice (fig. S10, F and G), so Shh signaling may function in the regulation of the central clock.

The enrichment of smoothened (SMO) on cilia is required to initiate Hedgehog signaling (*40*). We generated *Nms-Smo*$^{-/-}$ mice to block Shh signaling in the SCN (fig. S11A). Although *Nms-Smo*$^{-/-}$ mice did not exhibit overt developmental defects (fig. S11, B to E), we could not completely rule out subtle off-target developmental effects. Under experimental jet-lag conditions, *Nms-Smo*$^{-/-}$ mice re-entrained immediately to the LD cycle (Fig. 4, A and B, and fig. S11, F and G). We next applied an SMO inhibitor, vismodegib, to the SCN through an osmotic minipump in live animals during experimental jet-lag conditions. Vismodegib caused immediate re-entrainment to the LD cycle (Fig. 4, C and D, and fig. S12A). Moreover, vismodegib elicited a reversible dose-dependent suppression of *Per2::Luc* oscillations in SCN slices (fig. S12, B to D), and this inhibitory effect was abolished in *Nms-Smo*$^{-/-}$ SCN slices (fig. S12, E and F). We also found that the SMO agonist SAG induced *Per2* expression and significantly delayed the phase of the SCN circadian oscillation by up to 4 hours (fig. S12, G and H). These effects were abolished in *Nms-Smo*$^{-/-}$ SCN slices. These results demonstrate that Shh signaling is required for the resistance of the internal clock to environmental time cues.

We generated Shh conditional knockout mice by bilateral injection of adeno-associated virus (AAV)–expressing Cre recombinase to the SCN of *Shh*$^{fl/fl}$ mice (fig. S13, A and B). Similar to *Nms-Smo*$^{-/-}$ mice, mice lacking Shh in the SCN re-entrained immediately to the LD cycle under experimental jet-lag conditions (Fig. 4E and fig. S13, C and D). To test the effect of enhanced Shh signaling in the SCN, we deleted *Ptch1*, a key negative regulator of Shh signaling, in NMS neurons in mice (*41*) (fig. S13E). *Nms-Ptch1*$^{-/-}$ mice re-entrained immediately to the LD cycle under experimental jet-lag conditions (Fig. 4F and fig. S13, F and G). Thus, both rhythmic oscillation of Shh signaling and its amplitude influence coupling in the central clock.

To test whether Shh signaling also functions in interneuronal coupling in the SCN, we analyzed circadian rhythms in SCN slices using the single-cell real-time luciferase luminescence imaging assay. Similar to *Nms-Ift88*$^{-/-}$ neurons, *Nms-Smo*$^{-/-}$ neurons failed to recover their phase order after the washout of TTX (fig. S14). The Smo inhibitor vismodegib also reversibly disrupted the phase order of *Per2::Luc* in SCN slices (Fig. 4, G to I, and movie S6). Thus, Shh signaling may promote intercellular coupling among SCN neurons.

Ciliary Hedgehog signaling regulates the rhythms of clock genes and neuropeptides

Because the circadian clock controls the transcription of multiple genes that are important for interneuronal communications, we examined

the expression of core clock genes. The rhythmicity of core clock genes, including *Per1*, *Cry1*, *Bmal1*, and *Clock*, was altered in *Nms-Ift88*$^{-/-}$ and *Nms-Smo*$^{-/-}$ mice (Fig. 5A). We then invesgated the rhythmic expression of neuropeptides that are known to mediate intercellular coupling. The rhythmicity of several neuropeptide genes, including *Vip*, gastrin-releasing peptide (*Grp*), *Avp*, and prokineticin 2 (*Prok2*), was altered in *Nms-Ift88*$^{-/-}$ and *Nms-Smo*$^{-/-}$ mice (Fig. 5B). As shown by our immunofluorescence assay, the protein concentrations of Vip and Grp were significantly decreased in *Nms-Ift88*$^{-/-}$ and *Nms-Smo*$^{-/-}$ SCN (Fig. 5, C and D). Thus, cilia depletion in SCN neurons leads to dampened oscillations of core clock genes and neuropeptides.

Discussion

The SCN drives coherent and synchronized circadian oscillations that are resistant to environmental perturbations, and this resistance relies on interneuronal coupling. Our findings establish primary cilia in NMS neurons and downstream Shh signaling as critical regulatory mechanisms that promote interneuronal coupling, thereby maintaining SCN network synchrony and circadian rhythms (Fig. 5E). The rhythmic cilia changes in the SCN lead to rhythmic oscillation of Shh signaling, which in turn drives rhythmic expression of core clock genes and neuropeptides. This feedforward loop sustains robust and coherent oscillation at the cell population level, making the intrinsic clock resistant to environment perturbations.

Primary cilia are hubs for ACIII-mediated ciliary cyclic adenosine 3′,5′-monophosphate (cAMP) production. Cytoplasmic cAMP signaling is implicated in the SCN pacemaking function (*42*). Although the ratio between the volumes of whole cell and cilia is 5000:1, we speculate that ciliary cAMP could still influence the behavior of the entire cell through signaling amplication during SCN clock regulation. It will be interesting to investigate whether ciliary cAMP could also be involved in cytoplasmic cAMP signaling during the SCN pacemaking function.

Epidemiological studies have linked frequent cross-time-zone travel and shift work to high blood pressure, obesity, and other metabolic disorders. Our results show that pharmacological blockade of the Shh pathway accelerates recovery from experimental jet lag in mice. Targeting Shh signaling might be a potential therapeutic strategy for the treatment of human diseases related to circadian disruptions.

REFERENCES AND NOTES

1. L. S. Mure *et al*., *Science* **359**, eaao0318 (2018).
2. M. H. Hastings, E. S. Maywood, M. Brancaccio, *Nat. Rev. Neurosci.* **19**, 453–469 (2018).
3. M. H. Hastings, E. S. Maywood, M. Brancaccio, *Biology* **8**, 13 (2019).
4. A. C. Liu *et al*., *Cell* **129**, 605–616 (2007).
5. J. A. Mohawk, C. B. Green, J. S. Takahashi, *Annu. Rev. Neurosci.* **35**, 445–462 (2012).
6. V. Acosta-Rodríguez *et al*., *Science* **376**, 1192–1202 (2022).
7. J. S. Takahashi, H. K. Hong, C. H. Ko, E. L. McDearmon, *Nat. Rev. Genet.* **9**, 764–775 (2008).
8. A. Sancar, R. N. Van Gelder, *Science* **371**, eabb0738 (2021).
9. A. Patke, M. W. Young, S. Axelrod, *Nat. Rev. Mol. Cell Biol.* **21**, 67–84 (2020).
10. P. Xu *et al*., *Neuron* **109**, 3268–3282.e6 (2021).
11. M. Brancaccio *et al*., *Science* **363**, 187–192 (2019).
12. J. S. Takahashi, *Nat. Rev. Genet.* **18**, 164–179 (2017).
13. N. Koike *et al*., *Science* **338**, 349–354 (2012).
14. E. L. Morris *et al*., *EMBO J.* **40**, e108614 (2021).
15. J. A. Mohawk, J. S. Takahashi, *Trends Neurosci.* **34**, 349–358 (2011).
16. T. Sonoda *et al*., *Science* **368**, 527–531 (2020).
17. E. D. Buhr, S. H. Yoo, J. S. Takahashi, *Science* **330**, 379–385 (2010).
18. S. J. Aton, J. E. Huettner, M. Straume, E. D. Herzog, *Proc. Natl. Acad. Sci. U.S.A.* **103**, 19188–19193 (2006).
19. A. J. Harmar *et al*., *Cell* **109**, 497–508 (2002).
20. Y. Yamaguchi *et al*., *Science* **342**, 85–90 (2013).
21. Y. Shan *et al*., *Neuron* **108**, 164–179.e7 (2020).
22. E. S. Maywood *et al*., *Curr. Biol.* **16**, 599–605 (2006).
23. M. J. Parsons *et al*., *Cell* **162**, 607–621 (2015).
24. R. Rohatgi, L. Milenkovic, M. P. Scott, *Science* **317**, 372–376 (2007).
25. K. I. Hilgendorf *et al*., *Cell* **179**, 1289–1305.e21 (2019).
26. F. Hildebrandt, T. Benzing, N. Katsanis, *N. Engl. J. Med.* **364**, 1533–1543 (2011).
27. S. H. Sheu *et al*., *Cell* **185**, 3390–3407.e18 (2022).
28. J. S. Sun *et al*., *J. Clin. Invest.* **131**, e138107 (2021).
29. S. C. Phua *et al*., *Cell* **168**, 264–279.e15 (2017).
30. M. K. Bunger *et al*., *Cell* **103**, 1009–1017 (2000).
31. S. Ray *et al*., *Science* **367**, 800–806 (2020).
32. I. T. Lee *et al*., *Neuron* **85**, 1086–1102 (2015).
33. A. Vertii, A. Bright, B. Delaval, H. Hehnly, S. Doxsey, *EMBO Rep.* **16**, 1275–1287 (2015).
34. G. J. Pazour *et al*., *J. Cell Biol.* **151**, 709–718 (2000).
35. J. A. Follit, R. A. Tuft, K. E. Fogarty, G. J. Pazour, *Mol. Biol. Cell* **17**, 3781–3792 (2006).
36. D. Kopinke, E. C. Roberson, J. F. Reiter, *Cell* **170**, 340–351.e12 (2017).
37. J. J. Kovacs *et al*., *Science* **320**, 1777–1781 (2008).
38. S. Y. Wong *et al*., *Nat. Med.* **15**, 1055–1061 (2009).
39. E. E. Zhang *et al*., *Cell* **139**, 199–210 (2009).
40. K. C. Corbit *et al*., *Nature* **437**, 1018–1021 (2005).
41. Q. Deng *et al*., *eLife* **8**, e50208 (2019).
42. J. S. O'Neill, E. S. Maywood, J. E. Chesham, J. S. Takahashi, M. H. Hastings, *Science* **320**, 949–953 (2008).

ACKNOWLEDGMENTS

We thank E. E. Zhang for the gift of *Bmal1*$^{-/-}$ mice and *Per2::Luciferase* transgenic reporter mice (Jackson Laboratory); B. Li for the gift of *Ptch1*$^{fl/fl}$ mice; M. Luo for technique support with intracerebroventricular injections; and the Center of Biomedical Analysis, Tsinghua University, for two-photon microscopy imaging. **Funding:** This work was funded by the National Natural Science Foundation of China (grant 81790252) and the National Key Research and Development Program (grants 2017YFC1601100, 2017YFC1601101, 2017YFC1601102, 2017YFC1601104, and 2022YFC2505001). **Author contributions:** H.Y.L. and X.M.Z. supervised the project. H.Q.T., S.L., and Y.L.X. built the experimental system and performed most of the experiments. Y.C.Z. conducted locomotor activity assays. P.Y.L., L.Y.L., and G.P.S. performed the animal genotyping experiments. X.X.J., M.W., Z.Q.S., and T.T.L. analyzed the data and amended the original draft of the manuscript. H.B.H., J.F.Y., X.L.S., J.N.L., Q.Y.H., K.W., and T.Z. provided reagents and suggestions. T.Z. and A.L.L. analyzed the statistics. H.Q.T., Y.L.X., S.L., H.Y.L., and X.M.Z. wrote the paper. All authors discussed the results and commented on the manuscript. **Competing interests:** H.Y.L., H.Q.T., T.Z., A.L.L., M.W., H.B.H., and X.M.Z. are inventors on a pending patent application that covers the role of cilia in circadian clocks. The remaining authors declare no competing interests. **Data and materials availability:** All data are available in the main text or the supplementary materials.

License information: Copyright © 2023 the authors, some rights reserved; exclusive licensee American Association for the Advancement of Science. No claim to original US government works. https://www.science.org/about/science-licenses-journal-article-reuse

SUPPLEMENTARY MATERIALS

science.org/doi/10.1126/science.abm1962
Materials and Methods
Figs. S1 to S14
Tables S1 and S2
References (*43*–*47*)
Movies S1 to S6
MDAR Reproducibility Checklist

View/request a protocol for this paper from *Bio-protocol*.

10.1126/science.abm1962

TECHNICAL COMMENT

POLICY FORUM

Technical Comment on "Policy impacts of statistical uncertainty and privacy"

Yifan Cui[1], Ruobin Gong[2]*, Jan Hannig[3], Kentaro Hoffman[4]

Steed *et al.* (*1*) illustrates the crucial impact that the quality of official statistical data products may exert on the accuracy, stability, and equity of policy decisions on which they are based. The authors remind us that data, however responsibly curated, can be fallible. With this comment, we underscore the importance of conducting principled quality assessment of official statistical data products. We observe that the quality assessment procedure employed by Steed *et al.* needs improvement, due to (i) the inadmissibility of the estimator used, and (ii) the inconsistent probability model it induces on the joint space of the estimator and the observed data. We discuss the design of alternative statistical methods to conduct principled quality assessments for official statistical data products, showcasing two simulation-based methods for admissible minimax shrinkage estimation via multilevel empirical Bayesian modeling. For policymakers and stakeholders to accurately gauge the context-specific usability of data, the assessment should take into account both uncertainty sources inherent to the data and the downstream use cases, such as policy decisions based on those data products.

We motivate the proposed assessment framework by considering Title I funding allocation by the U.S. Department of Education using the U.S. Census Bureau's Small Area Income and Poverty Estimates (SAIPE) dataset studied by Steed *et al.* (*1*). Let $\mu = (\mu_1, ..., \mu_k)$ be the true population counts for children under poverty in districts $i = 1, ..., k$, and $x = (x_1, ..., x_k)$ be the official SAIPE poverty estimates. Denote by $y : \mathbb{N}^k \to (\mathbb{R}^+)^k$ the entitlement function, that is, $y(x) = (y_1(x), ..., y_k(x))$ are the districts' official entitlements (in USD) based on x, and $y(\mu)$ the *true* entitlements were the true poverty population μ known. Finally, let $\mathcal{L}(\cdot;\cdot)$ be a loss function that measures the misallocation of funding between $y(x)$ and $y(\mu)$. The assessment estimates the average loss between the ideal and the realized allocations:

$$\mathbb{E}(\mathcal{L}(y(\mu); y(x))|x) \tag{1}$$

with expectation taken over what we denote as $p_c(\mu|x)$, the available distributional information about the true poverty counts μ given the observed estimate x and any auxiliary parameter c. The parameter c may encode known information about the variability in the observed estimates, such as their sampling or model-based variance. When $p_c(\mu|x)$ is given, Eq. 1 can be approximated via simulation:

$$\frac{1}{T}\sum_{t=1}^{T}\mathcal{L}\left(y\left(\mu^{(t)}\right)y(x)\right) \tag{2}$$

where $\mu^{(t)} \sim p_c(\mu|x)$ i.i.d. for some T large. This assessment is uncertainty- and policy-aware by the specifications of $p_c(\mu|x)$ and $\mathcal{L}$, respectively.

Typically, the loss function $\mathcal{L}$ is chosen by the assessor depending on the policy context, whereas $p_c(\mu|x)$ relies on information available to the assessor. Following Steed *et al.* (*1*), the available information are (i) the coefficients of variation upper bounds $c = (c_1, ..., c_k)$ suggested by the Census Bureau; and (ii) that x is approximately normally distributed around μ. That is,

$$x|\mu \sim N(\mu, \mathrm{diag}(v)) \tag{3}$$

where $v = (v_1, ..., v_k), v_i = (c_i x_i)^2$ are the sampling variances of x.

Steed *et al.* employ a simulation procedure [section 2 of the supplementary materials in (*1*)] that approximates Eq. 1 by using x as a plug-in estimate for μ, and producing replicates of x using Eq. 3 based on this plug-in estimate. Understood within our proposal, this procedure amounts to simulating $\mu^{(t)}$ replicates ($T = 1000$) under the following choice of $p_c(\mu|x)$:

$$\mu|x \sim N(x, \mathrm{diag}(v)) \tag{4}$$

This is not ideal for two reasons. First, each $\mu^{(t)}$ generated through (Eq. 4) is *inadmissible* for the true poverty count μ, a classic observation from Charles Stein (*2*, *3*). Second, Eq. 3 and Eq. 4 together do not admit a consistent joint probability distribution for (μ, x) (*4*), exposing the procedure to potential paradoxical conclusions [e.g., (*5*)].

How should the assessor construct $p_c(\mu|x)$? There is unlikely a unique "best" approach for all contexts, but reasonable starting points exist. Here, we discuss a class of distributions derived via multi-level empirical Bayesian modeling that accord to admissible and minimax shrinkage estimates for μ. The class follows the general form

$$\mu_i|x \overset{ind}{\sim} N((1-B_i)x_i + B_i\beta, (1-B_i)v_i), \quad i = 1, ..., k \tag{5}$$

where β and all $B_i \in [0, 1]$ are functions of x and the auxiliary c. The method is called *shrinkage* because compared to Eq. 4, it adjusts each poverty estimate μ_i based on the observed x_i to account for a common baseline β with a $100B_i\%$ variance reduction. This restores consistency on the joint specification of (μ, x) whenever $B_i \neq 0$.

Two possible constructions of Eq. 5 are (i) The Hudson-Berger (HB) construction (*6*, *7*), for which $\beta = 0$ and

$$B_i^{HB} = \min\left(1, \frac{(k-2)/v_i}{\sum_{j=1}^{k}/(x_j/v_j)^2}\right) \tag{6}$$

and (ii) the Morris-Lysy (ML) construction (*8*), for which $\beta = \bar{x}$,

$$B_i^{ML} = \frac{v_i}{v_i + \bar{v}_h(1-\hat{B})/\hat{B}} \tag{7}$$

where $\bar{v}_h = k/\left(\sum_{i=1}^{k} v_i^{-1}\right)$ is the harmonic mean of the v_i's, $\hat{B} = (k-3)/(k-4)\hat{\sigma}^2$, and $\hat{\sigma}^2 = (k-1)^{-1}\sum_{i=1}^{k}(x_i - \bar{x})^2/v_i$ is the mean square error in the observed poverty counts.

Both constructions cater to unequal sampling variances v_i. They differ in that Hudson-Berger exerts stronger shrinkage for larger v_i whereas Morris-Lysy for smaller v_i. Due to the heavy tail of the SAIPE poverty estimates x and increasing c_i for larger x_i, we apply the Morris-Lysy method on the observed poverty proportion x_i/n_i (rather than x_i), where n_i is the total population of district i in order to mitigate overly strong shrinkage effects.

We compare the proposed approaches with the evaluation of Steed *et al.* (*1*). The top panel of Fig. 1 compares the quantiles of the expected Hudson-Berger and Morris-Lysy poverty estimates with the SAIPE estimates. The bottom panel displays poverty estimate replicates generated through the constructions of Hudson-Berger, Morris-Lysy, and Eq. 2 for four districts with different population sizes (at 1, 5, 50, and 100% quantiles). For small counts, Hudson-Berger shrinks strongly resulting in nearly constant $\mu^{(t)}$ replicates, whereas its replicates are comparable to that of Steed *et al.* (*1*) for larger counts. On the other hand, the Morris-Lysy method exhibits a varying and moderate shrinkage effect at all count levels.

Table 1 displays the estimated lost entitlement based on the three approaches, with data error alone and with differential privacy

[1]Center for Data Science, Zhejiang University, China. [2]Dept of Statistics, Rutgers University, New Brunswick, NJ. [3]Dept of Statistics & Operations Research, University of North Carolina at Chapel Hill, Chapel Hill, NC. [4]Johns Hopkins Institute for NanoBioTechnology, Baltimore, MD.
*Corresponding author. Email: ruobin.gong@rutgers.edu

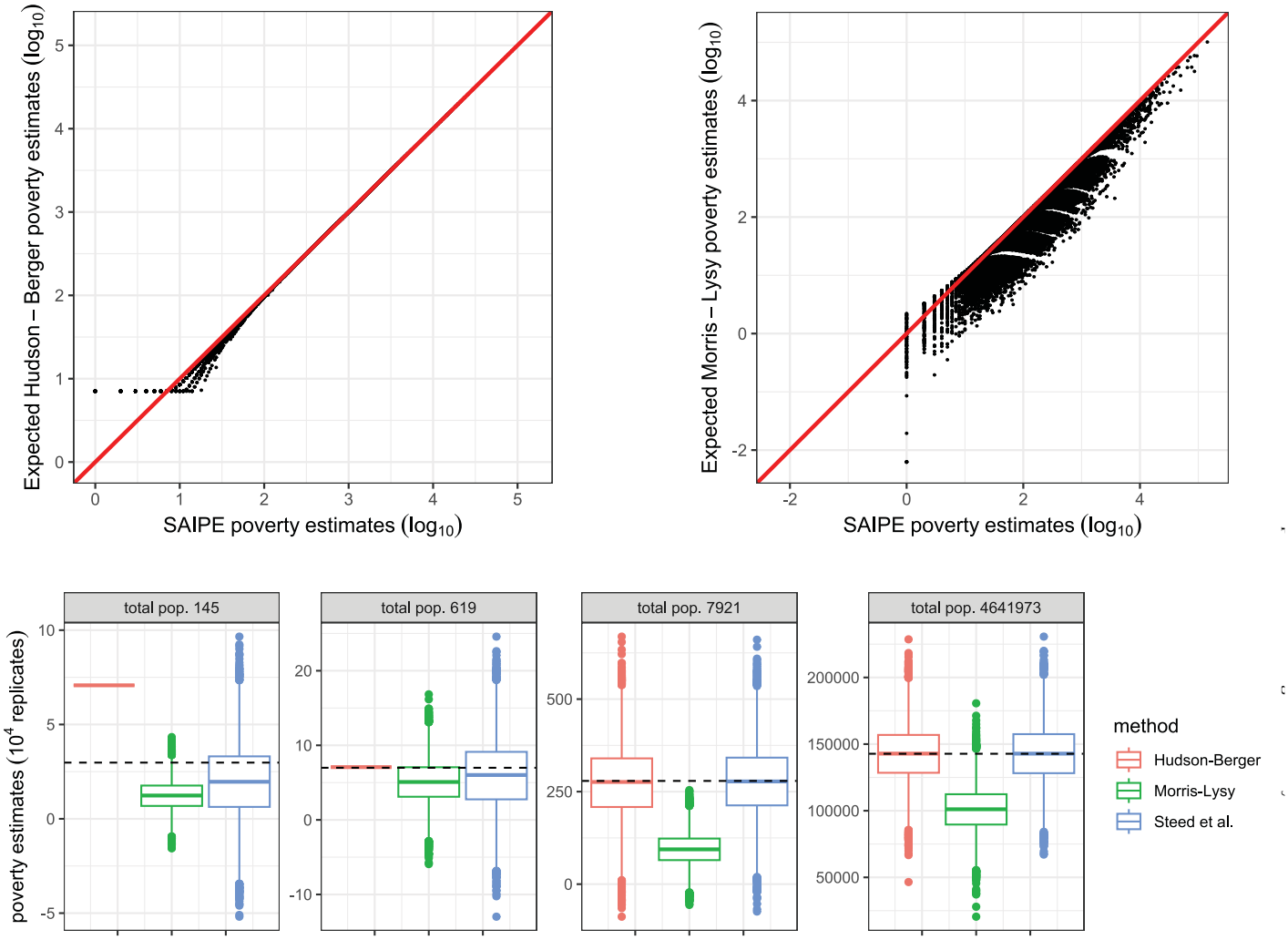


Fig. 1. (Top) quantile-quantile comparisons of expected Hudson-Berger (left) and Morris-Lysy (right) poverty estimates with SAIPE estimates ($\log_{10}$). (Bottom) Boxplots of 10^4 poverty estimate replicates from the Hudson-Berger, Morris-Lysy, and Steed *et al.* (*1*) constructions for four districts with total population sizes at 1, 5, 50, and 100% quantiles.

Table 1. Estimated lost entitlements (in USD, billions) due to data error (left) and due to data and privacy error (middle; $\epsilon = 0.1$) according to each assessment construction. Additional loss due to privacy (percent) is shown on the right.

	data error (s.e.)	data + privacy error (s.e.)	diff. (%)
Steed *et al.* (*1*)	1.058 (0.031)	1.109 (0.031)	4.756
Hudson-Berger	1.060 (0.032)	1.110 (0.033)	4.650
Morris-Lysy	2.385 (0.044)	2.429 (0.044)	1.840

protection ($\epsilon = 0.1$) applied to the observed SAIPE estimates first. These results are reproduced and/or implemented using the code provided by Steed *et al.* (*1*). The Hudson-Berger assessment agrees closely with the assessment by Steed *et al.* (*1*), putting the expected lost entitlement at $1.06 billion due to data error and an additional 4.65% due to privacy protection. The Morris-Lysy assessment estimates the lost entitlement at $2.385 billion due to data error, and an additional 1.84% due to privacy protection. The code we used to conduct these experiments relies in part on the public codebase that accompanies Steed *et al.* (*1*) and can be found at https://github.com/khoffm4/dp-policy-shrink.

The analysis by Steed *et al.* (*1*) is a timely companion to the rapid emergence of differential privacy as the new formal privacy standard for statistical disclosure limitation (SDL), anticipating possible adoption in complex survey programs at the Census Bureau (*9*, *10*) and at the IRS (*11*). The privacy revamp has been met with critical feedback from data users (*12*), who question the usability of differentially private data products after deliberate noise injection which instills distrust both in the data product and in the competence of the curator. The privacy innovation inadvertently ruptured, in the words of (*13*), a "statistical imaginary" that official statistics are somehow pristine. Steed *et al.* (*1*) point out that data users' distrust may be misplaced, as the impact of errors and uncertainty stemming from sampling, response, measurement, reporting, and editing may dominate that of errors from privacy. It exposes the need to examine, accurately and often, the extent to which every error source in an official statistical product affects policy decisions. The development of

quality assessment tools that are theoretically sound, substantively relevant, and practically deployable calls for quantitative research.

REFERENCES AND NOTES

1. R. Steed, T. Liu, Z. S. Wu, A. Acquisti, *Science* **377**, 928–931 (2022).
2. C. M. Stein, "Inadmissibility of the Usual Estimator for the Mean of a Multivariate Normal Distribution" in *Proceedings of the Third Berkeley Symposium on Mathematical Statistics and Probability, Volume 1: Contributions to the Theory of Statistics* (Univ. California Press, 1956), pp. 197–206.
3. The inadmissibility of $\mu^{(t)}$ generated through Eq. 4 means its estimation risk for μ based on the ℓ_2 loss can be uniformly dominated by an alternative and admissible estimate.
4. The inconsistency can be seen via a simple argument by the *law of iterated variances*. For each district i, the variance of the poverty estimate x_i may be written as a sum of two components,$\mathbb{V}(x_i) = \mathbb{E}(\mathbb{V}(x_i|\mu_i)) + \mathbb{V}(\mathbb{E}(x_i|\mu_i))$, where the first component is equal to v_i and the second is equal to $\mathbb{V}(\mu_i)$. Applying the same argument to $\mathbb{V}(\mu_i)$ we see that it is the sum of v_i and $\mathbb{V}(x_i)$. Since $\mathbb{V}(\mu_i)$, $\mathbb{V}(x_i)$, and v_i are all non-negative, both results can hold only when all v_i's are uniformly zero, leading to a contradiction.
5. A. P. Dawid, M. Stone, J. V. Zidek, *J. R. Stat. Soc. B* **35**, 189–213 (1973).
6. H. Hudson, Empirical Bayes estimation (technical report no. 58, Stanford Univ, 1974).
7. J. O. Berger, *Ann. Stat.* **4**, 223–226 (1976). http://www.jstor.org/stable/43590231.
8. C. N. Morris, M. Lysy, *Stat. Sci.* **27**, 115 (2012).
9. M. H. Freiman, R. A. Rodríguez, J. P. Reiter, A. Lauger, Formal Privacy and Synthetic Data for the American Community Survey (U.S. Census Bureau, 2018); https://www.census.gov/library/working-papers/2018/adrm/formal-privacy-synthetic-data-acs.html
10. A Roadmap for Disclosure Avoidance in the Survey of Income and Program Participation (SIPP) (National Academies of Sciences, Engineering, and Medicine, 2022); Https://www.nationalacademies.org/our-work/a-roadmap-for-disclosure-avoidance-in-the-survey-of-income-and-program-participation-sipp.
11. A. F. Barrientos, A. R. Williams, J. Snoke, C. M. Bowen, Differentially Private Methods for Validation Servers, (Urban Institute research report, 2021); https://www.urban.org/research/publication/differentially-private-methods-validation-servers.
12. V. J. Hotz, J. Salvo, A Chronicle of the Application of Differential Privacy to the 2020 Census. *HDSR* **2**, ff891fe5 (2022).
13. D. Boyd, J. Sarathy, *HDSR* **2**, 66882f0e (2022).

ACKNOWLEDGMENTS

The authors thank the authors of Steed *et al*. (*1*) for valuable comments and discussions. Y. C. was supported in part by the National Natural Science Foundation of China. J. H. was supported in part by the National Science Foundation under grant DMS-1916115, 2113404, and 2210337.

Submitted 25 November 2022; accepted 5 April 2023
10.1126/science.adf9724

TECHNICAL RESPONSE

POLICY FORUM

Response to comment on "Policy impacts of statistical uncertainty and privacy"

Ryan Steed[1]*, Alessandro Acquisti[1], Zhiwei Steven Wu[1], Terrance Liu[1]

We offer our thanks to the authors for their thoughtful comments. Cui, Gong, Hannig, and Hoffman propose a valuable improvement to our method of estimating lost entitlements due to data error. Because we don't have access to the unknown, "true" number of children in poverty, our paper simulates data error by drawing counterfactual estimates from a normal distribution around the official, published poverty estimates, which we use to calculate lost entitlements relative to the official allocation of funds. But, if we make the more realistic assumption that the published estimates are themselves normally distributed around the "true" number of children in poverty, Cui *et al.*'s proposed framework allows us to reliably estimate lost entitlements relative to the unknown, ideal allocation of funds—what districts would have received if we knew the "true" number of children in poverty.

Cui *et al.* show that when we measure losses relative to the ideal entitlements (rather than relative to fixed published estimates) with this assumption, the impacts of data error could be even larger. Using one possible approach under this framework (the Hudson-Berger construction), Cui *et al.*'s estimates of lost entitlements due to data error and privacy noise are very close to ours. Under another approach (Morris-Lysy), their estimate of lost entitlements due to data error nearly doubles, exceeding losses due to privacy noise by even more than we estimated.

We recommend Cui *et al.*'s framework to future studies of the effect of data quality on policy outcomes, and we look forward to future research in this area—in particular, guidance on which shrinkage constructions are most appropriate for a given evidence-based policy setting.

Submitted 17 February 2023; accepted 6 April 2023
10.1126/science.adh2297

[1]Carnegie Mellon University, 5000 Forbes Ave, Pittsburgh, PA 15213.
*Corresponding author. Email: ryansteed@cmu.edu

By **Greta Faccio**

One job wasn't enough

I sat at my desk wondering whether I would ever feel as engaged in and proud of my work as I had in academia. My job in the R&D division of a cosmetics company was coming easy to me and resulting in products on the shelves. But I thought constantly about what else I could do. I missed the feeling of risk and adventure that being a scientist at the edge of a discovery gives. I knew I didn't want to go back to academia, where I would have to hyperspecialize and study the same thing every day. But I couldn't picture myself in that industry job for years and years. It was time to get creative and find a different solution—or, as it turned out, a combination of them.

I had made the move to the private sector after 5 years as a postdoc, when I became disenchanted with the instability and lack of funding that is inherent in academia. I started my job search by reaching out to Ph.D.s in industry—people I'd worked with or found on social media. I asked about their career choices and what they liked and disliked about their jobs. Many told me they enjoyed the security that came with their long-term contracts, as well as their clearly defined job responsibilities. That sounded appealing.

Through one of those contacts, I landed a job identifying scientific evidence behind cosmetic ingredients and researching new technologies. The stability and great workplace atmosphere lifted my spirits. But the work was mostly literature searches and summaries, and after a while it didn't excite me anymore.

I thought back to what I loved about academia. I had always enjoyed that my days were varied, cycling through a range of activities: planning experiments, attending meetings, problem solving, lab work, discussing results, and other tasks. Research kept me on my toes and challenged me to devise creative solutions that could be communicated to a wider audience. I wasn't getting that with my position in industry.

I looked for other options in the private sector. But no one job offered the variety and chance to explore that I was missing. That's when I asked: Did I really have to choose just one? It might be time to experiment. So instead of pursuing a linear and conventional path, I decided to combine multiple jobs—all focusing on my passion for innovation, all with room for personal growth.

Part-time positions that offered what I was looking for were hard to find. But after casting a broad net and reaching out to companies that I thought might need support in their research and scientific communication, I met employers who were open to unconventional solutions. Through calls and lunches together, we identified interesting tasks that were too small to justify a full-time position.



"This work situation has given me the vibrant and varied workdays I was after."

I slowly built up my portfolio, eventually filling out my schedule with three part-time positions. I started by joining a global company as intellectual property manager, overseeing its patent and trademark portfolio—work that only requires a few mornings a week. Later, I added another role one to two mornings a week working as a patent scientist in a law firm that specializes in intellectual property. When I'm not doing those jobs, I'm an independent consultant for food and cosmetic startups, helping scout technology and communicate the scientific data behind their products.

This work situation has given me the vibrant and varied workdays I was after. My schedule is constantly changing and the series of projects I'm tasked to work on are always new, affording me opportunities to learn and grow. I may not be making new scientific discoveries. But I get to work on challenging and sometimes uncertain projects—especially when preparing patents—which gives me the rush of excitement I was looking for. The flexible schedule also gives me time to be a mum in the afternoons and the freedom to work remotely from a variety of locations, including from where my parents live in Italy.

It was risky for me to try to piece together a career from multiple part-time positions. But it has turned out to be more practical than I imagined—and as rewarding as I hoped. ■

Greta Faccio works in intellectual property and is based in St. Gallen, Switzerland. Send your career story to SciCareerEditor@aaas.org.